The Safety Pharmacology of Syk inhibitors: New preclinical screens to characterise cardiovascular adverse drug effects.

Marieke Van Daele
BSc, MSc, PharmD

A Thesis Submitted to the University of Nottingham for the Degree of Doctor of Philosophy

September 2023

I. Declaration

This thesis is entirely the candidate's work. The experiments described in this thesis were performed between September 2020 and September 2023 in the Cell Signalling research group at the Centre of Membrane Proteins and Receptors (COMPARE), University of Nottingham, UK. All *in vitro* experiments were completed solely by the author. All *in vivo* radiotelemetry work was performed as part of a secondment to Vivonics Ltd., by Marieke Van Daele (The Author: Experimenter) under supervision of Dr. Matt Skinner (Project Licence Holder and Surgeon) and Ed Hale (Surgeon and Experimenter). All *in vivo* Doppler flowmetry work was performed as part of a collaborative research team comprising of Marieke Van Daele (The Author: Experimenter and Surgical Assistant), Julie March (Surgeon and Senior Lab Technician), Prof. Jeanette Woolard (Principal Investigator, Project Licence Holder and Surgical Assistant) and Marleen Groenen (Surgical Assistant). All SPAR analysis was performed solely by the author, with collaborative discussions with Miquel Serna Pascual and Manasi Nandi (Nandi Lab, King's College London).

Additionally, to complete the scientific story of the thesis, one previously performed *in vivo* experiment has been included where a different researcher (Dr. Edward Wragg) completed the experiments before the authors' time in the lab. Express permission was obtained to present this experiment in this thesis and full credit was given to the experimenter in the appropriate Chapters' methodology section. No part of this material has been previously submitted for a degree or any other qualification at any university.

Funding: This work was funded by the European Union's H2020 Research & Innovation Program (GA 858070).

II. Abstract

Since the implementation of ICH S7A, the field of safety pharmacology has advanced radically. Current approaches for detection of cardiovascular (CV) adverse drug reactions (ADR), including evaluating mean arterial pressure (MAP) and heart rate (HR) often identify those safety risks. Nonetheless, high attrition rates due to safety issues remain an important challenge in drug development. Conventional analysis (MAP or HR) uses a minority of the recorded high-fidelity waveform data, overlooking a plethora of information. Potentially in-depth analysis of the CV waveform could provide early and mechanistically relevant markers to detect subtle CV ADR and aid in closing the current gaps in safety pharmacology. The Symmetric Projection Attractor Reconstruction (SPAR) is a novel in-depth wave analysis method that uses the entire waveform to generate an attractor which reflects and enlarges subtle changes in the wave. In this thesis, the application of SPAR on blood pressure and blood flow waves in CV safety pharmacology was explored. To perform this investigation, two tyrosine kinase inhibitors were selected and presented as an example of compounds with varying CV safety liabilities: (1) fostamatinib that targets Syk but is associated with the onset of hypertension due to off-target inhibition of Vascular Endothelial Growth Factor Receptor 2 (VEGFR2) and (2) entospletinib, a second-generation compound designed to not bind VEGFR2 and to achieve Syk inhibition without the onset of cardiovascular safety liabilities.

First, the cardiovascular effects of these two Syk inhibitors were assessed using radiotelemetry in rats, as is currently the golden standard for MAP and HR assessments in *in vivo* preclinical safety studies. This study showed that fostamatinib indeed caused a significant increase in MAP, while not affecting HR or pulse pressure (PP). Entospletinib did not affect MAP, HR or PP significantly.

Second, the blood pressure waveform data obtained in the radiotelemetry studies were analysed in-depth using SPAR. This analysis yielded insights that were not obtained from the conventional wave analysis. Firstly, SPAR metrics detected fostamatinib-induced CV effects within 8 h after fostamatinib administration, while MAP only changed significantly from the second day of the study. The changes in SPAR metrics indicated a fostamatinib-induced vasoconstriction, consistent with the anticipated mechanism of BP elevation. In addition,

entospletinib changed the SPAR metrics in a similar way as fostamatinib, suggesting that this second-generation compound might display subtle effects on the cardiovascular system that were not apparent from MAP, HR or PP.

Third, the two Syk inhibitors were assessed in the Doppler flowmetry model to interrogate their effect on the regional vascular conductances (VC) of the renal, mesenteric or hindquarters bed in rats. Subsequently, obtained blood flow waves were analysed using SPAR. Fostamatinib induced a decrease in renal and hindquarters VC, partially reflecting VC changes that are typically observed with VEGFR2-inhibitors. SPAR analysis indicated that fostamatinib caused a vasoconstriction in the mesenteric vascular bed, again reflecting effects typically observed with VEGFR2-inhibitors. Although entospletinib did not affect the renal, mesenteric or hindquarters VC in the conventional analysis, in the SPAR analysis this compound showed similar flow wave morphology changes to those observed with sunitinib, a known VEGFR2-inhibitor. These results indicated that entospletinib caused small changes in the compliance of blood vessels and may be associated with subtle CV effects.

Lastly, the effects of fostamatinib and entospletinib at VEGFR2 were evaluated *in vitro*. An intracellular nanoBRET assay in HEK293 cells was developed and employed to determine the compounds' direct binding affinities to the intracellular site of VEGFR2. Furthermore, an nuclear factor of activated T-cells (NFAT) reporter gene assay in HEK293 cells was performed to determine the compounds' effect on the downstream signalling of VEGFR2. These studies showed that fostamatinib bound to the receptor and inhibited its downstream signalling. Entospletinib did not directly bind to VEGFR2. Yet the latter inhibited both $VEGF_{165}$a- and ionomycin-induced NFAT signalling and did so with an approximately 100x higher potency than fostamatinib indicating entospletinib exerted off-target effects beyond its Syk inhibition.

In conclusion, results from this thesis showed that SPAR is a valuable method for detection of subtle cardiovascular side effects. For fostamatinib, SPAR detected CV ADR earlier than MAP, HR or PP could. Additionally, SPAR exposed entospletinib-induced CV effects that were consistent with an *in vitro* inhibition of the VEGFR2 signalling that might be relevant to its safety, in particular since this compound is in development in combination therapy with certain chemotherapeutics that have been associated with CV safety issues.

III. Publications

Research papers

Van Daele M, Kilpatrick LE, Woolard J, Hill SJ. Characterisation of tyrosine kinase inhibitor-receptor interactions at VEGFR2 using sunitinib-red and nanoBRET. Biochem Pharmacol. 2023;214(July):115672.

Review Articles

Van Daele M, Cooper SL, Pannucci P, Wragg ES, March J, de Jong I, et al. Monitoring haemodynamic changes in rodent models to better inform safety pharmacology: Novel insights from in vivo studies and waveform analysis. JRSM Cardiovasc Dis. 2022;11.

Conference proceedings

Van Daele M, Hill SJ, Woolard J. New preclinical screens in safety pharmacology: Haemodynamic assessment of VEGFR-2 inhibition. Oral presentation at COMPARE's 2021 Annual Symposium (2021, online event)

Van Daele M, Serna Pascual M, Nandi M, Skinner M, Woolard J. Exploring Waveform Analysis of Radiotelemetric Data to Improve Cardiovascular Safety Pharmacology using SPAR. Poster presentation at Joint Midlands 3Rs Symposium (2022, Nottingham, UK)

Van Daele M, Hill SJ, Woolard J. Waveform analysis of *in vivo* haemodynamic data to better inform safety pharmacology. Oral presentation at COMPARE Early Career Researcher Symposium (2022, Nottingham, UK)

Van Daele M, Hill SJ, Woolard J. Characterisation of kinase inhibitor-receptor interactions at VEGFR2 using sunitinib-red and nanoBRET. Poster presentation at SoLS UoN PGR Symposium (2022, Nottingham, UK)

Van Daele M, Serna Pascual M, Nandi M, Skinner M, Hill SJ, Woolard J. Exploring Waveform Analysis of Radiotelemetric Data to Improve Cardiovascular Safety Pharmacology using SPAR. Poster presentation and rapid-fire oral presentation at Safety Pharmacology Society Annual Meeting (2022, Montreal, Canada)

Van Daele M, Kilpatrick LE, Woolard J, Hill SJ. Characterisation of kinase inhibitor-receptor interactions at Vascular Endothelial Growth Factor Receptor 2 (VEGFR2) using sunitinib-red and nanoBRET. Oral presentation at SoLS UoN PGR Symposium (2023, Nottingham, UK)

Van Daele M, Kilpatrick LE, Woolard J, Hill SJ. Characterisation of kinase inhibitor-receptor interactions at Vascular Endothelial Growth Factor Receptor 2 (VEGFR2) using sunitinib-red and nanoBRET. Oral communication at World Congress of Basic & Clinical Pharmacology (2023, Glasgow, UK).

Van Daele M, Kilpatrick LE, Woolard J, Hill SJ. Characterisation of kinase inhibitor-receptor interactions at Vascular Endothelial Growth Factor Receptor 2 (VEGFR2) using sunitinib-red and nanoBRET. Poster presentation at COMPARE Annual Symposium (2023, Birmingham, UK)

Van Daele M, Serna Pascual M, Virk G, Skinner M, Nandi M, Hill SJ, Woolard J. Using SPAR to Analyse Arterial Blood Pressure Waves, Following Fostamatinib and Entospletinib Administration in Radiotelemetry in Rats, to Aid in Cardiovascular Safety Testing. Poster presentation at Safety Pharmacology Society Annual Meeting (2023, Brussels, Belgium)

IV. Acknowledgements

First of all, a massive thank you to my supervisors, Prof. Stephen J. Hill and Prof. Jeanette Woolard, who together made a wonderful supervisory team for me! Thank you to Jeanette for pushing me just far enough out of my comfort zone, so I was challenged to grow and develop myself. Thank you to Steve, for always keeping a close eye on the quality of my research and asking me 'what my data mean'. Your supervision has been a great guidance and example for me as a scientist and team member! This PhD project was realised thanks to many collaborations. First of all, thank you to Dr. Matt Skinner and Ed Hale, for hosting me for a 3-month placement at Vivonics Ltd and showing me the ropes of a small CRO. Thank you to Dr. Manasi Nandi, Miquel Serna Pascual and the team at King's College, for all their support and engaging discussions and for always being available to answer my many many SPAR-related questions. Thank you to Dr. Amy Pointon, Dr. Caroline Archer and their team at AstraZeneca, for hosting me for a short placement. Thank you to Prof. Pieter-Jan Guns, Paz Yanez and my fellow INSPIRE ESRs for creating a collaborative environment and for amazing times during the summer schools.

Thank you to Marleen Groenen, for endless support in CS8 and on F-floor, and most of all for being 'helden op sokken' with me in the lab. Your enthusiasm and ability to see the humour in everything made a world of difference for me! Thank you to Julie March, for passing on many years of experiences and all your hard work to keep the lab on F-floor running. Also, a big thank you to Marleen, Julie and Dr. Edward Wragg for your invaluable help with the data-preparation! Thanks to (at the time) PostDocs from the COMPARE lab, Dr. Laura Kilpatrick, Dr. Sam Cooper and Dr. Mark Soave for showing me around in the *in vitro* lab and for helpful discussions when setting up my nanoBRET assay.

To everyone in Cell Signalling, thank you for welcoming me into this amazing group. Thanks to Dehan, for sending me your podcasts and songs from time to time and making this crazy adventure even more crazy than it already was. I'm honestly so glad you were here to experience this rollercoaster (PhD and outside of the PhD) with me. Thanks to Noémi, for being there since day one, texting me on my very first day out of quarantining, and equally for being there on the very last day, helping me pack/sell all my stuff. To Hannah, for non-

stop interrupting my workflow and discussing everything there is possibly to discuss about our seasons, you made everything easier. Thank you for all the 'fat Tuesdays' (or fat any weekdays), which brings me seamlessly to Clare and Kelvin, thanks for making the best office mates, always ready to be distracted or to be a distraction, and to give me advice on whether it should be 'could, would or will'. Thanks Kelvin for being my RTK partner in crime in a world full of GPCRs!! Special mention goes to Gurleen, thanks for joining me in my SPAR journey and spending a chaotic summer with me in the lab. I'm left to thank many more people, that all make this lab the amazing group it is, James, Nikki, Simon, Julie S., Lydia, Patrizia, George C., Cemre, Natasha, and people that already left. You made Nottingham a home for me in the last 3 years.

Thank you to the members of 'my' Team Science Committee, Tamara, Aqfan, Jonas, Mae, James, Kelvin, Hannah, your enthusiasm was without limits and working with you was truly a pleasure and gave me so many chances to grow professionally.

Thank you to my parents, Lieve and Hans, siblings, Johanna, Hadewijch and Pieterjan, and my closest friends from Bruges and Antwerp, you might not directly have contributed to this work, but your calls and visits to the UK were invaluable! Last but certainly not least, thank you Tommaso, for being a steady rock in the storm that the last two years were, for endless patience and endless support. Sei il tulipano più bello!

V. Acronyms and abbreviations

2D	Two-dimensional
3D	Three-dimensional
ADR	Adverse drug effect
AIx	Augmentation index
AUC	Area Under the Curve
BF	Blood flow
BP	Blood pressure
BRET	Bioluminescence resonance energy transfer
BSA	Bovine serum albumin
CCB	Calcium channel blockers
CV	Cardiovascular
CVD	Cardiovascular disease
DBP	Diastolic blood pressure
DMEM	Dulbecco's Modified Eagle's Medium
DMSO	Dimethylsulfoxide
E. coli	*Escherichia coli*
EC	Endothelial cell
ECG	Electrocardiogram
ECM	Extracellular matrix
EDTA	Ethylenediaminetetraacetic acid
eNOS	Endothelial NO synthase
ESR	Early Stage Researcher
ET-1	Endothelin-1
FCS	Fetal calf serum
FGF	Fibroblast Growth Factor
GABA	γ-aminobutyric acid
HBSS	HEPES Buffered Salt Solution
HEK	Human Embryonic Kidney
hERG	Ether-a-go-go-Related gene
HR	Heart rate
HRV	Heart rate variability
ICH	International Conference on Harmonization
INSPIRE	INnovation in Safety Pharmacology for Integrated cardiovascular safety assessment to REduce adverse events and late stage drug attrition
IP	Intraperitoneal
ITAM	Immunoreceptor tyrosine-based activation motifs
ITP	Immune thrombocytopenia
IV	Intraveneous
LB	Luria broth
LPS	Lipopolysaccharide
MAP	Mean arterial pressure

NACWO	Named Animal Care and Welfare Officer
NFAT	Nuclear factor of activated T-cells
NL	NanoLuciferase
NP	Neuropilins
NSAID	Non-steroidal anti-inflammatory drug
PBS	Phosphate buffered saline
PDE-5	Phosphodiesterase 5
PDGF	Platelet Derived Growth Factor
PGI_2	Prostacyclin
PlGF	Placental growth factor
PP	Pulse pressure
PPA	Pulse pressure amplification
PWS	Pulse wave separation
RA	Rheumatoid arthritis
RCT	Randomized controlled trials
ReLuc	Renilla Luciferase
ROC	Receiver Operating Characteristic
RTK	Receptor tyrosine kinases
RTKI	Receptor tyrosine kinase inhibitor
SBP	Systolic blood pressure
SC	Subcutaneaous
SEM	Standard error of the mean
SH2	SRC homology 2
SHR	Spontaneously hypertensive rats
SP	Safety Pharmacology
SPAR	Symmetrical Projection Attractor Reconstruction
Syk	Spleen tyrosine kinase
T_i	Inflection point
TKI	Tyrosine kinase inhibitor
τ_w	Wave transit time
VC	Vascular conductance
VEGF	Vascular endothelial growth factor
VEGFR	Vascular endothelial growth factor receptor
VPF	Vascular Permeability Factor
WIS	Wave intensity analysis
WKY	Wistar-Kyoto

VI. Table of Contents

1. CHAPTER 1: GENERAL INTRODUCTION

1.1. Project introduction

This PhD project was part of the broader INSPIRE Marie Skłodowska-Curie European Training Network (ITN) programme. INSPIRE (INnovation in Safety Pharmacology for Integrated cardiovascular safety assessment to REduce adverse events and late stage drug attrition) is funded by the European Commission's H2020-MSCA-ITN programme and aims to make important contributions to the field of cardiovascular (CV) safety pharmacology (SP) (Guns et al., 2020). INSPIRE recruited 15 Early Stage Researchers (ESRs) with different training backgrounds, spanning disciples including pharmacology, physiology, biology and physics. Each ESR conducted an individual PhD project in safety pharmacology for a minimum period of 36 months. Furthermore, INSPIRE consisted of 10 beneficiaries, hosting the ESRs, and 9 partner organizations, providing training support. This multidisciplinary and international network promoted research on CV safety liabilities and fostered the training of the future generation of drug safety scientist (Guns et al., 2020).

This PhD project was conducted at the University of Nottingham under the supervision of Prof. J. Woolard and Prof. S. Hill. In their laboratories, the CV safety profile of Spleen Tyrosine Kinase (Syk) inhibitors and other multi-kinase inhibitors was evaluated, using both *in vivo* models (Doppler flowmetry and radiotelemetry in rats) and *in vitro* NanoBRET approaches. These kinase inhibitors were studied here to explore novel methods for sensitive detection of subtle cardiovascular adverse effects, as they are a prime example of compounds that failed late in drug development due to, amongst others, off-target safety issues. Under the supervision of Dr. M. Skinner, a secondment of 3 months was undertaken at Vivonics Preclinical Ltd to conduct an *in vivo* telemetry study, assessing effects of these drugs on CV safety in freely moving rats. The generated *in vivo* data were analysed using the innovative Symmetrical Projection Attractor Reconstruction (SPAR), to explore new biomarkers that could aid safety assessment of drug candidates; this SPAR work was undertaken in collaboration with the group of Dr. M. Nandi from Kings College, London.

1.2. Cardiovascular safety pharmacology

When developing a new chemical entity, three drug properties are required: sufficient primary target efficacy, a satisfactory pharmacokinetic profile and a suitable safety profile (i.e., it should not cause harm in patients) (Kenakin, 2014). To meet this last requirement, the assessment of potential adverse drug reactions (ADR) is crucial during drug development. Safety pharmacology is the branch of pharmacology that identifies and investigates those undesirable effects of a new chemical entity. Techniques used in this field range from *in vitro* cellular assays (e.g. receptor binding assays) and *ex vivo* studies (e.g. testing of vasoactive compounds in isolated pressurised vessels), to the use of rodents, dogs or primates in preclinical studies to provide translational *in vivo* pharmacological safety information on the drug candidate (International Conference on Harmonisation, 2001, 2005; Sager et al., 2013).

1.2.1. Introduction to cardiovascular safety pharmacology

CV adverse drug reactions comprise haematological toxicities and toxicity on the heart and vessels (Weaver & Valentin, 2019b). They can occur with drugs directly acting the CV system or by indirect effects, e.g., through modulation on the renal or nervous systems. Acute CV toxicity as well as CV ADR manifesting after chronic treatment may be observed (Laverty et al., 2011).

Currently, CV safety assessment is conducted as described in the guidelines of the International Conference on Harmonization (ICH) S7A (International Conference on Harmonisation, 2001) and S7B (International Conference on Harmonisation, 2005). These guidelines contain a core set of routine screenings and supplemental follow-up assays to address any compound-specific concerns arising during the different stages of drug development (International Conference on Harmonisation, 2001). For CV safety testing, ICH S7A and S7B describe among others: electrocardiogram (ECG) evaluation, testing for inhibitory effects on the human Ether-a-go-go-Related gene (hERG) and changes in heart rate (HR) and blood pressure (BP) (International Conference on Harmonisation, 2001, 2005). Through these screening approaches, safety liabilities are identified and can be managed (Weaver & Valentin, 2019b).

One area in CV safety pharmacology that is extensively studied, focuses on changes in the rhythm of the heart and its electrical activity (T. A. Collins et al., 2020). hERG is a potassium ion channel expressed on cardiomyocytes, that mediates ventricular repolarization by decreasing intracellular potassium levels upon activation and is therefore a crucial ion channel for heart rhythm control (Frommeyer & Eckardt, 2016; Vicente et al., 2018). Drugs that inhibit this channel can prolong the QT interval of the ventricular repolarisation in the ECG, increasing the risk of catastrophic ventricular arrhythmias (Frommeyer & Eckardt, 2016; Robertson & Morais-Cabral, 2020). There is a clear understanding of how the structure of a drug candidate is related to its activity on hERG and to proarrhythmic properties (T. A. Collins et al., 2020; Vicente et al., 2018). This enabled early attrition of drug candidates with a questionable effect on heart rhythm and, in the last decade, lead to a decrease in marketing of drugs with proarrhythmic safety issues (T. A. Collins et al., 2020; Weaver & Valentin, 2019a). This has been implemented in the CiPA (Comprehensive *in vitro* Proarrhythmia Assay) initiative. This initiative proposed the combination of *in silico* assays, *in vitro* screening in human stem cell-derived cardiomyocytes and early Phase I trial ECG readings to predict the proarrhythmic properties of a new compound in a comprehensive manner (Vicente et al., 2018; Yim, 2018).

In the meantime however, there are CV parameters that have been somewhat overlooked, such as BP, HR and contractility of the heart (T. A. Collins et al., 2020). These parameters are routinely assessed during drug development by taking single point averages of the blood pressure signal over time, resulting in parameters such as the diastolic pressure (DBP), systolic pressure (SBP) and mean arterial pressure (MAP) (Mynard et al., 2020; Segers et al., 2017). Yet the blood pressure is a periodic signal that displays cyclical waves following each heartbeat (discussed in more detail in section 1.5) and contains a lot more information than reported by these simplified parameters. Although MAP is an important parameter, providing an indication for normo-, hypo- or hypertension, the morphology of these high-fidelity BP signals is overlooked (Mynard et al., 2020). If evaluated in more depth, these wave signals could provide additional cues for safety liabilities, by elucidating subtle effects of compounds on the heart and vasculature, and therefore enhance the efficiency of safety assessment (T. A. Collins et al., 2020). Details on wave morphology analysis are introduced in section 1.5.

1.2.2. Current gaps in cardiovascular safety pharmacology

High attrition rates due to safety issues remain an important challenge in industry (Laverty et al., 2011; Waring et al., 2015). Analysing 800 compounds in drug development between 2000 and 2010, Waring *et al.* (2015) showed that toxicology issues are the most important cause for drug attrition in the preclinical stage. Furthermore, in Phase I and Phase II studies, clinical safety liabilities were found to be respectively the primary and secondary reason for termination of the development of the drug (Waring et al., 2015). In 2014, Cook *et al.* found similar results when reviewing AstraZeneca's small molecule drug development projects from 2005 to 2010; safety issues were the main cause of discontinuation of the drug development in both preclinical and clinical studies (Cook et al., 2014). In preclinical settings, CV toxicity was accountable for 17% of the failure and therefore the most common cause of drug attrition (Figure 1). During the clinical phase, safety issues linked to the central nervous system were the major cause of attrition (34%), followed by CV safety liabilities (24%) (Cook et al., 2014) (Figure 1).

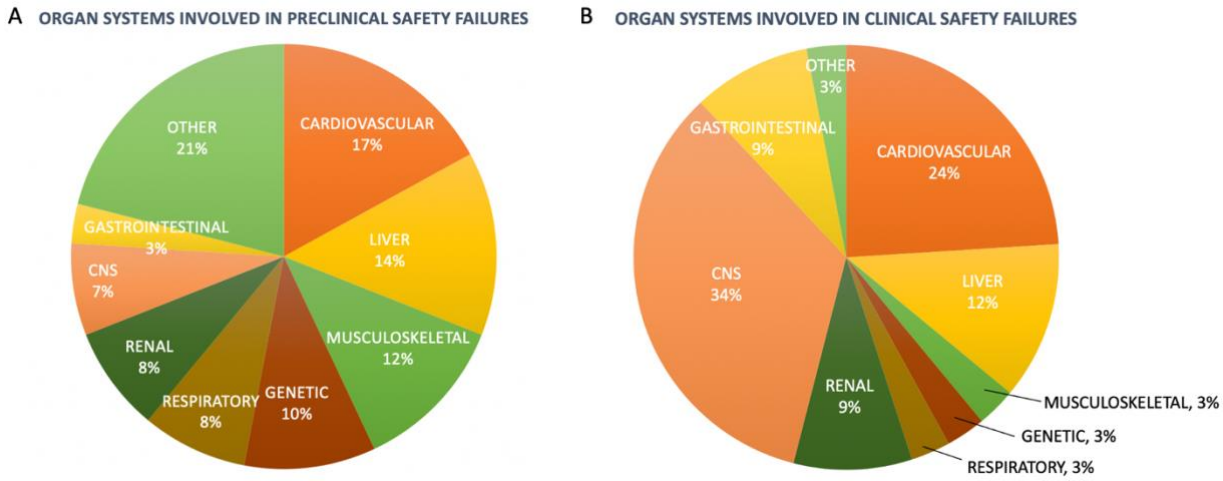

Figure 1: Organ systems involved in project closure due to safety issues in preclinical studies (A) and clinical studies (B). *Toxicity to the cardiovascular system remains a prominent contributor in both preclinical and clinical study closures. Charts based on data from Cook et al., reviewing AstraZeneca's small molecule projects from 2005 – 2010.* (Cook et al., 2014)

In post marketing surveillance, safety continue to be a significant issue. Qureshi *et al.* identified the main reasons for market withdrawal by analysing all FDA approved new chemical entities between 1980 and 2009 (Qureshi et al., 2011). Of all withdrawals, 22% were due to safety issues, with severe CV effects being one of the four major causes (Qureshi et al., 2011).

These data support the suggestion that there are current gaps in understanding of CV safety liabilities. Even though a reasonable number of cardiovascular safety liabilities are detected during preclinical testing, it remains one of the major organ systems involved in safety issues causing closure of clinical studies or post-marketing withdrawal (Cook et al., 2014; Qureshi et al., 2011). The current strategy of detecting CV safety liabilities as described in S7A is a quite effective approach to detect and assess acute high-risk CV toxicities in preclinical development and has obtained its goal of bringing safer medicines to clinical trials (Valentin & Leishman, 2023). However, more subtle and long term changes in CV parameters, such as small increases in MAP and associated long-term risks of CV events (Lewington et al., 2002; Sager et al., 2013) are not consistently addressed (Laverty et al., 2011). During preclinical development, these subtle changes can be overlooked or considered not clinically relevant, delaying the attrition of a drug candidate to later stages and therefore decreasing the productivity of R&D projects (Cook et al., 2014; Laverty et al., 2011). There is need for more robust and holistic safety characterization in the first stages of drug development, enabling earlier attrition of drug candidates with poor safety profiles (Bhatt et al., 2019; Morgan et al., 2018). Additionally, for a considerable number of adverse drug reactions, a full mechanistic understanding is lacking (Morgan et al., 2018; Weaver & Valentin, 2019b). Lastly, CV safety pharmacology would be reinforced if the quality of translation of *in silico*, *in vitro* and *in vivo* data to effects in man were improved (Morgan et al., 2018; Weaver & Valentin, 2019b). In summary, a more complete insight into the cause of CV toxicity could enhance our ability to identify safety liabilities early in drug development and to extrapolate preclinical data into clinical settings, potentially improving patient safety (Weaver & Valentin, 2019a).

1.2.2.1. Assessment of the blood pressure signal

The assessment of BP signals is an example of one interrogation that could be improved. During the early stage of drug discovery and development, there is routinely screening for *in vitro* effects on receptors involved in vasoconstriction and vasodilatation. Additionally, drug candidates may be tested in isolated vessels for effects on vascular resistance, and BP changes assessed in telemetered rats (International Conference on Harmonisation, 2001). This testing strategy detects acute and large changes in MAP, for example a 10 mmHg increase in MAP, a clinically meaningful event, and shows the direction for the first in man safety studies (Laverty et al., 2011). Nonetheless, due to the multiple complex mechanisms involved in regulation of the CV system, there is often a lack in understanding of the exact mechanism underlying these BP alterations (Laverty et al., 2011). In addition, the question remains concerning whether the current available assays are sensitive enough to detect small changes in BP that, when present for a long term, might lead to high risk CV outcomes (e.g. late failure of valdecoxib (Atukorala & Hunter, 2013) or torcetrapib (Joy & Hegele, 2008) due to CV ADR). Although BP is generally seen as a biomarker that is qualitatively translatable to clinical studies, quantitative prediction of long-term CV risk in patients is still a challenge (Bhatt et al., 2019; Budnitz et al., 2006; Stevens & Baker, 2009). As a sustained rise in BP increases stress on the heart and vessels, uncontrolled hypertension is a risk factor for several serious CV implications such as heart failure, intracerebral haemorrhage, coronary heart disease and chronic kidney disease (Fuchs & Whelton, 2020; Messerli et al., 2017) and it is important to identify these changes in BP early. CV complications such as heart failure and myocardial ischaemia may only be detected post-approval, indicating the failure of current R&D studies to note these liabilities during preclinical and clinical development (Atukorala & Hunter, 2013; Joy & Hegele, 2008; Weaver & Valentin, 2019a).

In summary, it is clear that drug-induced CV toxicity is a prominent issue in the field of safety pharmacology. These safety liabilities affect both the productivity of the pharmaceutical industry and, at least as important, the safety of patients treated with these drugs (Laverty et al., 2011). More sensitive systems to detect subtle changes in BP in preclinical settings, and to translate BP changes into long term risk in humans would improve our capability in safety testing (Laverty et al., 2011). The challenges that need to be addressed are (1) more detailed characterization of the current prevalence of CV ADR (2) understanding the mechanism of their origin and (3) verifying the reliability of preclinical CV biomarkers in clinical settings (Laverty et al., 2011; Weaver & Valentin, 2019b).

The spleen-associated tyrosine kinase (Syk) inhibitor fostamatinib is an example of a compound that causes off-target cardiovascular toxicity and was therefore, in combination with lack of efficacy reasons, withdrawn from clinical studies (AstraZeneca, 2013; Genovese et al., 2014; Taylor et al., 2015). To overcome these safety issues, a second generation of Syk inhibitors was developed, including entospletinib, differing from fostamatinib in their selectivity profile (Currie et al., 2014). In this thesis, the cardiovascular safety profile of these two Syk inhibitors is characterised and used as an example to explore novel approaches in cardiovascular safety pharmacology. Below, Syk is introduced in detail, followed by an overview of the clinical indications of the Syk inhibitors and their cardiovascular safety profile.

1.3. Syk inhibitors

1.3.1. Syk, linker molecule in immune cells

Spleen-associated tyrosine kinase (Syk) is a 72 kDa cytosolic tyrosine kinase mainly expressed in haematopoietic cells, including B-cells, macrophages and platelets, and plays a crucial role in the antibody-mediated adaptive immune response (Cooper et al., 2022; Kiefer et al., 1998; Mócsai et al., 2010). This tyrosine kinase serves as a regulatory linker molecule, coupling activated immunoreceptors to downstream signalling pathways (D. Liu & Mamorska-Dyga, 2017; J. Sharman et al., 2015; Westbroek & Geahlen, 2017). Additionally, Syk is found in non-haematopoietic cells (e.g. osteoclasts) and mediates other physiological functions, such as osteoclast maturation and vascular development (Inatome et al., 2001; Mócsai et al., 2010; Singh et al., 2012; L. Wang et al., 2021).

1.3.2. Intracellular signalling pathways of Syk

The N-terminus of Syk contains two SRC homology 2 (SH2) domains (linked by interdomain A) and a C-terminal kinase domain (linked to the second SH2 domain by interdomain B) (Figure 2) (Arias-Palomo et al., 2007; Turner et al., 2000; Wang L, Devarajan E, He J, Reddy SP, 2005). The SH2 domains bind phosphorylated tyrosine residues and, via intramolecular bindings to the kinase domain, maintain Syk in an inactive state in resting immune cells (Arias-Palomo et al., 2007; Grädler et al., 2013; Singh et al., 2012).

When B-cell receptors, Fc receptors or C-lectin receptors bind to their ligand, they associate with transmembrane proteins containing cytoplasmic immunoreceptor tyrosine-based activation motifs (ITAM) (Braselmann et al., 2006; Cambier, 1995; Reth & Alarcon B Wileman, 1989). This interaction leads to rapid phosphorylation of two tyrosine residues of the ITAM, regulated by tyrosine kinase of the SCR family (Geahlen, 2014; Johnson et al., 1995; Mkaddem et al., 2017; Quek et al., 2000). The dual phosphorylated ITAM recruits Syk through interaction with its two SH2 domains (Abram & Lowell, 2007; Johnson et al., 1995) (Figure 2). Furthermore, some proteins containing only one ITAM sequence (i.e. Hemi-ITAM) can provide a Syk interaction site by dimerizing (e.g. CLEC2 (Bauer & Steinle, 2017; C. E. Hughes et al., 2010) or dectin-1 (Tidu et al., 2021).

Additionally, several tyrosine residues in the linker and kinase domains of Syk are phosphorylated, by Lyn or through autophosphorylation. Together, this leads to disruption of the auto-inhibiting linker-kinase interactions, exposes of the ATP-pocket and provides docking site for the downstream signalling proteins (Johnson et al., 1995; Sada et al., 2001; Tsang et al., 2008). As a result, the kinase domain is activated and released for substrate interaction (De Castro et al., 2010; Johnson et al., 1995; Tsang et al., 2008). The activated kinase domain phosphorylates tyrosine residues in molecules essential in signalling transmission. Downstream signalling pathways include MAPK signalling pathway and NF-κB (De Castro et al., 2010; Takada & Aggarwal, 2004), NFAT (Bendickova et al., 2017; Tidu et al., 2021) and PI3K/Akt (L. Chen et al., 2013; Hatton et al., 2012). In this way, Syk is a central player in the activation of immune cells (Braselmann et al., 2006; Currie et al., 2014; Mócsai et al., 2010).

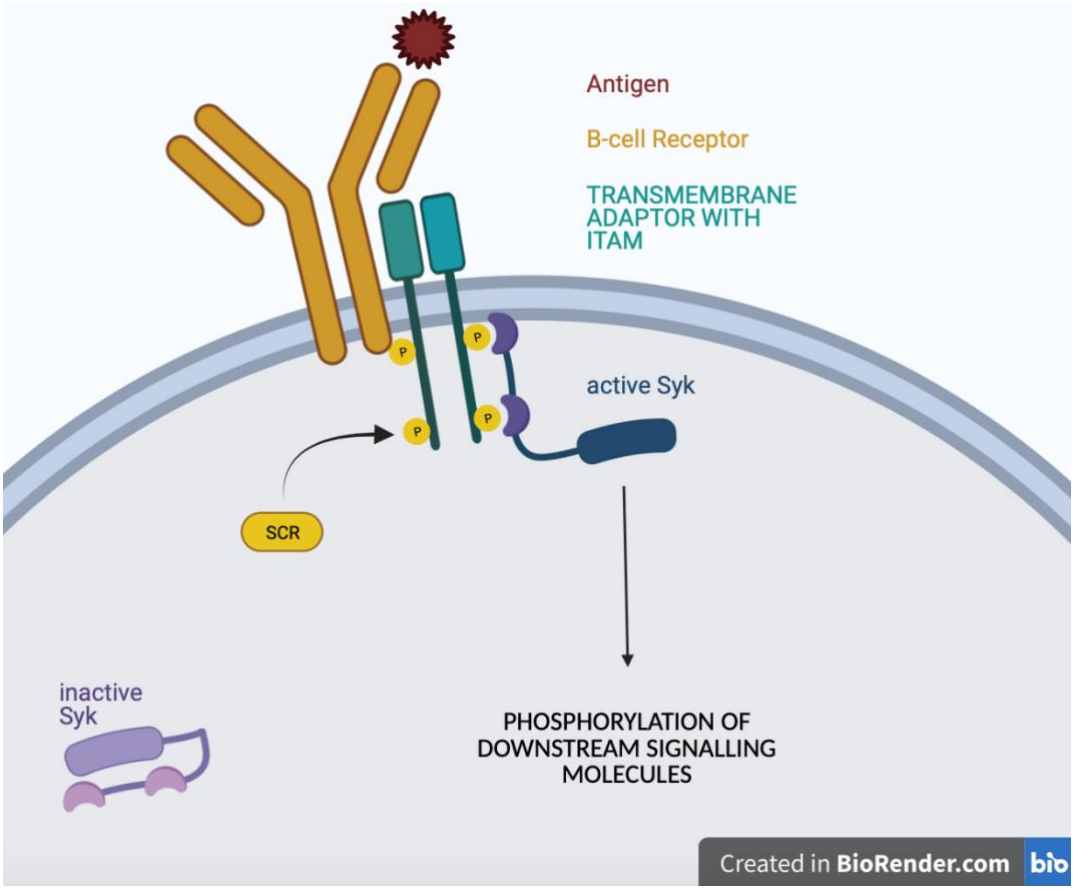

Figure 2: Syk as linker molecule in immune cells. *Figure represents B cell receptor activation, Fc-receptor and C-type lectins are linked to Syk in a similar way. Ligand binding to the immunoreceptor results in recruitment of transmembrane adaptors containing ITAMs. Subsequent phosphorylation on the ITAM allows interaction with the N-terminal SH2-domains of Syk, eventually leading to the activation of the kinase domain and phosphorylation of tyrosine residues in molecules important in downstream signalling of activated immune cells. Figure adapted from Mócsai, Ruland and Tybulewicz, (2010), created in BioRender.com.*

1.3.3. Indication for inhibition of Syk

As mentioned above, Syk is a master activator of inflammatory responses in immune cells, and as a result, inhibiting Syk activity broadly and comprehensively dampens inflammation (Singh, Masuda and Payan, 2012; Geahlen, 2014; N. Cooper *et al.*, 2022). Given Syk's location at the top of the signalling cascade, it is an ideal target for auto-immune disease management (Geahlen, 2014). Below, an overview of pathologies where Syk inhibition is investigated is given, followed by an introduction on the inhibitors fostamatinib and entospletinib, and their cardiovascular safety profile.

Syk is a crucial molecule in B-cell signalling and an important target in oncology, in particular B-cell lymphomas (Gobessi *et al.*, 2009; Hatton *et al.*, 2012; L. Chen *et al.*, 2013). Disruption of Syk in mice leads to a lack of mature B-cells and petechia-like haemorrhages that were later identified as blood-filled lymphatic vessels, showing that Syk is important in separation of lymphatic vessels from blood vessels (Abtahian *et al.*, 2003; Mócsai, Ruland and Tybulewicz, 2010).

Additionally, given its central role in Fc receptor signalling in macrophages, Syk is an interesting target for therapies in allergy and auto-immune diseases (Meltzer, Berkowitz and Grossbard, 2005; Tabeling *et al.*, 2017; Newland *et al.*, 2018; Wang *et al.*, 2021). Syk inhibition has shown positive results in these pathologies, but the exact mechanism of action of this inhibition is still not fully understood, due to Syk being involved in various pathways of diverse immune functions (Mócsai, Ruland and Tybulewicz, 2010; Currie *et al.*, 2014). Moreover, Syk is required for signalling of viral oncogenes, such as Epstein Barr virus (Lu *et al.*, 2006; Hatton *et al.*, 2012) and Kaposi's sarcoma-associated herpesvirus (Lagunoff, Lukac and Ganem, 2001), but, in contrast, it supresses tumour growth in some other non-haematopoietic tumours (Lei *et al.*, 2005; Nakashima *et al.*, 2006).

Recently, as Syk inhibition protected against lipopolysaccharide (LPS)-induced acute lung-injuries and thrombosis in mice, it has been explored to reduce the severity of COVID-19 infections (N. Cooper et al., 2022; Mallat et al., 2021; Strich et al., 2022; Vergis et al., 2021). This approach could attenuate the pro-inflammatory response and the platelet hyperactivity in response to COVID-19 complexes and therefore help in managing inflammation and coagulopathy in these patients (Apostolidis et al., 2022; Behnen et al., 2014; Bye et al., 2021; Strich et al., 2021).

1.3.4. First generation of Syk inhibitors: fostamatinib

1.3.4.1. Indications

Fostamatinib (Tavalisse®, active metabolite R406) is currently the only licenced Syk inhibitor, FDA approved in 2018 and EMA approved in 2020 for second-line treatment of chronic immune thrombocytopenia (ITP) (Connell & Berliner, 2019; Mullard, 2018; Newland & McDonald, 2020). In ITP, a defect in immune tolerance leads to a lack of platelet production and an increased destruction of platelets, resulting in excessive bleeding (Kistangari & McCrae, 2013; Zufferey et al., 2017). Binding of auto-antibody covered platelets to the Fcγ receptor of macrophages triggers activation of Syk, inducing cytoskeletal rearrangement and phagocytosis of antibody-covered platelets (Braselmann et al., 2006; Crowley et al., 1997; Nugent et al., 2009). Additionally, Syk plays a role in the production of the anti-platelet antibodies (Altomare et al., 2019; Crowley et al., 1997; Nugent et al., 2009). Inhibiting Syk is an attractive approach for treatment of ITP, as it attenuates both phagocytoses of platelets by macrophages and production of auto-antibodies by B-cells (Crowley et al., 1997; Mehta et al., 2022; Vicente-Manzanares & Sánchez-Madrid, 2004). Fostamatinib showed beneficial effects in ITP in mice and human (Podolanczuk et al., 2009) and Phase III clinical trials have proven its efficacy (Bussel et al., 2018; Duliege et al., 2018). Most frequent ADR were diarrhoea, hypertension and nausea (Bussel et al., 2018; D. Hughes et al., 2019).

Another indication where fostamatinib presented promising outcomes, is rheumatoid arthritis (RA). Syk gain of function mutations result in excessive osteoclast genesis in mice (L. Wang et al., 2021). Furthermore R406, the active metabolite of fostamatinib, blocked Syk-dependent activation of monocytes, macrophages and neutrophils, and reduces immune complex-mediated inflammation in RA models (Braselmann et al., 2006). Fostamatinib showed efficiency in animal models and human volunteers, reducing inflammatory processes and the severity of arthritis (Pine et al., 2007; M E Weinblatt et al., 2010; Michael E. Weinblatt et al., 2008). However, its development for RA was later discontinued, as fostamatinib failed to meet efficacy end-points (inferior in disease control of RA compared to marketed therapy) in Phase II and Phase III trials and showed dose-limiting toxicities (AstraZeneca, 2013; Genovese et al., 2014; Taylor et al., 2015). The reported ADR were similar as those observed in the ITP trials; diarrhoea, hypertension and neutropenia (Genovese et al., 2011; Mullard,

2018; Taylor et al., 2015). In a phase II clinical trial, an increase of systolic blood pressure (SBP) of 3 mmHg was reported, with 23% of patients requiring initiation or change of antihypertensive therapy (M E Weinblatt et al., 2010).

Additionally, fostamatinib is undergoing phase II trials for haematological malignancies, e.g., in chronic lymphoid leukaemia, as fostamatinib selectively inhibits the growth of malignant B-cell population (Barr et al., 2012; N. Cooper et al., 2022; Friedberg et al., 2010; Herman et al., 2013). In other malignancies, fostamatinib showed limited anti-tumour activity (Friedberg et al., 2010; D. Liu & Mamorska-Dyga, 2017; Mullard, 2018; S. R. Park et al., 2013). Lastly, as Syk inhibition could potentially decrease hyperimmune responses and thrombo-inflammation in COVID-19 (Apostolidis et al., 2022; Behnen et al., 2014; Bye et al., 2021; Strich et al., 2021), fostamatinib has been trialled in patients with mild-to-moderate COVID-19 (N. Cooper et al., 2022; Mallat et al., 2021; Strich et al., 2022; Vergis et al., 2021) (current clinical trials: ClinicalTrials.gov IDs: NCT04629703 and NCT04924660).

1.3.4.2. Pharmacology

Fostamatinib is an orally available prodrug, converted by intestinal phosphatases to its active metabolite tamatinib or R406 (Figure 3B and 3C) (Matsukane et al., 2022; Sweeny, Li, Clough, et al., 2010). R406 competitively binds to the ATP pocket in the catalytic domain of Syk and inhibits its kinase activity (Braselmann et al., 2006; Villaseñor et al., 2009). Beside Syk, R406 inhibits additional kinases involved in inflammatory processes, e.g. CD135, Jak, Lck, Fyn, Lyn and Src (Braselmann et al., 2006; Davis et al., 2011; Newland et al., 2018). This non-specific binding might add to the anti-inflammatory therapeutic benefits of fostamatinib (Braselmann et al., 2006; Connell & Berliner, 2019). However, the inhibition of a broad range of kinases is disadvantageous as well, as the off-target inhibition of VEGFR2 is likely the cause of the increased BP observed in clinical trials (Davis et al., 2011; Rolf et al., 2015; M. Skinner et al., 2014). Furthermore, R406 acts as inhibitor on VEGFR1 and VEGFR3 (Davis et al., 2011; Newland et al., 2018; Rolf et al., 2015). The selectivity profile of R406 for selected receptor tyrosine kinases (RTK) and intracellular tyrosine kinases, is represented in Figure 3. Outside of the kinases, R406 binds few non-kinase proteins, and at clinically relevant plasma concentrations only inhibits the adenosine A3 receptor (Braselmann et al., 2006; Rolf et al., 2015).

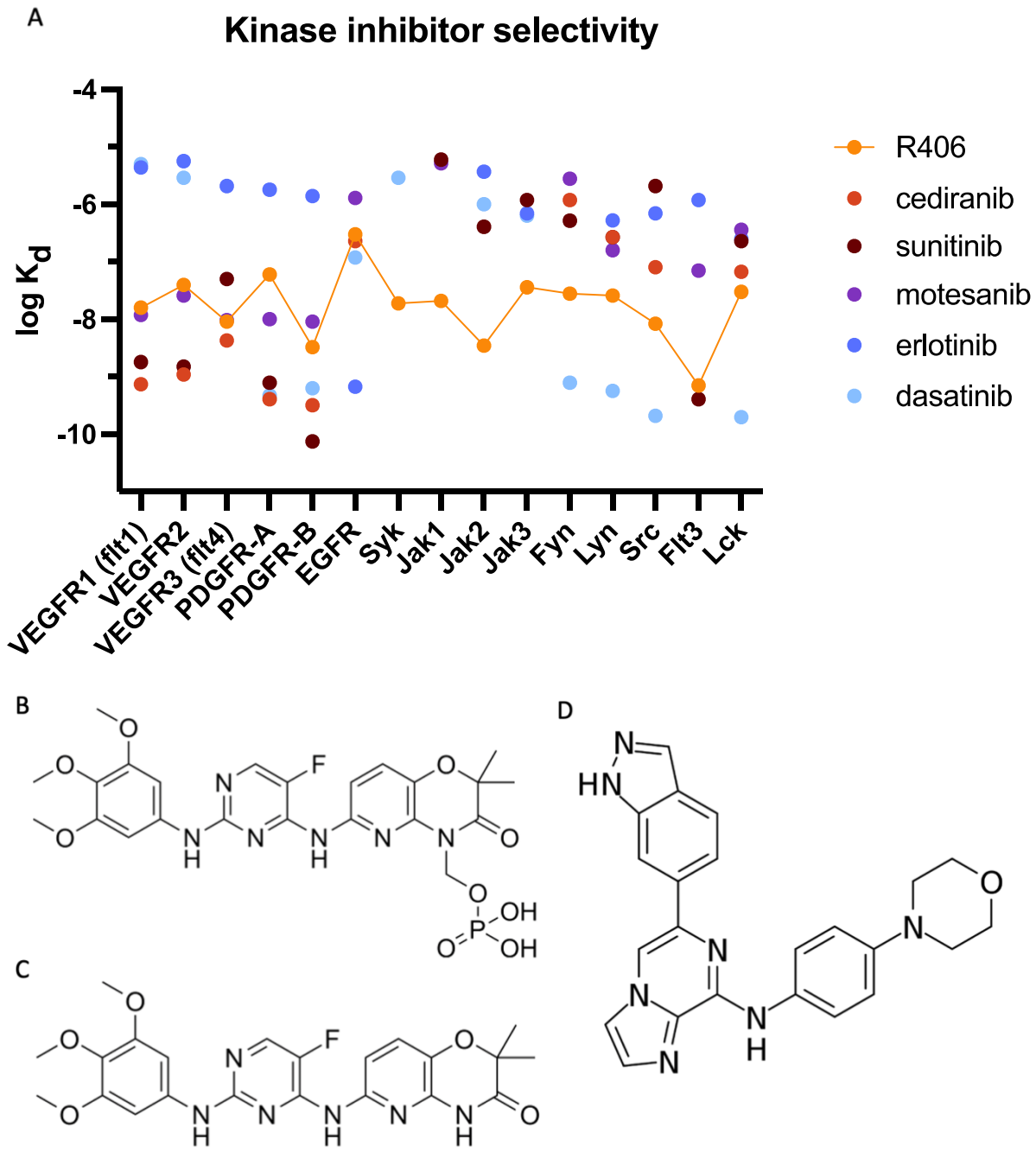

Figure 3: (A) Kinase selectivity of selected tyrosine kinase inhibitors*. The first 6 kinases shown on the x-axis are receptor tyrosine kinases, the 9 last kinases are cytoplasmic kinases. Cediranib, sunitinib and motesanib are multi-kinase inhibitors, inhibiting both VEGFRs and PDGFRs. Erlotinib is a selective EGFR inhibitor. R406 is not selective for Syk, but also inhibiting several receptor kinases and cytoplasmic kinases with similar affinities. Dasatinib is inhibiting several cytoplasmic kinases and the PDGFRs. Graph based on data from Davis et al. (2011).* ***(B), (C) and (D) Chemical structure of fostamatinib (B), R406 (C) and entospletinib (D).***

1.3.4.3. Cardiovascular safety concerns

The development of hypertension as a side effect is not surprising, as a rise in BP is commonly observed with tyrosine kinase inhibitors, especially VEGFR2 inhibitors (Lengel et al., 2015; Rolf et al., 2015). Skinner *et al.* (2014) demonstrated that fostamatinib increases BP and decreased femoral arterial conductance *in vivo*. Additionally, the active metabolite R406 reversed VEGF-induced hypotension and inhibited VEGFR2 phosphorylation and VEGF-stimulated NO production in EC (M. Skinner et al., 2014). These findings suggest that the increase in BP observed with fostamatinib caused an increased peripheral vascular resistance due to vascular constriction by VEGFR2 inhibition (Lengel et al., 2015; M. Skinner et al., 2014). Rolf *et al.* characterised the pharmacological profile of R406 at 314 targets and linked its inhibitory effects to BP observations of clinical studies, again showing that inhibition of VEGFR2 is most likely the underlying cause of the rise in BP (Rolf et al., 2015).

Lengel *et al.* evaluated the hypertensive effects of fostamatinib in conscious rats over a period of 4 weeks treatment days followed by 3 weeks without drug administration (Lengel et al., 2015). Administration of 30 mg/kg twice daily for 28 days resulted in a maximum effect of 15 mmHg increase in BP. The rise in BP followed the increase in plasma concentrations with little delay, reflecting clinical observations and suggesting a primary effect on the vasculature, rather than being secondary to renal toxicity (Lengel et al., 2015). After cessation of treatment, BP returned to initial values and it appeared there were no lasting effects, suggesting drug withdrawal in patients with raised BP should result in a reverse to normotension (Lengel et al., 2015). This observation was previously reported in clinical trials, showing that discontinuation of fostamatinib treatment quickly resolved hypertension (Friedberg et al., 2010). Moreover, standard anti-hypertensive drugs such as nifedipine, captopril or atenolol, attenuated the fostamatinib-induced hypertension in rats (Lengel et al., 2015). However, in a patient population with pre-existing cardiovascular morbidities, more variability in response to BP changes can be expected due to differences in efficient CV compensating reflexes. Therefore the results from studies in healthy rats should be translated with caution to safety assessment in elderly and immune-compromised patients (Lengel et al., 2015).

Multiple fostamatinib clinical trials reported hypertension as an adverse effect. A phase IIb trial by Taylor *et al.* reported 13% of patient receiving 100 mg twice daily developed hypertension (Taylor et al., 2015). Two phase III trials reported an elevated BP (>140/90 mmHg) in more than 1 visit in 40-47% of patients receiving fostamatinib 100 mg twice daily, versus 27% in placebo-treated patients (Genovese et al., 2014; Michael E. Weinblatt et al., 2014). A meta-analysis including 5 randomised controlled trials for fostamatinib in RA showed an increased risk of hypertension (17% vs 7.6% in control group) (Kunwar et al., 2016). Importantly, the magnitude of increase in BP following fostamatinib treatment is considerably lower than observed with other VEGFR2 inhibitors, for example sunitinib (Rolf et al., 2015). Clinical trials generally reported increases around 25 mmHg in systolic pressure and 15 mmHg in diastolic pressure following sunitinib treatment (George et al., 2012; Michael E. Weinblatt et al., 2008). Other VEGFR2-inhibitors such as cediranib and sorafenib results in increases in blood pressure of similar magnitudes (E. S. Robinson, Khankin, et al., 2010; Veronese et al., 2006). In contrast, fostamatinib was associated with a MAP increase smaller than 10 mmHg, which might reflect a lower efficacy for VEGFR2 inhibition (Rolf et al., 2015; M. Skinner et al., 2014).

Chen *et al.* performed a systematic review of the overall cardiovascular risk of fostamatinib in RA patients, analysing the results of 9 phase II trials and 4 phase III trials (Y. Chen et al., 2021). Fostamatinib therapy was associated with an increased risk for hypertension, but no increase in major cardiovascular events (including acute myocardial infarction, ischemic stroke, and cardiac death) or pulmonary heart disease was found (Y. Chen et al., 2021). However, the duration of the included trials ranged from 1 to 25 months. This follow-up period might be too short to detect major cardiovascular adverse effects, as these take longer to develop following onset of hypertension (Y. Chen et al., 2021; Messerli et al., 2017). Furthermore, due the relatively small sample sizes of trial included in this meta-analysis, they might not be sufficiently powered to detect these uncommon cardiovascular events. Therefore severe cardiovascular adverse events arising from fostamatinib therapy should remain a concern. (Y. Chen et al., 2021)

Treatment with fostamatinib is generally long-term, up to 24 months in the clinical trials (Duliege et al., 2018), so BP pressure changes should be carefully monitored and antihypertensive therapy should be set up if necessary. Patients with pre-existing hypertension should be treated adequately in order to manage high BP before starting fostamatinib (Connell & Berliner, 2019). Overall the rise in BP is seen as a manageable ADR, but dose reduction, treatment discontinuation or antihypertensive therapy can be necessary (Lengel et al., 2015; Newland & McDonald, 2020; Rolf et al., 2015).

Overall, fostamatinib has shown encouraging results in multiple *in vivo* models in treating inflammatory, autoimmune and oncological diseases (Braselmann et al., 2006; Gobessi et al., 2009; Podolanczuk et al., 2009). Moreover, clinical trials of fostamatinib in these pathologies have shown promising efficacy results, but ADR (neutropenia, gastro-intestinal side effects and hypertension) has limited its use in clinical settings and fostamatinib's safety profile stays a major limitation for full clinical use, especially in chronic applications (Y. Chen et al., 2021; Currie et al., 2014).

1.3.5. Second generation Syk inhibitor: entospletinib (GS-9973)

To improve the safety liabilities seen with fostamatinib, a second generation of Syk inhibitors with a better selectivity profile were developed (D. Liu & Mamorska-Dyga, 2017). These second generation compounds aimed to achieve higher levels of Syk inhibition, with minimal binding to other tyrosine kinases and without the associated dose-limiting ADR (Currie et al., 2014; J. Sharman & Di Paolo, 2016). One of those novel compounds is entospletinib (GS-9973) (Currie et al., 2014; J. Sharman et al., 2015). Currie *et al.* (2014) showed that entospletinib bound with a high affinity to Syk and displayed low affinities (>10 fold lower relative to Syk) for other off-target kinases, including VEGFR2. Hence entospletinib displayed a good selectivity for Syk. Moreover, entospletinib had a higher potency to inhibit Syk-mediated functional responses than R406 (EC_{50} 26 nM versus 53 nM), and lower potency to inhibit VEGFR2 phosphorylation (EC_{50} >1000 nM versus 36 nM) (Currie et al., 2014). Entospletinib is believed to have this higher selectivity for Syk over other tyrosine kinases as it has a more rigid structure than R406 and cannot adopt multiple conformations to bind to several kinases (Figure 3D) (Currie et al., 2014). Entospletinib is currently in development for lymphoid malignancies and leukaemia's, mostly in combination therapy with Bruton's tyrosine kinase inhibitors or new therapeutic antibodies (Currie et al., 2014; Danilov et al., 2020; D. Liu & Mamorska-Dyga, 2017; Morschhauser et al., 2021; J. Sharman et al., 2015). Compared to fostamatinib, entospletinib is generally well tolerated and shows fewer dose-limiting cardiovascular ADR (D. Liu & Mamorska-Dyga, 2017; J. Sharman et al., 2015). Except for one Phase I/II trial in AML that combined entospletinib with induction chemotherapy and reported hypertension as an adverse effect in 6 from 53 patients (Walker et al., 2020), no other Phase I or Phase II trials reported hypertension as an observed ADR with entospletinib (Burke et al., 2018; Danilov et al., 2020; Lam et al., 2021; Morschhauser et al., 2021; J. Sharman et al., 2015).

In summary, VEGFR2 is the main contributor to fostamatinib's safety issues (M. Skinner et al., 2014). On the other hand, entospletinib is more selective for Syk, doesn't bind VEGFR2 (Currie et al., 2014) and so far has not been associated with hypertension in clinical trials (Burke et al., 2018; Danilov et al., 2020; Lam et al., 2021; Morschhauser et al., 2021; J. Sharman et al., 2015). Below, the physiological and pathological functions of VEGFR2 are presented, followed by an introduction on its role in cardiovascular safety issues.

1.4. Vascular Endothelial Growth Factor (VEGF) inhibitors

1.4.1. The VEGF family

During the development of an embryo, the first organ to develop and become functional, is the heart and vasculature (Risau and Flamme, 1995). Vasculogenesis, the differentiation of vascular endothelial cells (EC) and development of the vascular system is a crucial step in this early stage of life (Risau and Flamme, 1995; Goldie, Nix and Hirschi, 2008). Similarly, in adults, the formation of new blood vessels out of pre-existing vessels, termed angiogenesis, is essential in several physiological processes, such as wound healing and the menstrual cycle (Felmeden et al., 2003; Koch et al., 2011; W. Risau, 1997). Vascular Endothelial Growth Factor (VEGF) is identified as the key signalling molecule in angiogenesis, through its potent action on ECs (Felmeden et al., 2003; Mabeta & Steenkamp, 2022; W. Risau, 1997). The VEGF family consists of five ligands: VEGF-A, VEGF-B, VEGF-C, VEGF-D and placental growth factor (PlGF) (Ferrara, 2004; Holmes et al., 2007; Koch et al., 2011) (Figure 4). The most important regulator of angiogenesis is VEGF-A, also referred to as Vascular Permeability Factor (VPF) or simply VEGF (Connolly et al., 1989; Ferrara & Adamis, 2016; Keck et al., 1989; Senger et al., 1983).

Alternative exon splicing of the human *VEGF-a* gene results in splice variants with a different number of amino acids, including $VEGF_{121}$, $VEGF_{165}$, $VEGF_{189}$ and $VEGF_{206}$ (Houck et al., 1992; Mabeta & Steenkamp, 2022; C. J. Robinson & Stringer, 2001) Structural differences in these isoforms are linked to their affinity for the VEGF-receptors and co-receptors (Ferrara, 2004; Holmes et al., 2007; Koch et al., 2011). Moreover, the different isoforms display different binding properties to cell surface heparin sulfate and the extracellular matrix (ECM). For example, $VEGF_{121}$ does not bind heparin and is freely diffusible (Houck et al., 1992; Mabeta & Steenkamp, 2022). Other isoform, such as $VEGF_{189}$ and $VEGF_{206}$ with a high affinity for heparin, are sequestered in the ECM by binding to heparin-like molecules, and are be released by heparin, heparinase or plasmin to diffusible forms (Houck et al., 1992; Mabeta & Steenkamp, 2022; Mamer et al., 2020; J. E. Park et al., 1993). This proteolytic release of VEGF is an important regulator of its activity and location (Ferrara, 2004; Künnapuu et al., 2021; Pepper, 2001).

$VEGF_{165}$a is the most abundant isoform and the major regulator of vessel growth and vascular permeability (Houck *et al.*, 1992; Robinson and Stringer, 2001). This isoform has intermediate diffusion properties, as it is secreted, but also found in significant amounts on the cell surface (Park, Keller and Ferrara, 1993; Robinson and Stringer, 2001). Paradoxically, $VEGF_{165}$b, an alternatively spliced variant of $VEGF_{165}$, is reported to act as an partial agonist on the VEGF receptors, and has an anti-angiogenic effect *in vivo* (David O. Bates *et al.*, 2002; Woolard, Wang, *et al.*, 2004; Peach *et al.*, 2018).

1.4.2. VEGF receptors

Ligands of the VEGF family act through binding to receptor tyrosine kinases (RTKs): VEGFR1, VEGFR2 and VEGFR3 (Figure 4) (Ferrara, 2004; Holmes et al., 2007). These receptors are expressed on the surface of a wide range of cells, including vascular and lymphatic Ecs (Jakeman et al., 1992; Monaghan et al., 2021; Soker et al., 1996) and bone marrow-derived cells, e.g. monocytes and macrophages (Adini et al., 2002; Broxmeyer et al., 1995; Ganta et al., 2019; Shen et al., 1993; Yamashita et al., 2022). VEGFR1 and VEGFR2 consist of seven extracellular immunoglobulin-like domains, a short transmembrane domain and an intracellular tyrosine kinase domain (Holmes et al., 2007; M. Shibuya et al., 1990; Terman et al., 1991). Both VEGFR1 and VEGFR2 bind VEGF-A (Kilpatrick et al., 2017; Olsson et al., 2006; Peach et al., 2018). VEGFR1 binds VEGF-A, VEGF-B and PlGF (Koch et al., 2011; Olsson et al., 2006) (Figure 4). The soluble form of VEGFR1 is reported to have inhibitory regulating effects on VEGF activity, as it binds VEGF-A with a high affinity and therefore hinders its binding to VEGFR2 (Aiello et al., 1995; Goldman et al., 1998; Kendall & Thomas, 1993; Mabeta & Steenkamp, 2022). Even though VEGFR2 binds VEGF-A with a 10-fold lower affinity than VEGFR1, the former is the key receptor in vascular endothelial cell development and proliferation, angiogenesis and permeability changes of the vasculature (Holmes et al., 2007; Mabeta & Steenkamp, 2022; Millauer et al., 1993; Terman et al., 1991). VEGFR3 is highly homologous to VEGFR1 and VEGFR2 and binds VEGF-C and VEGF-D, important regulators of lymphatic angiogenesis (Ferrara, 2004; Joukov et al., 1996; Karkkainen et al., 2002). Additionally, the neuropilins (NP) act as coreceptors for some isoforms of VEGF, enhancing the VEGF binding to VEGFR2 and the subsequent signal transduction (Fuh et al., 2000; Peach et al., 2018; Soker et al., 1996, 1998).

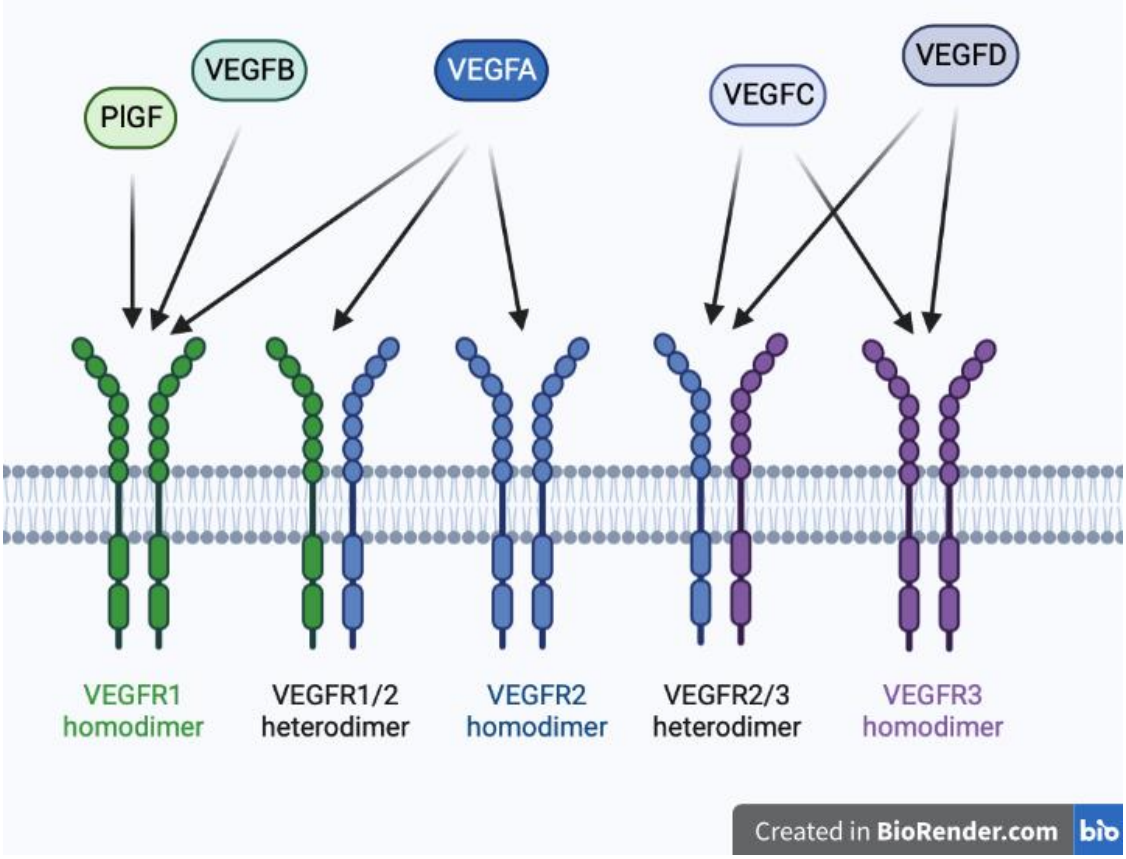

Figure 4: VEGF receptor ligand binding. *The VEGF family, consisting of 5 ligands, binds to three receptor tyrosine kinases: VEGFR1, VEGFR2, and VEGFR3, resulting in the formation of homo- or heterodimers of the receptor chains. Figure adapted from Olsson et al. (2006),* created in BioRender.

When VEGF binds to its receptor, receptor dimerization occurs. Both homodimers, where the two receptor chains are identical, and heterodimers, where the two receptor chains are similar, but not identical, can be formed (Figure 5). Upon dimerization, intracellular tyrosine residues of the receptor chains are phosphorylated, providing docking sides for subsequent adapter proteins and signalling molecules, and conformational changes will initiate the kinase activity of the receptor, activating downstream signalling pathways (Ferrara & Adamis, 2016; Koch et al., 2011; Manni et al., 2014). The full amino acid sequence of human VEGFR2 is given in the Appendix (section 8.2.).

1.4.3. Physiological actions of VEGF

Hypoxic conditions importantly promote the expression of the *VEGF-a* gene, mediated through hypoxia-inducible factor (Arcondéguy et al., 2013; Y. Liu et al., 1995; Minchenko et al., 1994; Pugh & Ratcliffe, 2003). In addition, there are several growth factors (e.g. transforming growth factors (Pertovaara et al., 1994) and epidermal growth factor (Frank et al., 1995)), hormones (e.g. corticotropin (Shifren et al., 1998) and the gonadotropins (Christenson & Stouffer, 1997)) that regulate the expression of VEGF (Arcondéguy et al., 2013; Pagès & Pouysségur, 2005). As described above, the binding of VEGF-A to VEGFR2 is the key factor in vascular development and angiogenesis, as it promotes the proliferation, survival and migration of vascular Ecs (Connolly et al., 1989; Keck et al., 1989; Mabeta & Steenkamp, 2022; Senger et al., 1983). VEGF-A increases vascular permeability and plays an important role in inflammation (Keck et al., 1989; Proescholdt et al., 1999; Senger et al., 1983; Thickett et al., 1999; Zhou et al., 2022). Lastly, activation of VEGFR2 causes an *in vitro* vasorelaxation in coronary arteries and *in vivo* hypotension, transient tachycardia and a decrease in cardiac output (D. D. Ku et al., 1993; M. Skinner et al., 2014; R. Yang et al., 1996).

Nitric oxide (NO) functions as a critical player in VEGF-induced angiogenesis, vascular permeability and its role in homeostasis of the BP (Eechoute et al., 2012; Fukumura et al., 2001; Gu et al., 2009). Furthermore, the hypotensive effect of VEGF-A is believed to be mediated through prostacyclin (PGI_2) generation and inhibition of endothelial endothelin-1 (ET-1) production (Colafella et al., 2020; Gliki et al., 2001; Herrmann et al., 2016; Lankhorst et al., 2014; Neagoe et al., 2005). Both NO and PGI_2 evoke vascular smooth muscle cell relaxation and endothelin-1 is a potent vasoconstrictor (Colafella et al., 2020; Fukumura et al., 2001; Lankhorst et al., 2014; Neagoe et al., 2005).

VEGF-A supports multiple vital processes, both in the embryonic and postnatal stages. It promotes blood vessel formation, affects haematopoiesis and plays a key role in skeletal growth. Through its angiogenetic effects, VEGF contributes in an important way to wound healing and a normal ovarian cycle (Ferrara, 2004; Koch et al., 2011).

1.4.4. VEGF signalling in tumour angiogenesis and inhibition of VEGF

Next to its importance in several physiological processes, VEGFR2 signalling plays a role in pathological conditions, e.g. diabetic retinopathy (Aiello et al., 1995; Malecaze et al., 1994) and cancer (D. I. Gabrilovich et al., 1996; Masabumi Shibuya, 2011; Soker et al., 1996). Where angiogenesis is a well-regulated process in normal physiological circumstances, this balance is disrupted in cancer. There is a so-called 'angiogenetic switch', where pro-angiogenic factors, secreted by the tumour cells, overrule the anti-angiogenic factors and create a pro-vascularization micro-environment (Carmeliet, 2005; Dey et al., 2015; Gotink & Verheul, 2010). Growth of a tumour beyond the size of 1 – 2 mm^3 is dependent on angiogenesis, in order to meet the high demand of cancer cells for nutrients and oxygen (Ferrara, 2004; Folkman, 2007). Most human tumours express VEGF-A mRNA and many *in vitro* tumour cell lines secrete VEGF and upregulate its receptor (Ferrara, 2004; Phillips et al., 1993; Senger et al., 1983; Tomisawa et al., 1999), emphasising its crucial role as mediator in tumour angiogenesis. These newly-formed blood vessels in a tumour are typically immature, disorganised and hyperpermeable and this allows cancer cells to enter the circulation and diffuse through the body, resulting in metastasis (D. O. Bates et al., 2002; Nagy et al., 2006; Senger et al., 1983; Tomita et al., 2021). Even more, VEGF-A decreases the development of dendritic cells, aiding in the escape of tumour cells from the immune system (D. Gabrilovich et al., 1998; D. I. Gabrilovich et al., 1996). An upregulated expression of VEGFR2 is seen as a marker for prognosis in patients with malignancies and overexpression of VEGF mRNA correlates with invasiveness of the tumour and higher recurrence (Ferrara & Adamis, 2016; Fine et al., 2000; Tomisawa et al., 1999).

To inhibit angiogenesis in cancer, therapeutic agents interfering with the VEGF signalling pathway have been developed (Faivre *et al.*, 2007; Gotink and Verheul, 2010; Tyler, 2012; Allegra *et al.*, 2013; Scott, 2015; Aljubran *et al.*, 2019). They reduce the vascularisation of the tumour and limit further tumour growth (Kim *et al.*, 1993; Faivre *et al.*, 2007; Scott, 2015). Additionally, these drugs normalise the vasculature in the tumour. By reducing hyperpermeability and disorganisation of the tumour vessels, VEGF inhibitors enable the delivery of chemotherapeutics to the centre of the tumour and decrease the chance of metastasis (Ferrara & Adamis, 2016; Jain, 2014; Willett et al., 2004).

The first marketed anti-VEGF therapy, bevacizumab (Avastin®), a VEGF-A targeting monoclonal antibody, was FDA approved as first-line treatment in metastatic colorectal cancer in 2004 (Bennouna et al., 2013; Giantonio et al., 2007; U.S. Food & Drug Administration, 2004), and more recently for treatment for several other cancer types including ovarian cancer (Burger et al., 2011), non-small cell lung cancer (Sandler et al., 2006) and renal cancer (J. C. Yang et al., 2003) (Ferrara & Adamis, 2016). Bevacizumab was generally well tolerated during Phase I clinical trials with typical side effects being hypertension and proteinuria (Cobleigh et al., 2003; Gordon et al., 2001). Subsequent studies revealed rare occurrence of serious side effects such as myocardial infarction and stroke (X. L. Chen et al., 2013; Tebbutt et al., 2011).

Another class of anti-VEGF therapeutics are the receptor tyrosine kinase inhibitors (RTKIs). These hydrophobic small molecule inhibitors easily pass through the cell membrane, where they target the intracellular ATP-binding site of the VEGFR2 and inhibit the downstream signalling pathways (Ferrara & Adamis, 2016; Gotink & Verheul, 2010; Holmes et al., 2007). One example is sunitinib (Sutent®), FDA and EMA approved in 2007 for advanced renal cell carcinoma (Faivre *et al.*, 2007; Motzer *et al.*, 2007; Ferrara and Adamis, 2016), and later also marketed for treatment of gastrointestinal stromal tumours, refractory or intolerant to imatinib and pancreatic cancer (Ferrara & Adamis, 2016; Kee & Zalcberg, 2012; Raymond et al., 2011). As with bevacizumab, hypertension and proteinuria were observed in this class of anti-VEGF therapies (Carter et al., 2017; Hayman et al., 2012; Møller et al., 2019; Zhang et al., 2014). Other side effects include fatigue, diarrhoea, skin discoloration and hand-foot syndrome (Ferrara & Adamis, 2016). More recently approved tyrosine kinase inhibitors targeting VEGFR2 are axitinib (Inlyta®, FDA approved for renal cell carcinoma in 2012 (Tyler, 2012), regorafenib (Stivarga®, FDA approved for metastatic colorectal cancer in 2012 (Aljubran et al., 2019; Leach, 2012) and lenvatinib (Lenvima®, FDA approved for thyroid cancer in 2015 (Scott, 2015). Hypertension remains a frequently reported side effect with these newer generation inhibitors (Agarwal et al., 2018; Møller et al., 2019; Scott, 2015; Tyler, 2012). Similarly, cediranib, a non-marketed VEGFR inhibitor, leads to rapid development of hypertension and proteinuria (E. S. Robinson, Matulonis, et al., 2010).

The ATP-binding site targeted by RTKIs is highly conserved across the kinome (Chakraborty et al., 2019; D. Huang et al., 2010). Many of VEGFR2 inhibitors do not only affect the VEGFR, but target a number of other kinases as well, e.g. the structurally related receptor for Platelet Derived Growth Factor (PDGF) and the structurally unrelated receptor for Fibroblast Growth Factor (FGF) (Davis et al., 2011; Ferrara & Adamis, 2016; Gotink & Verheul, 2010). Both PDGF and FGF are important mediators of angiogenesis. The antitumoral activity of the RTKIs is mediated through this multiple target inhibition and is, in some cases, not only affecting the Ecs but tumour cells as well (Ferrara & Adamis, 2016).

Targeting VEGF has been proven to be an effective anti-angiogenic approach both in animal models and in human cancers, and offers clinical improvement especially for patients with advanced cancers, left with limited treatment options (Dey et al., 2015; Ferrara & Adamis, 2016; Gotink & Verheul, 2010). However, two major issues have been hindering extensive use of the anti-VEGF therapies in clinical practice: therapy resistance and the occurrence of toxicity, as detailed below (Bergers & Hanahan, 2008; Dey et al., 2015; Gotink & Verheul, 2010).

1.4.5. Resistance to antiVEGF therapy

In preclinical and clinical studies, the benefits of anti-angiogenic therapy are often only transient and resistance to the RTKI-therapy emerges inevitably (Bergers & Hanahan, 2008). Both adaptive and intrinsic resistance are observed (Bergers & Hanahan, 2008; Ellis & Hicklin, 2008; Gotink & Verheul, 2010). In adaptive resistance, or evasive resistance, the therapy achieves clinical benefit at first, but fails to show lasting inhibition of tumour growth. Typically after a few weeks or months, the tumour is able to circumvent the inhibition and progresses further (Bergers & Hanahan, 2008; Ellis & Hicklin, 2008; Gotink & Verheul, 2010). Several escape routes have been suggested, but the development of resistance is most likely a multifactorial process and is still not fully understood (Broxterman et al., 2009; Itatani et al., 2018). Processes that are suggested to be involved are drug efflux, activation of alternative angiogenic pathways, mobilization of pro-angiogenic bone-marrow derived cells and vascular mimicry, wherein aggressive tumour cells differentiate and build vessel-like channels in a VEGF-independent manner (Bergers & Hanahan, 2008; Broxterman et al., 2009; Dey et al., 2015). Small molecule RTKIs are mostly multitargeting inhibitors, therefore resistance was initially not expected. However, as tyrosine kinases are not exclusive expressed on Ecs but can also be found in tumour cells, the hypothesis was raised that RTKIs target these dynamic and quickly adapting cells as well, and, through mutations and alternative signalling pathways, the tumour cells contribute to the reversal of initial response (Broxterman et al., 2009; Gotink & Verheul, 2010).

Moreover, pre-existing resistance or intrinsic resistance is reported, where no tumour regressions or retardation in tumour growth takes place after the onset of therapy (Rosenzweig, 2018; Y. Yang et al., 2022). Most likely one or multiple of the above mentioned mechanisms are already pre-existing in this type of resistant tumours, activated earlier in the development of the tumour (Bergers & Hanahan, 2008; Gotink & Verheul, 2010).

1.4.6. Cardiovascular safety concerns of VEGF-inhibition

Over the last decade, increasing attention has been given to CV care for cancer patients. As a result of the development of effective antitumoral agents, survival of cancer patients is prolonged. These improvements come with a demand for more CV care (Izzedine et al., 2009; Touyz et al., 2017b). Given that cancer patients are at higher risk of CV events and additionally, numerous chemotherapies display onset or worsening of systemic hypertension, it is important to prevent and monitor changes in haemodynamic parameters in this patient population (Herrmann et al., 2016; Izzedine et al., 2009). The antiangiogenic drugs are often used as an adjuvant or maintenance therapy, again underscoring the importance of considering the effects of long-term BP elevations (Dey et al., 2015). Small drug-induced increases in SBP are associated with an increased risk for major CV events, especially in patients with CV comorbidity or other CV risk factors (Lewington et al., 2002; Sager et al., 2013). On the other hand, hypertensive patients' risk for CV events are significantly decreased when their SBP is lowered by 5 mmHg (Blood Pressure Lowering Treatment Trialists Collarobation, 2008; Sager et al., 2013).

RTKs are expressed in multiple tissues, where they play an important role in the homeostasis of the CV system. In adulthood, Ecs remain mostly quiescent, therefore the angiogenesis inhibitors were not expected to affect the normal vasculature and little adverse drug reactions were foreseen (Carmeliet, 2005; Gotink & Verheul, 2010; Touyz et al., 2017a). Nonetheless, clinical studies have exposed various CV toxicities occurring upon VEGF-inhibition, including hypertension (Touyz et al., 2017b). The RTKI-induced hypertension is dose-dependent. A randomised trial with bevacizumab reported that with a dose of 3 mg/kg, 3% of patients developed hypertension, while hypertension rates of 36% were observed in the high-dose group (10 mg/kg) (J. C. Yang et al., 2003). Furthermore, drugs inhibiting VEGFR2 with a higher relative potency compared to other tyrosine kinases, result in higher rates of elevated BP than less potent VEGFR2 inhibitors (H. X. Chen & Cleck, 2009; T. Collins et al., 2018). For example, *in vivo*, 6 mg/kg cediranib (K_d for VEGFR2 = 1.1 nM) induced around 40% increase in MAP, while 12.5 mg/kg vandetanib (K_d for VEGFR2 = 820 nM) induced an MAP increase of approximately 20% (Carter et al., 2017). Similar observations have been made from clinical trials (H. X. Chen & Cleck, 2009), e.g. a 19 mmHg increase in BP observed with

cediranib (E. S. Robinson, Khankin, et al., 2010) versus 12 mmHg with vandetanib (Mayer et al., 2011).

In clinical settings, the dose of the RTKI often needs to be lowered or treatment needs to be interrupted due to the onset of this hypertension, resulting in a reduced efficacy of these therapies (Plummer et al., 2019; Touyz et al., 2017b). Moreover increased incidence of ischaemic heart disease, heart failure, QT prolongation leading to an enhanced risk of ventricular arrhythmia, thrombo-embolism and cerebrovascular events are reported (B. Liu et al., 2016; Touyz et al., 2017b). Failure to predict these serious CV adverse effects in early clinical trials might reflect the underestimation of the fact that many cancer patients are at predisposing risk of CV toxicity (Touyz et al., 2017b).

1.4.6.1. Incidence of CV toxicity

The reported incidence of hypertension and other CV side effects varies between clinical studies. Additionally, due to insufficient reports on post-marketing surveillance, overlap of CV symptoms and tumour progression symptoms, and under-reporting of ADR, the total risk of CV toxicity due to RTK inhibition is still not well quantified (Abdel-Qadir et al., 2017; B. Liu et al., 2016). It is clear however that patients receiving the small molecule VEGF-inhibitors are at a remarkably high risk of toxicity on the heart and vasculature, and their CV complications should be carefully monitored (B. Liu et al., 2016; Van Dorst et al., 2021).

A meta-analysis of 72 Phase II and Phase III randomized controlled trials (RCT) showed that the use of the VEGFR-TKIs enhanced the risk of developing all-grade hypertension with a ratio of risk of 3.85 (i.e. relative risk, the ratio of risk of hypertension in the treated group versus risk of hypertension in the non-treated group) and high-grade hypertensive incidents with a relative risk of 4.60 (B. Liu et al., 2016). Investigating the related risk of congestive heart failure, a meta-analysis of 5 Phase II and 16 Phase III RCT showed that treatment with a VEGF-RTKI is associated with higher risk for all grade congestive heart failure (relative risk of 2.69) (Ghatalia et al., 2015). Additionally, a meta-analysis with 10 Phase II and III randomized controlled trials reported arelative risk of 2.23 for fatal adverse drug events related to VEGF-RTKIs, with the two most common cause of death being haemorrhage and myocardial infarction (Schutz et al., 2012). A meta-analysis of 77 Phase III RCT and Phase IV post-marketing studies showed that the angiogenesis inhibitors were associated with an increased risk of hypertension (Odds ratio of 5.28, i.e. the ratio of odds of hypertension in the treated group versus the odds of hypertension in the non-treated group), Grade 3 or higher hypertension (Odds ratio 5.59), arterial thromboembolism (Odds ratio 1.52), cardiac dysfunction (Odds ratio 1.35) and cardiac ischaemia (Odds ratio 2.83) (Abdel-Qadir et al., 2017).

1.4.6.2. Renal toxicity

Besides this direct toxicity at the heart and vasculature, antiVEGF therapy is associated with renal toxicity. The VEGF/VEGFR2 interaction at the glomerular EC and podocytes is crucial for the normal kidney function (H. X. Chen & Cleck, 2009; Gurevich & Perazella, 2009) and VEGF is essential for the development and maintenance of the functional glomerular filtration barrier (Eremina et al., 2003; Gurevich & Perazella, 2009). Inhibiting the VEGF/VEGFR2 pathway is therefore associated with renal toxicity that mostly presents itself as proteinuria, a high level of proteins in the urine as the renal barrier function is disrupted (Camarda et al., 2022; Hayman et al., 2012; Van Dorst et al., 2021). Furthermore, VEGF is important in the regulation of the renal perfusion (Eremina et al., 2003). VEGF stimulates endothelial NO synthase (eNOS) and therefore increases NO production in the glomerulus (Gu et al., 2009). As NO regulates the renal perfusion and sodium excretion (Zou & Cowley, 1999), antiVEGF therapy may lead to sodium retention and contribute to an elevated blood pressure (Gu et al., 2009; Zou & Cowley, 1999).

Meta-analysis of 13 clinical trials showed that patients treated with sunitinib had an increased risk of renal dysfunction (relative risk of 1.36, i.e. the risk of renal dysfunction in sunitinib-treated-group compared to control group) (Zhu et al., 2009). Similarly, a meta-analysis of 32 clinical trials showed that patients receiving a VEGFR-inhibitor had an increased risk of developing all-grade and high grade proteinuria (Rixe et al., 2007; Zhang et al., 2014). More rarely, more severe renal toxicity is reported, such as thrombotic microangiopathy or focal segmental glomerulosclerosis (Eremina et al., 2008; Izzedine et al., 2014).

1.4.6.3. Mechanisms of anti-VEGF induced hypertension

As the rise in BP occurs typically within hours of the start of therapy and disappears quickly after treatment withdrawal, it has been suggested that this BP effect is due to functional changes in vasoreactivity (Herrmann et al., 2016; Touyz et al., 2017b). In 2020, Cooper *et al.* showed a sustained rise in BP in rats, up till 6 days after treatment with RTKIs. As these effects seemed to persist into the off-treatment period, it was suggested that structural changes also contribute to the CV side effects of these drugs (S. L. Cooper et al., 2020). The observed CV toxicity appears to be an "on-target" effect, as the CV safety issues are observed with all types of VEGF inhibition and a higher incidence of hypertension is seen with more potent anti-VEGF RKTIs (Carter et al., 2017; H. X. Chen & Cleck, 2009; T. Collins et al., 2018; Gordon et al., 2001).

While the exact mechanism of action causing hypertension and CV toxicity remains unclear (Camarda et al., 2022; Touyz et al., 2017a), several mechanisms have been proposed to explain the anti-VEGF hypertension (Figure 5). Direct effects on the endothelium include endothelial dysfunction and a decrease in NO production, due to a reduced eNOs activation, and subsequent decrease of its vasodilatory effects (Eechoute et al., 2012; Neves et al., 2018; Touyz et al., 2017a). Additionally, the endothelin system may be partly responsible, as an increase in circulating ET-1 levels by VEGF-inhibition causes vasoconstriction via the ET-A receptor on smooth muscle cells (Camarda et al., 2022; Colafella et al., 2020; Herrmann et al., 2016; Touyz et al., 2017a). Although less studied, prostacyclin, a potent vasodilator, could have a role in RTKI-induced hypertension as well, as anti-VEGF therapy could interfere with the physiological VEGF-induced production of prostacyclin (Colafella et al., 2020; Gliki et al., 2001; Neagoe et al., 2005).

Additionally, several mechanism contributing to vessel remodelling and increased vascular resistance have been suggested. For example, VEGFR2-inhibition leads to capillary rarefaction, a decrease in the number of micro-vessels and therefore reduction in microvasculature area in the capillary beds, that might increase the vascular resistance and contribute to elevated blood pressure levels (Kamba et al., 2006; Steeghs et al., 2010). Furthermore, Catino *et al.* have shown that sunitinib induced arterial stiffening and suggested this phenomenon to be involved in the development of RTKI-induced hypertension (Catino et al., 2018). Lastly, anti-VEGF induced renal toxicity may contribute to increased BP levels through sodium retention, as detailed above (section 1.4.6.2.) (Camarda et al., 2022; Van Wynsberghe et al., 2021).

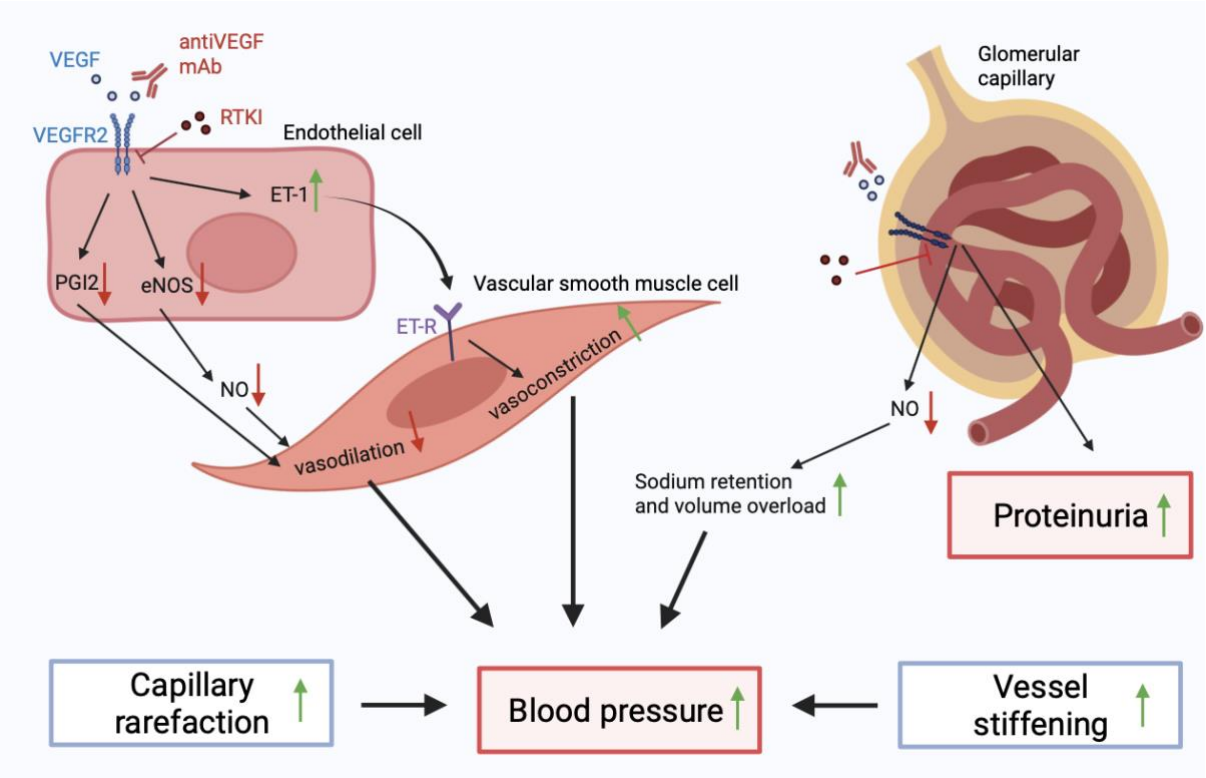

Figure 5: Mechanisms adding to antiVEGF-induced hypertension. *Inhibition of VEGF/VEGFR2 on the endothelial cells lead to a decrease in PGI_2 and NO, resulting in an attenuation of relaxation of the vascular smooth muscle cells and reducing of vasodilation. Simultaneously, inhibiting VEGFR2 at the endothelial cells leads to an increase in endothelin 1 (ET-1), that induces a vasoconstriction via its binding to its receptor on the vascular smooth muscle cells. Furthermore, antiVEGF therapy results in a decreased production of NO in the glomerular capillary, ultimately leading to an increase in sodium retention and blood volume overload. Additionally, RTKI-induced capillary rarefaction and arterial stiffness contribute to an elevation of the blood pressure. Arrows show the change induced by RTKIs (green; increase and red; decrease). Figure adapted from Camarda et al. (2022), and created in Biorender.com.*

1.4.6.4. Management of hypertension

It has been suggested that hypertension has predictive value of the efficacy of treatment, and therefore could serve as biomarker for superior survival outcomes (Bono et al., 2011; Hamnvik et al., 2015; Izzedine et al., 2009; Jesus-Gonzalez et al., 2012). Consequently, as the development of hypertension is associated with increased survival, it is important to ensure that the antihypertensive therapy doesn't interfere with the anti-tumour mechanism and activity of antiVEGF therapy (Camarda et al., 2022; George et al., 2012).

No clear recommendations on what antihypertensive agents are preferred in cancer patients treated with antiangiogenic drugs are available, because lack of controlled studies addressing different strategies in this patients population (Caletti et al., 2018; Herrmann et al., 2016; Izzedine et al., 2009). General guidelines for application of antihypertensive agents should be followed and BP management should be adjusted based on individual clinical circumstances (Izzedine et al., 2009; B. Liu et al., 2016; Plummer et al., 2019). Lifestyle modifications are encouraged, however this is not always the most suitable approach for debilitated cancer patients (Izzedine et al., 2009). Angiotensin-converting enzyme (ACE)-inhibitors and angiotensin receptor antagonists are the preferred choice of antihypertensive agents in patients with proteinuria, another common ADR of anti-VEGF drugs, and patients with chronic kidney risks (Herrmann et al., 2016; Izzedine et al., 2009; Jesus-Gonzalez et al., 2012). Another class of drugs that is often suggested as first-line treatment in these patients, are the calcium channel blockers (CCB). Non-dihydropyridine CCB however (i.e. verapamil and diltiazem) should be avoided, as they are inhibitors of CYP3A4 and small molecule RTKIs are CYP3A4 substrates (Herrmann et al., 2016; Izzedine et al., 2009). Nifedipine, a dihydropyridine CCB is known to induce VEGF secretion, therefore this agent should also be avoided. The preferred CCB is amlodipine, as it has the ability to reduce vasoconstriction through inhibition of the calcium-influx in vascular smooth muscle cells (Izzedine et al., 2009; Jesus-Gonzalez et al., 2012; Plummer et al., 2019). Others antihypertensive that can be used are diuretics and betablockers (Izzedine et al., 2009; Jesus-Gonzalez et al., 2012). Furthermore, drugs increasing NO activity are promising agents to bring BP back to pre-treatment levels. For example long-acting nitrates (activating NO signalling pathways (Tarkin & Kaski, 2018)), phosphodiesterase inhibitors (inhibiting the breakdown of cyclic guanosine monophosphate (cGMP), a second messenger that mediates the NO-induced vasodilation (Kukovetz et al.,

1987)) and betablocker nebivolol (that increases NO production and release (Maffei & Lembo, 2009; Weiss, 2006)) could be useful in the management of high BP in these patients, but more evaluation in clinical trials is needed (Caletti et al., 2018; Izzedine et al., 2009; Jesus-Gonzalez et al., 2012). Similarly, ET-receptor antagonists are under investigation for this indication (Caletti et al., 2018; Jesus-Gonzalez et al., 2012).

1.4.7. Remaining challenges

Antiangiogenic therapies are increasingly being used in treatment of solid advanced tumours, but their therapeutic use has been hindered by CV toxicity. Hypertension is often a dose-limiting factor, therefore this ADR should be carefully monitored and managed in patients receiving these drugs. No specific guidelines for antihypertensive strategies in patients treated with anti-VEGF RTKIs are available, so general guidelines should be followed. It is not yet clear to what extend the increased BP should be lowered (Izzedine et al., 2009; Jesus-Gonzalez et al., 2012; Plummer et al., 2019). Further research on the mechanisms of this anti-VEGFR2 hypertension is needed (Camarda et al., 2022; Herrmann et al., 2016; Touyz et al., 2017a). More complete understanding will facilitate the development of antiangiogenic strategies with a preserved therapeutic effect and more beneficial safety profile (Touyz et al., 2017b).

Not only the above-mentioned antiangiogenic drugs exhibit cardiovascular toxicity due to VEGFR2 inhibition. Other multikinase inhibitors that are binding VEGFR2 display a similar cardiovascular safety profile. An example of this is Syk inhibitor fostamatinib, as discussed above (Section 3.4), binding off-target at VEGFR2 and associated with a rise in BP (Connell & Berliner, 2019; Newland & McDonald, 2020; M E Weinblatt et al., 2010). In this thesis, alongside well-known VEGFR2 inhibitors, the cardiovascular safety profiles of Syk inhibitors fostamatinib and entospletinib are characterised and presented as an example to explore novel tools in cardiovascular safety pharmacology. A new approach for in-depth waveform analysis, SPAR, was applied on cardiovascular waveforms recorded in rats (blood pressure and blood flow waves) and novel markers for cardiovascular toxicity were investigated.

1.5. Cardiovascular waveform analysis

1.5.1. Generation and physiology of the cardiovascular waves

Both BP and blood flow are haemodynamic waves, defined as a change in pressure or flow that propagates along the blood vessel. They produce periodic pulse waveform signals, presenting as a repeating cycle at a particular location in the vasculature (Mynard et al., 2020; W. W. . Nichols et al., 2022). The characteristics of the profile of the BP waves and blood flow waves are the result of a complex interplay of several components in the cardiovascular system (Kelly et al., 1989; Kips et al., 2009; Namasivayam et al., 2009; Wilkinson et al., 2002). Left ventricular contractility and chronotropy, the diameter and wall elasticity of large arteries and the resistance in the microvasculature determine the pulse waveform, as discussed below. Theoretically the blood viscosity affects the waves as well, however this typically remains constant and therefore has a minimal effect on the overall wave (Avolio et al., 2009; Mynard et al., 2020; W. W. . Nichols et al., 2022).

Each cardiac contraction pumps blood out of the heart, generating a pulse that travels as a pressure through the vessels (Mynard et al., 2020; W. W. . Nichols et al., 2022; Townsend et al., 2015). At bifurcation points or at positions where properties of the vessel wall change (e.g. change in compliance or characteristic impedance of the vessel), part of the BP wave is reflected on the arterial wall, travels backwards and affects the pressure profile of the next wave (Figure 6A). In an arterial waveform, this reflection results in a second systolic peak and the anacrotic notch (indicated in Figure 7) (Avolio et al., 2009; S. Laurent et al., 2006; Townsend et al., 2015). The dicrotic notch in the aortic waveform is mostly attributed to the closing of the aortic valve in the heart (Figure 7) (Hoeksel et al., 1997; Kips et al., 2009).

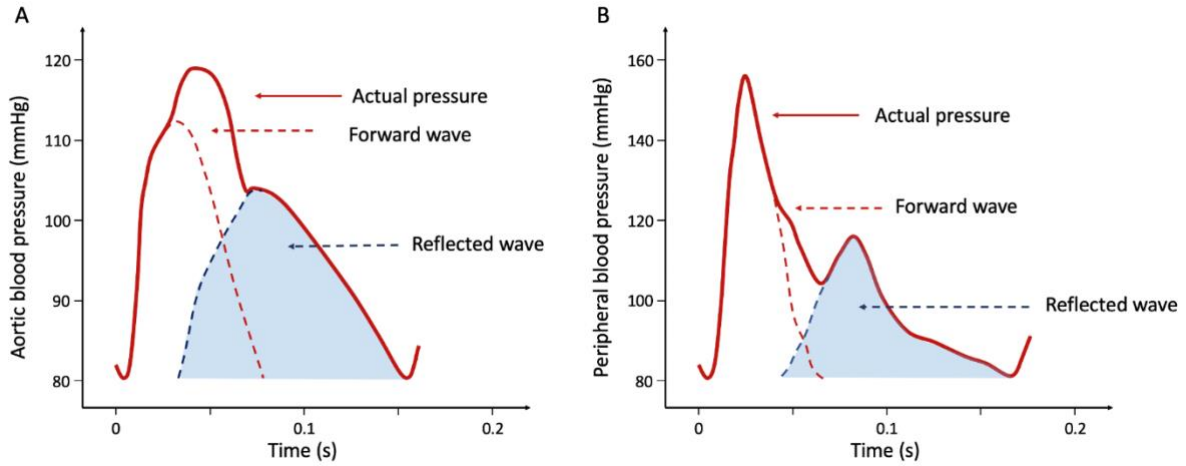

Figure 6: Differences in waveform reflection effects at different sites of the vascular tree. (A) *Schematic representation of the aortic pressure waveform. The reflected wave affects mostly the systolic part of the pulse.* ***(B)*** *Schematic representation of the peripheral wave. The reflected waveform creates an additional notch in the downstroke of the pulse. Figure adapted from Millasseau et al. (2003) and Avolio et al. (2009).*

It is important to note that wave reflections affect the peripheral waveforms in a different way than central waves. As shown in Figure 6B, in the a brachial wave, the reflected wave arrives during the late systole or diastole of the pulse and affects primarily the downstroke, rather than adding to the systolic peak pressure (Avolio et al., 2009; Kelly et al., 1989; Mills et al., 2000). Figure 6 is showing a simplified schema of the reflection effect from one wave. In reality, the final profile of the pressure wave is the sum of the forward wave and multiple reflected backward waves (Avolio et al., 2009; Mynard et al., 2020; Townsend et al., 2015).

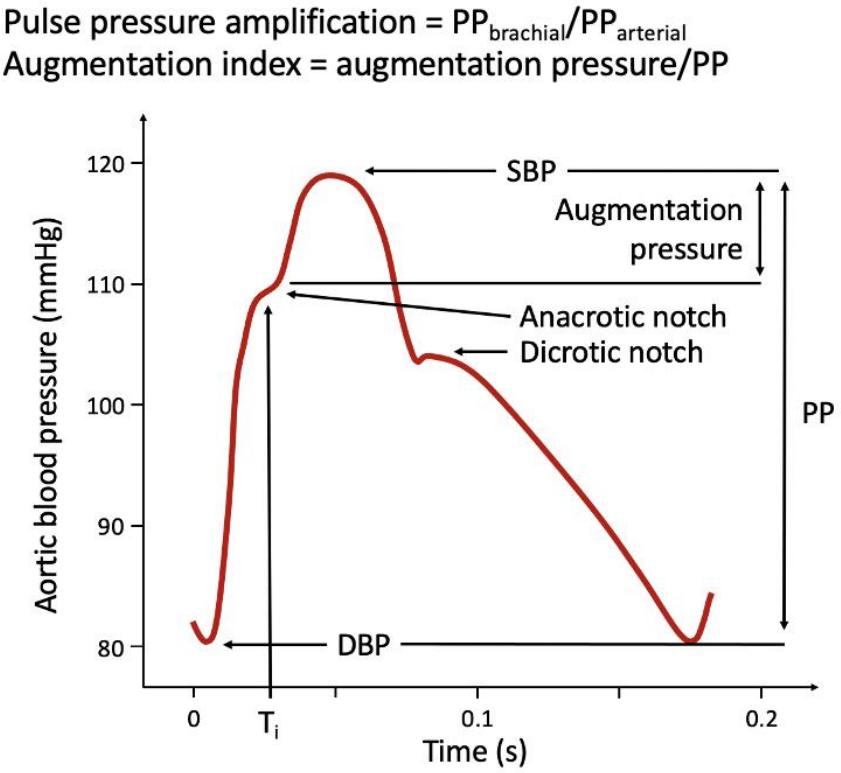

Figure 7: Components of the arterial pressure waveform. *The end-diastolic blood pressure (DBP) is the minimum pressure reached before the start of a new pulse. The systolic pressure (SBP) is the maximum pressure. Pulse pressure (PP) is defined as the difference between SBP and DPB. Due to waveform amplification, the PP is usually higher in peripheral waves than central waves. Pulse pressure amplification (PPA) is often reported as the ratio of brachial PP to central PP. The anacrotic notch indicates the onset of a reflected pressure waveform. The dicrotic notch in the aortic waveform is mostly attributed to the closing of the aortic valve in the heart. The augmentation pressure is defined as the difference between the pressure at the anacrotic notch and the SBP. The augmentation index (AIx) is the ratio of augmentation pressure to PP. The inflection time T_i indicates the time of onset of the reflected wave. Figure adapted from Millasseau et al. (2003) and Avolio et al. (2009).*

Importantly, the wave reflection effects are dependent on age, related to an increase in arterial stiffness and progressively earlier wave reflection (Kelly et al., 1989; Townsend et al., 2015). With aging, the aorta and arteries progressively stiffen due to strain, linked to a decrease in the compliance of the vessels (Namasivayam et al., 2009; W. W. Nichols et al., 2008). This typically leads to (1) an earlier return of the reflected wave and (2) a larger amplitude of the reflected wave, together resulting in an increase in aortic PP and SBP (Namasivayam et al., 2009; Phan et al., 2016).

To ensure tissue perfusion of all vital organs, MAP remains generally unchanged (minimum 60, typically between 70 and 110 mmHg) at different sites in the arterial vasculature and is maintained by several regulating mechanisms, such as the baroreflex of the autonomic nervous system and the renin-angiotensin-aldosterone system in the kidney (DeMers & Wachs, 2019; Leone et al., 2015). However, the amplitude of the waveform, i.e. the pulse pressure (PP), initially increases from the aorta to the elastic arteries, due to wave amplification effects (Avolio et al., 2009; W. W. . Nichols et al., 2022) followed by an attenuation of the PP as the pulse travels peripherally (Fritz et al., 2022), as shown in Figure 8.

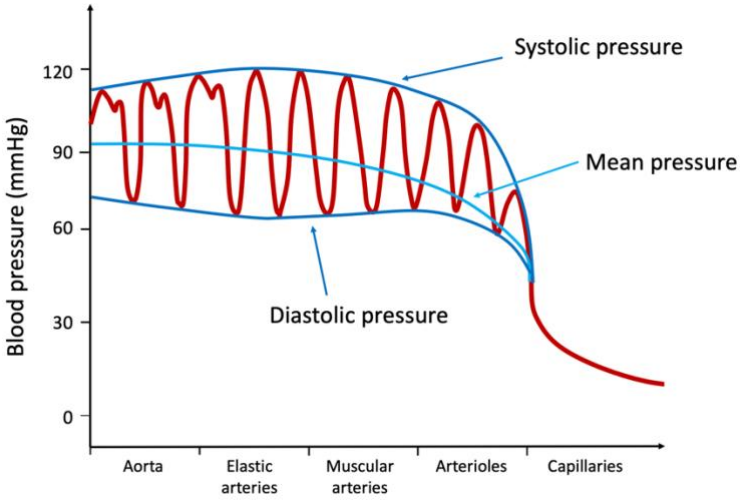

Figure 8: Typical pressure pulses in the systemic circulation. *Initially, an increase in amplitude of the pulse is observed (aorta to elastic arteries), followed by a decrease of the amplitude, as the wave travels peripherally. Figure adapted from Fritz et al. (2022).*

As described above, the blood flow presents as a pulsatile wave as well, that is affected by the contraction of the heart and wave reflection at impedance mismatches in the vascular tree (Holland et al., 1998; Masuda et al., 2013; Mynard et al., 2020). Blood flow is the movement of a volume of blood in the vessel, and is measured in volume/time (Hakim et al., 1994; Holland et al., 1998). Blood flow velocity refers to the speed at which the blood is moving through the vessel and is measured in distance/time (Gabe et al., 1969; Klarhöfer et al., 2001). Importantly, blood flow velocity is not to be confused with pulse wave velocity. The latter represents the velocity of the pulse wave – and not the blood itself – and is usually in the range of 5 m/s, thus approximately 10 times faster than the velocity of the blood (McEniery et al., 2008; Mynard et al., 2020).

Waveform reflection affects flow waves in the opposite way as pressure waves. As shown in Figure 9, instead of augmenting the overall flow - as observed in the BP - a reflected flow wave attenuates the wave, as it has the opposite direction of the forward wave. Indeed, flow waveforms therefore typically have an early-diastolic flow reversal (Masuda et al., 2013; Trihan et al., 2023).

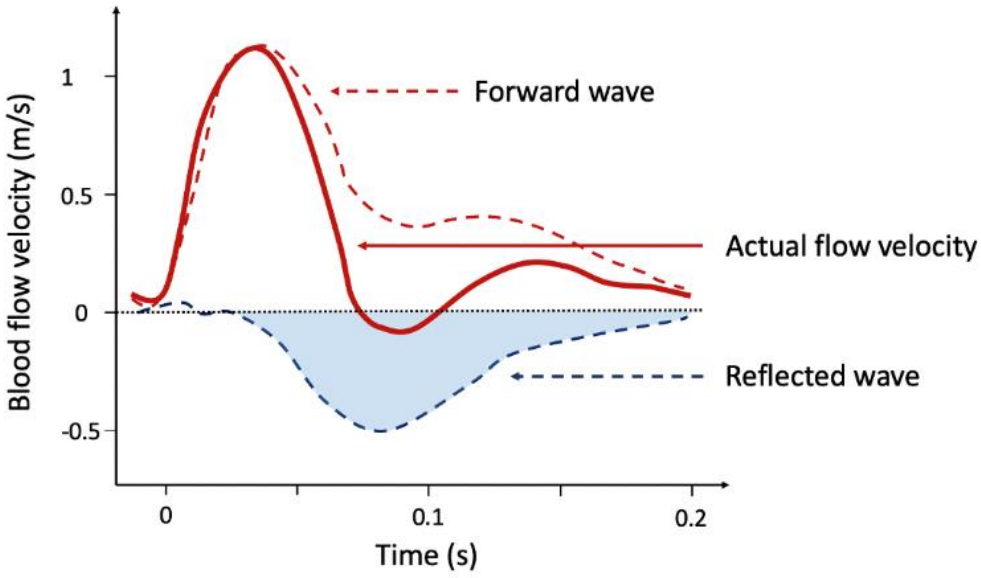

Figure 9: Schematic representation of blood flow wave reflection: *Reflected flow velocity wave will have a velocity opposite to the one of the forward wave, therefore attenuate the overall flow velocity. Figure based on Mynard et al. (2020) and Willemet and Alastruey (2015).*

1.5.2. High fidelity waveforms and conventional analysis

These BP and blood flow signals are recorded as high-fidelity numerical data, for example at a frequency of 500 Hz, i.e. 500 recorded data points per s (Greene et al., 2007; Wessel et al., 2007). To analyse the periodic signals, several mathematical methods can be employed to extract information of the waveform and report this as a simplified output that is easy to interpret (e.g. MAP or PP) (Laurent *et al.*, 2003; Papaioannou *et al.*, 2016). Conventionally, this analysis is performed by extracting peak values or single point averages from the BP waves; the systolic and diastolic BP (SBP and DBP, Figure 7) or MAP (Athaya & Choi, 2022). The SBP is defined as the maximum pressure reached, the DBP is the minimum pressure before the start of the next pulse (Avolio et al., 2009). Mean arterial pressure is calculated as:

$$MAP = \frac{2*DBP+SBP}{3}$$

where MAP is mean arterial pressure, DBP is diastolic blood pressure and SBP is systolic blood pressure.

The conventional analysis of MAP, SBP or DBP uses only a small subset of these data points and averages these out for further analysis (e.g. (S. L. Cooper et al., 2019) reporting on MAP, HR, SBP and SBP) (Mynard et al., 2020; Nandi et al., 2022; O'Rourke & Jiang, 2001). Although these values allow the calculation of important haemodynamic variables, this approach neglects a potential wealth of information hidden in subtle changes to the waveform morphology and variability (Aston et al., 2018; Mynard et al., 2020; Nandi & Aston, 2020). There is emerging evidence that changes in the waveform morphology reflect important physiological changes, for example a change in compliance of the vessels (W. W. Nichols et al., 2008) and arterial stiffness (O'Rourke et al., 2016). Subtle waveform changes have proven meaningful markers in several pathologies, amongst others coronary heart disease (Otsuka et al., 2006). These examples indicate that these high-fidelity waveforms contain information that could help answering important questions when assessing the safety of new drugs. In-depth characterisation beyond MAP, SBP and DBP, may provide more extensive information on the condition of the heart and vasculature when exposed to drugs and help in early detection of CV safety liabilities, serving as potential predictive markers.

1.5.3. Beyond MAP: approaches for in-depth analysis of cardiovascular waveforms

Wave analysis techniques aim to uncover the wave reflection effects and provide insight into how they change in the pulse waves (Mynard et al., 2020; O'Rourke & Jiang, 2001). The currently two most used approaches for waveform analysis are discussed below: HR variability and pulse wave analysis.

1.5.3.1. Heart rate variability

A well-established type of wave analysis is HR variability (HRV). HRV extracts the variation in HR over time, thus indicates fluctuations of the heart beat over time (Acharya et al., 2006; Karim et al., 2011). HRV is typically calculated from the ECG signal (as the RR intervals, the time interval between two consecutive R-peaks), but can also be determined from the pulse wave (as DBP intervals, the time interval between the DBP of two consecutive pressure waves) and is sometimes referred to as pulse rate variability (Kuang et al., 2022; Mejía-Mejía et al., 2021). This popular, non-invasive parameter reflects the ability of the heart and vasculature to adjust to changing circumstances and serves as an indicator for overall cardiac health. It has been proven useful in diagnosis and prognosis in several pathologies such as diabetes, renal failure, postinfarction follow-up, the myocardial infarction and sepsis and systemic inflammatory response syndrome. In Figure 10, examples of high and low HRV are presented. Generally, HRV is high in healthy subjects, but reduces under stress conditions. A reduction is HRV has been associated with an increased risk of cardiac events. Moreover, a decrease in beat-to-beat variation is an early marker for neuropathy in diabetic patients and for inflammation and infection (Acharya et al., 2006; Günther et al., 2012; Karim et al., 2011).

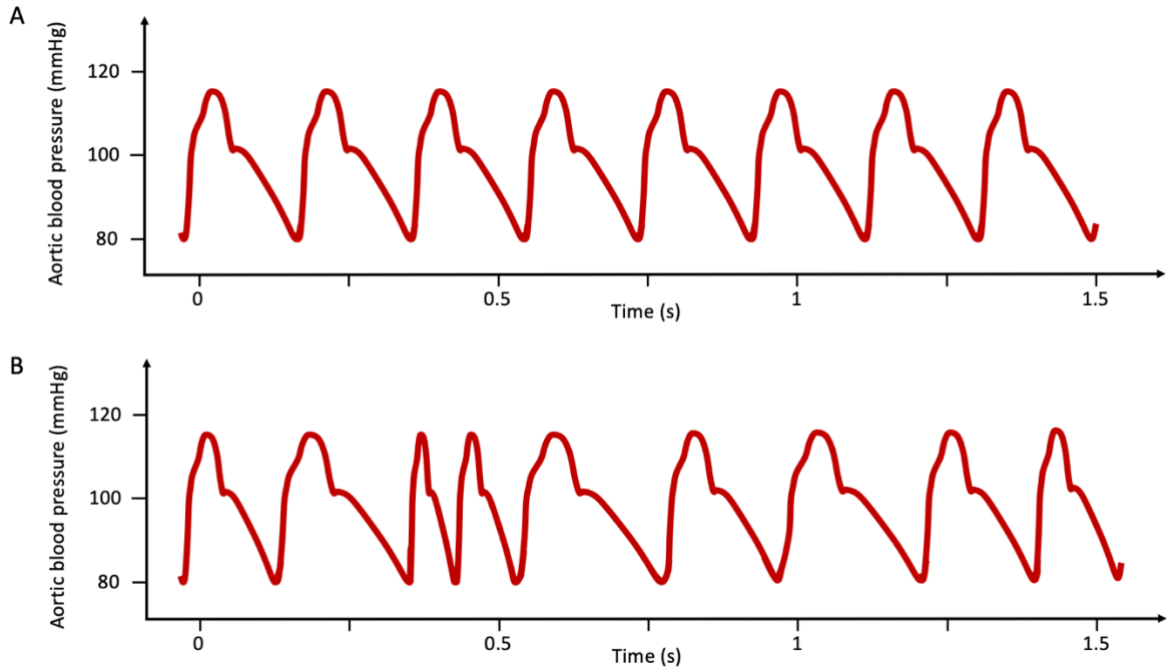

Figure 10: Heart rate variability (HRV) A. *Schematic example of a subject with low HRV.* ***B.*** *Schematic example of a subject with high HRV. Figure based on Kuang et al. (2022); Mejía-Mejía et al. (2021).*

1.5.3.2. Pulse wave analysis

In addition to HR variability analysis, the morphology of the waveform can be studied. There has been increasing interest in strategies to analyse the pulse waveform, the different components contributing to its profile, and the interpretation both central and peripheral waveform changes (Mynard et al., 2020; Townsend et al., 2015). The most used measures in pulse wave analysis are: (1) PP and pulse pressure amplification and (2) augmentation pressure, augmentation index and inflection time. An introduction to these parameters is given below.

Other parameters used in pulse wave analysis include pulse wave velocity, position of dicrotic notch (Figure 7) and upstroke gradient (Hermeling et al., 2009; Hoeksel et al., 1997; S. Laurent et al., 2006; D. P. Lyle et al., 1971; Nirmalan & Dark, 2014; Townsend et al., 2015; Weber et al., 2010).

Pulse pressure amplification

PP is the difference between SBP and DBP (Figure 7). Therefore the brachial PP is larger than the arterial PP and pulse pressure amplification (PPA, i.e. the ratio of brachial PP to central PP), is a valuable parameter in clinical settings (Avolio et al., 2009; S. Laurent et al., 2006; Townsend et al., 2015). Importantly, the HR affects PPA; a slower HR leads to a relatively earlier return of the reflected wave. Therefore the peak of the reflected wave will coincide with the SBP of the forward wave, resulting in an augmentation of the aortic SBP and PP (Millasseau et al., 2003; Wilkinson et al., 2002). Moreover, as detailed above (section 1.5.1.), with aging, arterial stiffening results in an increase in wave reflection and PP (Namasivayam et al., 2009; Phan et al., 2016). Given that HR, age and additionally sex appear to be the most influential predictors of PP, these variables should be taken into account when assessing PPA (Avolio et al., 2009).

A decreased PPA is associated with increased arterial stiffness and peripheral resistance, explained by the increase in wave reflection, thus increasing in central PP and decreasing the ratio of brachial over central PP. Indeed, traditional cardiovascular risk factors such as hypertension, hypercholesterolemia and diabetes have been associated with a decrease in PPA (Avolio et al., 2009; McEniery et al., 2008). Furthermore, in patients with end-stage renal disease, a low PPA was a predictor for CV mortality and again linked with an increase in arterial stiffness (Safar et al., 2002). Different classes of drugs display different effects on PPA (Laurent *et al.*, 2003; Avolio *et al.*, 2009). Some antihypertensive drugs with vasodilating actions increase the PPA due to a decrease in wave reflections. Examples are ACE-inhibitors, angiotensin receptors antagonists, calcium channel blockers and nitrates (Avolio et al., 2009). Atenolol, a beta adrenoceptor antagonist has been reported to decrease the PPA, most likely due to their bradycardia-inducing action and subsequent addition of reflection waveforms to the systolic peak in the central pressure wave (Dhakam et al., 2008). The extent to which this is clinically meaningful and whether this also applies to other beta-blockers is not entirely clear (Laurent *et al.*, 2003; Dhakam *et al.*, 2008; Avolio *et al.*, 2009; Pucci, Battista and Schillaci, 2014)

Rather than replacing the systolic, diastolic or mean pressure, PPA could serve as an additive prognostic value and help in decision making by providing additional information on the patient's cardiovascular health. A caveat of PPA is its need for simultaneous measurement of pressure waves at two sites of the vasculature (Avolio et al., 2009; Townsend et al., 2015) which is not routinely done in either preclinical or clinical settings.

Augmentation index and inflection time

Another parameter used in pulse wave analysis is the augmentation index (AIx), an indicator of wave reflection from peripheral vessels (Millasseau et al., 2003; Weber et al., 2010). The augmentation pressure is defined as the difference between pressure at the time of inflection and the SBP (Figure 7). Consecutively, the AIx is calculated as the ratio of the augmentation pressure over PP (González-clemente et al., 2021; Jeroncic et al., 2016; S. Laurent et al., 2006). Next to AIx, the time of inflection point (T_i) has been suggested as measure of transit time of waves to travel from the ventricle to the reflection site and back to the site of measurement (Hasanzadeh et al., 2020; Trudeau, 2014), however it's interpretation has been controversial (Mynard et al., 2020).

The AIx is determined by a combination of many factors, amongst others the ventricular ejection duration, the pulse wave velocity and naturally the stiffness of the large vessels (Millasseau et al., 2003; Obara et al., 2009; J. E. Sharman et al., 2009; Weber et al., 2004). Moreover, AIx is strongly dependent on HR. As stated above, a slower HR leads to a relatively earlier arrival of the reflected wave to the forward wave, therefore results in a larger augmentation of the SBP (Millasseau et al., 2003; Wilkinson et al., 2002).

An increase in aortic AIx indicates an increase in arterial stiffness and is predictive for severe cardiovascular events. On the other hand, pharmacological interventions resulting in a reduction of AIx are considered beneficial, as this indicates a destiffening of the arteries. Examples are ACE-inhibitors, angiotensin receptors blockers, CCBs and nitrates. AIx might help when identifying patients who might benefit from such treatment (Millasseau *et al.*, 2003; Weber *et al.*, 2010; Janić, Lunder and Šabovič, 2014; Townsend *et al.*, 2015).

Limitations of algorithms for pulse wave analysis

For correct calculation of the pulse wave parameters, high quality and sufficiently high frequency data are needed (Avolio et al., 2009; Millasseau et al., 2003; Mynard et al., 2020). Moreover backward and forward wave components need to be correctly identified. To determine parameters such as the inflection point and correctly calculate AIx, algorithms of pulse wave analysis are needed (Avolio et al., 2009; Mynard et al., 2020; N. Westerhof et al., 1972). These mathematical methods of pulse wave analysis use principles of fluid dynamics and time-domain principles to determine of the parameters of the pulse profile discussed above (Mynard et al., 2020; W. W. . Nichols et al., 2022; Parker, 2009; N. Westerhof et al., 1972). The two methods most studied to accurately label all components of the pulse wave are pulse wave separation (PWS) and wave intensity analysis (WIA) (Avolio et al., 2009; Hametner et al., 2013; Mynard et al., 2020). However, these methods require, additional to the pressure signal, simultaneous recording of a blood flow or blood flow velocity signal (Avolio et al., 2009; R. W. Chang et al., 2017; Mynard et al., 2020). The latter two are not routinely available during safety screening in preclinical models. Although some methods can perform wave analysis using a pressure signal only and are therefore more widely applicable (Kips et al., 2009; B. E. Westerhof et al., 2006), these methods are based on multiple assumptions and are therefore less informative (Kips et al., 2009; Parragh et al., 2015). Efforts have been made to improve the accuracy of these pressure-only methods by using estimations of the flow waveform simulated *in silico* (Hametner et al., 2013; Qasem & Avolio, 2008; B. E. Westerhof et al., 2006), however these have not yet been proven widely applicable due to poor correlations of the predicted and actual wave reflection (Kips et al., 2009; Mynard et al., 2020; Parragh et al., 2015).

Overall, both PWS and WIA are not broadly applied yet (Mynard et al., 2020). This is partly due to their need for further clinical validation, but also because of the need of simultaneously blood flow (velocity) recordings and the complexity of these methods (Kips et al., 2009; Mynard et al., 2020).

1.5.4. Blood flow waveform analysis

Although less extensively studied in the literature, the same principles of pressure waveform analysis can be applied on flow waves. With methods of wave separation, forward and backward waves components can be identified (Masuda et al., 2013).

Efforts have been made to understand several components of a flow pulse. For example, Masuda *et al.* (2013) have defined five characteristics of the simulated carotid artery flow velocity waves: first and second systolic peak of flow velocity (S1 and S2 respectively, Figure 11), minimal end diastolic velocity and maximum diastolic velocity and the notch between systole and diastole. They found a strong correlation between the ratio of S2/S1 and arterial elasticity. A decreased vessel elasticity caused a decrease in S1 and an increase in S2, due to an earlier arrival of the reflected waveform at the site of measurement (Masuda et al., 2013). Furthermore, Trihan et al. proposed acceleration time, i.e. the time of onset of the pulse until S1, and the maximum acceleration (Figure 11) as an diagnostic indicator for arterial stenosis (Trihan et al., 2023).

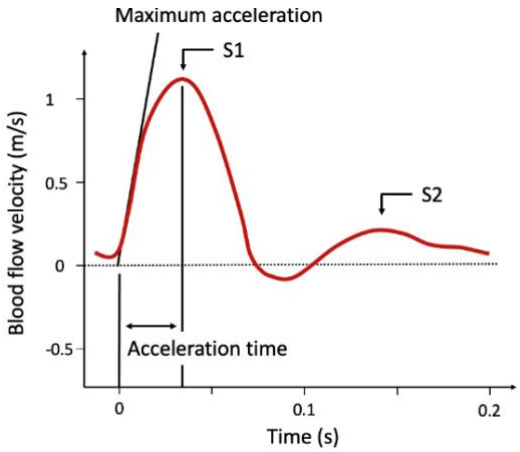

Figure 11: Examples of pulse wave analysis in the flow velocity wave. *Several parameters, such as S1 and S2, indicating the first and second peak of blood flow velocity respectively, maximum acceleration and the acceleration time are affected by waveform reflection and have been suggested as a useful tool for arterial stenosis diagnosis (Masuda et al. 2013, Trihan et al. 2023). Figure based on Mynard et al. 2020 and Willemet and Alastruey 2015.*

As with pressure waves, flow waves at different sites of the vasculature are affected in different ways by wave reflection and the actual flow is the result of the forward flow and multiple reflected flows (D. N. Ku, 1997; Masuda et al., 2013; Olufsen et al., 2000; Willemet & Alastruey, 2015).

1.5.5. Symmetrical Projection Attractor Reconstruction (SPAR)

The wave analysis methods mentioned above have obvious limitations, such as the requirement of simultaneous measurements of either BP at two sites, or BP combined with blood flow (Avolio et al., 2009; Mynard et al., 2020). Moreover, noise and natural variability often complicate the automated detection of the waveform analysis methods (Friesen et al., 1990; Nandi et al., 2022; Smulyan, 2019). A technique that may overcome these limitations is the mathematical signal processing method Symmetric Projection Attractor Reconstruction (SPAR) (Aston et al., 2018; Nandi & Aston, 2020). A scheme of the SPAR method is shown in Figure 12. Essentially, by applying the SPAR method on raw waveform data, an 'attractor' image is generated. Details on how the attractor is generated are described in Chapter 2, section 2.3.2.1. From this attractor image, distinct quantifiable features (e.g. colour or size of the inner triangle) can be extracted. These features reflect changes in variability or morphology of the raw waveform data (Aston et al., 2018; Nandi & Aston, 2020). SPAR does not take specific fiducial point measures from the waveform (such as the peak and trough), but uses the entire waveform data to generate an attractor which reflects and enlarges subtle changes in the wave (Aston et al., 2018; Nandi & Aston, 2020). In this way, SPAR facilitates the visualisation and quantification of waveform variability and morphology changes and is able to highlight subtle differences that would be less obvious when focusing on MAP, SBP or DBP alone (Aston et al., 2018; Nandi & Aston, 2020). The details of this method are described extensively in Chapter 2, section 2.3.

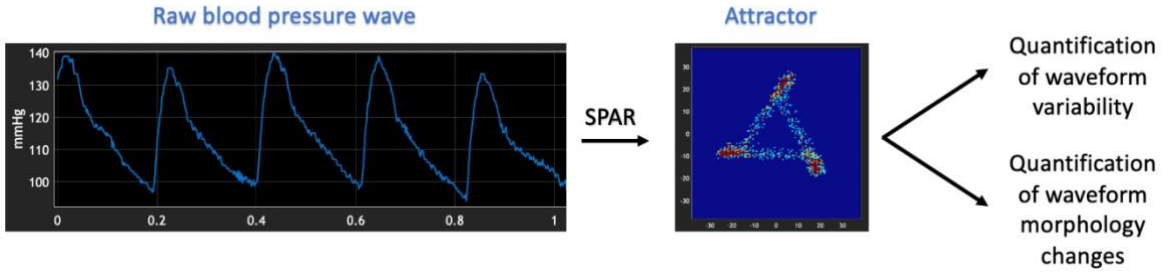

Figure 12: Schematic of the Symmetric Projection Attractor Reconstruction (SPAR)*: Raw waveform data are used to generate an attractor. This attractor reconstruction of the wave contains all data recorded in the raw wave, and furthermore enlarges small changes in the raw waveform. From this attractor, measures can be taken and quantified (e.g. e.g. colour or size of the inner triangle) that reflect these changes in the raw waveform.*

SPAR overcomes several issues that have impeded analysis of entire waveforms in the past. This method uses all the recorded datapoints, rather than taking single fiducial points of the waveform, and it can be used in the analysis of lengthy traces (Aston et al., 2014; Nandi et al., 2018). Additionally, unlike methods of PWS and WIA, SPAR does not need accompanying flow waves to quantify wave characteristics. Importantly, SPAR is a visual method, therefore may be easier to implement, which proved to be challenging with other wave analysis methods (Jin et al., 2023; Mynard et al., 2020). Lastly, a key step in SPAR means that it is largely unaffected by baseline wander of the original, making the method suitable for more noisy, real world data (Aston et al., 2014; Nandi et al., 2018).

SPAR is proven to be an effective method to detect small changes in human BP signals (Aston et al., 2018; Nandi & Aston, 2020). For example, cardiovascular diseases (CVDs) with different origins affected single point wave measurements in similar ways yet showed distinctive SPAR features (Aston et al., 2018; Nandi & Aston, 2020). Moreover, SPAR can be applied to any approximately periodic waveform, e.g. ECG (Bonet-Luz et al., 2020; J. V. Lyle et al., 2017) or respiratory waves (Pascual et al., 2021) and showed promising results regarding early and sensitive detection of physiological changes in these signals. So far, SPAR has been applied to *in silico* data (Aston et al., 2018; Nandi et al., 2018; Serna-Pascual et al., 2023), investigated in clinical settings (P. H. Charlton et al., 2015; Y. H. Huang et al., 2022; J. V. Lyle et al., 2017) and employed on ECG data recorded in a mouse model (Bonet-Luz et al., 2020). These studies reported promising results with SPAR showing high robustness, high sensitivity to classify between sexes, and high accuracy to detect particular arrythmias from short ECG recordings (Aston et al., 2018; Y. H. Huang et al., 2022; J. V. Lyle et al., 2017). Furthermore, in a proof-of-concept study exploring the application of SPAR on BP data and providing a first indication of the physiological relevance of the attractor metrics, SPAR has been employed in blood pressure data recorded in unrestrained mice (Aston et al., 2018). Therefore the analysis of the cardiovascular waveform in its whole, could aid in the diagnosis of CVD and enable earlier detection of CV disturbances. Next to its contributions in diagnosis, SPAR could be a useful tool in a preclinical settings, or when monitoring patients' response to certain drugs (Bonet-Luz et al., 2020; Y. H. Huang et al., 2022; Nandi & Aston, 2020).

1.5.6. Application of waveform analysis in preclinical models for safety pharmacology

The vast majority of waveform analysis examples mentioned above, including SPAR, are predominantly studied in clinical settings, where they are tested for their ability to diagnose pathologies, or predict the outcome of medical interventions. Nonetheless, the same principles could be applied in the preclinical stages of drug development.

Using measured pressure and an estimated triangular flow, Chang *et al.* (2017) investigated waveform reflection timing and magnitude in chronic kidney disease, diabetes, and healthy Wistar rats. Amongst others, the arterial wave transit time (τ_w) was determined, as an indicator of return time of a reflected wave back to the aorta. Compared to the healthy group, τ_w was shorter in both the chronic kidney disease and diabetes group, indicating an increase in pulse wave velocity due to increased arterial stiffness (R. W. Chang et al., 2017). Additionally, both disease groups exhibited a larger pulse wave reflection magnitude. The same group investigated waveform components in anaesthetised Long-Evans rats of different ages. They found no change in the forward pressure wave, but an increase in magnitude of the backwards pressure waves with age. This was associated with an increased AIx and a reduction of τ_w/cycle length, indicating arterial stiffness and earlier waveform reflections from the peripheral circulation (C. Y. Chang et al., 2017).

Laurent *et al.* (2003) measured pressure waves simultaneously in the proximal and distal aorta, in anesthetised Wistar-Kyoto (WKY) and spontaneously hypertensive rats (SHR). The SHR group showed a decreased PPA compared to WKY, due to an increase in central PP. Administration of adenosine decreased the MAP and, in SHR, partially brought back the PPA, due to an increase in peripheral PP. Administration of acetylcholine caused a MAP decrease comparable to the one observed with adenosine, however did not affect the PPA in both WKY and SHR (Laurent *et al.*, 2003). Overall this study showed that drugs causing a similar effect on MAP, could affect central and peripheral PP in different ways and therefore have opposing effects on PPA.

Even though the studies above have limitation (e.g. performed in anaesthetised animals or assumed a triangular flow instead of measuring the flow wave), they showcase the application of waveform analysis in *in vivo* studies. Looking at minimal and maximal values of BP data alone may have limited value. More in-depth analysis of its waveform morphology and variability is potentially useful when evaluating cardiovascular safety liabilities of a drug candidate in preclinical settings. The application of SPAR on BP waveforms and blood flow waveforms could provide more nuanced information in CV safety testing and contribute to the understanding of the mechanistic cause of safety liabilities. Ultimately, this could aid in more informed decisions and enable earlier attrition of compounds with a poor safety profile.

1.6. Thesis research aims

Whilst the field of safety pharmacology has advanced drastically since the implementation of ICH S7A in 2001, and current approaches for detection of CV adverse drug effects often identify those safety risks, high attrition rates due to safety issues remain an important challenge. This thesis aimed to explore novel methods in CV safety pharmacology, in particular the application of SPAR. Syk inhibitors fostamatinib and entospletinib were used as an example of compounds with off-target CV adverse effects, to explore the in-depth wave analysis of BP and blood flow pulse waves. Indeed, their *in vivo* CV safety was characterised, first by conventional analysis as usually performed in preclinical safety testing (Chapter 3), followed by more extensive interrogation of their CV effects, by the application of SPAR (Chapter 4) and in the Doppler flowmetry model (Chapter 5). Finally, the Syk inhibitors were screened *in vitro* for VEGFR2 binding affinity and functional inhibition (Chapter 6), to provide insights into the selectivity and potency of these Syk inhibitors at VEGFR2 and link those observations to the *in vivo* findings.

Chapter 3: The aim here was to assess the cardiovascular effects of fostamatinib and entospletinib *in vivo* using the conventional wave analysis approach. This was obtained by

- Assessing fostamatinib and entospletinib, alongside two vasodilators (vardenafil and molsidomine) and one RTKI (sunitinib), in radiotelemetry in rats.
- Performing conventional wave analysis and investigating the compounds' effects on MAP, HR and PP.

Chapter 4: This Chapter aimed to explore the application of SPAR on the BP data obtained in Chapter 3 and had the following objectives:

- To optimise SPAR for use in BP wave analysis recorded in rats.
- To validate SPAR for use in BP wave analysis recorded in rats (i.e. investigate if the method was able to detect variability and morphology changes in the waves).
- To assess the effects of the two Syk inhibitors on selected SPAR metrics and compare their effects to the ones observed with the vasodilators and sunitinib.

- Lastly, overall to explore if SPAR could provide any additional insights in the cardiovascular safety of these Syk inhibitors, that were not apparent from the conventional wave analysis in Chapter 3.

Chapter 5: This Chapter aimed to explore the application of SPAR on blood flow velocity waves by interrogating the effects of the Syk inhibitors on regional vascular conductances and the blood flow velocity waves. This was investigated by:

- Assessing the Syk inhibitors, alongside sunitinib, in the Doppler flowmetry model in rats.
- Analysing the obtained blood pressure and three blood flow velocity waves by conventional analysis (MAP, HR and vascular conductances).
- Extending the application of SPAR to the blood flow waves to investigate morphology and variability alterations in flow waves between different vascular beds and after different drug treatments.
- Lastly, overall exploring if SPAR could SPAR could provide any insights into the safety of fostamatinib and entospletinib, that were not apparent from the conventional vascular conductance analysis?

Chapter 6: The aim of this Chapter was to characterise the *in vitro* effects on the Syk inhibitors at VEGFR2. To give mechanistic insights into the observations made in the *in vivo* studies, the following objectives were set:

- To develop and optimise an *in vitro* nanoBRET assay to assess direct binding of the inhibitors at the intracellular site of VEGFR2, followed by the determination of the binding properties of fostamatinib and entospletinib at VEGFR2.
- To assess the VEGFR2-signalling inhibition by fostamatinib and entospletinib in the NFAT reporter gene assay, previously described by Carter *et al.* (Carter et al., 2015).

2. CHAPTER 2: MATERIALS AND METHODS

2.1. Radiotelemetry

2.1.1. Telemetry to monitor blood pressure in freely moving rats

2.1.1.1. Technique: history and overview

The use of implantable radiotelemetric devices as published for the first time in 1991, by Brockway *et al.*, describing accurate measurements of blood pressure (BP) and heart rate (HR) in conscious and freely moving rats (Brockway BP, Mills PA, 1991). Radiotelemetry in rats is now a routinely used model to evaluate the effects of a drug candidate on cardiovascular parameters (Kramer & Kinter, 2003; Sarazan et al., 2011), and a valuable tool for predicting the safety profile of therapeutics in humans (Iversen et al., 2013; Kramer & Kinter, 2003; Niemeyer, 2016). Small, implantable radiotelemetric devices are commercially available, allowing for wireless recording of physiological variables such as BP and HR, but also electrocardiogram (ECG), electroencephalogram, body temperature and activity (as a qualitative measurement of movement) (Kramer & Kinter, 2003; Niemeyer, 2016). In addition to short-term data recording (Isobe et al., 2014), radiotelemetry is an ideal tool for assessing long-term cardiovascular consequences and accurately representing clinical conditions in rodents (S. L. Cooper et al., 2019; Kramer & Kinter, 2003; Mills et al., 2000; Niemeyer, 2016).

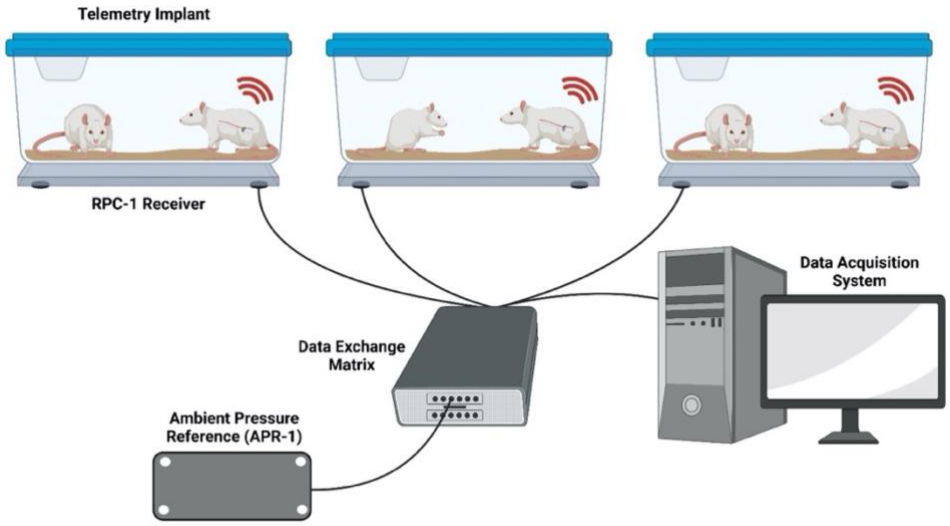

***Figure 13: General set-up of a radiotelemetry study**. Animals are generally co-housed with either an un-instrumented cage mate, or, in more recent multi-channel systems, with another instrumented rodent. Created with Biorender.com*

2.1.1.2. Technique advantages

In comparison to other methods of BP monitoring, radiotelemetry's two main advantages are its high data quality and advancements in animal welfare, detailed below (Kramer & Kinter, 2003; Niemeyer, 2016). Radiotelemetric data are collected in unrestrained animals, minimising stress effects (Kramer & Kinter, 2003). In contrast, BP measurement using, requires restraint of the animal. This leads to animal distress and subsequent alterations of BP, HR and body temperature, therefore artefacts in the recorded data (Crestani et al., 2010; Kramer & Kinter, 2003; Sharp et al., 2002). Data collection from undisturbed animals in their home cages is preferable as these conditions are more representative for the normal state of the animal and therefore the data have a higher predictive value (Kramer & Kinter, 2003; Niemeyer, 2016; Matt Skinner et al., 2019).

Radiotelemetry can be performed in conscious rats. Many anaesthetic drugs have a depressant effect on the respiratory and cardiovascular function (Flecknell, 2015). Additionally, these anaesthetics can affect homeostatic reflexes that influence HR and BP. For example, the arterial baroreflex is one of the major reflexes that contributes to acute changes in cardiovascular system. This neural reflex aims to regulate a constant blood pressure and a rise in BP will be counteracted by decrease in HR, vascular resistances and cardiac contractility, via a parasympathetic activation and sympathetic inhibition (Kougias et al., 2010; Pang, 2001). Several commonly used anaesthesia interfere with this baroreflex (Fluckiger et al., 1985; Rocchiccioli et al., 1989; Shimokawa et al., 1998). Recording of cardiovascular variables in anaesthetised animals is therefore not ideal, as the cardiovascular function might be impaired and anaesthetic drugs may interfere with the response to the test compound. In conscious rats however, the experiment is carried out in representative physiological conditions, better reflecting the normal state of the animal with baroreflex intact (Carter et al., 2017; Wragg et al., 2022). Hence, although surgeries to implant radiotelemetry devices might require expertise and invasive measurements in anaesthetised animals might in some cases be less time-consuming, radiotelemetry studies generally yield data with higher physiological relevance.

Additionally, telemetry improves animal welfare in several ways, presenting several other advantages over related techniques. Firstly, telemetry recordings can be conducted from socially housed rats (Figure 13) (Matt Skinner et al., 2019). New systems, such as the TSE Stellar telemetry used in this thesis, are allowing simultaneous recording of parameters from multiple instrumented animals in a single cage, reducing the number of animals used as there is no need for uninstrumented cage buddies (Kramer & Kinter, 2003; Rieux, 2008). Secondly, multiple variables can be recorded from one animal, decreasing the need for separate studies and further reducing the total number of animals used (Kramer & Kinter, 2003; Niemeyer, 2016). Furthermore, with suitable precautions about long-term drug effects, animal reuse is possible, thanks to the long lifetime of the implant's battery (Kramer & Kinter, 2003). Lastly, as mentioned above, radiotelemetry can be performed in freely moving animals, in contrast to related techniques, for example the Doppler flowmetry model described below (Section 2.2), where animals are tethered during experimentation.

2.1.1.3. Technique details

To monitor blood pressure, a catheter with blood pressure sensor is positioned intravascularly in the carotid or femoral artery or in the abdominal aorta (Woolard et al., 2003). In this thesis, TSE Stellar real time telemetry implants were used. This set-up uses solid-state catheter tips, consisting of a silicon chip as pressure sensor (TSE systems, 2020). Compared to gel- or fluid-filled pressure catheters, solid-state tips are suggested to deliver pressure data with higher accuracy, sharper peaks and less artifacts (AD Instruments & Williams, 2022). Gel- or fluid-filled sensors measure the pressure indirectly; detection of the pressure relies on transmission of the signal through the gel or liquid in the tip of the sensor. This indirect measurement can be compromised by changes in the gel/liquid properties, bubble formation or movement of the animal, possible leading to dampening of the signal (AD Instruments & Williams, 2022). Solid tips don't suffer from these disadvantages as the silicon chip is in direct contact with the site of interest, and measures pressure directly. They would therefore be more suitable for acquiring high quality data for further in-depth waveform analysis (AD Instruments & Williams, 2022).

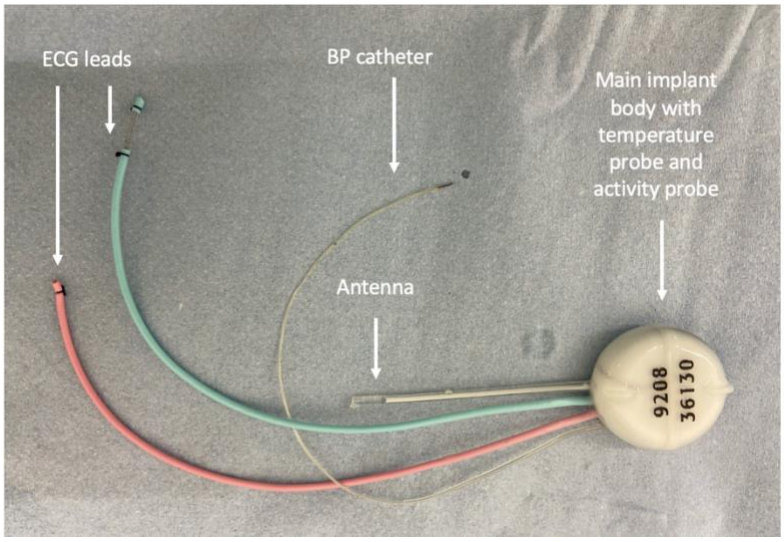

Figure 14: TSE Stellar telemetry implants. *The implant consists of a main body, that contains the temperature and activity probe and battery. This body is connected to the ECG leads and BP catheter. Furthermore, a transmitter inside of the body leads the antenna, sending radio signals to the receiver outside of the cage.*

The catheter is connected to an implantable radio telemetry device that contains a battery and electronic module, the transmitter, that processes the information measured by the sensor and transmits it, via the antenna, to the receiver outside of the cage (Figure 13). The radiotelemetry receiver is placed below or on top of the cage and receives radio signals from the transmitter antenna (Figure 13). The TSE Stellar set-up is able to receive radio signals at different frequencies from up to two transmitters, therefore allowing the use of one receiver per cage housing two animals (TSE systems, 2020). Digitalised signal are then transferred to the data acquisition system for analysis (Kramer & Kinter, 2003; Niemeyer, 2016).

Overall, the TSE Stellar set-up uses a solid-tip blood pressure sensor and allows for the transmission from two implanted devices to one receiver per cage, therefore simultaneous measurements from two animals in one cage can be made. Given these advantages over e.g. the DSI telemetry system that uses a gel-filled catheter, the Stellar set-up was chosen for the telemetry studies performed in this thesis.

Besides the blood pressure sensor, the implantable device contains two ECG leads, a sensor for temperature and for activity (Figure 14). This allowed for measurement of ECG, body temperature and activity of the animals as well. However, in this thesis, the focus was on BP waveforms recorded with this telemetry set-up. Heart rate was derived from the ECG measurements.

2.1.2. Materials

Vardenafil HCl was obtained from Merck KgaA (Darmstadt, Germany). Molsidomine, fostamatinib (R935788), entospletinib (GS-9973) and sunitinib-malate were purchased from Generon (Slough, UK). Test compounds were dissolved in 10% hydroxypropyl beta cyclodextrin (Trappsol®, CTD, Inc) in water for injection.

Isoflurane was used as anaesthetic (Merial Animal Health, UK). Isoflurane acts on γ-aminobutyric acid (GABA), glutamate and glycine receptors and NMDA receptors, causing muscle relaxation, induction of analgesia by reducing pain sensitivity and induction and maintenance of anaesthesia (Capey, 2007). As post-operative analgesics, buprenofine (Bettinger et al., 2021) and meloxicam (Pacheco et al., 2020) were used. Buprenofine (Buprevet®,) a semi-synthetic opioid derivative was obtained from Virbac, Richter Pharma, Austria. Meloxicam (Metacam®), a non-steroidal anti-inflammatory drug (NSAID), was purchased from Boehringer Ingelheim, Germany. Bupivacaine hydrochloride was used as local anaesthetic (Marcaine®, Mercury Pharma, UK) (Shah et al., 2018).

2.1.3. Animals and surgery

2.1.3.1. Housing of the animals

Male Wistar Han rats (Charles River, Margate, UK), weighing > 400 g, were pair-housed in double-decker individually ventilated rodent cages either with another telemetry animal or, in case of an uneven number of telemetry animals, a non-instrumented cage mate. Environmental enrichment (tubes and nesting material) was provided. The animal room was illuminated by artificial light on a 12 h light/dark cycle, in a temperature (19-23°C) and humidity (40-70%) controlled environment. Animals had free access to food (Teklad global rodent diet, 18% protein) and water.

2.1.3.2. Surgery

All *in vivo* experimentation was approved by the Animal Welfare and Ethical Review Body (University of Nottingham) and performed under the Scientific Procedures Animals Act (1986), with UK Home Office approved Project Licence PP1632406, Protocol 3 and Personal Licence authority. Telemetry implant surgeries were carried out by Dr. Matt Skinner and Ed Hale, prior to the start of the student's placement at Vivonics Ltd.

The animal was placed in an anaesthesia Induction box with isoflurane (2 – 4%) until the animal righting reflex had disappeared. The animal was then removed from the induction box and placed on a facemask to maintain anaesthesia with 2% isoflurane. Before the start of the surgery, depth of anaesthesia was checked by the response to a hind paw pinch. The abdominal midline and the right side of the thorax were shaved and cleaned using Clinell® 2% chlorhexidine gluconate and 70% isopropyl alcohol wipes. To protect the eyes from drying out during surgery, an ocular gel was applied (Geltears® 0.2% w/w Carbomer eye gel, Bauch & Lomb). Buprenorphine (0.05 mg/kg) and meloxicam (1 mg/kg) was administered subcutaneously (SC). Animals were wrapped in clear surgical drape and a 4 cm cut was made to expose the area for laparotomy. Bupivacaine hydrochloride was applied down the midline of the peritoneum and the foot withdrawal and inguinal reflex were evaluated prior to the start of the surgery, to ensure anaesthesia. Surgeries were performed under aseptic conditions. To implant the telemetry device, an incision was made along the *linea alba* from below the sternum to the umbilical region. The aorta was occluded, a hole was made in the top and the blood pressure catheter was inserted into the aorta and advanced towards the cranial ligature. The position of the end of the catheter was checked under the microscope, to ensure parallel placement to the aorta. Tissue adhesive was applied around the catheter insertion site and a microscope check was done again to ensure no leakage of blood. A cellulose patch was placed over the vessel and catheter, and tissue adhesive was applied over the middle and edges of the patch. The telemetry device body, connected to the blood pressure catheter, was placed in the midline of the abdominal cavity wall and secured with a suture. ECG electrodes were implanted, one on the ventral surface of the xiphoid and one SC over the right pectoral muscle. The peritoneal cavity was irrigated with 5 mL of warm saline solution and skin incisions were closed. Isoflurane level was dropped during suturing to ensure quicker recovery. Once fully closed, bupivacaine hydrochloride was applied on top of

the wound. Buprenorphine (0.05 mg/kg) was administered SC on day 1 post-surgery. Additional doses of meloxicam (1 mg/kg) were administered SC on day 1 and 2 post-surgery. The animal's bodyweight, body condition, and behaviours were monitored every day for 7 days then once weekly thereafter. Animals were given a minimum of 14 days for recovery before the commencement of any experiments. Signal checks were performed prior to study start to assess the quality of the telemetry signal.

2.1.4. Experimental set-up

As the animals were housed in the dosing room, no acclimatisation before experimentation was necessary. On telemetry session days, recordings were made in the home cage. Each drug was administrated for 2 consecutive days. To ensure no overlap of drug effects, 7 days were left between different treatments as a wash out period. Details on the plasma half-lives of each compound are given in Chapter 3, section 3.2.3. An overview of the timing of the studies can be found in Table 1. All drugs were dissolved or suspended in 10% (w/V) hydroxypropyl beta cyclodextrin (CTD Inc.) in water for injection. This solution was used as vehicle in the control groups as well, dosed at 10 mL/kg. Every drug-treated group was compared with its corresponding vehicle group recorded in the preceding or following week.

Table 1: Timing of telemetry studies *- drug treatment and corresponding vehicles. Vehicles 1, 2 and 3 are the same (10% HPB CD in water), these were repeated to ensure comparisons between the drug-treated group and vehicle group could be made.*

	Timing	**Compound**	**Dose**	**Route of administration**
Week 1	16/5/22-17/5/22	vardenafil	10 mg/kg	Oral gavage dosing
Week 2	30/5/22-1/6/22	vehicle 1	10 mL/kg	
Week 3	8/6/22-9/6/22	sunitinib	7 mg/kg	
Week 4	15/6/22-16/6/22	entospletinib	6 mg/kg	
Week 5	22/6/22-23/6/22	vehicle 2	10 mL/kg	
Week 6	18/7/22-19/7/22	fostamatinib	20 mg/kg	
Week 7	26/7/22-27/7/22	vehicle 3	10 mL/kg	
Week 8	3/8/22-4/8/22	molsidomine	10 mg/kg	

Fostamatinib and entospletinib were evaluated as they are a first and second generation Syk inhibitor, respectively (Currie et al., 2014; Davis et al., 2011; D. Liu & Mamorska-Dyga, 2017). Additionally, two vasodilators were tested. Vardenafil induces a vasodilation by inhibiting phosphodiesterase 5 (PDE-5). Molsidomine acts as an NO-donor and has therefore similar effects as vardenafil on mean arterial pressure (MAP) and HR. These two compounds were selected as they are often used as reference compounds in safety studies, and cause a validation by acting on the same pathway, although through a different mechanism. Lastly, sunitinib was evaluated using telemetry. This drug is a non-specific receptor tyrosine kinase inhibitor (RTKI) developed for anti-angiogenic action in various cancer types and associated with VEGF2-induced hypertension (Davis et al., 2011; Neves et al., 2020).

Drug solutions or vehicle were dosed using oral gavage, in 10 mL/kg vehicle. As vehicle, 10% (w/V) hydroxypropyl beta cyclodextrin (CTD Inc.) in water for injection was used. Dose levels were chosen after literature review, with the aim to achieve therapeutic plasma levels while ensuring the dose was well tolerated over at least two days. On each day, prior to the experiment, animals were weighed, and dosing volume was adjusted accordingly. All animals were given a full examination by the Study Director or Licensee prior to the study and at the end of the study by the Named Veterinary Surgeon. When considered necessary by the Named Veterinary Surgeon, Study Director or Licensee, additional examinations were performed.

On each day of dosing, recording was done for at least 1 h before administration of the drug or vehicle, and up to 23 h post-dose for data collection. Arterial BP, HR, ECG, body temperature and activity were recorded continuously via the antenna placed near the cage. Animals were removed from their cages temporarily for dosing but were placed back directly after and not restrained during the remaining of the recording period. Animal welfare and behaviour were monitored immediately after dosing and throughout the day. Formal cage-side observations were made at approximately 1 h and 5 h post-dose.

2.1.5. Data collection software and statistical analysis

Data were recorded at 500 Hz and transferred through the TSE antenna to a PC-based data acquisition system using HEM software (Notocord Inc). Telemetry data were analysed and extracted into Excel for further analysis. For conventional waveform analysis (MAP, HR and pulse pressure (PP), data were extracted as means of superintervals, averages of time durations ranging from 1 h to 6 h. For in-depth waveform analysis, i.e SPAR, raw waveform numbers were extracted for further analysis in SPARKS (Section 2.3.3.).

All data were expressed as mean ± SEM. Statistical analysis was performed in Prism 9.5.1 (GraphPad Software, San Diego, CA, USA). As there were two categorical, independent variables (time and treatment) and one quantitative outcome variable (MAP, HR or PP), a two-way ANOVA was performed. This tested (1) if MAP/HR/PP was significantly different over time, (2) if MAP/HR/PP was significantly different between groups, and (3) if MAP/HR/PP was significantly different between groups over time. If the result of the two-way ANOVA were significant, multiple comparisons test were performed; a Dunnett test to determine where changes over time from baseline were significant and a Sídák test to determine where changes between groups were significant. Results were considered significant at $p < 0.05$.

2.2. Pulsed Doppler flowmetry

2.2.1. Measuring regional haemodynamic changes in conscious rats

2.2.1.1. Technique: history and overview

The use of pulsed Doppler flowmetry was reported for the first time in 1974, by Hartley and Cole, who used the *in vivo* approach for measuring regional blood flow in dogs (Hartley & Cole, 1974). Haywood *et al.* developed the method for application in rodents (Haywood et al., 1981) and Gardiner and Bennett further refined the model, as used in this thesis, at the University of Nottingham (Gardiner & Bennett, 1988). The implantation of up to three miniature ultrasonic probes allows for measurement of Doppler shift, and subsequent calculation of vascular conductance (VC) in several regional beds, including the renal, superior mesenteric, and hindquarters vascular beds (Figure 15) (Bennett et al., 2004; Gardiner et al., 1996). Additionally, BP and HR are monitored using intra-arterial catheters (Bennett et al., 2004; Carter et al., 2017; Gardiner et al., 1996).

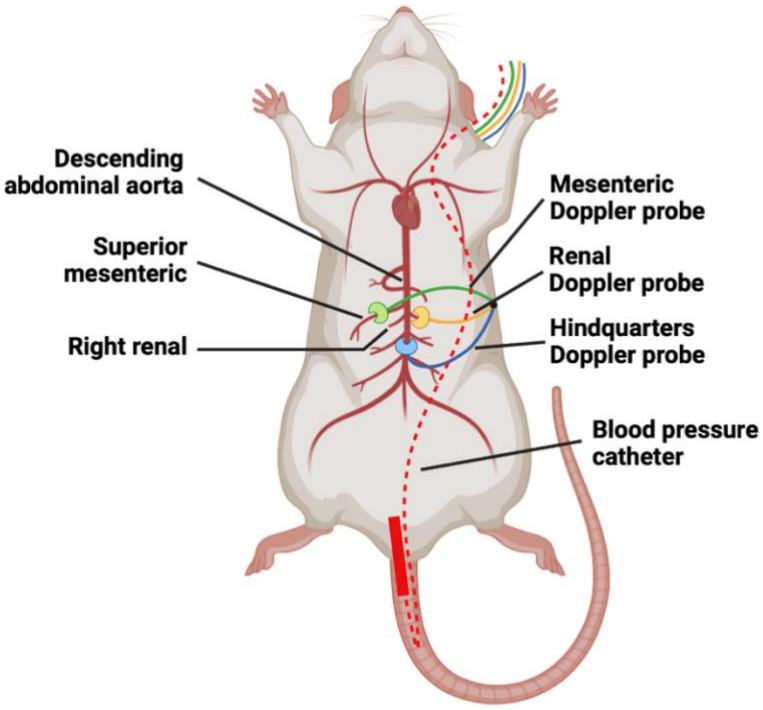

Figure 15: Position of the pulsed Doppler probes and blood pressure catheter. *Up to three Doppler probes for monitoring blood flow can be implanted. Additionally, a fluid-filled catheter is implanted to record blood pressure in the distal abdominal aorta. Created with Biorender.com. Figure adapted from Van Daele et al. (2022).*

2.2.1.2. Technique advantages

Compared to the pulsed Doppler probes, traditional electromagnetic probes to monitor blood flow are larger, heavier and often difficult to calibrate (Hartley & Cole, 1974). Similarly, continuous-wave transonic Doppler probes are large in size and hard to place correctly on the vessel (Haywood et al., 1981). In contrast, the pulsed Doppler system utilizes a small piezoelectric crystal (~ 1 mm), that emits and receives pulsed ultrasonic energy, and can easily be positioned around small vessels (Hartley & Cole, 1974; Haywood et al., 1981). This technique therefore provided a significant advancement in measuring blood flows and additionally captures around 70% of cardiac output.

As with radiotelemetry, the Doppler flowmetry model uses conscious, freely moving rats, with the advantages mentioned above (section 2.1.1.2) (Gardiner & Bennett, 1988; Woolard, Bennett, et al., 2004). Cardiovascular radiotelemetry is, however, mostly restricted to monitoring BP, ECG and HR. Nonetheless, pharmacological agents can affect peripheral haemodynamic variables without evoking a significant change in overall BP (e.g. regional vasoconstrictions or vasodilatations) (Bennett et al., 2004; Gardiner et al., 1996; Woolard, Bennett, et al., 2004). As demonstrated before (Bennett et al., 2004; Carter et al., 2017; Gardiner et al., 1996; Woolard, Bennett, et al., 2004), different vascular beds may respond differentially, and even in opposing ways. These changes may go undetected when evaluating cardiovascular safety using radiotelemetry. In contrast, Doppler flowmetry measures the regional effects on distinct vascular beds and is thus an ideal tool to obtain critical and comprehensive information on peripheral responses to drug exposure.

2.2.1.3. Technique details

The flow probes used in this Doppler model are produced in-house, to the design as proposed by Haywood *et al.* (Haywood et al., 1981). The piezoelectrical crystal for flow detection is attached to insulated copper wires, and mounted inside the silastic cuff, so that the crystal sits at a 45° angle to the lumen for the blood vessel (Figure 16). Probes for the renal and superior mesenteric arteries are made to have a lumen diameter of 1 mm, probes for the descending aorta have a lumen diameter of 1.7 mm. To ensure no detection of flow signals from other vessels than the one of interest, an accoustic baffle of syrofoam is placed around the back and sides of the cuff (Gardiner et al., 1990; Haywood et al., 1981). Silk sutures are put at lumen side of the cuff to secure the probe around the vessel.

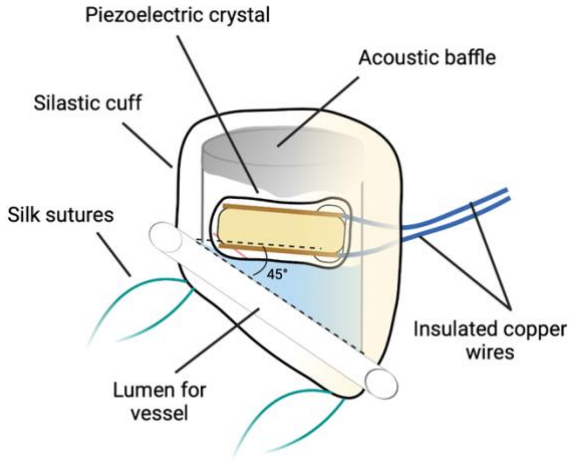

***Figure 16: Pulsed Doppler probe**. In-house produced probes consist of the piezoelectric crystal bedded in a silastic cuff. To isolate the probe and prevent detection of other signals, an acoustic baffle is used to surround the cuff. The crystal is attached to copper wires for signal transduction. At 45 °of the crystal, there is a lumen where the vessel is to be positioned and tied in place with silk sutures. Created in Biorender.com. Figure adapted from Van Daele et al. (2022).*

The piezoelectric crystal in the probe is 1 mm in diameter and emits short bursts of pulsed ultrasonic energy (20 MHz) to the section of the blood vessel in the cuff lumen. Moving erythrocytes in the blood vessel reflect the signal and this reflected signal is detected again by the crystal in the probe (S. L. Cooper et al., 2020; Gardiner et al., 1996; Woolard, Bennett, et al., 2004). Following the principle of the Doppler effect (a change in frequency of a wave as an object moves towards or away from the wave source), the reflected signal is at a slightly shifted frequency and, relative to the transmitted signal, referred to as the Doppler shift. The Doppler shift is proportional to the velocity of the erythrocytes and thus reflects the blood flow velocity in the downstream vascular bed (Gardiner et al., 1996; Hartley & Cole, 1974; Haywood et al., 1981).

The Doppler shift can be described by the following equation:

$$\Delta_f = 2\frac{f_0\, V}{c\, .cos\theta} \quad (1)$$

Where Δ_f is the Doppler frequency difference, f_0 the frequency of the transmitted signal, V the velocity of the blood, c the velocity of the sound in the blood and the angle between crystal and vessel. As f_0 and c are constant and the angle between crystal and vessel is constant at 45°, is directly proportional to the velocity of the erythrocytes, hence the velocity of the blood they are flowing in. Additionally, MAP can be calculated using the following equation:

$$MAP = \frac{2*DBP+SBP}{3} \quad (2)$$

Where MAP is mean arterial pressure, DBP is diastolic blood pressure and SBP is systolic blood pressure. Subsequently, using the Doppler shift and MAP, the vascular conductance can be calculated using the following equations:

$$Vascular\ conductance = \frac{mean\ \Delta f}{MAP} \quad (3)$$

$$\%\Delta\ Vascular\ conductance = \ \%\Delta\ \frac{mean\ \Delta f}{MAP} \quad (4)$$

The vascular conductance is an indicator for the ease with which the blood flows through the regional vascular bed downstream the Doppler probe. Vascular resistance is reciprocal to the conductance. An increase in vascular conductance indicates a vasodilatation, a decrease indicates a vasoconstriction in the vascular bed downstream the probe.

The distance from the crystal to the object from which the reflected signal is measured, can be altered by adjusting the range gate control in the flowmeter. Adjusting the range so that the signal is the highest, ensures that the sampling is done in the centre of the vessel, where the velocity of the erythrocytes is highest. Chronical implantation of the probes leads to the formation of a fibrous cap on the cuff and vessel, therefore the diameter of the vessel is constant and the Doppler shift is an index of the velocity of flow into the vascular bed downstream of the probe (Hartley & Cole, 1974; Haywood et al., 1981).

The implantation of the flow probes, a fluid-filled intravascular BP catheter and intravenous (IV) lines involves a two-stage surgery (detailed in section 2.2.3.2.). During the first stage, the probes with a piezoelectric crystal are positioned on the appropriate vessels (Figure 15) (S. L. Cooper et al., 2020; Gardiner et al., 1996; Woolard, Bennett, et al., 2004). Following a recovery period of at least 10 days, the second surgery consists of the implantation of catheters into the right jugular vein (for IV drug administration) and a fluid-filled catheter into the distal abdominal aorta to monitor BP and HR (S. L. Cooper et al., 2020; Gardiner et al., 1996; Woolard, Bennett, et al., 2004).

Contrary to wireless recording in telemetry studies, animals are tethered during the recording of the Doppler data (Figure 17). The rat wears a fitted harness. This allows for the fixation of the probe wires to a miniature plug and connector for signal transduction. To protect the catheters, they are passed through a flexible spring that is connected to the harness and counterbalanced over the rat's head (Figure 17) (S. L. Cooper et al., 2020; Gardiner et al., 1996; Woolard, Bennett, et al., 2004). This set-up allows for the rat to move freely during experimental protocols.

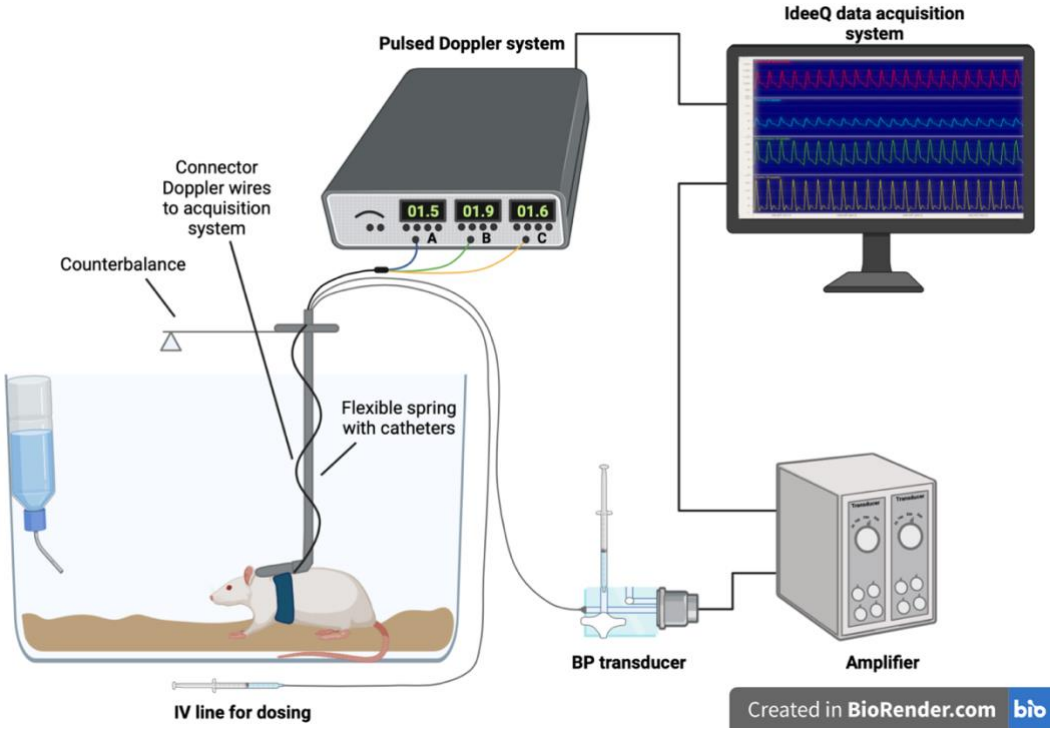

Figure 17: Doppler flowmetry set-up. *The rat wears a harness, connecting Doppler probes to the connector and data acquisition system. The catheters are tunnelled through a flexible spring and attached to the transducer for blood pressure recording or syringes for IV dosing. Both the pressure amplifier and the Doppler system are connected to a computer running bespoke software (IdeeQ) to allow real-time visualisations of the data being collected. Created in Biorender.com. Figure adapted from Van Daele et al. (2022).*

2.2.2. Materials

Entospletinib and R406 were obtained from ApexBio (Houston, USA). Drugs were dissolved in 5% PEG400 (Fisher Chemicals, Hampton, New Hampshire, USA), 20% ethanol (99%) (SigmaAldrich, Gillingham, UK) in sterile water as vehicle. To improve the solubility of entospletinib, the pH was adjusted to ~1 using a 1 M HCl solution and subsequently brought back to a neutral pH using a 1 M NaOH solution.

At the start of the surgical procedures, the anaesthetic agents medetomidine (Sedastart®) and fentanyl citrate were used. Medetomidine, an α_2-adrenoreceptor agonist and commonly used sedative and analgesic agent, was obtained from Animalcare Ltd. (York, UK). Fentanyl is a μ-opioid agonist and was obtained from Martindale Pharmaceuticals (Essex, UK). Lidocaine was used as local anaesthetic, as it blocks voltages-gated sodium channels and inhibits nociceptive signalling, and was obtained from Antigen Pharmaceuticals (Southport, UK). As reversal agents atipamezole and buprenorphine were used. Atipamezole (Sedastop®, Animalcare Ltd, York, UK) is a α_2-adrenoceptor antagonist and therefore reverses the effects of medetomidine. Buprenorphine (Buprecare®, Animalcare Ltd, York, UK) is a semi-synthetic opioid derivative and acts as a partial μ-opioid agonist, thus competes with fentanyl and reverses its anaesthetic effects. Furthermore meloxicam (Boehringer Ingelheim Animal Health UK, Berkshire, UK), an NSAID, was used as analgesic. Lastly, pentobarbitone (Euthalal, Alstoe Animal Health, York, UK), was used a schedule one anaesthetic at the termination of studies. This compound acts on $GABA_A$ and causes respiratory depression, followed by cardiorespiratory failure and, when administered in a lethal dose, death.

During the experiments heparin and plasmin were used as anti-blood clotting agents. Heparin (Wockhardt, Wrexham, UK) activates antithrombin and promotes its inactivation of coagulation enzymes (Beurskens et al., 2020). Plasmin (Merck KGaA, Darmstadt, Germany) is a serine protease that proteolyzes fibrin in blood clots (Keragala & Medcalf, 2021).

2.2.3. Animals and surgery

2.2.3.1. Housing of the animals

Adult male Sprague-Dawley rats (Charles River, Margate, UK), weighing 350 – 450 g at the start of the study, were pair-housed in individually ventilated rodent double-decker cages with bedding. Environmental enrichment (tubes and nesting material) was provided. The animal room was illuminated by artificial light on a 12 h light/dark cycle, in a temperature (21-23°C) and humidity (40-70%) controlled environment. Animals had free access to food (18% protein rodent diet, Envigo, Madison WI, USA) and water. Welfare checks were carried out daily by a Named Animal Care and Welfare Officer (NACWO).

2.2.3.2. Surgeries

All *in vivo* experimentation was approved by the Animal Welfare and Ethical Review Body (University of Nottingham, establishment license (X653228F4); which has representation from The National Centre for the Replacement, Refinement and Reduction of Animals in Research (NC3R)) and performed in keeping with the Scientific Procedures Animals Act (1986), under UK Home Office approved Project Licence (PFOF2A6EC) and Personal License authority for all members of the *in vivo* research team.

Animals were giving an aclimatisation period of at least 7 days after arrival before any surgical intervention. Anaesthesia was induced using fentanyl citrate and medetomindine hydrochloride (0.3 mg/kg, intraperitoneal (IP), supplemented if needed). Furthermore, meloxicam (1 mg/kg, SC) was given pre-operative to provide additional analgesia. To protect the eyes from drying out during surgery, an ocular gel was applied. Animals were wrapped in clear surgical drape for surgery and all surgeries were performed in aseptic conditions. The toe pinch withdrawal was checked prior to the start of the surgeries.

At the end of the surgeries, atopamezole (1 mg/kg, SC) and buprenorphine (30 μg/kg) were administered as reversal agents and post-operative analgesics. Additionally, after the first surgery, meloxicam was given for a further 3 days (1 mg/kg, SC) for post-operative analgesia.

Doppler flow probe implantation

Under anaesthesia, an abdominal incision was made along the *linea alba* and the body wall was opened. Under the microscope, the distal abdominal aorta supplying the hindquarters, superior mesenteric artery and left renal artery were cleared and a miniature pulsed flow probe was positioned and sutured around these vessels. The probe wires were stutured to the left abdominal wall and SC tunnelled to the posterior of the neck, where they were secured to the nape of the neck. Excess of the probe wires were coiled up and sutured into a pouch under the skin of the left flank. Warm saline solution (5 mL) was used to irrigate the peritoneal cavity and the peritoneum and skin incisions were closed. After administration of reversal agents, animals were individually housed and closely monitored, with formal welfare checks every 15 min for at least 4 h. The following morning, rats were paired-housed again with their original cage mate.

Catheter implantation

Following probe implantation, a minimum 10-day recovery period and welfare check from the Named Veterinary Surgeon or NACWO was required prior to performing the second surgery. Firstly, under anaesthesia as described above for probe implantation, the Doppler probe wires were released from the neck. Doppler signals were checked and the wire ends were soledered into a miniature plug (Omnetic, USA) to be attached to the connector to the Doppler recording system. Secondly, catheters were inserted into the vessels. An incision was made into the neck, to expose the right jugular vein. Lidocaine (0.5% m/v, Hameln Pharma Ltd., UK) was applied to this vessel and the vein was ligated with a suture at the rostral end of the vein towards the head. A small incision was made and two polyethylene catheters (Braintree Scientific, LD 0.28 mm, 100 cm) were inserted approximately 1.5 cm and tied in place, using a 3/0 Mersilk suture (Ethicon, UK). The remaining of the IV catheters was then tunneled subcutaneously to the back of the neck (approximetely 6 cm) and tied within the incision in the neck with 3/0 Mersilk suture, followed by closing of the incision. Next, to insert the pressure catheter, an incision was made on the underside of the tail. The ventral caudal artery was exposed and ligated at the caudal end. An incision in the vessel was made and the catheter inserted, advanced to the distal abdominal aorta (appoximately 6 cm) and tied in place using a 4/0 Vicryl suture (Ethicon, UK). The catheter line was tunnelled SC to the back

of the neck and exteriorised through same hole as probe wires and venous lines. Lastly, the incision at the tail was closed.

Preparation of the experimental set-up

The soldered plug with probe wire end was mounted into a harness fitted for the rat. This harness allowed for the free movement of the rats in their cage. Catheters were put through a protective, flexible metal spring that was secured to the harness, to ensure rats could not acces the lines and damage them. Rats were put in their cage for experimentation and the spring and harness were counterbalanced with a pivot system (Figure 17). A connection extension lead was connected to the miniature plug with probe wire ends, to allow for the transfer of Doppler signals to the recording system (Figure 17), and taped to the spring. Anaesthesia reversal agents and analgesics were administered as described above and animals were single-housed during the remaining of the experiment, with access to food and water. The arterial catheter line for blood pressure monitoring was connected to a fluid-filled swivel and continiously infused with heparinsed saline (20 I.U./mL at 4 mL/h) to preserve the patency of the signal.

After the surgery, animals were closely monitored, with formal welfare checks carried out and recorded every 15 min for at least 5 h. Post-surgery analgesia was administered as described above. Experiments began approximately 24 h after the second surgery, following a satisfactory welfare check and sign off by the NACWO, allowing for recovery and acclimatisation of the animals.

2.2.4. Experimental set up

The arterial line was disconnected from the swivel and pump and connected to the pressure transducer and computer of data acquisition. During experimentation, the arterial catheter was flushed with heparin (40 I.U./mL, 0.1 mL every 15 min) to prevent formation of blood clots and loss of patency of the arterial line. If the pressure signal was lost or severely dampened, plasmin (1 I.U./mL in heparinised saline) was administered through the arterial line as an initial bolus of 0.4 mL, followed by 0.1 mL flushes every 10 min, to dissolve a blood clot if present at the tip of the catheter. The pressure signal was calibrated at the start of each study for each animal. Next, the Doppler system was connected to the connector and Doppler shift signals were checked and ranges adjusted if necessary. The patency of the IV line was checked by flushing the line with 0.2 mL of heparinised saline (20 I.U. /mL).

Three compounds were analysed in the Doppler flowmetry model: fostamatinib, entospletinib and sunitinib. The sunitinib study was carried out by Dr. Edward Wragg. Each animal was dosed with the one compound or vehicle for 3 consecutive days. Solutions were dosed using one of the IV catheters, therefore animals could remain in their cage for the full length of the study and were not disturbed during drug administration. Drug were administered as a 0.2 mL bolus, followed by an infusion of 0.4 mL at a rate of 0.4 mL/h. Concentrations of drug solution was adjusted to weight recorded on the day of the second surgery, to maintain correct dosage of each animal, according to their weight. The sunitinib dose was selected to produce a sustained hypertension. Fostamatinib and entospletinib doses were chosen to reflect plasma concentrations obtained in patients treated with these compounds, according to the literature. On each day of dosing, recording was done for at least 0.5 h before administration of the drug or vehicle, and 5 h post-dose for data collection. Arterial BP, HR and Doppler shifts were recorded continuously. Animal welfare and behaviour were monitored immediately after dosing and throughout the day. When pressure was not recorded, the arterial line was connected back to the swivel and pump and infused with heparinsed saline (20 I.U./mL at 4 mL/h).

2.2.5. Data collection software and statistical analysis

2.2.5.1. IdeeQ

Measurements of HR and BP, together with renal, mesenteric, and hindquarters Doppler shifts, were recorded using bespoke software (IdeeQ; Maastricht Instruments, version 2.5, Maastricht, The Netherlands). The same algorithm was used to analyse the BP and Doppler shift waveforms. First, the positive and negative maximum slope of the wave was determined by means of differentiation, followed by detection of the beginning and end of each beat. In this way, each beat (i.e. cardiac pulse) was detected in the signal. DBP or minimum flow was defined as the minimum value of the curve prior to the start of the beat, the systolic pressure or flow was defined as the maximum value of the curve before the slope of the curve turns negative. By using this analysis, systolic and diastolic values for each beat in the BP waveform or Doppler shift waveform were generated and used to calculate the mean Doppler shift or MAP, using the equations described in section 2.2.1.3.

For in-depth waveform analysis, i.e. SPAR, raw waveform numbers were extracted for further analysis in SPARKS (section 2.3.3.).

2.2.5.2. Statistics

All data were expressed as mean ± SEM. As there were two categorical, independent variables (time and treatment) and one quantitative outcome variable (MAP, HR or VC), a two-way ANOVA test was performed. This tested (1) if MAP/HR/VC was significantly different over time, (2) if MAP/HR/VC was significantly different between groups, and (3) if MAP/HR/VC was significantly different between groups over time. If the result of the two-way ANOVA were significant, multiple comparisons test were performed; a Dunnett test to determine where changes over time from baseline were significant and a Sídák test to determine where changes between groups were significant. Results were considered significant at $p < 0.05$.

2.3. Symmetric Projection Attractor Reconstruction

2.3.1. Conventional waveform analysis

The telemetry and Doppler flowmetry model described above, record BP and blood flow (BF) as approximately periodic waveforms. In the current analysis of these data, single point averages (e.g. MAP or mean VC) are typically evaluated. Although these values allow for the calculation of important haemodynamic variables, this approach reduces a complex waveform to one single value, therefore potentially overlooks changes to the waveform morphology and variability. In-depth characterisation of recorded waveforms may provide more extensive information on the condition of the heart and vasculature when exposed to pharmacological agents (Aston et al., 2018; Bonet-Luz et al., 2020; Y. H. Huang et al., 2022; J. V. Lyle et al., 2017; Nandi & Aston, 2020).

2.3.2. In-depth waveform analysis

The Symmetric Projection Attractor Reconstruction (SPAR) is a mathematical method that transforms high fidelity waveform data and extracts information on subtle changes to physiological waveforms. Using all raw numerical data captured by conventional monitoring devices, SPAR facilitates the visualisation and quantification of waveform variability and morphology changes (Aston et al., 2018; Nandi & Aston, 2020).

2.3.2.1. Step-by-step generation of a 2D Signal

SPAR is based on a combination of two mathematical models, the Lorenz attractor (Lorenz, 1963) and Takens' delay coordinates (Takens, 1981) (Aston et al., 2018). In brief, the waveform data are reconstructed into an attractor reconstruction in five steps, shown in Figure 18**:** and Table 2. First, three points are plotted on the waveform, each separated by a time delay that equals one third of the average duration of the cycle. For each window of data, the time delay is adjusted to always equal one third of the cycle length. This set of three delay coordinates (x, y and z) can be placed anywhere on the waveform, with each position resulting in one point in the three-dimensional (3D) space with x-, y- and z-axis (Nandi & Aston, 2020). To transform the waveform into a 3D representation in step 2, the three delay coordinates run over the entire recorded time trace (Nandi & Aston, 2020). Each pulse of the

wave corresponds to one loop in the 3D space (Nandi & Aston, 2020). Next, the 3D cube is rotated and the attractor is viewed down one line, transforming it into a two-dimensional (2D) image (step 3) (Nandi et al., 2018; Nandi & Aston, 2020). In so doing, the more noisy 3D attractor is transformed into a clearer, more symmetrical triangular 2-D shape, as displayed in step 4 (Nandi et al., 2018; Nandi & Aston, 2020). In the last step, the density (colour) of the attractor reconstruction can be added, pointing out where the individual loops (where one loop is one heartbeat) overlap and thus providing information on the waveform shape variability (Nandi & Aston, 2020). In a low variability signal, every waveform pulse is similar as the previous, therefore the loops in the attractor overlap, showing as red - high density - in the attractor. A blue - low density - attractor indicates high variability in the recorded waveform as there is little overlap of the attractor loops (Nandi & Aston, 2020). Other measures of the attractor, such as the attractor size or rotation, give an indication of waveform morphology changes. An example of morphology changes in two selected blood pressure waves and corresponding attractors are shown in Figure 18. Density and other attractor features can be quantified and used in further analysis (Aston et al., 2018; Nandi et al., 2018; Nandi & Aston, 2020). These metrics have been developed using retrospective preclinical and clinical datasets.

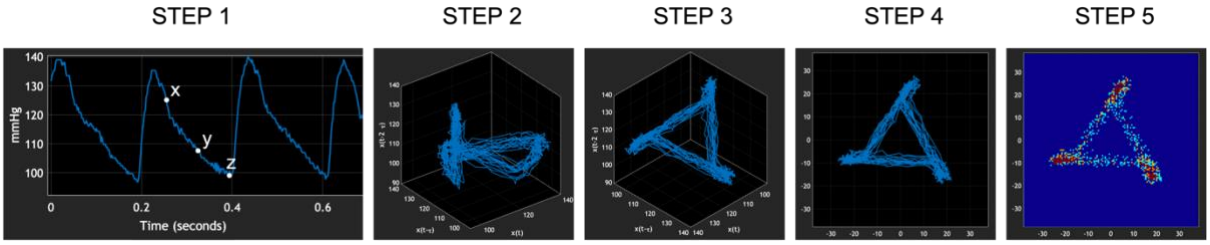

Figure 18: Step-by-step 2D construction of a physiological waveform. *On the recorded waveform, three delay coordinates are plotted, x, y and z. These three delay coordinates are separated by a time delay that equals one third of the average duration of a waveform cycle. This set of three delay coordinates corresponds to one value in a 3D space with a x-, y- and z-axis. When the set of x, y and z runs over the entire waveform, a 3D presentation of the recorded time trace is obtained, as shown in step 2. When this set of loops is rotated and observed from a certain angle, a triangle-like shape is achieved, shown in step 3. This 3D image is easily projected into a symmetrical 2D image (step 4). In the last step a heat map, showing the overlap of the individual loops, is added. Figure adapted from Nandi and Aston, (2020).*

Table 2: SPAR principle: An overview of the steps taken to generate an attractor from a wave. *Each step is illustrated in Figure 18.*

STEP 1	Three points are plotted on the waveform, each separated by a time delay that equals one third of the average duration of the cycle. This set of three delay coordinates (x, y and z) can be placed anywhere on the waveform.
STEP 2	Each position of the set of delay-coordinates results in one point in the three-dimensional (3D) space with x-, y- and z-axis. To transform the waveform into a 3D representation in step 2, the three delay coordinates run over the entire recorded time trace. Each pulse of the wave corresponds to one loop in 3D space
STEP 3	Next, the 3D cubicle is rotated, and the attractor is viewed down one particular line.
STEP 4	The chaotic 3D attractor is transformed into a clearer, symmetrical triangular 2D shape.
STEP 5	In the last step, the density (colour) of the attractor reconstruction is added, pointing out where the individual loops overlap and thus providing information on the waveform shape variability.

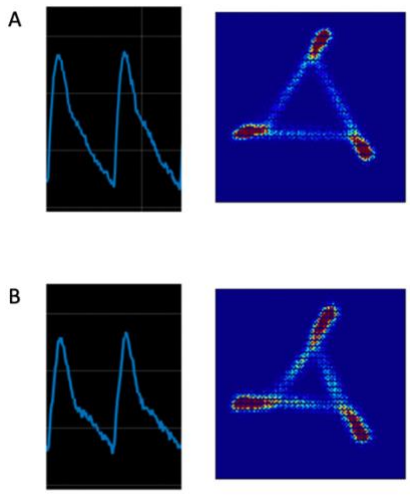

Figure 18: Attractor morphology reflects wave morphology. *An example to two selected blood pressure waves from a 1-minute recording, and their corresponding attractor. Small changes in the wave (less wave reflection in B versus A) result in clear changes in the associated attractors (a closed attractor in B: longer arms towards the centre of the attractor versus A).*

2.3.2.2. Advantages of SPAR

SPAR is a robust method and has several advantages over other mathematical methods of waveform analysis (Aston et al., 2014; Nandi & Aston, 2020). A common problem in waveform analysis is baseline variation. Depending on the active state of the subject, the signal varies naturally and gives disturbances in waveform analysis. Other methods of wave analysis, such as heart rate variability for example, complex algorithms are required to eliminate baseline wander (Aston et al., 2014). SPAR does not need these, as baseline variation is removed automatically when projecting the 3D attractor into a 2D plane. This step creates an attractor that is independent from absolute measured BP (or other) numbers, thus baseline variation doesn't affect the attractor morphology (Aston et al., 2014, 2018). SPAR can be applied on any signal that has a periodic structure, providing the sampling frequency is sufficiently high (Bonet-Luz et al., 2020; Y. H. Huang et al., 2022; Pascual et al., 2021). For that reason, this method can be applied not only on regularly repeating waveforms recorded in restrained laboratory animals, but also more disordered signals recorded in freely moving animals or in hospital settings (Y. H. Huang et al., 2022; Nandi & Aston, 2020; Pascual et al., 2021). Moreover, since SPAR does not require extensive pre-processing of the data, this simplifies the application of the technique further and reduces bias that can occur through preselection of regions of interest (Nandi et al., 2018; Nandi & Aston, 2020).

2.3.3. SPAR data analysis

2.3.3.1. Data extraction and preparation

Per recorded hour of data, a 1 min window of raw waveform data was extracted. This window length was chosen for optimal attractor quality and physiologically relevant analysis time. The full optimisation process is described in Chapter 4 (section 4.3.1.). For telemetry data, data were extracted into Excel using Notocord HEM software and saved as .txt file. Doppler data were extracted as .txt file from IdeeQ. At times where drop-out occurred during the selected 1 min window (e.g. when connection between implant antenna and the TSE receiver was interrupted), the frame was moved for a maximum of 5 min. If no signal without drop-out was present within this range, the timepoint was discarded and excluded from further analysis.

2.3.3.2. SPARKS application

All SPAR analysis was done in the SPARKS application, developed by Miquel Serna Pascual at School of Cancer and Pharmaceutical Sciences, King's College London (Nandi Lab). This application allows for importing of different formats of files (among other .txt) and streamlined SPAR analysis (Figure 20A). Moreover, predefined SPAR features can be determined and quantitative metrics are provided in the app. An overview of the application and the four available tabs are shown in Figure 20. In the first tab, raw waveform data are imported for analysis (Figure 20A). The second tab shows all input parameters for the SPAR algorithm and allows for adjustment of some parameters, as required (Figure 20B). In the third tab, the attractors are generated from the raw waveform data and visualised (Figure 20C). Lastly, in the fourth tab, the calculated metrics for each attractor can be found and exported for further analysis (Figure 20D).

The app offers the possibility of down sampling or bandpass filtering of data, however this option was not used in this thesis. Most importantly, the estimated rate range of the signal is crucial to input. In the app, predefined sets of parameters for SPAR analysis are available for different types of data (Figure 20A). The details of the three available predefined sets of parameters are presented in the thesis appendix (section 8.1., Table 22). As there was not yet a specified set for rat BP or rat blood flow, the set 'HumanBP' was selected, and two parameters were changed to facilitate optimal SPAR analysis for data obtained in rats; 'Ratemin' and 'Ratemax' were changed from 40 and 180 (for humans), to 230 and 550 respectively, as the mean HR of healthy rats is generally in the range of 300 bpm up to 400 bpm in resting conditions (S. L. Cooper et al., 2019) and some compounds tested in this study are known to increase the HR (Figure 20B). The full optimisation of these parameters is detailed in Chapter 4 (section 4.3.1.1.). Furthermore, to allow for sufficiently 'coloured' attractor in the qualitative, visual analysis, the 'nbins_density' was decreased to 125 (Figure 20B). This parameter is related to the brightness of the attractor and its full optimisation is discussed in Chapter 4 (section 4.3.1.2.) In the SPAR tab, the window length used to create one attractor was selected (1 min, optimised in Chapter 4, section 4.3.1.3.). When attractors were generated, each window of raw waveform data and its corresponding attractor were visualised and could be exported (Figure 20C). In the last tab of the application, the attractor measures (e.g. colour, length of arms, rotation) were displayed in a table format and could be exported as well (Figure 20D).

A. SPARKS: Data loading tab

The application allows importing of different file formats (among other .txt).

Predefined sets of parameters for SPAR analysis. In this thesis, the HumanBP set was selected and adjusted to fit data obtained in rats.

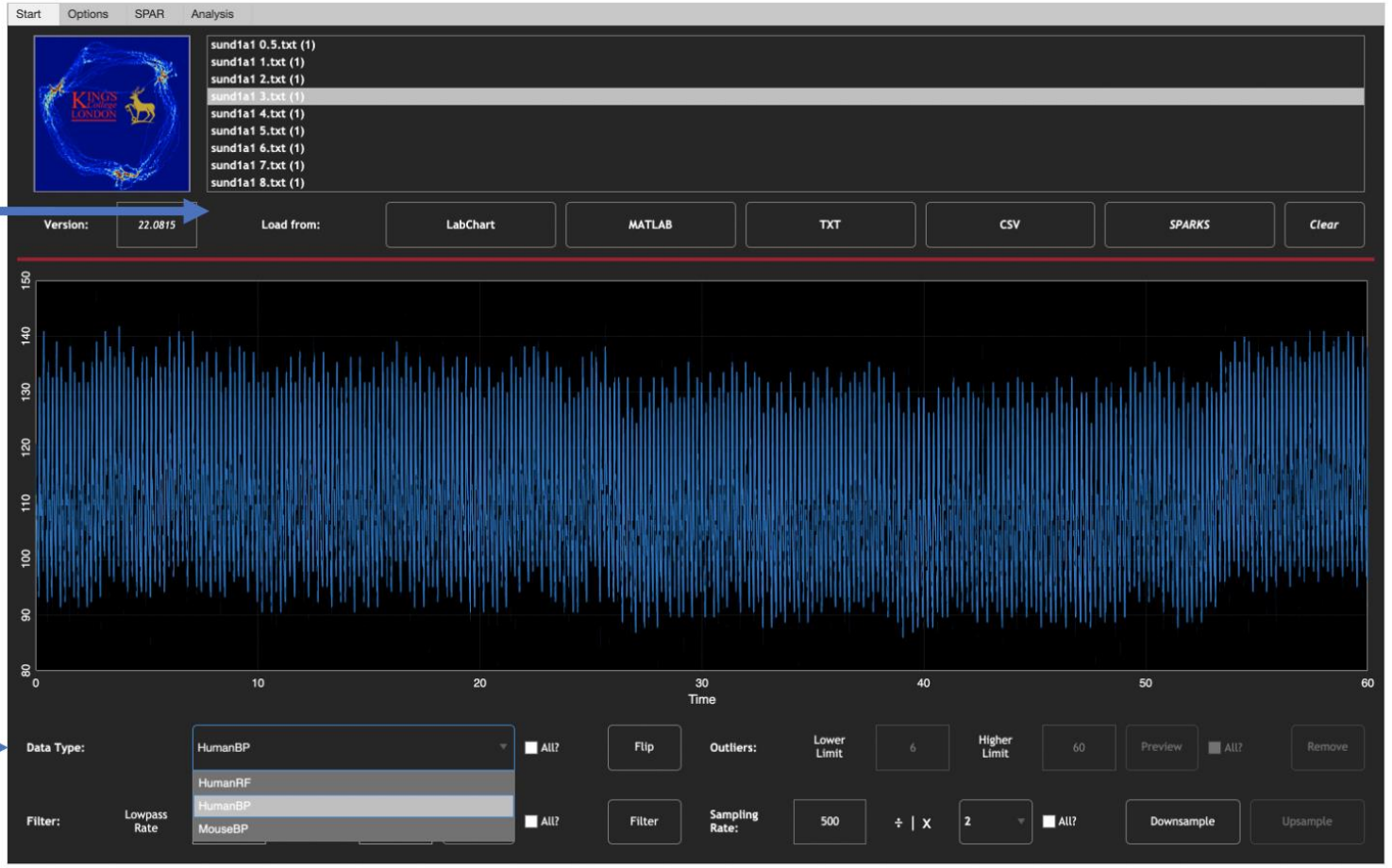

Figure 19A: *In the first tab of SPARKS, data files of different formats can be loaded (upper window), here the raw waveform data are loaded and visualised. Additionally predefined parameters for SPAR analysis can be selected in this tab (lower panel: HumanRF, HumanBP and MouseBP). These predefined sets provide characteristics of the data type, such as expected rate ranges and expected signal ranges to SPAR, so each pulse is correctly detected by the algorithm and attractors are correctly generated.*

B. SPARKS: Options for parameters

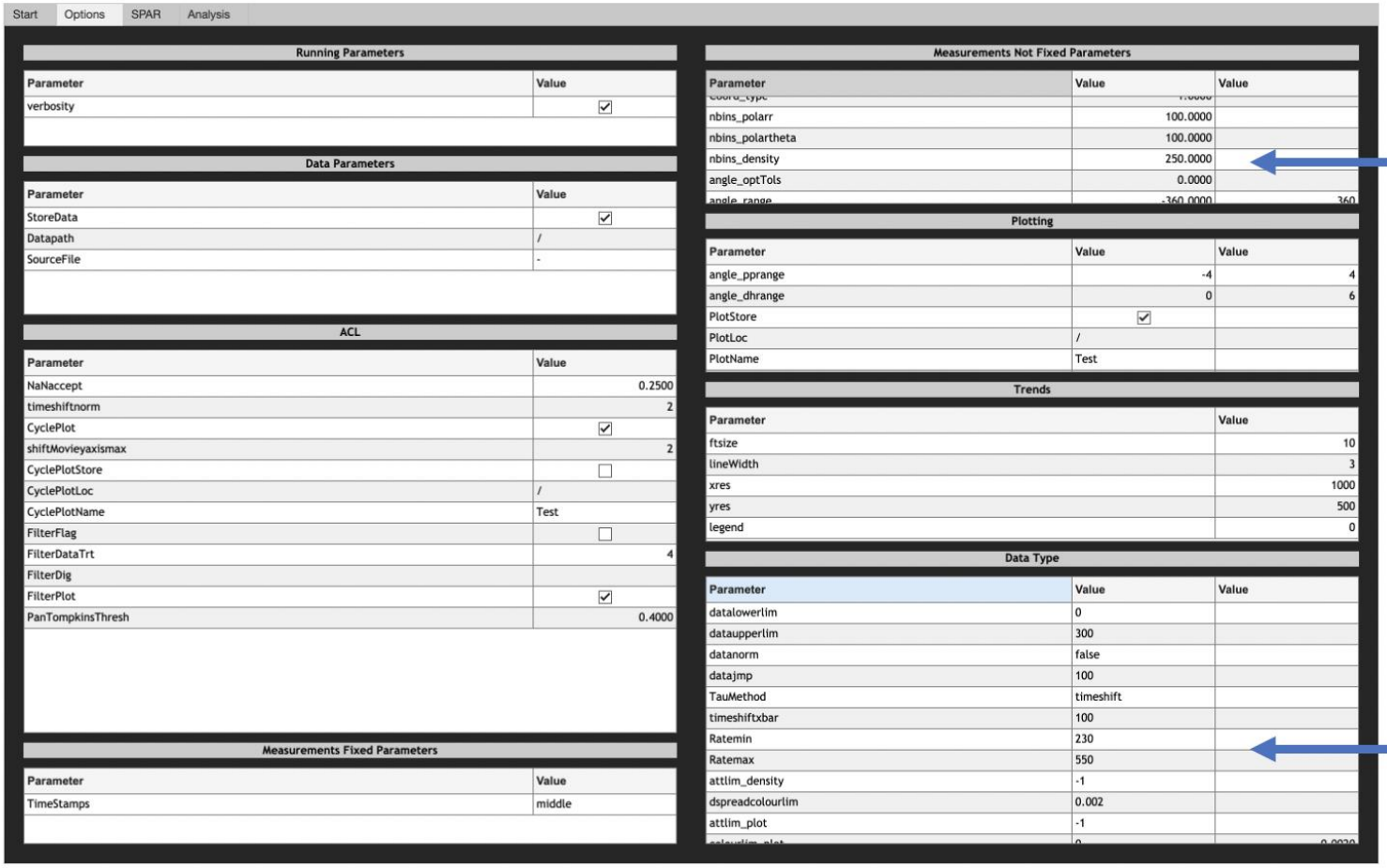

Figure 20B: *In the second tab of SPARKS, all parameters used in the algorithm are displayed and several can be adjusted for optimal analysis of different data type. Selecting a certain data type in the first tab, will result in distinct parameters in this second tab providing input for the SPAR algorithm. Relevant input parameters are indicated by the blue arrows. N_binsdensity relates to the brightness of the attractor. To ensure sufficiently high colour spread to meaningfully map variability differences and improve the brightness of attractors for easier quantitative analysis, this parameter was decreased to 125. Ratemax and Ratemin represent the expected rate ranges. For BP and blood flow data, this is the heart rate. These parameters were adjusted to 230 and 550, to mirror typical HR in rats and ensure correct detection of each cycle of the raw waveform data.*

C. SPARKS: SPAR analysis and visualisation

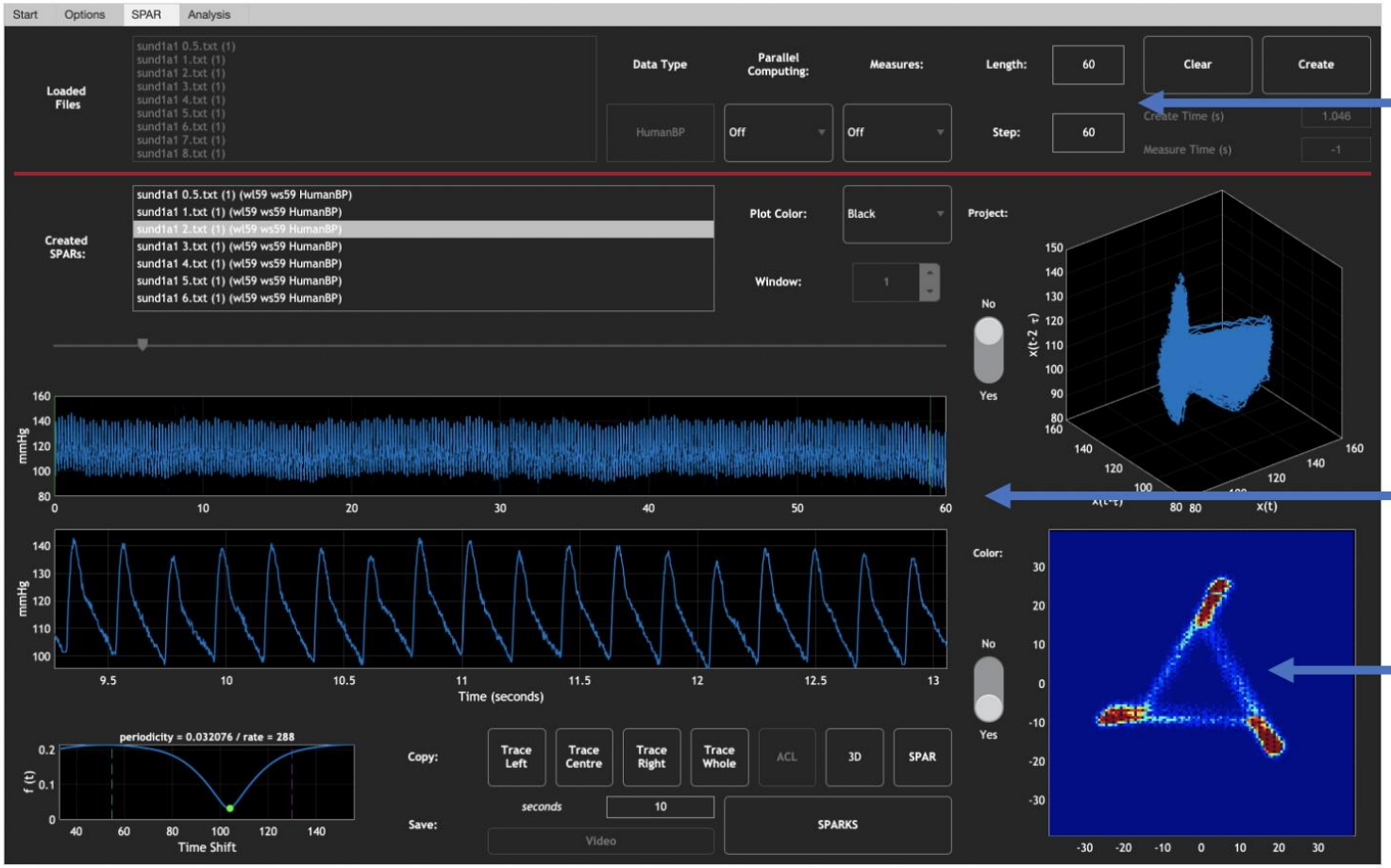

Selection of window length (s) and steps (s) to create consecutive attractors.

Visualisation of raw waveform in selected time window.

Visualisation of attractor with or without heatmap to indicate density.

Figure 20C: *In the third tab, attractors are generated. The chosen length of window and step between consecutive windows to create one attractor should be indicated (upper panel, right hand sight). After running the algorithm, a list of files from which an attractor was created is given, accompanied of the visualisation of each raw waveform signal, and a window that allows for zooming in on waves of interest. The attractor of the selected file can be found on the lower, right-hand side corner. Each trace and attractor can be exported.*

D. SPARKS: measures for quantitative analysis

Figure 20D: *In the last SPARKS tab, all computed SPAR metrics for quantitative analysis are presented in a table (upper panel). Furthermore, all plots derived from the attractor and used for calculations of these SPAR metrics are shown in the lower panel. Again, the table with metrics or attractor plots can be exported for further analysis and statistics.*

2.4. *In vitro* methods

2.4.1. Materials

Human Embryonic Kidney (HEK) 293 cells were selected as a widely utilised cell line for expression of recombinant proteins. This immortalised cell line, isolated in 1977 by Graham *et al.* (Russell et al., 1977), is extensively used due to its easy reproduction and maintenance in cell culture and its high transfection efficiency and protein expression (Thomas & Smart, 2005). The NFAT-ReLuc2P HEK293 cell line was obtained from Promega Corporation (Madison, USA). The NFAT-ReLuc2P NL-VEGFR2 HEK293 cell line has been described previously (Kilpatrick et al., 2017). HEK293T cells were obtained from ATCC (Virginia, USA). This cell line was used in all NFAT assays. Bioluminescence Resonance Energy Transfer (BRET) experiments were done in HEK293 T cells. This variant of the HEK293 cell line was established by stable expression of the SV40 large T-antigen (DuBridge et al., 1987), allowing for an improved vector transfection (Tan et al., 2021). These cells were transiently transfected with the VEGFR2-NL construct. This cDNA construct was a generous gift from Promega Corporation (Madison, USA).

Recombinant human Vascular Endothelial Growth factor 165a ($VEGF_{165}a$) was purchased from R&D Systems (Abingdon, UK). Sunitinib-red was purchased from PerkinElmer Ltd (Beaconsfield, UK). $VEGF_{165}a$ was aliquoted at a concentration of 10^{-6} M in phosphate buffered saline (PBS, Sigma Aldrich, Gillingham, UK) containing 0.1% protease free Bovine Serum Albumin (BSA, Sigma Aldrich, Gillingham, UK) to prevent interactions with plasticware, according to the manufacturer instructions. Aliquots were stored at -20°C. Sunitinib, cediranib, erlotinib, dasatinib, motesanib, fostamatinib, R406, cerdulatinib and entospletinib were purchased from ApexBio (Houston, USA). These inhibitors were stored at -20°C as 10^{-2} M stocks in dimethylsulfoxide (DMSO, Sigma Aldrich, Gillingham, UK). FuGENE HD Transfection Reagent, One-Glo® luciferase, furimazine and NanoGlo® HiBit lytic buffer were purchased from Promega Corporation (Madison, USA). Opti-MEM reduced serum medium was bought from Thermo Fischer Scientific (Loughborough, UK). Unless otherwise stated, cell culture reagents, laboratory equipment and chemical stocks were purchased from Sigma

Aldrich (Gillingham, Dorset, UK). Cell culture plasticware was purchased from Thermo Fischer Scientific (Loughborough, UK).

2.4.2. Cell culture

2.4.2.1. Cell maintenance and passaging

Cell culture was performed in a microbiological safety cabinet (TriMAT Class 2; Contained Air solutions, UK), to maintain a sterile environment. All HEK293 cell lines were cultured as a monolayer in 75 cm^2 flasks, in Dulbecco's Modified Eagle's Medium (DMEM) containing 2 mM L-glutamine, supplemented with 10% fetal calf serum (FCS) as growth supplement. This medium contained all inorganic salts, amino acids, vitamins and pyruvate required for cell survival. Moreover, a pH indicator, phenol red, was present in this medium, transitioning from pink to yellow with increasing acidity, indicating cell metabolism or microbial infection. All cells were grown in incubators at 37°C in a humidified atmosphere containing 95% air/5% CO_2. Cell morphology and confluence was checked daily with an inverted microscope (Pan Apochromat 10X objective, Zeiss Primovert) and cells were regularly tested for the presence of mycoplasma.

Cells passaging was performed at 70 – 80% confluency to ensure maximal cell health. All media used during cell passages was warmed up to room temperature before use. Medium was removed from the flask and cells were washed with 5 mL PBS. Adherent cells were then detached from the flasks using 1 mL trypsin (0.25% w/v in ethylenediaminetetraacetic acid (EDTA) solution, Gillingham, UK). Trypsin is a serine protease that cleaves the adhesion molecules holding cells to each other and the flask. EDTA was also present to chelate Ca^{2+} and Mg^{2+} present in the medium and improving trypsin's ability to detach adherent cells. Cells were incubated for 3 – 5 min and washed off into 10 mL DMEM/10% FCS. FCS contains a protease inhibitor that inhibit the proteolytic activity of trypsin. Cell suspensions were centrifuged at 1000 rpm for 4 min. Supernatants was discarded and pellets were resuspended by pipetting gently up and down in 2 mL of DMEM/10% FCS, to achieve single cell suspensions. Cells were then diluted into 10 mL DMEM/10% FCS and passaged into a new 75 cm^2 flask containing 20 mL DMEM/10% FCS. For experimental purposes, cells were used until passage 30.

2.4.2.2. Freezing

Multiple passages of the HEK293 cells were stored in liquid nitrogen dewars for long-term storage (LS6000, Taylor Wharton, Scientific Laboratory Supplies). Cells were bulked up in 75 cm^2 or 175 cm^2 flasks until 70 – 80% confluency and detached from the flask as described above. After centrifugation, the cell pellet was resuspended into 3 mL of cryopreservation medium containing 90% FCS and 10% DMSO, that had been filtered through a sterile 0.2 μm pore filter before the cells were added, to remove potential contamination. FCS provides cell support and protects against cellular stress and DMSO prevents lysing of the cells. The resuspended cells were aliquoted into cryogenic vials and placed into a Mr Frosty™ freezing container. The isopropyl alcohol present in this freezing container ensured a slow freezing rate of the cells, reducing the formation of ice crystals which cause cell lysis upon thawing. The Mr Frosty™ freezing container was frozen to -80 °C and transferred to the liquid nitrogen vapour phase on the next day for long-term storage.

To recover cells from frozen, an aliquot was removed from storage and thawed rapidly. Once defrosted, 10 mL of DMEM/10% FCS was added to the aliquot and the cell suspension was seeded into a 25 cm^2 flask, to ensure sufficient cell contact. After 24 h, cell medium was replaced by fresh DMEM/10% FCS to remove any dead cells and remaining DMSO. At 70% confluency, cells were passaged into a 75 cm^2 flask as described above, using 2 mL of PBS and 0.5 mL of trypsin. Cells were passaged at least twice before experimental use, to ensure full recovery.

2.4.2.3. Seeding

For experimental use, cells were seeded into white, clear bottom 96-well plates. The plates were coated with poly-D-lysine hydrobromide to encourage cell attachment to the surface of the well, so that cells would not be removed when replacing medium for assay buffers on the experimental day. Poly-D-lysine hydrobromide, a positively charged amino acid, interacts with the negatively charged ions in the plasma membrane encourages adherence of the cells to the bottom of the well. Ten μg/mL poly-D-lysine in PBS was prepared, filter-sterilised using a 0.2 μm pore filter and stored at -20 °C. On the day of seeding, 50 μL of poly-D-lysine in PBS was added in each well and plates were incubated for 30 min at room temperature. Poly-D-lysine was removed from the wells before seeding the cells. The appropriate cell line was grown in 75 cm^2 and passaged as described above. After resuspension of the cell pellet, the density of the cells was determined, to ensure the optimal number of cells seeded per well. Cells were counted using a haemocytometer (BRAND® counting chamber), averaging the read of 4 chambers. The cell suspension was diluted in the appropriate volume of DMEM/10 FCS% and seeded at 20 000 cells/well in a total volume of 100 μL/well.

2.4.3. Recombinant cell line

2.4.3.1. Stable cell line

NFAT-ReLuc2P NL-VEGFR2 HEK293 were obtained from Dr. Laura Kilpatrick and colleagues at Promega Corporation (USA).

2.4.3.2. Transient transfected cell lines

NanoBRET experiments were performed in HEK293T cells transiently transfected with VEGFR2-NL. Unlike cell lines stably expressing the transfected protein, transient transfected cells do not incorporate the plasmid DNA into their genome. A transfection reagent aids the delivery of the plasmid DNA into the cytoplasm of the target cell, followed by transcription into mRNA and translation into the protein of interest. Transiently transfected cells are suitable for only one experiment, requiring newly transfected cells for each experimental replicate.

HEK293 T cells were seeded in 96-well plates as described above. After 24 h, transfection solution was added directly into the medium in the wells. Transient transfections were performed using FuGENE® HD. In a sterile tube, plasmid DNA was diluted in OptiMEM® to a concentration of 20 ng/μL. FuGENE® HD was added at a ratio of 1 μg cDNA to 3 μL reagent, according to the manufacturer's instructions. Transfection solution was incubated at room temperature for 5 min to ensure optimal formation of cDNA/FuGENE® complexes. Transfection solution (5 μL/well) was added to each well, resulting in 100 ng cDNA/well. Cells were then incubated for a further 20 h at 37°C/5% CO_2 before experimentation.

2.4.4. Molecular biology

2.4.4.1. VEGFR2-NL cDNA construct

The VEGFR2-NL plasmid was provided by Promega Corporation (USA) (Figure 21). An expression vector should ensure transcription of the insert, mRNA processing for protein translation, propagation in prokaryotic cells and selection in mammalian cells. The cytomegalovirus (CMV) enhancer and promotor facilitate protein transcription in mammalian cells. The vector also contained a chimeric intron, to enhance mRNA processing and increase expression levels. Furthermore, a polyadenylation tail (SV40 poly(A) signal) was introduced, to protect mRNA from degradation. A neomycine/kanamycine-resistance gene was present in the plasmid, allowing for selection of transfected bacterial cells (kanamycin-resistant, see section 2.4.4.2) and kill non-transfection, therefore non-resistant cells. The stop codon of KDR was removed, and the C-terminus of KDR was genetically fused to NL (19.1 kDa luciferase subunit), using a flexible 18 amino acid linker (VSLGGSGGGGSGGGSSGG).

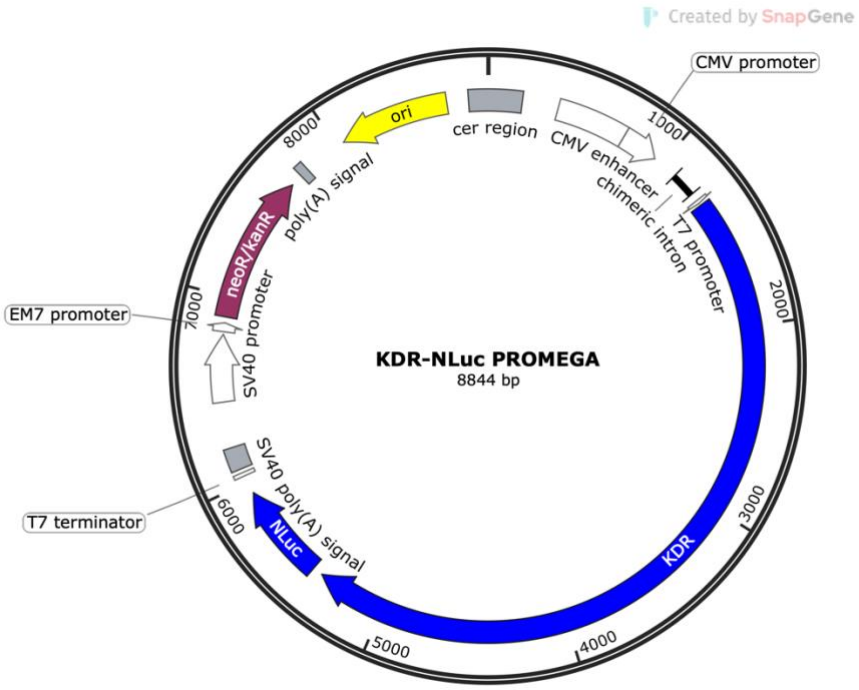

Figure 20: Plasmid map of KDR-NL construct. *The C-terminal end of KDR was fused to NL. Furthermore, the plasmid contained a neo-resistance gene for selection of transfected cells during transformation into E. coli and DNA amplification. Map created in SnapGene.*

2.4.4.2. Plasmid transformation into E. coli

To propagate plasmid cDNA for transfection, DNA was transformed in Subcloning Efficiency DH5α cells (Invitrogen), competent *E. coli* cells engineered to maximise transformation efficiency. Cells were thawed on ice and 25 μL was transferred to a cool, sterile 0.5 mL tube. Depending on the concentration of the plasmid preparation, 2 – 5 μL DNA was added to the DH5α cells. To ensure associating of the plasmid with the outer membrane of the cells, the tube was left for 30 min on ice. Next, the mixture was heat shocked for 30 s at 42°C, to enable the uptake of the plasmid into the competent cells. Bacterial cells were cooled on ice for 3 min before 250 μL Luria Broth (LB) Lennox was added to the tube. This rich medium contained tryptone, yeast extract and sodium chloride, allowing for optimal *E. coli* replication. To further encourage exponential bacterial growth, the mixture was shaken for 60 min at 225 rpm/37°C using the SI600 Large Shaking Incubator (Stuart Equipment). In the meanwhile, LB agar plates were prepared. The LB agar solution was sterilised in the autoclave. To prevent inactivation of the antibiotic, kanamycin was added after the agar had cooled down to approximately 45°C. Per petri dish, 20 mL sterile LB agar containing 30 μg/mL kanamycin sulphate (Gibco) was poured and left to solidify at room temperature. After the 60 min incubation, 250 μL of transformed *Escherichia coli* (*E. coli*) were added to the agar plate and spread using a sterile plastic L-shaped spreader. The plates were incubated overnight at 37°C, placed upside down to prevent condensation. The transformed DNA plasmid contained a kanamycin resistance gene. *E. coli* that did not incorporate the plasmid, were killed or prevented from growing on the kanamycin containing agar plates. Only successfully transformed *E. coli*, hence *E. coli* expressing the prokaryotic antibiotic resistance gene, could grow on the kanamycin plates. As bacterial colonies grew from a single bacterium, the populates within one colony was genetically identical. Agar plates with these colonies were stored at 4°C for up to 1 month.

2.4.4.3. DNA amplification – maxiprep

To bulk up plasmid DNA, a single colony was picked from the agar plate, using a sterile pipette tip. The pipette tip with starter culture was placed into 5 mL of LB broth containing 30 μg/mL kanamycin and shaken for 8 h at 225 rpm/37°C in the SI600 Large Shaking Incubator, to establish bacterial growth. After this initial incubation, the 5 mL culture was transferred into a 500 mL conical flask containing 120 mL of LB broth/30 μg/mL kanamycin. This flask was shaken overnight at 225 rpm/37°C, stimulating further exponential bacterial growth.

The following morning, the plasmid was extracted from the bacteria, using Promega's PureyieldTM Plasmid Maxiprep System. The bacterial cultures were transferred into plastic bottles and centrifuged for 10 min at 5000 x g/4°C (Eppendorf Centrifuge). Supernatant was discarded. Following the Maxiprep kit instructions, the bacterial cell pellet was resuspended in 12 mL of Cell Resuspension Solution (50 mM Tris-HCl, 10 mM EDTA, 100 μg/ml RNase A) by pipetting. 12 mL of Lysing Solution (0.2 M NaOH, 1% sodium dodecylsulfate–polyacrylamide) was added, followed by 12 mL of Neutralization Solution (4.09 M guanidine hydrochloride, 759 mM potassium acetate, 2.12 M glacial acetic acid). The lysate was then transferred into a container suitable for superspeed centrifugation and centrifuged at 14 000 x g for 20 min at room temperature. This step allowed for the plasmid to be separated from precipitate. The pellet was discarded and supernatant, containing the plasmid, was used for further purification.

The blue PureYield™ Clearing Column and white PureYield™ Maxi Binding Column were assembled on the vacuum manifold (Vac-Man, Promega Corporation, USA) and the lysate supernatant was transferred into the clearing column. By applying vacuum to the columns, the lysate passed through both the clearing and binding column. The clearing column was discarded, and 5 mL of Endotoxin Removal Wash was added to the binding column, followed by 20 mL Column Wash (60% ethanol, 60 mM potassium acetate, 8.3 mM Tris-HCl and 0.04 mM EDTA), to remove contaminants. The vacuum was applied for a further 5 min, until the membrane of the binding column appeared dry. Next, the binding column was placed on the Eluator Vacuum Elution Device, so that the tip of the column was positioned into a sterile 1.5 mL tube in the device. Plasmid DNA was eluted into the tube by adding 1 mL of nuclease free

water to the binding column and, after 1 min, applying maximum vacuum, until all liquid passed through the membrane into the tube. This Maxiprep protocol typically resulted in 700 μL DNA preparation with a yield of approximately 300 ng/μL. DNA samples were further aliquoted and stored at -20°C.

2.4.4.4. DNA quantification and sequencing

The DNA concentration of plasmid preparations were quantified using the NanoDrop 2000 Spectrophotometer (ThermoFisher Scientific). DNA concentration was determined by the absorbance at 260 nm of a 1 μL sample, using nuclease-free water as blank. The nucleic acid purity was calculated by the ratio of the readings at 260 nm and at 280 nm. A ratio close to 1.8 indicated pure DNA, a higher ratio suggested the presence of RNAs, a lower ratio suggested contamination with proteins.

Plasmid sequencing was carried out by the DNA Sequencing Facility in the School of Life Science of the University of Nottingham, using Sanger sequencing with primers T7T (TAT GCT AGT TAT TGC TCA GCG G) and T7P (TAA TAC GAC TCA CTA TAG GG), annealing the regions on both sides of the open reading frame. DNA chromatograms were checked to ensure sufficient clear peaks and sequences aligned with a reference plasmid.

Additionally, whole plasmid sequencing was done by Plasmidsaurus®. Whole plasmid sequencing does not require amplification steps and primers to detect specific regions of the plasmid. Instead, this method linearizing the plasmid in a sequence-independent manner and sequences every nucleotide within a long, single read, using R10.4.1 flow cells (Oxford Nanopore Technologies, UK). Therefore, it can reveal any structural abnormalities in a sample, e.g. degraded DNA or contaminants. The histogram below (Figure 22) shows the detection of one main peak around 9000 base pairs, indicating the sample was pure and contained the KDR-NL plasmid (8840 base pairs). Furthermore, a data consensus score was reported, showing a high confidence of nucleotide detection. As with the Sanger sequencing results, sequences were aligned with a reference plasmid to ensure no mutations in the DNA.

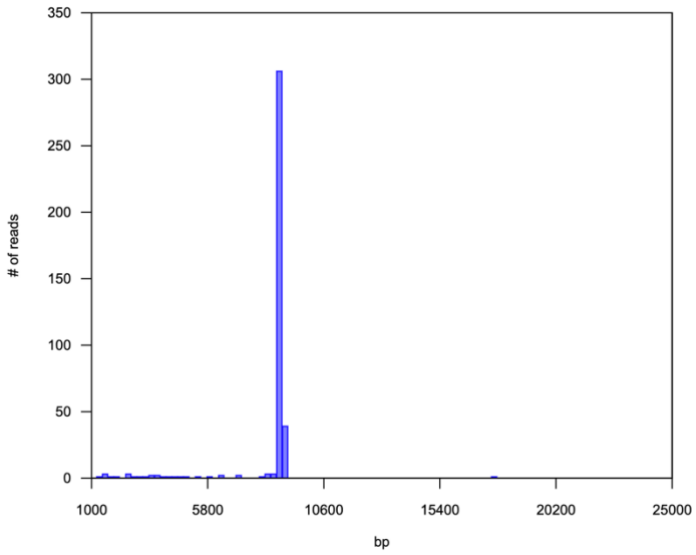

Figure 21: Histogram showing number of reads for each base pair length. *One main peak was detected around 9000 base pairs, indicating the sample was pure and contained the KDR-NL plasmid (8840 base pairs).*

2.4.5. NanoBRET ligand binding assay

2.4.5.1. Bioluminescence Resonance Energy Transfer

Bioluminescence Resonance Energy Transfer (BRET) is a quantitative technique that allows the investigation of interaction of ligands at the receptor in living cells (Stoddart et al., 2018). Unlike a functional reporter gene assay (Carter et al., 2015), that monitors effects on the downstream signalling pathway after receptor activation, BRET measures direct binding affinity of the inhibitor to the receptor. The technique requires two components: a luciferase, serving as the bioluminescent energy donor, and a fluorophore, serving as the energy acceptor (Stoddart et al., 2018). Upon addition of the nanoluciferase's substrate, furimazine, bright bioluminescence is emitted (Figure 23B). When within a distance of <10 nm, the excess energy from the luciferase is transferred to the fluorophore. An electron from the fluorophore is excited into a higher energy state and, when falling back into its relaxation state, emits light at a different wavelength than the luciferase (Figure 23C). In this way, an energy transfer takes place from luciferase to fluorophore, i.e. BRET.

Previously done N-terminal (Kilpatrick et al., 2017), here a C-terminal NanoLuc-tagged VEGFR2 was used (Figure 23A). NanoLuc is a small luciferase, derived from deep-sea shrimp luciferase, and emits bright bioluminescence at 460 nm (Hall et al., 2012). Following binding of fluorescently tagged sunitinib (i.e. sunitinib-red) to ATP pocket of the receptor, the fluorescent tracer comes in close proximity (<10 nm) to NanoLuc, resulting in emission at 670 nm. As shown in Figure 23C, there is minimal overlap between the emission spectra NanoLuc and sunitinib-red, making this fluorescent tracer an ideal compound for BRET detection. Simultaneous measurement of bioluminescent and fluorescent light allows for the monitoring of sunitinib-red binding at the receptor and displacement of sunitinib-red by unlabelled inhibitors.

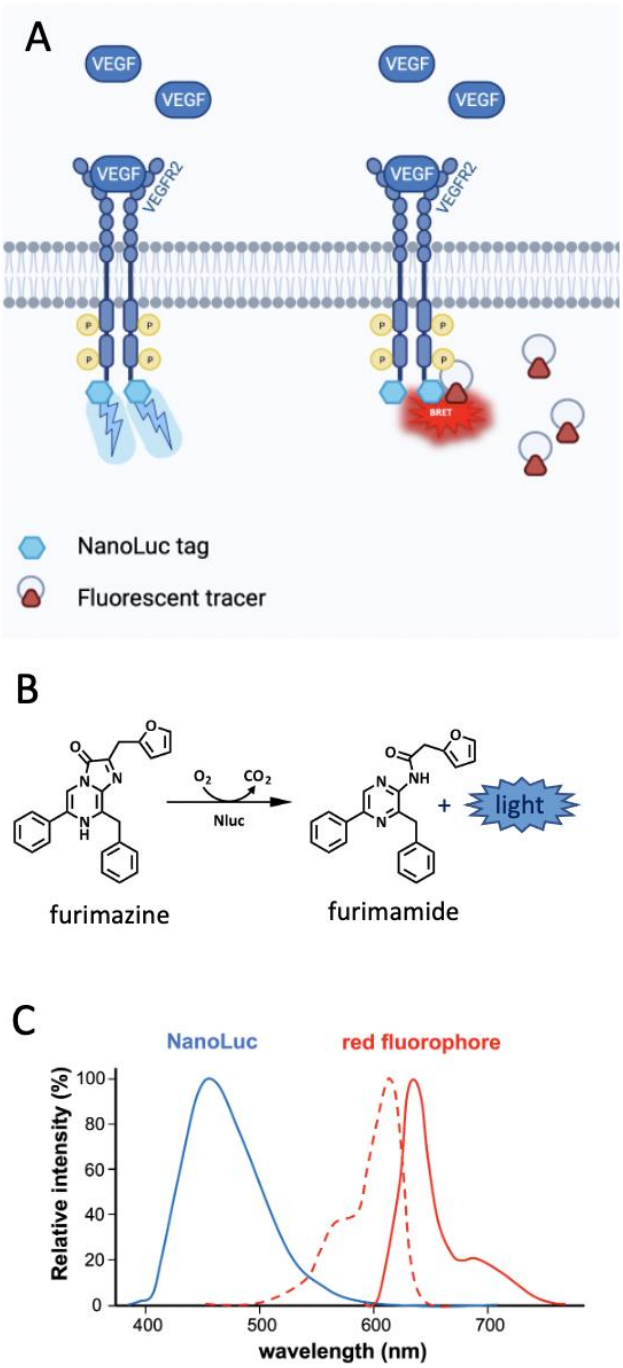

Figure 22: NanoBRET assay. A. *Bioluminescence resonance energy transfer. Upon addition of NanoLuc's substrate, luminescence is emitted. Proximity of a fluorophore, here sunitinib-red, results in an energy transfer and emission of red fluorescence. Created with Biorender.com* ***B.*** *NanoLuciferase catalyses the conversion of furimazine to furimamide, with emission of bright luminescence as by-product. Chemical reaction adapted from Hall et al. (2012).* ***C.*** *NanoLuc emission spectra (blue, peak at 460 nm) and sunitinib-red excitation (red dashed, peak at 650 nm) and emission (full red, peak at 670 nm) spectra. Figure adapted from Stoddart et al., (2018).*

2.4.5.2. HEPES Buffered Saline Solution (HBSS)

All BRET experiments were carried out in HEPES Buffered Saline Solution (HBSS). This solution was prepared at a 10X stock solution of 1 L. The pH was adjusted to 7.45 (with 3 M NaOH) and the stock solution was autoclaved and stored at 4 °C. 1X solution was prepared by a 1:10 dilution in ddH_2O and addition of 18 g D-Glucose 100 mM. The final composition of the 1X HBSS solution was:

Calcium chloride dihydrate	1.3 mM
D-Glucose	10 mM
HEPES	10 mM
Magnesium sulphate heptahydrate	1 mM
Potassium chloride	5 mM
Sodium pyruvate	2 mM
Sodium chloride	145 mM
Sodium bicarbonate	1.5 mM
	in ddH_2O

2.4.5.3. Sunitinib-red saturation binding and displacement

HEK293 T cells were grown to 80% confluency in DMEM/10% FCS. Cells were seeded 48 h prior to assay at 20 000 cells/well in DMEM/10% FCS in white 96 well plates (Greiner Bio-One, UK), coated with 0.01 mg/mL poly-D-lysine in PBS. The next day, cells were transfected with VEGFR2-NL construct (100 ng cDNA/well) and incubated for a further 20 h. On the day of the experiment, medium was removed and replaced by HBSS/0.1% protease-free BSA. Cells were pre-treated with 1 nM $VEGF_{165}a$ for 15 min, followed by fluorescent ligand and inhibitor where appropriate, in a total volume of 50 μL per well, and incubated for 1 h at 37 °C/5% CO_2. Furimazine (1:400) was added to each well and plates were incubated for a further 10 min at 37 °C/5% CO_2 before BRET was measured. Cells were then lysed using NanoGlo® lytic buffer at room temperature for 10 min before BRET was measured a second time. Fluorescence and bioluminescence were read at room temperature using a PHERAstar FS plate reader (BMG Labtech, Germany) using a filter for 460 – 80 nm for donor NanoLuc emission and a > 610 nm longpass filter for acceptor sunitinib-red emission or a > 550 nm longpass filter for acceptor unlabelled sunitinib emission. BRET ratios were calculated as acceptor/donor emission values from the second of three cycles.

2.4.5.4. NanoBRET kinetics assay, pre-incubated with sunitinib-red

For kinetic experiments, HEK293T cells were seeded and transfected as described above. Cells were pre-treated with 1 nM $VEGF_{165}a$ for 15 min, followed by sunitinib-red and the appropriate inhibitor in triplicates. Plates were incubated at 37 °C/5% CO_2 for 1 h before furimazine (1:400) was added. Baseline BRET was taken for an initial 10 min every 60 s. Cell lysis was then performed, and BRET was measured for a further 50 min. Kinetics experiments were carried out in a temperature-controlled environment at 25 °C or 37 °C.

2.4.5.5. NanoBRET kinetics assay in lysed cells

HEK293T cells were seeded and transfected as described above. Cells were pre-treated with 1 nM $VEGF_{165}a$ for 15 min. Furimazine (1:400) and NanoGlo® lytic buffer were added simultaneously and baseline BRET measurement commenced immediately after. After 10 min of initial reads, sunitinib-red and the appropriate inhibitor were added in triplicates, and BRET was measured for a further 50 min.

2.4.6. Functional reporter gene assay

2.4.6.1. NFAT ReLuc2P reporter gene

To assess the pharmacological inhibition of VEGFR2 downstream signalling by TKIs, a functional reporter gene assay was used (Figure 24B). Carter *et al*. (Carter et al., 2015) have previously described this nuclear factor of activated T-cells (NFAT)-luciferase assay to quantitively assess the interaction of RTKIs on $VEGF_{165}a$/VEGFR2 signalling. In stably transfected cells, the Firefly luciferase ReLuc2P was inserted downstream the NFAT promotor so that the luciferase is produced in response to NFAT-induced gene transcription. $VEGF_{165}a$/VEGFR2 downstream signalling leads, via an increase in Ca^{2+} concentration and activation of calcineurin, to dephosphorylation of NFAT and its translocation into the nucleus (Carter et al., 2015; Hill et al., 2001). Through binding to the NFAT response element, NFAT promotes subsequent transcription of the ReLuc2P gene (Carter et al., 2015; Hill et al., 2001) (Figure 24B). The luciferase catalyses the conversion of its substrate, 5-fluoroluciferin, to oxyfluroluciferin, and luminescence is emitted (Figure 24A) allowing for quantification of VEGF2 activation and signalling.

2.4.6.2. $VEGF_{165}a$ concentration response assay

NFAT-ReLuc2P HEK293 cells stably expressing NL-VEGFR2 were grown to 80% confluency in DMEM/10% FCS. Cells were seeded 48 h prior to experimentation at 20 000 cells/well in DMEM/10% FCS in white 96 well plates, coated with 0.1 mg/mL poly-D-lysine in PBS. After 24 h, medium was replaced by 100 μL serum-free DMEM and cells were incubated for a further 24 h. On the day of the experiment, medium was replaced by serum-free DMEM containing 0.1% BSA and $VEGF_{165}a$ (10 pM – 10 nM) was added to the wells in a total volume of 100 μL/well. Plates were incubated for 5 h at 37 °C/5% CO_2. Consequently, medium was replaced by 50 μL/well serum-free DMEM/0.1% BSA and 50 μL/well ONE-Glo luciferase reagent (Promega Corporation, USA). Following a 5-minute delay, luminescence was measured using a TopCount plate reader (Perkin Elmer, UK).

A

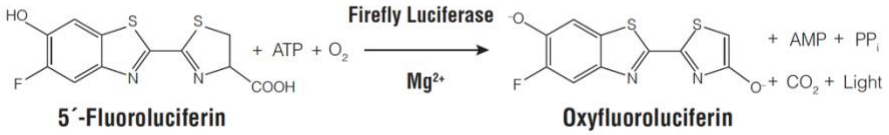

B

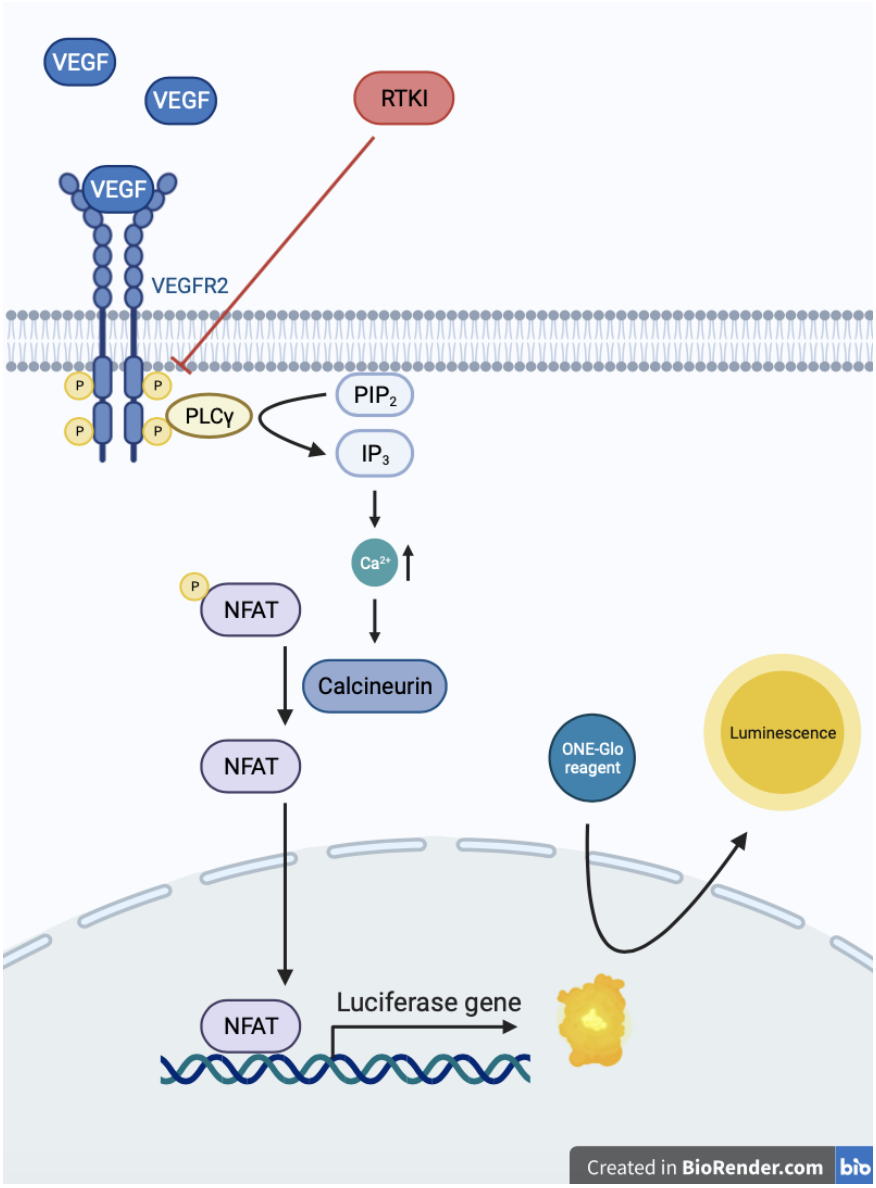

Figure 23: NFAT luciferase reporter gene assay. A. *the firefly luciferase catalyses conversion of its substrate, 5'-fluoroluciferin, into oxyfluoroluciferin emitting bright luminescence as a by-product. Chemical reaction taken from Hawkins et al. (2007).* ***B.*** *Binding of VEGF-A to VEGFR2 activates the intracellular domain of the receptor, inducing its signalling cascade and ultimately resulting in translocation of NFAT into the nucleus. NFAT acts as a transcription factor and stimulates the luciferase gene expression. The luciferase converts its substrate, 5-fluoroluciferin, to oxyfluoroluciferin, emitting luminescence. The produced luminescence serves as read-out for activation of the VEGFR2 signalling pathway. RTKI inhibiting VEGFR2 signalling will decrease luminescence levels. Created in Biorender.com*

2.4.6.3. Pharmacological inhibition of NFAT-induced response

To determine the effect of the inhibitors on NFAT signalling, cells were seeded and starved as described above. On the day of the experiment, cells were pre-treated with increasing concentrations of inhibitor (10 pM – 10 μM) in triplicates for 1 h. $VEGF_{165}a$ (1 nM) or ionomycin (1 μM) was then added to the wells in a total volume of 100 μL/well and plates were incubated for 5 h, before medium was replaced by ONE-Glo luciferase reagent and luminescence was read.

2.4.7. Data analysis and statistical tests

2.4.7.1. Software

All data are presented as mean ± SEM. All *in vitro* data were analysed using Prism 6 (GraphPad Software, San Diego, CA, USA).

2.4.7.2. BRET binding assay

The sunitinib-red saturation curve was fitted simultaneously for total and non-specific binding using a one site fit, to the following equation:

$$Total\ binding = B_{max} \cdot \frac{[L]}{[L] + K_D} + M.[L] + C \quad (5)$$

where B_{max} is the maximal specific binding, [L] is the concentration of sunitinib-red (nM), K_D is the equilibrium dissociation constant of sunitinib-red (nM), M is the slope of the non-specific binding component and C the y-axis intercepts.

Displacement curves of unlabelled inhibitors, in the presence of a fixed concentration of sunitinib-red were fitted to the following equation:

$$Specific\ Binding = 100 - \frac{100 \text{ x } [I]^{Hc}}{[I]^{Hc} + IC_{50}^{Hc}} \quad (6)$$

where Specific Binding is the specific binding of 30 nM sunitinib-red, [I] is the concentration of inhibitor, IC_{50} is the concentration of inhibitor required to generate 50% of inhibition, and Hc is the Hill coefficient, describing the steepness of the curve.

Binding affinities (K_i) of unlabelled inhibitors were calculated using the Cheng-Prusoff equation:

$$K_i = \frac{IC_{50}}{1 + \frac{[L]}{K_D}} \quad (7)$$

where IC_{50} is the inhibitor concentration required to generate 50% of inhibition, [L] is the concentration of sunitinib-red used (nM), and K_D was derived from the sunitinib-red saturation binding curve.

The displacement curve for inhibition of sunitinib-red binding by unlabelled sunitinib was fitted to the following equation:

$$Specific\ Binding = (100 - \frac{100 \text{ x } [Sun]}{[Sun] + IC_{50}}) + \frac{E_{MAX} \text{ x } [Sun]}{[Sun] + EC_{50}} \quad (8)$$

where Specific Binding is the specific binding of 30 nM sunitinib-red alone, [Sun] is the concentration of non-fluorescent sunitinib, IC_{50} is the concentration of sunitinib required to inhibit 50% of the specific binding of 30 nM sunitinib-red and E_{MAX} and EC_{50} are the maximal BRET signal and concentration of sunitinib required to stimulate a direct BRET response.

In the kinetic associated curves, data were simultaneously fitted to the follow equation:

$$Y = Y_{max}\ (1 - e^{-k_{obs}.t}) \quad (9)$$

$$k_{on} = \frac{k_{obs} - k_{off}}{[L]} \quad (10)$$

where Y_{max} is the level of binding at infinite time (t), k_{obs} is the rate constant for the observed rate of association at a particular concentration of L, [L] is the ligand concentration in M, k_{off} is the dissociation rate constant of the ligand (in min^{-1}) and k_{on} is the association rate constant (in $min^{-1}\ M^{-1}$). From this, the kinetic dissociation constant (K_d) is determined with the following equation:

$$K_d = \frac{k_{off}}{k_{on}} \quad (11)$$

2.4.7.3. Functional NFAT assay

The $VEGF_{165}a$ concentration-response data were normalized to responses to 10 nM $VEGF_{165}a$ and fitted to a non-linear regression with the following equation:

$$Response = \frac{E_{max} \text{ x } [A]^{Hc}}{[A]^{Hc} + EC_{50}^{Hc}} \quad (12)$$

where E_{max} is the maximal response, [A] is the concentration of $VEGF_{165}a$, EC_{50} is the concentration of $VEGF_{165}a$ required to generate 50% of the E_{max} and Hc is the Hill coefficient, representing the slope of the curve.

Inhibition curves of unlabelled inhibitors, in the presence of a fixed concentration of $VEGF_{165}a$ were fitted to the following equation:

$$Response = 100 - \frac{100 \text{ x } [I]^{Hc}}{[I]^{Hc} + IC_{50}^{Hc}} \quad (13)$$

where Response is the response to 1 nM $VEGF_{165}a$ alone, [I] is the concentration of inhibitor, IC_{50} is the concentration of inhibitor required to generate 50% of inhibition, and Hc is the Hill coefficient, describing the steepness of the curve.

2.4.7.4. Statistical tests

Statistical significance was determined by two-tailed Student's paired t-test (for changes in response between two paired conditions), two-tailed unpaired t-test (for changes in response between two unpaired conditions) or one-way ANOVA (for changes between more than two conditions) with post hoc Tukey's multiple comparison test. Results were considered significant where $p<0.05$.

3. RESULTS CHAPTER 3: RADIOTELEMETRY TO ASSESS THE CARDIOVASCULAR EFFECTS OF SYK INHIBITORS

3.1. Chapter introduction

Cardiovascular side effects are one of the leading causes for drug attrition from clinical and post-marketing stages of drug development (Cook et al., 2014; Qureshi et al., 2011). More sensitive systems to detect subtle changes in preclinical settings, and to translate these preclinical observations into long term risk in humans, could improve the reliability of preclinical safety assessment (Laverty et al., 2011; Weaver & Valentin, 2019b). Importantly, the analysis of BP signals needs improvement, as the traditional analysis includes few single points measures and overlooks the majority of recorded signals (Bhatt et al., 2019; Laverty et al., 2011; Mynard et al., 2020; O'Rourke & Jiang, 2001). In this Chapter, the traditional analysis of BP signals was performed (i.e., assessing MAP, HR and PP), allowing for comparison with more in-depth approaches discussed in later Chapters (Chapter 4 and Chapter 5).

One class of drugs that is known to cause severe cardiovascular toxicity are tumour angiogenesis inhibitors, used in advanced cancers (Ferrara & Adamis, 2016; Møller et al., 2019). These drugs are VEGFR2 inhibitors and have proven effective as adjuvant therapy, but their clinical application is restricted due to, in part, cardiovascular toxicity (Ferrara & Adamis, 2016; Møller et al., 2019). For example, sunitinib, a non-selective VEGFR2 inhibitor, is reported to cause or worsen persistent hypertension in 38% of patients (Bono et al., 2011). Even though the exact mechanism remains to be fully elucidated, it is clear that VEGFR2 inhibition leads to an increase in blood pressure and subsequent cardiovascular risks, including heart failure and myocardial infarction (Camarda et al., 2022; S. L. Cooper et al., 2019; Ghatalia et al., 2015; Schutz et al., 2012).

Equally, off-target inhibition of VEGFR2 presents a safety concern. The Syk inhibitor fostamatinib, FDA and EMA approved for treatment of ITP and in clinical trials for several other hyperimmune pathologies, is an example of this (D. Liu & Mamorska-Dyga, 2017; Newland & McDonald, 2020). Its non-selective binding to VEGFR2 leads to a safety profile similar to that observed with anti-angiogenesis therapies (Lengel et al., 2015; M. Skinner et al., 2014). Although the cardiovascular toxicity appears to be less severe, fostamatinib's safety liabilities limit its full clinical potential, especially in chronic applications (Y. Chen et al., 2021; Currie et al., 2014).

To improve the safety of Syk inhibition, a second generation of more selective inhibitors was developed. Of these, entospletinib is the one of the most extensively studied (Currie et al., 2014; Lam et al., 2021; D. Liu & Mamorska-Dyga, 2017; Morschhauser et al., 2021; J. Sharman et al., 2015). This compound exhibits a better selectivity for Syk and was expected to display an improved cardiovascular safety profile (Currie et al., 2014). So far, Phase I and Phase II clinical trials seem to confirm this anticipation (Burke et al., 2018; Danilov et al., 2020; Lam et al., 2021; Morschhauser et al., 2021; J. Sharman et al., 2015).

The aim of this Chapter was to characterise the cardiovascular safety of these Syk inhibitors using the typical approach currently applied in preclinical studies. According to the guideline for preclinical safety pharmacology ICH S7A (The International Conference on Harmonisation 'S7A Safety Pharmacology Studies for Human Pharmaceuticals'), preclinical cardiovascular core testing should include an evaluation of BP and HR (International Conference on Harmonisation, 2001). The guideline recommends performing these assessments in conscious animals, for example by telemetry in unrestrained rodents (International Conference on Harmonisation, 2001). Therefore, in this Chapter, this method was used for the initial safety evaluation of the Syk inhibitors. Radiotelemetry in rats was employed to monitor changes in BP and HR before and after drug administration. Arterial BP signals were analysed as MAP and PP, as is currently the conventional method for BP wave analysis (Mynard et al., 2020). ICH S7A states that safety pharmacology studies are generally performed by single dose administration, nonetheless in this Chapter animals were dosed once daily for two consecutive days and pressure signals were monitored for 48 h, to allow for slightly longer-term monitoring and detection of potential lag- or accumulation- effects.

In summary, the results in this Chapter 3 provide the initial characterisation of the safety of the selected Syk inhibitors and serves as reference points for further Chapters (Chapter 4 and Chapter 5).

3.2. Chapter methodology

3.2.1. Radiotelemetry set-up

To monitor MAP and HR, the TSE Stellar telemetry system was used. As detailed in Chapter 2 (section 2.1.1.2.), this set-up offers multiple advantages compared to other methods for blood pressure measurement. Firstly, radiotelemetry can be performed in conscious and freely moving animals that are housed in pairs, therefore data are representative for the normal state of the animal (Crestani et al., 2010; Kramer & Kinter, 2003; Matt Skinner et al., 2019). This contrasts with tail-cuff manometry, where animals are restrained, or the Doppler flowmetry model described in Chapter 5, where animals are single housed and tethered during experimentation, potentially increasing stress in animals. Moreover, the TSE Stellar receiver is able to simultaneously detect signals from two different animals in the same cage (TSE systems, 2020), therefore reduces the numbers of animals used, as there is no need of non-instrumented cage buddies. Lastly, the Stellar set-up uses a solid tip catheter which is suggested to detect more accurate and sharp blood pressure waves (AD Instruments & Williams, 2022; TSE systems, 2020). These high-quality data were required for further in-depth waveform analysis in the next Chapter (Chapter 4). In summary, the TSE Stellar system was chosen to perform the telemetry studies in this thesis as it offers advances in animal welfare and high-quality data acquisition.

3.2.2. Animals and surgery

All *in vivo* experimentation was approved by the Animal Welfare and Ethical Review Body (University of Nottingham) and performed under the Scientific Procedures Animals Act (1986), with UK Home Office approved Project Licence PP1632406, Protocol 3 and Personal Licence authority. Adult Male Wistar Han rats (400 - 550 g) were implanted with the telemetry devices (n=6). The BP sensor tip was positioned in the abdominal aorta and ECG electrodes were implanted, one on the ventral surface of the xiphoid and one subcutaneous over the right pectoral muscle. The body of the telemetry device was secured in the abdominal cavity. This device body contained a temperature probe and activity probe, the battery of the wireless implant and the transmitter that, via the antenna, transmits recorded data to the receiver outside of the cage. Full details of the surgery and experimental set-up can be found

in Chapter 2 (section 2.1.4.). Animals were given a minimum of 14 days for recovery before the commencement of any experiments.

3.2.3. Experimental protocol

In total, five compounds were tested, alongside the appropriate vehicles. Besides the Syk inhibitors (fostamatinib, 20 mg/kg and entospletinib, 6 mg/kg), three reference compounds were tested; two compounds decreasing MAP (vardenafil, 10 mg/kg and molsidomine, 10 mg/kg) and one increasing MAP (sunitinib-L-malate, 7 mg/kg). All solutions were dosed via oral gavage once daily for two consecutive days, at a volume of 10 mL/kg. An overview of the study protocol can be found in Figure 24. At least 7 days were left between two studies (drug or vehicle), to ensure complete wash-out of the previously administered compound. Plasma half-lives of each compound are specified below; none were sufficiently long to result in relevant plasma concentrations after 7 days. Indeed baseline values after 7 days were similar to those recorded before the first test (e.g. Figure 26).

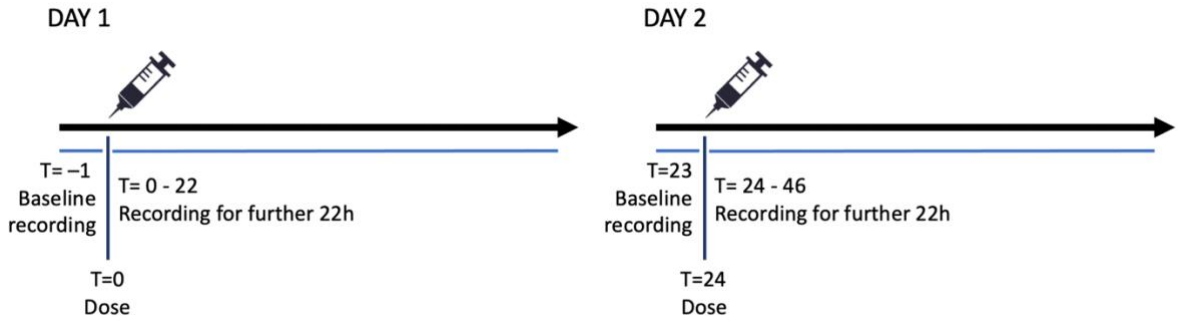

Figure 24: Telemetry study protocol. *Telemetry recordings were done 1 h before dosing on the first day, and up to 22 h after dosing. The same protocol was followed on the second day. Each drug was administered once daily, for two consecutive days.*

Most groups were composed of 6 animals (n=6), however, as one telemetry implant became faulty after the 5th group, the n-number was reduced by one, therefore the last three groups were run with 5 animals (n=5).

3.2.3.1. Fostamatinib

As described in Chapter 1 (section 1.3.4.), fostamatinib is the first and only marketed Syk inhibitor (D. Liu & Mamorska-Dyga, 2017). Due to the non-selectivity of its active metabolite R406, this compound displayed hypertension as an adverse drug reaction in clinical trials (Davis et al., 2011; Kunwar et al., 2016). Fostamatinib has been administered previously to rats at an oral dose of 8.5 mg/kg and 30 mg/kg twice daily. These dosing schedules resulted in maximal free plasma concentrations of 27 nmol/L and 106 nmol/L respectively (Lengel *et al.* 2015). Lengel *et al.* dosed twice daily and in this study dosed fostamatinib once daily, therefore plasma concentrations are not directly comparable, nonetheless this study was used as a guide when choosing the dose here. In this study, the aim was to reflect relevant clinical plasma concentrations. The clinical mean peak free plasma concentration in clinical trials was approximately 49 nmol/L (Lengel et al. 2015), therefore fostamatinib was dosed at 20 mg/kg once daily. This dose theoretically (based on the study by Lengel *et al.*) resulted in a peak plasma concentration of 35 – 60 nmol/L. The oral route is the therapeutic route in man (Connell & Berliner, 2019). The plasma half-life of R406 is 4.2 h in rats (Pine et al., 2007).

3.2.3.2. Entospletinib

As described in Chapter 1 (section 1.3.5.), entospletinib is a second generation Syk inhibitor with a better selectivity profile and expected to display less cardiovascular side effects (Currie et al., 2014). Entospletinib has been administered previously to rats at a dose of 3 mg/kg twice daily, this dose resulted in plasma concentrations sufficient to significantly reduce arthritis disease scores on the second day (Currie et al., 2014). Again, here the aim was to obtain plasma concentration *in vivo* that were relevant to clinical settings, therefore entospletinib was dosed 6 mg/kg once daily in this study. The microsomal half-life of entospletinib in rats is 35 min (Currie et al., 2014).

3.2.3.3. Vardenafil

Besides the Syk inhibitors, two vasodilators were tested. Vardenafil is a potent phosphodiesterase type 5 (PDE-5) inhibitor (Keating & Scott, 2003). This compound inhibits the breakdown of cGMP, a second messenger that mediates the NO-induced vasodilation (Ghiadoni et al., 2008). By sustaining the activity of NO and thus enhancing its vasodilating effects, it causes a decrease in BP (Ghiadoni et al., 2008; Keating & Scott, 2003). Vardenafil had been administered to rats at a dose of 10 mg/kg in a previous study at Vivonics Ltd. and is known to be well tolerated. The oral route is the therapeutic route in man (Keating & Scott, 2003). The plasma half-life of vardenafil in rats is 1.38 h (Matsumoto et al., 2009).

3.2.3.4. Molsidomine

Molsidomine acts as an NO-donor and is therefore a potent vasodilating compound (Chander & Chopra, 2005; Nayak B et al., 2021), displaying similar effects as vardenafil on MAP and HR. Molsidomine has been administered previously to rats at an oral dose of 10 mg/kg and was well tolerated (Chander & Chopra, 2005; Nayak B et al., 2021). No literature on the half-life of molsidomine (or its active metabolite SIN-1) in rats could be found, however in humans, SIN-1 is quickly metabolised to release NO and the plasma half-life is less than 2 h (Rosenkranz et al., 1996).

3.2.3.5. Sunitinib

Lastly, sunitinib was evaluated in the radiotelemetry set-up. Sunitinib is a non-specific receptor tyrosine kinase inhibitor (RTKI), targeting VEGFR2 and PDGRRs developed for anti-angiogenic effects in various cancer types, and associated with antiVEGFR2-induced hypertension (Davis et al., 2011; Neves et al., 2020). The malate salt of sunitinib was used, as it has a higher solubility in aqueous solutions. Sunitinib-L-malate has been administered previously to rats at a dose of 7 mg/kg, this dose resulted in systemic concentrations comparable with those reached in patients treated with a standard daily dose of sunitinib of 50 mg (Lankhorst et al., 2015). The oral route is the therapeutic route in man. In rats, sunitinib's plasma half-life is 8 h (Speed et al., 2012).

3.2.3.6. Vehicle

All drugs were dissolved or suspended in 10% (w/V) hydroxypropyl beta cyclodextrin (CTD Inc.) in water for injection. This solution was used as vehicle in the control groups as well, dosed at 10 mL/kg. Every drug-treated group was compared with its corresponding vehicle group recorded in the preceding or following week.

3.2.4. Statistics

All data were expressed as mean ± SEM. Statistical analysis was performed in Prism 9.5.1 (GraphPad Software, San Diego, CA, USA). Delta changes (e.g. ΔMAP) are changes in reference to the baseline value on day 1. As there were two categorical, independent variables (time and treatment) and one quantitative outcome variable (MAP, HR or PP), a two-way ANOVA test was performed. This tested (1) if MAP/HR/PP was significantly different over time, (2) if MAP/HR/PP was significantly different between groups, and (3) if MAP/HR/PP was significantly different between groups over time. If the result of the two-way ANOVA were significant, multiple comparisons test were performed; a Dunnett test to determine where changes over time from baseline were significant and a Sídák test to determine where changes between groups were significant. Results were considered significant at $p < 0.05$.

3.3. Chapter results: Conventional waveform analysis

3.3.1. Vardenafil

Vardenafil caused an immediate large decrease in MAP and ΔMAP (Figure 25A and 26D). The maximum effect was reached on day 2, within the first hour after dosing (ΔMAP = -11.0 ± 1.2 mmHg for vardenafil (n=5) versus 0.8 ± 1.9 mmHg for vehicle (n=6), Table 3, Sídák test $p<0.05$). This decrease in blood pressure was accompanied by an increase in HR (Figure 25B and 26E). The maximum effect on HR was observed on day 1, within the first hour after dosing (ΔHR = 108.6 ± 8.0 bpm for vardenafil versus 16.0 ± 14.6 bpm for vehicle, Table 3, Sídák test $p<0.0005$). The elevation in ΔHR was temporary and not significantly different from vehicle after 2 – 3 h post dosing. Furthermore, a simultaneous decrease of PP was observed in vardenafil-treated rats (Figure 26C and 26F). The biggest difference in ΔPP was observed on the first day, 2 – 3 h after dosing (ΔPP = -7.0 ± 0.8 mmHg for vardenafil versus -0.8 ± 1.2 mmHg for vehicle, Table 3, Sídák test $p<0.05$). This decrease sustained throughout the day. All numerical data showing the effect of vardenafil on the cardiovascular variables are displayed in Table 3.

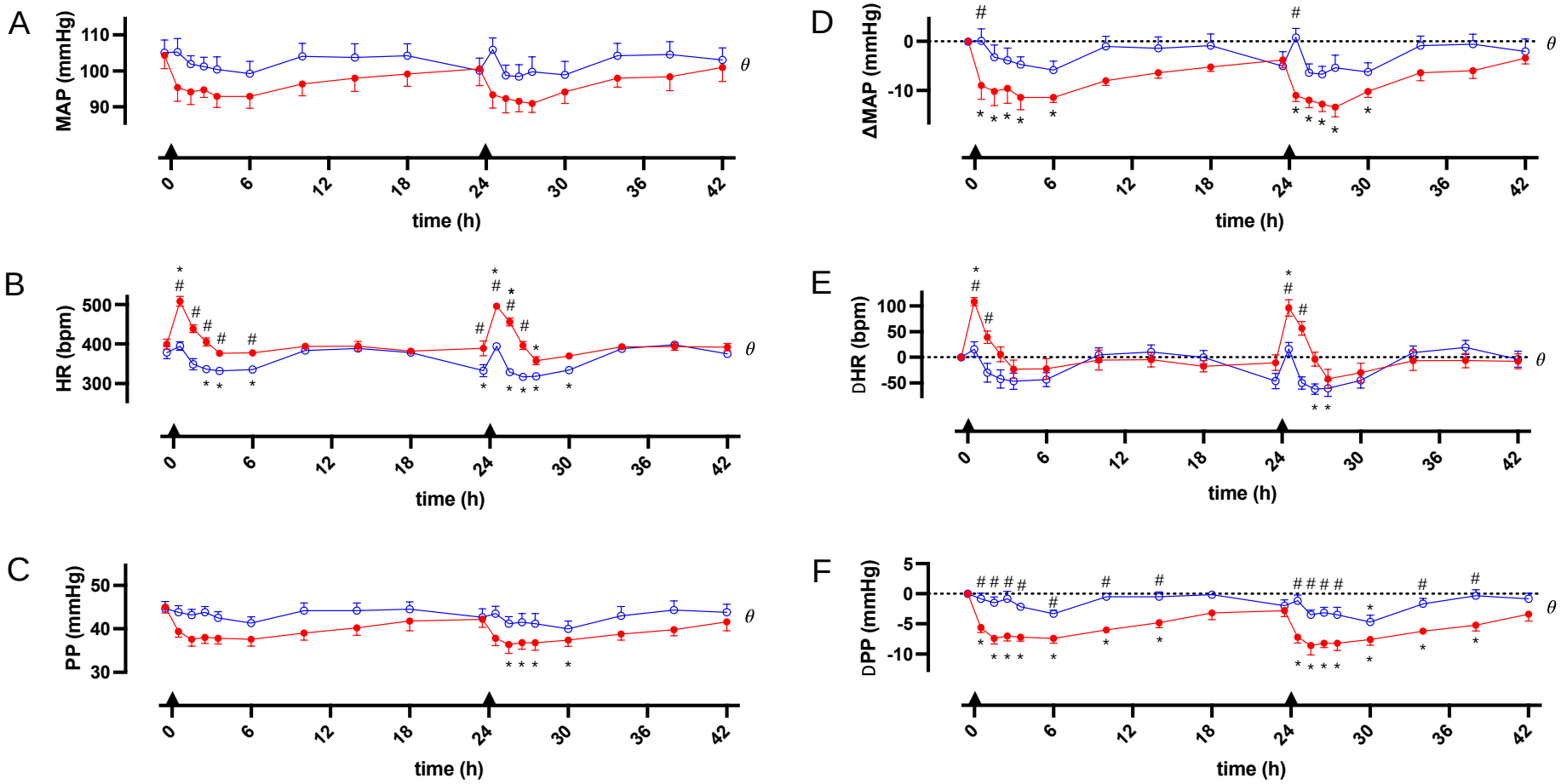

Figure 25: Cardiovascular effects of vardenafil. *Changes in MAP* ***(A)****, HR* ***(B)*** *and PP* ***(C)*** *of rats dosed with vardenafil 10 mg/kg p.o. (n=5, red, filled circles) and vehicle p.o. (n=6, blue, open circles). Data were normalised to baseline recording for each animal individually, presented in* ***(D)****,* ***(E)*** *and* ***(F)****. Black triangles on time-axis indicate time of administration of vardenafil or vehicle. Data are presented as mean ± SEM, were binned per hour (baseline and first 4 h after dosing) or per 4 h (from 4 h after dosing) and plotted at the time points half-way through the 1 h or 4 h interval. A two-way ANOVA test was conducted to test for overall differences between two groups (θ = p<0.05), followed by multiple comparison by Sídák to test for differences between the groups at each time point (# = p<0.05) Furthermore, if there was a significant change over time within a group (two-way ANOVA), each timepoint of the group was compared to the group's corresponding baseline (T=-0.5 h), by Dunnett test, performed on the raw, non-normalised data (* = p<0.05).*

Table 3: Changes in ΔMAP, ΔHR and ΔPP after vardenafil administration. *Mean ± SEM changes from baseline (defined as T=-0.5 h) from rats dosed with vardenafil (10 mg/kg/day, n=5) or vehicle (10 mL/kg/day, n=6). Data were binned per hour (baseline and first 4 h after dosing) or per 4 h (from 4 h after dosing). Blue line indicated dosing via oral gavage. Statistics: Significant changes between treated and vehicle group overall are indicated by θ (two-way ANOVA, p<0.05), followed by significant changes for each individual timepoint between the groups, indicated by # (Sídák, p<0.05). Significant changes within the group from baseline are indicated by * (two-way ANOVA, p<0.05).*

Time (h)	ΔMAP (mean ± SEM) (mmHg)		ΔHR (mean ± SEM) (bpm)		ΔPP (mean ± SEM) (mmHg)	
	Vardenafil$^{\theta}$	Vehicle	Vardenafil$^{\theta}$	Vehicle	Vardenafil$^{\theta}$	Vehicle
-1 – 0	0.0 ± 0.0	0.0 ± 0.0	0.0 ± 0.0	0.0 ± 0.0	0.0 ± 0.0	0.0 ± 0.0
0 – 1	-9.0 ± 2.8$^{\#,*}$	0.2 ± 2.4	108.6 ± 8.0$^{\#,*}$	16.0 ± 14.6	-5.6 ± 0.8$^{\#,*}$	-0.8 ± 0.9
1 – 2	-10.2 ± 2.9*	-3.2 ± 2.5	39.2 ± 11.9$^{\#}$	-29.8 ± 18.4	-7.4 ± 0.9$^{\#,*}$	-1.5 ± 1.0
2 – 3	-9.6 ± 3.0*	-3.8 ± 2.5	5.8 ± 14.2	-42.2 ± 17.8	-7.0 ± 0.8$^{\#,*}$	-0.8 ± 1.2
3 – 4	-11.4 ± 2.5*	-4.7 ± 1.6	-23.4 ± 17.8	-46.7 ± 16.2	-7.2 ± 0.7$^{\#,*}$	-2.2 ± 0.5
4 – 8	-11.4 ± 1.0*	-5.9 ± 1.9	-22.4 ± 30.4	-43.3 ± 13.8	-7.4 ± 0.8$^{\#,*}$	-3.3 ± 0.6
8 – 12	-8.0 ± 1.0	-1.0 ± 2.1	-5.6 ± 19.4	4.8 ± 14.2	-6.0 ± 0.5$^{\#,*}$	-0.5 ± 0.5
12 – 16	-6.4 ± 1.1	-1.3 ± 2.3	-4.8 ± 14.0	10.3 ± 13.7	-4.8 ± 0.8$^{\#,*}$	-0.5 ± 0.8
16 – 20	-5.2 ± 0.9	-0.8 ± 2.4	-17.4 ± 10.8	0.0 ± 13.3	-3.2 ± 1.1	-0.2 ± 0.5
23 – 24	-3.8 ± 1.6	-5.0 ± 2.9	-10.6 ± 15.1	-46.2 ± 15.3	-2.8 ± 1.0	-2.0 ± 1.0
24 – 25	-11.0 ± 1.2$^{\#,*}$	0.8 ± 1.9	96.6 ± 16.0$^{\#,*}$	15.8 ± 13.4	-7.2 ± 1.0$^{\#,*}$	-1.2 ± 0.9
25 – 26	-12.0 ± 1.5*	-6.3 ± 1.8	56.4 ± 13.3$^{\#}$	-50.0 ± 12.0	-8.6 ± 1.5$^{\#,*}$	-3.5 ± 0.8
26 – 27	-12.8 ± 1.5*	-6.7 ± 1.6	-3.6 ± 13.5	-62.2 ± 10.4*	-8.2 ± 0.7$^{\#,*}$	-3.2 ± 0.9
27 – 28	-13.4 ± 2.0*	-5.3 ± 2.6	-42.2 ± 18.8	-60.5 ± 15.7*	-8.2 ± 1.2$^{\#,*}$	-3.5 ± 1.3
28 – 32	-10.2 ± 1.2*	-6.2 ± 1.9	-30.0 ± 18.7	-44.8 ± 15.2	-7.6 ± 1.0*	-4.7 ± 1.1*
32 – 36	-6.4 ± 1.6	-0.8 ± 2.0	-6.4 ± 19.0	9.5 ± 13.1	-6.2 ± 0.5$^{\#,*}$	-1.7 ± 0.9
36 – 40	-6.0 ± 1.5	-0.5 ± 2.0	-6.0 ± 14.2	19.5 ± 13.9	-5.2 ± 1.0$^{\#,*}$	-0.3 ± 1.0
40 – 44	-3.4 ± 1.2	-2.0 ± 2.6	-7.6 ± 15.0	-3.7 ± 15.5	-3.4 ± 1.1	-0.8 ± 0.9

3.3.2. Molsidomine

Administration of molsidomine resulted in a rapid large decrease in MAP and ΔMAP that returned to baseline values throughout the day (Figure 26A and 27D). The maximum decrease in ΔMAP was observed on the first day, within the first hour after dosing (ΔMAP = -10.6 ± 2.7 mmHg for molsidomine (n=5) versus 3.0 ± 1.3 mmHg for vehicle (n=5), Table 4, Sídák test $p<0.05$). Similar to vardenafil, this decrease in MAP was accompanied by a rapid increase in HR, that was sustained during the first three h after dosing (Figure 26B and 27E). The maximum effect on HR was observed on day 1, 1 – 2 h after dosing (ΔHR = 112.2 ± 10.7 bpm for molsidomine versus -23.6 ± 14.1 bpm for vehicle, Table 4, Sídák test $p<0.05$). Lastly, the PP was consistently and significantly decreased in molsidomine-treated rats (Figure 26C and 27F), with the maximum effect observed on the first day, within the first hour after dosing (ΔPP = -14.4 ± 1.4 mmHg for molsidomine versus -0.2 ± 0.4 mmHg for vehicle, Table 4, Sídák test $p<0.05$). All numerical data showing the effect of molsidomine on the cardiovascular variables are displayed in Table 4.

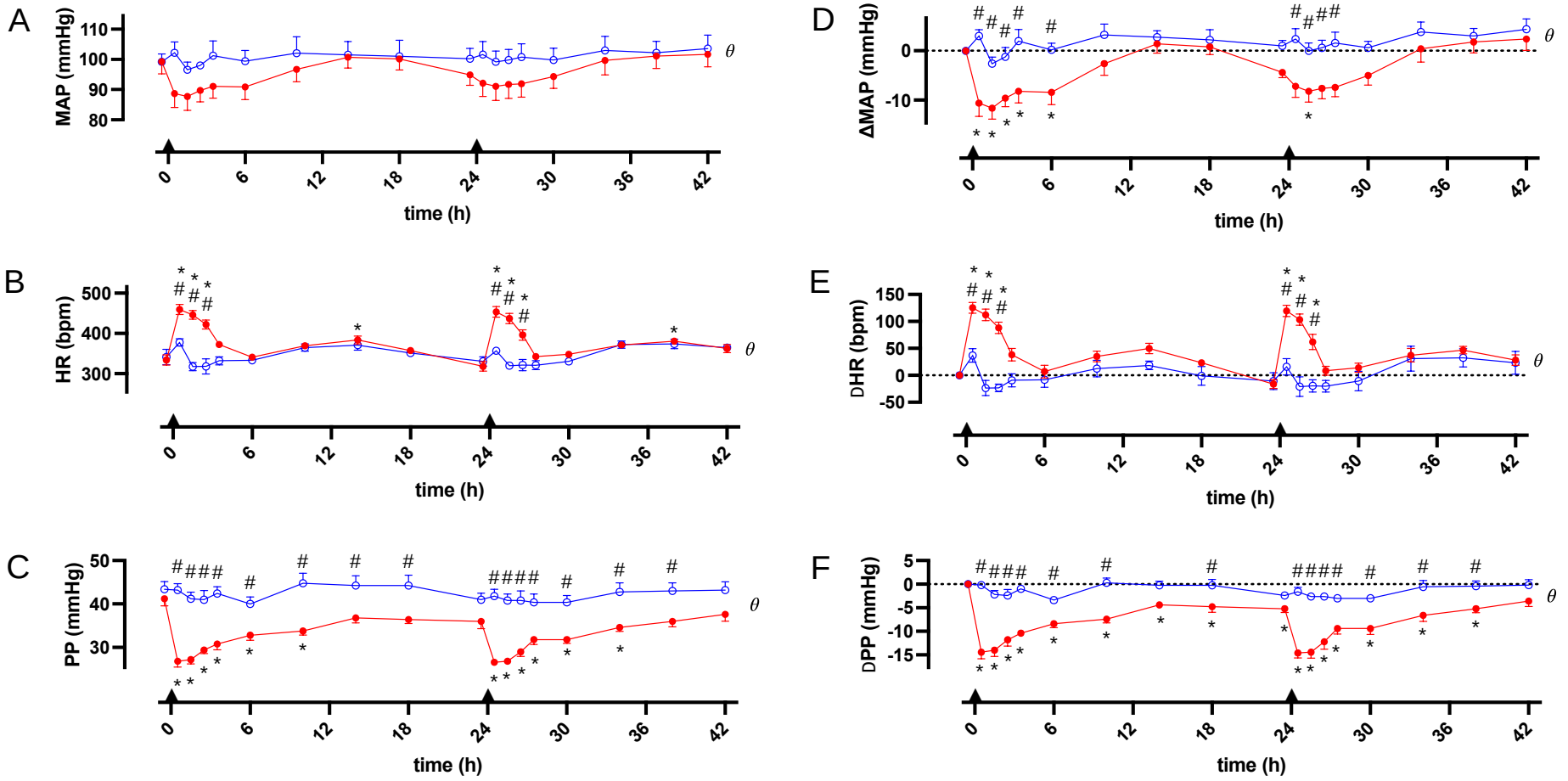

Figure 26: Cardiovascular effects of molsidomine. *Changes in MAP* ***(A)****, HR* ***(B)*** *and PP* ***(C)*** *of rats dosed with molsidomine 10 mg/kg p.o. (n=5, red, filled circles) and vehicle p.o. (n=5, blue, open circles). Data were normalised to baseline recording for each animal individually, presented in* ***(D)****,* ***(E)*** *and* ***(F)****. Black triangles on time-axis indicate time of administration of molsidomine or vehicle Data are presented as mean ± SEM, were binned per hour (baseline and first 4 h after dosing) or per 4 h (from 4 h after dosing) and plotted at the time points half-way through the 1 h or 4 h interval. A two-way ANOVA test was conducted to between two groups (θ = p<0.05), followed by multiple comparison by Sídák to test for differences to test for overall differences between the groups at each time point (# = p<0.05) Furthermore, if there was a significant change over time within a group (two-way ANOVA), each timepoint of the group was compared to the group's corresponding baseline (T=-0.5 h), by Dunnett, performed on the raw, non-normalised data (* = p<0.05).*

Table 4: Changes in ΔMAP, ΔHR and ΔPP after molsidomine administration. *Mean ± SEM changes from baseline (defined as T=-0.5 h) from rats dosed with molsidomine (10 mg/kg/day, n=5) or vehicle (10 mL/kg/day, n=5). Data were binned per hour (baseline and first 4 h after dosing) or per 4 h (from 4 h after dosing). Blue line indicated dosing via oral gavage. Significant changes between treated and vehicle group overall are indicated by θ (two-way ANOVA, p<0.05), followed by significant changes for each individual timepoint between the groups, indicated by # (Sídák, p<0.05). Significant changes within the group from baseline are indicated by * (two-way ANOVA, p<0.05).*

Time (h)	**ΔMAP (mean ± SEM) (mmHg)**		**ΔHR (mean ± SEM) (bpm)**		**ΔPP (mean ± SEM) (mmHg)**	
	Molsidomine $^{\theta}$	**Vehicle**	**Molsidomine** $^{\theta}$	**Vehicle**	**Molsidomine** $^{\theta}$	**Vehicle**
-1 – 0	0.0 ± 0.0	0.0 ± 0.0	0.0 ± 0.0	0.0 ± 0.0	0.0 ± 0.0	0.0 ± 0.0
0 – 1	-10.6 ± 2.7$^{\#,*}$	3.0 ± 1.3	125.4 ± 10.0$^{\#,*}$	36.8 ± 12.8	-14.4 ± 1.4$^{\#,*}$	-0.2 ± 0.4
1 – 2	-11.6 ± 2.2$^{\#,*}$	-2.6 ± 1.3	112.2 ± 10.7$^{\#,*}$	-23.6 ± 14.1	-14.0 ± 1.3$^{\#,*}$	-2.2 ± 0.9
2 – 3	-9.6 ±1.7$^{\#,*}$	-1.2 ± 1.8	88.2 ± 10.8$^{\#,*}$	-23.4 ± 7.2	-11.8 ± 1.4$^{\#,*}$	-2.4 ± 1.3
3 – 4	-8.2 ± 2.4$^{\#,*}$	2.0 ± 2.3	38.4 ± 11.5	-9.4 ± 12.4	-10.4 ± 0.6$^{\#,*}$	-1.0 ± 0.6
4 – 8	-8.4 ± 2.5$^{\#,*}$	0.2 ± 1.4	7.0 ± 11.8	-8.0 ± 14.1	-8.4 ± 0.8$^{\#,*}$	-3.4 ± 0.2
8 – 12	-2.6 ± 2.4	3.3 ± 2.1	35.2 ± 10.2	12.5 ± 15.7	-7.4 ± 0.8$^{\#,*}$	0.25 ± 1.0
12 – 16	1.4 ± 1.8	2.8 ± 1.3	49.8 ± 9.5	18.5 ± 7.8	-4.4 ± 0.7*	-0.25 ± 0.9
16 – 20	0.8 ± 1.6	2.3 ± 2.1	23.4 ± 6.3	-1.0 ± 17.5	-4.8 ± 1.2$^{\#,*}$	-0.25 ± 1.3
23 – 24	-4.4 ± 1.0	1.0 ± 1.1	-16.2 ± 8.2	-10.8 ± 15.5	-5.2 ± 0.8*	-2.4 0.7
24 – 25	-7.2 ± 2.2$^{\#}$	2.4 ± 2.1	119.6 ± 10.2$^{\#,*}$	15.8 ± 15.3	-14.6 ± 1.0$^{\#,*}$	-1.6 ± 0.9
25 – 26	-8.2 ± 2.2$^{\#,*}$	0.0 ± 1.6	103.2 ± 10.6$^{\#,*}$	-21.2 ± 18.4	-14.4 ± 1.3$^{\#,*}$	-2.6 ± 0.6
26 – 27	-7.6 ± 2.1$^{\#}$	0.6 ± 1.5	62.0 ± 14.0$^{\#,*}$	-19.6 ± 11.5	-12.2 ± 1.6$^{\#,*}$	-2.6 ± 0.7
27 – 28	-7.4 ± 1.9$^{\#}$	1.6 ± 2.2	8.4.0 ± 8.2	-20.4 ± 10.7	-9.4 ± 1.2$^{\#,*}$	-3.0 ± 0.3
28 – 32	-5.0 ± 1.9	0.6 ± 1.4	14.0 ± 8.5	-10.6 ± 18.1	-9.4 ± 1.3$^{\#,*}$	-3.0 ± 0.7
32 – 36	0.4 ± 2.7	3.8 ± 2.1	37.2 ± 12.8	31.0 ± 23.4	-6.6 ± 1.3$^{\#,*}$	-0.6 ± 1.4
36 – 40	1.8 ± 2.2	3.0 ± 1.5	47.0 ± 7.2	32.4 ± 16.9	-5.2 ± 0.9$^{\#,*}$	-0.4 ± 1.0
40 – 44	2.4 ± 2.3	4.4 ± 2.0	28.4 ± 9.7	23.4 ± 21.2	-3.6 ± 1.1	-0.2 ± 1.2

3.3.3. Sunitinib

Administration of sunitinib resulted in an increase in BP (Figure 27A and 28D). From the first day, ΔMAP was significantly different between the sunitinib-group (n=6) and the vehicle group (n=6). On the second day, an even larger increase in ΔMAP was observed, with the maximum effect at 3-4 h after dosing (ΔMAP = 8.2 ± 1.6 mmHg for sunitinib versus -5.3 ± 2.6 for vehicle, Table 5, Sídák test $p<0.05$). Although overall the HR and ΔHR were changed significantly between the sunitinib group and vehicle group (two-way ANOVA, $p<0.05$ for both HR and ΔHR), no individual time point was significantly different between the groups (Figure 27B and 28E). ΔPP slightly increased following sunitinib administration, with the only significant difference from vehicle at 16-20 h after dosing on the second day (Figure 27F, ΔPP = 2.8 ± 0.7 mmHg for sunitinib versus -0.8 ± 0.9 mmHg for vehicle, Sídák test $p<0.05$, Table 5). All numerical data showing the effect of sunitinib on the cardiovascular variables are displayed in Table 5.

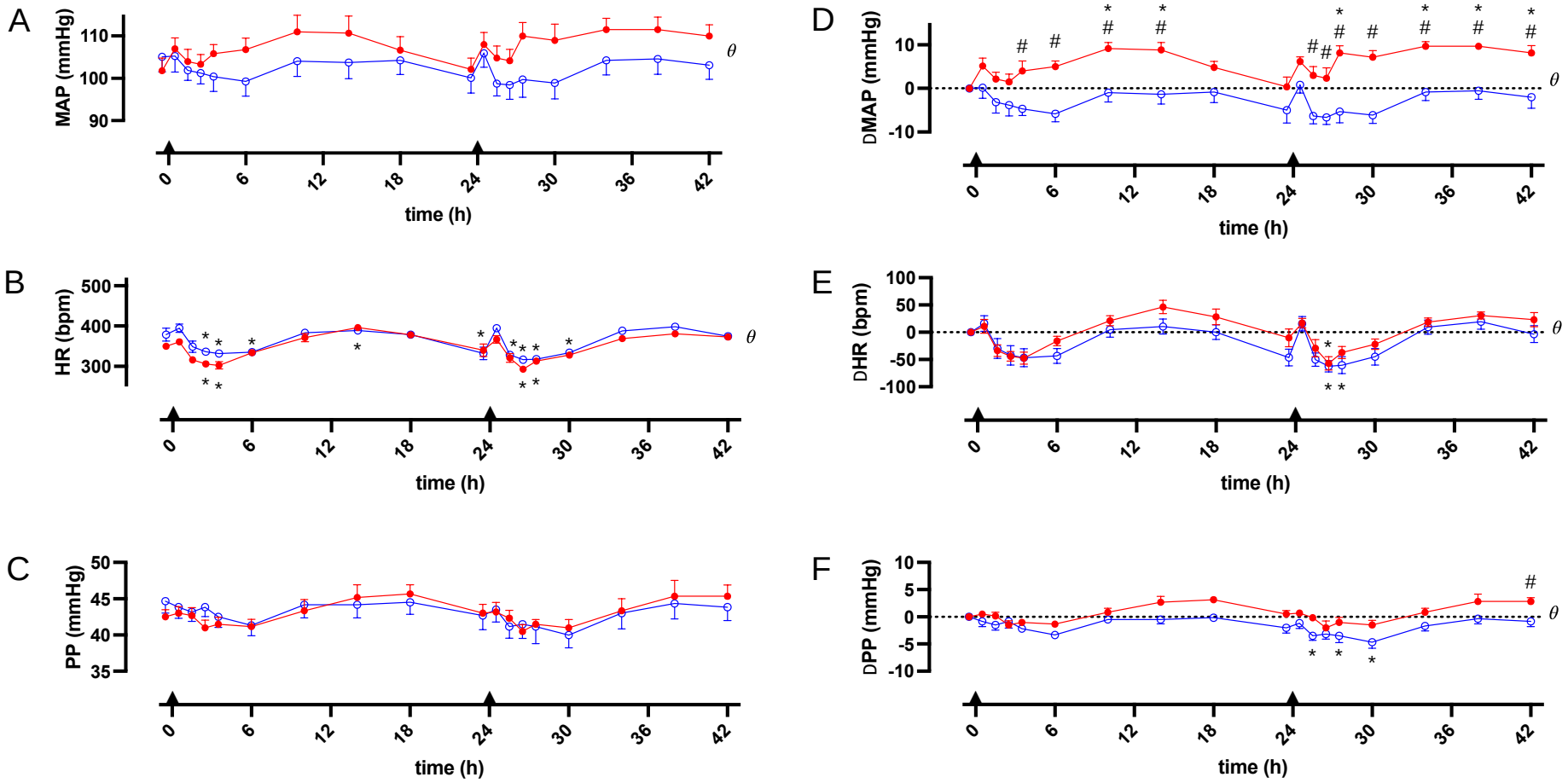

Figure 27: Cardiovascular effects of sunitinib. *Changes in MAP **(A)**, HR **(B)** and PP **(C)** of rats dosed with sunitinib 7 mg/kg p.o. (n=6, red, filled circles) and vehicle p.o. (n=6, blue, open circles). Data were normalised to baseline recording for each animal individually, presented in **(D)**, **(E)** and **(F)**. Black triangles on time-axis indicate time of administration of sunitinib or vehicle. Data are presented as mean ± SEM, were binned per hour (baseline and first 4 h after dosing) or per 4 h (from 4 h after dosing) and plotted at the time points half-way through the 1 h or 4 h interval. A two-way ANOVA test was conducted to test for overall differences between two groups (θ = p<0.05), followed by multiple comparison by Sídák to test for differences between the groups at each time point (# = p<0.05) Furthermore, if there was a significant change over time within a group (two-way ANOVA), each timepoint of the group was compared to the group's corresponding baseline (T=-0.5 h), by Dunnett, performed on the raw, non-normalised data (* = p<0.05).*

Table 5: Changes in ΔMAP, ΔHR and ΔPP after sunitinib administration. *Mean ± SEM changes from baseline (defined as T=-0.5 h) from rats dosed with sunitinib (7 mg/kg/day, n=6) or vehicle (10 mL/kg/day, n=6). Data were binned per hour (baseline and first 4 h after dosing) or per 4 h (from 4 h after dosing). Blue line indicated dosing via oral gavage. Significant changes between treated and vehicle group overall are indicated by θ (two-way ANOVA, p<0.05), followed by significant changes for each individual timepoint between the groups, indicated by # (Sídák, p<0.05). Significant changes within the group from baseline are indicated by * (two-way ANOVA, p<0.05).*

Time (h)	ΔMAP (mean ± SEM) (mmHg)		ΔHR (mean ± SEM) (bpm)		ΔPP (mean ± SEM) (mmHg)	
	Sunitinib$^{\theta}$	Vehicle	Sunitinib$^{\theta}$	Vehicle	Sunitinib$^{\theta}$	Vehicle
-1 – 0	0.0 ± 0.0	0.0 ± 0.0	0.0 ± 0.0	0.0 ± 0.0	0.0 ± 0.0	0.0 ± 0.0
0 – 1	5.2 ± 1.8	0.2 ± 2.4	11.0 ± 12.6	16 ± 14.6	0.5 ± 0.4	-0.8 ± 0.9
1 – 2	2.2 ± 1.6	-3.2 ± 2.5	-33.8 ± 10.7	-29.8 ± 18.4	0.2 ± 0.7	-1.5 ± 1.0
2 – 3	1.5 ± 1.8	-3.8 ± 2.5	-44.0 ± 9.1	-42.2 ± 17.8	-1.5 ± 0.8	-0.8 ± 1.2
3 – 4	4.0 ± 2.3$^{\#}$	-4.7 ± 1.6	-47.5 ± 11.2	-46.7 ± 16.2	-1.0 ± 0.6	-2.2 ± 0.5
4 – 8	5.0 ± 1.3$^{\#}$	-5.9 ± 1.9	-16.0 ± 8.6	-43.3 ± 13.8	-1.3 ± 0.5	-3.3 ± 0.6
8 – 12	9.2 ± 1.4$^{\#,*}$	-1.0 ± 2.1	21.3 ± 9.3	4.8 ± 14.2	0.8 ± 0.7	-0.5 ± 0.5
12 – 16	8.8 ± 1.7$^{\#,*}$	-1.3 ± 2.3	46.3 ± 12.2	10.3 ± 13.7	2.7 ± 1.1	-0.5 ± 0.8
16 – 20	4.8 ± 1.4	-0.8 ± 2.4	28.3 ± 14.5	0.0 ± 13.3	3.2 ± 0.5	-0.2 ± 0.5
23 – 24	0.3 ± 2.2	-5.0 ± 2.9	-10.0 ± 16.6	-46.2 ± 15.3	0.5 ± 0.7	-2.0 ± 1.0
24 – 25	6.2 ± 1.1	0.8 ± 1.9	16.7 ± 8.7	15.8 ± 13.4	0.7 ± 0.4	-1.2 ± 0.9
25 – 26	3.0 ± 2.0$^{\#}$	-6.3 ± 1.8	-29.2 ± 15.0	-50.0 ± 12.0	-0.2 ± 0.5	-3.5 ± 0.8*
26 – 27	2.3 ± 2.4$^{\#}$	-6.7 ± 1.6	-57.0 ± 12.1*	-62.2 ± 10.4*	-2.0 ± 1.2	-3.2 ± 0.9
27 – 28	8.2 ± 1.6$^{\#,*}$	-5.3 ± 2.6	-37.0 ± 11.1	-60.5 ± 15.7*	-1.0 ± 0.9	-3.5 ± 1.3*
28 – 32	7.2 ± 1.5$^{\#}$	-6.2 ± 1.9	-22.0 ± 9.6	-44.8 ± 15.2	-1.5 ± 0.8	-4.7 ± 1.1*
32 – 36	9.7 ± 1.1$^{\#,*}$	-0.8 ± 2.0	18.7 ± 7.7	9.5 ± 13.1	0.8 ± 0.7	-1.7 ± 0.9
36 – 40	9.7 ± 0.8$^{\#,*}$	-0.5 ± 2.0	30.8 ± 6.8	19.5 ± 13.9	2.8 ± 1.4$^{\#}$	-0.3 ± 1.0
40 – 44	8.2 ± 1.6$^{\#,*}$	-2.0 ± 2.6	23.0 ± 13.0	-3.7 ± 15.5	2.8 ± 0.7	-0.8 ± 0.9

3.3.4. Fostamatinib

Fostamatinib (n=5) caused a small increase in MAP (Figure 28A). There was no significant difference in MAP between fostamatinib and vehicle-treated animals (both groups, n=5) on the first day (two-way ANOVA). On the second day, ΔMAP significantly increased (Figure 28D), with the maximum effect observed 3-4 h after dosing (ΔMAP = 8.8 ± 0.7 mmHg for fostamatinib versus 1.6 ± 2.2 mmHg for vehicle, Table 6, Sídák test $p<0.05$). There were no significant changes in ΔHR between the two groups (Figure 28E, two-way ANOVA). No significant change was observed in PP (Figure 28B). ΔPP was increased after fostamatinib administration (Figure 28F), with the only significant change observed 1-2 h after dosing on the second day (ΔPP = 2.2 ± 1.3 mmHg for fostamatinib versus -2.6 ± 0.5 mmHg for vehicle, Sídák test $p<0.05$, Table 6). All numerical data showing the effect of fostamatinib on the cardiovascular variables are displayed in Table 6.

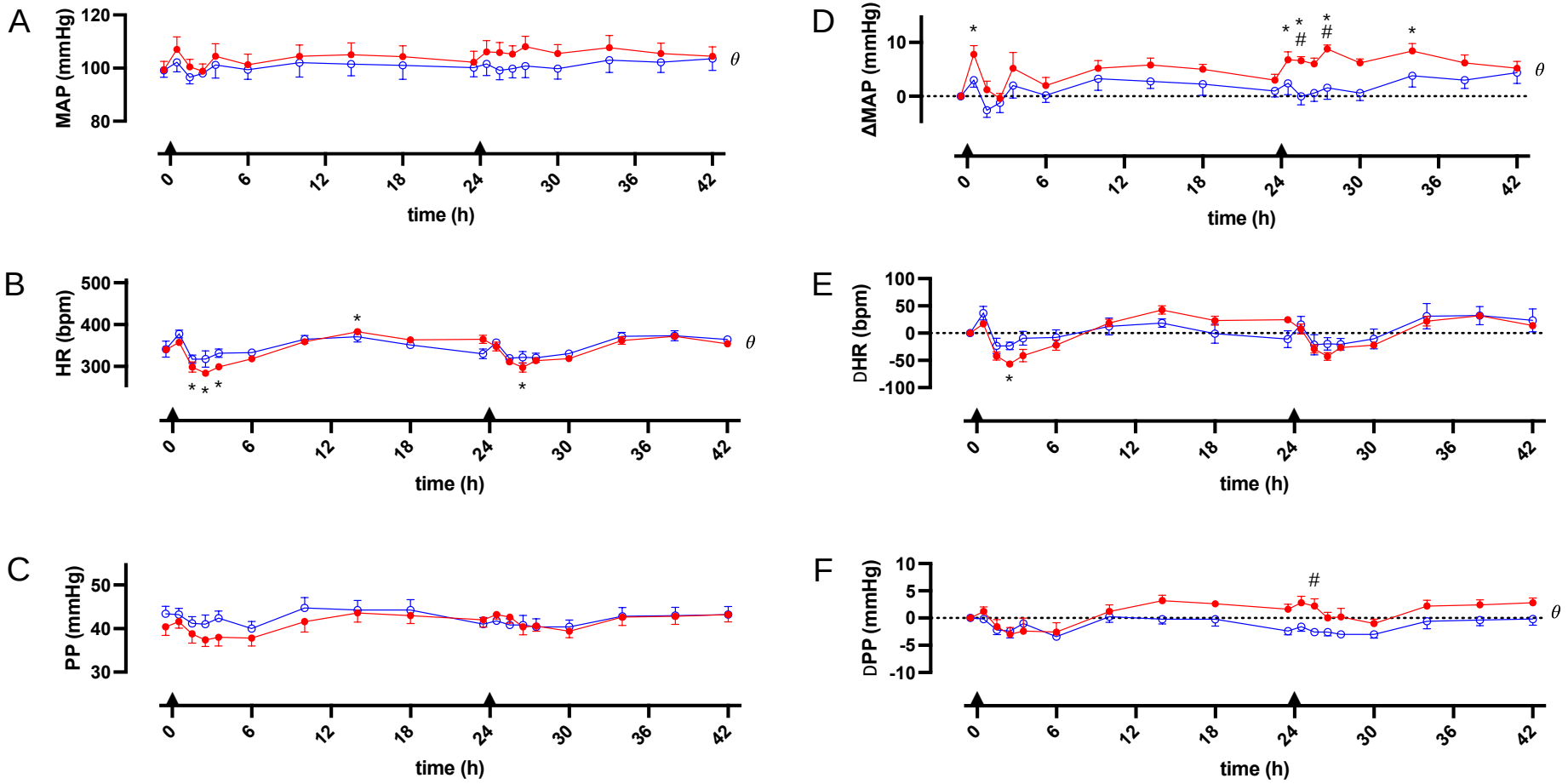

Figure 28: Cardiovascular effects of fostamatinib. *Changes in MAP* ***(A)****, HR* ***(B)*** *and PP* ***(C)*** *of rats dosed with fostamatinib 20 mg/kg p.o. (n=5, red, filled circles) and vehicle p.o. (n=5, blue, open circles). Data were normalised to baseline recording for each animal individually, presented in* ***(D)****,* ***(E)*** *and* ***(F)****. Black triangles on time-axis indicate time of administration of fostamatinib or vehicle. Data are presented as mean ± SEM, were binned per hour (baseline and first 4 h after dosing) or per 4 h (from 4 h after dosing) and plotted at the time points half-way through the 1 h or 4 h interval. A two-way ANOVA test was conducted to test for overall differences between two groups (θ = p<0.05), followed by multiple comparison by Sídák to test for differences between the groups at each time point (# = p<0.05) Furthermore, if there was a significant change over time within a group (two-way ANOVA), each timepoint of the group was compared to the group's corresponding baseline (T=-0.5 h), by Dunnett, performed on the raw, non-normalised data (* = p<0.05).*

Table 6: Changes in ΔMAP, ΔHR and ΔPP after fostamatinib administration. *Mean ± SEM changes from baseline (defined as T=-0.5 h) from rats dosed with fostamatinib (20 mg/kg/day, n=5) or vehicle (10 mL/kg/day, n=5). Data were binned per hour (baseline and first 4 h after dosing) or per 4 h (from 4 h after dosing). Blue line indicated dosing via oral gavage. Significant changes between treated and vehicle group overall are indicated by θ (two-way ANOVA, p<0.05), followed by significant changes for each individual timepoint between the groups, indicated by # (Sídák, p<0.05). Significant changes within the group from baseline are indicated by * (two-way ANOVA, p<0.05).*

Time (h)	ΔMAP (mean ± SEM) (mmHg)		ΔHR (mean ± SEM) (bpm)		ΔPP (mean ± SEM) (mmHg)	
	Fostamatinib$^{\theta}$	Vehicle	Fostamatinib	Vehicle	Fostamatinib$^{\theta}$	Vehicle
-1 – 0	0.0 ± 0.0	0.0 ± 0.0	0.0 ± 0.0	0.0 ± 0.0	0.0 ± 0.0	0.0 ± 0.0
0 – 1	7.8 ± 1.6*	3.0 ± 1.3	17.2 ± 4.7	36.8 ± 12.8	1.2 ± 0.8	-0.2 ± 0.4
1 – 2	1.2 ± 1.6	-2.6 ± 1.3	-41.8 ± 7.6	-23.6 ± 14.1	-1.6 ± 1.3	-2.2 ± 0.9
2 – 3	-0.4 ± 0.9	-1.2 ± 1.8	-56.8 ± 3.4*	-23.4 ± 7.2	-3.0 ± 1.3	-2.4 ± 1.3
3 – 4	5.2 ± 2.9	2.0 ± 2.3	-41.0 ± 11.2	-9.4 ± 12.4	-2.4 ± 2.4	-1.0 ± 0.6
4 – 8	2.0 ± 1.5	0.2 ± 1.4	-22.0 ± 9.8	-8.0 ± 14.1	-2.6 ± 1.7	-3.4 ± 0.2
8 – 12	5.2 ± 1.4	3.3 ± 2.1	18.8 ± 6.8	12.5 ± 15.7	1.2 ± 1.2	0.3 ± 1.0
12 – 16	5.8 ± 1.3	2.8 ± 1.3	42.6 ± 7.6	18.5 ± 7.8	3.2 ± 1.0	-0.3 ± 0.9
16 – 20	5.0 ± 0.9	2.3 ± 2.0	23.2 ± 8.2	-1.0 ± 17.5	2.6 ± 0.6	-0.3 ± 1.3
23 – 24	3.0 ± 1.0	1.0 ± 1.1	24.4 ± 6.1	-10.8 ± 15.5	1.6 ± 0.9	-2.4 ± 0.7
24 – 25	6.8 ± 1.4*	2.4 ± 2.1	7.4 ± 9.2	15.8 ± 15.3	2.8 ± 1.2	-1.6 ± 0.9
25 – 26	6.6 ± 0.7$^{\#,*}$	0.0 ± 1.6	-29.0 ± 7.3	-21.2 ± 18.4	2.2 ± 1.3$^{\#}$	-2.6 ± 0.5
26 – 27	6.0 ± 1.1	0.6 ± 1.5	-42.8 ± 7.3	-19.6 ± 11.5	0.0 ± 1.0	-2.6 ± 0.7
27 – 28	8.8 ± 0.7$^{\#,*}$	1.6 ± 2.2	-26.2 ± 5.8	-20.4 ± 10.7	0.2 ± 1.6	-3.0 ± 0.3
28 – 32	6.2 ± 0.7	0.6 ± 1.4	-21.8 ± 4.1	-10.6 ± 18.1	-1.0 ± 0.8	-3.0 ± 0.7
32 – 36	8.4 ± 1.4*	3.8 ± 2.1	21.8 ± 9.2	31.0 ± 23.4	2.2 ± 1.1	-0.6 ± 1.4
36 – 40	6.2 ± 1.5	3.0 ± 1.5	31.8 ± 6.4	32.4 ± 16.9	2.4 ± 0.9	-0.4 ± 1.0
40 – 44	5.2 ± 1.2	4.4 ± 2.0	14.0 ± 6.5	23.4 ± 21.2	2.8 ± 0.9	-0.2 ± 1.2

3.3.5. Entospletinib

Entospletinib (n=6) did not cause significant changes in MAP or ΔMAP compared to vehicle (n=6) (Figure 29A and 30D, two-way ANOVA). Similarly, HR did not change after entospletinib administration (Figure 29B, two-way ANOVA). Even though overall ΔHR was significantly different between entospletinib and vehicle, no individual time point was significantly different between the groups (Figure 29E, two-way ANOVA ($p<0.05$), Sídák test for multiple comparisons; no significant differences between the groups). PP and ΔPP did not differ between the entospletinib group and vehicle group (Figure 29C and 30F, two-way ANOVA). All numerical data showing the effect of entospletinib on the cardiovascular variables are displayed in Table 7.

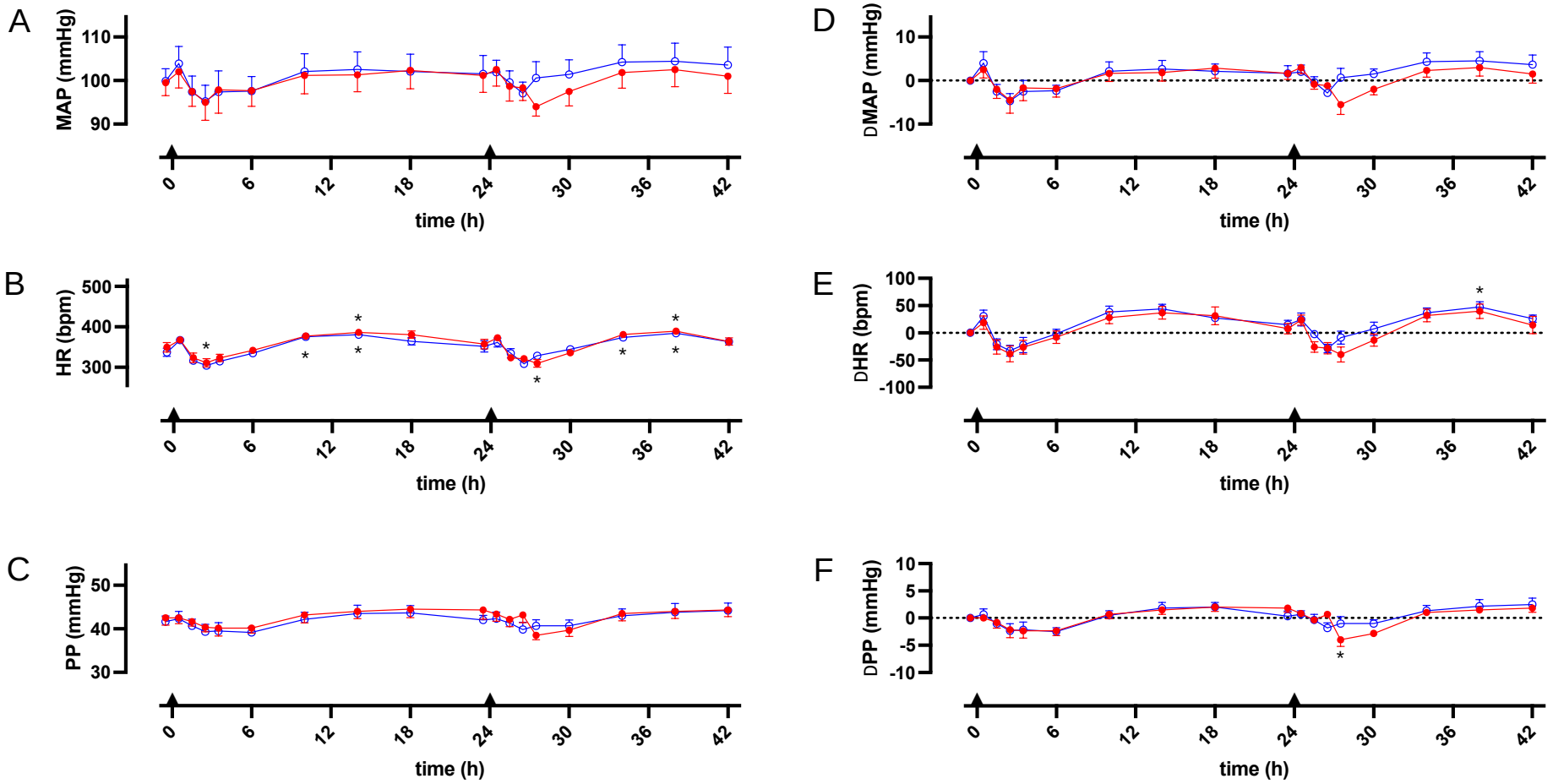

Figure 29: Cardiovascular effects of entospletinib. *Changes in MAP* ***(A)****, HR* ***(B)*** *and PP* ***(C)*** *of rats dosed with entospletinib 6 mg/kg p.o. (n=6, red, filled circles) and vehicle p.o. (n=6, blue, open circles). Data were normalised to baseline recording for each animal individually, presented in* ***(D)****,* ***(E)*** *and* ***(F)****. Black triangles on time-axis indicate time of administration of entospletinib or vehicle. Data are presented as mean ± SEM, were binned per hour (baseline and first 4 h after dosing) or per 4 h (from 4 h after dosing) and plotted at the time points half-way through the 1 h or 4 h interval. A two-way ANOVA test was conducted to test for overall differences between two groups (θ = p<0.05), followed by multiple comparison by Sídák to test for differences between the groups at each time point (# = p<0.05) Furthermore, if there was a significant change over time within a group (two-way ANOVA), each timepoint of the group was compared to the group's corresponding baseline (T=-0.5 h), by Dunnett, performed on the raw, non-normalised data (* = p<0.05).*

Table 7: Changes in ΔMAP, ΔHR and ΔPP after entospletinib administration. *Mean ± SEM changes from baseline (defined as T=-0.5 h) from rats dosed with entospletinib (6 mg/kg/day, n=6) or vehicle (10 mL/kg/day, n=6). Data were binned per hour (baseline and first 4 h after dosing) or per 4 h (from 4 h after dosing). Blue line indicated dosing via oral gavage. Significant changes between treated and vehicle group overall are indicated by θ (two-way ANOVA, p<0.05), followed by significant changes for each individual timepoint between the groups, indicated by # (Sídák, p<0.05). Significant changes within the group from baseline are indicated by * (two-way ANOVA, p<0.05).*

Time (h)	ΔMAP (mean ± SEM) (mmHg)		ΔHR (mean ± SEM) (bpm)		ΔPP (mean ± SEM) (mmHg)	
	Entospletinib	Vehicle	Entospletinib θ	Vehicle	Entospletinib	Vehicle
-1 – 0	0.0 ± 0.0	0.0 ± 0.0	0.0 ± 0.0	0.0 ± 0.0	0.0 ± 0.0	0.0 ± 0.0
0 – 1	2.5 ± 1.9	4.0 ± 2.6	18.5 ± 12.4	30.3 ± 11.5	0 ± 0.6	0.7 ± 1.0
1 – 2	-2.0 ± 2.1	-2.5 ± 1.6	-26.0 ± 12.9	-20.8 ± 10.0	-0.8 ± 1.0	-1.0 ± 0.6
2 – 3	-4.5 ± 3.0	-4.7 ± 1.7	-38.5 ± 14.5	-33.2 ± 10.1	-2.2 ± 1.4	-2.3 ± 1.3
3 – 4	-1.7 ± 2.9	-2.5 ± 2.5	-26.3 ± 13.8	-22.5 ± 14.2	-2.3 ± 1.3	-2.2 ± 1.4
4 – 8	-1.8 ± 2.0	-2.3 ± 1.3	-7.8 ± 11.6	-2.2 ± 8.5	-2.3 ± 0.9	-2.5 ± 0.7
8 – 12	1.7 ± 1.9	2.2 ± 2.1	28.0 ± 11.0	38.3 ± 10.9	0.7 ± 0.8	0.5 ± 0.8
12 – 16	1.8 ± 1.9	2.7 ± 2.0	36.8 ± 11.4	44.0 ± 8.5	1.5 ± 0.8	1.8 ± 1.0
16 – 20	2.8 ± 2.2	2.2 ± 1.6	31.2 ± 16.2	27.2 ± 5.4	2.0 ± 0.8	2.0 ± 0.9
23 – 24	1.7 ± 1.4	1.2 ± 1.8	7.7 ± 9.6	15.0 ± 8.1	1.8 ± 0.8	0.3 ± 1.0
24 – 25	3.0 ± 1.4	2.0 ± 1.6	23.3 ± 9.5	24.5 ± 11.8	0.8 ± 0.4	0.7 ± 0.7
25 – 26	-0.8 ± 1.1	-0.3 ± 1.2	-25.8 ± 9.9	-2.5 ± 5.3	-0.3 ± 0.4	-0.3 ± 1.0
26 – 27	-1.2 ± 0.7	-2.8 ± 1.5	-28.3 ± 10.3	-28.7 ± 7.8	0. 7 ± 0.6	-1.8 ± 0.9
27 – 28	-5.5 ± 2.3	0.7 ± 2.2	-39.8 ± 13.8	-8.7 ± 12.0	-4.0 ± 1.2*	-1.0 ± 1.3
28 – 32	-2.0 ± 1.3	1.5 ± 1.2	-13.3 ± 11.2	7.3 ± 12.3	-2.8 ± 0.7	-1.0 ± 0.7
32 – 36	2.3 ± 1.5	4.33 ± 2.0	32.0 ± 12.1	36.7 ± 9.1	1.0 ± 0.4	1.3 ± 0.9
36 – 40	3.0 ± 2.0	4.5 ± 2.1	39.8 ± 13.4	47.5 ± 9.7*	1.5 ± 0.6	2.2 ± 1.3
40 – 44	1.5 ± 2.1	3.7 ± 2.2	14.3 ± 16.0	26.2 ± 6.9	1.8 ± 0.8	2.5 ± 1.2

3.3.6. Summary

A summary of the effects of vardenafil, molsidomine, sunitinib, fostamatinib and entospletinib on MAP, HR and PP are shown in Table 8. All changes in the Table were significant from the first day of dosing, except the increase in MAP following fostamatinib administration, which was significantly different from vehicle only from the second day.

Table 8: Overview of the effects on cardiovascular variables (MAP, HR and PP) of vardenafil, molsidomine, sunitinib, fostamatinib and entospletinib. *All changes shown were significantly different from vehicle from the first day ($p<0.05$, two-way ANOVA), except for the fostamatinib-induced increase in MAP, which was significantly different from vehicle only from the second day (D2) ($p<0.05$, two-way ANOVA). '↑↑' indicates a large increase in the parameter, '↑' indicates an increase in the parameter, '↓↓' indicates a large decrease in the parameter, '↓' indicates a decrease in the parameter, '=' indicates parameter was not significantly changed.*

	Vardenafil	Molsidomine	Sunitinib	Fostamatinib	Entospletinib
MAP	↓↓	↓↓	↑↑	↑ (on D2)	=
HR	↑	↑↑	=	=	=
PP	↓	↓↓	=	=	=

Vardenafil and molsidomine caused a decrease in MAP and PP, associated with an increase in HR. Sunitinib caused a large increase in MAP and did not affect HR or PP. Fostamatinib caused a smaller increase in MAP, that was significant only after dosing on the second day, and did not change HR or PP. Lastly, entospletinib did not affect any of the cardiovascular variables analysed in this Chapter.

3.4. Chapter discussion

In this Chapter the effect on cardiovascular variables, in particular MAP, HR and PP, after administration of vardenafil, molsidomine, sunitinib, fostamatinib and entospletinib was investigated, using radiotelemetry in conscious freely moving rats. This Chapter performed conventional wave analysis, showing an increase in MAP (significant from the second day) following fostamatinib administration, and no changes in the cardiovascular parameters following entospletinib administration, and serving as a point of comparison for the next Chapters.

3.4.1. Vasodilators

Firstly, the effects of two vasodilators were investigated. Both inhibitor's mechanisms of action are displayed in Figure 31. Vardenafil is a PDE-5 inhibitor (Keating & Scott, 2003) and therefore, by blocking degradation of cGMP, prolongs NO's action as smooth muscle cell relaxation agent (Ghiadoni et al., 2008). On the other hand, molsidomine is an NO-donor, quickly metabolised to release NO, which activates soluble guanylyl cyclase and generates cGMP (da Silva et al., 2021; Rosenkranz et al., 1996).

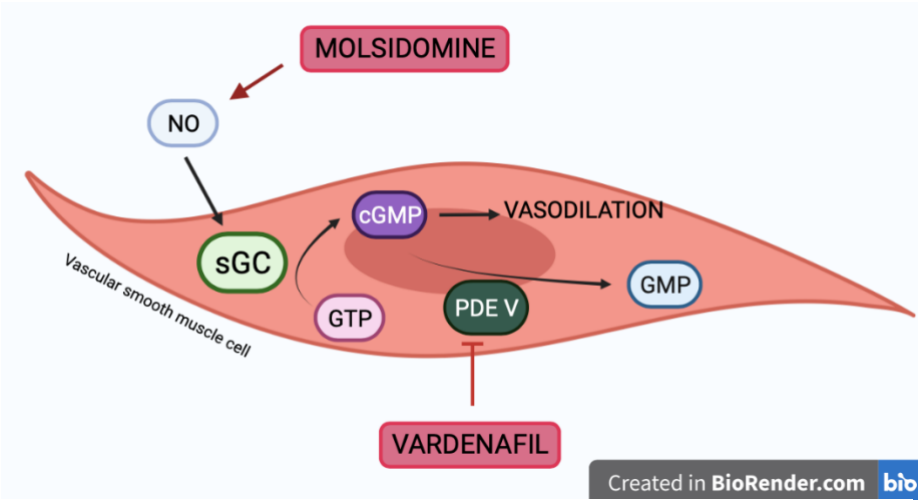

Figure 30: Schematic representation of molsidomine and vardenafil's mechanism of action. *In vascular smooth muscles cells, nitric oxide (NO) leads to activation of soluble guanylyl cyclase (sGC), converting guanosine triphosphate (GTP) to cyclic guanosine monophosphate (cGMP). Through further secondary messenger pathways, cGMP induces vasodilation. cGMP is degraded to GMP by phosphodiesterase 5 (PDE-V). Molsidomine is a NO-donor, quickly metabolised to NO and therefore mimicking its action. Vardenafil is a PDE-V inhibitor, prolonging the action of cGMP. Figure created in BioRender.com, adapted from da Silva et al. (2021).*

Vardenafil and molsidomine displayed similar effects on MAP, HR and PP. Administration of vardenafil led to an immediate and temporary decrease in MAP. The maximum difference between vardenafil and vehicle in ΔMAP was 11.8 mmHg. Molsidomine displayed a similar effect, quickly but temporarily decreasing MAP after drug administration. The maximum difference between molsidomine and vehicle in ΔMAP was 13.6 mmHg. These decreases in MAP were accompanied by a rapid increase in HR. This reflex tachycardia, an increase in HR to compensate for the decreased BP, attempting to raise it back to normal levels, has been described in the literature for both vardenafil (Fossa et al., 2011) and molsidomine (Bergstrand et al., 1984). The reflex tachycardia observed with molsidomine had a larger magnitude (maximum difference between vehicle and molsidomine in ΔHR = 135.8 bpm) than the one observed with vardenafil (maximum difference between vehicle and vardenafil in ΔHR = 92.6 bpm). Similarly, PP decreased quickly after both vardenafil and molsidomine administration, and this effect was sustained throughout the day with both compounds. Again, the effect was larger with molsidomine (maximum difference in ΔPP = 14.2 mmHg) than with vardenafil (maximum difference in ΔPP = 6.2 mmHg). Vasodilators are known to decrease PP. As they induce a vasorelaxation, these compounds attenuate wave reflection due to an increased vessel compliance (discussed in Chapter 1, section 1.5.1.) (Avolio et al., 2009; Schroeder et al., 2019). As a reflected wave augments the SBP of the forward wave, a decrease in amplitude of the reflected wave leads a decrease of the overall magnitude of the pressure wave, i.e. PP, of the arterial wave (Avolio et al., 2009; S. Laurent et al., 2006; Townsend et al., 2015). These alterations on waveform reflection were further investigated in Chapter 4, by applying SPAR to the obtained blood pressure waves.

3.4.2. Sunitinib

Secondly, the cardiovascular effects of sunitinib, an RTKI known to induce hypertension in patients, were studied. As expected, sunitinib had opposing effects on MAP compared to the vasodilators. Sunitinib caused a large and sustained increase in MAP. On the first day, the maximum difference between vehicle and sunitinib in ΔMAP was 10.9 mmHg and ΔMAP returned to vehicle levels in the last 4 h of the first day. These results are consistent with literature reporting a MAP increase of approximately 10 mmHg after administration of sunitinib-L-malate 7 mg/kg (Lankhorst et al., 2015). On the second day, a larger increase in MAP was observed (maximum difference in ΔMAP = 13.5 mmHg) and this raised pressure remained significantly different from vehicle until the end of day 2.

This larger response on the second day is likely linked to the plasma half-life of sunitinib. As a rule, after 4 to 5 times the half-life of a compound, 97% of the compound is eliminated and plasma concentrations are considered below clinically relevant levels (Hallare & Gerriets, 2020; Ito, 2011). On the other hand, if the compound is dosed again before the end of this '4 to 5 x half-life window', the drug will accumulate in the plasma (Hallare & Gerriets, 2020; Ito, 2011). In the case of sunitinib, this window is around 32 – 40 h, as its half-life is 8 h in rats (Speed et al., 2012). Sunitinib was dosed for the second time 24 h after the first administration, therefore not all sunitinib administered on the first day was eliminated yet and total plasma concentrations were accumulating. In conclusion, the larger response in ΔMAP on the second day is most likely due to accumulation of sunitinib in the blood.

Furthermore, sunitinib caused a small increase in HR, nonetheless this was not significantly different from the vehicle group at any time point. Over time, HR changed significantly from baseline within the sunitinib group, however these effects were also found in the vehicle group and are probably due to circadian oscillations in HR. Similar observations were made by Cooper *et al.* (2019), assessing the effects of RTKIs in radiotelemetry in rats. Lastly, sunitinib caused an increase in ΔPP. This effect only reached significance during the last 4 h of the second day (maximum difference in ΔPP = 3.6 mmHg). This increase, although small, indicates sunitinib causes a vasoconstriction. As mentioned above, vasodilators decrease PP by attenuation of wave reflection. Conversely, vasoconstrictors have the opposite effect on PP, as they cause an increase of stiffness of the vessel wall, therefore increase wave reflection and the overall magnitude of the pressure wave (PP) (Avolio et al., 2009; S. Laurent et al., 2006; Townsend et al., 2015).

Vardenafil, molsidomine and sunitinib were included in this study as reference compounds, as their effect on cardiovascular parameters is quite well established. Although this was not the aim of this study, the results discussed above show that the TSE Stellar telemetry set-up delivered reproducible data; both the vasodilators and sunitinib induced responses that have been reported extensively in literature and were anticipated prior to the start of the study.

3.4.3. Syk inhibitors

Next, the cardiovascular effects of the two Syk inhibitors were investigated in the radiotelemetry in rat model. Fostamatinib caused a small increase in MAP. Interestingly, on the first day, MAP in the fostamatinib group did not reach levels significantly different from vehicle (two-way ANOVA). Only on the second day, MAP reached levels that were significantly different from vehicle (two-way ANOVA and Sídák test). The maximum difference in ΔMAP between fostamatinib and vehicle was 7.2 mmHg. These results are consistent with literature reporting no significant differences in MAP on the first day of twice daily oral dosing with fostamatinib 8.5 mg/kg in rats (Lengel et al., 2015) and furthermore coincides with a reported increase of approximately 10% in MAP following oral administration of 10 mg/kg and 30 mg/kg once daily in rats (M. Skinner et al., 2014).

When comparing HR between vehicle- and fostamatinib-treated animals, no significant changes were found. In both fostamatinib group and the vehicle group, HR changed over time within the group, however as mentioned above this is likely due to circadian oscillations rather than a drug effect. Lastly, fostamatinib caused a small increase in ΔPP (maximum difference in ΔPP = 4.8 mmHg). Similar to the one observed following sunitinib administration, this effect on PP, although small, indicates vasoconstricting actions (Avolio et al., 2009; S. Laurent et al., 2006; Townsend et al., 2015).

Previous studies reported rapid conversion of fostamatinib to R406 following oral dosing in rats, indicated by maximum plasma concentrations reached within 1 to 2 h after fostamatinib administration (Lengel et al., 2015; Pine et al., 2007). Furthermore, no prodrug was detected in the plasma, indicating a complete conversion of fostamatinib to R406 (Pine et al., 2007). According to the rule of '4 – 5 x half-life window' and given the plasma half-life of R406 is 4.2 h in rats, plasma concentrations should have returned to levels below clinically relevant concentrations after 16.8 – 21 h after dosing. However, given that fostamatinib needs to be converted into R406 (1 – 2 h delay as stated above), these two factors add up to a time window of close to 23 h, needed for R406 concentrations to attenuate to clinically irrelevant levels. Furthermore, the drug formulation used in this study could contribute to the accumulating effect as well. Fostamatinib was suspended in a 10% cyclodextrin solution.

Cyclodextrins consist of a hydrophobic pocket and hydrophilic outer surface (Feng et al., 2021; D. Zheng et al., 2020). They allow for the solution of hydrophobic molecules in a hydrophilic vehicle, and are often used to obtain slow release of drug in the gastro-intestinal tract (Feng et al., 2021; D. Zheng et al., 2020). Given this formulation was used to dose, fostamatinib was potentially released slowly from the cyclodextrins, resulting in lower but more consistent plasma concentrations. Overall, it is possible that R406 accumulated in the blood, due to a plasma half-life of 4.2 h that was prolonged by slow drug release from the cyclodextrins and delayed R406 peak concentrations due to its conversion from fostamatinib. This presents a potential explanation for the larger effects in MAP observed on day 2. However, no definite statements could be made about R406 plasma concentrations throughout the study as no blood samples were taken during this study. Taking regular blood samples would be a useful addition in follow-up studies.

As mentioned above, ICH S7A, the current guideline for cardiovascular safety testing, recommends monitoring BP and HR after single dose administration (International Conference on Harmonisation, 2001). In the present study, if looking at the data from the first day alone, no significant changes in MAP or HR would have been detected following fostamatinib administration. Only from 3 h after the second dose administration, MAP was significantly different between the two groups. Theoretically, when using these routine approaches looking at MAP and HR alone after single administration, the subtle fostamatinib-induced changes could be missed in preclinical studies or considered not relevant. Nonetheless clinical trials demonstrated otherwise by now, showing considerable effects on cardiovascular parameters after repeated fostamatinib administration (Y. Chen et al., 2021; Kunwar et al., 2016).

Another example of such missed cardiovascular effects leading to safety issues and decreases in drug development productivity, is presented by torcetrapib (Joy & Hegele, 2008; Tanne, 2006). This compound is a cholesteryl ester transfer protein inhibitor, increasing HDL levels and thus antiatherogenic drug. Although the results from its preclinical trials are not available, later *in vivo* characterisation of the CV effects of this compound showed that torcetrapib induced an increase in MAP of 10 – 15 mmHg in both anaesthetised and conscious rats (Forrest et al., 2008). Reports from a Phase II clinical trial showed small increases in SBP and

DBP (mean 0.9 – 2.2 mmHg) with this compound (McKenney et al., 2006). Nonetheless torcetrapib continued to Phase III trials, where larger increases in SBP were found (4.6 – 6.6 mmHg) (Bots et al., 2007; Nissen et al., 2007). Lastly, ILLUMINATE, a large Phase III clinical trial involving over 15 000 patients at high cardiovascular risk, investigated the effects of torcetrapib over 12 months (Barter et al., 2007). This trial was prematurely terminated due to an increased risk of death and cardiac events associated with torcetrapib (Barter et al., 2007) and these findings led to the termination of the other ongoing torcetrapib trials and the failure of this compound (Joy & Hegele, 2008; Tanne, 2006). Similar examples are the late withdrawal of valdecoxib (Atukorala & Hunter, 2013), sibutramine (James et al., 2010), pergolide (Zanettini et al., 2007) and tegaserod (Thompson, 2007) from the market, indicating that preclinical safety testing could potentially benefit from a more elaborate analysis of the BP signal, providing earlier and more sensitive detection of these changes and preventing late failure of new drugs.

Lastly, the effect of entospletinib on the cardiovascular variables was assessed. Entospletinib did not significantly affect MAP, HR or PP. These results are consistent with the purpose of this drug to achieve selective Syk inhibition without the onset cardiovascular toxicity. In this study, a lower concentration was used to dose entospletinib (6 mg/kg), compared to fostamatinib for example (20 mg/kg). This dose selection might impact on whether cardiovascular effects are seen. However, the aim of the study was to represent CV adverse drug effects that might occur at plasma concentrations relevant to the clinical applications of each drug and the selected doses of both entospletinib and fostamatinib gained this objective.

3.4.4. Chapter conclusion

Overall, this Chapter provided an initial screening of the cardiovascular effects of three reference compounds (vardenafil, molsidomine and sunitinib) and two Syk inhibitors (fostamatinib and entospletinib). Using the conventional approach for preclinical assessment of cardiovascular safety, the results in this Chapter indicated that the TSE Stellar telemetry system recorded reproducible data, showing anticipated responses to the reference compounds and responses to Syk inhibitors that are consistent with literature. Importantly, if MAP and HR would have been studied solely after a single dose administration – as recommended by ICH S7A – no significant changes would be observed following fostamatinib treatment. Only from the second day and after repeated fostamatinib dosing, MAP changed significantly from vehicle-treated animals. In-depth wave analysis could potentially perform better than conventional analysis in detecting these cardiovascular effects. Therefore, in the next Chapter the SPAR method was applied on the waveform data obtained in the telemetry studies of this Chapter, to interrogate if in-depth wave analysis could detect any effects that were not apparent from the conventional analysis, or detect those effects earlier post drug administration than the conventional analysis, for example in the case of fostamatinib.

4. RESULTS CHAPTER 4: SPAR ANALYSIS OF BLOOD PRESSURE WAVES

4.1. Chapter introduction

Preclinical cardiovascular safety pharmacology could benefit from improved assessments (Bhatt et al., 2019; Weaver & Valentin, 2019a). The importance of this current gap is underscored in reports from the clinical and post-marketing stages of drug development, where high attrition rates due to cardiovascular adverse drug reactions are observed (Cook et al., 2014; Qureshi et al., 2011). Cardiovascular parameters currently used, such as MAP and HR, give important indications of cardiovascular drug effects, however these variables provide only limited insight into the complete CV profile of a compound (Mynard et al., 2020; Nandi & Aston, 2020). A theoretical example is shown in Figure 31, where two aortic blood pressure waves present obvious visual changes that could indicate important differences in cardiac and vascular health or disrupted regulatory mechanisms, yet would return similar MAP and HR values.

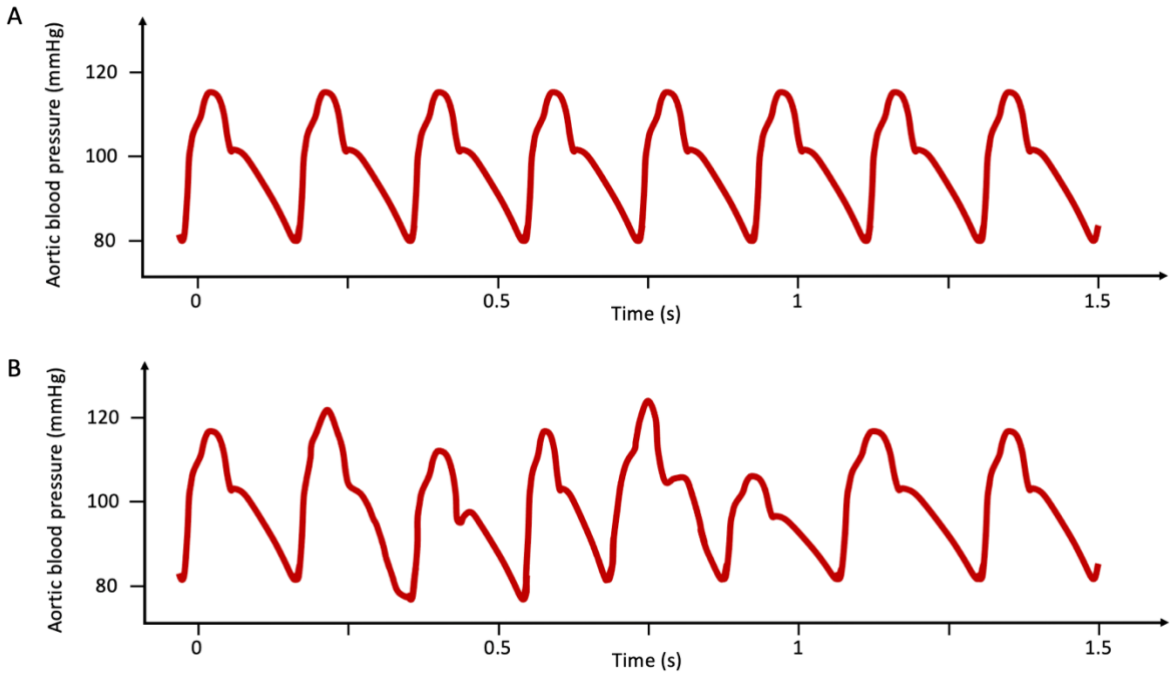

Figure 31: Theoretical examples of blood pressure waves recorded in rats, *with* ***(A)*** *displaying little variability and* ***(B)*** *displaying high waveform variability. Although the waves are visually different, both have a HR of approximately 320 bpm and MAP of approximately 100 mmHg. These reductive parameters can therefore be inadequate to provide a full understanding of a compounds effect on the cardiovascular system.*

In the last decades, novel methods of blood pressure wave analysis, looking beyond MAP, SBP or DBP, and HR, have been developed, aiming to detect more subtle changes and providing more insight into the mechanisms behind the observed cardiovascular effects (Mynard et al., 2020; Townsend et al., 2015). As described in Chapter 1 (section 1.5.3.), these novel parameters have mostly been explored in clinical settings. For example, Safar *et al.* (2002) showed that PPA is a predictor for CV mortality in end-stage renal disease. Similarly, AIx has been described as a strong predictor for severe cardiovascular events (Millasseau et al., 2003; Townsend et al., 2015; Weber et al., 2010). Moreover, HRV has been suggested to be a helpful marker in diagnosis of neuropathy in diabetes patients (Acharya et al., 2006; Karim et al., 2011). Besides their application in clinical studies, similar novel wave metrics have been explored in preclinical studies. For example, Laurent *et al.* (2003) showed that vasodilators that displayed a similar effect on MAP, affected PPA in different ways in rats. Additionally, Chang *et al.* reported a shortened arterial wave transit time in rats with chronic kidney disease or diabetes, compared to healthy animals (R. W. Chang et al., 2017). Altogether, these studies indicate that detailed analysis of blood pressure waves beyond MAP may provide further insights in disease development or drug effects and could potentially help closing the current gap in cardiovascular safety pharmacology.

Despite these promising developments, some important limitations should be considered. Firstly, these novel parameters remain reductionist. They extract only one specific component of the waveform (e.g. the amplitude of the wave or the position of the dicrotic notch) and, like MAP, under-analyse the data (Hametner & Wassertheurer, 2017; Hashimoto & Ito, 2010; Nandi et al., 2022). Secondly, the application of these parameters has been hindered by the complexity of the mathematical methods needed to derive them from the wave (Nandi et al., 2022; Sassi et al., 2015). For example, parameters reporting on wave reflection are determined by pulse wave separation, a method that needs a simultaneous blood flow or blood flow velocity recording for accurate calculation (R. W. Chang et al., 2017; Mynard et al., 2020). These blood flow measurements are not routinely available in both clinical and preclinical settings. Similarly, for the calculation of PPA, blood pressure should be recorded at two sites in the vasculature (Avolio et al., 2009; Townsend et al., 2015). Lastly, HRV requires complex and often manual data pre-processing to eliminate baseline wander and occasional

artifacts (Aston et al., 2014; Sassi et al., 2015). This need for extensive pre-processing of the data has hindered its full application (Nandi et al., 2022; Sassi et al., 2015).

SPAR is a novel way of waveform analysis that overcomes several of these limitations (Aston et al., 2018; Nandi et al., 2018, 2022). Firstly, as described in detail in Chapter 1 (section 1.5.5.) and Chapter 2 (section 2.3.), one of the main advantages of SPAR is its ability to transform lengthy wave traces into compact attractors. The method takes all recorded data into account when generating the attractor, and by doing so, is not reducing the analysis of the waveform to only one component or fiducial point of the wave (Nandi et al., 2018). As all data are utilised, SPAR can detect waveform changes that other reductionist parameters would overlook (Aston et al., 2018). Changes in waveform variability are reflected in a change in colour of the attractor; blue indicates a high variability wave, red indicates a low variability wave (Aston et al., 2018; Nandi et al., 2018). On the other hand, changes in the morphology of the wave present as a change in the shape of the attractor (Aston et al., 2018; Nandi et al., 2018). Additionally, this method does not need an accompanying flow measurement or multiple pressure signals for its analysis. Lastly, SPAR removes naturally occurring baseline variation by projecting the chaotic 3D structure into a 2D plane (detailed in Chapter 2, section 2.3.2.2.) (Aston et al., 2014). At the same time, SPAR a robust method; small artifacts in the signal won't affect the analysis significantly (Aston et al., 2014). In summary, SPAR provides a novel way of visualising and quantifying physiological wave morphology and variability and overcomes several issues that have limited wide application of wave analysis methods until now (Aston et al., 2018; Nandi et al., 2018).

In this Chapter, SPAR was explored as a toolbox in preclinical safety pharmacology. Indeed, the attractor reconstruction of BP waves was studied, using data obtained from radiotelemetry in rats discussed in Chapter 3. First, to validate the method for this type of data, the effect of reference compounds (vardenafil, molsidomine and sunitinib) on the attractors was investigated. Secondly, the effect of novel Syk inhibitors (fostamatinib and entospletinib) on the attractors was assessed. In this way, this Chapter aimed to answer the following questions:

- Can SPAR features detect changes in wave morphology and waveform variability in blood pressure data recorded using radiotelemetry in rats?
- How do vasoconstrictors and vasodilators affect the attractors and conversely how do attractor features translate to physiologically relevant changes in the cardiovascular system?
- Can SPAR features provide insights in the cardiovascular safety of the Syk inhibitors, that were not apparent from MAP, HR or PP analysis in Chapter 3?

4.2. Chapter methodology

4.2.1. Radiotelemetry data recording

The data analysed in this Chapter were obtained using radiotelemetry in rats, as described in Chapter 3 (section 3.2.). BP waves were recorded using the solid-tip BP sensor of the TSE Stellar telemetry implant, for 1 h before and up to 22 h after drug administration on two consecutive days.

4.2.2. Data extraction and analysis in SPARKS

4.2.2.1. Data extraction

For SPAR analysis, blood pressure data were extracted into Microsoft Excel®, using the Notocord-hem™ add-in. This Notocord-hem™ toolbar allowed for efficient reporting of the raw data sequences of blood pressure values at 500 Hz into Excel®.

4.2.2.2. Optimisation

To obtain optimal analysis of the blood pressure data recorded with radiotelemetry in rats, several input parameters of the SPAR algorithm were adjusted, in collaboration with the Nandi Lab (King's College London). Details on how the final input parameters were decided is described in Chapter 2, section 2.3.3.2 and further detailed below in section 4.3.1., where the optimisation of the parameters is presented. In brief, three sets with pre-determined algorithm parameters were available in the SPARKS app. These sets were 'HumanRF', 'HumanBP' and 'MouseBP', differing in for example what limits of cycle frequency the algorithm should use to detect each cycle, what minimum and maximum values are expected for the signal, and the units in which the application should display the given signal. The full set of input parameters for each pre-defined set are shown in the Appendix (section 8.1.). In this thesis, the set of 'HumanBP' was used as a starting point and then adapted to accommodate optimal analysis of the blood pressure signals from rat.

Firstly, the HR limits were adjusted, from 40 and 180, to 230 and 550 respectively, as these cover the expected HR in rats (S. L. Cooper et al., 2019). More details on how these HR limits were determined are discussed in section 4.3.1.1.

Secondly, nbins_density was adjusted. This parameter determines the numbers of pixels in the presentation of the attractor. Essentially, the higher the bins, the smaller the pixels in the attractor image, and the lower the bins, the bigger the pixels in the image. This parameter is not necessarily linked to the physiology of the wave but relates to the representation (brightness) of the attractor. Examples of several nbins_densities and how they affect the presentation of attractors are shown below, in section 4.3.1.2.

In this thesis, 1 min windows were extracted per timepoint of interest. As specified below (section 4.3.1.3) using longer time windows did not enhance attractor quality but did complicate data extraction. The recommended number of cycles per attractor is at least 100, to incorporate variability and morphology patterns providing a representative attractor for a physiological window. Therefore the 1 min window of BP data (300 – 400 cycles) contained sufficient cycles to generate a robust and representative attractor.

4.2.2.3. Standard protocol

Following the optimisation of HR limits, nbins_density and the window length, the following standard protocol was followed for SPAR analysis:

1. One min of raw wave numbers were extracted into Excel® using the Notocord-hem™ add-in. Per animal, per day, per drug treatment, one window was extracted during the baseline recording, followed by one window at 30 min and at 1 h after dosing, and at every hour afterwards.

2. The only pre-processing of data that was performed, was removal of non-physiological artefacts, meaning non-cyclic data. This was the case when prolonged drop-out of the data recording took place, due to the loss of connection between a telemetry implant and its receiver outside of the cage. An example of data drop-out is shown in Figure 34. If this drop-out occurred, the time window was moved backwards or forwards for a maximum of 5 min. If the drop-out occurred longer than 5 min, this timepoint was discarded and data excluded from further analysis. In this study, approximately 2% of the chosen windows was discarded due to drop-out.

3. For each individual 1-min window, the sequence of blood pressure values was saved as a .txt file. These .txt files were then loaded into the SPARKS app, the application developed by Miquel Serna Pascual (Nandi Lab, King's College London), facilitating streamlined SPAR analysis.

4. For SPAR analysis, the pre-set of parameters of HumanBP was used, with adjusted nbins_density and HR limits as described above. For quantitative analysis of the attractors, an nbins_density of 250 was set. For visual inspection and presentation of the attractors, an nbins_density of 125 was set (as detailed below in section 4.3.1.2., this resulted in brighter attractors, simplifying visual comparisons). HR limits were adjusted to maximum 550 and minimum 230.

5. Next, the attractors were generated in the SPARKS app. One attractor was generated per 1 min window. Additionally, from each attractor 49 metrics were taken, to enable quantification of attractor changes.

6. For further quantitative analysis, the attractor metrics of interest were imported into Prism 9.5.1 (GraphPad Software) and binned in the same way as for MAP, HR and PP in Chapter 3; per hour in the first 4 h after dosing, and per 4 h afterwards until the end of the day.

4.2.3. Statistics

All data were expressed as mean ± SEM. Statistical analysis was performed in Prism 9.5.1 (GraphPad Software, San Diego, CA, USA). As there were two categorical, independent variables (time and treatment) and one quantitative outcome variable (SPAR metric), a two-way ANOVA test was performed. This tested (1) if the SPAR metric was significantly different over time, (2) if the SPAR metric was significantly different between groups, and (3) if SPAR metric was significantly different between groups over time. If the result of the two-way ANOVA were significant, multiple comparisons test were performed; a Dunnett test to determine within the group at which time points changes from baseline were significant, and a Sídák test to determine at which time points changes between the groups were significant. Results were considered significant at $p < 0.05$.

4.3. Chapter results: SPAR analysis

4.3.1. Optimisation of the method for BP waves from radiotelemetry in rats

4.3.1.1. Optimising the limits for minimum and maximum cycle frequency

For correct detection of each cycle of the physiological signal, SPARKS needs an estimation of the minimum and maximum cycle frequency of the signal. Setting a threshold range supports computational efficiency, otherwise the system would systematically assume cycle lengths increasing to infinity. For the blood pressure signals used in this thesis, the cycle frequency is the HR. Mean HR of healthy rats is generally in the range of 300 bpm up to 400 bpm under resting conditions (S. L. Cooper et al., 2019). As some compounds in this thesis increased or decreased the HR, a wider range was applied in SPARKS to ensure correct detection of each cycle. Multiple combinations of minimum and maximum rate values were tried in SPARKS, and limits of 230 bpm and 550 bpm respectively were found to be optimal for this study. If the limits were set lower, two consecutive cycles could be detected as one, causing a faulty rotation of the attractor and affecting SPAR metrics. An example of this is shown in Figure 32; administration of molsidomine induced an increase in HR and when HR limits were set too low (e.g. 150 – 400 bpm), SPARKS did not detect each cycle correctly and generated incorrect attractors. On the other hand, if the limits were set higher than 230 and 550, SPARKS was unable to generate attractors from signals with a low HR.

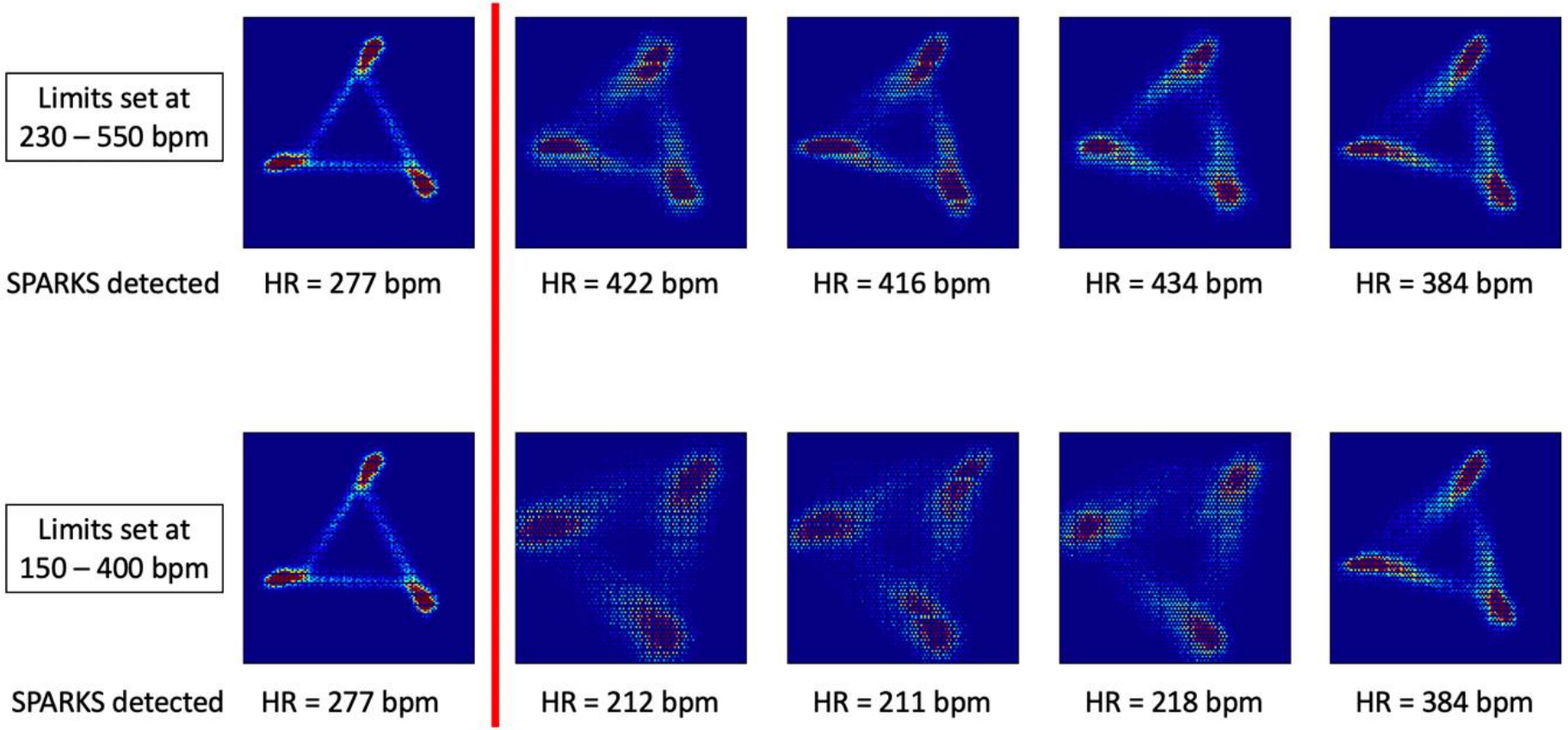

Figure 32: Optimising limits for cycle frequency detection. *In the upper row, HR limits of 230 – 550 bpm were set. In the lower row, lower HR limits (150 – 400 bpm) were set. The red line indicates dosing with molsidomine (10 mg/kg, p.o.). On the left-hand side of the red line is a baseline attractor, on the right-hand side attractors after 1, 2, 3 and 4 h after dosing. Analysis of molsidomine in the telemetry study indicated a large increase in HR following molsidomine administration (>100 bpm increase compared to baseline, Chapter 3, section 3.3.2.) The upper row shows correct detection of all HR by SPARKS, and correct generation of each attractor. The lower row shows incorrect detection of HR after molsidomine dosing, and associated faulty attractor generation, leading to a change in rotation and distribution of data points over the attractor.*

4.3.1.2. Optimising nbins_density

Several values for nbins_density were tested to achieve attractors optimal for both visual and quantitative analysis. As shown in Figure 33, decreasing the nbins_density increased the brightness of the attractor. Less bins (i.e. less pixels) per image, leads to grouping of more data points into one pixel and presents a brighter image. For visual evaluation and to present the attractors, a nbins_density of 125 was used. However, due to technical limitations of the SPARKS at the time of analysis, the application was not able to measure several attractor metrics from such attractors. For example, no radial density plot was generated in SPARKS from such attractors (Figure 33), therefore radial density metrics could not be calculated. Therefore, for quantitative analysis of attractor changes, the default nbins_density of 250 was kept.

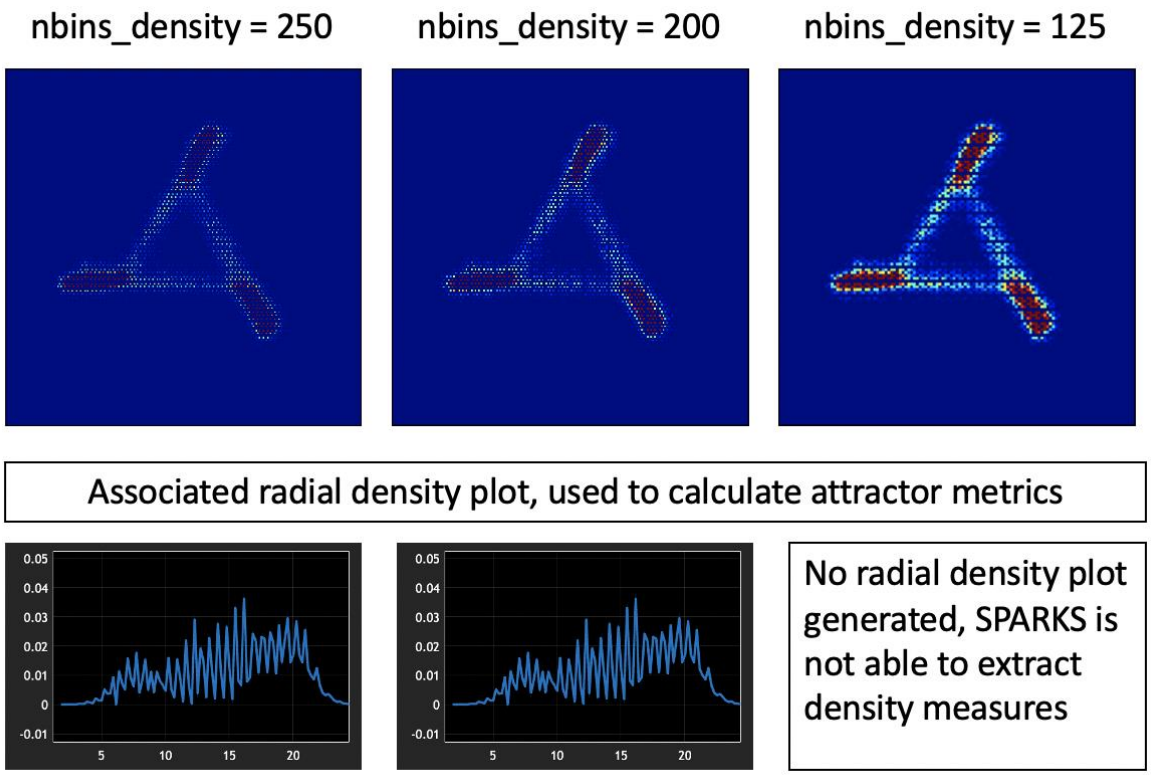

Figure 33: Optimising nbins_density. *Attractor and their associated radial density plots are shown, at 250, 200 and 125 nbins_density. The radial density plot on the bottom row shows how the data are distributed over the attractor. This plot is used in SPARKS for the calculation of certain metrics. Decreasing the nbins_density (right-hand side) resulted in a brighter image of the attractor, therefore an nbins_density of 125 was used for quantitative analysis of the attractor changes. SPARKS was not able to generate radial density plots from such attractors. For this reason, the default nbins_density of 250 was used to measure all metrics for quantitative analysis of attractor changes.*

4.3.1.3. Optimising the window length for one attractor

To optimise the window length of data per attractor, attractors were generated from 1 min, 2 min and 5 min blood pressure data (Figure 34). When using data containing prolonged drop-out of the blood pressure signal (Figure 34D), SPARKS is not able to generate an attractor. A shorter period of signal drop-out does not affect the attractor reconstruction (Figure 34C), however the longer the window, the higher the chances of selecting a window with signal drop-out. When comparing a 1-minute window and 2-minutes window (Figure 34A and 35B), the attractors did not visually change. The recommended number of cycles per attractor is at least 100, hence 1 min of data contained sufficient cycles (300 – 400) to generate a robust and representative attractor. Additionally, the shorter the window, the lower the required computational power and the faster the analysis. In conclusion, a 1-minute window was found optimal, as it resulted in representative attractors, while keeping the computational power low and facilitating easy window selection without signal drop-out.

Taking together these optimisation steps, the standard protocol was obtained, as presented in section 4.2.2.3.

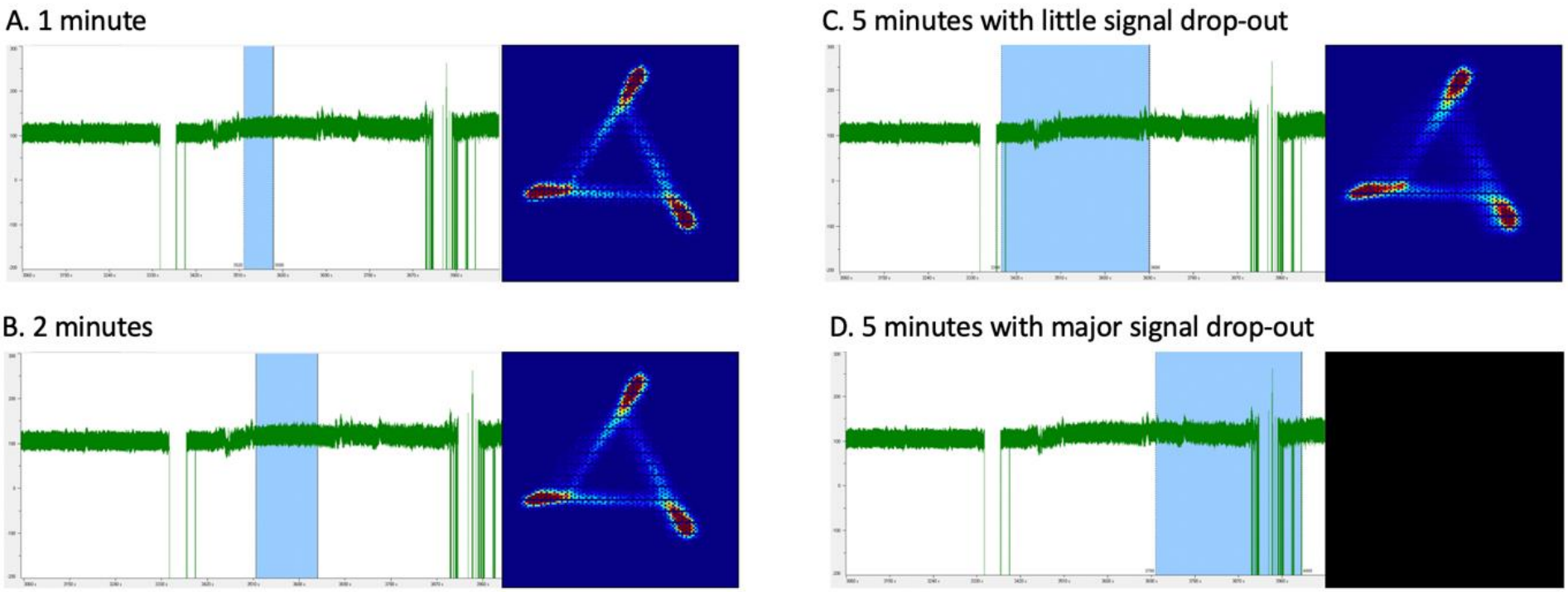

Figure 34: Optimising the window length for one attractor. *Blood pressure traces (shown in green), selected time windows to generate an attractor (indicated in blue, 1, 2 and 5 min) and associated attractor reconstructions.* ***(A)*** *Using 1 min of blood pressure data, a high-quality attractor was generated.* ***(B)*** *Doubling the data used to generate one attractor did not affect the attractor visually, indicating 1 min of data are sufficient to obtain a representative attractor.* ***(C)*** *and* ***(D)*** *display a longer time window, of 5 min, with little or major signal drop-out. SPARKS is able to cope with short signal-drop out (C), however it cannot generate an attractor if longer drop-out is present in the signal (D).*

4.3.2. Qualitative (visual) investigation of attractors

Following optimisation of the method, the standard protocol as stated in 4.2.2.3 was followed to generate all attractors. Firstly, as a validation step, a visual comparison of these attractors was carried out. An investigation of visual changes in both attractor colour (reflecting waveform variability) and attractor shape (reflecting waveform morphology) was performed manually, to explore how these fluctuated throughout the day or altered after drug administration.

4.3.2.1. Waveform variability changes

Firstly, changes in waveform variability were visually examined. The variability of the signal is represented by the heatmap added on the attractor (Aston et al., 2018; Nandi & Aston, 2020). The heatmap indicates the density of each pixel in the attractor image. When each cardiac pulse is similar to the preceding and following one (i.e. a signal with low waveform variability), each pulse will result in a similar loop in the attractor. As many loops of the attractor are overlapping in such case, the density of the pixels will be high (red). Conversely, a signal with high waveform variability (i.e. each cardiac pulse is morphologically different from the preceding and following one), will result in an attractor with few overlapping loops, therefore will appear blue (low density in the pixels of the attractor image) (Aston et al., 2018; Nandi & Aston, 2020).

In Figure 35, an example of attractors from a vehicle-treated animal are shown (n=1). During the hours where the lights were on and animals were usually asleep (6:00 – 18:00, thus before dosing until 7 h post dosing, and 19 h post dosing until the end of the day), the attractors were comparable to each other and showed clear red arms. On the other hand, during the dark half of the day (18:00 – 6:00, thus 7 h post dosing until 19 h post dosing) when animals are expected to be awake, attractors were fuzzier and bluer, indicating a higher variability in waveforms during the night-time active period.

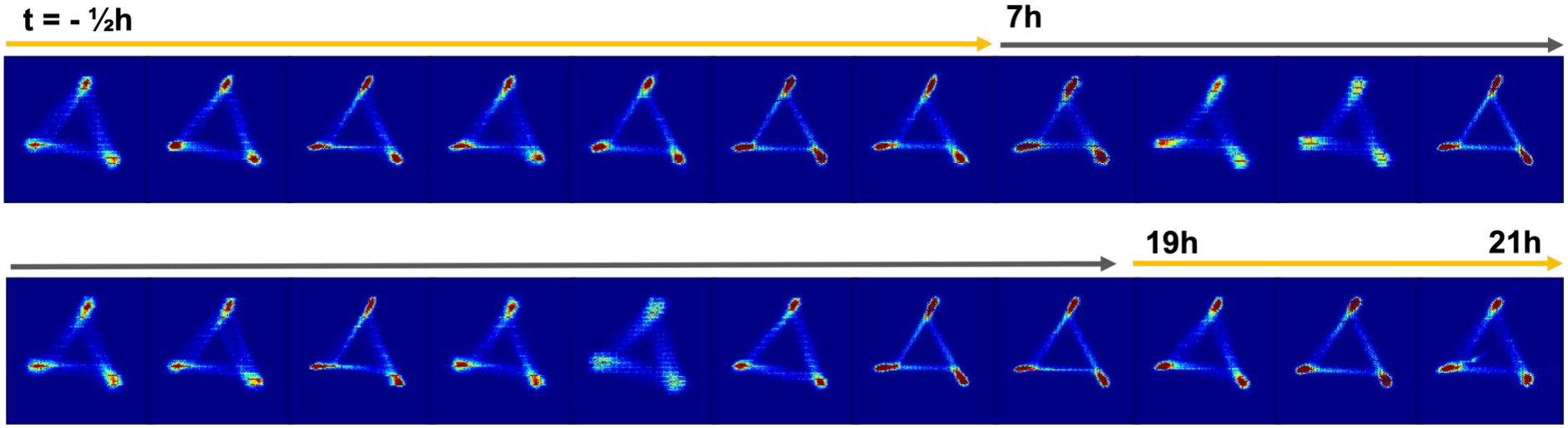

Figure 35: Visual assessment of waveform variability. *Attractors of every hour on day 2, generated from 1-minute recordings from an exemplar vehicle-treated animal. Yellow arrows indicate the part of the day where the lights were on, grey arrows indicate the part of the day where the lights were off. Attractors during the dark part of the cycle were bluer and fuzzier, indicating an increase in waveform variability.*

4.3.2.2. Morphology changes in the wave

Secondly, a visual analysis of the changes in attractor shape was performed. Figure 36 shows blood pressure waves and corresponding attractors at four selected timepoints of a representative vardenafil-treated animal (n=1). After vardenafil administration, the dicrotic notch in the downstroke of the pulse disappeared. This change in morphology of the wave was reflected in a change in the attractor shape; the red arms of the attractor became smaller and overall the attractor changed from triangular shape to a more circular shape.

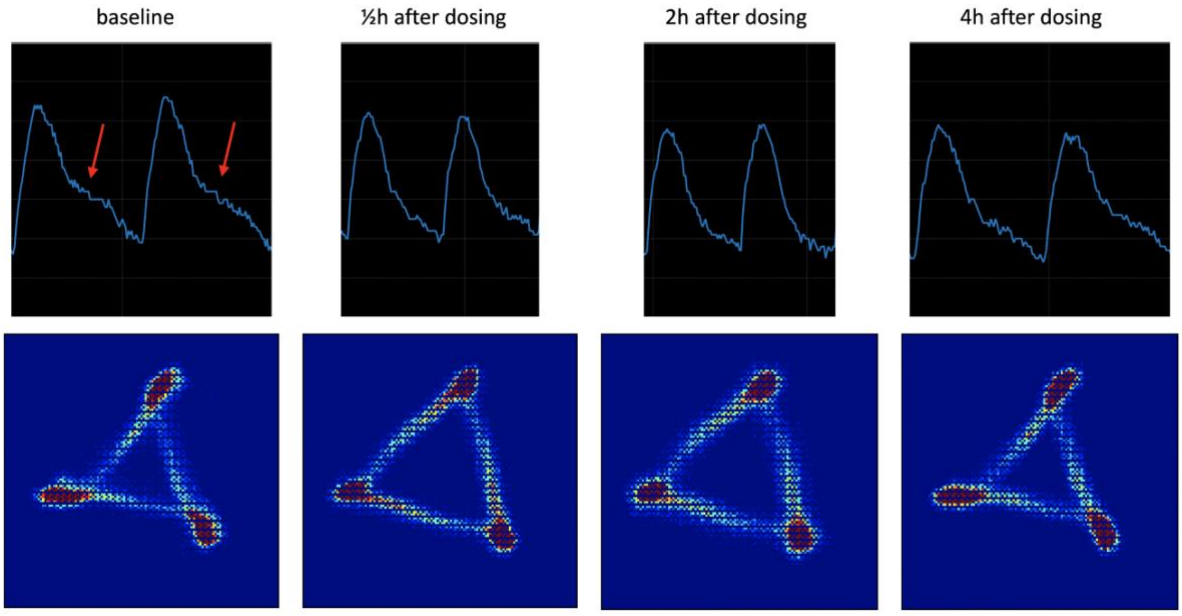

Figure 36: Visual assessment of waveform morphology changes. *Waveforms (top row) and corresponding attractors (bottom row) of selected time points, generated from 1-minute recordings from an exemplar vardenafil-treated animal. The dicrotic notch is indicated by a red arrow in the baseline wave. Administration of vardenafil caused an elimination of the dicrotic notch, indicating a decrease in waveform reflection. This change in waveform morphology was noticeable in the shape of the attractors; vardenafil caused a decrease in the size of the red attractor arms and increased the attractor opening.*

4.3.3. Selection of metrics relevant to observed attractor changes

To quantify changes in waveform variability (attractor colour) and waveform morphology (attractor shape), SPAR metrics were taken from each attractor. As mentioned above, currently a total of 49 attractor metrics can be calculated, developed on analysis of historical data sets, including ECG, by the groups of Nandi and Aston. Some of these metrics were not suitable for analysis of the BP data used here. For example, the number of arms of each attractor was the same in the entire study therefore this was not an informative metric. Moreover, due to technical limitations at the time of analysis, SPARKS was not able to calculate some other metrics correctly, e.g. the length of the attractor arms. For these two reasons, 13 metrics were excluded in this Chapter. This resulted in 36 metrics that could be analysed, displayed in a heatmap in Figure 39. To evaluate the performance of each metric for classification of drug-treated or vehicle-treated group, the Receiver Operating Characteristic (ROC) value was used. Examples of ROC plots are shown in Figure 38, it presents a graphical representation of how well a metric can distinguish the drug-treated animal from the vehicle-treated animal. By plotting the true positive rate (Y-axis) against the false positive rate (X-axis), the cut-off value can be identified for which an animal is assigned to the drug-treated or vehicle-treated group. A perfect metric would result in a ROC curve along the top-left corner, as all treated animals would be identified as treated, and all vehicle animals would be identified as vehicle. A metric that does not distinguish well between the groups, displays a ROC curve at 45 degrees from the left bottom to the right upper corner, as the metric is not able to classify the groups. Thus, the area under the ROC curve (ROC AUC) indicates the overall performance of the metric to classify drug-treated versus vehicle treated animals. The closer to 1 the ROC AUC, the better the separation between the two groups. ROC AUC values were automatically calculated in SPARKS and presented per metric in the heatmap in Figure 39.

To quantify drug-induced changes, metrics were selected based on these ROC AUCs; metrics with ROC AUCs closest to 1 over the 5 drug-treated groups compared to their vehicle were found most suitable for characterisation of drug-induced waveform changes. Firstly, metrics to quantify changes in waveform morphology were chosen. Metrics related to the roundness of the attractor (highlighted in purple in Figure 39), in particular maxrdenspos, rspread and rQ25, resulted in ROC AUCs closest to 1 over the different drug-treated groups and were

therefore selected to quantify morphology changes. How these three metrics are calculated and how they relate to changes in attractors and waves are detailed in 4.3.5. Furthermore, to enable quantification of waveform variability, one of the three metrics related to the colour of the attractor (highlighted in blue in Figure 39) was selected: dspread3. Dspread3 is a metric that represents the amount of red colour in an attractor. The redder the attractor, the higher dspread3, representing a low variability waveform. The bluer the attractor, the lower dspread3, representing a high waveform variability. This is further described in Figure 39 below (section 4.3.4.). Table 11 displays an overview of all SPAR metrics used in this Chapter.

Interestingly, in the heatmap the more conventional metrics 'CycleRate' (i.e. HR) and metrics related to PP (e.g. 'sminPP', 'smaxPP', 'stdPP' etc.) resulted in more orange ROC AUCs than the SPAR metrics (e.g. rQ metrics mentioned above and dspread3), suggesting that these metrics extracted from the attractor were better at distinguishing drug-treated animals from vehicle animals, compared to the conventional metrics.

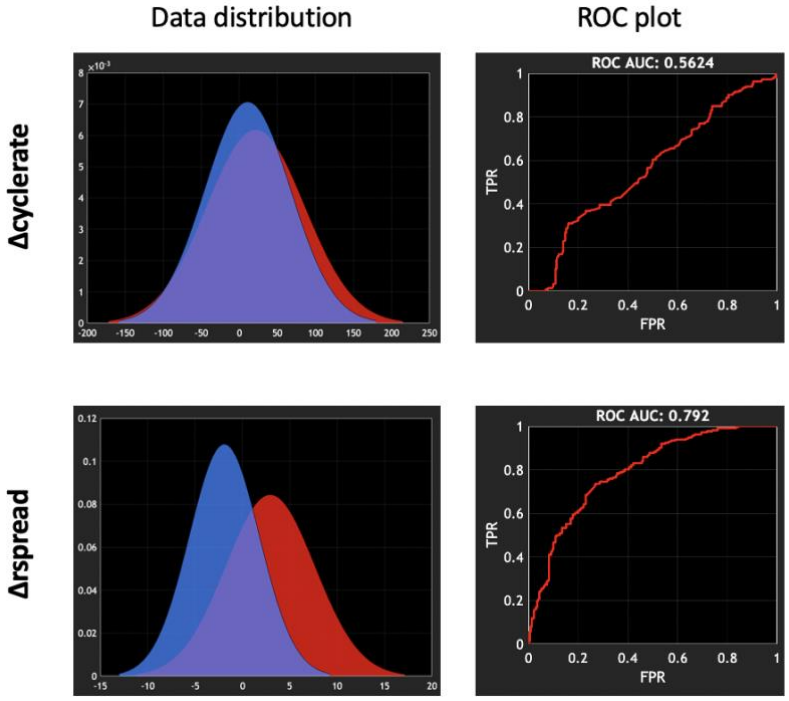

Figure 37: Receiver Operating Characteristic area under the curve (ROC AUC). *On the left-hand side of the figure, data distribution plots are shown, with vehicle animals displayed in blue, and fostamatinib-treated animals in red. Cycles rates (i.e. HR, upper row) were overlapping between the two groups, while rspread (a metric related to the roundness of the attractor, lower row) was increased in the fostamatinib-group. On the right-hand side, corresponding ROC plots are shown. Indeed, cycle rate resulted in a diagonal ROC curve, indicating a mediocre classification of true fostamatinib-treated animals when using this metric (ROC AUC 0.56). On the other hand, the rspread ROC curve moved closer to the upper left corner of the plot, indicating a better identification of fostamatinib- and vehicle-treated animals based on this metric (ROC AUC 0.79). TPR; true positive rates, FPR; false positive rates.*

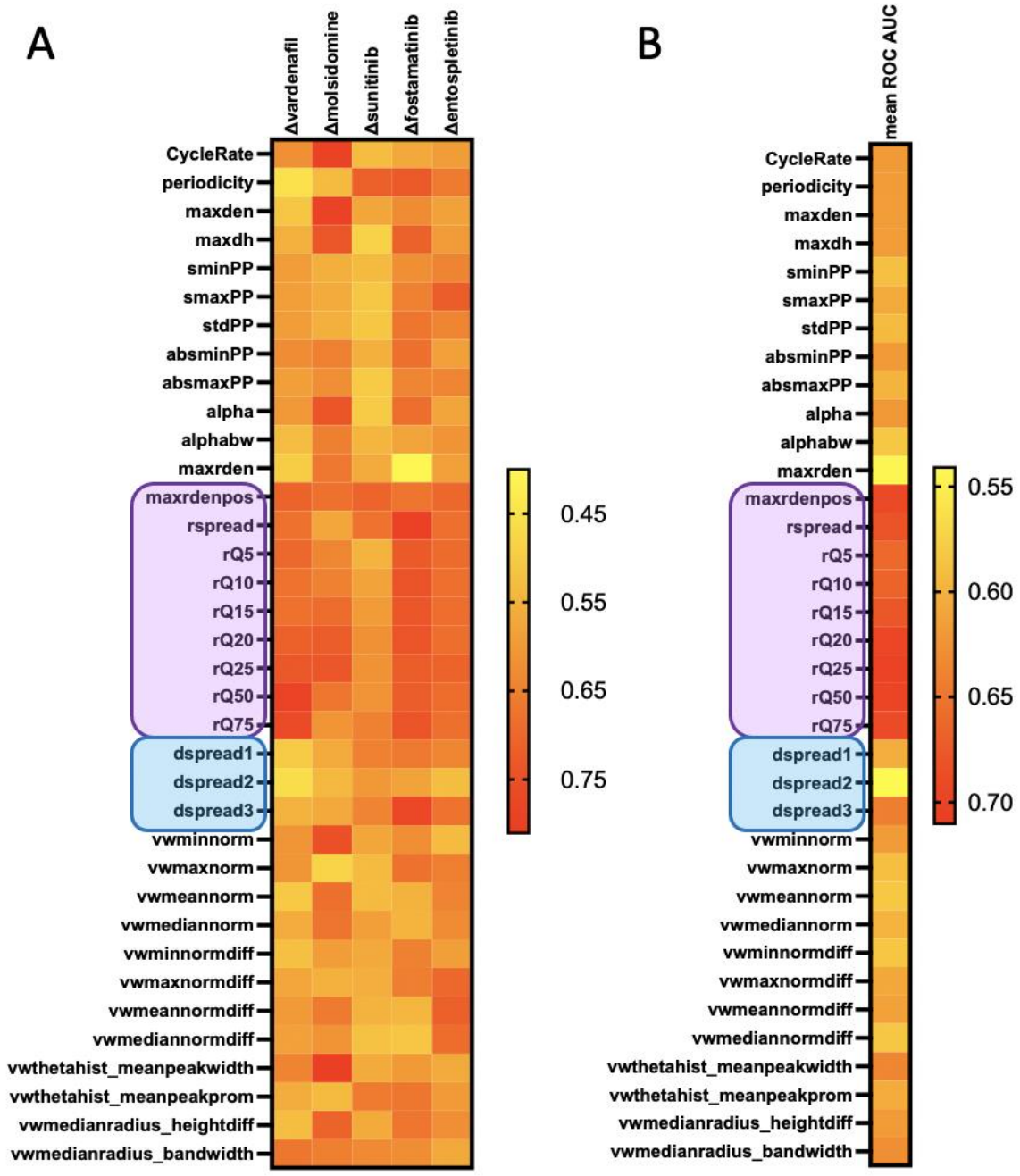

Figure 38: Heatmap of ROC AUC values to select attractor metrics for quantifying waveform changes. (A) *All 36 attractor metrics are listed with their ROC AUC value, per drug compared to its corresponding vehicle. The higher the ROC AUC (red in the heatmap), the better the metric can distinguish drug-treated animals from vehicle-treated animals. The lower the ROC AUC (yellow in heatmap), the more overlapping the metric is between the drug-treated and vehicle-treated group. Overall, metrics related to the roundness (or opening) of the attractor (highlighted in purple) were best at discriminating the attractors from drug-treated animals from those from vehicle-treated animals.* ***(B)*** *The mean ROC AUCs across all drug-treated groups per attractor metric. Attractor metrics related to waveform variability are highlighted in blue. Dspread3 had the ROC AUC closest to 1 and was therefore selected for further quantification of waveform variability changes.*

4.3.4. Quantification of waveform variability

Following selection of SPAR metrics suitable to analyse attractor changes in this study, waveform variability changes throughout the day were quantified using dpsread3. As described above (section 4.3.2.1) and presented below in Figure 39, during the daytime, red attractors were observed and during the night-time, blue attractors were observed. Subsequently, higher dspread3 values were measured during the phase of the day where the lights were on (as described above indicating low variability), and lower dspread3 values were measured during the phase of the day where the lights were off (as described above, indicating high variability) (Figure 39, vehicle-treated animals).

Next, the effects of the 5 compounds on dspread3 tested in the radiotelemetry study (Chapter 3) were assessed (Figure 40). The two vasodilators, vardenafil (Figure 40B) and molsidomine (Figure 40C), increased dspread3 significantly compared to vehicle (indicating redder attractor, two-way ANOVA, $p<0.05$). Vardenafil only changed dspread3 significantly on the first day, on the second day there was no significant difference from vehicle. The maximum effect was observed on the first day, at 11 – 12 h after vardenafil dosing. Molsidomine increased dspread3 significantly from vehicle on both days. Again, the maximum effect was observed 11 – 12 h after dosing. Sunitinib (Figure 40D) did not significantly affect dspread3 over the two days monitored. Fostamatinib (Figure 40E) decreased dspread3 significantly from baseline within the group (indicating bluer attractor, two-way ANOVA $p<0.05$, Dunnett's multiple comparisons test within group from baseline $p<0.05$), however this was not significantly different from the vehicle-treated group. Entospletinib did not significantly affect dspread3 overall (Figure 40F).

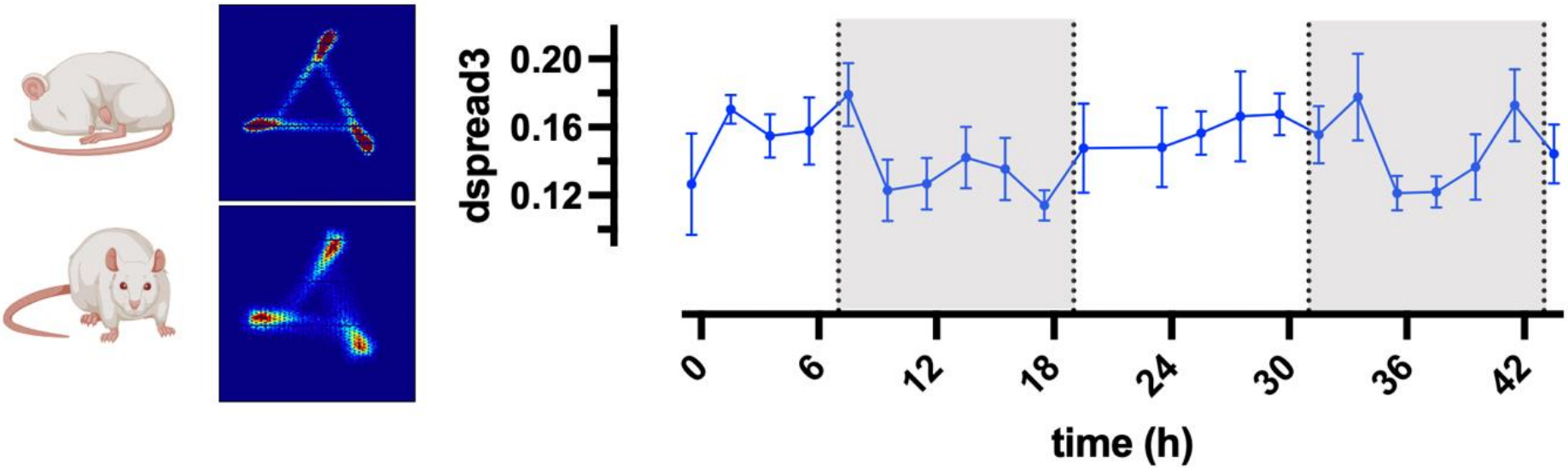

Figure 39: Dspread3 to quantify waveform variability changes throughout the day. *Dspread3 represents the amount of red in the attractor. The redder the attractor, the higher dspread3, the bluer the attractor, the lower dpsread3. Top attractor is an example of an attractor generated from a 1-minute recording during the lights-on half of the day, when the animals are expected to be asleep. These attractors were usually defined and had clear red arms, representing a low waveform variability, and therefore have a high dspread3. The bottom attractor is an example of an attractor generated from a 1-minute recording during the lights-off half of the day, when the animals are expected to be awake. These attractors are usually less well defined and bluer, representing a higher waveform variability, and therefore have a lower dspread3. The graph on the right-hand side shows dspread3 changes throughout the day of vehicle-treated animals (n=6, data are presented as mean ± SEM and were binned per two h). Grey bars indicate light-off half of the day. Dspread3 decreases during the light-off half of the day (not significant, One-way ANOVA, p>0.05). This graph confirms an increase in waveform variability when the animals are awake.*

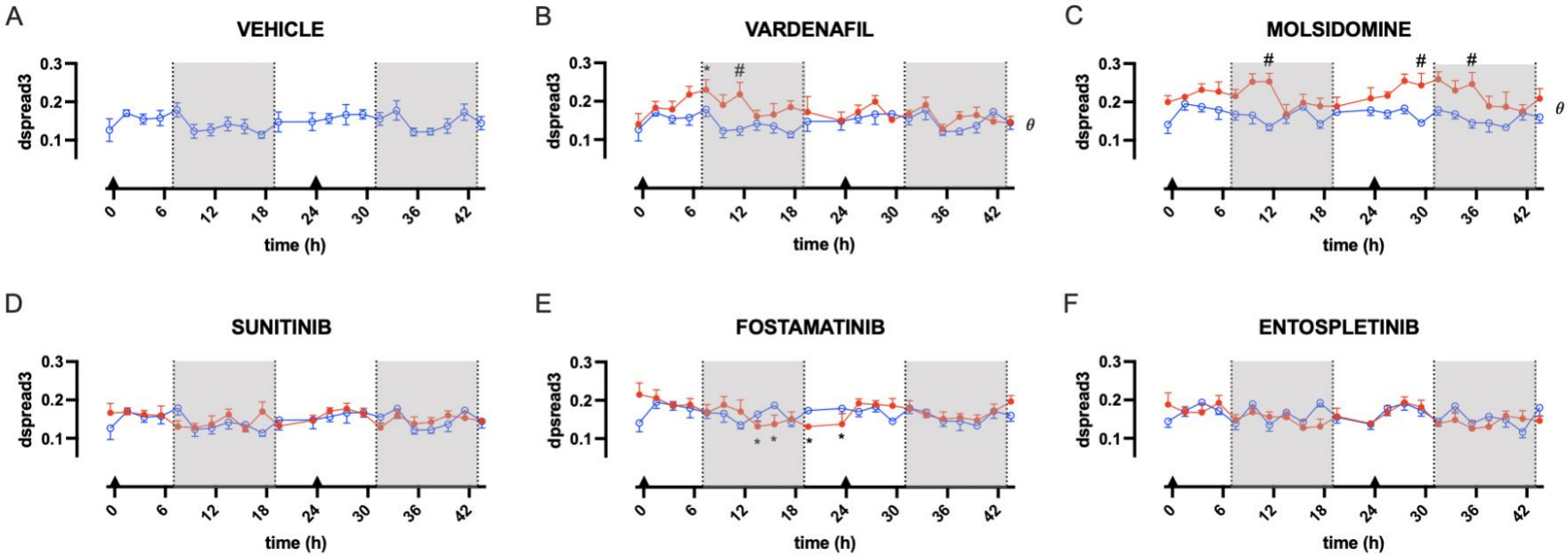

Figure 40: Changes in dspread3 in drug-treated groups. *Vehicle-treated groups are presented in blue, open circles. Drug-treated groups are presented in red, filled circles. Grey bars indicate light-off half of the day, black triangles on time-axis indicate time of administration of drug or vehicle. Data are presented as mean ± SEM and were binned per two h.* ***(A)*** *Changes in dspread3 in vehicle-treated group (10 mL/kg, p.o., n=6).* ***(B)*** *Vardenafil (10 mg/kg, p.o., n=6) caused an increase in dspread3 on the first day.* ***(C)*** *Molsidomine (10 mg/kg p.o., n=5) caused an increase in dspread3 that sustained over the two days.* ***(D)*** *Sunitinib (7 mg/kg, p.o., n=6) did not affect dspread3.* ***(E)*** *Fostamatinib (20 mg/kg, p.o., n=5) caused a decrease in dspread3 within the group from baseline, however this was not significantly different from vehicle.* ***(F)*** *Entospletinib (6 mg/kg, p.o., n=6) did not significantly change dspread3. Statistical tests: a two-way ANOVA test was conducted to test for overall differences between two groups (θ = p<0.05), followed by multiple comparison by Sídák to test for differences between the groups at each time point (# = p<0.05) Furthermore, if there was a significant change over time within a group (two-way ANOVA), each timepoint of the group was compared to the group's corresponding baseline (T=-0.5 h), by Dunnett test (* = p<0.05).*

4.3.5. Quantification of waveform morphology changes

As described above (section 4.3.3.), three attractor metrics were selected to quantify morphology changes: rQ25, maxrdenspos and rspread. The section below shows the effects of the five tested compounds on these metrics. Additionally, the metrics normalised to baseline value for each animal are presented, as each animal had its own distinct attractor before dosing on the first day.

4.3.5.1. Vardenafil

Figure 41 shows an example of how vardenafil affected the wave, attractor, radial density plot and metrics (n=1). In SPARKS, from each attractor, a radial density plot is extracted. These plots are generated via a growing circle that measures the density over the attractor. The centre of the circle is 0 units on the x-axis of the radial density plot. As the diameter of the circle grows, the density values are recorded and reported on the y-axis of the radial density plot. Essentially this plot represents how the data points are radially distributed over the attractor. The metrics rQ25, rspread and maxrdenspos can be measured from this plot. rQ25 represents at which radial position 25% of the data is captured (blue arrow in Figure 41). If the data are concentrated in the outer edges of the attractor, rQ25 is high. If the data points are coming more towards the inside of the attractor (e.g. after vardenafil dosing), the rQ25 decreases. Similarly, maxrdenspos indicated at which radial position the maximum density can be found (pink arrow in Figure 41). If the highest density is found at the outer edges of the attractor, maxrdenspos is high. If the highest density is closer to the centre of the attractor, maxrdenspos decreases. Lastly, rspread represents at which radial density 99% of the data is captured, thus indicates how the data in the outer edges of the attractor are distributed (green arrow in Figure 41). The physiological relevance of these metrics is interpreted and discussed later in this Chapter (Section 4.4.2.2., Table 11). As shown in Figure 41, vardenafil decreased rQ25, maxrdenspos and rspread. This was the result of a change in distribution of the data over the attractor; vardenafil caused the high-density arms to come more towards the middle of the triangle and spread the data more evenly over the attractor. As discussed below (section 4.4.2.2., Table 11), this was associated with a decrease in wave reflection.

It's important to mention that these metrics are inevitably affected by a change in attractor size, and therefore by a change in PP (Nandi et al., 2018). For example, vardenafil decreases PP (Chapter 3, section 3.3.1.). This was indeed reflected in a decrease in size of the attractors, and subsequently a decrease in radial density measures. In Figure 41 for example, the top attractor has a size of approximately 37 units in the radial density plot, and its rspread is 36,32. The bottom attractor has a size of approximately 29 units, so automatically its rspread will be lower (in this case 28,78). To circumvent this issue and make sure metrics were comparable between different sized attractors, each metric was normalised to its own attractor size. In this way, reported changes in rQ25, maxrdenspos and rspread were a result of changes in the radial distribution of the data in the attractor, rather than changes in PP. This normalisation step was available in SPARKS and was done in a window-by-window basis. Before the metrics were computed, the waveform itself was normalised to its Euclidean norm (a common mathematical algorithm for normalisation, defined as the square root of the inner product of a vector with itself). This produced equally sized attractors for each window, whose radial metrics were comparable.

Importantly, data were normalised in a second way; to the baseline recording on the first day. Each animal had its unique BP wave morphology and thus attractor at the beginning of each study, therefore each attractor metric was normalised to its value at baseline recording on the first day. This allowed for informative reporting of changes of the metric in each group of animals.

In summary, SPAR metrics were normalised in two ways. Firstly, the metrics were normalised to size (represented in panel A, B and C of Figures 43, 45, 46, 48 and 49) to ensure metrics indicated relative changes in data distribution, rather than changes dependent on drug-induced PP changes. Secondly, data were normalised to their baseline recording value, to account for inter-animal variability. Δmetrics presented in panel D, E and F of Figures 43, 45, 46, 48 and 49 are normalised both to size and to baseline. The radial density plots in this thesis are shown in absolute units (not normalised to size). The sole purpose of these figures was to illustrate how the metrics were taken and how drug-induced attractor changes were related to changes in the radial density plots.

Figure 42 shows the effects of the vardenafil-treated animals, compared to vehicle-treated animals (n=6). Vardenafil did not cause a significant change in rQ25 (Figure 42A), maxrdenspos (Figure 42B) or rspread (Figure 42C) if the data were not normalised to their baseline recording. When normalising each animal to its individual baseline metric, vardenafil decreased all three metrics (Figure 42D, E and F). ΔrQ25 decreased significantly from the first day (two-way ANOVA, $p<0.05$), with the maximum effect reached 4 – 8 h after dosing on the first day. Similarly, Δmaxrdenspos was decreased significantly from day 1 (two-way ANOVA, $p<0.05$), maximum effect observed within the first hour after dosing on the second day. Lastly, also Δrspread was decreased after vardenafil administration from the first day (two-way ANOVA, $p<0.05$), with the maximum effect observed on the first day, 12 – 16 h after dosing. As discussed below (section 4.4.2.2. Table 11), these changes of these metrics were typically associated with a decrease in wave reflection.

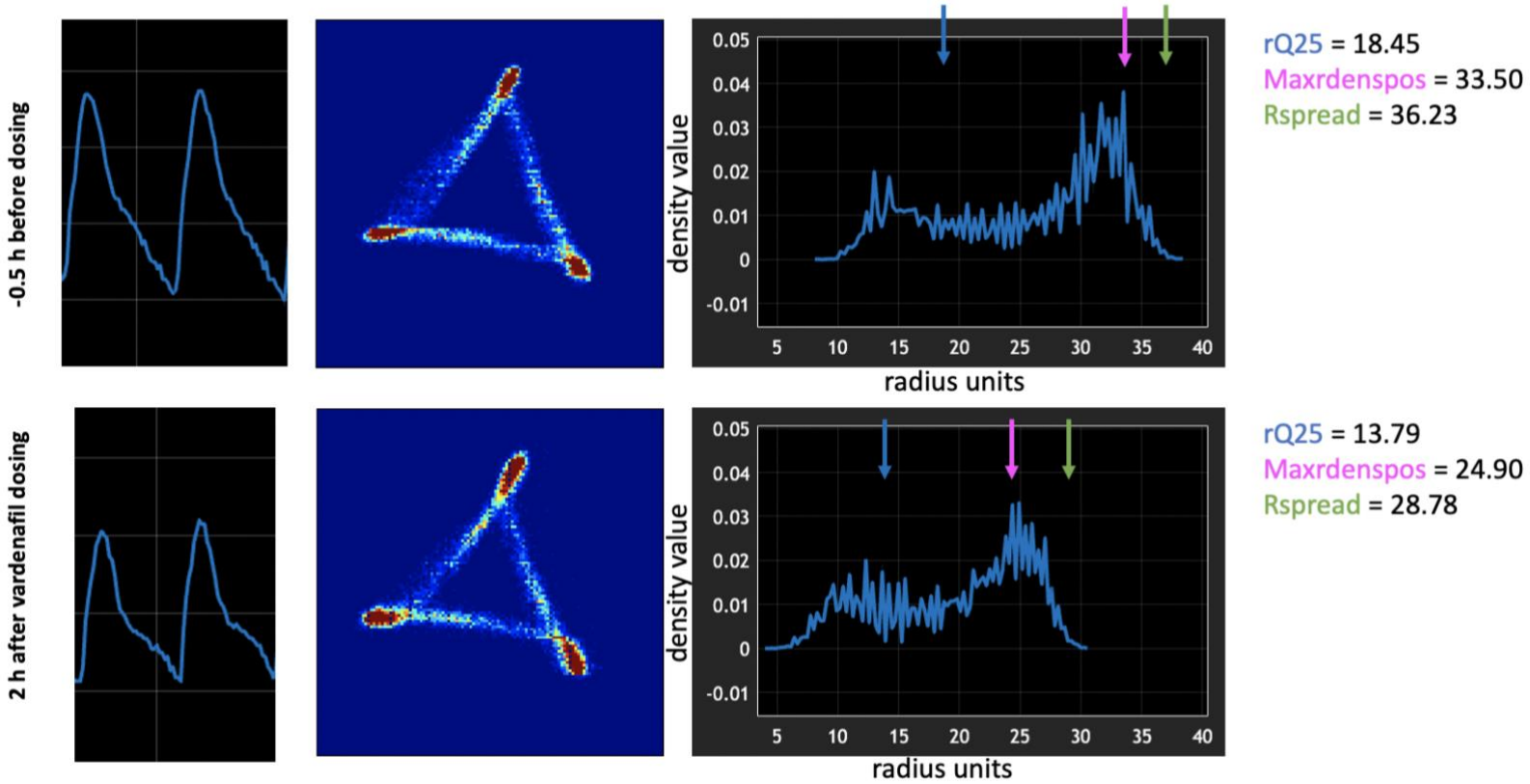

Figure 41: Effects of vardenafil of the waveform, attractor, radial density plot and attractor metrics (n=1). *The top row is generated from a blood pressure recording before dosing, the bottom row is generated from a blood pressure recording 2 h after vardenafil dosing. The data shown here are a representative example of changes observed in vardenafil-treated animals. Changes in blood pressure waves were reflected in a change in attractors; after vardenafil administration, the red arms of the attractor were increased in size. On the right-hand side of the attractors, corresponding radial density plots are shown (with x-axis representing radius units of growing concentric circle, y-axis indicating density values). These plots are generated via a growing circle over the attractor density. The centre of the circle is 0 on the x-axis of the radial density plot. As the diameter of the circle grows, the density values are recorded and reported on the y-axis of the radial density plot. Essentially the radial density plot represents how the data points are radially distributed over the attractor. From the radial density plots shown in this figure, it is apparent that vardenafil decreased the size of the attractor and shifted the distribution of the data to the inside of the attractor. From this radial density plot, the three metrics discussed above are extracted. rQ25 represents at which growing circle 25% is captured (blue arrow), rspread represents at which growing circle 99% is captured (green arrow), and maxrdenspos indicated at which radial position the maximum density can be found (pink arrow). Vardenafil decreased all three metrics.*

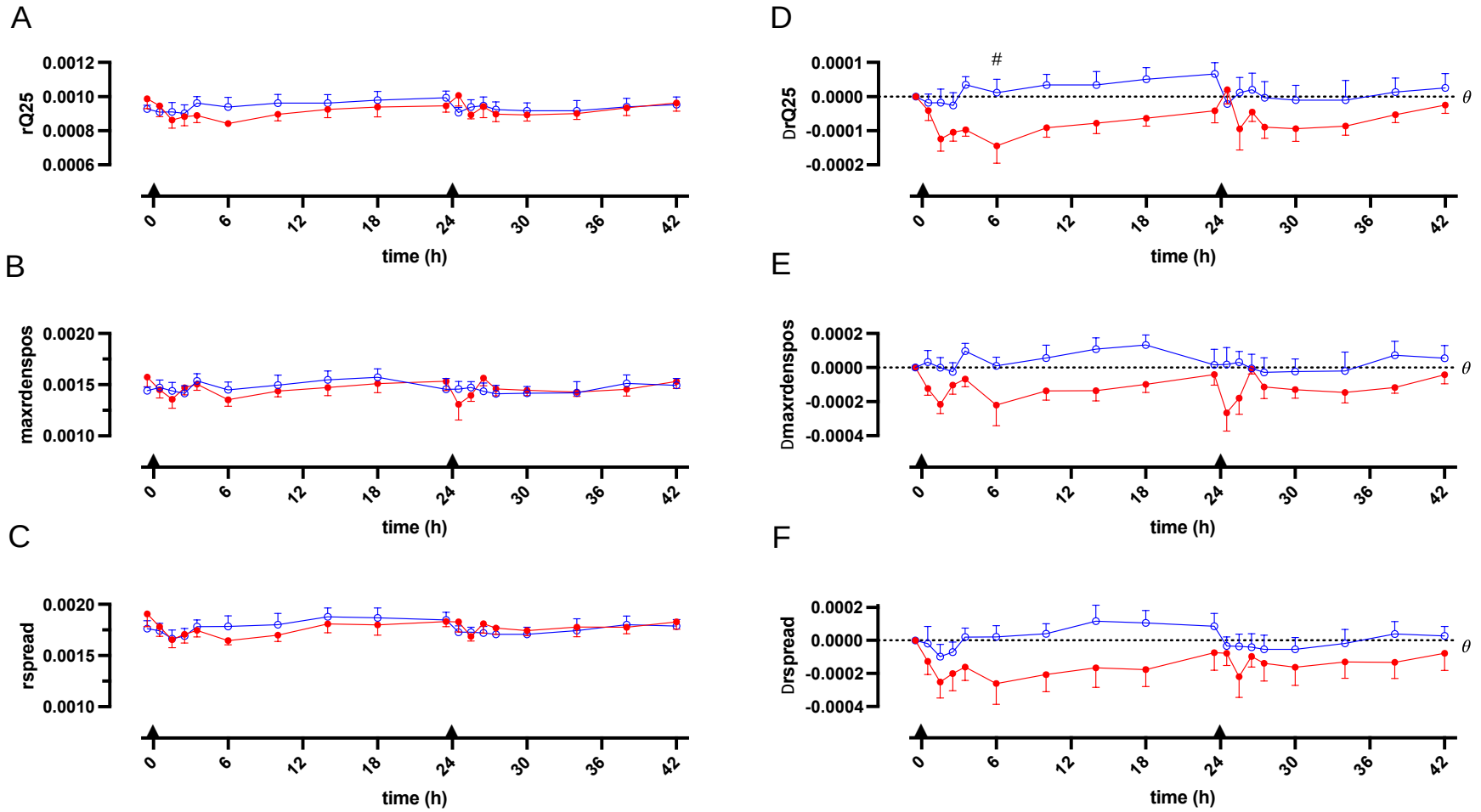

Figure 42: Vardenafil-induced changes of the attractor metrics. *Changes in rQ25* ***(A)****, maxrdenspos* ***(B)*** *and rspread* ***(C)*** *(normalised to attractor size only) of rats dosed with vardenafil 10 mg/kg p.o. (n=6, red, filled circles) and vehicle p.o. (n=6, blue, open circles). Data normalised additionally to baseline recording for each animal individually, are presented in* ***(D)****,* ***(E)*** *and* ***(F)****. Black triangles on time-axis indicate time of administration of vardenafil or vehicle. Data are presented as mean ± SEM and were binned per hour (baseline and first 4 h after dosing) or per 4 h (from 4 h after dosing). A two-way ANOVA test was conducted to test for overall differences between two groups (θ = p<0.05), followed by multiple comparison by Sídák to test for differences between the groups at each time point (# = p<0.05) Furthermore, if there was a significant change over time within a group (two-way ANOVA), each timepoint of the group was compared to the group's corresponding baseline (T=-0.5 h), by Dunnett test (* = p<0.05).*

4.3.5.2. Molsidomine

Similarly as vardenafil, molsidomine caused a inwards shift of the high density arms of the attractor. An example of this effect is shown in Figure 43 (n=1); at 3 h after molsidomine dosing the red arms were redistributed towards the centre of the attractor. This change in attractor data spread resulted in a large decrease in rQ25 and maxrdenspos. Rspread was not affected majorly in this example, however as mentioned above these metrics should be normalised to their attractor size. These plots were only included to demonstrate examples of drug-induced changes in the attractor shape and how metrics were taken, not to indicate quantitative drug-effects. The normalised-to-size and normalised-to-size-and-baseline metrics are presented in Figure 44 (n=5).

Molsidomine decreased rQ25 (Figure 44A), maxrdenspos (Figure 44B) and rspread (Figure 44C) significantly. When normalising the metric to the baseline recording values, ΔrQ25 (Figure 44D) and Δmaxrdenspos (Figure 44E) were significantly decreased from the first day of dosing (two-way ANOVA, $p<0.05$). The maximum effect on ΔrQ25 was observed 8 – 12 h after dosing on the first day. The maximum effect on Δmaxrdenspos was observed 2 h after dosing on the second day (Sídák test, $p<0.05$). These changes indicated the attractor closed following molsidomine administration, and as discussed below (section 4.4.2.2., Table 11) were typically associated with a decrease in wave reflection. Interestingly, when normalised to baseline, Δrspread significantly increased from the first day of molsidomine dosing, compared to vehicle (Figure 44F, two-way ANOVA, $p<0.05$), with the maximum effect seen 4 – 8 h after dosing (Sídák test, $p<0.05$).

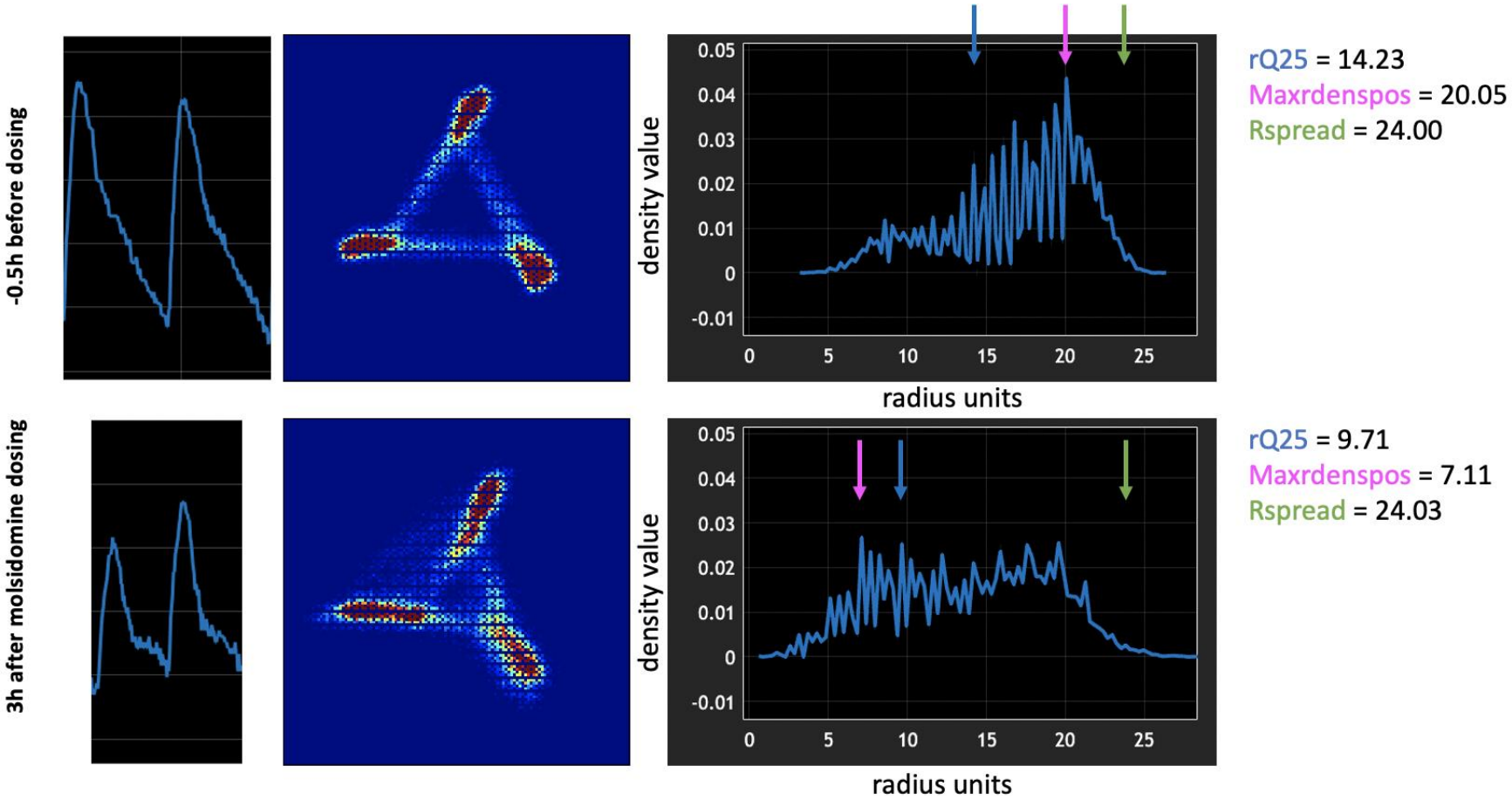

Figure 43: Effects of molsidomine of the waveform, attractor, radial density plot and attractor metrics. *The top row is generated from a blood pressure recording before dosing, the bottom row is generated from a blood pressure recording 3 h after molsidomine dosing. The data shown here are a representative example of changes observed in molsidomine-treated animals. Changes in blood pressure waves were reflected in a change in attractors; after molsidomine administration, the red arms of the attractor were larger and spread towards the centre of the attractor. On the right-hand side of the attractors, corresponding radial density plots are shown. From the radial density plots shown in this figure, it is apparent that molsidomine shifts the distribution of the data to the inside of the attractor, resulting in a decrease in rQ25 (blue arrow) and maxrdenspos (pink arrow).*

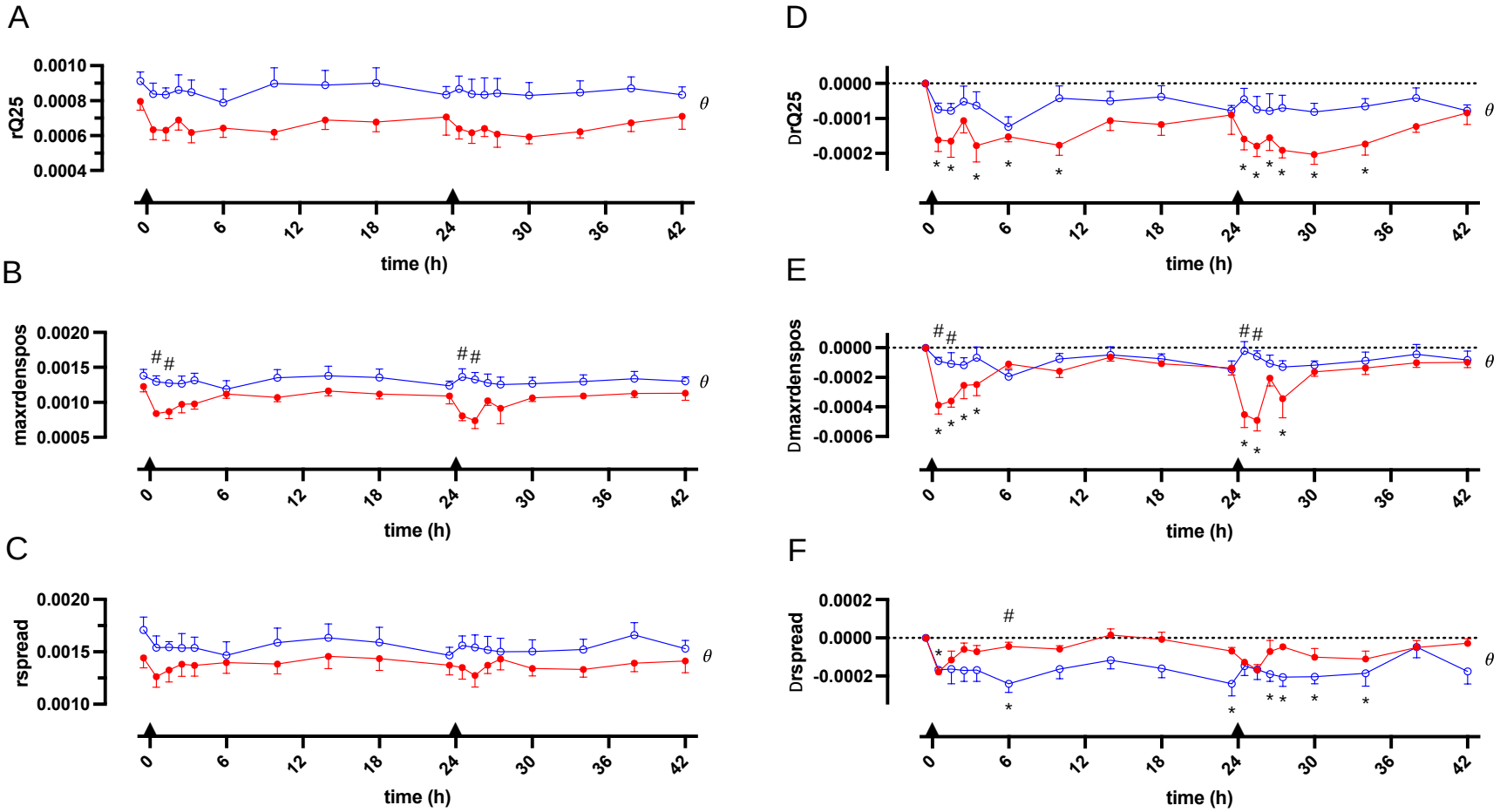

Figure 44: Molsidomine-induced changes of the attractor metrics. *Changes in rQ25* ***(A)****, maxrdenspos* ***(B)*** *and rspread* ***(C)*** *(normalised to attractor size only) of rats dosed with molsidomine 10 mg/kg p.o. (n=5, red, filled circles) and vehicle p.o. (n=5, blue, open circles). Data normalised additionally to baseline recording for each animal individually, are presented in* ***(D)****,* ***(E)*** *and* ***(F)****. Black triangles on time-axis indicate time of administration of vardenafil or vehicle. Data are presented as mean ± SEM and were binned per hour (baseline and first 4 h after dosing) or per 4 h (from 4 h after dosing). A two-way ANOVA test was conducted to test for overall differences between two groups (θ = p<0.05), followed by multiple comparison by Sídák to test for differences between the groups at each time point (# = p<0.05) Furthermore, if there was a significant change over time within a group (two-way ANOVA), each timepoint of the group was compared to the group's corresponding baseline (T=-0.5 h), by Dunnett test (* = p<0.05).*

4.3.5.3. Sunitinib

Sunitinib (n=6) caused in small decrease in rQ25 (Figure 45A) and ΔrQ25 (Figure 45B), however this effect was only significant from the second day (two-way ANOVA, $p<0.05$). Maxrdenspos (Figure 45B) and rspread (Figure 45C) were slightly decreased as well, both significantly different from vehicle from the first day of sunitinib administration (two-way ANOVA, $p<0.05$). These effects were lost when the latter two metrics were normalised to the baseline recording (Δmaxrdenspos, Figure 45E, and Δrspread, Figure 45F). Overall, SPAR detected little changes following sunitinib administration.

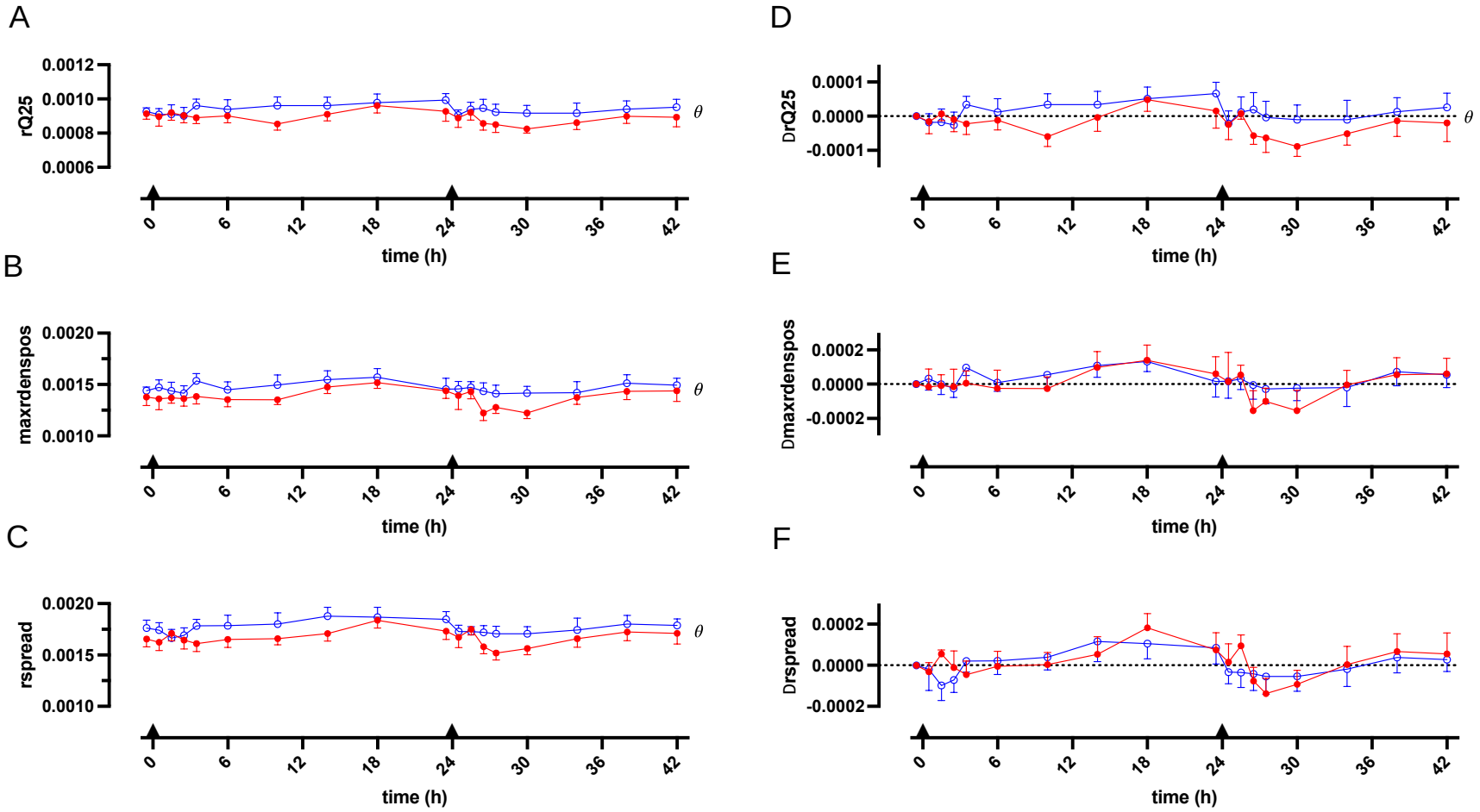

Figure 45: Sunitinib-induced changes of the attractor metrics. *Changes in rQ25* ***(A)****, maxrdenspos* ***(B)*** *and rspread* ***(C)*** *(normalised to attractor size only) of rats dosed with sunitinib 7 mg/kg p.o. (n=6, red, filled circles) and vehicle p.o. (n=6, blue, open circles). Data normalised additionally to baseline recording for each animal individually, are presented in* ***(D)****,* ***(E)*** *and* ***(F)****. Black triangles on time-axis indicate time of administration of vardenafil or vehicle. Data are presented as mean ± SEM and were binned per hour (baseline and first 4 h after dosing) or per 4 h (from 4 h after dosing). A two-way ANOVA test was conducted to test for overall differences between two groups (θ = p<0.05), followed by multiple comparison by Sídák to test for differences between the groups at each time point (# = p<0.05) Furthermore, if there was a significant change over time within a group (two-way ANOVA), each timepoint of the group was compared to the group's corresponding baseline (T=-0.5 h), by Dunnett test (* = p<0.05).*

4.3.5.4. Fostamatinib

Figure 46 shows an example of how fostamatinib affected the waveform, attractor, radial density plot and associated measures (n=1). Fostamatinib caused a shortening of the red attractor arms, towards the outer edge of the attractor. From the radial density plot, an increase in rQ25 and maxrdenspos was measured. Equally, rspread increased, following an increase in attractor size due to an increase PP of the wave. To ensure changes in these metrics were due to changes in attractor shape, rather than solely due to PP changes, each metric was then normalised to the size of its attractor. The normalised-to-size and normalised-to-size-and-baseline metrics are presented in Figure 47 (n=5).

Administration of fostamatinib resulted in a small decrease in rQ25 (Figure 47A), maxrdenspos (Figure 47B) and rspread (Figure 47C), significantly different from vehicle from the first day (two-way ANOVA, $p<0.05$). When the metrics were normalised to baseline, fostamatinib had the opposite effect; the Δmetrics increased following fostamatinib dosing. ΔrQ25 increased significantly from the first day (Figure 47D, two-way ANOVA, $p<0.05$), with the maximum effect observed at baseline recording on the second day (T=23.5 h, Sídák test, $p<0.05$). Δmaxrdenspos was significantly increased from the first day as well (Figure 47E, two-way ANOVA, $p< 0.005$), with the maximum response observed at 12 – 16 h on the first day of dosing. Lastly, Δrspread was increased significantly from the first day of fostamatinib dosing (Figure 47F, two-way ANOVA, $p<0.05$). The maximum difference between fostamatinib and vehicle was observed at baseline recording on the second day (T=23.5 h, Sídák test, $p<0.05$). In general, for all three metrics, the effects of fostamatinib were larger in the second half of each day (12 – 24 h and 36 – 46 h) than immediately after dosing.

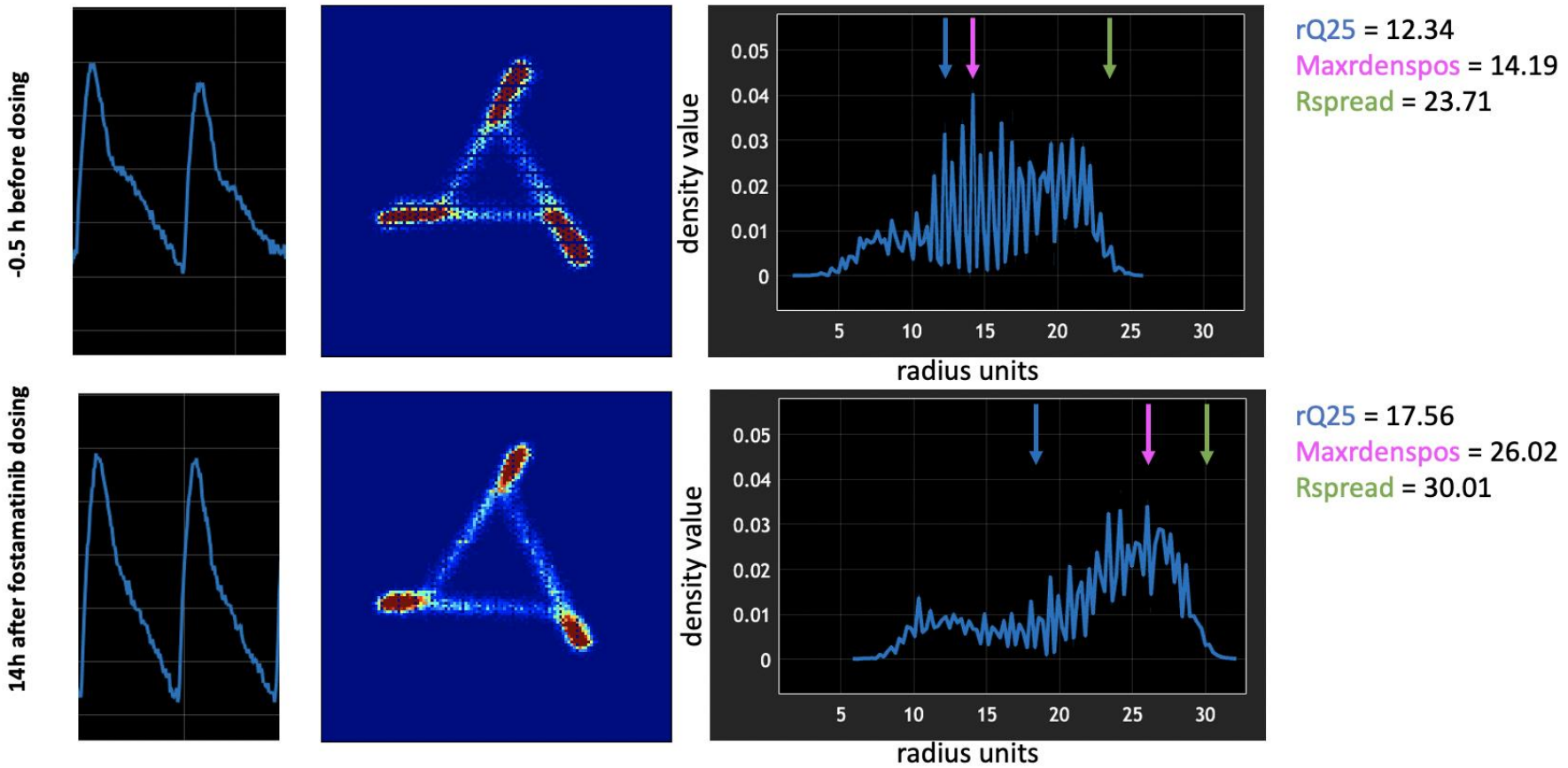

Figure 46: Effects of fostamatinib of the waveform, attractor, radial density plot and attractor metrics. *The top row is generated from a blood pressure recording before dosing, the bottom row is generated from a blood pressure recording 14 h after fostamatinib dosing. The data shown here are a representative example of changes observed in fostamatinib-treated animals. Following fostamatinib administration, the red arms of the attractor were smaller compared to baseline. On the right-hand side of the attractors, corresponding radial density plots are shown. From the radial density plots shown in this figure, it is apparent that fostamatinib increased the size of the attractor and shifter the distribution of the data to the outside of the attractor, associated with an increase in rQ25, maxrdenspos and rspread.*

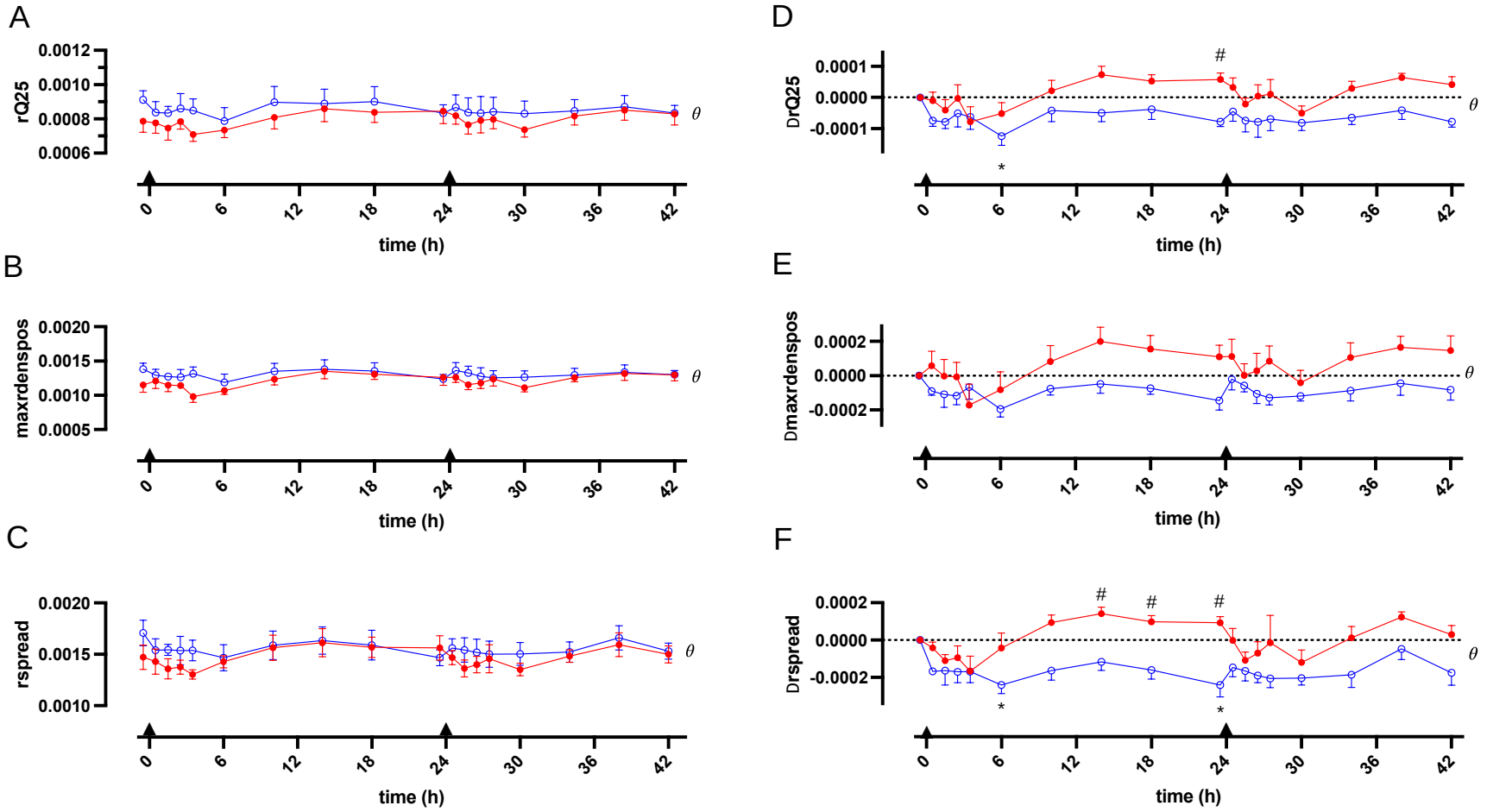

Figure 47: Fostamatinib-induced changes of the attractor metrics. *Changes in rQ25* ***(A)****, maxrdenspos* ***(B)*** *and rspread* ***(C)*** *(normalised to attractor size only) of rats dosed with fostamatinib 20 mg/kg p.o. (n=5, red, filled circles) and vehicle p.o. (n=5, blue, open circles). Data normalised additionally to baseline recording for each animal individually, are presented in* ***(D)****,* ***(E)*** *and* ***(F)****. Black triangles on time-axis indicate time of administration of vardenafil or vehicle. Data are presented as mean ± SEM and were binned per hour (baseline and first 4 h after dosing) or per 4 h (from 4 h after dosing). A two-way ANOVA test was conducted to test for overall differences between two groups (θ= p<0.05), followed by multiple comparison by Sídák to test for differences between the groups at each time point (# = p<0.05) Furthermore, if there was a significant change over time within a group (two-way ANOVA), each timepoint of the group was compared to the group's corresponding baseline (T=-0.5 h), by Dunnett test (* = p<0.05).*

4.3.5.5. Entospletinib

Entospletinib (n=5) did not affect rQ25, maxrdenspos or rspread significantly (Figure 48A, 49B and 49C). When the metrics were normalised to baseline recordings, ΔrQ25 (Figure 48D) and Δrspread (Figure 48F) increased. ΔrQ25 in the entospletinib group changed significantly from vehicle on the first day (two-way ANOVA, $p<0.05$), with the largest increase observed at 2 – 3 h after dosing on the second day (Sídák test, $p<0.05$). Similarly, Δrspread was significantly different in the entospletinib group compared to the vehicle group, from the first day (two-way ANOVA, $p<0.05$). The maximum difference in Δrspread between entospletinib and vehicle was at 2 – 3 h after dosing on the second day. Overall, both ΔrQ25 and Δrspread changed rapidly after dosing and these effects sustained throughout the day. Entospletinib did not significantly change Δmaxrdenspos (Figure 48E, two-way ANOVA, $p>0.05$).

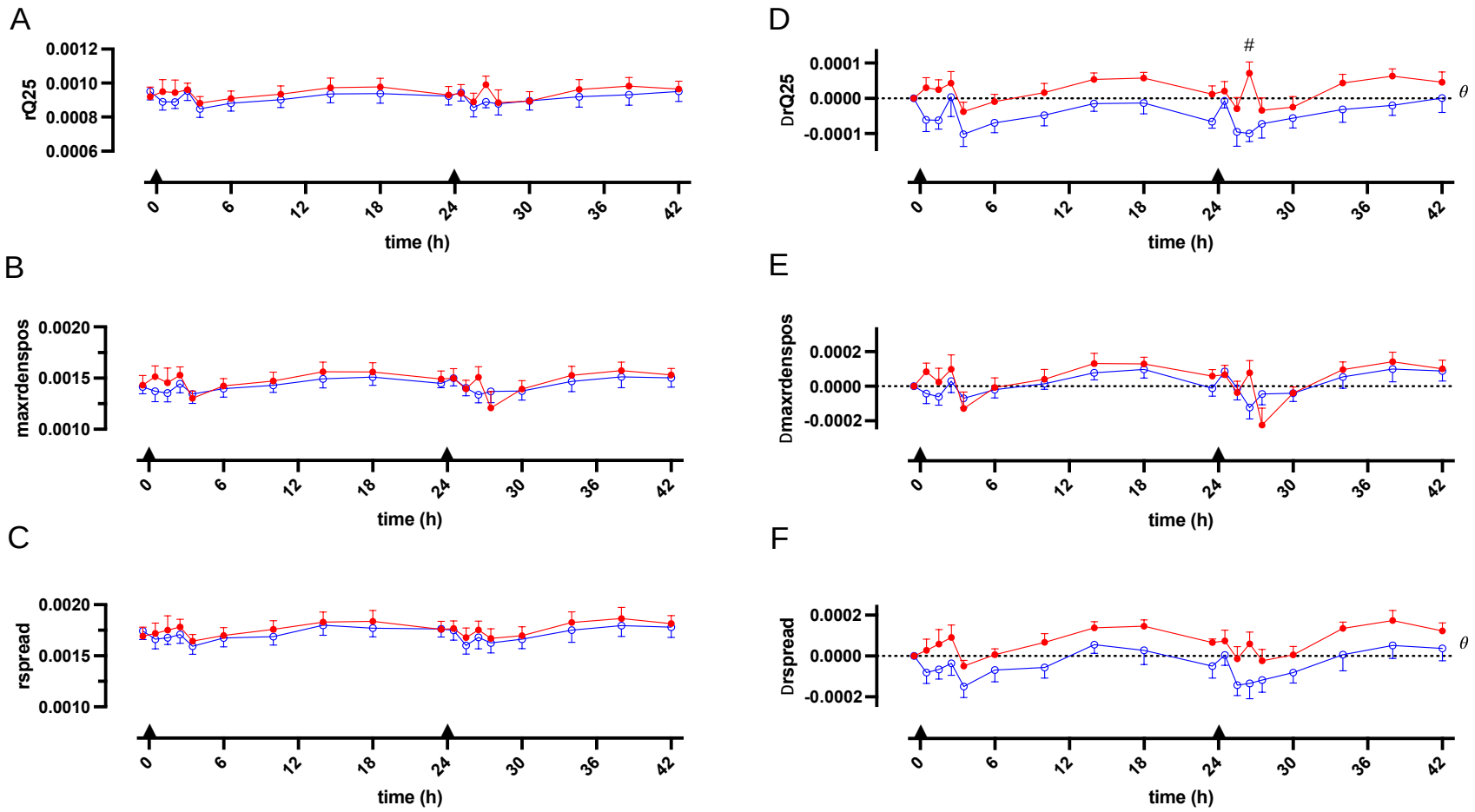

Figure 48: Entospletinib-induced changes of the attractor metrics. *Changes in rQ25* ***(A)****, maxrdenspos* ***(B)*** *and rspread* ***(C)*** *(normalised to attractor size only) of rats dosed with entospletinib 6 mg/kg p.o. (n=5, red, filled circles) and vehicle p.o. (n=5, blue, open circles). Data normalised additionally to baseline recording for each animal individually, are presented in* ***(D)****,* ***(E)*** *and* ***(F)****. Black triangles on time-axis indicate time of administration of vardenafil or vehicle. Data are presented as mean ± SEM and were binned per hour (baseline and first 4 h after dosing) or per 4 h (from 4 h after dosing). A two-way ANOVA test was conducted to test for overall differences between two groups (θ = p<0.05), followed by multiple comparison by Sídák to test for differences between the groups at each time point (# = p<0.05) Furthermore, if there was a significant change over time within a group (two-way ANOVA), each timepoint of the group was compared to the group's corresponding baseline (T=-0.5 h), by Dunnett test (* = p<0.05).*

4.3.6. Summary

A summary of the effects of vardenafil (Figure 42), molsidomine (Figure 44), sunitinib (Figure 45), fostamatinib (Figure 47) and entospletinib (Figure 48) on attractor metrics are shown in Table 9. The normalised-to-baseline attractors metrics are displayed Table 10. All changes shown in the tables were significant from the first day of drug administration, except the sunitinib-induced rQ25 decrease and ΔrQ25 decrease, which were significantly different from vehicle only from the second day of the study. A similar table for conventional parameters MAP, HR and PP can be found in Chapter 3, section 3.3.6.

Table 9: Overview of the effects on attractor metrics (dspread3, rQ25, maxrdenspos and rspread) of vardenafil, molsidomine, sunitinib, fostamatinib and entospletinib. *All changes shown were significantly different from vehicle from the first day ($p<0.05$, two-way ANOVA), except for the sunitinib-induced decrease in rQ25 which was significantly different from vehicle only from the second day (D2). '↑↑' indicates a large increase in the metric, '↑' indicates an increase in the metric, '↓↓' indicates a large decrease in the metric, '↓' indicates a decrease in the metric, '=' indicates metric was not significantly changed.*

	Vardenafil	Molsidomine	Sunitinib	Fostamatinib	Entospletinib
dspread3	↑	↑	=	=	=
rQ25	=	↓↓	↓ (on D2)	↓	=
maxrdenspos	=	↓↓	↓	↓	=
rspread	=	↓↓	↓	↓	=

Table 10: Overview of the effects on normalised attractor morphology metrics (ΔrQ25, Δmaxrdenspos and Δrspread) of vardenafil, molsidomine, sunitinib, fostamatinib and entospletinib. *All changes shown were significantly different from vehicle from the first day ($p<0.05$, two-way ANOVA), except for the sunitinib-induced decrease in ΔrQ25, which was significantly different from vehicle only from the second day (D2). '↑↑' indicates a large increase in the metric, '↑' indicates an increase in the metric, '↓↓' indicates a large decrease in the metric, '↓' indicates a decrease in the metric, '=' indicates metric was not significantly changed.*

	Vardenafil	Molsidomine	Sunitinib	Fostamatinib	Entospletinib
ΔrQ25	↓	↓	↓ (on D2)	↑	↑
Δmaxrdenspos	↓	↓↓	=	↑	=
Δrspread	↓	↑	=	↑↑	↑

As mentioned above (section 4.3.5.1.), attractors were normalised in two ways for quantitative analysis; once to size and once to baseline. This allowed for more representative reporting of changes of the metric and the discussion of the waveform morphology changes below is focussed on these metrics normalised to both size and baseline (Δmetrics). The two vasodilators vardenafil and molsidomine decreased ΔrQ25 and Δmaxrdenspos. They had an opposing effect on Δrspread; vardenafil decreased Δrspread while molsidomine increased Δrspread. Sunitinib did not affect Δmaxrdenspos or Δrspread, and ΔrQ25 was decreased significantly only after the second administration of sunitinib. Fostamatinib increased all three normalised attractor metrics. Lastly, entospletinib did not affect Δmaxrdenspos but did increase ΔrQ25 and Δrspread.

4.4. Chapter discussion

In this Chapter, the application of a novel method for physiological wave analysis, SPAR, was explored using the blood pressure data obtained with radiotelemetry in rats, discussed in Chapter 3. The main aim of this Chapter was to optimise and validate the method for application on rat blood pressure data, and subsequently, utilise the method for in-depth analysis of the Syk-inhibitors' effect on the blood pressure wave.

4.4.1. Optimisation of the methods

To ensure optimal analysis of the blood pressure waves from rats, several parameters of the SPAR algorithm were adjusted. As a starting point for algorithm input parameters, the set of 'HumanBP' was used, however this set was optimised for analysis of human blood pressure data. To adjust these parameters for pressure data from rats, firstly, the minimum expected HR was increased from 40 to 230, and the maximum expected HR was increased from 180 to 550. Next, for qualitative, visual analysis of the attractors, the nbins_density was decreased from 250 to 125, as this generated brighter attractors, facilitating easier visual assessment of the attractor changes. Furthermore, a 1 min window of data was found to be the optimal length to generate an attractor; this window contained sufficient data (> 100 cycles) to generate a representative attractor and allowed for easy window selection without signal drop-out while keeping the required computational power low. These optimisation steps led to the standard protocol of SPAR analysis used in this Chapter.

4.4.2. Validation of the method

Next, to validate the use of SPAR on blood pressure data recorded with radiotelemetry in rats, the changes attractor colour and attractor shape were examined after administration of vehicle or reference compounds, to assess whether they exhibited the expected changes in waveform variability and waveform morphology respectively.

4.4.2.1. Waveform variability changes

Firstly, the changes in waveform variability were studied. Waveform variability changes are reflected in the attractor colour (Aston et al., 2018; Nandi & Aston, 2020). As rats are nocturnal animals, they are expected to be awake when the lights are off ('night-time') and display more active behaviour (Stephan & Zucker, 1972). This would result in higher waveform variability. Conversely, during the half of the day where the lights are on ('daytime'), the animals are expected to be asleep and less active (Stephan & Zucker, 1972), thus show lower waveform variability. To confirm if SPAR could detect these variability fluctuations, attractors from vehicle-treated animals were examined (Figure 35). Indeed, more blue attractors were observed in the night-time (7 – 19 h after dosing), indicating higher waveform variability in the pressure signal, than during the daytime. This observation was quantified by dspread3 changes (Figure 39). Dspread3 did decrease during the night-time, again confirming an increase in waveform variability, compared to day-time recordings. These changes were not significant, however following the circadian rhythm fluctuations was not the primary purpose of the study. Animals were visited at multiple occasions during the day for drug administration and welfare checks. These disruptions inherently influenced their circadian rhythm. Nonetheless, the reported dspread3 changes indicated that SPAR is able to detect changes in waveform variability of the rat blood pressure data and presented confirmation that the SPAR method is suitable to map physiological changes.

Interestingly, HRV is reported to increase during night-time in humans (Sammito et al., 2016). However so far, findings on variability changes following the circadian rhythm are contradictory (Honkalampi et al., 2021). Furthermore, it is important to mention that HRV and SPAR detect different aspects of wave variability. HRV reports how the HR varies, reducing the pulse wave to one metric (peak-to-peak interval changes) (Honkalampi et al., 2021). SPAR however reports on the variability in the wave morphology. Theoretically, HRV and SPAR could fluctuate differently throughout the day, especially in different species.

Sunitinib did not affect dspread3. The two vasodilators, vardenafil and molsidomine, caused an increase in dspread3 (Figure 40), indicating a decrease in waveform variability. Potentially this effect was observed because vardenafil and molsidomine caused large decreases in MAP and therefore would decrease the blood supply to vital organs. In response, several autoregulatory mechanisms are activated to maintain a constant blood supply (Carlström et al., 2015; Post & Vincent, 2018). One example is the baroreflex, resulting in a rapid increase in the HR in response to the drop in BP (DeMers & Wachs, 2019), as was indeed observed with both vasodilators in Chapter 3 (section 3.3.1. and 3.3.2.). Other autoregulatory mechanisms involve the myogenic and tubuloglomerular feedback pathways and the renin-angiotensin-aldosterone system (Carlström et al., 2015; DeMers & Wachs, 2019; Post & Vincent, 2018). These autoregulatory changes aim to control the blood flow to the kidney and other organs, therefore permit little changes in the blood pressure wave. Altogether, the activation of such regulating mechanisms could lead to a controlled cardiovascular system, resulting in a sequence of nearly identical waves and a reduction in waveform variability.

On the other hand, the observed decrease in waveform variability by the vasodilators could be indicating that these compounds compromise the ability of the cardiovascular system to adapt to changing circumstances, resulting in little wave variation, as no regulating mechanisms were affecting the wave. This hypothesis would be supported by literature reporting a high wave variability (reported as HRV) in subjects with a good cardiovascular health (Dong, 2016; McNarry & Lewis, 2012), and decreased variability with age or occupational stress (thus indicating impaired autoregulation) (Järvelin-Pasanen et al., 2019; Nunan et al., 2010; Van Ravenswaaij-Arts et al., 1993). However, given that these experiments were performed in healthy adult rats, it is unlikely that the vasodilators impaired the cardiovascular system in such way that all autoregulatory mechanisms would be compromised, therefore the first reasoning is more likely the cause of the observed variability decrease.

4.4.2.2. Waveform morphology changes

Secondly, the effects of wave morphology changes on the attractors were assessed to validate if SPAR could indeed pick up these morphology changes. Figure 36 shows an example of how changes in the waveform were indeed reflected in a change in shape of the attractor. Using 3 metrics (rQ25, maxrdenspos and rspread), the effects of the reference compounds (vardenafil, molsidomine and sunitinib) were characterised, allowing attractor metrics to be linked to physiological changes in the cardiovascular system, as discussed below.

Vasodilators

Firstly, the effect of vardenafil and molsidomine were assessed. As the additionally normalised-to-baseline metrics consider inter-individual variability and are therefore more representative for qualitative, visual changes, the discussion below is focussed on these Δmetrics (Table 2). Vardenafil decreased all three metrics related to attractor shape studied in this Chapter. Within the first 24 h after vardenafil dosing, ΔrQ25 and Δmaxrdenspos decreased significantly from vehicle. Molsidomine had similar effects on ΔrQ25 as vardenafil and showed an even larger decrease in Δmaxrdenspos. These effects on the radial density distribution, are linked to a shift of data in the attractor, from the outside towards the centre (Figure 41 and Figure 43). These observations are most likely due to the vasodilating effects of these two compounds. Vasodilatory compounds cause a decrease in wave reflection (W. W. Nichols et al., 2008; Su et al., 2018). This effect was observed in the exemplar waves included in Figure 41 and Figure 43; after administration of the vasodilator, the upstroke and first part of the downstroke were symmetrical, followed by a smaller wave reflection effect on the last third of the cycle, compared to the baseline waves. This effect is most clearly visible in Figure 43. In summary, the vasodilating effects of vardenafil and molsidomine caused an attenuating in wave reflection, resulting in an increase in size of the red attractor arms, which subsequently led a decrease in ΔrQ25 and Δmaxrdenspos.

A summary of the attractor metrics, how they related to changes in the attractor and waveform, and their physiological relevance is presented in Table 11.

Interestingly, molsidomine and vardenafil affected ∆rspread in opposing ways. Vardenafil decreased ∆rspread and molsidomine increased ∆rspread. Nonetheless literature indicates that these two compounds display comparable effects in the cardiovascular system, causing a vasodilation in both veins and arteries, systemically (Grund et al., 1978; Ried et al., 2017) and in the pulmonary bed (Detry et al., 1981; Ried et al., 2017). This would be expected, as both vardenafil and molsidomine perform their effect through the NO-pathway (Chander & Chopra, 2005; Ghiadoni et al., 2008; Keating & Scott, 2003; Nayak B et al., 2021). Therefore, so far the reason why these compounds were affecting rspread in opposing ways is not apparent and the interpretation of this metric is not entirely clear. As ∆rspread represents at which radial position 99% of the data can be found, the changes observed must be related to changes in the outer edges of the attractor. Most likely ∆rspread changes as the attractor edges become more sharp or soft (as for example in a circular attractor). However, no certain conclusions can be taken from the data available in this study. To further explore how rspread is related to changes in the attractors and waves, *in silico* generated data could be employed. This approach of analysing *in silico* data in SPAR has successfully been used before to characterise other SPAR metrics (Aston et al., 2018). Similarly, here it could potentially help to obtain a clear understanding of waveform changes leading to rspread changes.

Of important note, other SPAR metrics would have been interesting to study as well in this Chapter. For example, rcentspread, a metric that detects the length of the attractor arms, would likely be a good predictor of waveform morphology changes as well. Some preliminary analysis seemed to confirm this anticipation. However, at the time of analysis, due to technical limitations of the algorithm, SPAR was not able to measure rcentspread for each attractor, leading to many missing data points and low n-numbers for analysis. Furthermore, a decreased resistance and compliance of peripheral vasculature, associated with an increased concavity of downstroke, results in a clockwise rotation of attractor (Aston et al., 2018). These clockwise rotations were observed after vasodilator dosing, however SPARKS was not able to correctly compute the angle of rotation for each attractor at the time of analysis, therefore this metric was not further analysed. Optimising the detection of these metrics for the blood pressure attractors generated in the study, would be a useful next step, as this could perhaps detect morphology changes in an even more sensitive way.

When comparing the detection of cardiovascular effects by conventional wave analysis (MAP, HR and PP), SPAR was able to detect the changes following vasodilator administration with the same sensitivity; ΔrQ25 and Δmaxrdenspos were significantly different from vehicle from the first day of dosing, and indicated a decrease in waveform reflection.

Measure	Change in attractor	Change in waveform	Physiological interpretation
dspread3	Density in attractor **High** = high density, lot of red **Low** = low density, lot of blue	Variability in waveform **High** = low variability **Low** = high variability	Some drugs might affect variability, indicating activation of several autoregulating mechanisms to maintain blood flow to vital organs.
rQ25	Radial position that includes 25% of data, indication of how data points are spread over attractor. **Low** = closed attractor = high density points close to centre, e.g. high density arms are large or data are evenly spread over attractor. **High** = open attractor = high density points at outer sides of the attractor, e.g. in small high density arms.	**Low** = wave is more symmetrical, followed by flat interbeat interval. **High** = reflected waveform affects entire downstroke rather than only the last part of diastole.	**Decrease** is observed with vasodilators, effect of reflected pressure on forward wave becomes smaller as the vessel is more compliant. **Increase** is observed with Syk inhibitors, could indicate a vasoconstriction.
Maxrdenspos	Radial position of maximum density **Low** = closed attractor = maximum density is closer to centre of attractor **High** = open attractor = maximum density is on outer sides of attractor		
Rspread	Radial position that includes 99% of data, indication of how data are spread at the outer edges of the attractor. **Low** = low density end of arms, rounder attractor, density more evenly spread over attractor? **High** = density in end of arms increases, sharp edges?	?	**Decrease** is observed with vardenafil. **Increase** is observed with molsidomine and Syk inhibitors.

Table 11: Each attractor measures analysed in this Chapter, with its corresponding change in attractor and wave, and its physiological relevance.

Sunitinib

Administration of sunitinib did not affect any of the radial density plot ∆metrics discussed in this Chapter, except ∆rQ25 after the second day of dosing. Interestingly, ∆rQ25 was increased after sunitinib dosing, thus showing the same effects as vardenafil and molsidomine.

Sunitinib induces hypertension, this was indeed detected in Chapter 3; sunitinib caused a large increase in MAP, significantly different from vehicle from the first day. Furthermore, sunitinib is known to increase vessel stiffness in the large artery, and increase the total peripheral resistance due to systemic vasoconstrictions (Catino et al., 2018; Kappers et al., 2012; Thijs et al., 2015). An increased risk of heart failure is reported as well with sunitinib, due to direct cardiotoxicity or indirect effects on the heart (Gupta & Maitland, 2011; Reis Brandão et al., 2022). Given these cardiovascular effects, sunitinib was expected to affect the waveform reflection, and therefore attractor changes, in the opposite way to that observed with the vasodilators. When visually assessing the attractors following sunitinib dosing, some animals indeed displayed a shortening of the red attractor arms (e.g. animal 3 Figure 50), however this was not consistently the case for all sunitinib-treated animals (e.g. animal 1 and animal 2 in Figure 50) and indeed did not result in a consistent increase in rQ25, maxrdenspos or rspread. Moreover, as mentioned above, a decreased resistance and compliance of peripheral vasculature results in a clockwise rotation of attractor (Aston et al., 2018). Subsequently, after sunitinib administration, an anticlockwise rotation of the attractor was expected. Indeed, in some animals (e.g. animal 1 and 2 in Figure 50), this was the case, however attractors from other sunitinib-treated animals did not show this effect. Moreover, at the time of data analysis, SPARKS was not able to detect rotation of the attractor correctly for all generated attractors therefore this effect could not be quantified. Again, this was due to technical limitations of the algorithm at the time and optimisation of analysis is needed to ensure the attractor rotation is accurately computed.

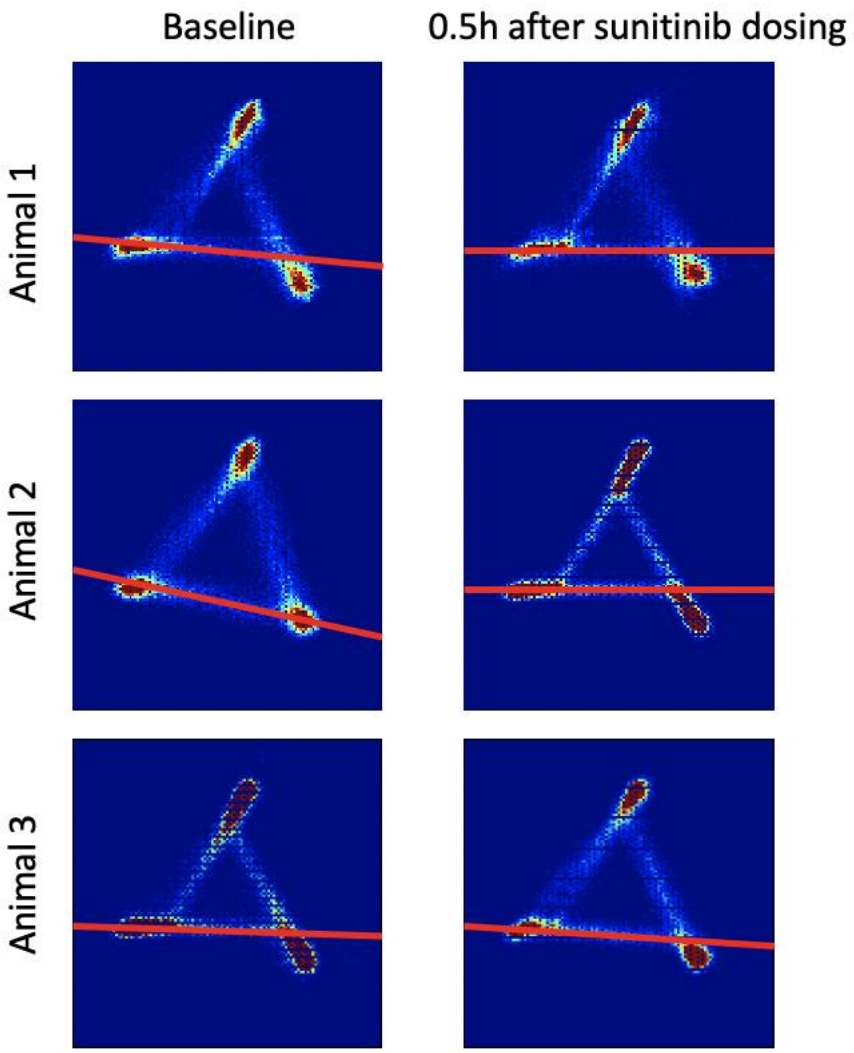

Figure 49: Examples of attractor changes following sunitinib administration. *The baseline attractor, and attractor generated 0.5 h after sunitinib dosing on the first day are shown for three animals. Animal 1 and 2 showed an anticlockwise rotation of the attractor (indicated by the red bar through the base of the triangle). The attractors of animal 3 did not change rotation, but a shortening of the red arms was observed.*

Additionally, changes in the cardiac contraction have previously been linked to changes in the uniformity of density along the edges of the attractor, and variability in the right hand side of the attractor (Aston et al., 2018). However, also these changes were not unambiguously detected or could not be quantified at the moment of data analysis.

In summary, the 3 SPAR metrics used in this Chapter could not clearly detect changes in waveform reflection after sunitinib administration. On the other hand, given that sunitinib caused large and obvious changes in MAP, arguably there was no need for follow-up analysis with SPAR. The aim of applying SPAR in preclinical settings was not to replace the conventional wave analysis parameters, but to provide additional insights where needed, particularly where changes are perhaps more subtle over the longer term. Nonetheless, to understand better why sunitinib did not affect the attractor metrics as anticipated, it would have been useful to repeat this study including another reference compound with a well-understood vasoconstricting action, to see if it would affect the SPAR metric differently than sunitinib.

4.4.3. Effect of Syk inhibitors on blood pressure wave

4.4.3.1. Fostamatinib

Fostamatinib caused an increase in all three radial density plots metric analysed in this Chapter (Figure 47 and Table 10), thus exhibiting the opposing effect on the attractor shape compared to the vasodilators. These observations could potentially indicate a vasoconstriction downstream of the location of pressure wave recording (Table 3), consistent with literature showing that fostamatinib caused an increase in the peripheral vascular conductance and impaired a VEGF-induced vasodilation (M. Skinner et al., 2014) and the wider literature reporting vasoconstrictions with VEGFR2-inhibitors, leading to an increase in peripheral resistance (Carter et al., 2017; Kappers et al., 2012; Zhu et al., 2009). These vasoconstrictor effects were not markedly visible when looking at the waveform alone; some changes in waveform morphology were observed, however these were subtle (Figure 46). Nonetheless, distinct changes in the corresponding attractors were visible, and these changes were consistently reflected in an increase of ΔrQ25, Δmaxrdenspos and Δrspread. These results confirmed once again that SPAR is indeed able to expose subtle changes in waveform morphology and reflects these systematically in its shape.

Additionally, the radial density plot measures detected an alteration in the cardiovascular system earlier than the conventional measures of wave analysis could. Indeed, in Chapter 3, only during the second day, following the second dose administration, MAP reached levels that were significantly different in the fostamatinib group compared to the vehicle group, and HR and PP did not change overall (Chapter 3 section 3.3.4.). In contrast, within the first 24 h after the first dose, SPAR metrics ΔrQ25, Δmaxrdenspos and Δrspread (and rQ25, maxrdenspos and rspread) were significantly different between fostamatinib and vehicle. ICH S7A currently recommends monitoring of MAP and HR following single dose administration of the test compound (International Conference on Harmonisation, 2001). SPAR detected a potential cardiovascular safety liability after this single fostamatinib administration, from 8 h after dosing. In summary, using the same data set, SPAR was able to extract more information from the waveform and detect fostamatinib-induced cardiovascular effects earlier than conventional analysis could.

4.4.3.2. Entospletinib

Lastly, the effect of entospletinib on the SPAR measures was assessed. Entospletinib did not affect dspread3, thus did not affect waveform variability. Importantly, entospletinib caused an increase in ΔrQ25 and Δrspread, that was significant from the first day (Figure 48). Indeed, smaller but similar effects as the ones observed with fostamatinib were found with this second-generation compound. As explained above, the interpretation of rspread is not entirely clear. Nonetheless, the increase in ΔrQ25 and Δrspread indicated some subtle effects on the cardiovascular system. These effects were not detecting using the conventional wave analysis; MAP, HR or PP were not significantly changed during the 48 h of monitoring following entospletinib administration (Chapter 3 section 3.3.5.).

Entospletinib was developed with the purpose of achieving higher Syk inhibition levels, without binding to other, off-target, kinases (Currie et al., 2014). In this way, entospletinib was anticipated to be safer than fostamatinib, as it should not induce VEGFR2-inhibition mediated hypertension (Currie et al., 2014). So far, little cardiovascular adverse drug reactions have been reported in clinical trials (Burke et al., 2018; Danilov et al., 2020; Lam et al., 2021; Morschhauser et al., 2021; J. Sharman et al., 2015). Yet little literature is available that describes the *in vivo* or *ex vivo* effects of entospletinib on vascular compliance or cardiac function.

Entospletinib is currently in development in combination therapy regimes for leukaemias and lymphomas (Borate et al., 2022; N. Cooper et al., 2022; Kittai et al., 2021; Lam et al., 2021; Walker et al., 2020). Patients suffering from these pathologies might already have a compromised cardiovascular system, and additionally, multiple drugs combined in one therapy schedule can affect and exacerbate each other's CV effects. Examples of such treatment schedules are discussed in the general discussion (Chapter 7, section 7.1.). Given these drug combinations, it is important to fully understand the CV effects of a new compound to make informed decisions on the cardiovascular safety of the drug, alone or in combination therapy. SPAR could aid in this, as the method can detect CV effects that MAP, HR and PP cannot.

4.4.4. Chapter conclusion

The aim of this Chapter was to validate SPAR for use in radiotelemetric studies in rat, and to explore whether SPAR could provide insights into the cardiovascular effects of Syk inhibitors that were not captured by conventional waveform analysis in Chapter 3.

This Chapter showed that SPAR could indeed detect changes in waveform variability and waveform morphology, likely relating to the diastolic downstroke and notch position and thus indicating an augmentation or attenuation of reflected waves. SPAR metrics rQ25 and maxrdenspos were found most suitable to quantify the changes observed in this study. SPAR detected fostamatinib-induced changes in the cardiovascular system earlier than MAP, HR or PP could; from the first day, the Δmetrics were different from vehicle, while MAP was only significantly different from day 2 (Chapter 3) and HR or PP were not affected. When animals are only monitored after single dose administration, SPAR could detect safety issues in more sensitive way than MAP. Furthermore, SPAR detected entospletinib-induced changes in the blood pressure wave as well, even though this compound didn't affect any of the conventional wave measures. Overall, the results in this Chapter indicated that:

- SPAR is a suitable method to monitor waveform variability and waveform morphology changes in blood pressure data recorded with radiotelemetry in rats.
- SPAR metrics ΔrQ25 and Δmaxrdenspos were able to indicate the vasodilating actions of vardenafil and molsidomine, and conversely, suggested a vasoconstriction following fostamatinib and entospletinib treatment.
- SPAR detected changes in cardiovascular system earlier than MAP, HR or PP could for fostamatinib-treated animals.
- SPAR detected entospletinib-induced cardiovascular effects that went unnoticed when looking at MAP, HR or PP alone.

In conclusion, SPAR could potentially contribute to a more nuanced understanding of cardiovascular liabilities and help to mitigate risk in distinct patient populations (e.g. in combination with other oncology therapies). Employing in-depth waveform analysis in preclinical settings could help in making informed decision about the cardiovascular safety profile of new drugs.

4.4.5. Future directions

More validation of SPAR is needed to confirm the findings in this Chapter. Firstly, improved detection of all SPAR metrics of the attractors (e.g. attractor rotation and rcentspread, measuring the length of the attractor arms) would allow more complete application of the method. Secondly, to enhance the understanding of the link between each metric and what it represents in wave changes, it would be helpful to get insights from *in silico* data. This approach has been successfully applied so far for a couple of other SPAR metrics (Aston et al., 2018), but not for the ones used in this Chapter. For example, using *in silico* generated waves could give insights into how changes in rspread are related to waveform morphology changes. Moreover, to further validate the method, the effects on attractor metrics of more compounds need to be tested. It would also be informative to further explore sensitivity limits of both SPAR metrics and MAP (for example by assessing the effects of different concentrations of the same compound). Another useful study would be to assess the effect of two compounds that show similar MAP and HR profiles, but obtain these through different mechanism (e.g., a direct effect on the heart versus a reflex tachycardia). Lastly, applying deep learning on the attractor images themselves would be helpful, as not all features visualised by human eye are exactly computed by the metrics available at the moment. Together, these studies could further illustrate the advantages of SPAR beyond MAP, in detecting cardiovascular changes more sensitive, or by providing additional insights into mechanistic causes of cardiovascular effects.

Little literature was available on distinct *ex vivo* or *in vivo* effects of Syk inhibitors on regional vascular beds. From the data in this Chapter, it was suggested that entospletinib caused subtle but significant effects on the CV system, similar to those observed with fostamatinib. To add to the comprehensive assessment of the cardiovascular safety profile of fostamatinib and entospletinib, these compounds were interrogated in the Doppler flowmetry model in the next Chapter (Chapter 5).

5. RESULTS CHAPTER 5: DOPPLER FLOWMETRY AND SPAR TO ASSESS THE CARDIOVASCULAR EFFECTS OF SYK INHIBITORS

5.1. Chapter introduction

As described in Chapter 1, section 1.5.4., the contraction of the heart generates a pulsatile flow of blood in the arteries (Masuda et al., 2013; Mynard et al., 2020). Each cardiac beat results in an increase of blood flow (Masuda et al., 2013; Mynard et al., 2020). Moreover, the profile of the blood flow wave is affected by wave reflection; a reflected blood flow wave attenuates the forward wave (section 1.5.4. Figure 9) (Masuda et al., 2013; Trihan et al., 2023). The mean blood flow velocity in an artery is affected as well by the state of its downstream vascular bed (W. W. . Nichols et al., 2022). A vasoconstriction attenuates the mean blood flow velocity (decrease in vascular conductance (VC), the ease with which the blood flows through a vascular bed), while a vasodilation increases the blood flow to the vascular bed (increase in VC) (W. W. . Nichols et al., 2022).

It has previously been shown that the increase in MAP induced by VEGFR2-inhibitors, is associated with regionally selective vasoconstrictions in rats (Carter et al., 2017). The most pronounced vasoconstriction was observed in the hindquarters vascular bed (measured in the abdominal aorta), suggested to be the main vascular bed involved in the VEGFR2-inhibition related hypertension (Carter et al., 2017). Some RTKIs induced mesenteric and renal vasoconstrictions as well, but these effects differed between RTKIs, likely depending on the selectivity and potency of VEGFR2-inhibition (Carter et al., 2017). Similarly, Kappers *et al.* (2012) demonstrated that sunitinib caused a regionally selective vasoconstriction in swine, affecting the systemic, but not coronary or pulmonary haemodynamic profiles (Kappers et al., 2012).

Skinner *et al.* showed that fostamatinib decreased the arterial blood flow and VC in the femoral artery in anaesthetised rats, indicating an increase in peripheral vascular resistance (M. Skinner et al., 2014). Furthermore, fostamatinib impaired a VEGF-induced vasorelaxation. Nonetheless this compound did not display constriction of isolated human cutaneous vessels or isolated femoral rat arteries (M. Skinner et al., 2014). Additionally, similar as sunitinib in swine, the fostamatinib metabolite R406 did not affect the coronary blood flow in rats (M. Skinner et al., 2014).

Entospletinib has been reported to interfere with platelet activation (Series et al., 2020; T. J. Zheng et al., 2021) and Syk inhibition has been proposed as an approach to inhibit progression of atherosclerosis and other related inflammatory cardiovascular pathologies (Li et al., 2023). Nonetheless, no literature is available on how entospletinib affects blood flow in vascular beds, either *ex vivo* or *in vivo*. As described in Chapter 4, entospletinib caused subtle but significant changes in SPAR metrics of the BP (section 4.3.5.5.). When present for a long time, subtle changes in the cardiovascular system might lead to an increased risk for severe cardiovascular events, therefore adequate detection and management of such safety liabilities is required (Curigliano et al., 2010; Vallerio et al., 2022; Wu et al., 2008).

To further investigate the risk of cardiovascular adverse drug effect of Syk inhibitors beyond BP alone, their effects on three vascular beds in conscious rats was characterised in this Chapter. The pulsed Doppler flowmetry model has previously been proven to be a translational, powerful and sensitive approach to determine drug-induced changes in distinct vascular beds (Carter et al., 2017; S. L. Cooper et al., 2020, 2022; Wragg et al., 2022). Using this model, this Chapter determined the effects of fostamatinib and entospletinib on renal, mesenteric and aortic blood flow velocity. The signals obtained during these experiments were first analysed using the conventional VC analysis to answer the following questions:

1. How do fostamatinib and entospletinib affect the VC of these three vascular beds?
2. By comparison to sunitinib, do the Syk inhibitors display similar regional haemodynamic effects as reported with VEGFR2 inhibitors?

Next, blood flow and BP waves were analysis with SPAR, to:

1. Explore the application of this method on the signals recorded in the Doppler flowmetry model, and
2. Determine if SPAR could provide any insights into the safety of fostamatinib and entospletinib, that were not apparent from the conventional VC analysis.

5.2. Chapter methodology

5.2.1. Doppler flowmetry set-up

To monitor the effects of the Syk inhibitors on the blood flow in three vascular beds, the pulsed Doppler flowmetry model was used. As detailed in Chapter 2 (section 2.2.1.1.), this model uses a BP catheter and three implanted miniature ultrasonic Doppler probes, allowing for the recording of arterial BP and Doppler shift; the latter provides an index of blood flow velocity. In this thesis, the blood flow velocity waves to the following vascular beds were recorded: the renal, mesenteric and hindquarters bed. The latter is referred to as the aortic flow throughout the thesis. Subsequently, multiple cardiovascular parameters were calculated: VC in the vascular beds downstream of each Doppler probe and MAP and HR. How these parameters were derived is described in Chapter 2, section 2.2.1.3. The use of small pulsed Doppler probes offers several advantages over other blood flow measurement techniques that use larger probes, are harder to calibrate and less fit for use at the small rat arteries of interest (Haywood et al., 1981). Furthermore, the Doppler model utilises IV lines for drug administration, therefore animals are not disturbed during the recording of the haemodynamic parameters.

5.2.2. Animals and surgeries

The details of the two surgeries to implant vascular probes, pressure catheter and IV lines are described in Chapter 2, section 2.2.3.2. In brief, during the first surgery, three in-house produced Doppler probes were implanted around the left renal artery, superior mesenteric artery and descending abdominal aorta (referred to as aortic below) of adult Male Sprague-Dawley (350 – 450 g). The second surgery, carried out a minimum 10 days after the first, and following welfare sign-off from the Named Veterinary Surgeon, involved the implantation of the fluid-filled BP catheter in the distal abdominal aorta and three IV catheter lines in the right jugular vein. Following the second surgery, animals were moved to their cage for experimentation. Probe wires and catheters were tunnelled through a protective metal spring fixed to a harness that was worn by the rat around the torso. This allowed for the animals to move around freely for the duration of the experiment. Animals were given approximately 24 h for recovery before the commencement of the experiments.

5.2.3. Experimental protocol

In total, three compounds were tested, alongside the appropriate vehicles. Firstly, the effects of sunitinib (16 mg/kg) were assessed in the Doppler model. This study was carried out by Dr. Edward Wragg. Secondly, fostamatinib was tested. As drugs were dosed IV in this study, R406 (2.5 mg/kg) was administered, to ensure the presence of the active compound in the plasma, rather than the pro-drug. Lastly, the haemodynamic effects of entospletinib (0.4 mg/kg) were investigated. All drugs were dissolved in their appropriate vehicle (detailed below) and administered IV via the inserted lines in the jugular vein. Each drug was dosed as a bolus (0.2 mL), containing half of the daily dose, followed by an infusion (0.4 mL) over 1 h, containing the second half of the daily dose. An overview of the study protocol is presented in Figure 51. Animals were dosed for three consecutive days.

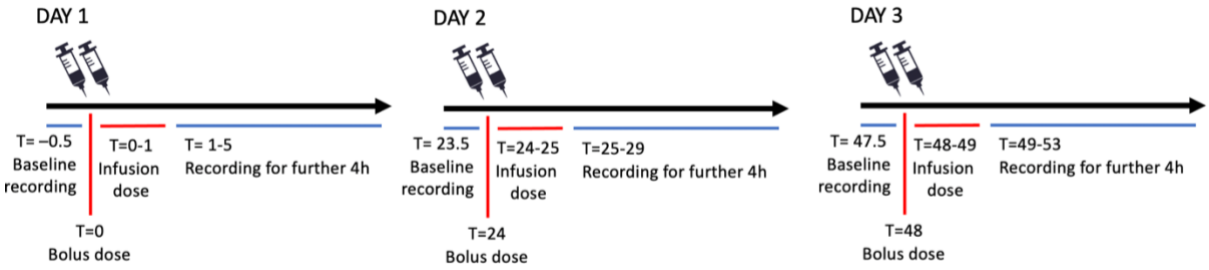

Figure 50: Doppler study protocol. *Cardiovascular recordings were performed at least 30 min before dosing on the first day. At T=0, animals were dosed with a bolus, containing half of the daily dose, immediately followed by a 1h-infusion, containing the other half of the daily dose. Cardiovascular recordings continued for a further 4h after the completion of the infusion (at T=1). The same protocol was followed on the second and third day.*

5.2.3.1. Sunitinib

This study was carried out by Dr. Edward Wragg (experimentation and conventional analysis of MAP, HR and VC). Subsequent SPAR analysis was done by Marieke Van Daele. These historical data were included here as sunitinib is a compound known to cause hypertension due to VEGFR2-inhibition (Davis et al., 2011; Neves et al., 2020). Sunitinib was dosed at 16 mg/kg/day. This dose was chosen following a pilot study assessing the effect of 4, 8 and 16 mg/kg/day sunitinib. Unlike the lower two doses, 16 mg/kg/day caused sustained hypertension over the 3 days of experimentation, displaying the typical response observed with VEGFR2-TKIs. Once daily, sunitinib was administered as 8 mg/kg in 0.2 mL bolus, immediately followed by 8 mg/kg in 0.4 mL infusion (at a rate of 0.4 mL/h). The vehicle used for these experiments was 5% propylene glycol, 2% Tween 80 in sterile saline.

5.2.3.2. Fostamatinib (R406)

As fostamatinib is rapidly metabolised to the active compound R406 in the intestines (Connell & Berliner, 2019; Mócsai et al., 2010), here R406 was used to dose IV. R406 was dosed at 2.5 mg/kg/day, as 1.25 mg/kg in in 0.2 mL bolus, immediately followed by 1.25 mg/kg in 0.4 mL infusion (at a rate of 0.4 mL/h). This dose was selected to reflect plasma concentrations in patients treated with fostamatinib (Lengel et al., 2015; M. Skinner et al., 2014). The vehicle used for these experiments was 5% ethanol, 20% PEG400 in water. Before dosing, the pH of the drug solution was checked to ensure the pH was not too acidic or alkaline for administration. If needed, the pH was adjusted to neutral (pH 6 – 8) using 1 M HCl or 1 M NaOH.

5.2.3.3. Entospletinib

Entospletinib was dosed at 0.4 mg/kg/day, as 0.2 mg/kg in in 0.2 mL bolus, immediately followed by 0.2 mg/kg in 0.4 mL infusion (at a rate of 0.4 mL/h). This dose was selected to reflect estimated plasma concentrations in patients treated with this drug (Currie et al., 2014). The vehicle used for these experiments was 5% ethanol, 20% PEG400 in water. Before dosing, the pH of the drug solution was checked to ensure administration of a neutral solution.

5.2.4. Conventional analysis: MAP, HR and VC

Full details on data-analysis in IdeeQ can be found in Chapter 2, section 2.2.5.1. Summarised, HR, BP and renal, mesenteric, and aortic Doppler shifts were recorded using the bespoke IdeeQ software. The time-averages of MAP, HR and VCs were calculated within IdeeQ. The equations used for this analysis are given in Chapter 2, section 2.2.1.3. Areas for analysis were taken at baseline, followed by one at half an hour and at one hour after bolus dosing, and at every hour afterwards. Data are presented as change from baseline recording on day 1 to account for intra-animal variability.

5.2.5. SPAR analysis

5.2.5.1. Data extraction

For in-depth analysis of the recorded waveforms, BP data and Doppler shift data were extracted directly from IdeeQ, imported into Notepad and saved as .txt files. From each area selected to perform conventional analysis (as described above in section 5.2.4.), a 1-minute window of raw waveform data was extracted in the same time window to analyse in SPARKS.

5.2.5.2. Method optimisation for blood flow waves and protocol for SPAR analysis

The telemetry studies (Chapter 3) and Doppler studies (this Chapter) were both performed in rats and recordings were conducted at 500 Hz in both instances. Therefore, the standard protocol developed for SPAR analysis of telemetry data (Chapter 4, section 4.2.2.3) was utilised here as well. Use of one minute of raw waveform data was sufficient to generate a robust and reliable attractor (Chapter 4, section 4.3.1.3.), so this was kept consistent here. The 'HumanBP' pre-set of parameters was used, with adjusted HR (230 and 550) and nbins_density of 125 for quantitative analysis. Full details on how this protocol was obtained can be found in Chapter 4, section 4.3.1.

In brief, the following protocol was applied:

1. One minute of raw wave numbers were extracted from IdeeQ into Notepad. Per animal, per day, per drug treatment, per signal, one window was extracted during the baseline recording, followed by one window at half an hour and at one hour after bolus dosing, and at every hour afterwards.
2. The only pre-processing of data that was performed, was removal of obvious outliers, for example where catheters were blocked or Doppler probes disconnected. This happened only sporadically, for example when the lines in and around the flexible metal spring needed untangling.
3. For each individual 1-minute window, the sequence of BP/Doppler shift values was saved as a .txt file.
4. These .txt files were then loaded into the SPARKS app.
5. For SPAR analysis, the pre-set of parameters of HumanBP was used, with adjusted nbins_density and HR limits. For quantitative analysis of the attractors, an nbins_density of 250 was used. For qualitative, visual analysis and presentation of the attractors, an nbins_density of 125 was used. HR limits were adjusted to maximum 550 and minimum 230.
6. Next, the attractors were generated in the SPARKS app. One attractor was generated per 1 min window. Additionally, from each attractor 49 metrics were taken, to enable quantification of attractor changes.
7. For further quantitative analysis, the attractor metrics of interest were imported into Prism 9.5.1 (GraphPad Software).

A qualitative analysis was carried out to identify any visual changes in attractors after drug administration. Next, ROC AUCs were used to select SPAR metrics that were suitable for quantifying attractor changes.

5.2.6. Statistics

All data were expressed as mean ± SEM. Statistical analysis was performed in Prism 9.5.1 (GraphPad Software, San Diego, CA, USA). As there were two categorical, independent variables (time and treatment) and one quantitative outcome variable (MAP, HR, VC or SPAR metric), a two-way ANOVA test was performed. This tested (1) if the outcome variable was significantly different over time, (2) if the outcome variable was significantly different between groups, and (3) if the outcome variable was significantly different between groups over time. If the result of the two-way ANOVA were significant, multiple comparisons test were performed; a Dunnett test to determine where changes within a group from baseline were significant and a Sídák test to determine where changes between groups were significant. Results were considered significant at $p < 0.05$.

Outliers were detected using the ROUT method. This method first fits the data to a model using a robust method that is impacted little by outliers. Next, outliers are identified based on the false discovery rate, to determine which points are far enough from the model prediction to be considered outliers.

5.3. Chapter results

5.3.1. Conventional analysis: MAP, HR and VC

5.3.1.1. Sunitinib

Administration of sunitinib (16 mg/kg/day) resulted in a decrease in HR and an increase in BP (Figure 52). From the first day, HR was significantly decreased in the sunitinib group, compared to vehicle (two-way ANOVA, $p<0.05$ and follow-up Sídák test $p<0.05$). This effect was sustained during the day, and enlarged over the three days of experimentation, with the maximum effect reached on day 3, 1h after bolus dosing. No significant differences in HR were observed within each group from baseline (two-way ANOVA, $p>0.05$). Sunitinib increased MAP from 4h after bolus dosing of the first day. From the second day, this effect was significantly different from baseline within the group (Dunnett-test $p<0.05$). Although MAP increased from baseline in the vehicle-treated group as well (maximum effect observed 1h after bolus dosing on day 3, Dunnett-test $p<0.05$), sunitinib still caused an increase in MAP that was significantly different from vehicle over the three days of experimentation (two-way ANOVA, $p<0.05$).

It was clear the sunitinib caused a vasoconstriction in all three vascular beds assessed (Figure 52). Sunitinib evoked a decrease in the renal VC, compared to vehicle. Although no individual time point was significantly different between the groups (Sídák test, $p>0.05$), overall % renal VC was significantly smaller in the sunitinib group (two-way ANOVA, $p<0.05$). This effect was most apparent on the third day. No significant differences were observed within each group from baseline (two-way ANOVA, $p>0.05$). Secondly, mesenteric VC was incrementally decreased by sunitinib. From the second day, % mesenteric VC was significantly different from baseline in the sunitinib treated group (Dunnett-test, $p<0.05$). No significant changes were obtained within the vehicle group (Dunnett-test, $p>0.05$). Overall, a significant decrease in % mesenteric VC was observed in the sunitinib group, compared to vehicle (two-way ANOVA, $p<0.05$). Lastly, a similar profile was seen in the abdominal aortic VC; from the first day, 4h after bolus dosing, sunitinib caused a reduction of % aortic VC (Dunnett-test, $p<0.05$), while no significant changes were observed within the vehicle group (Dunnett-test, $p>0.05$). Overall, sunitinib caused a significant decrease of % aortic VC compared to vehicle (two-way ANOVA, $p<0.05$), with the effect of sunitinib enlarging every day (individual time points being significantly different from vehicle on day 3, Sídák test, $p<0.05$). All baseline parameters are shown in Table 12.

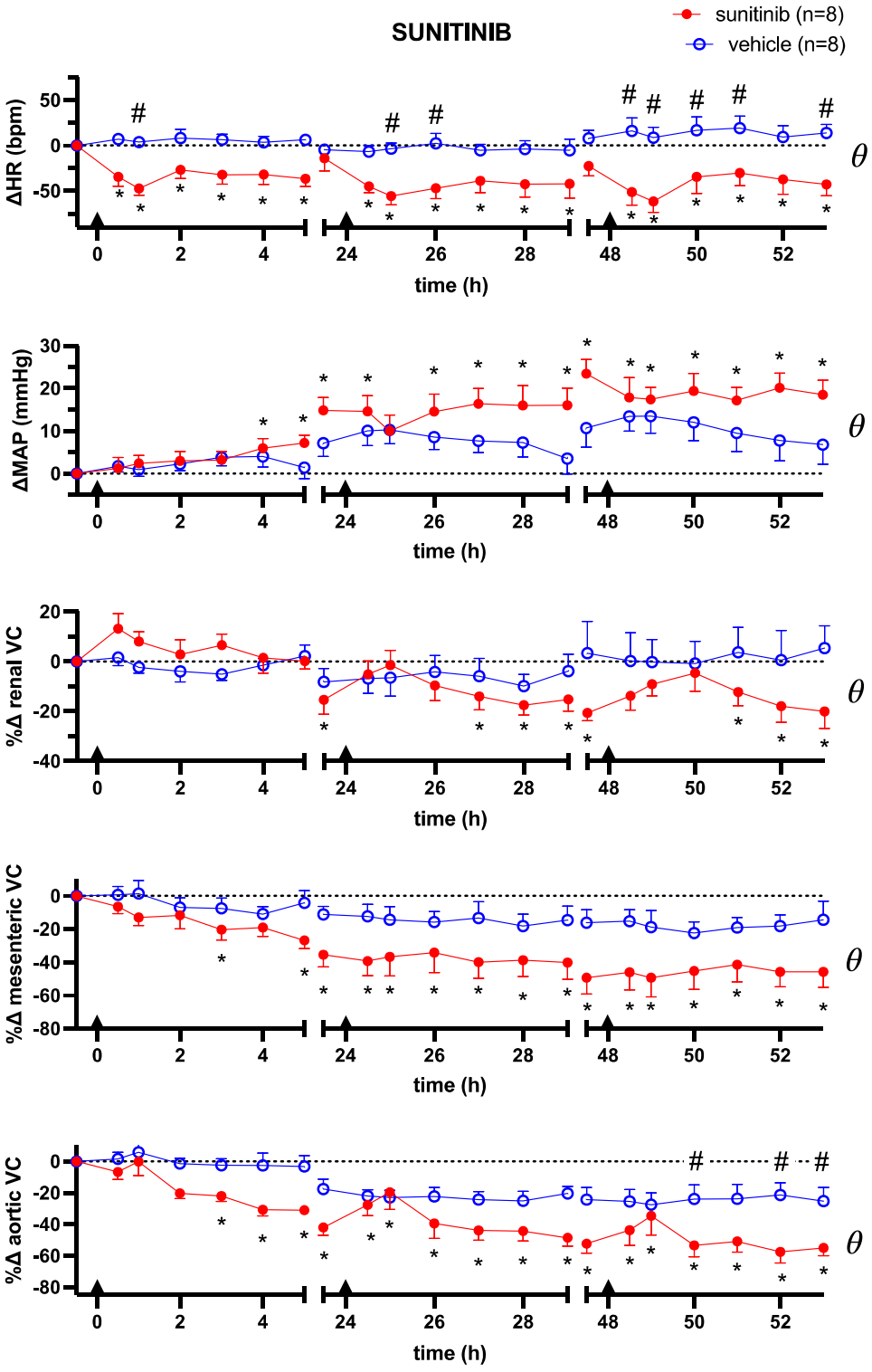

Figure 51: Cardiovascular effects of sunitinib. *Changes in ΔHR, ΔMAP and %ΔVC (renal, mesenteric and aortic) of rats dosed with sunitinib 16 mg/kg IV (n=8, red, filled circles) and vehicle IV (n=8, blue, open circles). Data were normalised to baseline recording of day 1 for each animal individually. Black triangles on time-axis indicate time of drug administration. Data are presented as mean ± SEM. A two-way ANOVA test was conducted to test for overall differences between two groups (θ = p<0.05), followed by multiple comparison by Sídák to test for differences between the groups at each time point (# = p<0.05) Furthermore, to test for significant changes over time within a group, each timepoint of the group was compared to the group's corresponding baseline (T=-0.5h), by Friedmann performed on the raw, non-normalised data (* = p<0.05).*

***Table 12: Overview of cardiovascular parameters before drug or vehicle administration**, corresponding to t=-0.5h. Values are presented as mean ± SEM. Abbreviations: U, units; VC, vascular conductance. Units (U) of VC are kHz.mmHg^{-1}.10^{3}.*

Parameter at t=-0.5h (mean ± SEM)	Sunitinib	Vehicle	R406	Vehicle	Entospletinib	Vehicle
MAP (mmHg)	100 ± 3	106 ± 4	108 ± 3	102 ± 1	100 ± 3	102 ± 1
HR (bpm)	342 ± 11	340 ± 8	341 ± 16	347 ± 8	339 ± 10	347 ± 8
RVC (U)	105 ± 6	96 ± 6	84 ± 13	61 ± 6	91 ± 15	61 ± 6
MVC (U)	100 ± 7	72 ± 9	52 ± 9	62 ± 13	83 ± 15	62 ± 13
AVC (U)	41 ± 5	45 ± 6	24 ± 8	30 ± 2	46 ± 8	30 ± 2

5.3.1.2. R406

Treatment with R406 (2.5 mg/kg/day), the active metabolite of fostamatinib, resulted in no significant changes in HR or MAP, when compared within the group to baseline and when compared to the vehicle group (Figure 53, two-way ANOVA, $p>0.05$). An upwards trend was seen in MAP over three days of R406 administration, however a similar observation was made in the vehicle group, and these were not significantly different.

Importantly, one animal was, as described below, identified as an outlier in the mesenteric signal of the R406-treated group and these data were excluded in figures and statistical analysis. In Figure 54A, the individual mesenteric traces of all six animals are shown. Animal 6 showed an abnormal increase in % mesenteric VC (note: the y-axis was adjusted to 120%) compared to the other animals (maximum increase in %MVC of 34.55%). To objectively identify any outliers, the ROUT method was used. Indeed, this test reported 10 data points of animal 6 to be outliers in the R406-treated group. The timepoints considered outliers are shown in the table in Figure 54B. These data were excluded when plotting the graphs and performing the statistical analysis.

R406 caused a decrease of the renal VC (Figure 53). Although no individual time points were different between the two treatment groups (Sídák test, $p>0.05$), overall R406 displayed a reduction in % renal VC compared to vehicle (two-way ANOVA, $p<0.05$). No changes from baseline were significant in either of the groups (two-way ANOVA, $p>0.05$). The mesenteric VC was not affected by R406, compared to vehicle or within the group from baseline (two-way ANOVA, $p>0.05$). The aortic VC was not significantly different between the two treatment groups (two-way ANOVA, $p>0.05$). A downwards trend in % aortic VC was observed over the three days of R406 treatment, reaching significance after the 1h bolus dosing on the last day (within group from baseline; Dunnett test, $p<0.05$). All baseline parameters are shown in Table 12.

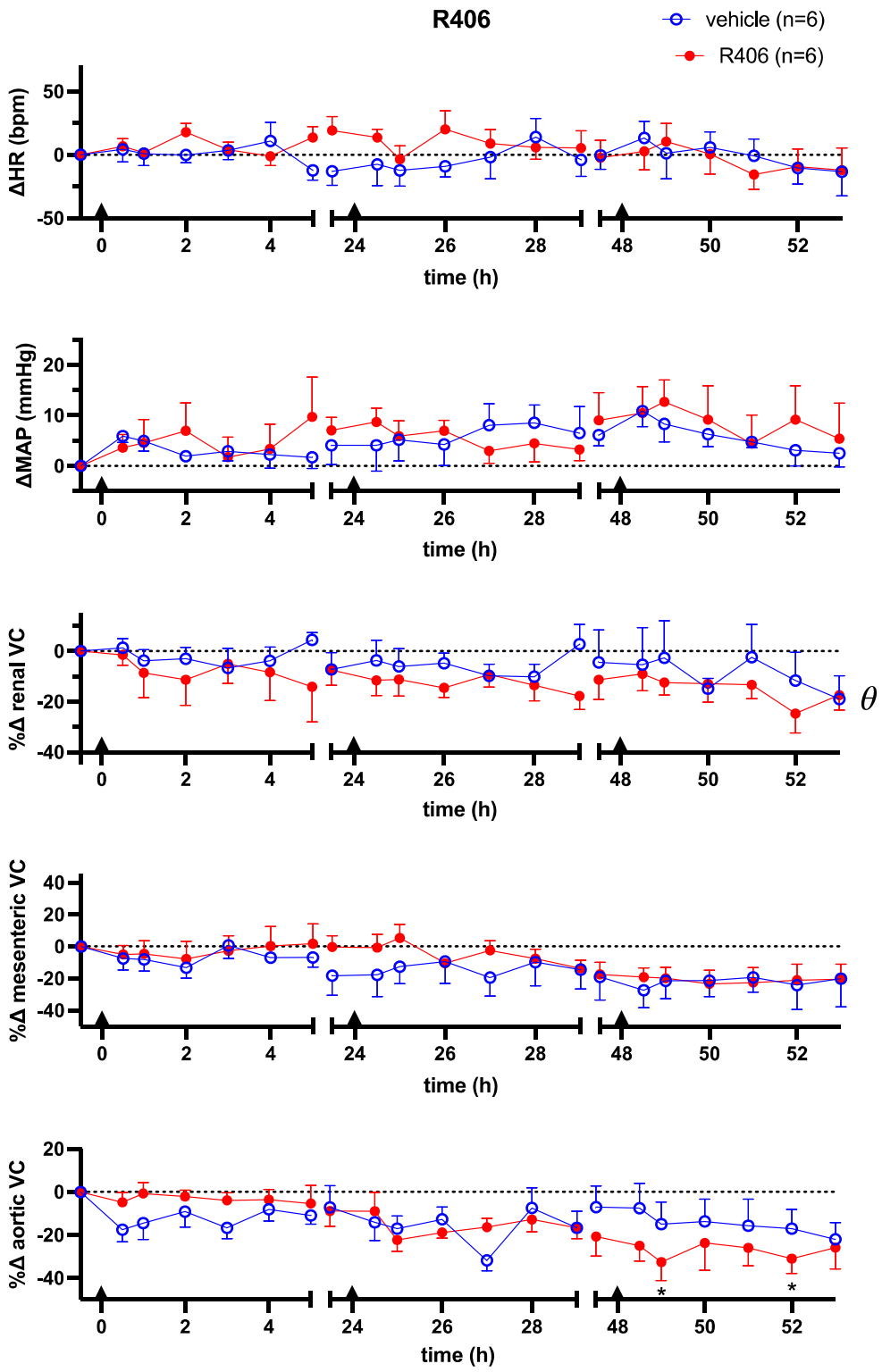

Figure 52: Cardiovascular effects of R406. *Changes in ΔHR, ΔMAP and %ΔVC (renal, mesenteric and aortic) of rats dosed with R406 2.5 mg/kg IV (n=6, red, filled circles) and vehicle IV (n=6, blue, open circles). Data were normalised to baseline recording of day 1 for each animal individually. Black triangles on time-axis indicate time of drug administration. Data are presented as mean ± SEM. A two-way ANOVA test was conducted to test for overall differences between two groups (θ = p<0.05), followed by multiple comparison by Sídák to test for differences between the groups at each time point (# = p<0.05) Furthermore, to test for significant changes over time within a group, each timepoint of the group was compared to the group's corresponding baseline (T=-0.5h), by Friedmann performed on the raw, non-normalised data (* = p<0.05).*

A

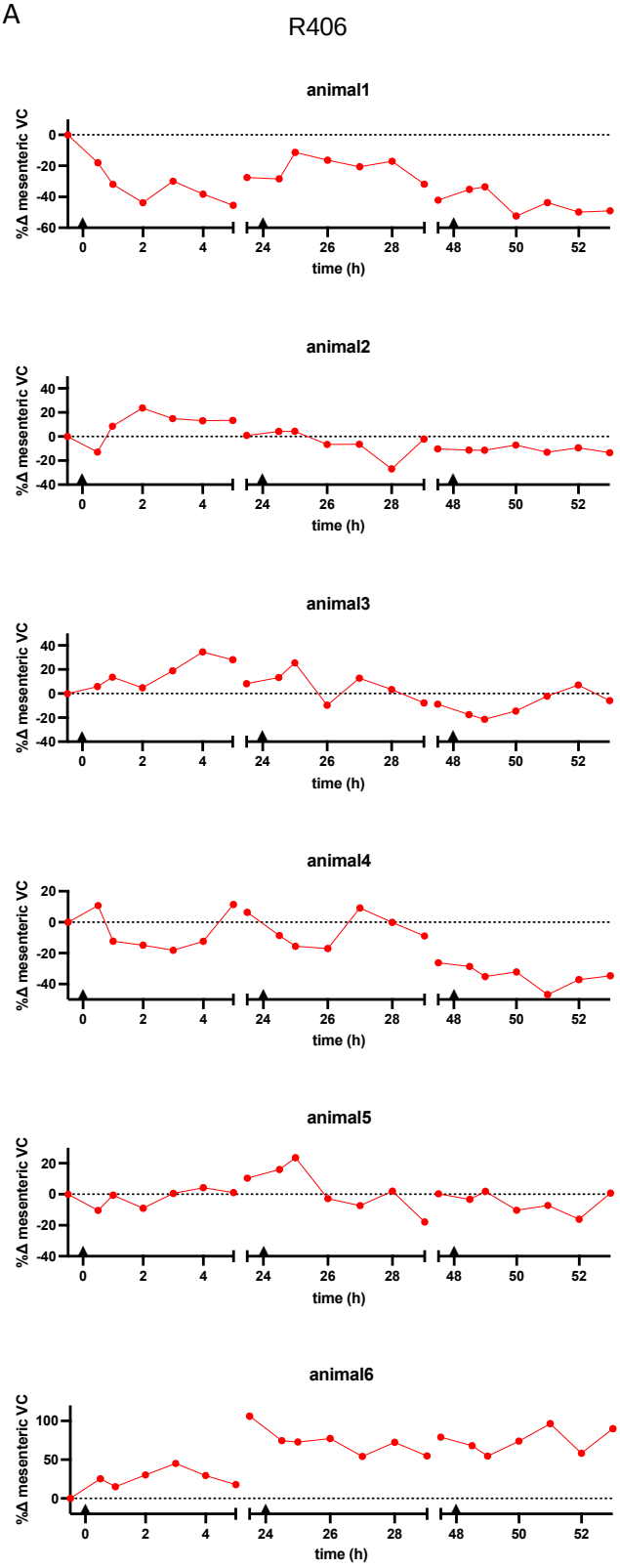

B

Animal nr	Timepoint (h)	%ΔMVC	Mean %ΔMVC
6	23.5	106.27	17.45
6	24.5	74.67	11.86
6	25	72.8	16.57
6	26	77.33	4.14
6	28	72.54	5.65
6	47.5	79.21	-1.34
6	48.5	68.09	-4.64
6	50	73.97	-7.13
6	51	96.66	-2.74
6	53	90.05	-2.04

Figure 53: Identification of outliers in the mesenteric conductances in the R406-treated group. (A) *%Δ mesenteric VC was plotted for each animal individually to identify the general trend of the signal. All animals showed a stable or downwards trend in %Δ mesenteric VC, except for animal 6, that showed an increase in mesenteric VC of up to 100%.* ***(B)*** *Table of outliers in this group, identified by the ROUT method. The table shows the animal number (in all cases, 6), timepoint and %Δ mesenteric VC value of data points considered outliers, combined with the mean of %Δ mesenteric VC of the group at that timepoint, for reference. These outliers were potentially caused by an incorrect adjustment of the probe frequency at the start of day 2.*

5.3.1.3. Entospletinib

Entospletinib (0.4 mg/kg/day) affected HR and MAP in the opposite way to that observed with sunitinib (Figure 55). Firstly, a significant increase in HR was observed between entospletinib and vehicle (two-way ANOVA, $p<0.05$), with the biggest effect seen on the third day. Within the groups, there were no significant changes from baseline HR. MAP was significantly lower in the entospletinib-treated group, compared to the vehicle-treated group (two-way ANOVA, $p<0.05$). Again, no changes over time within either group were present. Entospletinib did not affect the renal, mesenteric or aortic VC significantly within the group or between treatment groups (Figure 55, two-way ANOVA, $p>0.05$ in all cases).

Similar to the data obtained with R406 for the mesenteric signal, one animal was identified as an outlier in the entospletinib-treated group and these data were excluded in figures and statistical analysis. Figure 56A shows the individual mesenteric traces of all six animals. Animal 5 showed an abnormal increase in % mesenteric VC (note: the y-axis was adjusted to 150%) compared to the other animals (maximum increase in %MVC of 25.85%). To objectively identify any outliers, the ROUT method was used. Indeed, this test reported 11 data points of animal 5 to be outliers in the entospletinib-treated group. The timepoints considered outliers are presented in the table in Figure 56B. These data were excluded when plotting the graphs and performing the statistical analysis. All baseline parameters are shown in Table 12.

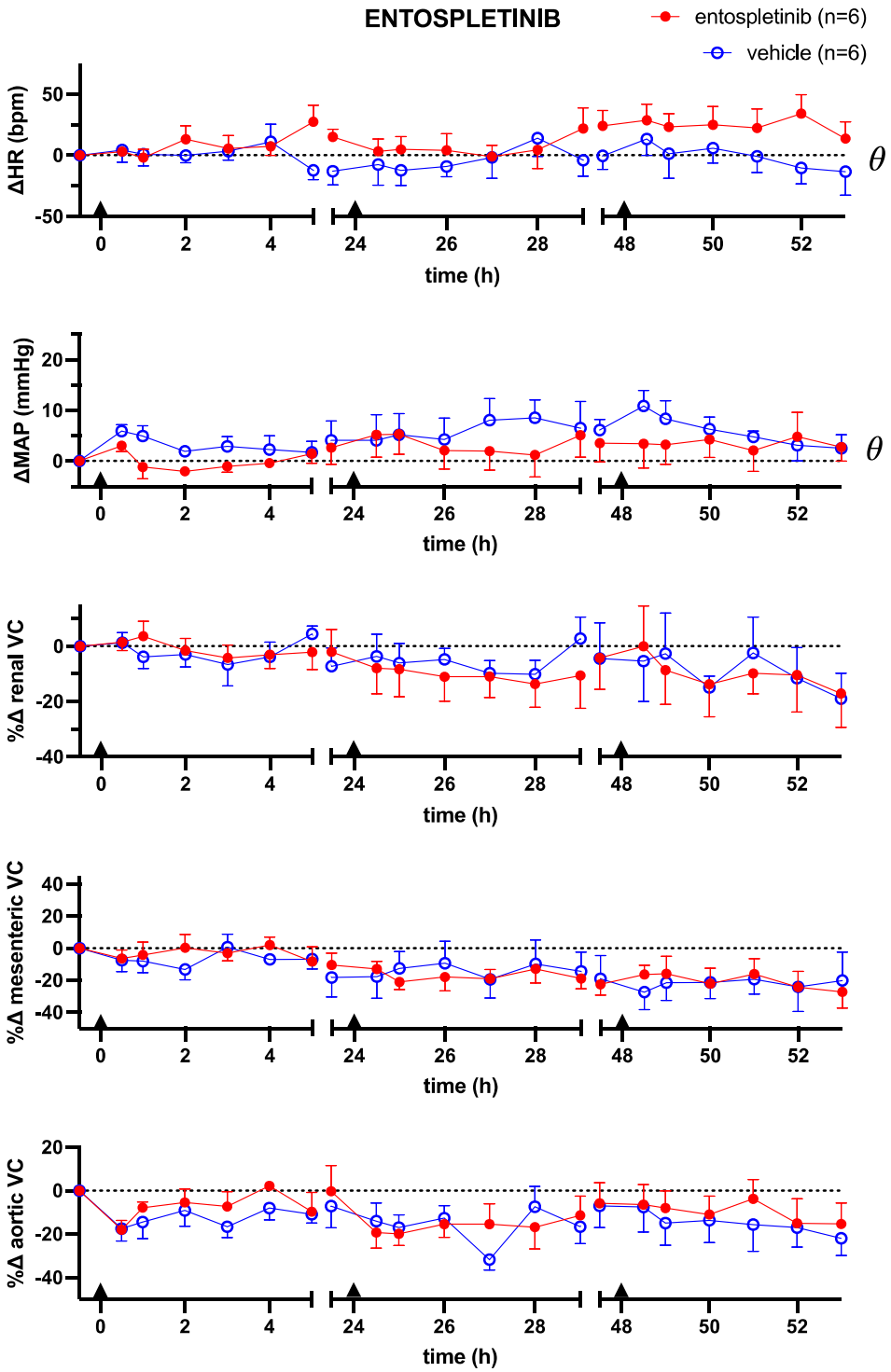

Figure 54: Cardiovascular effects of entospletinib. *Changes in ΔHR, ΔMAP and %ΔVC (renal, mesenteric and aortic) of rats dosed with entospletinib 0.4 mg/kg IV (n=6, red, filled circles) and vehicle IV (n=6, blue, open circles). Data were normalised to baseline recording of day 1 for each animal individually. Black triangles on time-axis indicate time of drug administration. Data are presented as mean ± SEM. A two-way ANOVA test was conducted to test for overall differences between two groups (θ = p<0.05), followed by multiple comparison by Sídák to test for differences between the groups at each time point (# = p<0.05). Furthermore, to test for significant changes over time within a group, each timepoint of the group was compared to the group's corresponding baseline (T=-0.5h), by Friedmann performed on the raw, non-normalised data (* = p<0.05).*

A

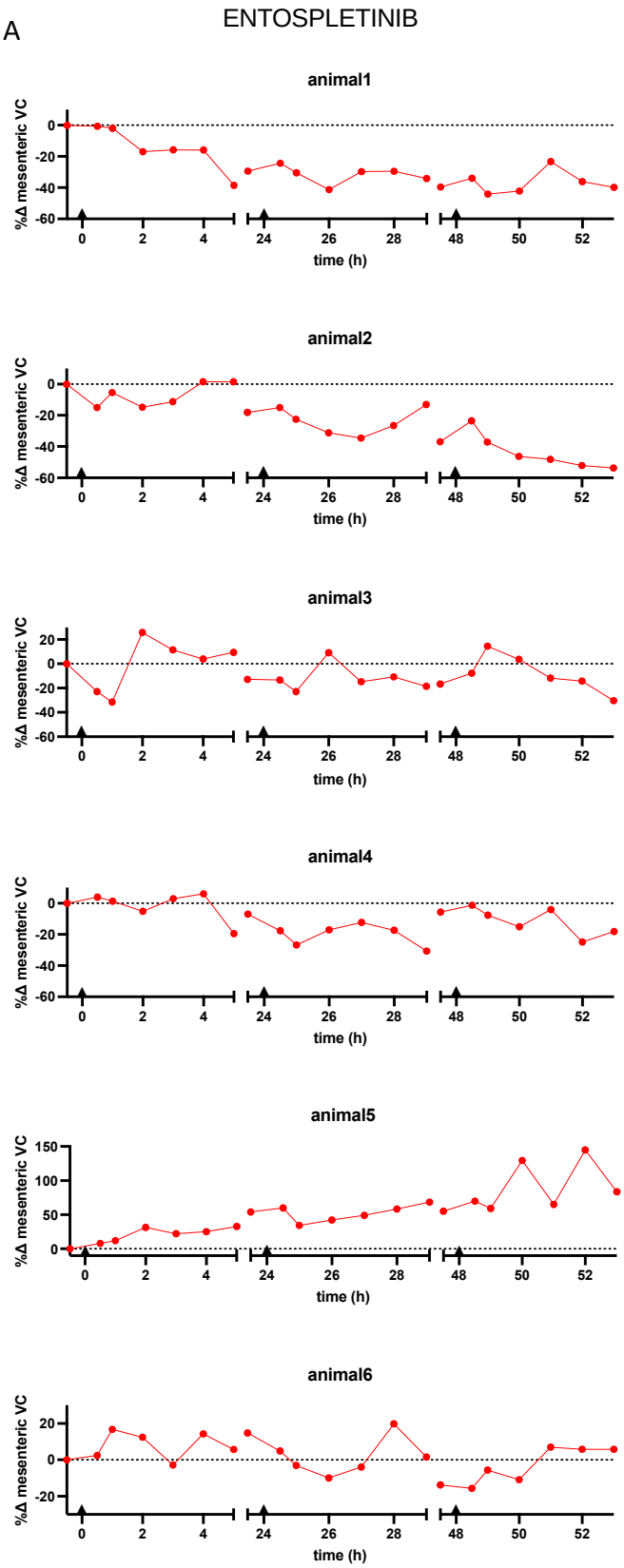

B

Animal nr	Timepoint (h)	%ΔMVC	Mean %ΔMVC
5	23.5	54.03	0.27
5	24.5	59.97	-0.90
5	28	58.26	-1.01
5	29	68.47	-4.42
5	47.5	55.13	-9.59
5	48.5	69.83	-2.05
5	49	59.17	-3.48
5	50	129.54	3.16
5	51	65.17	-2.54
5	52	144.84	3.90
5	53	83.58	-8.77

Figure 55: Identification of outliers in the mesenteric conductances in the entospletinib-treated group. (A) *%Δ mesenteric VC was plotted for each animal individually to identify the general trend of the signal. All animals showed a stable or downwards trend in %Δ mesenteric VC, except for animal 5, that showed an increase in mesenteric VC of up to 140%.* ***(B)*** *Table of outliers in this group, identified by the ROUT method. The table shows the animal number (in all cases, 5), timepoint and %Δ mesenteric VC value of data points considered outliers, combined with the mean of %Δ mesenteric VC of the group at that timepoint, for reference. These outliers were potentially caused by malfunctioning of the probe, given the large differences in VC observed over day 3.*

5.3.1.4. Summary of conventional analysis results

A summary of the results obtained with the conventional analysis is shown in Table 13. Sunitinib caused a significant decrease in HR and increase in MAP. All three VC were attenuated following sunitinib administration. R406 did not affect HR, MAP or the % mesenteric VC, however showed small decreases in the renal and aortic flow velocity. No changes in VCs were detected with entospletinib, but a small increase in HR and decrease in MAP were present.

Table 13: Selected drug-induced changes of the conventional Doppler wave analysis. *Changes reported in the table were significant between treated and vehicle group (θ: two-way ANOVA, p<0.05) and/or significantly different from baseline within the treated group (* two-way ANOVA, p<0.05). '↑' indicates an increase in the parameter, '↓' indicates a decrease in the parameter, '=' indicates parameter was not significantly changed.*

	Sunitinib	**R406**	**Entospletinib**
ΔHR	$\downarrow\downarrow^{\theta}$	=	$\uparrow^{\theta}$
ΔMAP	$\uparrow\uparrow^{\theta,*}$	=	$\downarrow^{\theta}$
%ΔRVC	$\downarrow^{\theta}$	$\downarrow^{\theta}$	=
%ΔMVC	$\downarrow\downarrow^{\theta,*}$	=	=
%ΔAVC	$\downarrow\downarrow^{\theta,*}$	$\downarrow^{*}$	=

5.3.2. SPAR analysis

Following the conventional wave analysis, the BP waves and Doppler shift waves were analysed using SPAR. Following the protocol described above in section 5.2.5.2., attractors were generated, and ROC AUC values determined for each SPAR metric. These values indicated how well a metric can distinguish the drug-treated group from its control group (vehicle). The closer to 1, the larger the difference; the closer to 0.5, the more similar the metric is in both groups. An overview of all ROC AUCs is presented in Figure 57. Figure 57A represents a heatmap of ROC AUCs per signal per group (drug-treated versus vehicle). It was clear that the renal blood flow wave was least affected overall (yellow/light orange for most metrics). The aortic flow metrics were more variable, especially in the sunitinib-treated group. Furthermore, the mesenteric metrics were changing between the drug-treated and vehicle group as well, mostly with entospletinib and sunitinib. Lastly, some BP metrics were relatively good to distinguish between groups (e.g. maxden, maxdh and some vw-metrics; ROC AUCs around 0.65 – 0.70), but less so than the mesenteric and aortic flow. Similar observations were made when the ROC AUCs for each metric per signal were averaged out over the drug-treated groups (Figure 57B): aortic flow and mesenteric flow differed the most in drug-treated versus vehicle groups and the renal metrics were affected the least.

Overall, from the heatmap, it appeared that R406 made the least changes in waveform morphology and variability, compared to entospletinib and sunitinib.

In the sections below, each signal (i.e. BP or renal, mesenteric or aortic flow), its relevant metrics and changes in waves are presented. Metrics were selected for quantification of waveform changes according to the following criteria: (1) the mean ROC AUC was over 0.6 and (2) the metric showed a reasonable change (ROC AUC>0.6) in at least two of the drug-treated groups and (3) ease of interpretation of the metric. Cycle rate was excluded for all signals, as this indicates the HR, already discussed in section 5.3.1.

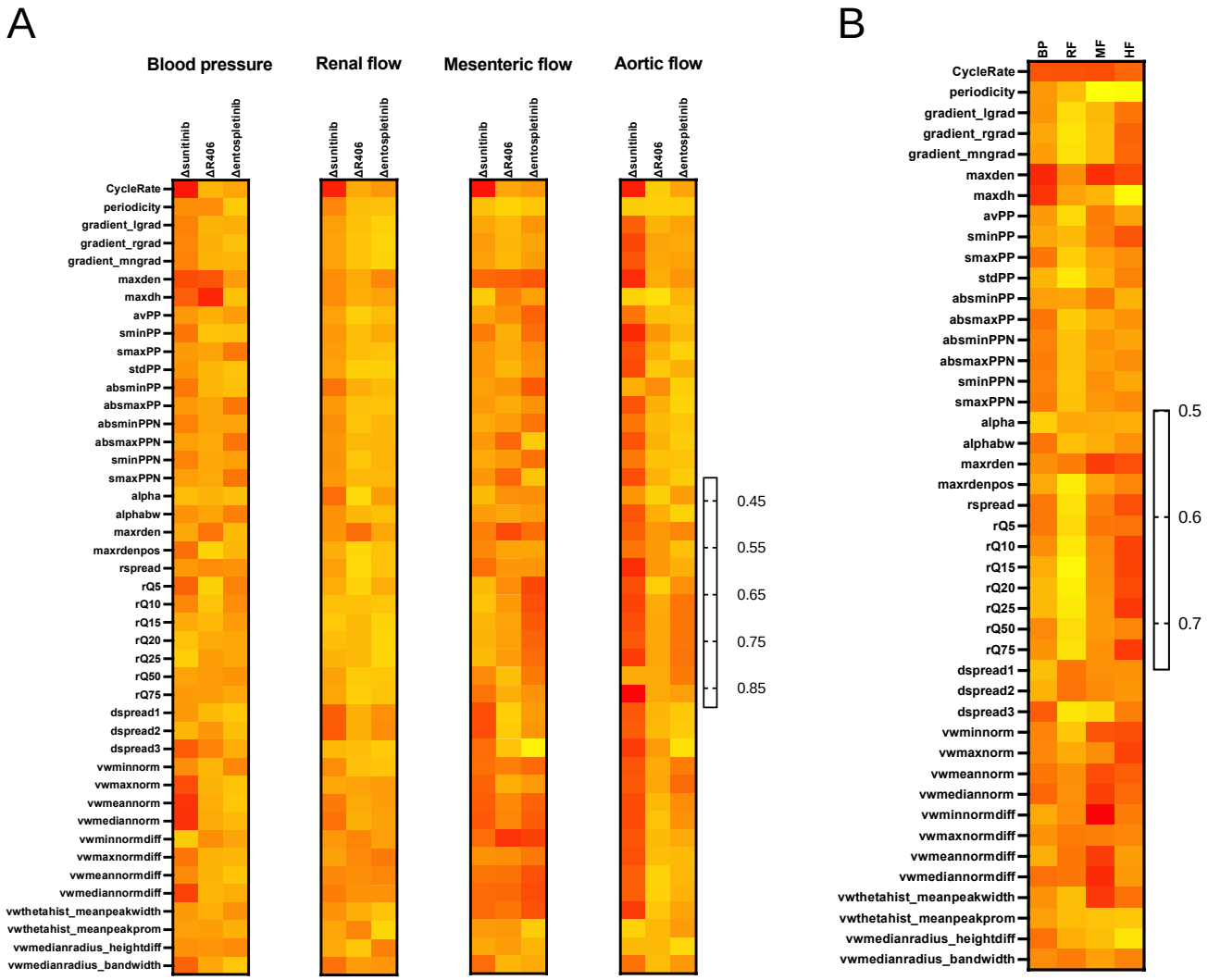

Figure 56: Heatmap of ROC AUC values of all Doppler studies. (A) *All 36 attractor metrics per signal are listed with their ROC AUC value, per drug compared to its corresponding vehicle. The higher the ROC AUC (red in the heatmap), the better the metric can distinguish drug-treated animals from vehicle-treated animals. The lower the ROC AUC (yellow in heatmap), the more overlapping the metric is between the drug-treated and vehicle-treated group.* ***(B)*** *Per signal, mean ROC AUCs across all drug-treated groups per attractor metric.*

5.3.2.1. Blood pressure waves

First, the SPAR analysis of BP waves was performed.

Selection of metrics to quantify changes in BP waves.

Figure 58 shows the heatmap of ROC AUCs values for the arterial BP wave signals. Based on this heatmap, following the criteria mentioned above, 4 metrics were selected: (1) maxden, (2) dspread3, (3) vwmedianradio_heightdiff and (4) rQ5. Below a summary of how each metric related to waveform morphology or variability changes is given. The metrics in this section, and how they were derived from the attractor, are represented in the Appendix (section 8.3., Table 23).

Firstly, maxden was included here, as it showed a good ROC AUC to distinguish between drug-treated groups and their corresponding vehicle group. This metrics is representing the maximum recorded attractor density and inversely related with the waveform variability. Dspread3 and rQ5 have been discussed previously, in Chapter 4, section 4.3.4 and 4.3.5. In summary, dspread3 indicates the amount of red colour in an attractor, hence the higher dspread3, the lower the waveform variability. rQ5 is extracted from the radial density plot and indicates at which radial position respectively 5% of the data are captured. An attractor with a high density in the centre, is therefore associated with a low rQ5 value. Vwmedianradio_heightdiff is another metric that relates to the roundness of the attractor. This metric is taken from the polar map of the attractor. How this plot is generated and vwmedianradio_heightdiff is determined is shown in the Appendix (section 8.3., Figure 90 and 91). In short, a decrease vwmedianradio_heightdiff is related the opening of attractor and an increase in waveform reflection. This metric is referred to as heightdiff throughout the rest of the thesis.

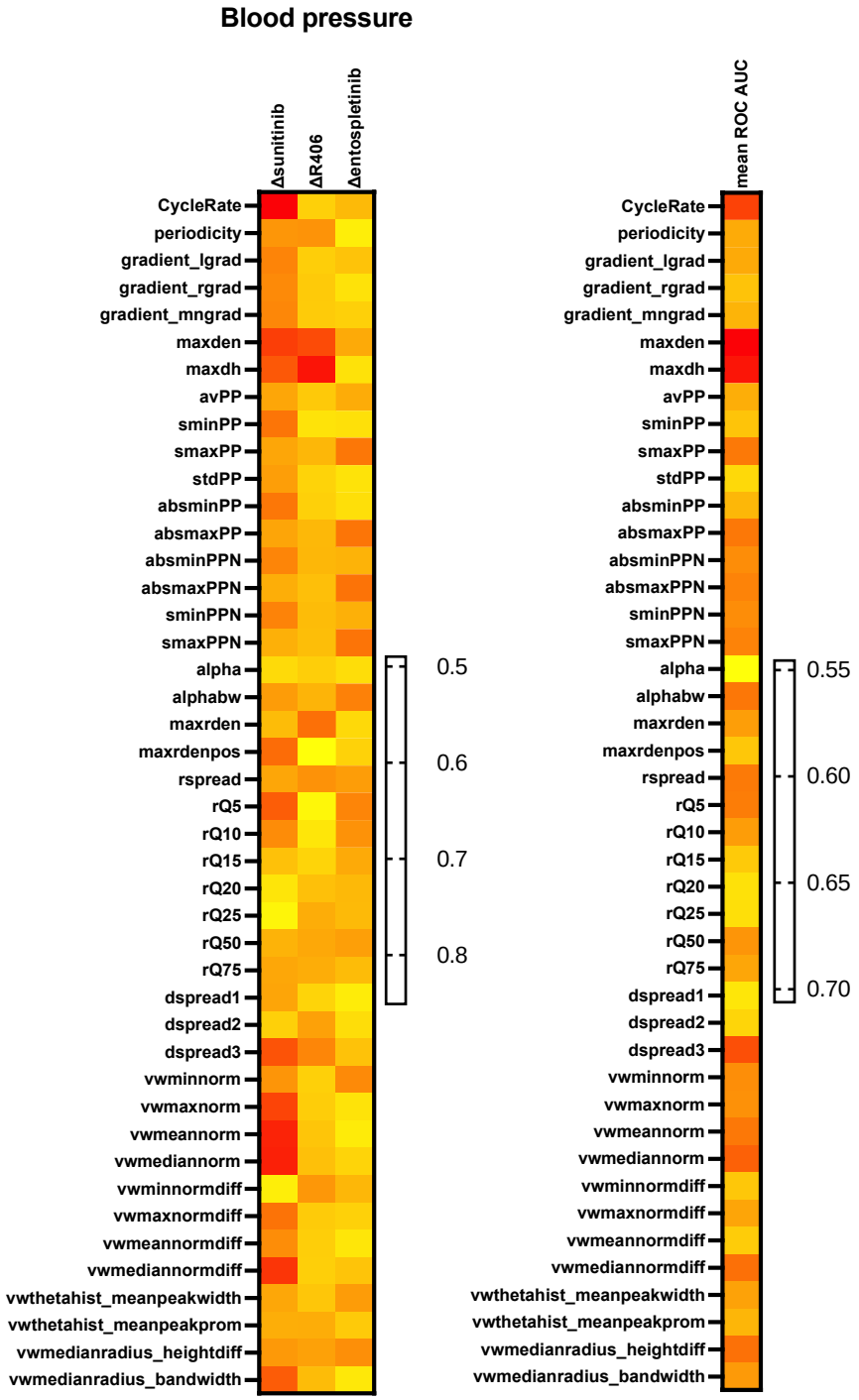

Figure 57: Heatmap of ROC AUC values of arterial BP wave signal. *All 44 attractor metrics are listed with their ROC AUC value, per drug compared to its corresponding vehicle. The higher the ROC AUC (red in the heatmap), the better the metric can distinguish drug-treated animals from vehicle-treated animals. The lower the ROC AUC (yellow in heatmap), the more overlapping the metric is between the drug-treated and vehicle-treated group. Mean ROC AUCs across all drug-treated groups per attractor metric are presented on the right-hand side.*

Quantitative changes

Following the selection of the SPAR metrics, changes of the metrics following drug treatment were quantified and are shown in Figure 59, 60 and 61.

Figure 59 represents the changes induced in the BP wave following sunitinib treatment. Metrics inversely related to waveform variability – maxden and dspread3 – were increased by sunitinib compared to vehicle. Within the group, the metrics did not increase significantly over time (two-way ANOVA, $p>0.05$). However, both maxden and dspread3 increased significantly from the first day of treatment compared to the vehicle-treated group (two-Way ANOVA, $p<0.05$). This effect was sustained during the three days of experimentation, with the largest effect observed on the second day. Metrics related to the waveform morphology changed as well. Metric rQ5 was increased with sunitinib, again significant from the first day of dosing (two-Way ANOVA, $p<0.05$). This effect wore off during the day, returning to baseline values after 2 or 3 h after bolus-dosing on every day. The maximal effect was observed on the third day, 1 h post bolus-dosing (Šídák test, $p<0.05$). Unlike the sunitinib-group, in the vehicle-group significant changes over time were observed within the group (two-way ANOVA, $p<0.05$), with the maximum effect observed in the last hour of the last day (Dunnett test, $p<0.05$). Lastly, heightdiff decreased following sunitinib administration. This effect was only significantly different from vehicle from the second day (two-way ANOVA, $p<0.05$). Within the sunitinib-group, a significant decrease compared to baseline was observed from the third day (two-way ANOVA, $p<0.05$, maximum effect observed 1h post bolus-dosing on the third day, Dunnett test, $p<0.05$). Together, these changes indicated sunitinib caused an increase in waveform reflection and thus vasoconstriction.

Figure 60 shows the changes induced in the BP wave following R406 treatment, compared to vehicle. In contrast to sunitinib, R406 showed a decrease in maxden and dspread3. From the first day, maxden was significantly decreased with R406 compared to vehicle (two-way ANOVA, $p<0.05$). This decrease was sustained during the three days. No significant changes were detected within the group from baseline (two-way ANOVA, $p>0.05$). Dspread3 was affected in a similar way; within the treatment groups no significant changes were observed from baseline (two-way ANOVA, $p>0.05$), but from the first day, dspread3 was significantly decreased in the R406 group compared to vehicle (two-way ANOVA, $p<0.05$) and this effect sustained during the three days of monitoring. Related to the waveform morphology, rQ5 was not differently affected by vehicle or R406 (two-way ANOVA, $p>0.05$). Lastly, heightdiff increased following R406 administration. This effect was overall significant (two-way ANOVA, $p<0.05$) due to the effect on the second day; on the first and third heightdiff was not significantly different between the two groups (two-way ANOVA, $p>0.05$).

In Figure 61, the effect of entospletinib on the BP SPAR metrics are presented. Entospletinib resulted in similar but smaller effects on the variability metrics as R406; both maxden and dspread3 were decreased. For maxden, this effect was significant from the second day (two-way ANOVA, $p<0.05$), dspread3 decreased significantly, compared to vehicle, from the third day only (two-way ANOVA, $p<0.05$). Both metrics were not significantly affected within the groups over time (two-way ANOVA, $p>0.05$). The metric rQ5 was increased following entospletinib administration compared to vehicle (two-way ANOVA, $p<0.05$) and this effect grew larger over the three days of dosing. No significant changes were observed within either of the groups from baseline. Lastly, heightdiff was decreased with entospletinib, compared to vehicle (two-way ANOVA, $p<0.05$), with no changing within the group from baseline. These changes in morphology metrics were similar to the ones observed with sunitinib.

A summary of the drug-effects on the BP SPAR metrics is shown in Table 14.

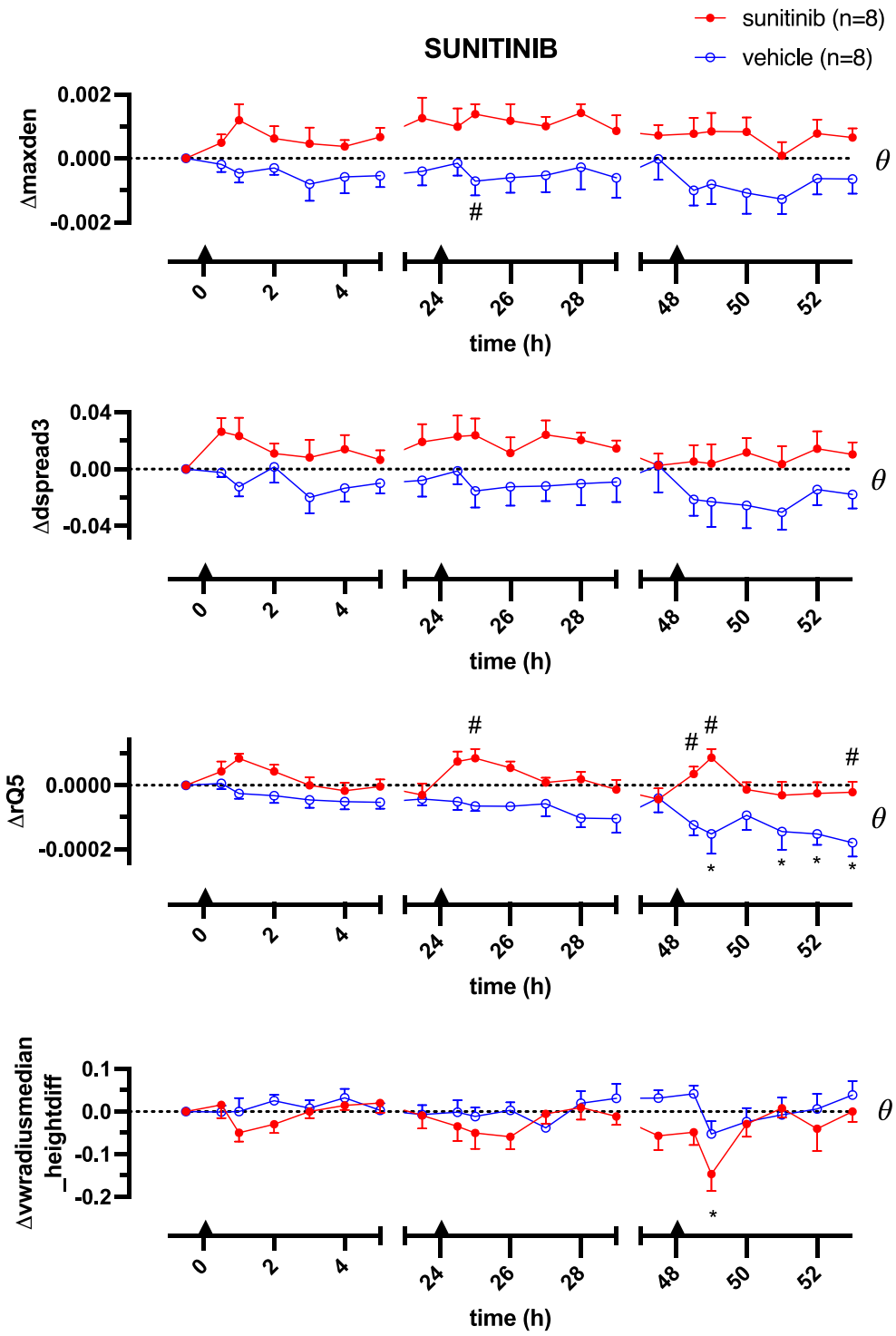

Figure 58: Effect of sunitinib on selected BP SPAR metrics. *Changes in Δmaxden, Δdspread3, ΔrQ5 and Δheightdiff of rats dosed with sunitinib 16 mg/kg IV (n=8, red, filled circles) and vehicle IV (n=8, blue, open circles). Data were normalised to baseline recording of day 1 for each animal individually. Black triangles on time-axis indicate time of drug administration. Data are presented as mean ± SEM. A two-way ANOVA test was conducted to test for overall differences between two groups (θ = p<0.05), followed by multiple comparison by Sídák to test for differences between the groups at each time point (# = p<0.05) Furthermore, if there was a significant change over time within a group (two-way ANOVA), each timepoint of the group was compared to the group's corresponding baseline (T=-0.5h), by Dunnett (* = p<0.05).*

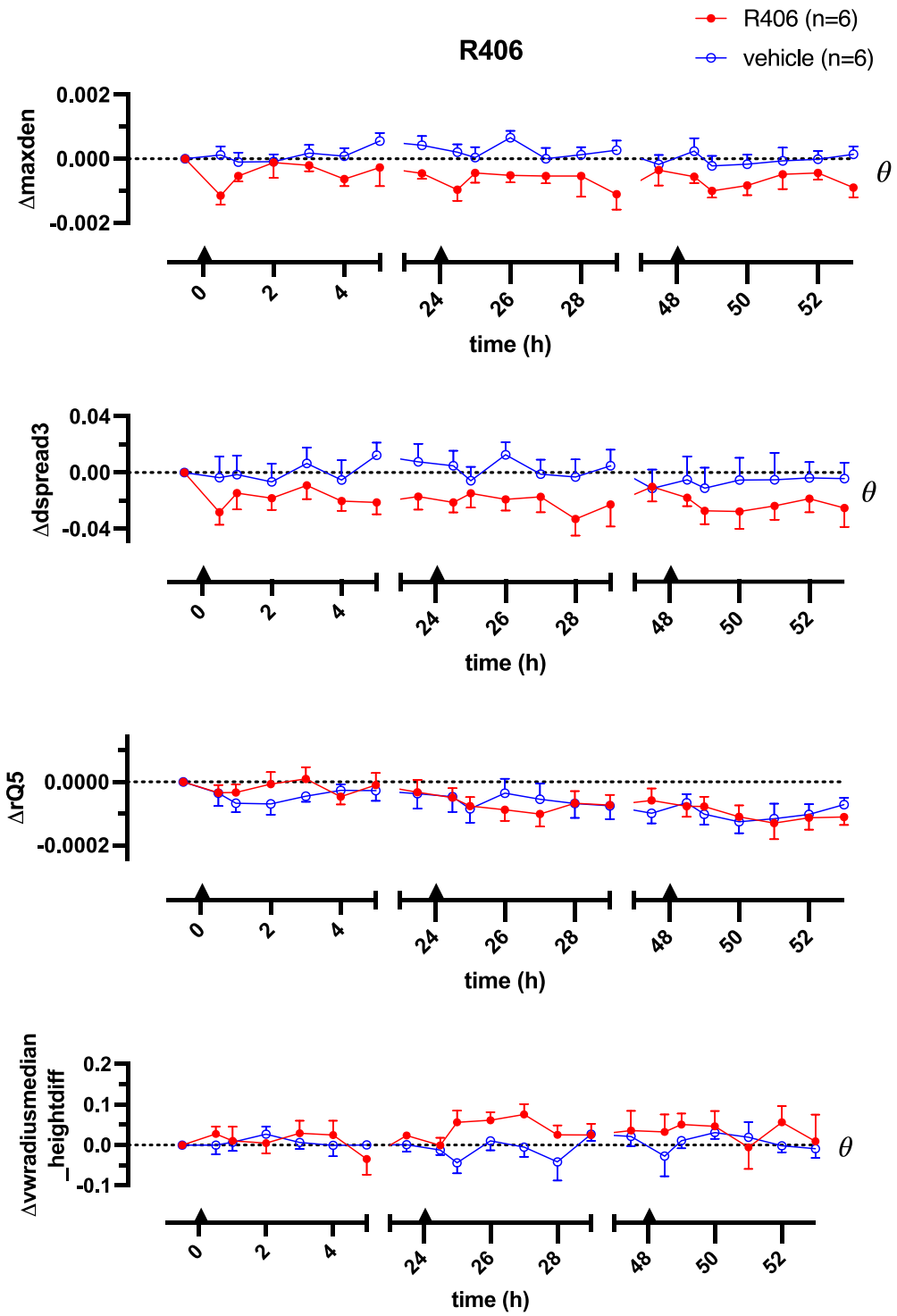

Figure 59: Effect of R406 on BP SPAR metrics. *Changes in Δmaxden, Δdspread3, ΔrQ5 and Δheightdiff of rats dosed with R406 2.5 mg/kg IV (n=6, red, filled circles) and vehicle IV (n=6, blue, open circles). Data were normalised to baseline recording of day 1 for each animal individually. Black triangles on time-axis indicate time of drug administration. Data are presented as mean ± SEM. A two-way ANOVA test was conducted to test for overall differences between two groups (θ = p<0.05), followed by multiple comparison by Sídák to test for differences between the groups at each time point (# = p<0.05) Furthermore, if there was a significant change over time within a group (two-way ANOVA), each timepoint of the group was compared to the group's corresponding baseline (T=-0.5h), by Dunnett (* = p<0.05).*

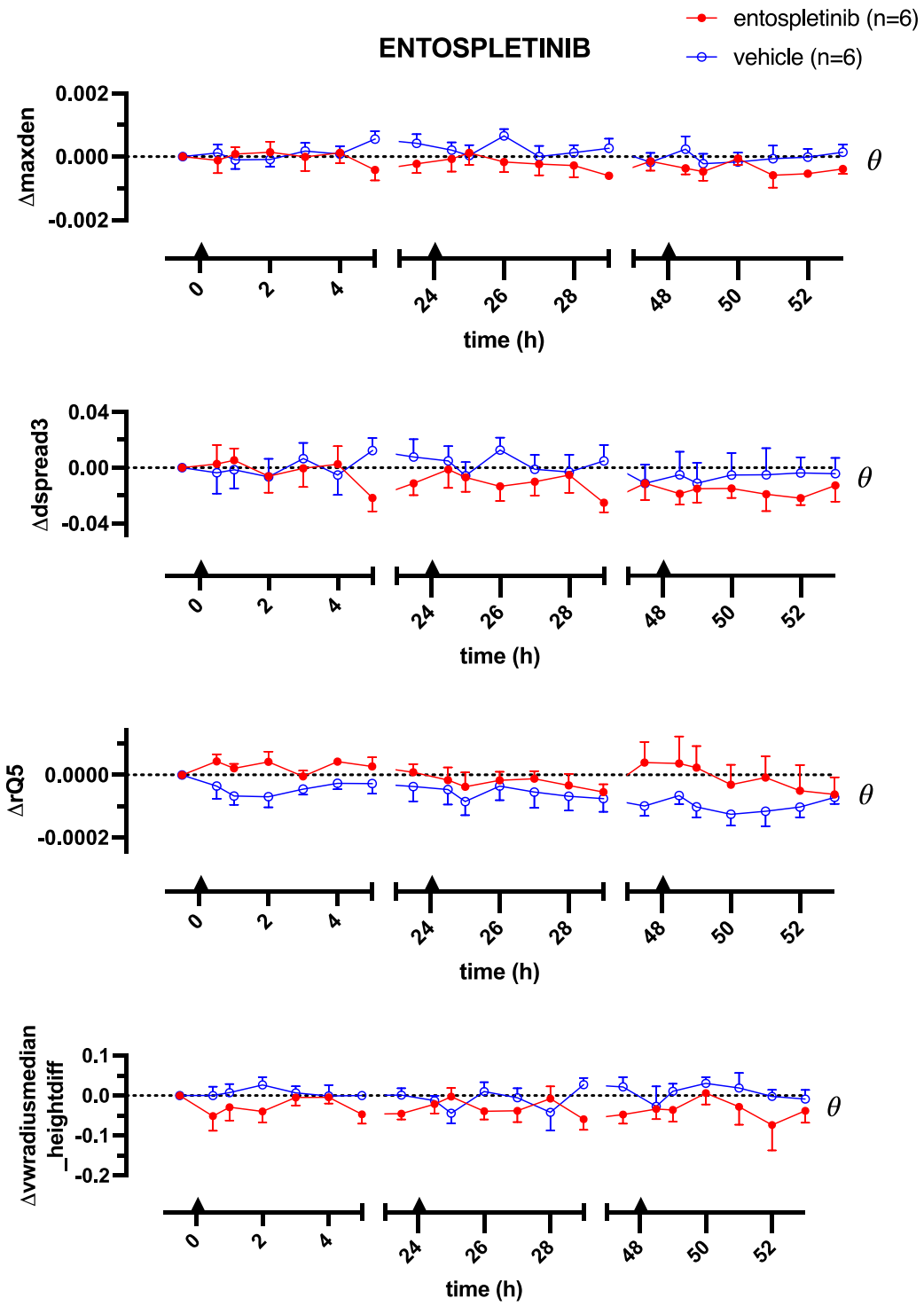

Figure 60: Effect of entospletinib on BP SPAR metrics. *Changes in Δmaxden, Δdspread3, ΔrQ5 and Δheightdiff of rats dosed with entospletinib 0.4 mg/kg IV (n=6, red, filled circles) and vehicle IV (n=6, blue, open circles). Data were normalised to baseline recording of day 1 for each animal individually. Black triangles on time-axis indicate time of drug administration. Data are presented as mean ± SEM. A two-way ANOVA test was conducted to test for overall differences between two groups (θ = p<0.05), followed by multiple comparison by Sídák to test for differences between the groups at each time point (# = p<0.05) Furthermore, if there was a significant change over time within a group (two-way ANOVA), each timepoint of the group was compared to the group's corresponding baseline (T=-0.5h), by Dunnett (* = p<0.05).*

Table 14: Selected BP SPAR metrics, drug-induced changes and the interpretation of the metric. *Changes reported in the table were significant between treated and vehicle group (two-way ANOVA, p<0.05). '↑' indicates in increase in the metric, '↓' indicates a decrease in the metric, '=' indicates metric was not significantly changed.*

	Sunitinib	**R406**	**Entospletinib**	**Interpretation of metric**
Δmaxden	↑	↓	↓	↑: decreased waveform variability ↓: increased waveform variability
Δdspread3	↑	↓	↓	↑: decreased waveform variability ↓: increased waveform variability
ΔrQ5	↑	=	↑	↑: opening of attractor, more wave reflection ↓: closing of attractor, less wave reflection
Δheightdiff	↓	↑	↓	↑: closing of attractor, less wave reflection ↓: opening of attractor, more wave reflection
Summary of drug effect	Decreases variability and opens attractor	Increases variability and closes attractor	Increases variability and opens attractor	

5.3.2.2. Renal flow wave

Selection of metrics

Overall, changes in renal attractor metrics were less pronounced than in other vascular beds and signals had a much higher variability than the mesenteric and aortic flow. Nonetheless, based on the heatmap shown in Figure 62, three SPAR metrics were selected to quantify renal blood flow wave changes following drug treatment: (1) maxrden, (2) dspread1 and (3) vwmedianradius_bandwidth. How these metrics are determined and how they relate to attractor and wave changes is detailed in the Appendix (section 8.3., Table 24). In summary, these three metrics are related to the variability of the wave:

1. Maxrden indicates the maximum density, calculated from the radial density plot, as explained in Chapter 4, section 4.3.5. The higher this metric, the lower the waveform variability.
2. Secondly, dspread1 is the opposite metric of dspread3; whereas dspread3 indicates the amount of red colour in an attractor, dspread1 indicates the amount of blue colour in an attractor. Thus, the higher the value of dspread1, the less overlap of attractor loops and the higher the variability of the waveform.
3. Lastly, vwmedianradius_bandwidth was extracted from the polar map of the attractor. How this metric is calculated and relates to waveform variability is detailed in the Appendix (section 8.3., Table 24 and Figure 92 and 93). Briefly, the vwmedianradius_bandwidth is directly related to the waveform variability. This metric is referred to as bandwidth throughout the rest of the thesis.

Thus, these three metrics are calculated from different plots of the attractor but are all related with waveform variability. An increase in waveform variability is associated with a decrease in maxrdens and increase in dspread1 and bandwidth.

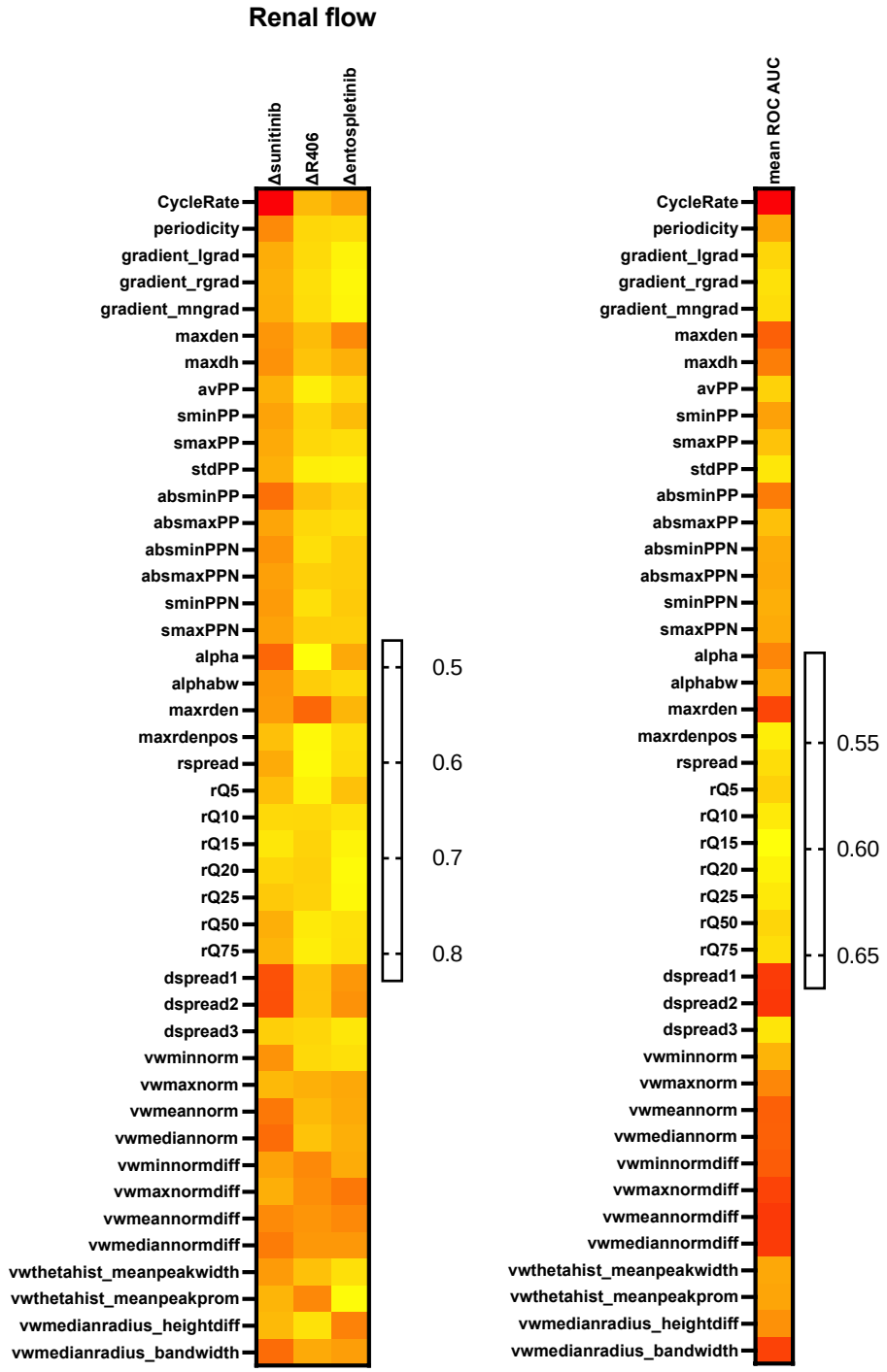

Figure 61: Heatmap of ROC AUC values of RF signals. *All 44 attractor metrics are listed with their ROC AUC value, per drug compared to its corresponding vehicle. The higher the ROC AUC (red in the heatmap), the better the metric can distinguish drug-treated animals from vehicle-treated animals. The lower the ROC AUC (yellow in heatmap), the more overlapping the metric is between the drug-treated and vehicle-treated group. Mean ROC AUCs across all drug-treated groups per attractor metric are presented on the right-hand side.*

Quantitative changes

Following the selection of the SPAR metrics, changes of the metrics following drug treatment were quantified and are shown in Figure 63, 64 and 65.

In Figure 63, the effects of sunitinib on the renal metrics (and thus renal blood flow wave variability) are presented. The metric marxden was not affected over the three days of data recording. On the other hand, dspread1 and Δbandwidth both decreased following sunitinib administration. Interestingly, rather than a decrease compared to baseline in the sunitinib-group, the metrics increased in the vehicle-treated group and sunitinib seemed to offset that effect. Metric dspread1 was significantly lower in the sunitinib group, compared to vehicle, from the first day of dosing (two-way ANOVA, overall $p<0.05$), with the maximum effect observed on the third day, 2h after bolus dosing (Šídák test, $p<0.05$). The metric bandwidth was significantly different between the two groups from the second day (two-way ANOVA, overall $p<0.05$), with no individual timepoints being significantly different between the groups (Šídák test, $p>0.05$). Both the vehicle group and sunitinib group did not show a significant change from baseline within the group. In summary, these changes indicated sunitinib evoked a decrease in renal flow waveform variability.

The effect of R406 on the renal wave variability metrics are presented in Figure 64. This compound caused a significant decrease in maxrden compared to vehicle, indicating an increase in waveform variability. However, this effect was again rather due to offsetting of effects observed in the vehicle group, than a change from baseline within the R406-group. From the first day, there was a significant change between the groups (two-way ANOVA, overall $p<0.05$, largest effect on day 2, Šídák test, $p<0.05$) and no significant effects were observed within either group from baseline. A trend for increasing dspread1 and bandwidth was observed with R406, however these changes were not significant within the group, or compared to the vehicle group (two-way ANOVA, $p>0.05$).

In Figure 65, the effects of entospletinib on the renal flow SPAR metrics are shown. Firstly, a decrease in marxden was observed, compared to vehicle (significant from the first day, two-way ANOVA, overall $p<0.05$). On the other hand, dspread1 and bandwidth were, similar to R406, increased in the entospletinib-group. Metric dspread1 was significantly decreased from the second day in the entospletinib-group compared to vehicle (two-way ANOVA, overall $p<0.05$), with no significant changes over time from baseline observed within either group (two-way ANOVA, $p>0.05$). The increase in bandwidth was significant from the second day (two-way ANOVA, overall $p<0.05$). The effect was the largest on the second day, but again, within both groups, no significant changes from baseline were detected. Taken together, these changes indicated an entospletinib-induced increase in renal blood flow waveform variability.

The effects of these three compounds on the SPAR metrics extracted from the renal flow are summarised in Table 15.

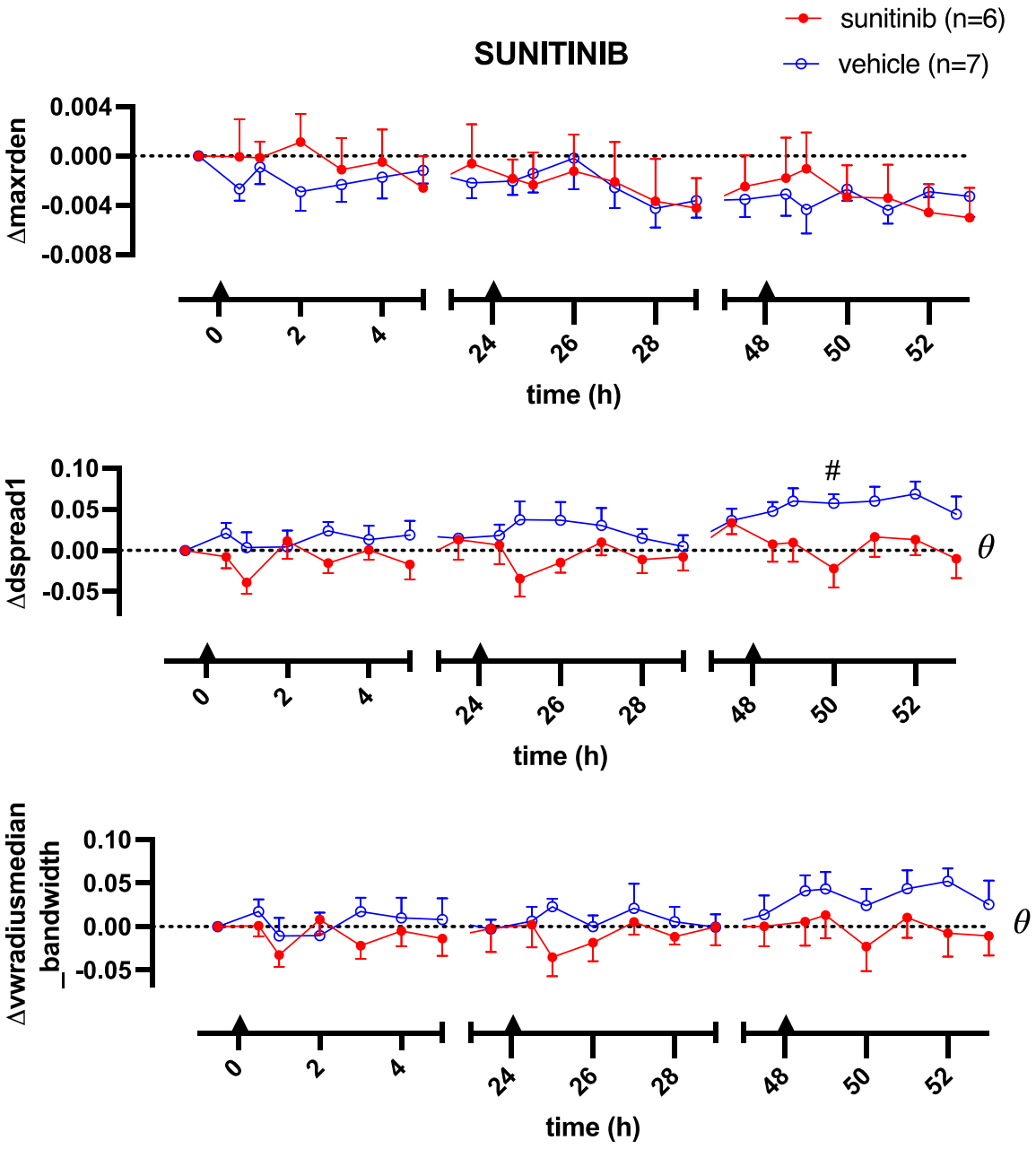

Figure 62: Effect of sunitinib on selected renal flow SPAR metrics. *Changes in Δmaxrden, Δdspread1 and Δbandwidth of rats dosed with sunitinib 16 mg/kg IV (n=6, red, filled circles) and vehicle IV (n=7, blue, open circles). Data were normalised to baseline recording of day 1 for each animal individually. Black triangles on time-axis indicate time of drug administration. Data are presented as mean ± SEM. A two-way ANOVA test was conducted to test for overall differences between two groups (θ = p<0.05), followed by multiple comparison by Sídák to test for differences between the groups at each time point (# = p<0.05) Furthermore, if there was a significant change over time within a group (two-way ANOVA), each timepoint of the group was compared to the group's corresponding baseline (T=-0.5h), by Dunnett (* = p<0.05).*

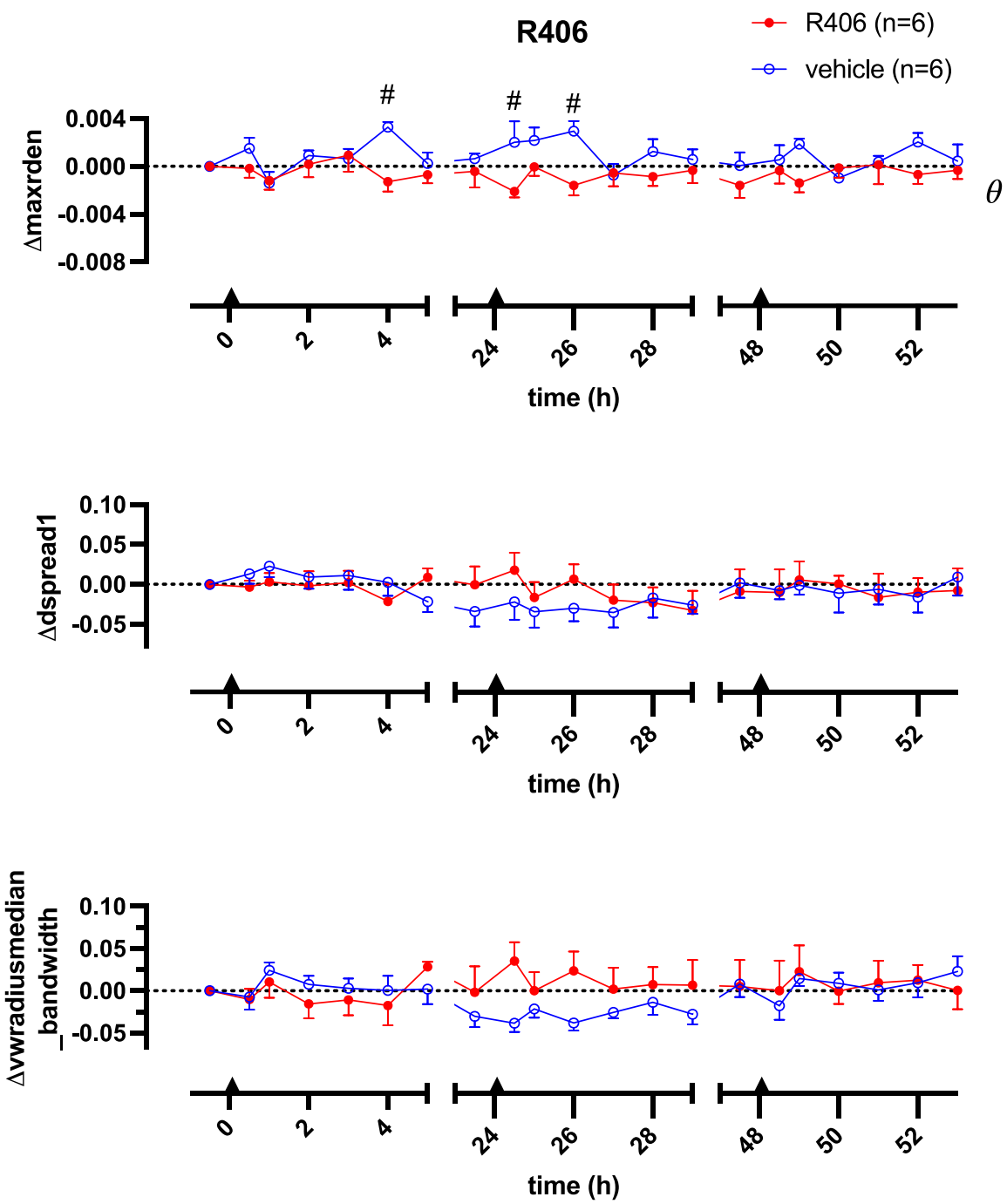

Figure 63: Effect of R406 on selected renal flow SPAR metrics. *Changes in Δmaxrden, Δdspread1 and Δbandwidth of rats dosed with R406 2,5 mg/kg IV (n=6, red, filled circles) and vehicle IV (n=6, blue, open circles). Data were normalised to baseline recording of day 1 for each animal individually. Black triangles on time-axis indicate time of drug administration. Data are presented as mean ± SEM. A two-way ANOVA test was conducted to test for overall differences between two groups (θ = p<0.05), followed by multiple comparison by Sídák to test for differences between the groups at each time point (# = p<0.05) Furthermore, if there was a significant change over time within a group (two-way ANOVA), each timepoint of the group was compared to the group's corresponding baseline (T=-0.5h), by Dunnett (* = p<0.05).*

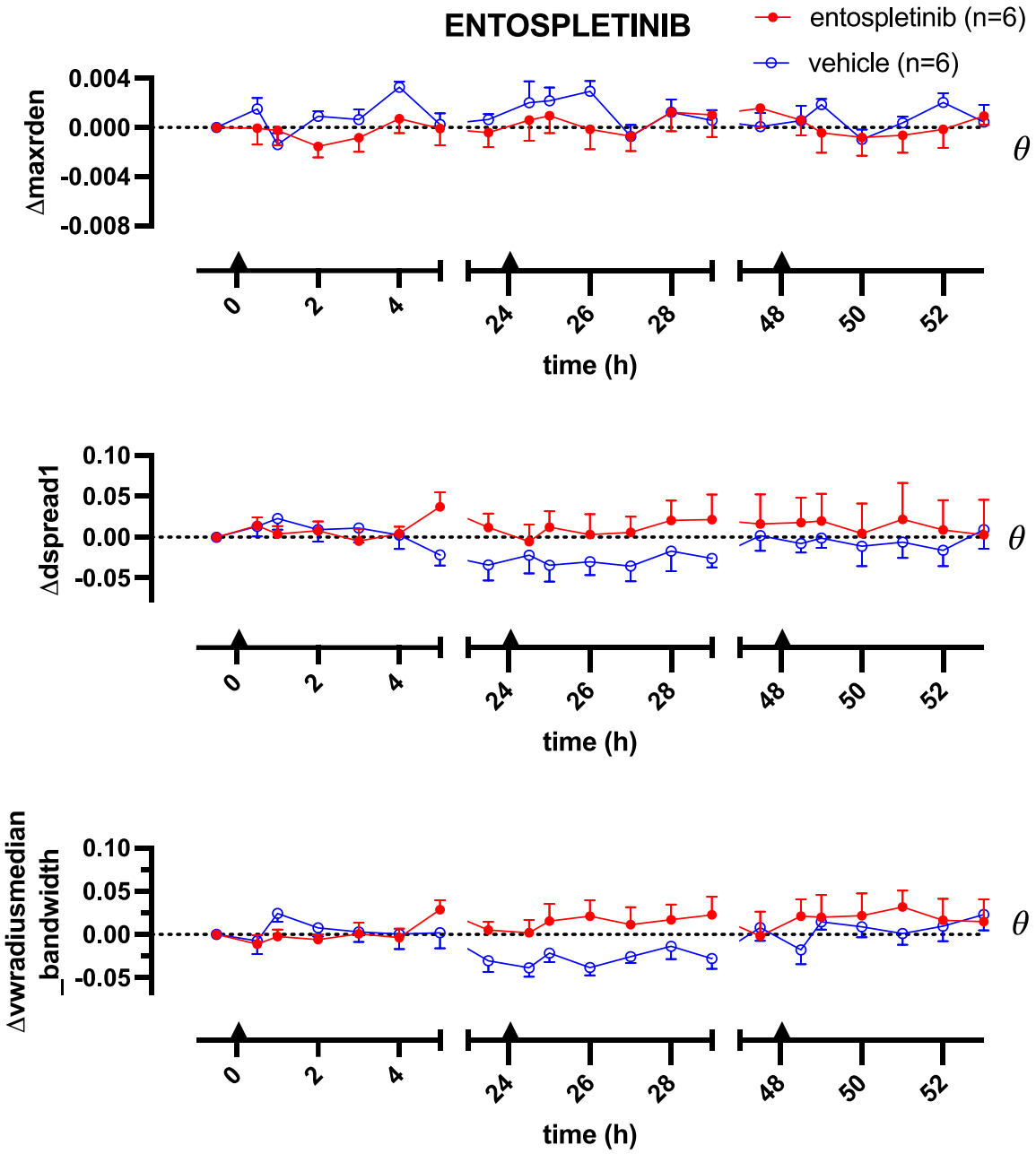

Figure 64: Effect of entospletinib on selected renal flow SPAR metrics. *Changes in Δmaxrden, Δdspread1 and Δbandwidth of rats dosed with entospletinib 0.4 mg/kg IV (n=6, red, filled circles) and vehicle IV (n=6, blue, open circles). Data were normalised to baseline recording of day 1 for each animal individually. Black triangles on time-axis indicate time of drug administration. Data are presented as mean ± SEM. A two-way ANOVA test was conducted to test for overall differences between two groups (θ = p<0.05), followed by multiple comparison by Sídák to test for differences between the groups at each time point (# = p<0.05) Furthermore, if there was a significant change over time within a group (two-way ANOVA), each timepoint of the group was compared to the group's corresponding baseline (T=-0.5h), by Dunnett (* = p<0.05).*

Table 15: Selected renal flow SPAR metrics, drug-induced changes and the interpretation of the metric. *Changes reported in the table were significant between treated and vehicle group (two-way ANOVA, p<0.05). '↑' indicates in increase in the metric, '↓' indicates a decrease in the metric, '=' indicates metric was not significantly changed.*

	Sunitinib	**R406**	**Entospletinib**	**Interpretation of metric**
Δmaxrden	=	↓	↓	↑: decreased waveform variability ↓: increased waveform variability
Δdspread1	↓	=	↑	↑: increased waveform variability ↓: decreased waveform variability
Δbandwidth	↓	=	↑	↑: increased waveform variability ↓: decreased waveform variability
Summary of drug effect	Decreases variability	Increases variability	Increases variability	

5.3.2.3. Mesenteric flow wave

Selection of metrics

Based on the heatmap of ROC AUCs, presented in Figure 66, four metrics were selected to quantify changes in the mesenteric flow wave: (1) maxden, (2), avPP, (3) rQ75 and (4) vwmediannorm. The extraction and interpretation of the metrics are detailed in the Appendix (section 8.3., Table 25). Below an overview of the metrics is given.

1. Maxden, as described in section 5.3.2.1., indicates the number of data in the highest density bin of the attractor, and is therefore inversely related to the wave variability.
2. The metric avPP indicates the average 'pulse pressure' of the signal. When the downstream vascular bed is constricted, a larger flow wave amplitude is measured, as wave reflection increases (W. W. . Nichols et al., 2022). A lower flow wave amplitude indicates less wave reflection, hence a dilation in the downstream vascular bed (W. W. . Nichols et al., 2022). An illustrative example is shown in the Appendix (section 8.3. Figure 94).
3. The metric rQ75 is extracted from the radial density plot, as described in Chapter 4, section 4.3.5, and indicated at which radial density 75% of the data are captured. The larger this metric, the more high-density points at the outer edges of the attractor. The lower rQ75, the more high-density points at the centre of the attractor. For the mesenteric signal, a high rQ75 was related to a flat interbeat interval, and thus indicated an increase in blood flow wave reflection and vasoconstriction. An example is shown in the Appendix (section 8.3.3., Figure 95).
4. Lastly, vwmediannorm was determined. How this metric is derived from the polar attractor map, and how it relates to changes in waveform morphology is detailed in the Appendix (section 8.3., Table 25 and Figure 96). In brief, a decrease in vwmediannorm was linked to a flattening of the interbeat interval, thus indicating an increase in wave reflection of the mesenteric blood flow wave, observed with vasoconstrictors.

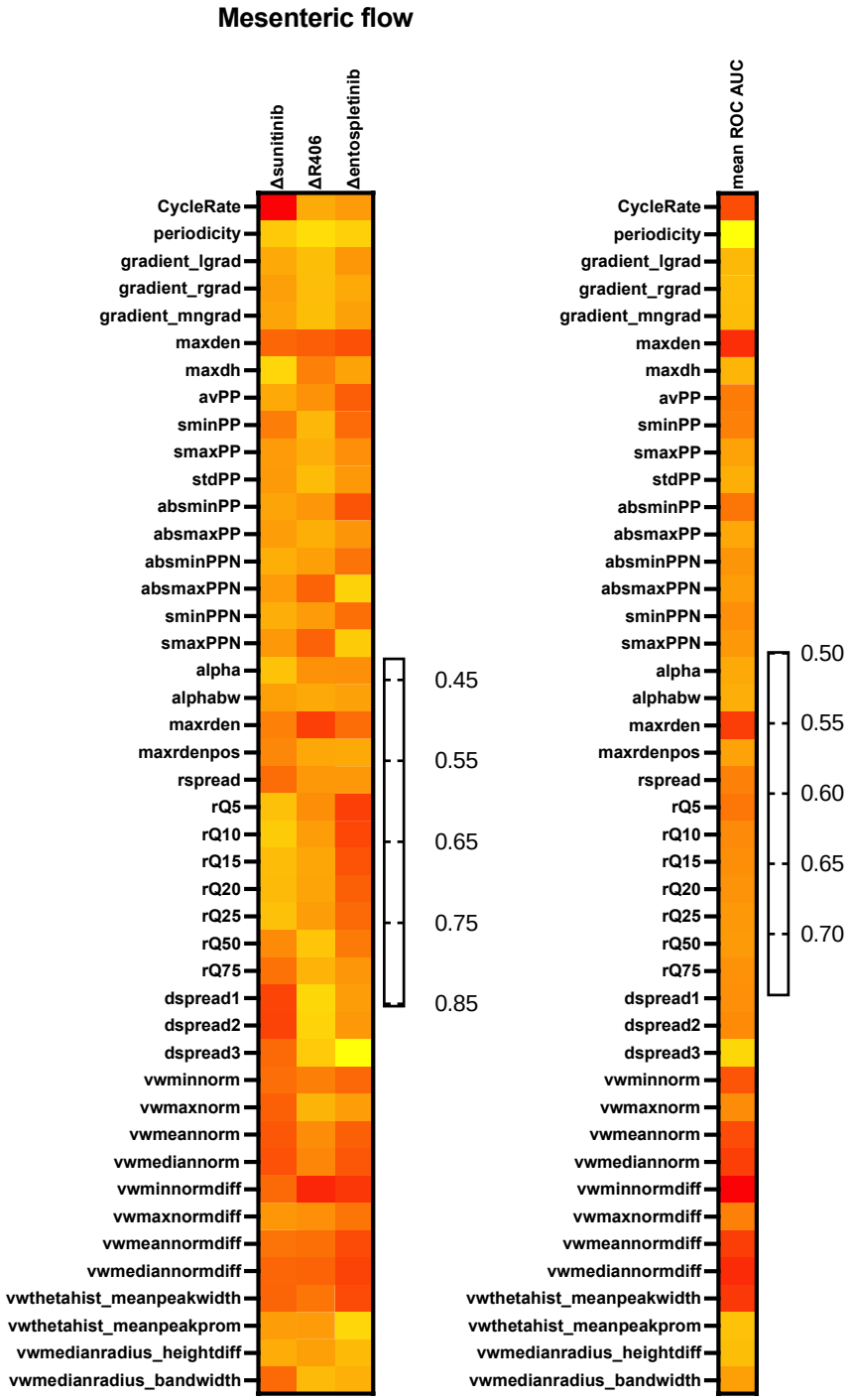

Figure 65: Heatmap of ROC AUC values of MF signals. *All 44 attractor metrics are listed with their ROC AUC value, per drug compared to its corresponding vehicle. The higher the ROC AUC (red in the heatmap), the better the metric can distinguish drug-treated animals from vehicle-treated animals. The lower the ROC AUC (yellow in heatmap), the more overlapping the metric is between the drug-treated and vehicle-treated group. Mean ROC AUCs across all drug-treated groups per attractor metric are presented on the right-hand side.*

Quantitative changes

Using these selected metrics, the drug-induced changes in attractors were quantified and the results are shown in Figure 67, 68 and 69. A summary of the effects of the three compounds on the mesenteric SPAR metrics, and their link to waveform changes is given in Table 16.

The effects of sunitinib on the mesenteric attractors are displayed in Figure 67. Firstly, sunitinib induced an increase in maxden, that was significantly different from vehicle from the first day (two-way ANOVA, overall $p<0.05$). The maximal difference was observed on the second day, 4 h after bolus dosing (Šídák test, $p<0.05$). Within the groups, there was no significant change from baseline in maxden. Secondly, a large increase in avPP was observed following sunitinib administration (two-way ANOVA, $p<0.05$). This effect sustained during the day and increased incrementally over the three days of monitoring. From the first day, the increase in avPP was significantly different from vehicle and the maximum effect was observed 1 h post bolus dosing on the second day (Šídák test, $p<0.05$). Furthermore, within the sunitinib-treated group, avPP incrementally and significantly increased over the three days compared to baseline (two-way ANOVA, $p<0.05$, maximum effect 1 h post bolus dosing on the second day, Dunnett test, $p<0.05$). A similar trend was observed in the metric rQ75; a large increase was observed in the sunitinib group, significantly different from the vehicle group from the first day (two-way ANOVA, overall $p<0.05$) and the maximum effect was observed on the second day, 1 h post sunitinib bolus dosing (Šídák test, $p<0.05$). This effect was sustained and grew over the three days of experimentation. Also, within the group, sunitinib caused a significant increase in rQ75 from baseline (two-way ANOVA, $p<0.05$, maximum effect at 1 h post dosing on the third day, Dunnett test, $p<0.05$). Lastly, Δvwmediannorm was reduced by sunitinib, compared to vehicle. This effect was smaller than the ones observed in avPP and rQ75, but significant at the last day (two-way ANOVA, $p<0.05$). These data indicated sunitinib evoked an attenuation of the mesenteric wave variability, and increased wave reflection from the mesenteric bed, thus causing a vasoconstriction in the mesenteric bed.

The R406-induced effects of the selected mesenteric SPAR metrics are shown in Figure 68. R406 had similar but smaller effects on the metrics, compared to sunitinib. Overall, the effects of R406 were however mostly due to nullifying the effect observed in the vehicle group; the metrics did not change largely within the R406 group and generally stayed close to baseline values. Firstly, maxden was increased following R406 dosing, compared to vehicle (two-way ANOVA, $p<0.05$). Within each group, no significant changes from baseline were observed. Metric avPP was increased following R406 administration, compared to vehicle (two-way ANOVA, $p<0.05$), significantly so from the second day. While rQ75 was not affected, R406 decreased vwmediannorm compared to vehicle (two-way ANOVA, $p<0.05$), with the maximum difference observed at the baseline of day 3 (Šídák test, $p<0.05$). In the vehicle group, vwmediannorm was significantly increased from baseline (two-way ANOVA, $p<0.05$), with the maximum effect observed on the third day, 30 min after bolus dosing (Dunnett test, $p<0.05$). No significant changes from baseline were detected within the R406 group.

Changes in the mesenteric flow metrics following entospletinib administration are displayed in Figure 69. Overall, entospletinib showed similar effects as R406 on these metrics; this compound changed the metrics in the same direction as sunitinib, but with a smaller magnitude, and effects were mostly due to offsetting increases or decreases observed in the vehicle group. The metric maxden was significantly different between the entospletinib and vehicle treated group by the first day (two-way ANOVA, overall $p<0.05$). The metric decreased in the vehicle group, however this effect was not significant within the group compared to baseline (two-way ANOVA, $P>0.05$). Both avPP and rQ75 were higher in the entospletinib group compared to the vehicle group. These effects were small, but significant between the two treatment-groups (two-way AONVA< $p<0.05$ for ΔavPP and $p<0.05$ for ΔrQ75). Lastly, the increase in vwmediannorm observed in the vehicle group, was attenuated by entospletinib (two-way AONVA, $p<0.05$), with the largest effect observed 30 min after bolus dosing on the third day (Šídák test, $p<0.05$). In the vehicle group, vwmediannorm was significantly increased from baseline (two-way ANOVA, $p<0.05$, maximum increase on the third day, 30 min after bolus dosing, Dunnett test, $p<0.05$). Within the entospletinib group, no significant changes from baseline were detected.

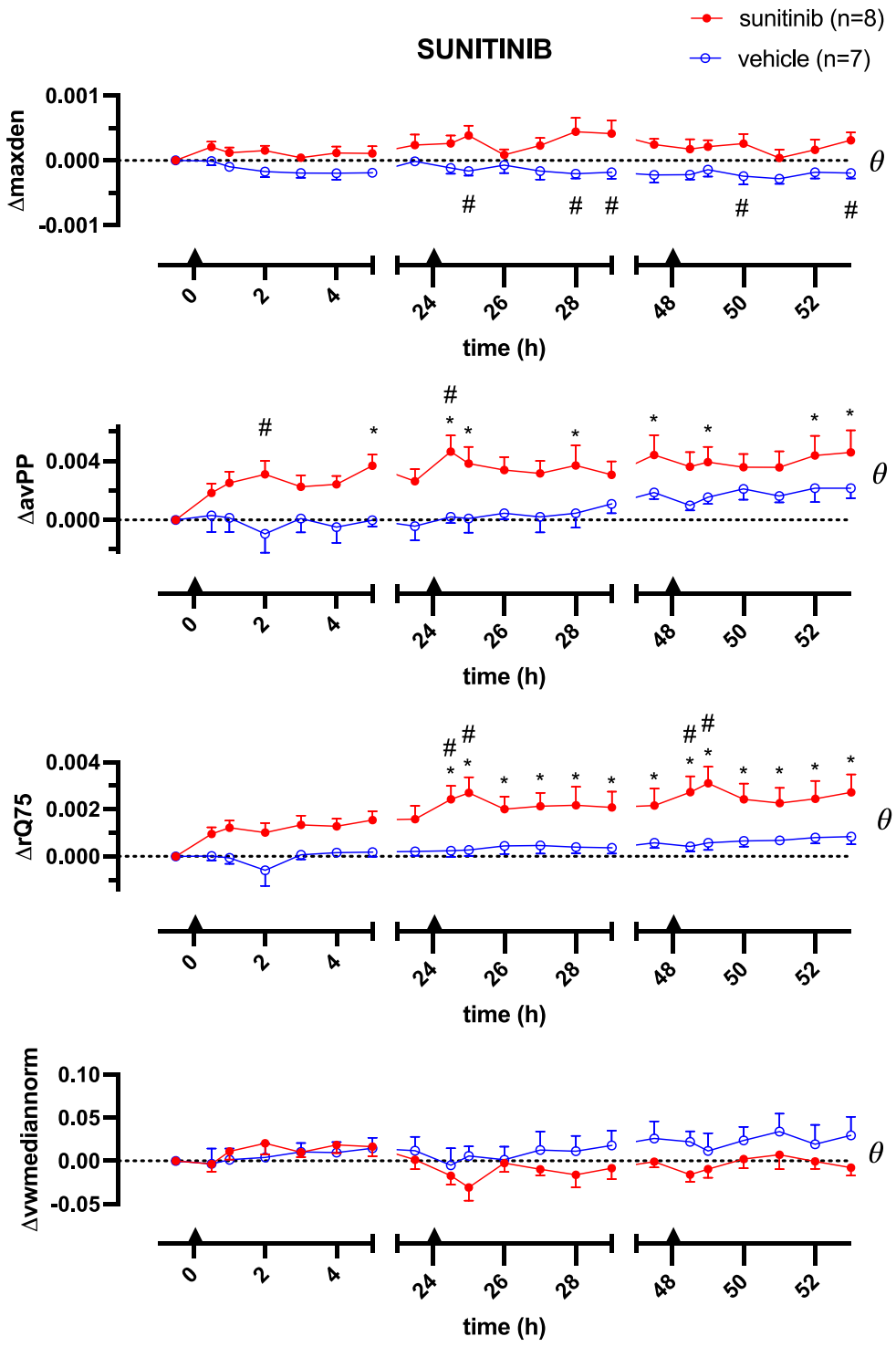

Figure 66: Effect of sunitinib on selected mesenteric flow SPAR metrics. *Changes in Δmaxden, ΔavPP, ΔrQ75 and Δvwmediannorm of rats dosed with sunitinib 16 mg/kg IV (n=8, red, filled circles) and vehicle IV (n=7, blue, open circles). Data were normalised to baseline recording of day 1 for each animal individually. Black triangles on time-axis indicate time of drug administration. Data are presented as mean ± SEM. A two-way ANOVA test was conducted to test for overall differences between two groups (θ = p<0.05), followed by multiple comparison by Sídák to test for differences between the groups at each time point (# = p<0.05) Furthermore, if there was a significant change over time within a group (two-way ANOVA), each timepoint of the group was compared to the group's corresponding baseline (T=-0.5h), by Dunnett (* = p<0.05).*

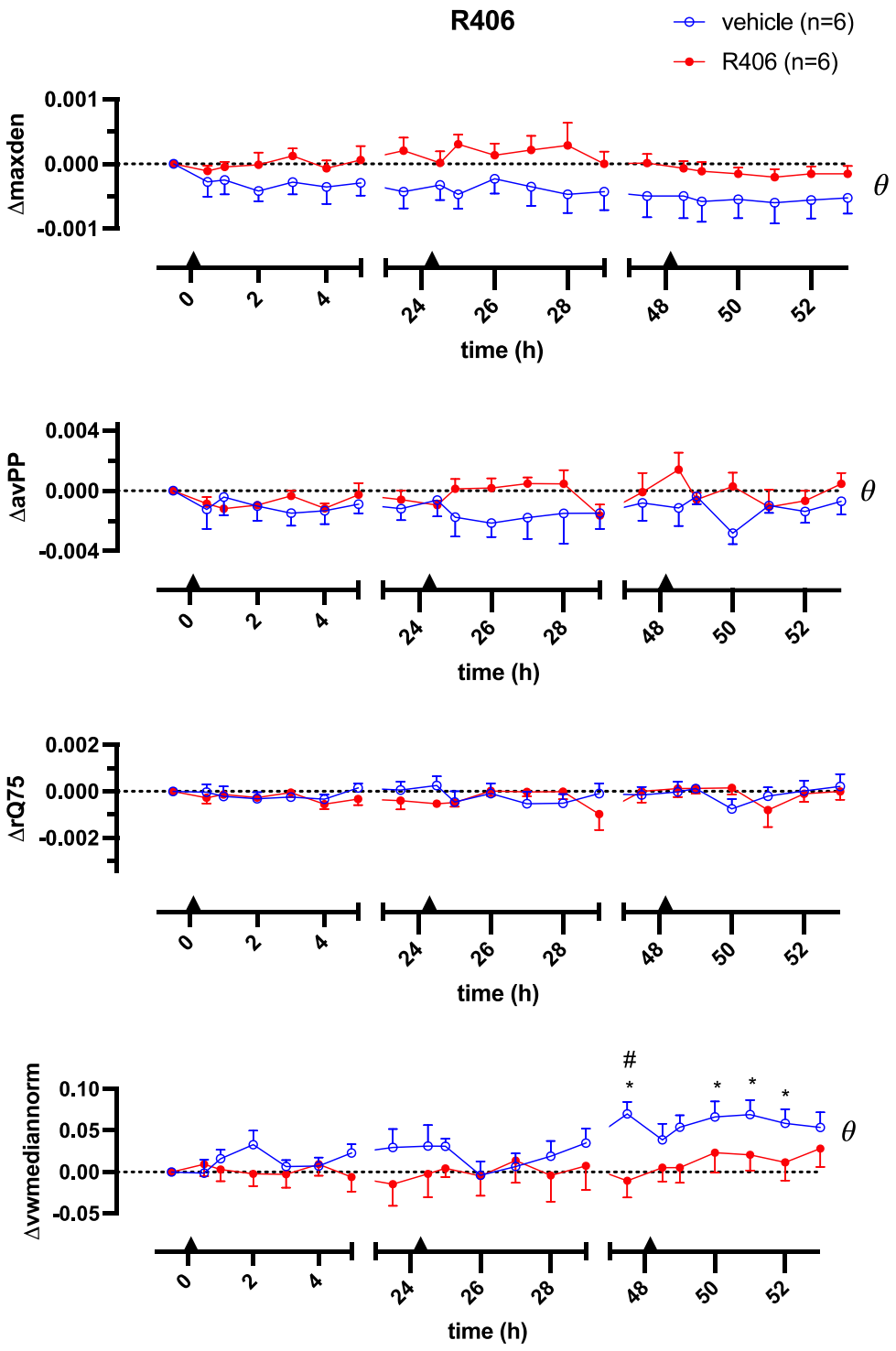

Figure 67: Effect of R406 on selected mesenteric flow SPAR metrics. *Changes in Δmaxden, ΔavPP, ΔrQ75 and Δvwmediannorm of rats dosed with R406 2.5 mg/kg IV (n=6, red, filled circles) and vehicle IV (n=6, blue, open circles). Data were normalised to baseline recording of day 1 for each animal individually. Black triangles on time-axis indicate time of drug administration. Data are presented as mean ± SEM. A two-way ANOVA test was conducted to test for overall differences between two groups (θ = p<0.05), followed by multiple comparison by Sídák to test for differences between the groups at each time point (# = p<0.05) Furthermore, if there was a significant change over time within a group (two-way ANOVA), each timepoint of the group was compared to the group's corresponding baseline (T=-0.5h), by Dunnett (* = p<0.05).*

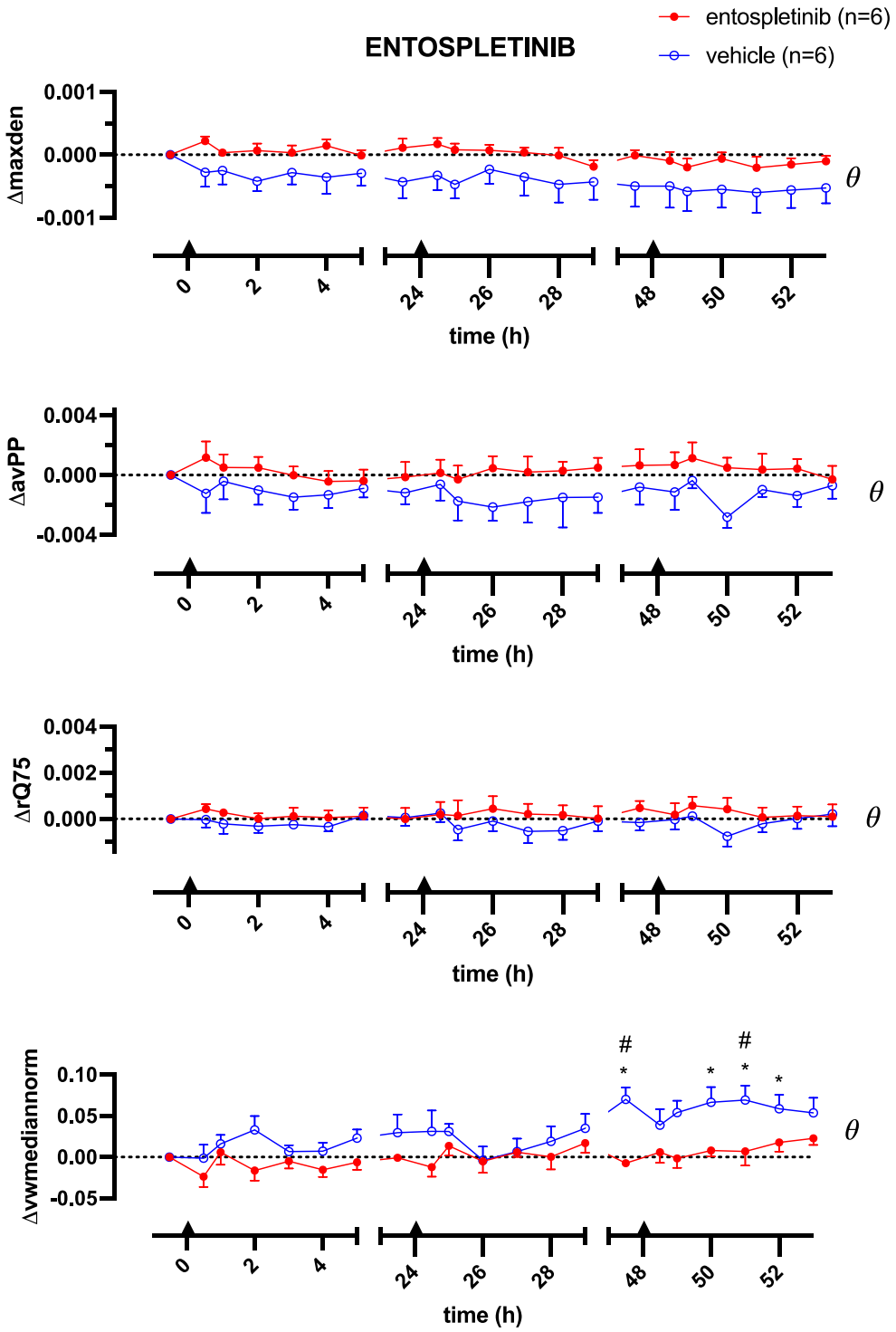

Figure 68: Effect of entospletinib on selected mesenteric flow SPAR metrics. *Changes in Δmaxden, ΔavPP, ΔrQ75 and Δvwmediannorm of rats dosed with entospletinib 0.4 mg/kg IV (n=6, red, filled circles) and vehicle IV (n=6, blue, open circles). Data were normalised to baseline recording of day 1 for each animal individually. Black triangles on time-axis indicate time of drug administration. Data are presented as mean ± SEM. A two-way ANOVA test was conducted to test for overall differences between two groups (θ = p<0.05), followed by multiple comparison by Sídák to test for differences between the groups at each time point (# = p<0.05) Furthermore, if there was a significant change over time within a group (two-way ANOVA), each timepoint of the group was compared to the group's corresponding baseline (T=-0.5h), by Dunnett (* = p<0.05).*

Table 16: Selected mesenteric flow SPAR metrics, drug-induced changes and the interpretation of the metric. *Changes reported in the table were significant between treated and vehicle group (two-way ANOVA, p<0.05). '↑' indicates in increase in the metric, '↓' indicates a decrease in the metric, '=' indicates metric was not significantly changed.*

	Sunitinib	**R406**	**Entospletinib**	**Interpretation of metric**
Δmaxden	↑	↑	↑	↑: decreased waveform variability ↓: increased waveform variability
ΔavPP	↑	↑	↑	↑: increased wave amplitude ↓: decreased wave amplitude
ΔrQ75	↑	=	↑	↑: high density at outer edges of attractor (in wave: flat interbeat interval) ↓: high density at centre of attractor
Δvwmediannorm	↓	↓	↓	↑: increase in rotational symmetry of attractor ↓: decrease in rotational symmetry of attractor (in wave: flat interbeat interval)
Summary of drug effect	Decrease in waveform variability and flattening of interbeat interval in wave (increase in wave reflection)			

5.3.2.4. Aortic flow wave

Selection of metrics

Based on the heatmap of ROC AUCs shown in Figure 70, and following the criteria mentioned in section 5.3.2., 4 metrics were selected to quantify drug-induced changes in the aortic flow waveform; (1) maxrden, (2) dspread3, (3) rQ25 and (4) vwmaxnorm. All metrics (extraction, change in attractor and change in wave) are detailed in the Appendix (section 8.3., Table 26).

1. The metric maxrden has been described in section 5.3.2.2. In brief, this metric is derived from the radial density plot of the attractor and is inversely related to waveform variability.
2. Dspread3 is mentioned above (section 5.3.2.1.) and is inversely related to waveform variability as well.
3. rQ25 is, in a similar way as rQ5 (section 5.3.2.1.) and rQ75 (section 5.3.2.3.), derived from the radial density plot and indicates at which radial position 25% of the data is captured. In the aortic flow wave, this metric was inversely related to wave reflection. This is illustrated by an example in the Appendix (section 8.3., Figure 97).
4. Lastly, the metric vwmaxnorm is derived in a similar way as vwmediannorm (section 5.3.2.3.) from stacked polar maps (detailed in the Appendix, section 8.3. Table 26). In the aortic flow wave, this metric was inversely related to wave reflection (Figure 98 in the Appendix).

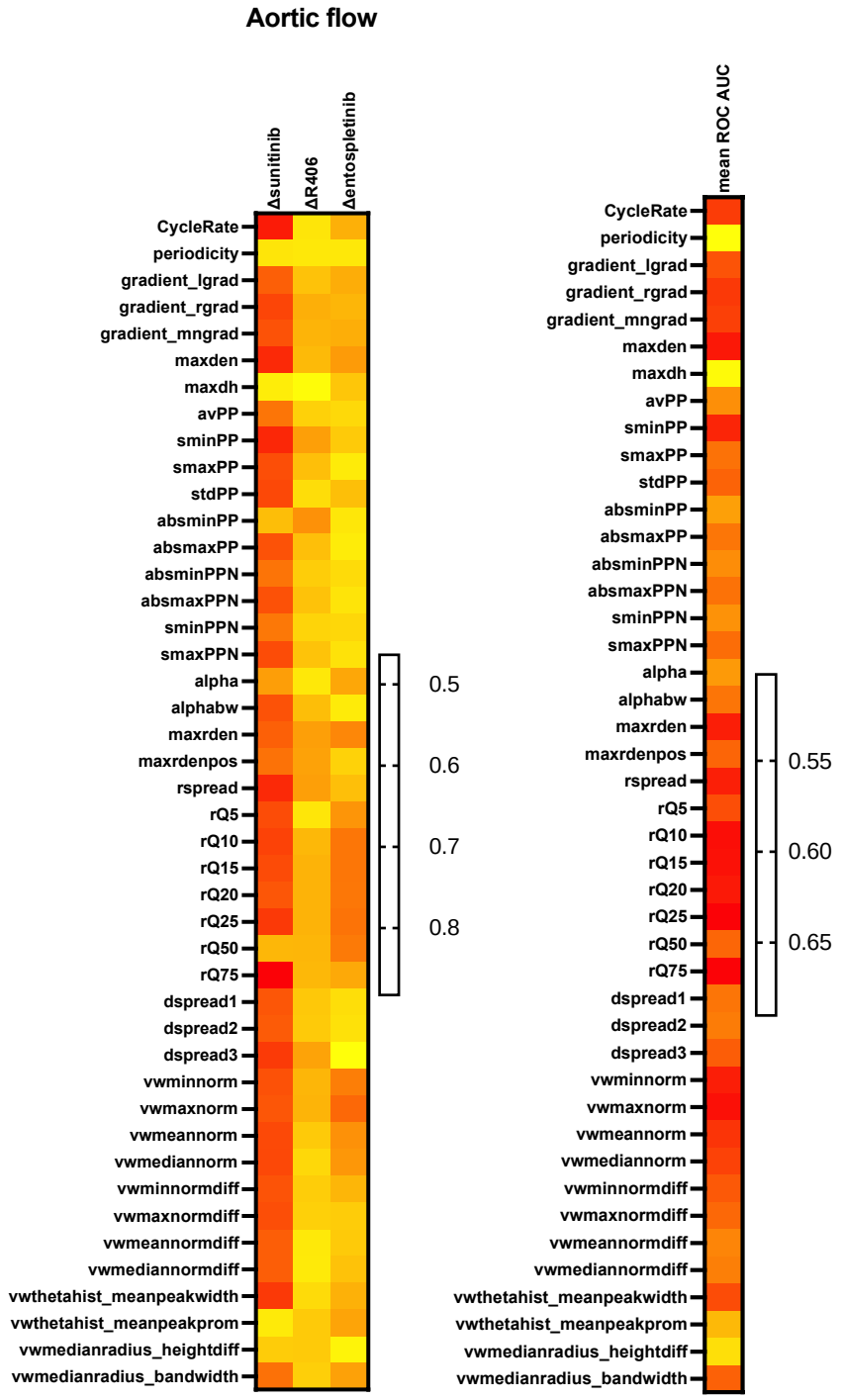

Figure 69: Heatmap of ROC AUC values of aortic flow signals. *All 44 attractor metrics are listed with their ROC AUC value, per drug compared to its corresponding vehicle. The higher the ROC AUC (red in the heatmap), the better the metric can distinguish drug-treated animals from vehicle-treated animals. The lower the ROC AUC (yellow in heatmap), the more overlapping the metric is between the drug-treated and vehicle-treated group. Mean ROC AUCs across all drug-treated groups per attractor metric are presented on the right-hand side.*

Quantitative changes

Using these selected metrics, the drug-induced changes in the aortic flow attractor were quantified and the results are shown in Figure 71, 72 and 73. A summary of the effects of the three compounds on the aortic SPAR metrics, and their link to attractor/waveform changes is given in Table 17.

Figure 71 presents the sunitinib-induced changes in the aortic SPAR metrics. Overall, sunitinib induced clear changes in both metrics related to the waveform variability and wave morphology. Firstly, maxrden was increased following sunitinib administration, compared to vehicle (two-way ANOVA, $p<0.05$). This effect was largest on the second day of dosing (maximum effect 4h after bolus dosing, Šídák test, $p<0.05$) and declined slightly on the last day. Within both groups, no significant changes from baseline were reached. Similarly, dspread3 was increased in the sunitinib group compared to the vehicle group (two-way ANOVA, $p<0.05$), with the maximum effect observed on the second day, 4h after bolus dosing (Šídák test, $p<0.05$) and wearing off slightly on the last day. Again, within either group, no significant differences from baseline were detected over the three days of recording. Related to the waveform morphology changes, both rQ25 and vwmaxnorm were largely attenuated by sunitinib. From the first day, the metric rQ25 was significantly different between the two groups (two-way ANOVA, overall $p<0.05$) and over time within the sunitinib group from baseline (two-way ANOVA, overall $p<0.05$). Within the group, the maximum effect was observed during the last hour of the second day (Dunnett test, $p<0.05$). Between the two groups, the maximum effect was observed at 4h after bolus dosing on the first day (Šídák test, $p<0.05$).

The effects of R406 treatment on the selected aortic SPAR metric are presented in Figure 72. R406 did not changes the variability metrics (maxrden and dspread3) significantly within the group or compared to vehicle. Small effects on the morphology metrics (rQ25 and vwmaxnorm) were detected. A slight increase in rQ25 was observed following R406 dosing, however this effect was only apparent and significant on the first day (two-way ANOVA, $p<0.05$) and did not last on the second and third day of experimentation. The metric vwmaxnorm was increased in the R406 group as well compared to vehicle. This effect was largest and significant on the second day (two-way ANOVA, $p<0.05$). No significant changes were found within either the vehicle group or R406 group.

In Figure 73, the effects of entospletinib on the selected SPAR metric of aortic flow are shown. Entospletinib caused a small but significant increase in maxrden compared to vehicle (two-way ANOVA, $p<0.05$). No changes over time within the group from baseline were detected. In contrast, dspread3 was incrementally decreased by entospletinib over the three days, compared to vehicle. This effect was significant from the third day (two-way ANOVA, $p<0.05$). Again, no changes within either group were significant over time. On the other hand, rQ25 was significantly increased by entospletinib compared to vehicle (two-way ANOVA, $p<0.05$). This effect was clear on the first day, fell back on the second day, and reappeared smaller on the third day. Lastly, also vwmaxnorm was increased following entospletinib treatment. This effect was sustained during the three days, and significantly different from vehicle (two-way ANOVA, $p<0.05$), but not within the group from baseline.

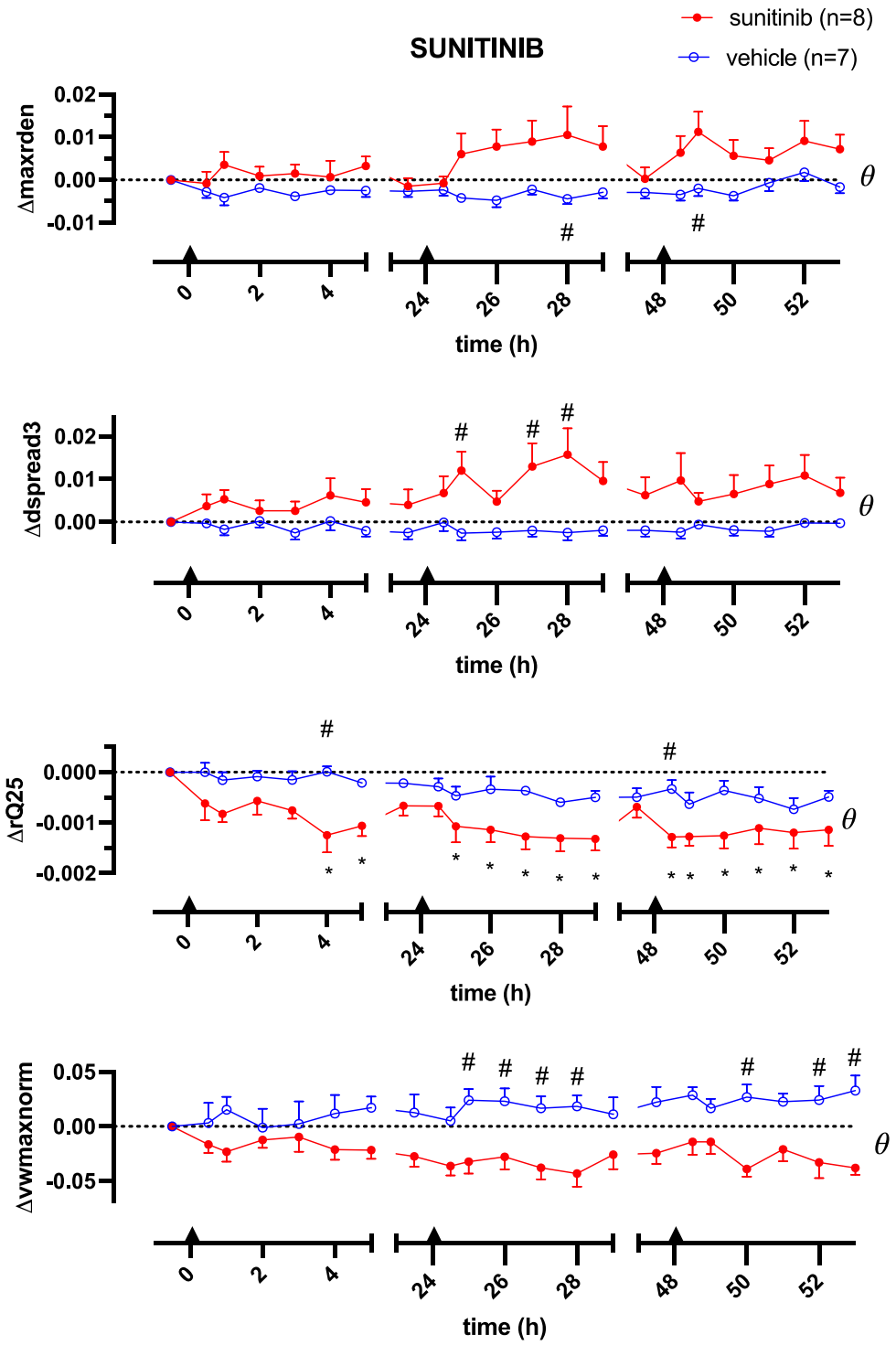

Figure 70: Effect of sunitinib on selected aortic flow SPAR metrics. *Changes in Δmaxrden, Δdspread3, ΔrQ25 and Δvwmaxnorm of rats dosed with sunitinib 16 mg/kg IV (n=8, red, filled circles) and vehicle IV (n=7, blue, open circles). Data were normalised to baseline recording of day 1 for each animal individually. Black triangles on time-axis indicate time of drug administration. Data are presented as mean ± SEM. A two-way ANOVA test was conducted to test for overall differences between two groups (θ = p<0.05), followed by multiple comparison by Sídák to test for differences between the groups at each time point (# = p<0.05) Furthermore, if there was a significant change over time within a group (two-way ANOVA), each timepoint of the group was compared to the group's corresponding baseline (T=-0.5h), by Dunnett (* = p<0.05).*

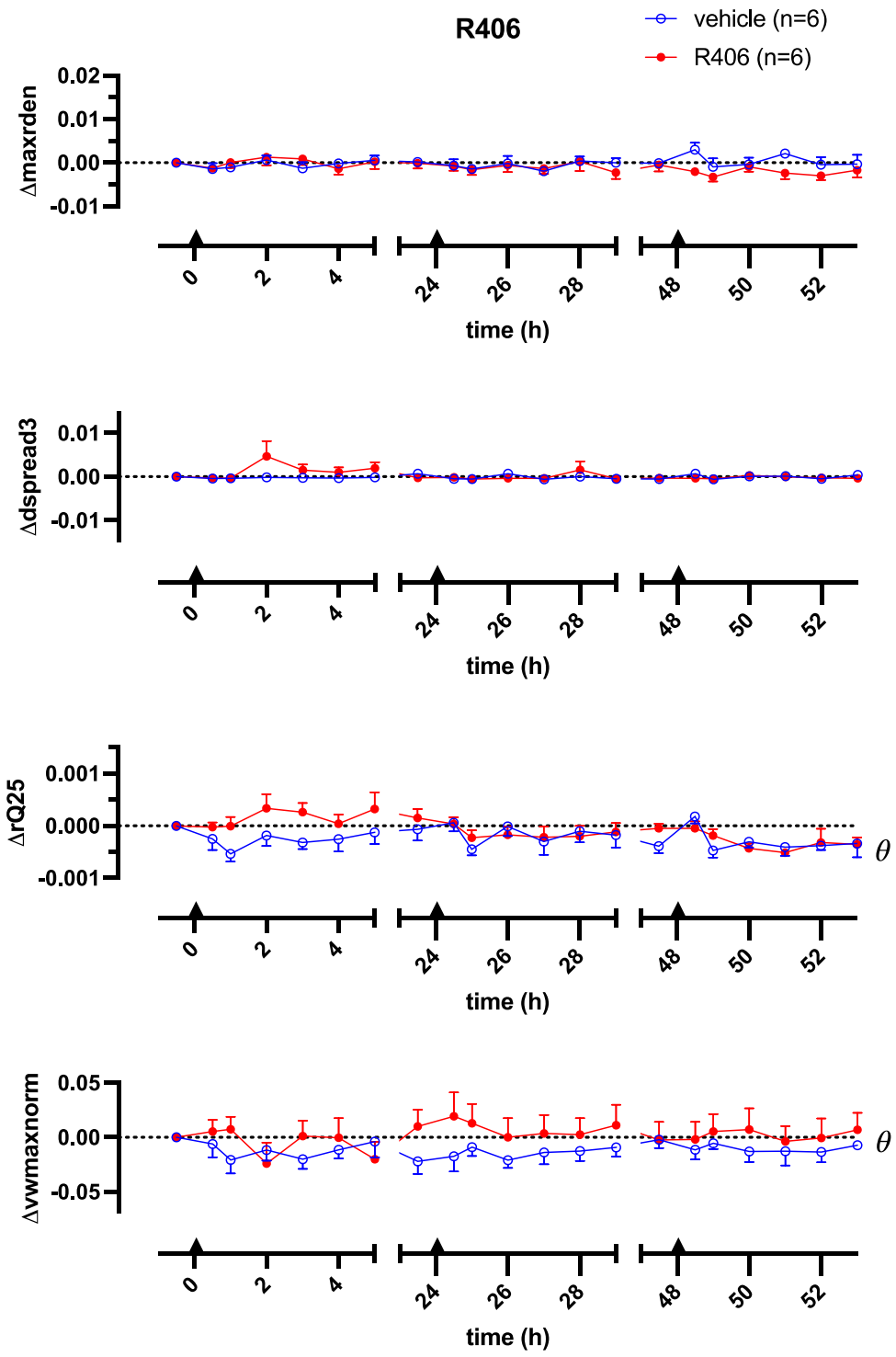

Figure 71: Effect of R406 on selected aortic flow SPAR metrics. *Changes in Δmaxrden, Δdspread3, ΔrQ25 and Δvwmaxnorm of rats dosed with R406 2.5 mg/kg IV (n=6, red, filled circles) and vehicle IV (n=6, blue, open circles). Data were normalised to baseline recording of day 1 for each animal individually. Black triangles on time-axis indicate time of drug administration. Data are presented as mean ± SEM. A two-way ANOVA test was conducted to test for overall differences between two groups (θ = p<0.05), followed by multiple comparison by Sídák to test for differences between the groups at each time point (# = p<0.05) Furthermore, if there was a significant change over time within a group (two-way ANOVA), each timepoint of the group was compared to the group's corresponding baseline (T=-0.5h), by Dunnett (* = p<0.05).*

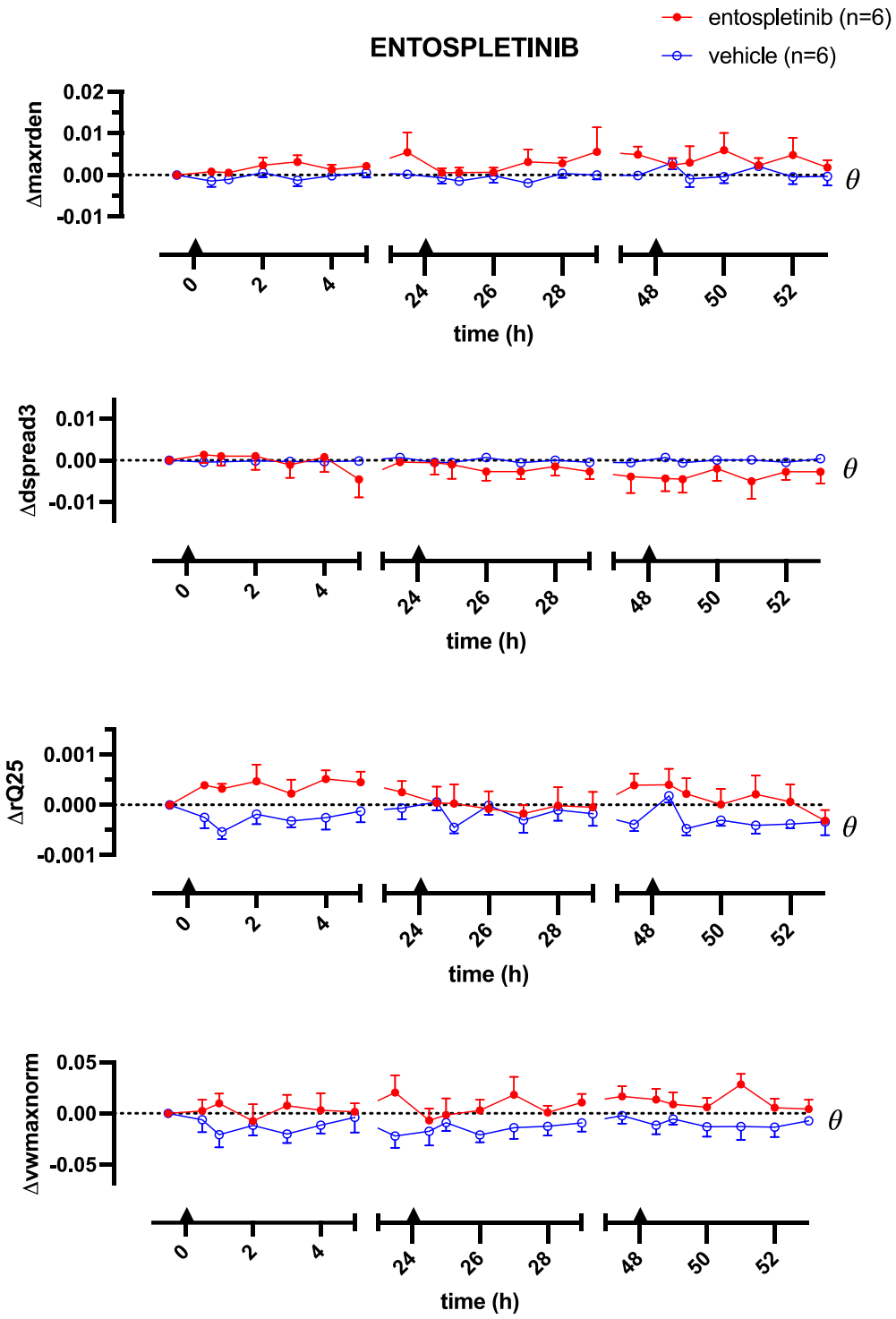

Figure 72: Effect of entospletinib on selected aortic flow SPAR metrics. *Changes in Δmaxrden, Δdspread3, ΔrQ25 and Δvwmaxnorm of rats dosed with entospletinib 0.4 mg/kg IV (n=6, red, filled circles) and vehicle IV (n=6, blue, open circles). Data were normalised to baseline recording of day 1 for each animal individually. Black triangles on time-axis indicate time of drug administration. Data are presented as mean ± SEM. A two-way ANOVA test was conducted to test for overall differences between two groups (θ = p<0.05), followed by multiple comparison by Sídák to test for differences between the groups at each time point (# = p<0.05) Furthermore, if there was a significant change over time within a group (two-way ANOVA), each timepoint of the group was compared to the group's corresponding baseline (T=-0.5h), by Dunnett (* = p<0.05).*

Table 17: Selected aortic flow SPAR metrics, drug-induced changes and the interpretation of the metric. *Changes reported in the table were significant between treated and vehicle group (two-way ANOVA, p<0.05). '↑' indicates in increase in the metric, '↓' indicates a decrease in the metric, '=' indicates metric was not significantly changed. Some drug effects are indicated with a question mark, as these effects were observed visually in the flow wave, but not unambiguously detected by the selected SPAR metrics, as discussed below in section 5.4.2.).*

	Sunitinib	**R406**	**Entospletinib**	**Interpretation of metric**
Δmaxrden	↑	=	↑	↑: decreased waveform variability ↓: increased waveform variability
Δdspread3	↑	=	↓	↑: decreased waveform variability ↓: increased waveform variability
ΔrQ25	↓	↑	↑	↑: high density at outer edges of attractor ↓: high density at centre of attractor
Δvwmaxnorm	↓	↑	↑	↑: decrease in rotational symmetry of attractor ↓: increase in rotational symmetry of attractor
Summary of drug effect	Decrease in waveform variability	No changes in waveform variability	No clear changes in waveform variability	
	Increase in wave reflection?			

5.3.2.5. Summary of SPAR analysis results

The effects of sunitinib, R406 and entospletinib on each selected metric per signal can be found at the end of each section above (Table 14, BP signal; Table 15, renal flow signal; Table 16, mesenteric flow signal; and Table 17, aortic flow signal). Here, in Table 18, a summary of the overall effects on the attractor and/or wave of each drug per signal are given.

Table 18: Summary of drug-effects per signal on the wave and/or attractor. *Effects on the aortic flow morphology are indicated with a question mark, as these effects were observed visually in the flow wave, but not unambiguously detected by the selected SPAR metrics. (BP, blood pressure; RF, renal flow; MF, mesenteric flow; AF, aortic flow)*

	Sunitinib	**R406**	**Entospletinib**
BP	Decreases variability and opens attractor, increases reflection	Increases variability and closes attractor	Increases variability and opens attractor, increases reflection
RF	Decreases variability	Increases variability	Increases variability
MF	Decreases variability and flattening of interbeat interval in wave (increases wave reflection)		
AF	Decreases variability. Increases reflection?	Increases reflection?	Increases reflection?

Overall, sunitinib decreased the wave variability and showed indications of an increase in wave reflection, both in the BP signal and flow signals. R406 induced an increase in waveform variability in the BP and renal flow and decreased the variability of the mesenteric signal. SPAR did not detect large changes in wave reflection of the BP signal following R406 administration, however in the mesenteric and aortic flow, indications of an increase in wave reflection were found. Entospletinib showed an increase in the variability of the BP and renal flow waves. On the other hand, in the mesenteric signal a decrease in waveform variability was detected. Moreover, entospletinib administration showed hints of an increase of reflection of both pressure and flow waves in the SPAR analysis.

5.4. Chapter discussion

This Chapter investigated the cardiovascular effects of sunitinib, R406 and entospletinib in conscious and freely moving rats in the Doppler flowmetry model. First, obtained wave data were assessed using the conventional analysis, looking at MAP, HR and mean conductances in the renal, mesenteric and hindquarter vascular beds. Next, SPAR was used to perform more in-depth analysis of recorded BP and blood flow waves. By conducting this analysis and providing detailed results on entospletinib's and fostamatinib's effects on the blood flow velocities, these studies contributed to the wider understanding of the subtle cardiovascular safety liabilities that might occur with fostamatinib and entospletinib.

5.4.1. Doppler experiments and conventional analysis

For all three compounds, animals were dosed once daily, using a bolus containing half of the dose/day, followed by a one-hour infusion containing the other half of the dose/day. This protocol was followed for 3 consecutive days.

In this Chapter, two different vehicles were used as control groups. The sunitinib group used the following vehicle: 5% propylene glycol, 2% Tween 80 in sterile saline. R406 and entospletinib solubility was found optimal in a vehicle containing 5% ethanol, 20% PEG400 in water, with adjusted pH to neutral values (pH 6 – 8). Interestingly, in both vehicle groups a trend of increasing MAP and decreasing mesenteric and aortic VC was observed. This effect has been observed previously, especially in the aortic flow (Carter et al., 2017) and is potentially related to stress-induced vasoconstrictions (Hayashi et al., 2006; Zukowska-Grojec et al., 1996), as animals were single-housed during experimentation and recovering from surgery. Nonetheless, with the exception of one time-point in the vehicle group of the sunitinib study, the CV parameters were not significantly changing within the vehicle groups from baseline, therefore relevant comparisons between vehicle- and drug-treated groups could still be performed.

Firstly, the effects of sunitinib on MAP, HR and VCs in the three vascular beds were presented (section 5.3.1.1., Figure 52). As mentioned, this study was performed by Dr. Edward Wragg and included here to display the response typically expected with a compound inhibiting VEGFR2. Indeed, sunitinib caused a large increase in MAP and decrease in HR, as previously reported with this drug (Isobe et al., 2014; Lankhorst et al., 2015) and in general with VEGFR2-inhibitors (Carter et al., 2017; S. L. Cooper et al., 2019; Touyz et al., 2018), and reflected clinical responses (Catino et al., 2018; Zhu et al., 2009). MAP increased incrementally over the three days of experimentation, reaching a 23.5 mmHg increase from baseline. This is likely the result of accumulation of sunitinib in the plasma, related to the dosing schedule and its plasma half-life as discussed in Chapter 3, section 3.4.2. The observed decrease in HR is likely the consequence of the elevated BP, as a result of the activation of the baroreflex (Kougias et al., 2010). Associated with the increase in MAP, a significant reduction in the VC of the renal, mesenteric and hindquarters vascular bed was observed. In particular, the decrease in aortic flow velocity was significant within 5h after bolus-dosing on the first day, compared to vehicle. The mesenteric flow velocity was rapidly reduced as well. Effects in the renal bed were smaller, nonetheless also significant. All reductions of VC grew larger over the three days, likely the result of accumulating plasma concentrations, and contributing to the overall increase in MAP. Again, these observations were consistent with previously reported VEGFR2-inhibitor induced regional vasoconstrictions (Carter et al., 2017; Kappers et al., 2012).

Next, the effect of the two Syk-inhibitors was investigated in the Doppler model. Both in the R406-group and entospletinib-group an outlier was identified in the mesenteric signal (ROUT-methods, Figure 54 and 56). To ensure reported results were physiologically relevant, these data were excluded. This brought the number of animals per group down to n=5. According to power calculations performed by Prof. Jeanette Woolard using the NC3Rs EDA (experimental design assistant) tool, a minimum of 4 animals per group was sufficient for a power calculation with 80% confidence (the minimum) to detect changes of 10 mmHg (and other clinically meaningful differences) between two groups in the Doppler model. Therefore, even when excluding these outliers, the data obtained should be sufficient to perform statistical tests and obtain valuable results. Nonetheless, it would have been worthwhile to include one more animal in both groups, to have a powered study of n=6 for all signals as was the originally set goal.

The effects of fostamatinib are shown in Figure 53 (section 5.3.1.2.). To ensure the presence of the active metabolite in the blood, rather than the prodrug, R406 was used to dose IV. Based on literature (Lengel et al., 2015; M. Skinner et al., 2014), a dose of 2.5 $mg.kg^{-1}.day^{-1}$ was selected with the aim to obtain plasma levels that are representative for the plasma concentrations in patients treated with fostamatinib in clinic. With this concentration, an upwards trend in MAP was observed with a similar magnitude of the one observed in the telemetry studies of Chapter 3. However, as discussed above, in the vehicle group a similar elevation of MAP was observed and the effects of R406 were not significantly different from this. Moreover, no change in HR or % mesenteric VC was detected. In the renal vascular bed, a small decrease in VC was observed over time (significantly different between the two groups) and also in the hindquarters, a reduction of VC was found (significantly different within the R406-group compared to baseline). These subtle changes indicated R406-induced vasoconstrictions in those beds, consistent with literature showing a femoral artery constriction following R406-treatment (M. Skinner et al., 2014).

Lastly, the effects of entospletinib on the three VC was investigated. Again, the dose selection of entospletinib was based on literature (Currie et al., 2014) and aimed to present relevant concentrations in patients treated with this compound. Although this drug caused a small decrease in MAP and increased HR slightly, the VC in kidney, mesentery and hindquarters was not affected.

In summary, this study showed that R046 had similar effects on the cardiovascular parameters as sunitinib, but in a smaller extend, as only the renal and aortic VC were affected and not BP, HR or the mesenteric VC. Entospletinib caused subtle changes in HR and MAP, however these effects were of a much smaller magnitude than the ones observed with sunitinib and did not sustain over the three days of experimentation. Furthermore, entospletinib did not affect any of the measured blood flow velocities significantly.

5.4.2. Flow waveform analysis

Following the conventional wave analysis (MAP, HR and %VC), raw BP wave and blood flow wave data were extracted and analysed in SPAR. This analysis produced additional insights into the subtle drug-induced changes in waveform variability and wave morphology, that were overlooked in the conventional wave analysis. Below, the application of SPAR per signal is discussed (section 5.4.2.1.), followed by a description and interpretation of how the three compounds affected the selected SPAR metrics (section 5.4.2.2.).

5.4.2.1. Discussion of the SPAR metrics: fit to quantify blood flow wave changes?

Blood pressure signal

Overall, the metrics selected to assess the changes in BP waveform morphology and variability were suitable to detect such effects. Firstly, changes in two metrics related to the waveform variability, dspread3 and maxden, were quantified. These metrics are calculated in a different way; maxden is determined from a single bin of the attractor, while dspread3 reports on the overall density of the attractor. Nonetheless they are both inversely related to wave variability and did indeed change consistently. From the morphology metrics selected, rQ25 showed a more consistent course and larger changes in the sunitinib group, compared to vwmedianradio_heightdiff. The latter was less stable overall and showed some seemingly random changes over time. Therefore, rQ25 is potentially a better metric to quantify BP wave changes in the Doppler model.

The quality of the BP signal obtained in this model is presumably not ideal for in-depth wave analysis for the following reason. A common issue in the Doppler flowmetry model is the dampening of the BP signal over time, as small blood clots form at the fluid-filled pressure catheter and decrease the patency of the arterial line. This dampening of the signal usually does not affect the calculation of MAP majorly, but naturally affects the morphology of the wave drastically as the detailed pulse profile is lost. An example is shown in Figure 74. To prevent this loss of patency of the catheter and maintain a good quality of the signal, the arterial line was flushed with heparin during experimentation. Moreover, efforts were made to select windows of waves where little pressure signal dampening occurred to generate attractors. However, given these fluctuations in quality of the signal, it was challenging to

identify drug-induced wave changes unrelated to signal diminution. As the signal dampening was a trend that was seen in a major part of the animals, it is important to note that some SPAR effects observed in these studies may have little physiological relevance, as morphology changes might be artefacts rather than true drug-induced effects. Related to this, some metrics (e.g. rQ5 in Figure 59) were significantly attenuated over the course of three days in the vehicle group. This drift in waveform morphology could be an indication of such reduction of signal quality. Another possible explanation for these changes of metrics in the vehicle groups could be stress-related, as animals were single-housed during experimentation and recovering from surgery, which can affect cardiovascular parameters as mentioned above (section 5.4.1.).

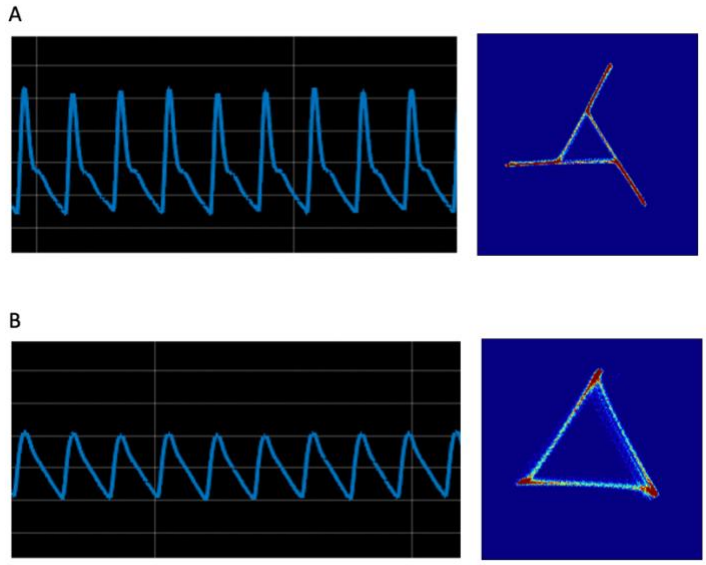

Figure 73: Example of signal dampening and effects on the attractor. *Waveforms and associated attractors are taking from a recording in the same animal on the same day.* ***(A)*** *shows a good quality BP signal, with sharp peaks and clear effects of wave reflection (dicrotic notch).* ***(B)*** *shows a dampened signal, with an overall smaller magnitude and lacking subtle wave reflection effects on the downstroke. This dampening of the signal had obvious effects on the shape of the attractor.*

Despite these challenges, the observations made from the BP waves in this Chapter were roughly in line with results from previous Chapters, as discussed below in more detail (section 5.4.2.2.).

Renal flow signal

The renal signal displayed a lot of natural variability. This was observed when looking at the flow waves directly, but also noticeable from the very blue colour and little defined edges of the attractors (e.g. Appendix Figure 92 and 93). This high variability has been reported previously, both in rats (Pires et al., 2001) and human (Krejza et al., 2005). Given this high degree of variability, small drug-induced changes in the waveform morphology likely got lost and were not consistently detectable as they were overwhelmed by naturally occurring changes. Indeed, the majority of SPAR metrics related waveform morphology were not suitable to detect drug-induced changes in the renal signal, as shown in the heatmap in Figure 62. On the other hand, a couple of metrics related to changes in variability stood out; maxrden, dspread1 and bandwidth displayed ROC AUC values between 0.60 and 0.70. As detailed in section 5.3.2.2., maxrden is inversely related to wave variability and dspread1 and the bandwidth are directly related to the variability. These metrics indeed detected drug-induced changes. Potentially, an increase in wave variability could be related to a small physiological change in the cardiovascular system, while a decrease in wave variability could be indicating a large disruption of the blood supply to the kidney and subsequent activation of auto-regulatory mechanisms, leading to a controlled environment and little wave variability. This is further discussed below, in section 5.4.2.2.

Mesenteric signal

To quantify the variability changes in the mesenteric flow wave, maxden was selected, which was a good indicator for wave variability changes in this study. Furthermore, the mesenteric Doppler signal showed less natural variability than the renal signal, therefore changes in morphology metrics were less variable and could be linked to changes in wave morphology. Three metrics to quantify morphology changes were selected: avPP, rQ75 and vwmediannorm. These three metrics showed large differences between the sunitinib- and vehicle-treated groups and appeared suitable metrics to detect an increase in wave reflection in the mesenteric wave.

With several metrics, in particular vwmediannorm, large changes in metrics in the vehicle group were observed. Subsequently, drugs were often offsetting that effect rather than directly changing the metric from baseline. This observation was made especially in the R406 and entospletinib studies. For example, in Figure 68, a significant increase in vwmediannorm within the vehicle group was detected. Another example is the changes in metric maxden; in vehicle group in Figure 68, a large decrease in maxden was present (indicating an increase in wave variability), while the drug treatment nullified that effect and resulted a stable Δmaxden around baseline throughout the three days. These changes in the SPAR metrics over time in the vehicle-treated animals could indicate two possibilities: (1) an increase in variability suggesting that the animals had a low variability at the beginning of experiment and needed perhaps more time to recover from surgeries before the start of study, or (2) animals were exposed to stress (e.g. due to single-housing) during three days of study and this directly affected the waveforms. Ideally no large drifts would be observed in the metrics in vehicle group, so that effect observed in drug-treated group can be related to true drug-induced effects alone, instead of the changing metric over time combined with the drug-induced effects. A potential solution to improve these drifts from baseline would be to use a telemetry set-up to detect the flow waves. This concept is described more in detail below (section 5.4.3.).

Aortic (hindquarters) signal

The flow wave recorded in the abdominal aorta (to hindquarters) generally showed very pronounced effects of wave reflection, as shown by the flow waves in the Appendix, Figure 97. Therefore, associated attractor showed a slightly different morphology, displaying large loops (Figure 97) rather than thin arms. Given that the waves and attractor had such different morphologies to start with, compared to the mesenteric signal for example, extra care was taken when interpreting the physiological meaning of each selected metric.

To quantify changes in wave variability, two metrics were selected: maxrden and dspread3. Both these metrics are inversely related to wave variability and were therefore expected to change in the same direction within treatment groups. This was the case for sunitinib (Table 17). However, these two metrics yielded contradicting results regarding the effect of entospletinib. An increase in maxrdens indicated a decrease in variability, while the decrease in dspread3 suggested an increase in variability. Despite the fact that these changes were indicating opposite variability changes, the magnitude of the entospletinib-induced changes was small compared to the effects observed in the sunitinib group and perhaps these contradictory observations were of little physiologically relevance.

To quantify the wave morphology changes, rQ25 and vwmaxnorm were selected, and showed significant changes, linked to a vasoconstriction, in the sunitinib group. Entospletinib-induced changes in the morphology metrics rQ25 and vwmaxnorm were however hard to link to attractor changes. As described in section 5.3.2.4., in the sunitinib-treated animals a decrease in these metrics was linked to an increase in wave reflection, thus to a vasoconstriction in the downstream vascular bed. With entospletinib, an increase in these metrics was observed. The increase in rQ25 was linked with opening of attractor and lower density in the centre of the attractor, as expected (Figure 75). However, when looking at the raw waveform, this was not associated with a decrease in wave reflection. In contrary, a flattening of the interbeat interval was observed (Figure 75B), indicating an increase in wave reflection. In summary, both an increase and decrease in rQ25 could be linked to an increase in wave reflection, therefore this metric is likely not ideal for detection of waveform changes of aortic flow.

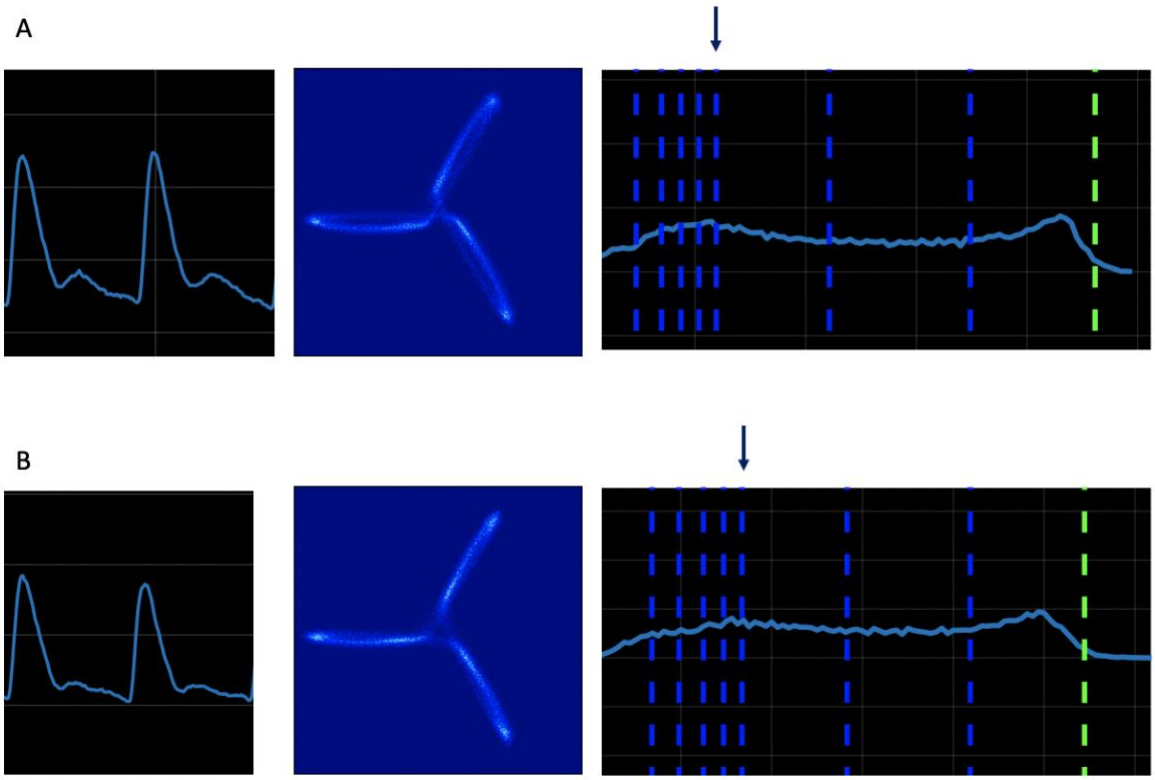

Figure 74: Example of increase in metric rQ25 in the aortic flow wave following entospletinib administration. (A) *shows the wave, attractor and radial density plot of an animal during the baseline recording.* ***(B)*** *shows the wave, attractor and radial density plot of the same animal, 5h after entospletinib-bolus dosing. The increase in rQ25 (0.0023833 units in (A) versus 0.003539 units in (B) was linked with a decrease in density in the centre of the attractor. However, in the waveform, an increase in wave reflection (demonstrated by flatter interbeat interval) was observed, indicating a vasoconstriction downstream of the aortic probe.*

Similarly, changes in vwmaxnorm in the entospletinib group were hard to link to attractor changes and waveform changes for the following two reasons: (1) changes within the group were small and the increasing effect on vwmaxnorm was due to offsetting of the decrease of this metric in the vehicle group, rather than a direct increase in the entospletinib group, and (2) waves had variable baseline morphologies and therefore it was challenging to identify trends in wave morphology changes within the group.

Overall, the selected metrics were not particularly useful to detect changes in the aortic wave here. Although these metrics were initially selected based on their good ROC AUC values (section 5.2.3.4.), perhaps other (new) attractor metrics would be better to quantify subtle drug-induced changes as observed visually in the waves. Assessing the effect of a vasodilator on the aortic flow wave and related SPAR metrics would be a helpful additional study, providing clarification in the relationship between the metrics and physiological changes in the cardiovascular system.

Summary

In summary, SPAR was able to detect changes in the four waves discussed in this Chapter, however caution is required when interpreting changes in its metric. Given that a large amount of data became available following this analysis, more work is needed to pinpoint relevant metrics and clarify their interpretation. Vasoconstrictions affected the flow waves differently than BP, therefore not all interpretation of the SPAR metrics in BP waves could be transferred to the blood flow waves. For example, an increase in wave reflection of a blood pressure wave was correlated to the opening of an attractor. In contrast, an increase in wave reflection was linked to the closing of the attractor in the mesenteric flow. Similarly, flows recorded at different positions in the vasculature showed distinct differences in morphology and in morphology changes following drug treatment, hence each individual metric should be properly validated per signal type. In this study, the appropriate controls to perform such validation were lacking as for example no compounds with vasodilatory actions were included. In particular the interpretation of aortic flow metrics should be conducted with caution as for now.

Nonetheless, the findings in this Chapter served as a proof of principle that SPAR is a feasible method for in-depth wave analysis of the blood flow waves. The method has potential to be further developed and validated for in-depth analysis to provide detailed information on blood flow wave changes. Optional further steps for validation of SPAR in the Doppler model are detailed below (section 5.4.3).

5.4.2.2. Discussion of drug effects

Below, the drug-induced effects on SPAR metrics are discussed.

Sunitinib

In contrast to findings from Chapter 4, where sunitinib caused little changes in the BP SPAR metrics, here clear and significant changes were observed in the BP SPAR metrics. This is most likely due to the difference in dosing schedule between the two studies; in Chapter 4, animals were orally dosed at 7 $mg.kg^{-1}.day^{-1}$, while in this Chapter, animals received 16 $mg.kg^{-1}.day^{-1}$ via an IV line. This larger dose was linked with large decrease in waveform variability and an increase in wave reflection, indicating a general vasoconstriction (Figure 59 and Table 14). Furthermore, from the SPAR metrics extracted from the mesenteric flow similar conclusions were drawn; the changes in avPP, rQ75 and vwmediannorm indicated a flattening of the interbeat interval of the flow wave, indicating a vasoconstriction in the mesenteric bed (Figure 67 and Table 16). Furthermore, a decrease in the variability of the renal signal was observed following sunitinib dosing (Figure 63 and Table 15). This is presumably the result of the large increase in BP and decrease of renal VC induced by sunitinib, as demonstrated by the conventional analysis (Figure 52). To maintain a constant blood flow supply, several autoregulatory mechanisms are activated, such as the myogenic and tubuloglomerular feedback (Carlström et al., 2015; Post & Vincent, 2018). These autoregulatory changes aim to control the blood flow to the kidney, therefore permit little changes in the blood flow velocity and decrease the variability of the renal flow wave. Moreover, renal toxicity, in particular proteinuria and kidney disfunction, is a reported adverse drug effect of VEGFR2-inhibition (Hayman et al., 2012; Van Wynsberghe et al., 2021; Zhang et al., 2014), which could contribute as well to changes in waveform variability. Overall, this decrease in waveform variability was indicating stress on the cardiovascular system, as is indeed expected with sunitinib (Catino et al., 2018; Lankhorst et al., 2015; Van Wynsberghe et al., 2021). Lastly, in the aortic waves a decrease in waveform variability and increase in wave reflection was observed as well, once more indicating a regional vasoconstriction (Figure 71 and Table 17).

In summary, the SPAR analysis of the sunitinib study indicated (1) an overall decrease in waveform variability, indicating stress on the cardiovascular system and (2) an overall (from

BP) and regional (from mesenteric and aortic flow) vasoconstriction. These effects were the anticipated response of this VEGFR2-inhibitor (Carter et al., 2017), and in line with results so far in this thesis. Indeed, in Chapter 3, telemetry studies showed a sunitinib-induced increase in BP, and the conventional analysis in this Chapter (section 5.3.1.) reported vasoconstrictions in all three vascular beds assessed.

R406

Overall, the effects on SPAR metrics observed following R406 dosing, were minimal. A decrease in the variability in the BP wave and renal flow wave was observed (Table 14 and 16). These effects were opposite to the ones observed with sunitinib, suggesting that R406 did not disrupt the balance of cardiovascular system to the same extent as sunitinib did. In contrast, the morphology variability of the mesenteric flow was increased (Table 16) and aortic flow variability was not affected (Table 17). Furthermore, the morphology metrics of the flow waves were little affected by R406-treatment (Table 14, 16 and 17). The mesenteric attractors and wave changed in a similar way as sunitinib, indicating a vasoconstriction in the mesenteric bed. This effect was not detected by the conventional analysis (section 5.3.1.2.) and indicated that SPAR was able to detect subtle effects on the mesenteric bed that were overlook in the VC analysis. On the other hand, the metrics extracted from the aortic flow changed in the opposite direction as observed with sunitinib. As detailed above (section 5.4.2.1.), both an increase and decrease in these aortic metrics were linked to an increase in wave reflection, therefore theoretically, these observations were in line with the small vasoconstriction observed following the conventional analysis of the aortic VC.

As stated before, the dose of R406 was chosen based on literature to reflect plasma concentrations of patients undergoing fostamatinib treatment. However, in typical preclinical safety studies, the dose of the test compound includes and exceeds the primary pharmacodynamic or therapeutic range (International Conference on Harmonisation, 2001). These doses often reach 10x the expected clinical plasma concentration. Perhaps a higher dose (e.g. 5 mg/kg (M. Skinner et al., 2014), i.e. double the dose used in this study) would have produced more clear results regarding the regional effects of R406.

Entospletinib

Lastly, the effects of entospletinib on the SPAR metrics were investigated. Even though entospletinib didn't affect the renal, mesenteric or aortic VC (section 5.3.1.3.), in-depth blood flow wave analysis using SPAR implied that entospletinib affected the flow velocity waves. Entospletinib caused an increase in wave variability in all signals, except for the mesenteric flow. Similar as with R406, this increase in variability of the waveform indicated rather subtle effects on the cardiovascular system, slightly increasing the variability of the waves. In terms of morphology, entospletinib changed all metrics in the same direction as observed with sunitinib (Table 14, 16 and 17). Although this effect was not detected in the conventional VC analysis, this observation indicated that entospletinib displayed vasoconstricting effects overall (conclusion from BP signal) and regionally (conclusion from mesenteric and aortic flow signal). Thus, consistent with the SPAR analysis in the telemetry studies (Chapter 4), the results from the SPAR analysis of Doppler flowmetry study suggested that entospletinib exerted subtle effects on the vasculature.

Summary

Overall, the SPAR analysis performed in this Chapter provided additional insights into the cardiovascular safety profile of the Syk-inhibitors. Even though no changes in mesenteric VC were observed following R406 administration, SPAR metrics indicated a regional vasoconstriction in the mesenteric bed with this compound. This finding supports literature describing VEGFR2-inhibition as the main contributor to fostamatinib-induced hypertension (M. Skinner et al., 2014). Similarly, entospletinib did not affect the VCs but showed clear indications of increased wave reflection in the SPAR analysis, again in line with results from Chapter 4 and suggesting subtle vasoconstricting effects in both the mesenteric and hindquarters bed. In summary, as far as the selected SPAR metrics were interpretable and changed consistently within each group of drug treatment, this analysis supported conclusions from pervious Chapters that R406 and entospletinib showed effects of vasoconstriction. Hence, SPAR is a method with potential to detect subtle changes in the cardiovascular system that are overlooked when assessing mean VCs only.

5.4.3. Limitations of this study and further directions

As mentioned throughout the discussion, several limitations have impeded this study. Firstly, no compounds with vasodilating effects were included. Investigating how vasodilators affect the SPAR metrics in the Doppler model would potentially shed light on how the flow attractors metrics are related to changes in the waveform. This would aid in understanding the metrics' interpretation, in particular for the aortic signal, and assist in the further validation of the SPAR method.

Another issue in this study was related to the quality of the wave signals. Firstly, the dampening of the BP wave over time complicated the SPAR analysis of this signal. Additionally, both in the BP metrics and flow metrics, large drifts over time in morphology metrics were observed in the vehicle-treated animals, potentially indicating stress of the animals. Both these issues could be prevented by using a radiotelemetry set-up to measure the flow waves. Telemetry methods using a solid-state tip in the blood pressure catheter are available. Such solid-state tips measure BP directly, instead of indirectly as the fluid-filled tip, and do not suffer from signal diminution as often (AD Instruments & Williams, 2022). Moreover, using a telemetry set-up would reduce the stress-exposure to the animals, as (1) animals can be chronically instrumented and given sufficient time to recover from surgery before the start of the experiment and (2) animals can be freely moving and housed with a cage mate. This is in contrast to the Doppler model, where experiments started within 24h post-surgery and rats were single-housed and tethered during experimentation. Indeed, telemetry methods using transit-time flow probes to record blood flow waves are currently being developed (Arnall et al., 2017; Brijs et al., 2019).

In this study, doses were selected to reflect plasma concentrations in patients undergoing therapy with these compounds. This resulted in a dose of 2.5 $mg.kg^{-1}.day^{-1}$ for R406 and 0.4 $mg.kg^{-1}.day^{-1}$ for entospletinib, which were considerably lower concentrations than used for sunitinib (16 $mg.kg^{-1}.day^{-1}$). Administering higher dose of R406 and entospletinib would have mirrored typical safety pharmacology studies, where doses usually exceed the therapeutic range (International Conference on Harmonisation, 2001). Moreover, the lack of clear SPAR results of R406 could be connected to the low dose used and administration of higher doses would perhaps have yielded more apparent changes induced by R406. Lastly, it would be helpful to understand if higher doses of entospletinib displayed an effect on the MAP or VC.

Lastly, a couple of factors compromised the interpretation of the SPAR metrics for the flow signal. A lot of inter-animal variability was observed in the aortic and renal flow waves, for example indicated by smaller mean dspread3 values in the renal signal (0.001) compared to the BP signal (0.028) and larger mean dspread1 values (0.82 in renal signal versus 0.68 in BP signal). This high variability impeded the visual detection of wave reflection effects to link those to SPAR metric changes. Therefore, a useful follow-up analysis would be to assess simulated flow waves in SPARKS. Using computational data presents the opportunity to tweak certain parts of the wave and investigate subsequent effects on the attractors, facilitating the investigation of single components of the wave, rather than deciphering a constantly changing wave from an animal (Alastruey et al., 2016; Willemet & Alastruey, 2015). As such databases are publicly available (Peter H. Charlton et al., 2019), this is an evident next step to further validate the SPAR model for its application on blood flow velocity waves. Furthermore, performing multivariate analysis could strengthen the potential application of SPAR, as combining several attractor metrics with conventional parameters could probably characterise the cardiovascular effects of a compound more comprehensively than either analysis alone, and aid in classifying the safety risk of new drugs.

5.5. Chapter conclusion

The aim of this Chapter was to follow-up on the findings of Chapter 4, where subtle changes in waveform morphology were found following fostamatinib or entospletinib administration in rats. Here, the cardiovascular risk of these Syk-inhibitors was further characterised by assessing the two compounds in the pulsed Doppler flowmetry model and determining their effect on the renal, mesenteric and aortic blood flow velocity. The conventional analysis, looking at VC, was performed, followed by in-depth analysis of both pressure and flow waves. Furthermore, the sunitinib study performed by Dr. Edward Wragg was included here, serving as a reference point for the typical responses obtained with a VEGFR2-inhibitor.

Results showed that R406 did not affect the HR, MAP or mesenteric VC, but displayed small decreases in the VC to the renal and hindquarters beds. These decreases in VC mirrored results of sunitinib but had a smaller magnitude. Changes in the variability of the renal flow wave, and in the morphology of the mesenteric and hindquarters flow waves were reported by SPAR analysis. Even though the interpretation of these results was sometimes ambiguous, overall the changes indicated a vasoconstriction following R406 administration.

Entospletinib showed small responses in HR and MAP but did not affect the VC in any vascular bed in the conventional analysis. However, SPAR detected entospletinib-induced changes in both the pressure wave and the flow waves, similar to the ones observed with sunitinib. Again, these effects were generally smaller than the ones of sunitinib but nonetheless suggested that entospletinib displayed some subtle vasoconstricting effects in the cardiovascular system.

From the results in this Chapter, SPAR seemed a suitable method to perform detailed analysis of the blood flow waves recorded in the Doppler model and provided insights into the cardiovascular safety of entospletinib that went undetected in the conventional analysis. Yet more validation of the method is needed before interpretation of these results can be performed confidently and conclusive evidence can be provided.

6. RESULTS CHAPTER 6: *IN VITRO* CHARACTERISATION OF VEGFR2 INHIBITION BY SYK INHIBITORS

6.1. Chapter introduction

The main driver of fostamatinib-induced hypertension is VEGFR2-inhibition (Rolf et al., 2015; M. Skinner et al., 2014). Entospletinib, one of the second generation Syk inhibitors, is more selective (Currie et al., 2014; D. Liu & Mamorska-Dyga, 2017). This second compound has been suggested to have a more rigid chemical structure, and is therefore structurally more restricted to a conformation that does not fit into the kinase domain of VEGFR2 (Currie et al., 2014). So far, no VEGFR2-related cardiovascular safety liabilities have been reported in Phase I and Phase II clinical trials of entospletinib (Burke et al., 2018; Danilov et al., 2020; Lam et al., 2021; Morschhauser et al., 2021; J. Sharman et al., 2015).

VEGFR2 is expressed on the cell surface of endothelial cells (EC), lymphatic endothelial cells, adipocytes and several epithelial cell types and acts as the key regulator in EC proliferation and migration (Ferrara, 2004; Holmes et al., 2007; Koch et al., 2011). In this way, VEGFR2 plays an important role in angiogenesis and permeability changes of the vasculature (Ferrara, 2004; Holmes et al., 2007; Koch et al., 2011). In oncology, VEGF and its receptor are well known to be involved in tumour development and metastasis (Carmeliet, 2005; Ferrara & Adamis, 2016; Gotink & Verheul, 2010). The activation of the VEGF/VEGFR2 pathway in cancer promotes the formation of new blood vessel branches to the tumour from pre-existing vasculature, providing the cancer cells with nutrients and oxygen and allowing for further tumour growth (Carmeliet, 2005; Ferrara & Adamis, 2016; Gotink & Verheul, 2010). Therapies targeting this angiogenic pathway have been partially successful as adjuvants therapies in late stages of cancer, however their effective inhibition of tumour growth is accompanied by cardiovascular toxicity (Bono et al., 2011; Ferrara & Adamis, 2016; B. Liu et al., 2016). With antibodies targeting VEGF-A, as well as small molecule VEGFR2 inhibitors, elevated blood pressure and proteinuria are frequently reported adverse drug effects (Bono et al., 2011; Ferrara, 2004). High potency VEGFR2-inhibitors and multikinase inhibitors with low selectivity are associated with a higher incidence of hypertension than more moderate VEGFR2 inhibitors (H. X. Chen & Cleck, 2009; T. Collins et al., 2018). With growth factor receptor inhibition therapy in cancer, this anti-VEGF hypertension is often a dose-limiting factor (Izzedine et al., 2009; Jesus-Gonzalez et al., 2012; Plummer et al., 2019), emphasizing the importance of adequate identification of drugs binding to this receptor.

As previously described in this thesis, entospletinib induced changes in the blood pressure and blood flow waveform (Chapter 4, section 4.4.3.2. and Chapter 5, section 5.3.2.), despite not changing the overall MAP or VC. To interrogate the mechanism behind these *in vivo* observations, a potential effect of entospletinib on VEGFR2 signalling was elucidated. For this, it was assessed whether entospletinib binds to VEGFR2 and whether it interferes with VEGF's NFAT signalling.

Firstly, an assay was designed that monitors direct interactions of the inhibitors at the kinase domain of VEGFR2, using nanoBRET and sunitinib-red. This BRET technique monitors the proximity of two component (e.g. proteins or small molecule inhibitors) (S. L. Cooper et al., 2022; Stoddart et al., 2018; Wragg et al., 2022). The full details of the principle behind BRET are described before (section 2.4.5.). In brief, a nanoLuciferase tag was put on the C-terminal tail of VEGFR2, allowing for monitoring of close proximity (binding to the kinase domain) of sunitinib-red. This Chapter reports on how the different TKIs inhibited sunitinib-red binding, thus indicating which TKIs were binding directly at the intracellular site of VEGFR2. Secondly, a nuclear factor of activated T-cells (NFAT) reporter gene assay was used to determine inhibition of $VEGF_{165}$a-induced VEGFR2 signalling. Previously described by Carter *et al*. (Carter et al., 2015), this assay was used here to identify TKIs that were interfering with the downstream signalling following VEGFR2 activation.

In summary, to complement *in vivo* findings from previous Chapters and provide mechanistic insight, here the pharmacological interaction of fostamatinib and entospletinib at VEGFR2 were characterised *in vitro* by:

1. Optimising the use of sunitinib-red as a fluorescent tracer binding at VEGFR2-NL in the intracellular nanoBRET assay.
2. Assessing binding affinities for VEGFR2-NL of the Syk inhibitors and a range of TKIs, using the intracellular nanoBRET assay, to confirm the selectivity profiles of entospletinib and fostamatinib.
3. Assessing functional inhibition of the VEGFR2/NFAT signalling pathway by the Syk inhibitors and a range of TKIs.

6.2. Chapter methodology

6.2.1. Selected TKIs to assess *in vitro* effects

Nine compounds were selected to test *in vitro*, with the aim of covering a range of inhibitors targeting cytoplasmic kinases and receptor kinases, with a varying affinity for VEGFR2. An overview of the nine inhibitors, their main targets and clinical applications are presented in Table 19. First, four Syk inhibitors were selected; first-generation compound fostamatinib and its active metabolite R406, and second-generation compounds entospletinib and cerdulatinib. The latter two are reported not to bind VEGFR2 at clinically relevant concentrations (Coffey et al., 2014; Currie et al., 2014; D. Liu & Mamorska-Dyga, 2017). Additionally, five other TKIs were selected. These compounds were selected to obtain a range of TKIs with varying VEGFR2 affinities. Cediranib, sunitinib and motesanib are known growth factor receptor inhibitors that are binding VEGFR2 (Davis et al., 2011) and displaying the cardiovascular side effects mentioned above (Catino et al., 2018; Gotink & Verheul, 2010; E. S. Robinson, Matulonis, et al., 2010). Dasatinib does not target VEGFR2 primarily but inhibits several other membrane and cytoplasmic tyrosine kinases (targets BCR-ABL and the PDGFRs) (Cheng & Force, 2010; Davis et al., 2011). This compound causes pulmonary hypertension (Guignabert et al., 2016; Montani et al., 2012; Weatherald et al., 2017). Lastly, erlotinib is a selective EGFR inhibitor, included here as negative control as it does not bind to VEGFR2 (Davis et al., 2011).

Table 19: Overview of nine tested compounds, their main targets and clinical application.

Compound	Main targets (non-exhaustive)	Applications in clinic (non-exhaustive)	References
Cediranib	VEGFRs, PDGFRs	Anti-angiogenic agent, in development for various cancer types (metastatic colorectal cancer and ovarian cancer)	(Davis et al., 2011; Ferrara & Adamis, 2016; J. F. Liu et al., 2014; Neves et al., 2020)
Sunitinib	VEGFRs, PDGFRs, c-KIT	Anti-angiogenic agent in various cancer types (advanced renal cell carcinoma, gastrointestinal stromal tumours and pancreatic cancer)	(Sun *et al.*, 2003; Davis *et al.*, 2011; Ferrara and Adamis, 2016; Neves *et al.*, 2020)
Motesanib	VEGFRs, PDGFRs	Anti-angiogenic agent, in development for various cancer types (thyroid tumor and non-small cell lung cancer)	(Coxon et al., 2012; Davis et al., 2011; Polverino et al., 2006; Rijavec et al., 2014)
Dasatinib	BCR-ABL, PDGFRs	Antineoplastic agent in chronic myeloid leukemia and Ph^+ acute lymphoid leukemia	(Cheng & Force, 2010; Conchon et al., 2011; Davis et al., 2011; Montani et al., 2012)
Erlotinib	EGFR	Antineoplastic agent in non-small cell lung cancer and pancreatic cancer	(Cheng & Force, 2010; Davis et al., 2011; Van Cutsem et al., 2009)
Fostamatinib and active metabolite R406	Syk (1st generation)	Chronic immune thrombocytopenia, failed clinical trials for rheumatoid arthritis	(Connell & Berliner, 2019; Davis et al., 2011; Mócsai et al., 2010; M E Weinblatt et al., 2010)
Cerdulatinib	Syk (2nd generation) and Janus kinase	In development for B-cell lymphoma and leukemia, atopic dermatitis	(Coffey et al., 2014; D. Liu & Mamorska-Dyga, 2017; Piscitelli et al., 2021)
Entospletinib	Syk (2nd generation)	In development for chronic lymphocytic lymphomas, non-Hodgkin lymphomas and autoimmune disorders	(Currie et al., 2014; D. Liu & Mamorska-Dyga, 2017; J. Sharman et al., 2015)

6.2.2. NanoBRET assay

Full details on the nanoBRET experimental technique are described in Chapter 2, section 2.4.5.3. In brief, HEK293 T cells were transiently transfected with the VEGFR-NL construct, approximately 20 h before experimentation. On the day of experimentation, cells were pre-treated with 1 nM $VEGF_{165}$a for 15 min, followed by increasing concentrations of sunitinib-red (0.1 nM – 1000 nM) in the absence or presence of 100 μM cediranib to obtain a saturation binding curve. Competition experiments were performed with 30 nM sunitinib-red in the presence of unlabelled inhibitor (0.01 nM – 100 μM). Cells were incubated for 1 h at 37 °C to reach equilibrium. Furimazine (1:400) was added to each well and plates were incubated for a further 10 min at 37 °C/5% CO_2 before BRET was measured. Cells were then lysed using NanoGlo® lytic buffer at room temperature for 10 min before BRET was measured a second time. Donor and acceptor emissions were read at room temperature using a PHERAstar FS plate reader (BMG Labtech, Germany) using a filter for 460 – 80 nm for donor NanoLuc emission (gain 1400) and a > 610 nm longpass filter for acceptor sunitinib-red emission (gain 3600). BRET ratios were calculated as acceptor/donor emission values from the second of three cycles. All luminescence and fluorescence signals were read with a white backing tape (PerkinElmer, Beaconsfield, UK) attached to the bottom of the plate. Figure legends state where different experimental conditions were used.

6.2.3. NFAT assay

The experimental details of the NFAT assay used in this thesis are described fully in Chapter 2, section 2.4.6. As previously described by Carter *et al.* (Carter et al., 2015), NFAT-ReLuc2P HEK293 cells stably expressing NLuc-VEGFR2 were serum-starved for 24 h before experimentation, i.e. incubated in FCS-free medium. This was done to reduce the interference of FCS on the NFAT pathway, as this serum contains several growth factors that activate several cell signalling pathways (Hill et al., 2001). Incubating the cells for 24 h in medium without FCS reduces this effect and produces a response specific to the investigated activator (Hill et al., 2001), in this case $VEGF_{165}a$. A concentration-response curve was obtained with increasing concentrations of $VEGF_{165}a$ (10 pM – 10 nM), and to determine the interference of inhibitors on the signalling pathway, cells were pre-treated with increasing concentrations of inhibitor (10 pM – 10 μM) for 1 h, followed by $VEGF_{165}a$ (1 nM) or ionomycin (1 μM). Plates were incubated for 5 h at 37 °C to allow for luciferase gene transcription and translation. Next, ONE-Glo luciferase reagent was added and following a 5-minute delay, luminescence was measured using a TopCount plate reader (Perkin Elmer, UK). All luminescence was read with a white backing tape attached to the bottom of the plate.

6.3. Chapter results

6.3.1. Optimisation of the use of sunitinib-red in the nanoBRET assay

Firstly, to characterise the use of sunitinib-red as a fluorescent tracer in this intracellular nanoBRET assay, BRET ratios were determined following 1 h incubation with 100 nM sunitinib-red in intact cells and lysed cells (Figure 76). In intact cells, when comparing the vehicle-treated wells to sunitinib-red treated wells, no increase in BRET ration was observed under any experimental conditions (Figure 76A). After cell lysis (Figure 76B), BRET ratio was increased in the wells treated with sunitinib-red compared to the vehicle-treated wells (paired t-test, $p<0.05$). Increasing the furimazine concentration did not improve the signal window. With prolonged furimazine incubation (1 h instead of 10 min), the signal window was decreased (One-way ANOVA with post hoc Tukey's multiple comparison test, $p<0.05$). The absence or presence of $VEGF_{165}a$ did not affect the BRET signal significantly (One-way ANOVA with post hoc Tukey's multiple comparison test).

Based on this initial optimisation step, the standard protocol for further experimentation was established as described in section 6.2.2; cells were pre-treated with 1 nM $VEGF_{165}a$ for 15 min, followed by a 1 h incubation with sunitinib-red and inhibitor. Next, cells were incubated with furimazine (1:400) at 37 °C for 10 min and then lysed for 10 min at room temperature before BRET ratios were determined. Under this standard protocol, a saturation binding curve of sunitinib-red at VEGFR2-NL was obtained (Figure 77). Sunitinib-red showed saturable binding at the receptor, and this binding was inhibited by 100x molar excess of cediranib, an unlabelled RTKI (Figure 77A). Specific binding of sunitinib-red is showed in Figure 77B ($-\log K_D = 7.29 \pm 0.06$).

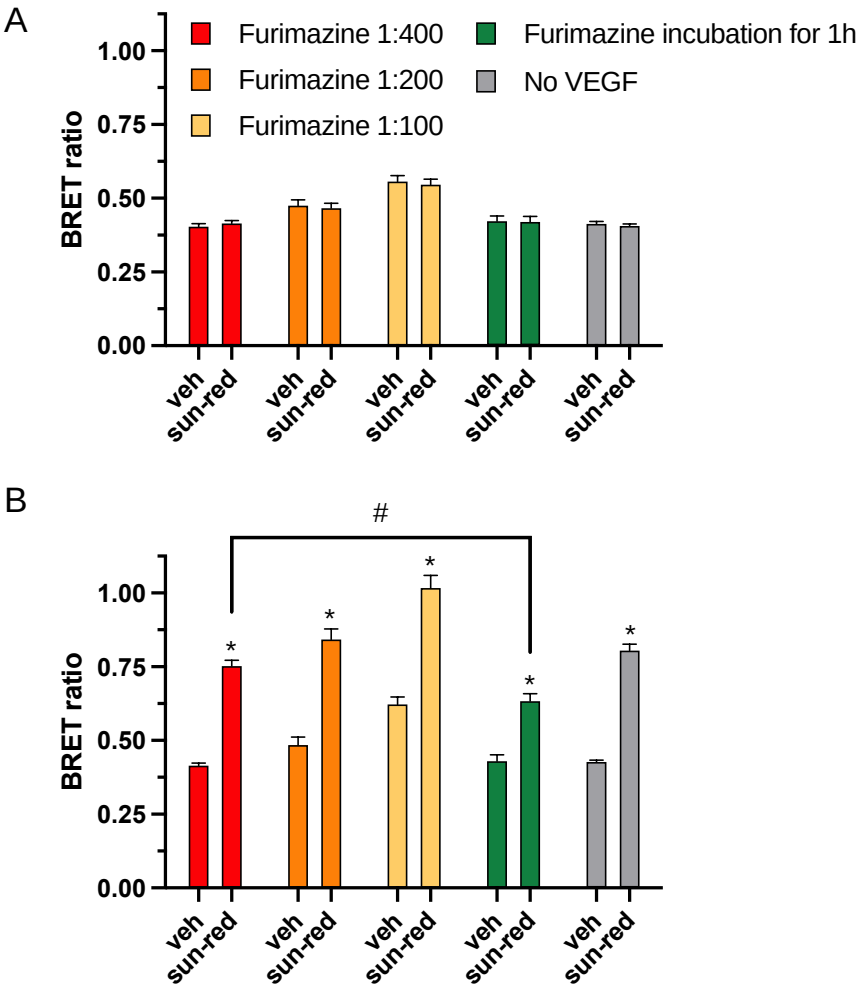

Figure 75: Binding of 100 nM sunitinib-red VEGFR2-NL. (A) *HEK293T cells expressing VEGFR2-NL were pre-incubated in the presence (in **red**) or absence (in **grey**) of 1 nM $VEGF_{165}$a for 15 min, followed by 100 nM sunitinib-red for a further 1 h at 37 °C/5% CO_2. Furimazine (1:400) was added to each well and the plates were incubated for a further 10 min at 37 °C/5% CO_2 before BRET ratios were determined. In some wells, furimazine was added at higher concentrations (1:200 or 1:100; **orange** and **yellow** respectively). In other wells, furimazine (1:400) was added at the same time as sunitinib-red (in **green**). **(B)** The cells in (A) were lysed using NanoGlo® lytic buffer at room temperature for 10 min and BRET measured a second time. Data are presented as mean ± S.E.M from 5 individual experiments (n=5) in triplicates. A paired t-test was conducted to test for differences between vehicle-treated wells and sunitinib-red-treated wells within the same experimental conditions (* = p<0.05). Furthermore, a one-way ANOVA with post hoc Tukey's multiple comparison test was used to test for significant differences between sunitinib-red treated wells following lysis in the presence of furimazine 1:400 (# = p<0.05). There was no significant difference between the data obtained in the presence or absence of 1 nM $VEGF_{165}$a (p>0.05; one-way ANOVA with post hoc Tukey's multiple comparison test).*

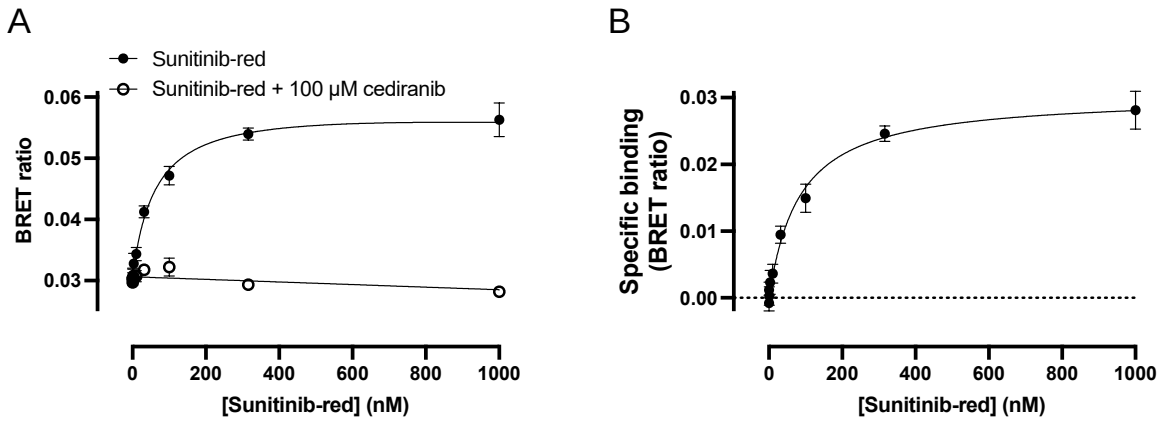

Figure 76: Saturation binding of sunitinib-red to VEGFR2-NL. (A) *HEK293T cells expressing VEGFR2-NL were treated with increasing concentrations of sunitinib-red. Graph shows total binding (filled circles, sunitinib-red) and non-specific binding (open circles, sunitinib-red + 100 µM cediranib) after cell lysis. To conserve sunitinib-red, this assay was performed in white half-well 96 well plates (Corning Incorporated, New York, USA). A total volume of 25 µL was used and cells were plated at 10,000/well and transfected with 0.05 µg cDNA. The gain for the 460 nm channel was adjusted to 2400 for an optimal signal window.* ***(B)*** *Specific binding of sunitinib-red, calculated as BRET ratio(total binding) – BRET ratio(non-specific binding). Data are presented as mean ± S.E.M from 5 individual experiments (n=5) in triplicates.*

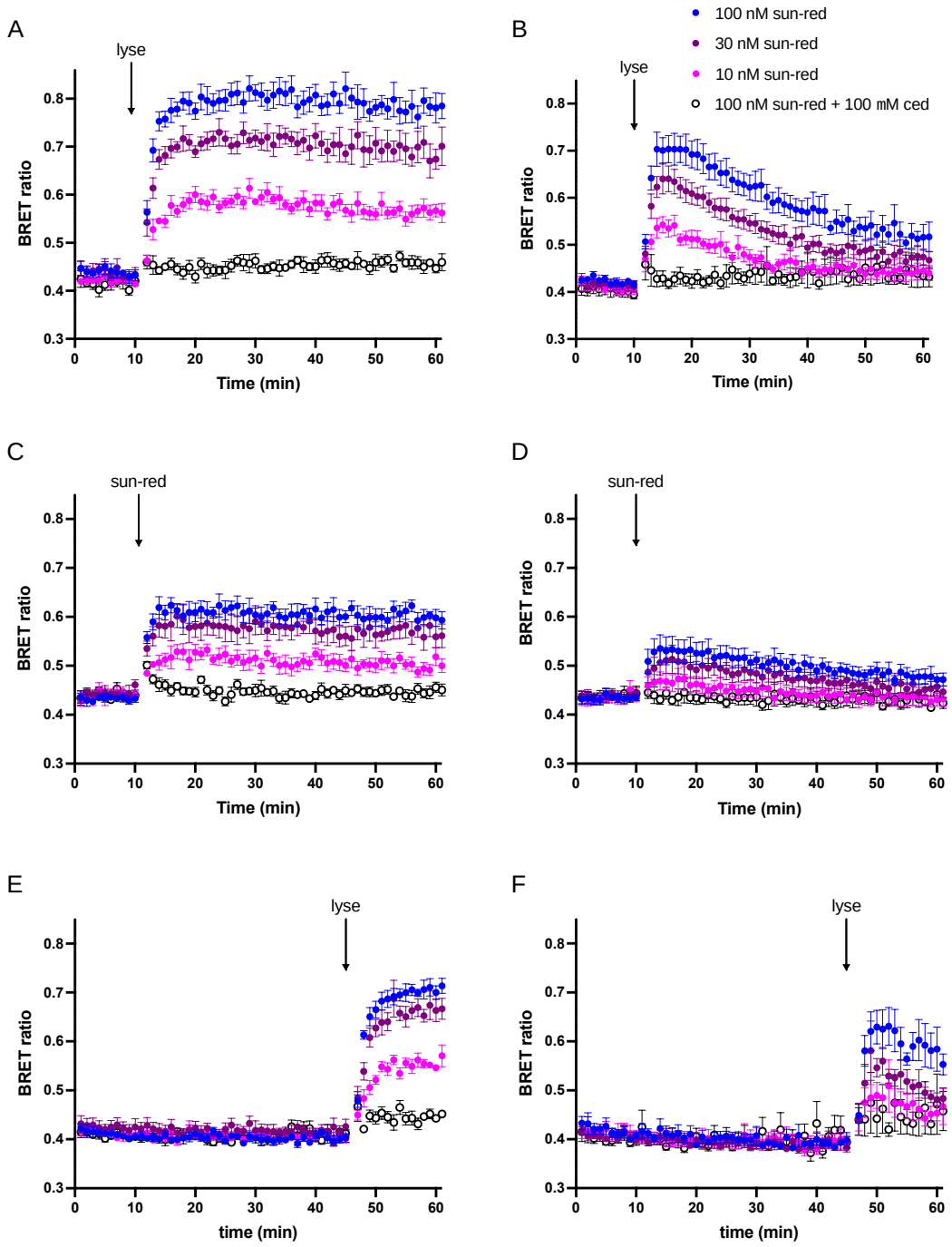

Figure 77: Time course of sunitinib-red-induced changes in BRET ratio, under different experimental conditions. (A) *Standard conditions as described before; cells were pre-incubated with 1 nM $VEGF_{165}$a for 15 min, followed by sunitinib-red (100 nM, 30 nM or 10 nM) and cediranib (100 μM) as required, for a further 1 h at 37 °C/5% CO_2. Furimazine (1:400) was then added to each well (t=0) and BRET was measured at 25 °C, every 60s. After 10 min (t=10), lysing buffer was added to each well, and BRET was measured at 25 °C for a further 50 min.* ***(B)*** *was obtained in the same conditions at (A), except that incubation from t=0 was at 37 °C.* ***(C)*** *Following the 15-minute pre-incubation with 1 nM $VEGF_{165}$a, furimazine (1:400) and lysing buffer were added at the same time (t=0) and BRET was measured at 25 °C, every 60s. After 10 min (t=10), sunitinib-red and cediranib were added in the appropriate wells and BRET was measured at 25 °C for a further 50 min.* ***(D)*** *was obtained in the same conditions at (C), except that incubation from t=0 was at 37 °C.* ***(E)*** *was obtained in the same conditions as (A), except that incubation with furimazine was performed for 45 min, before lysing buffer was added (t=45).* ***(F)*** *was obtained under the same conditions as (E), except that incubation from t=0 was at 37 °C. Data are presented as mean ± S.E.M from 5 individual experiments (n=5) in triplicates.*

To further characterise the sunitinib-red-induced BRET signal before and after cell lysis, kinetic experiments under different conditions were performed (Figure 78). The standard protocol as described in section 6.2.2. is represented in Figure 78A and 78B (BRET measured at 25 °C and 37 °C respectively). In both cases, no BRET signal was observed before cells were lysed. Lysing of the cells resulted in a rapid increase in the BRET signal, indicating sunitinib-red was able to bind to the intracellular site of the receptor. At 25 °C, the BRET signal was stable, at 37 °C the BRET signal declined more quickly. Next, the effect of simultaneous addition of furimazine and lysing buffer, before sunitinib-red treatment, was investigated (Figure 78C and 78D, BRET measurements at 25 °C and 37 °C respectively). In both cases, additon of sunitinib-red resulted in a rapid increase in BRET ratio, however smaller maximum responses were obtained than in Figure 78A and 78B. Interestingly, an initial increase in BRET signal was observed in sunitinib-red+cediranib treated wells in Figure 78C, before the signal returned to baseline values, indicating sunitinib-red bound faster to VEGFR2 than cediranib. This was further investigated and reported in section 6.3.4. below. Lastly, to investigate if prolonged furimazine incubation, prior to cell lysis, would recapitulate findings from Figure 78A and 78B, were cells were incubated for 1 h with sunitinib-red+inhibitor, followed by furimazine addition and 45 min of BRET baseline recording before cells were lysed. The results of these experiments are displayed in Figure 78E and 78F (BRET measurements performed at 25 °C and 37 °C respectively). Within this 45 min furimazine incubation, no BRET signal developed. Only after cell lysis, the BRET ratio increased. This result was in line with Figure 76A, showing that 1 h incubation with furimazine and sunitinib-red, without cell lysis, was not able to produce a BRET signal. In summary, these experiments showed that sunitinib-red was only able to produce a BRET signal after cell lysis, indicating this fluorescent derivative of sunitinib is not cell-membrane permeable.

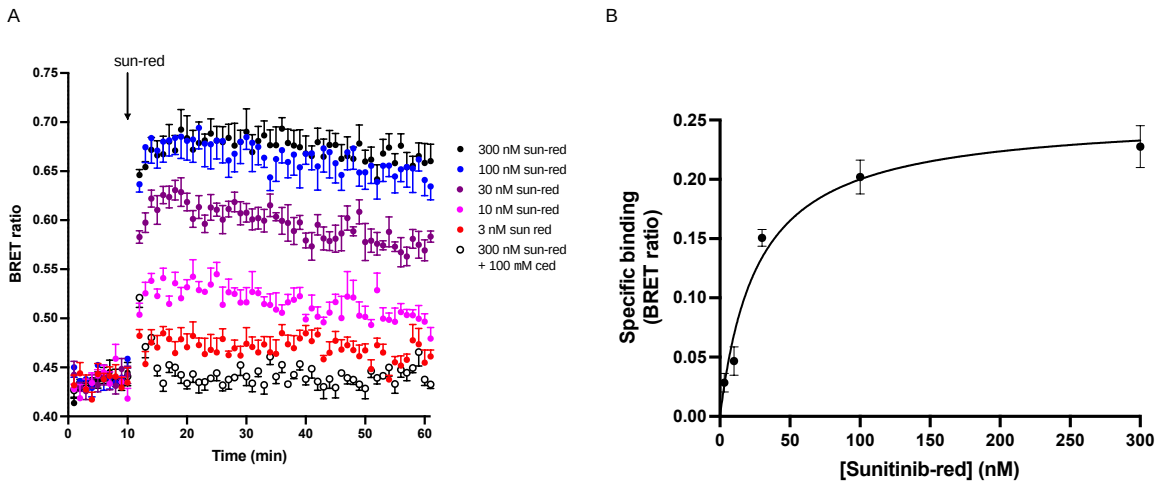

Figure 78: Time course of changes in BRET ratio induced by five different sunitinib-red concentrations. (A) *was obtained under the same experimental conditions as Figure 3C, with 2 additional concentrations of sunitinib-red (300 nM and 3 nM). Graphs shows total binding (filled circles, sunitinib-red) and non-specific binding (open circles, sunitinib-red + 100 µM cediranib). From these data, common values for k_{on} and k_{off} rate constants were obtained for sunitinib-red binding in the absence of inhibitor in GraphPad Prism.* ***(B)*** *Specific binding of sunitinib-red obtained at 61 min, calculated as BRET ratio(total binding) – BRET ratio(non-specific binding) at different concentrations of sunitinib-red. Data are presented as mean ± S.E.M from 5 individual experiments (n=5) in triplicates.*

Kinetic parameters of sunitinib-red binding to VEGFR2 were determined by repeating the experimental conditions of Figure 78C with 2 additional sunitinib-red concentrations (Figure 79A). Using the data obtained during the 20 min after addition of 3 nM, 10 nM, 30 nM and 100 nM sunitinib-red, the shared values of k_{on}, k_{off}, and K_D were determined in GraphPad prism and are shown in Table 20. Sunitinib-red displayed a quick association rate constant (k_{on} = 3.96 x 10^7 $M^{-1}.min^{-1}$) and short retention time at the receptor ($1/k_{off}$ = 1.32 min). Furthermore, from the 61st min of this experiment, a saturation binding curve was obtained by plotting the specific binding BRET ratio (Figure 79B). This plot yielded a -log K_D of 7.57, similar to the one obtained in Figure 77.

6.3.2. Displacement of sunitinib-red at VEGFR2-NL by TKIs

Next, the nine selected TKIs (Table 19) were tested for their ability to displace 30 nM sunitinib-red at VEGFR2-NL (Figure 79). Five inhibitors were able to inhibit the BRET signal: unlabelled sunitinib (Figure 80A), cediranib (Figure 80B), motesanib (Figure 80C), fostamatinib (Figure 80D) and its active metabolite R406 (Figure 80E). Interestingly, with increasing concentrations of unlabelled sunitinib a biphasic curve was obtained, showing an increase in BRET ratio at sunitinib concentrations above 1 μM. This indicated autofluorescence of the unlabelled version of sunitinib and was further explored in section 6.3.6. This BRET signal was fitted to bespoke equation 8 in Chapter 2 (section 2.4.7.2.) and resulted in a $\log K_I$ of -8.20 ± 0.13. Cediranib and motesanib showed similar affinities as unlabelled sunitinib, displacing 30 nM sunitinib-red with a $\log K_I$ of -8.24 ± 0.12 and -8.01 ± 0.10 respectively (Cheng-Prusoff equation). Fostamatinib and R406 displayed a more moderate inhibition of the BRET signal, with $\log K_I$ of -6.71 ± 0.12 and -6.44 ± 0.11 respectively. All values of $\log K_I$ are displayed in Table 21. Erlotinib, a selective EGFR inhibitor (Figure 80F), and dasatinib, targeting BCR-ABL and the PDGFRs (Figure 80H), were not affecting the BRET ratio at concentrations up to 1 μM. Similarly, the selective Syk inhibitors entospletinib and cerdulatinib did not affect the BRET signal at concentrations relevant to clinical plasma levels of these compounds (Figure 80G and 80I).

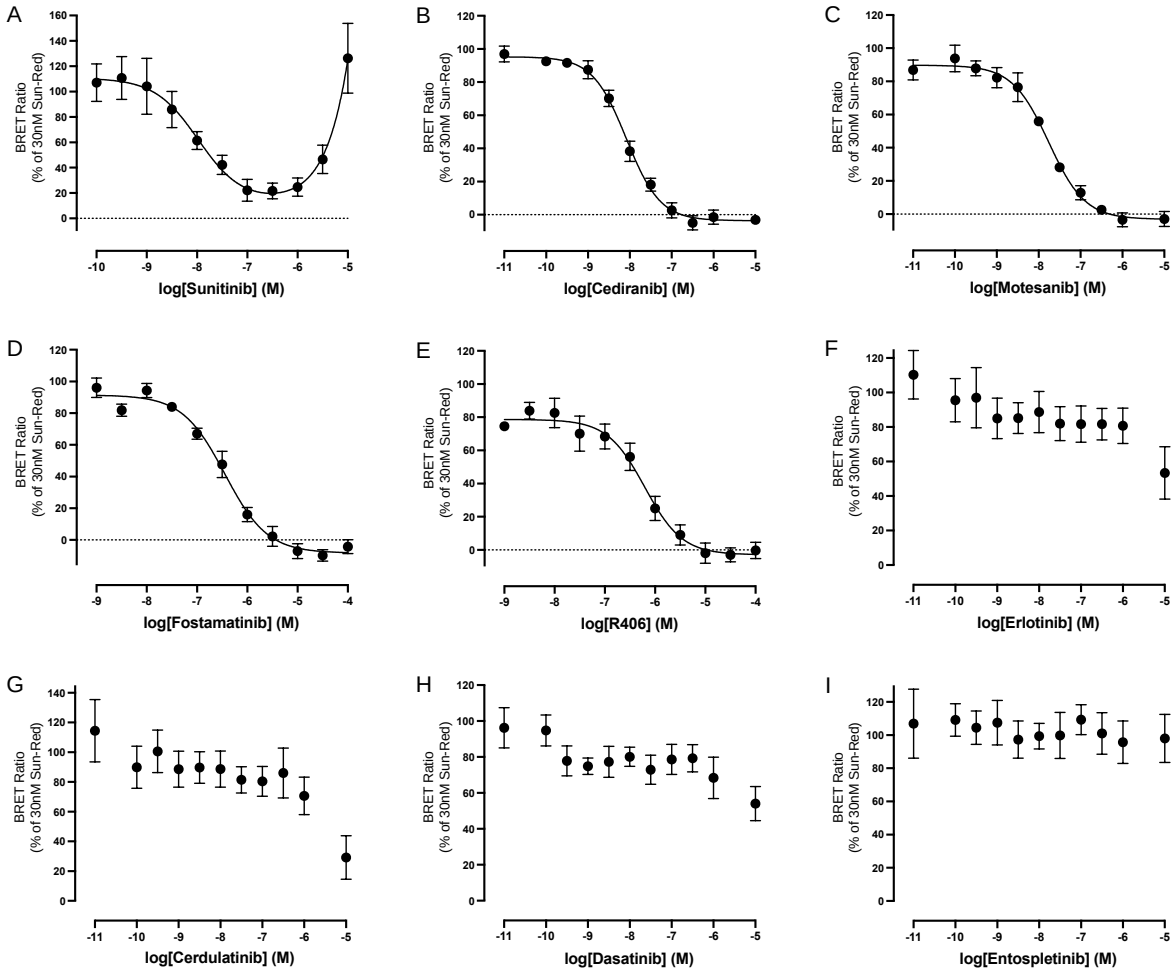

Figure 79: Inhibition of binding of 30 nM sunitinib-red to VEGFR2-NL by selected TKIs. *BRET ratios are presented as a percentage of the specific binding of 30 nM sunitinib-red. Non-specific binding was determined in the presence of 100 μM cediranib. Data were obtained under the standard experimental conditions as described in section 6.2.2. and BRET ratio was determined in lysed cells. Data are presented as mean ±S.E.M from 5 individual experiments (n=5) in triplicates.* ***(A)*** *unlabelled sunitinib;* ***(B)*** *cediranib;* ***(C)*** *motesanib;* ***(D)*** *fostamatinib;* ***(E)*** *R406;* ***(F)*** *erlotinib;* ***(G)*** *cerdulatinib;* ***(H)*** *dasatinib;* ***(I)*** *entospletinib.*

6.3.3. Inhibition of VEGFR2 signalling by TKIs

Following the determination of binding affinities at VEGFR2 of the nine TKIs, their effect on the functional signalling of VEGFR2 was assessed. First, an NFAT response curve with increasing concentration of $VEGF_{165}a$ (1 pM – 10 nM) was obtained as described in section 6.2.3. With increasing concentrations, $VEGF_{165}a$ showed a clear increase in luminescence (Figure 81), with a $-logEC_{50}$ of 9.85 ± 0.11.

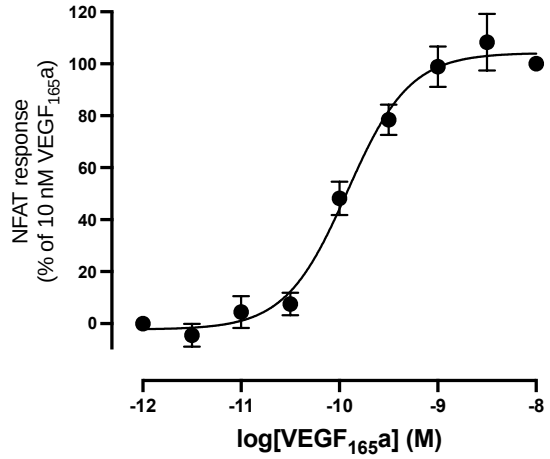

Figure 80: NFAT-mediated gene transcription in response to $VEGF_{165}a$. *HEK293 cells stably expressing the NFAT ReLuc2P vector and NL-VEGFR2 were stimulated for 5 h with increasing concentrations of $VEGF_{165}a$ (1 pM – 10 nM) at 37℃ before luminescence was measured. Values are normalised to the 10 nM $VEGF_{165}a$ response. Data are presented as mean ± S.E.M from 5 individual experiments (n=5) in triplicates.*

Next, to determine the functional inhibition of the TKIs, cells were treated with 1 nM $VEGF_{165}a$ combined with increasing concentrations of the inhibitor. First, the effect of sunitinib-red on the NFAT-induced luciferase production was assessed. With concentrations that induced a clear response in the BRET assay (3 nM – 300 nM), no significant effect on the NFAT response was observed (Figure 82), indicating that over the 5 h period of incubation, sunitinib-red was likely not entering the intact cells and therefore not inhibiting VEGFR2 signalling.

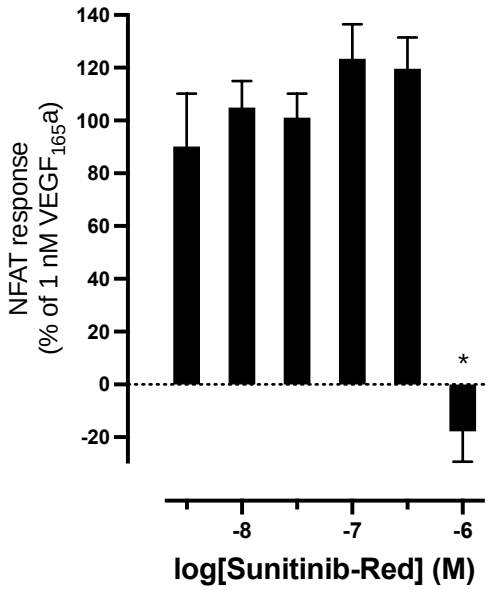

***Figure 81: The effect of different concentrations of sunitinib-red on the $VEGF_{165}$a-induced NFAT response**. HEK293 cells stably expressing the NFAT ReLuc2P vector and NL-VEGFR2 were pre-treated for 1 h with sunitinib-red. Next, 1 nM $VEGF_{165}$a was added and cells were incubated for a further 5 h at 37℃ before luminescence was measured. Data are normalized to the maximal response to 1 nM $VEGF_{165}$a in the absence of sunitinib-red. Data are presented as mean ± S.E.M from 5 individual experiments (n=5) in triplicates. A one-way ANOVA with post hoc Tukey's multiple comparison test was conducted to test for significant differences from the response obtained with 1 nM $VEGF_{165}$a (*=p<0.05).*

Figure 83 displays the effects of the nine inhibitors on the $VEGF_{165}$a-induced NFAT response. The most potent inhibitor was cediranib ($logIC_{50}$ = -8.73 ± 0.02, Figure 83B), followed by motesanib ($logIC_{50}$ = -7.97 ± 0.10, Figure 83C) and unlabelled sunitinib ($logIC_{50}$ = -7.90 ± 0.12, Figure 83A). Similar as observed in the nanoBRET experiments, treatment with fostamatinib and R406 resulted in a more moderate inhibition of the NFAT response, with a $logIC_{50}$ of -6.58 ± 0.32 and -6.87 ± 0.06 respectively (Figure 83D and 83E). Erlotinib (Figure 83F) and cerdulatinib (Figure 83G) did not affect the NFAT response, consistent with the nanoBRET results. Surprisingly, despite not binding to VEGFR2 directly (section 6.3.2.), dasatinib and entospletinib were both able to interfere with the functional signalling of the receptor. Dasatinib inhibited the NFAT response with a $logIC_{50}$ of -6.96 ± 0.19 (Figure 83H). Entospletinib ($logIC_{50}$ of -8.28 ± 0.21, Figure 83I) displayed an inhibition with potency similar to cediranib and a 100x fold higher potency than fostamatinib and R406. All $logIC_{50}$ values are shown in Table 21.

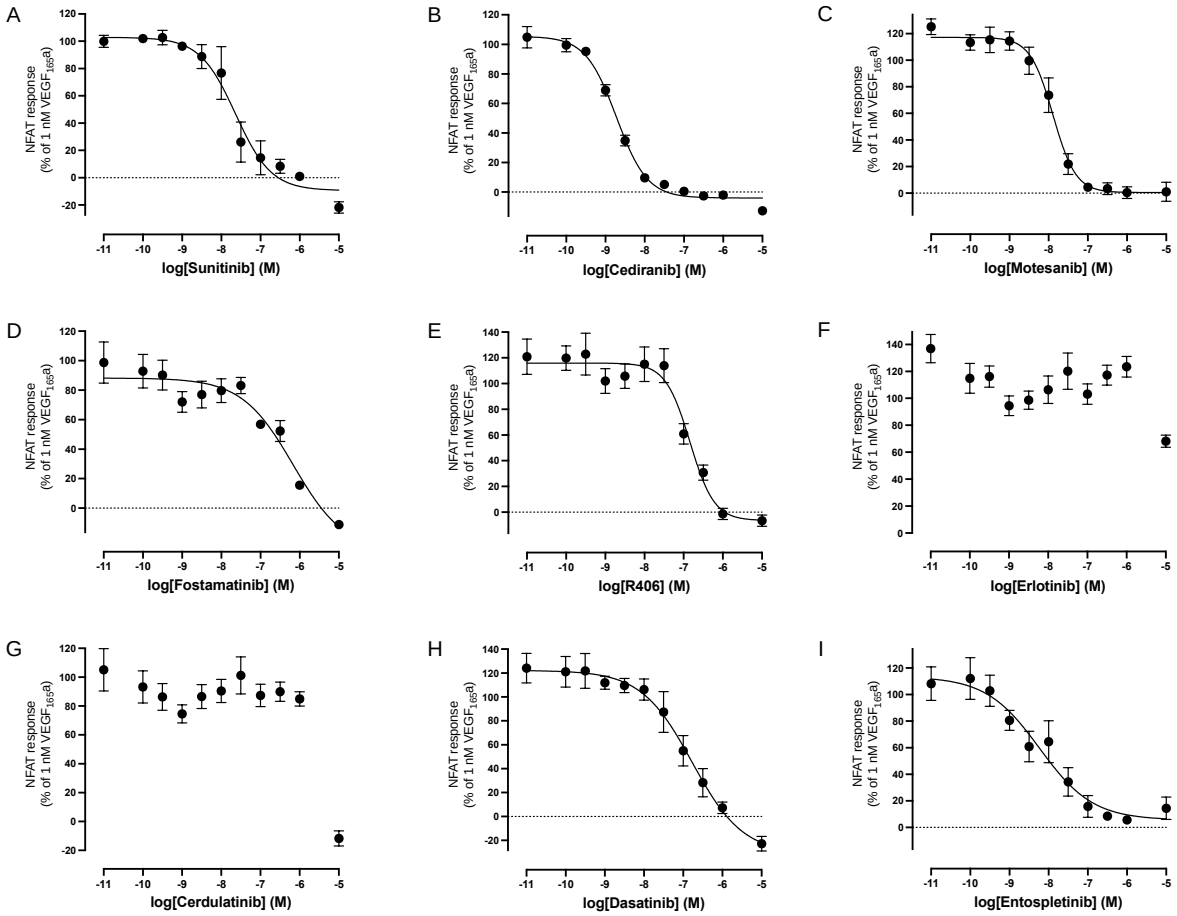

Figure 82: Inhibition of the $VEGF_{165}a$-induced NFAT response by selected TKIs. *HEK293 cells stably expressing the NFAT ReLuc2P vector and NL-VEGFR2 were pre-treated for 1 h with increasing concentrations of the appropriate inhibitor. Next, 1 nM $VEGF_{165}a$ was added and cells were incubated for a further 5 h at 37℃ before luminescence was measured. Data are normalized to the maximal response to 1 nM $VEGF_{165}a$ in the absence of inhibitor. Data are presented as mean ± S.E.M from 5 individual experiments (n=5) in triplicates.* ***(A)*** *unlabelled sunitinib;* ***(B)*** *cediranib;* ***(C)*** *motesanib;* ***(D)*** *fostamatinib;* ***(E)*** *R406;* ***(F)*** *erlotinib;* ***(G)*** *cerdulatinib;* ***(H)*** *dasatinib;* ***(I)*** *entospletinib.*

6.3.4. Kinetics of sunitinib-red displacement by TKIs

As mentioned in section 6.3.1 (Figure 78C), when adding sunitinib-red and cediranib simultaneously after cell lysis, sunitinib-red was able to induce an initial response before cediranib displaced sunitinib-red at the receptor and return BRET values to baseline. This suggested that, under these experimental conditions, sunitinib-red had a faster kinetic binding profile at VEGFR2 than cediranib. To confirm these findings, kinetic parameters of cediranib and fostamatinib at the receptor were assessed. Figure 84 shows the results obtained under the same experimental conditions as Figure 78C, looking at the displacement of 30 nM sunitinib-red by increasing concentrations of cediranib (1 nM – 100 nM, Figure 84A) or fostamatinib (30 nM – 3000 nM, Figure 84B). As anticipated, both inhibitors showed a concentration-dependent inhibition of the sunitinib-red induced BRET signal. Furthermore, an initial increase in BRET ratio was indeed observed, indicating sunitinib-red binding prior to antagonism by high concentrations of the unlabelled inhibitor. To determine values of k_{on}, k_{off} and $logK_D$, data were baseline corrected as shown in Figure 85. Using the Motulsky and Mahan method of competitive ligand association, the shared values of k_{on} and k_{off} for each inhibitor were calculated (Table 20). Indeed, cediranib showed a slower association rate constant (k_{on} = 1.16 x 10^7 $M^{-1}.min^{-1}$) and longer retention time (111.11 min) than sunitinib-red. Fostamatinib showed the slowest association and dissociation rate constants (k_{on} = 3.17 x 10^5 $M^{-1}.min^{-1}$ and retention time of 140.86 min).

Table 20: Kinetic parameters of sunitinib-red, cediranib and fostamatinib binding to VEGFR2*. k_{on} = association rate constant; k_{off} = dissociation rate constant; Retention time = 1/k_{off} and logK_D = k_{off}/k_{on}. Parameters for sunitinib-red were obtained from Figure 79, parameters for cediranib and fostamatinib were extracted from Figure 85.*

TKI	k_{on} (M^{-1},min^{-1})	k_{off} (min^{-1})	Retention time (min)	Kinetic log K_D
Sunitinib-red	3.96 x 10^7	0.76	1.32	-7.72
Cediranib	1.16 x 10^7	0.0090	111.11	-9.12
Fostamatinib	3.17 x 10^5	0.0071	140.86	-7.65

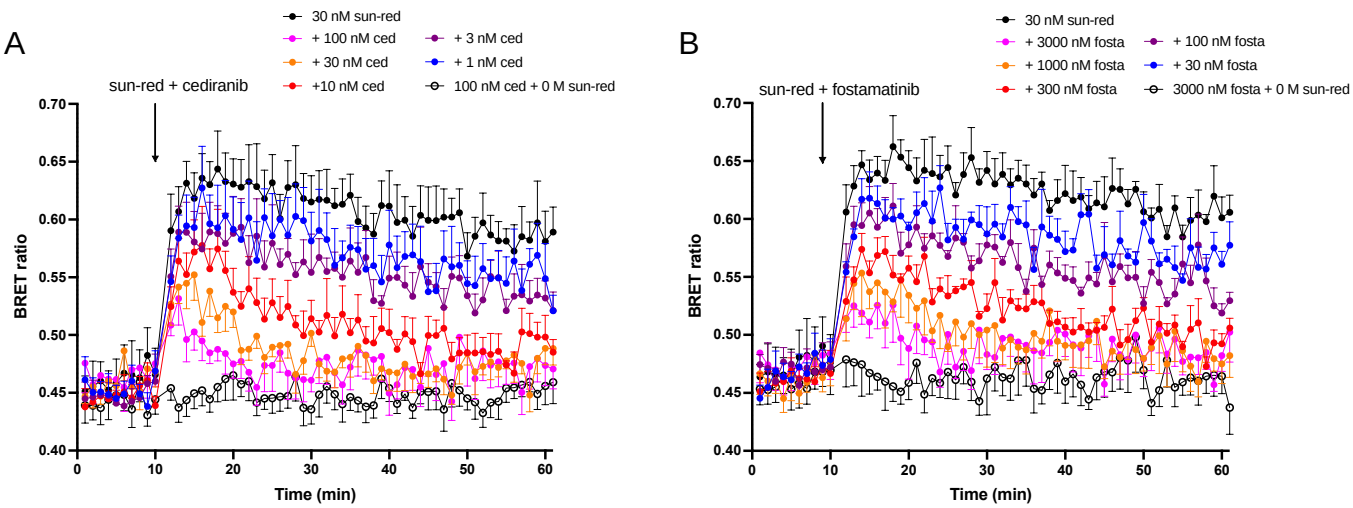

Figure 83: Time course of the inhibition of 30 nM sunitinib-red binding by different concentrations of cediranib (A) and fostamatinib (B). *To determine binding kinetics of cediranib and fostamatinib at VEGFR-NL, experiments were conducted under the same conditions as used in Figure 78C; following the 15-minute pre-incubation with 1 nM $VEGF_{165}a$, furimazine (1:400) and lysing buffer were added at the same time (t=0) and BRET was measured at 25 ℃, every 60s. After 10 min (t=10), sunitinib-red (30 nM) and different concentrations of unlabelled inhibitor (cediranib in (A) or fostamatinib in (B)) were added simultaneously in the appropriate wells and BRET was measured at 25 ℃ for a further 50 min. Open circles represent BRET ratio after inhibitor treatment in the absence of sunitinib-red. Data are presented as mean ± S.E.M from 5 individual experiments (n=5) in triplicates.*

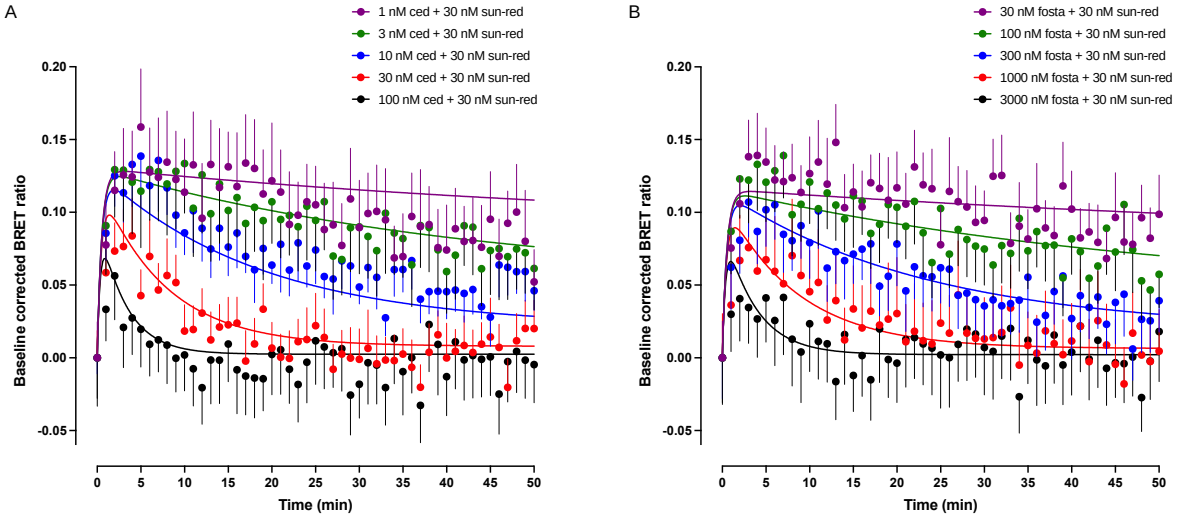

Figure 84: Baseline corrected BRET ratio of the inhibition of 30 nM sunitinib-red binding by different concentrations of cediranib (A) and fostamatinib (B). *Data were taken from Figure 84A and 84B respectively. Baseline corrected BRET ratios were obtained by subtracting the BRET ratio(immediately before sunitinib-red+inhibitor addition) from the BRET ratio at subsequent time points. T=0 represents time of sunitinib-red+inhibitor addition. For both inhibitors, data points at each concentration were fitted with shared values for k_{on} and k_{off} using the Motulsky and Mahan method of competitive ligand association (Motulsky and Mahan 1984) in GraphPad Prism. Curves through each data set represent the best-fit from this analysis.*

6.3.5. Investigating the effects of entospletinib and dasatinib at VEGFR2

To further investigate the discrepancy between data obtained in the nanoBRET assay and in the NFAT assay, seen with entospletinib and dasatinib, two additional experiments were carried out.

Firstly, to monitor inhibitor binding over a longer time rather than evaluating a single time point (as in Figure 80), a time-course experiment was performed for both dasatinib and entospletinib. In this way, slow association rates could be confirmed or ruled out as a cause for lack of antagonism in the nanoBRET assay. Under the same experimental conditions as Figure 84, the effect of increasing concentration dasatinib (0.1 nM – 1000 nM, Figure 86A) or entospletinib (0.1 nM – 1000 nM, Figure 86B) on sunitinib-red-induced BRET response was measured. For both inhibitors, no concentration-dependent effect was found over the 60-minute recording of BRET ratio. The presence of dasatinib or entospletinib did not attenuate the maximum BRET signal observed with 30 nM sunitinib-red alone, indicating that these inhibitors did indeed not displace sunitinib-red at VEGFR2-NL over the time measured.

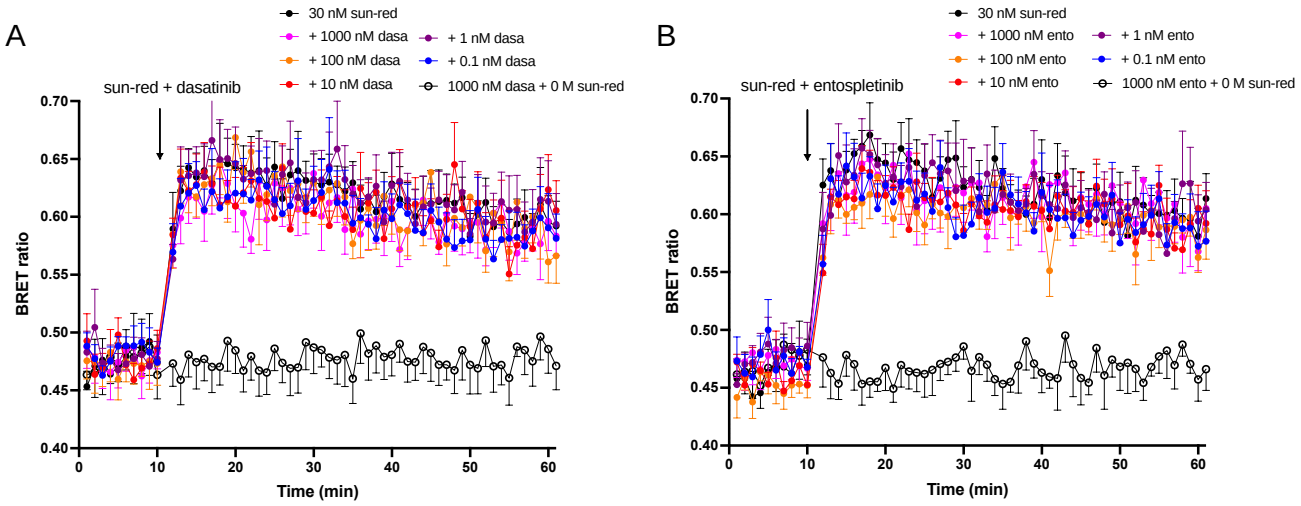

Figure 85: Time course of the inhibition of 30 nM sunitinib-red binding by different concentrations of dasatinib (A) and entospletinib (B). *To investigate if dasatinib and entospletinib displayed any slower inhibition of sunitinib-red binding at VEGFR2-NL, experiments were conducted under the same conditions as used in Figure 9; furimazine (1:400) and lysing buffer were added at the same time (t=0). Following a 10-minute incubation at 25℃ (t=10), sunitinib-red (30 nM) and different concentrations of unlabelled inhibitor (dasatinib in (A) or entospletinib in (B)) were added simultaneously in the appropriate wells and BRET was measured at 25℃ for a further 50 min. Open circles represent BRET ratio after inhibitor treatment in the absence of sunitinib-red. Data are presented as mean ±S.E.M from 5 individual experiments (n=5) in triplicates.*

Secondly, to assess whether the inhibition of the NFAT response was specific for $VEGF_{165}a$-activation of VEGFR2, NFAT experiments as in Figure 83 were repeated, however cells were stimulated with ionomycin, a calcium ionophore, instead of $VEGF_{165}a$. This calcium ionophore was used to generate an increase in intracellular calcium, so that calcineurin could be directly stimulated, leading to the translocation of NFAT into the nucleus, without the need for VEGFR2 activation. Both inhibitors were able to inhibit the NFAT response to 1 μM ionomycin (Figure 87). Potency obtained here ($logIC_{50}$ = -7.16 ± 0.22 for dasatinib and $logIC_{50}$ = -8.18 ± 0.08 for entospletinib) were not significantly different from the ones obtained in the $VEGF_{165}a$-induced NFAT assay (unpaired t-test). This experiment suggested that dasatinib and entospletinib inhibited the NFAT response in a non-specific way and were able to interfere with the luciferase production independently from VEGFR2 activation.

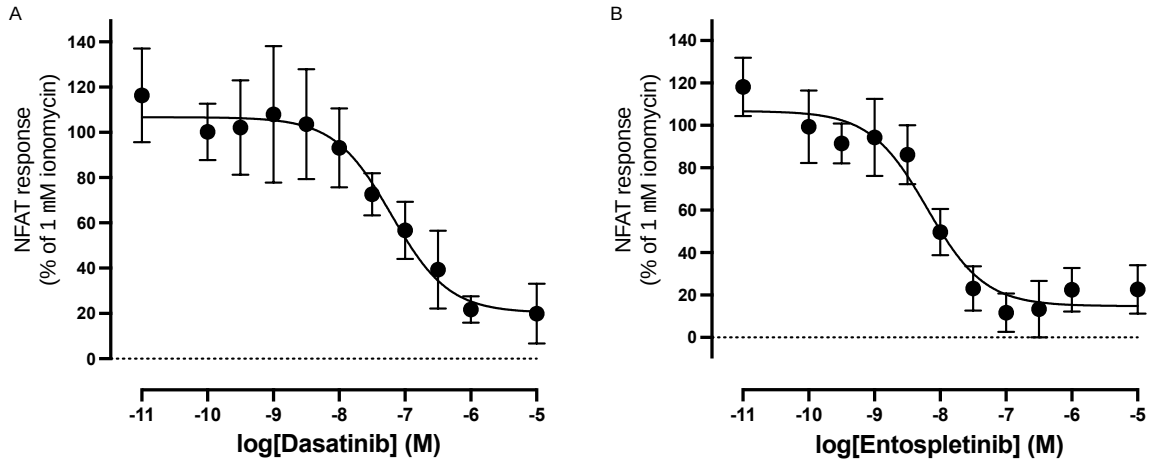

Figure 86: Inhibition of the ionomycin-induced NFAT response by dasatinib (A) and entospletinib (B). *HEK293 cells stably expressing the NFAT ReLuc2P vector and NL-VEGFR2 were pre-treated for 1 h with increasing concentrations of the appropriate inhibitor. Next, 1 μM ionomycin was added and cells were incubated for a further 5 h at 37°C before luminescence was measured. Data are normalized to the maximal response to 1 μM ionomycin in the absence of inhibitor. Data are presented as mean ± S.E.M from 5 individual experiments (n=5) in triplicates.*

6.3.6. Unlabelled sunitinib as a fluorescent tracer in the nanoBRET assay

As described above (section 6.3.2.), the concentration-response curve of unlabelled sunitinib in the nanoBRET assay had a biphasic profile. The initial decrease in BRET ratio, indicating that unlabelled sunitinib was displacing sunitinib-red at the receptor, was followed by a sharp increase in BRET ratio with sunitinib concentration higher than 1 μM (Figure 80A). These data suggested that unlabelled sunitinib is inherently fluorescent. Indeed, sunitinib has a bright yellow colour and it has been reported in the literature to display light emission in the green spectrum (maximum emission at 540 nm) (Nowak-Sliwinska et al., 2015). To confirm this, the fluorescent intensity spectra from unlabelled sunitinib and sunitinib-red were measured on a CLARIOStar plate reader (BMG Labtech, Ortenberg, Germany). Unlabelled sunitinib, when excited over 415 – 515 nm, indeed showed an excitation peak around 450 nm, and emission peak around 545 nm (Figure 88A), confirming autofluorescence of the unlabelled molecule.

The fluorescent tag on sunitinib-red (Cisbio's fluorescent dye 'd2') is reported to have a maximum absorption at 650 nm and maximum emission at 670 nm (Cisbio, 2023b). This profile of fluorescence absorption and emission is similar the one of Cy5 (Fernández-Suárez & Ting, 2008). Cy5 is a cell membrane-impermeable fluorophore, with maximum excitation and emission wavelengths reported to be 649 nm and 664 nm respectively (Fernández-Suárez & Ting, 2008). The emission spectrum of Cy5 following excitation over 560 nm – 675 nm is displayed in Figure 88B, showing maximal fluorescent intensity around 665 nm. When sunitinib-red was excited over these same wavelengths (560 nm – 675 nm, Figure 88D), the emission peak was observed around 670 nm, as anticipated. In this case, a higher fluorescent intensity was observed compared to the one observed following excitation over 415 nm – 515 nm (Figure 88C).

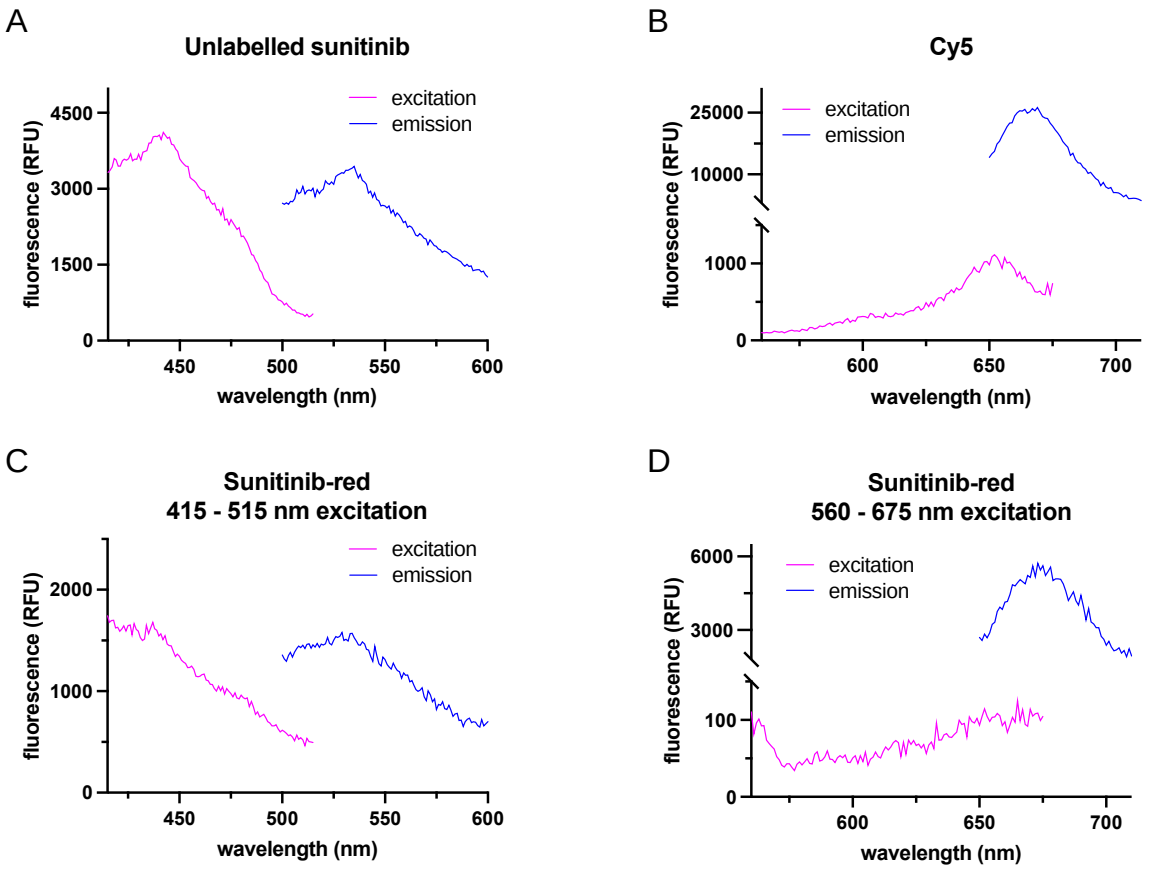

Figure 87: Fluorescence intensity of unlabelled sunitinib (A) and labelled sunitinib-red (C and D). *Unlabelled sunitinib* ***(A),*** *Cy5* ***(B)*** *or sunitinib-red* ***(C and D)*** *were added in triplicates to a white 96 well plates without any cells present. Fluorescence intensity was measured on a CLARIOStar plate reader (BMG Labtech, Ortenberg, Germany) with excitation at 415 – 515 nm and emission detection at 500 – 600 nm (**A** and **C**), or excitation at 560 – 675 nm and emission detection at or 650 – 710 nm (**B** and **D**). Data are presented as mean from one experiment in triplicates.*

To explore the use of unlabelled sunitinib as a fluorescent tracer in the nanoBRET assay, a concentration response curve was obtained with unlabelled sunitinib (1 nM – 100 μM). Figure 89 shows the BRET response to increasing concentrations of unlabelled sunitinib, obtained under the same experimental conditions as Figure 77. Here, a > 550 nm longpass filter was used to detect acceptor emission. A clear increase in BRET ratio was observed, however only at concentrations above 10 μM. This was consistent with observations from Figure 80A and indicated that sunitinib is a dim fluorescent molecule. Furthermore, lysing of the cells did not change the BRET response.

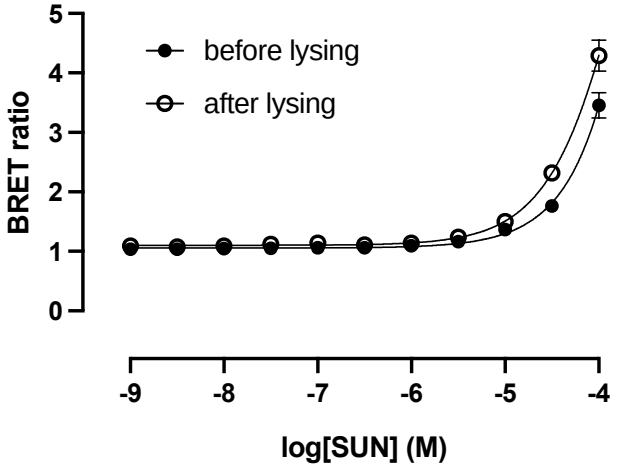

Figure 88: Autofluorescence of unlabelled sunitinib. *Cells were pre-incubated with 1 nM $VEGF_{165}a$ for 15 min, followed by increasing concentrations of unlabelled sunitinib (1 nM – 100 μM) for a further 1 h at 37 °C/5% CO_2. Furimazine (1:400) was added to each well and the plates were incubated for a further 10 min at 37 °C/5% CO_2 before BRET ratios were determined (filled circles). The cells were then lysed using NanoGlo® lytic buffer at room temperature for 10 min and BRET measured a second time (open circles). Consistent with Figure 77, this assay was performed in white half-well 96 well plates, in a total volume of 25 μL. To detect acceptor emission (from unlabelled sunitinib), a > 550 nm longpass filter was used, as the expected maximum emission was at 540 nm. BRET ratios were calculated as acceptor/donor emission values from the second of three cycles. Data are presented as mean ± S.E.M from 5 individual experiments (n=5) in triplicates.*

6.3.7. Summary

In summary, treatment of the VEGFR2-NL transfected cells with sunitinib-red resulted in a concentration-dependent BRET response in lysed cells. Sunitinib-red displayed relative quick binding to the receptor, compared to cediranib and fostamatinib.

Unlabelled sunitinib, cediranib and motesanib displayed a high affinity for VEGFR2 and high potency for inhibition of the $VEGF_{165}a$-induced NFAT response. Fostamatinib and its active metabolite showed a more moderate inhibition of the responses in the nanoBRET assay and in the NFAT assay. Erlotinib and cerdulatinib did not affect the sunitinib-red-induced BRET signal and $VEGF_{165}a$-induced NFAT signal. Surprisingly, dasatinib and entospletinib did interfere with the NFAT signalling, despite not binding VEGFR2-NL directly. An overview of all values for $\log K_I$ (affinity, nanoBRET assay) and $\log IC_{50}$ (potency, NFAT assay) of the nine inhibitors can be found in Table 21.

Table 21: Overview of the affinity and potency of the nine tested inhibitors for VEGFR2. *$LogK_I$ and K_I represent the inhibitor's affinity for VEGFR2, determined using the nanoBRET assay. $LogIC_{50}$ and IC_{50} represent the potency for inhibition of the $VEGF_{165}$a-induced VEGFR2 signalling, determined using the NFAT assay. (NI, no inhibition)*

TKI	Inhibition of sunitinib-red binding $LogK_I$	Inhibition of sunitinib-red binding K_I (nM)	Inhibition of NFAT response to $VEGF_{165}$a $LogIC_{50}$	Inhibition of NFAT response to $VEGF_{165}$a IC_{50} (nM)
Sunitinib	-8.20 $\pm$ 0.13	6.3	-7.90 $\pm$ 0.12	12.6
Cediranib	-8.24 $\pm$ 0.12	5.8	-8.73 $\pm$ 0.02	1.9
Motesanib	-8.01 $\pm$ 0.10	9.8	-7.97 $\pm$ 0.10	10.7
Fostamatinib	-6.71 $\pm$ 0.12	195.0	-6.58 $\pm$ 0.32	263.0
R406	-6.44 $\pm$ 0.11	363.1	-6.87 $\pm$ 0.06	134.9
Erlotinib	NI	NI	NI	NI
Cerdulatinib	NI	NI	NI	NI
Dasatinib	NI	NI	-6.96 $\pm$ 0.19	109.6
Entospletinib	NI	NI	-8.28 $\pm$ 0.21	5.2

6.4. Chapter discussion

6.4.1. Sunitinib-red as a fluorescent tracer in the intracellular nanoBRET assay

In this Chapter, first the nanoBRET assay was optimised for the binding of sunitinib-red to VEGFR2-NL. Sunitinib-red is a fluorescent TKI, linking sunitinib to PerkinElmer's red 'D2' dye. Interestingly, sunitinib-red did not induce a BRET response in intact cells (Figure 76A). Lysing the cells however, lead to a significant increase in BRET ratio in sunitinib-red treated wells compared to vehicle-treated wells (Figure 76B), in a concentration-dependent manner (Figure 77). This suggested that the addition of the D2 dye on sunitinib led to a cell impermeable molecule. A concentration of furimazine of 1:400 was found ideal in this assay, as increasing the concentration did not improve the signal window (Figure 76B). Furthermore, pre-treatment with $VEGF_{165}a$ did not significantly change the BRET response to 100 nM sunitinib-red (Figure 76B). In subsequent nanoBRET assays cells were pre-treated with 1 nM $VEGF_{165}a$, to be consistent with the NFAT protocol. Time-course experiments revealed a fast association of sunitinib-red at the intracellular kinase domain of VEGFR2 in lysed cells (Figure 78 and Figure 79). In the NFAT assay, in contrast to unlabelled sunitinib, sunitinib-red did not affect the $VEGF_{165}a$-response (Figure 82), again suggesting this fluorescent sunitinib-derivative did not enter the intact cells. The D2 dye showed similar characteristics as Cy5, a cell membrane-impermeable fluorophore with a similar fluorescent emission spectrum as sunitinib-red (maximum excitation at 649 nm and maximum emission at 664 nm (Fernández-Suárez and Ting 2008, Figure 88).

As unlabelled sunitinib showed autofluorescence (Figure 80A and Figure 88A), is cell membrane permeable and is less costly, its use as a fluorescent tracer in the nanoBRET assay was explored. However, high concentrations (> 10 μM) of the non-labelled version of sunitinib were needed to induce a response in BRET signal (Figure 89). Moreover, unlike inorganic fluorophores, used to fluorescently tag proteins of interest, unlabelled sunitinib is a naturally fluorescent compound and emits dim light over broad wavelengths (Figure 88A). Unlabelled sunitinib exhibited maximum emission at a lower wavelength than sunitinib-red (λ_{max} 540 nm versus 665 nm respectively), resulting in more spectral overlap between unlabelled sunitinib and NLuc (λ_{max} 450 nm). For these reasons, unlabelled sunitinib was not suitable as a fluorescent tracer to determine binding affinities of other TKIs in the nanoBRET competition experiments in this Chapter.

6.4.2. Inhibitory effects of nine TKIs at VEGFR2

Binding affinities of selected TKIs were determined in the nanoBRET assay (Figure 80) and compared to functional responses in the NFAT assay (Figure 83). All inhibitors that were binding VEGFR2, displayed inhibition of the downstream signalling NFAT pathway. Sunitinib, cediranib and motesanib were the most potent inhibitors of VEGFR2. Fostamatinib showed a less potent inhibition of sunitinib-red binding to the receptor and NFAT luminescence response. The active metabolite R406 displayed similar affinities and potencies as its prodrug. Given that fostamatinib is converted to R406 by phosphatases in the intestinal mucosa (Sweeny, Li, Clough, et al., 2010; Sweeny, Li, Grossbard, et al., 2010) and several phosphatases are expressed in HEK293 cells, potentially fostamatinib was rapidly converted in these assays, resulting in similar responses as direct R406 treatment. As anticipated, EGFR-inhibitor erlotinib and Syk inhibitor cerdulatinib did not display any effect in both NFAT and nanoBRET assay. Interestingly, entospletinib and dasatinib were not binding directly to the receptor, but nonetheless inhibited its downstream signalling in the NFAT assay. This functional inhibition effect was recapitulated in the ionomycin-induced NFAT response, indicating entospletinib and dasatinib interfered with the NFAT response independent from VEGFR2 activation, and downstream of the event of intracellular calcium increase, as shown in Figure 24 (Chapter 2).

6.4.3. Syk in VEGFR2 signalling

As Syk is expressed in HEK cells (The Human Protein Atlas, 2023), the effect of entospletinib in the NFAT assay might be directly related to the inhibition of Syk and independent from binding to VEGFR2.

As mentioned in Chapter 1, section 1.3.2., the two SH2 domains of Syk bind to dual phosphorylated ITAMs associated with immunoreceptors. This leads to conformational changes of Syk and activation of its tyrosine kinase domain (Mócsai et al., 2010). Alternatively, two hem-ITAMs (a single phosphorylated residue) on two separate but dimerised receptors may provide docking sites for the SH2-domains of Syk (Bauer & Steinle, 2017; Mócsai et al., 2010). Interestingly, tyrosine residue Y1175 in VEGFR2 can provide hemi-ITAMs for Syk binding and activation (Kazerounian et al., 2011). Additionally, Kazerounian *et al.* reported that Syk increases phosphorylation of Y1175 of VEGFR2 (Kazerounian et al., 2011), a tyrosine residue in the C-terminal part of the receptor, and key phosphorylation site for the induction of its downstream signalling (Peach et al., 2018; X. Wang et al., 2020). However, others has shown that silencing or inhibition of Syk did not affect VEGF-induced VEGFR2 Y1175 phosphorylation (Chu et al., 2013). Lastly, increased phosphorylation of Syk following VEGFR2 receptor dimerization has been reported (Kazerounian et al., 2011).

Given this interplay of Syk and VEGFR2, the observed inhibition of the NFAT response by entospletinib might be related to its on-target inhibition of Syk, independent from direct binding at the kinase domain of the receptor. However, cerdulatinib, the other Syk inhibitor that was tested, did not affect the NFAT response, thus the entospletinib-induced signalling inhibition was likely not Syk-mediated. Moreover, entospletinib inhibited the ionomycin-induced NFAT response with a similar potency as the $VEGF_{165}$a-induced NFAT response, indicating that this compound is exhibiting its effect independent from VEGFR2 activation.

6.4.4. Cardiovascular adverse drug effects of dasatinib

Dasatinib displayed a similar inhibitor profile for VEGFR2 as entospletinib. Interestingly, this compound is associated with pulmonary arterial hypertension, that persist after treatment-discontinuation in one third of patients (Guignabert et al., 2016; Weatherald et al., 2017). This adverse drug reaction has been linked to a dasatinib-induced elevation in serum markers for vascular damage and endothelial dysfunction (Guignabert et al., 2016). Dasatinib targets BCR-ABL, but multiple other tyrosine kinases as well, such as PDGFRs, the SRC kinase family, KIT and ABL (Cheng & Force, 2010; Davis et al., 2011; El-Dabh & Acharya, 2019). Inhibition of SCR kinases has been suggested as a potential cause of the dasatinib-induced pulmonary hypertension, however SCR-independent pathways might be involved as well (El-Dabh & Acharya, 2019). Given this non-specific kinase inhibition of dasatinib, it is likely that the decrease in NFAT response observed with this drug is due to interference with one or several cytoplasmic kinases that are involved in the VEGFR2 signalling pathway. In particular the kinases from the SRC family are involved in multiple receptors signalling pathways, and inhibition of these kinases might result in multiple off-target effects. Dasatinib for example inhibits Lyn, which phosphorylates Syk and ITAMs (Davis et al., 2011; Mócsai et al., 2010; Singh et al., 2012), but also Src, which is involved in VEGFR2 signalling (Davis et al., 2011; X. Wang et al., 2020).

6.4.5. Selectivity of entospletinib for Syk

Both dasatinib and entospletinib did not bind to VEGFR2 directly but interfered with its downstream signalling, and dasatinib is known to cause vascular damage in the lungs (Guignabert et al., 2016; Weatherald et al., 2017). Entospletinib is selective for Syk, however it still binds other tyrosine kinases with a ~10 fold lower affinity (e.g. Src and KIT) (Currie et al., 2014). Plasma concentrations of entospletinib easily reach 1 μM to achieve therapeutic effect (Currie et al., 2014; Ramanathan et al., 2017) and entospletinib inhibited the NFAT response with a high efficacy (IC_{50} = 5.2 nM), suggesting that, at relevant plasma concentrations, this second generation compound might exhibit VEGFR2 signalling inhibition and associated cardiovascular safety liability.

6.4.6. Further experiments

Given that dasatinib-red (dasatinib linked to the D2 dye, (Cisbio, 2023a)) is commercially available, an interesting follow-up experiment would be to characterise its binding to several nanoLuciferase-tagged cytoplasmic kinases, combined with a competition experiment by entospletinib, to investigate binding affinities of these two compounds for shared inhibited kinases. Moreover, looking at inhibition of VEGFR2 signalling other than NFAT, for example the ERK pathway, would potentially provide additional insights into how entospletinib established the functional signalling inhibition.

6.5. Chapter conclusion

The aim of this Chapter was to provide complementary information about the interference of fostamatinib and entospletinib in VEGFR2 activation and signalling. Firstly, a nanoBRET assay was developed to monitor intracellular binding of TKIs at VEGFR2, using sunitinib-red. Sunitinib-red was not cell membrane-permeable, but did induce a robust BRET response in lysed cells. Secondly, performing a competition experiment with sunitinib-red in the nanoBRET assay, the affinities of nine selected TKIs for VEGFR2 were determined. Lastly, these binding affinities were compared to the compounds' potencies to inhibit the $VEGF_{165}$a-induced NFAT response.

Fostamatinib and R406 displayed a moderate binding affinity to the receptor and inhibited VEGFR2 signalling, consistent with literature (Lengel et al., 2015; M. Skinner et al., 2014). Entospletinib did not bind to the receptor directly, as previously reported (Currie et al., 2014). The latter however did interfere in the VEGFR2 signalling pathway. Dasatinib, a non-selective kinase inhibitor that is associated with vascular toxicity and pulmonary hypertension (Davis et al., 2011; Guignabert et al., 2016), showed similar characteristics as entospletinib. Jak/Syk inhibitor cerdulatinib did not interfere with the VEGFR2 NFAT response. Altogether, the data in this Chapter indicated that entospletinib exhibits effects beyond Syk inhibition alone and, although the exact mechanism was not identified, these effects could potentially be involved in subtle cardiovascular safety liabilities.

7. CHAPTER 7: GENERAL DISCUSSION

7.1. Research summary and general discussion

Safety pharmacology aims to identify and investigate new compounds that exert undesired drug effects. Since 2001, the implementation of ICH S7A, the current guideline for conducting preclinical safety assessment, has enhanced the detection and understanding of adverse drug reactions, yet safety related drug attrition remains a prominent issue in drug development, in particular in late stages of the R&D pipeline and at post-marketing stages (section 1.2.2.). The conventional core approach of *in vivo* CV safety assessment includes evaluation of the ECG, MAP and HR (section 1.2.1.). The latter two measurements indeed demonstrate acute effects of therapeutics on the cardiovascular system, with consequent hypotension or hypertension, and tachycardia or bradycardia, respectively. Yet the signals from which MAP and HR are derived are high-fidelity waves, containing a greater amount of information than reported by MAP and HR (section 1.5.2.). Therefore, the experiments described in this thesis were designed to interrogate the entire physiological waveform to potentially identify new CV safety markers and to aid in closing the current gaps in safety pharmacology. For this, two Syk inhibitors were selected: fostamatinib, associated with a BP elevation due to off-target inhibition of VEGFR2 (section 1.3.4.3.) and entospletinib, a more selective Syk inhibitor and associated with little overt CV ADR (section 1.3.5.). The objective was to explore the application of SPAR, a novel approach to wave analysis that allows for in-depth characterisation of waveform morphology and variability (section 1.5.5.), on BP and blood flow waves in rats following administration of the Syk inhibitors. Additionally, the inhibitory effects of these Syk inhibitors at VEGFR2 were evaluated *in vitro* to provide mechanistic insights.

Chapter 3 provided the conventional assessment of the Syk inhibitors' cardiovascular effects, as typically performed in preclinical safety studies. Alongside two vasodilators (vardenafil and molsidomine) and an established VEGFR2-inhibitor (sunitinib) with known cardiovascular effects, the Syk inhibitors were evaluated using radiotelemetry in rats. Both vasodilators induced a hypotension that was associated with a rapid increase in HR and decrease in PP (section 3.3.1. and 3.3.2.). Sunitinib evoked a hypertensive response, with little effect on HR or PP (section 3.3.3.). Fostamatinib increased MAP, that was significant from the second day of the study and did not affect HR or PP (section 3.3.4.). Lastly, entospletinib did not affect

any of the conventional wave analysis parameters (section 3.3.5.). This analysis served as a representation of current approaches in safety pharmacology and results were used for comparison to novel SPAR analysis in the next Chapter.

In **Chapter 4**, the BP waves obtained in the telemetry studies were analysed in SPAR. Firstly, the method was optimised for use in this model (section 4.3.1.) and validated using the vasodilator data, showing a decrease in metrics related to the roundness of the attractor, such as rQ25, and indicating a vasodilation-associated decrease in wave reflection. These data demonstrated the ability of SPAR to detect changes in BP waveform morphology and variability (section 4.3.2., 4.3.5.1 and 4.3.5.2.). Sunitinib did not cause clear changes in the SPAR metrics analysed (section 4.3.5.3.). Potentially other SPAR features, that could not be quantified at the time of analysis, could pick up sunitinib-induced changes in the waveform. SPAR reported fostamatinib-induced wave changes that were opposite to the ones observed with the vasodilators (increasing metrics such as rQ25, indicating an increase in wave reflection, section 4.3.5.4.), demonstrating a vasoconstriction as anticipated. These effects were detected from the first day of the experiment, thus highlighting fostamatinib-induced CV ADR earlier than MAP. Furthermore, SPAR revealed entospletinib-induced wave changes that were similar to the ones observed with fostamatinib, providing a first indication of potential cardiovascular effects of this compound (section 4.3.5.5.). In summary, SPAR detected cardiovascular effects of both fostamatinib and entospletinib in a more sensitive way than the conventional analysis and thus could serve as a novel approach to characterise the cardiovascular safety profile of other compounds at preclinical or clinical stages.

Chapter 5 aimed to characterise the effects of the two Syk inhibitors, alongside sunitinib, on the VC in three vascular beds in the Doppler flowmetry model in rats, combined with their effects on SPAR metrics derived from the blood flow waves. Sunitinib induced changes in MAP, HR and the three VC that mirrored those typically observed with VEGFR2-inhibitors (section 5.3.1.1.). SPAR indicated large decreases in waveform variability and increases in wave reflection following sunitinib-administration (section 5.3.2.). Fostamatinib partially reflected those effects, showing a small decrease in the renal and aortic VC in the conventional analysis (section 5.3.1.2.) and indications of a vasoconstriction in the mesenteric bed in the SPAR analysis (section 5.3.2.). Entospletinib did not display any effects on the VC in the conventional analysis (section 5.3.1.3.) but in-depth wave analysis of the BP, mesenteric and hindquarters flow uncovered a vasoconstricting effect of entospletinib (section 5.3.2.), again suggesting potential CV safety issues of this compound.

Lastly, in **Chapter 6** an *in vitro* nanoBRET assay was developed to determine the Syk inhibitors' binding affinities to VEGFR2. This assay showed an intermediate affinity of fostamatinib for VEGFR2 and no binding of entospletinib at the level of the receptor (section 6.3.2.). In the NFAT reporter gene assay however, both Syk inhibitors inhibited the downstream signalling of VEGFR2 and entospletinib displayed an approximately 100-fold higher potency for this effect than fostamatinib (section 6.3.3.).

Data were discussed in detailed at the end of each Chapter. Below, a general discussion is presented about (1) the application of SPAR in preclinical safety pharmacology and (2) the findings around entospletinib's cardiovascular effects.

7.1.1. General discussion of application of SPAR in safety pharmacology

The experiments performed in this thesis demonstration that SPAR was a suitable method to detect changes in waveform variability and morphology of both blood pressure of blood flow waveforms. The body of work performed in this thesis implied that this novel wave analysis method can potentially (1) produce markers that have physiological significance, (2) detect CV ADR earlier than MAP, HR or PP and (3) detect CV ADR more sensitive than MAP, HR, PP or VC. Previous studies indeed indicated that more comprehensive CV wave analysis could provide additional insights beyond MAP and HR, both in clinical settings (Janić et al., 2014; Masuda et al., 2013; McEniery et al., 2008; Millasseau et al., 2003; Safar et al., 2002) and *in vivo* (C. Y. Chang et al., 2017; R. W. Chang et al., 2017; P. Laurent, Safar, et al., 2003). However the real-life application of these methods has been limited as they require simultaneous pressure or flow recordings at two site in the vasculature or employ mathematical models that rely on estimations and therefore are less informative (Avolio et al., 2009; Kips et al., 2009; Mynard et al., 2020). SPAR is a method that overcomes these complications and is easier to implement. Moreover, it is a visual method that reports on several waveform components simultaneously from one analysis, rather than combining several methods to characterise the full profile of the CV wave, thus SPAR provides a single comprehensive approach to wave analysis.

Yet effort is needed to fully characterise and further develop SPAR ahead of its implementation in safety pharmacology studies. For example, in this thesis sunitinib was anticipated to induce effects opposite to those observed with the vasodilators in the BP metrics from telemetry, however this was not consistently the case. On the other hand, SPAR metrics derived from the BP wave recorded with the Doppler model did show large changes following sunitinib administration. Potential reasons for the lack of SPAR metric changes in the telemetry study are discussed in section 4.2.2. In brief, it could be that the metrics selected in Chapter 4 were not appropriate to detect sunitinib-induced changes and other, new SPAR features would be able to detect those. Indeed, from visual analysis of the attractors, some sunitinib-induced changes were observed. However as the SPARKS application was still being developed at the moment of analysis, the algorithm was not yet developed in a way that allowed for calculation of these characteristics of the attractor, therefore these changes could not be objectively quantified. Moreover, a higher dose of sunitinib was used in the Doppler study compared to the telemetry study (16 $mg.kg^{-1}.day^{-1}$ IV versus 7 $mg.kg^{-1}.day^{-1}$ orally), which likely contributed to larger effects observed in the Doppler SPAR metrics. Another example of where more validation of the method is needed, is presented by the aortic SPAR metrics. The interpretation of these metrics was not clear as some positive and negative controls were lacking in this study. Potential future steps to further explore the use of SPAR in safety pharmacology are detailed below (section 7.2.).

Although the measurement of blood flow changes is an approach that is not widely applied in industry settings, it highlights important regional vasoactive properties of a drug. Recently efforts have been made to develop telemetric Doppler probes (Arnall et al., 2017; Brijs et al., 2019; Neary et al., 2017). Although this technique measures only two flows simultaneously at the moment, the emerge of such telemetry methods to determine blood flows in freely moving animals will allow for easier and less labour-intensive monitoring of blood flow velocity changes alongside BP, compared to the Doppler flowmetry model, and may make this approach more widely available. In that case, SPAR analysis of recorded blood flow waves would be a helpful addition besides MAP, HR and VC in drug development, as it provides more comprehensive information without the need of supplementary animals or experiments.

The findings of this thesis served as a proof of concept of the application of SPAR in safety pharmacology. Other studies utilising SPAR to interrogate physiological waves have reported promising results as well. For example, Lyle *et al.* showed that SPAR performed better than standard ECG interval measures at identifying a subjects sex from clinical ECG signals (J. V. Lyle et al., 2017). Using short mouse ECG recordings, Bonet-Luz *et al.* (2020) showed that utilising SPAR metrics, a better accuracy for classifying genotypes associated to arrythmias was obtained than with standard ECG metrics, and that the combination of both SPAR and standard metrics resulted in the highest classification accuracy (Bonet-Luz et al., 2020). Moreover, Huang *et al.* reported that SPAR metrics combined in a machine learning approach generated a model with high sensitivity to detect arterial fibrillation from short ECG-recordings of equine athletes (Y. H. Huang et al., 2022). Not only cardiovascular waves can be examined in SPAR; Pascual *et al.* employed the method to identify novel biomarkers for hypercapnia from respiratory waveforms (Pascual et al., 2021).

Altogether, the above-mentioned studies and this thesis indicate that SPAR is a valuable method to explore further in detail. Incorporation of SPAR in preclinical safety testing could extend findings from existing parameters such as MAP and HR and provide a more comprehensive safety profile. Most likely a multifactorial analysis combining conventional metrics with novel SPAR metrics is most suitable for risk assessment and risk management of new compounds.

7.1.2. General discussion of entospletinib findings

Findings from Chapter 5, 6 and 7 raised the question whether entospletinib is associated with CV ADR, as it induced SPAR metric changes similar to those observed with fostamatinib, and inhibited VEGFR2 signalling. No literature was found to support this finding. Tabeling *et al.* reported that in lungs of mice, inhibition of Syk rapidly reversed pulmonary vasoconstriction independent from NO (Christoph Tabeling et al., 2018). Hwan *et al.* showed that Syk is involved in the ET-1-induced vasoconstriction of isolated rat thoracic aorta and Syk inhibition attenuated this vasoconstriction (Hwan et al., 2007). These studies suggested opposite vasoactive effects of Syk inhibition than those observed with entospletinib here. However, Tabeling *et al*. only investigated the pulmonary vascular bed, and these findings do not necessarily translate to other vascular beds. Furthermore, both studies mentioned above were performed *ex vivo* and perhaps did not reflect physiological events *in vivo*. In contrast, in this thesis, the *in vivo* experiments were carried out in unanaesthetised rats. More importantly, the *in vitro* findings in Chapter 6 indicated that the observed inhibition of VEGFR2 signalling by entospletinib is independent from its on-target inhibition of Syk (section 6.4.3.). Likewise, its *in vivo* CV effects may be due to off-target inhibition of other tyrosine kinases and unrelated to the vasoactive properties of Syk.

Given the clues of CV effects presented in this thesis, it is important to further characterise entospletinib's CV safety liabilities (as detailed below, section 7.2.) and take these findings into account when designing combination therapies with entospletinib. For example, entospletinib is currently being evaluated for acute myeloid leukemia in combination with cytarabine and daunorubicin (Borate et al., 2022; Walker et al., 2020), two drugs that have been associated with cardiotoxicity (Conrad, 1992; Kikukawa et al., 2012; Neuendorff et al., 2020; Samosir et al., 2021; Yeh et al., 2004). Likewise, entospletinib is being investigated for chronic lymphocytic leukemia and B-cell malignancies in combination with obinutuzumab (Kittai et al., 2021; Lam et al., 2021), a monoclonal antibody that has been associated with an increased risk of cardiac events, including acute myocardial infarction, bradycardia, atrial fibrillation and heart failure (Marcus et al., 2017; Vitolo et al., 2017). Although in this thesis the CV effects observed with entospletinib were subtle, they might appear more severely over the longer term, especially in combination with other cardiotoxic drugs. Hence, proper risk assessment before marketing, and post-marketing monitoring of cardiovascular complications is warranted (Curigliano et al., 2010; Vallerio et al., 2022).

7.2. Future directions

As stated above, validation and optimisation of the SPAR method should be continued. First, advancing the SPAR algorithm so that it can quantify all features of the attractor would allow an even more comprehensive characterisation of the CV effects of each test compounds. Additionally, more work is needed to validate the model and link its metrics to their physiological interpretation. Below examples of studies to perform are given:

- Assessing reference compounds *in vivo* such as:
    - Vasodilators, e.g. clonidine, centrally acting vasodilator or hydralazine, an arteriole vasodilator,
    - Other RTKIs to see if similar SPAR metric changes are observed as with sunitinib, e.g. axitinib or cediranib,
    - Vasoconstrictors, e.g. endothelin-1 or norepinephrine, two endogenous vasoconstrictors,
    - Atropine, a muscarinic receptor antagonist that induces tachycardia,
    - Negative controls not displaying CV ADR, e.g. cerdulatinib, a second generation Syk inhibitor with no affinity or potency for VEGFR2 inhibition or erlotinib, a selective EGFR-inhibitor.

  These studies may include historical *in vivo* data of compounds with a well-characterised CV profile and dose-escalation studies to compare at what plasma level SPAR versus MAP or HR can detect ADR and determine the relative sensitivity of both approaches.
- Additionally, as performing *in vivo* studies can be time-consuming, using *in silico* databases containing simulated blood pressure/flow waves (Boccadifuoco et al., 2018; Peter H. Charlton et al., 2019; Hewlin & Kizito, 2018; Willemet et al., 2016) may be a valuable approach. As components of the waveform are easily adjusted in a simulated wave and corresponding attractor changes can be determined consistently, using *in silico* waveform data enables identification of relevant SPAR metrics and link those to waveform changes and could additionally serve as a further validation of *in vivo* findings as well.

Secondly, in light of SPAR results indicating small entospletinib-induced vasoconstrictions, a follow-up experiment testing the vasoactive effects of entospletinib in isolated rat arteries and veins *ex vivo* could investigate this further. Myography is a technique that could be employed for this study, as it monitors the vascular function, structure and biomechanical properties (Wenceslau et al., 2021). An isolated vessel is mounted onto glass pipettes (pressure myography) or stretched by wires or pins that are passed through the lumen on the vessel (isometric force myography) and changes in vessel diameter are measured, indicating a vasoconstriction or dilations (Buus et al., 1994; Falloon et al., 1995). The vasoactive effect of entospletinib on several arteries, e.g. mesenteric and distal abdominal aortic isolated from rats could be evaluated using this set-up, followed by the evaluation of entospletinib-induced changes in vessel reactivity in preconstricted (e.g. by phenylephrine) or predilated (e.g. by $VEGF_{165}a$) vessels. Fostamatinib, sunitinib, erlotinib and cerdulatinib could be included as positive and negative controls.

Lastly, further experiments should identify kinases involved in the VEGFR2 signalling inhibition established by entospletinib. As discussed in Chapter 6 (section 6.4.6.), dasatinib-red is commercially available and the use of this fluorescently tagged non-selective TKI in a NanoBRET proximity assay could shed some light on the selectivity profile of entospletinib as well. The cell permeability of labelled dasatinib in HEK cells should be evaluated first, as the red tag seemed to hinder the cell membrane permeability of sunitinib (section 6.4.1.). Next, performing displacement experiment of dasatinib-red by entospletinib, as done in this thesis with sunitinib-red, at several NL-tagged intracellular kinases (including SCR kinases and KIT) could highlight where these two TKIs are binding and indicate pathways behind the observed inhibition of VEGFR2 signalling. Moreover, evaluating entospletinib's potency to inhibit other VEGFR2 signalling pathways than NFAT, e.g. ERK, could provide additional insights into how entospletinib established the functional signalling inhibition. Again sunitinib, fostamatinib, erlotinib and cerdulatinib can be included as positive and negative controls.

7.3. Key conclusions

This thesis explored novel approaches in cardiovascular safety pharmacology. In particular the application of SPAR, a novel in-depth wave analysis method, was assessed on blood pressure and blood flow waves. **First**, the CV effects of two Syk inhibitors, fostamatinib and entospletinib, were interrogated in a radiotelemetry model in rats. Conventional analysis of obtained blood pressure waves indicated a BP elevation following fostamatinib administration but did not display any effects with entospletinib. **Second**, BP waves obtained in the telemetry study were analysed in SPARKS, an application for streamlined SPAR analysis. This revealed subtle entospletinib-induced effects in the wave morphology, similar to those observed with fostamatinib. Moreover, this analysis highlighted fostamatinib-induced CV ADR earlier than the conventional analysis did. **Third**, the two Syk inhibitors were evaluated in the Doppler flowmetry model in rats, to investigate their effects on blood flow velocity and blood flow waveforms. Conventional analysis indicated regional vasoconstrictions in the kidney and hindquarters by fostamatinib and no effects by entospletinib. Again, SPAR detected changes that were unnoticed in the conventional analysis. Although more work is needed to unambiguously link the SPAR metrics to physiological changes, SPAR analysis demonstrated vasoconstrictions with both Syk inhibitors. This effect was anticipated with fostamatinib, however was remarkable for entospletinib as this compound was designed to show fewer CV ADR than fostamatinib. **Lastly**, the *in vitro* inhibition of VEGFR2 by fostamatinib and entospletinib was evaluated in HEK cells, showing that fostamatinib but not entospletinib bound to the intracellular site of VEGFR2. Yet both compounds inhibited the $VEGF_{165}$a-induced VEGFR2 downstream signalling, possibly indicating a cause behind the observed entospletinib effect *in vivo*.

By exploring for the first time the application of SPAR on preclinical BP and blood flow waveform data following drug treatment, this thesis added to the overarching aim of INSPIRE to advance the field of cardiovascular safety pharmacology.

8. CHAPTER 8: APPENDIX

8.1. SPAR parameters

Table 22: Predefined sets of SPAR parameters as available in the SPARKS application. *In this thesis, the HumanBP set was used, with adjusted values for Ratemin and Ratemax to mirror typical HR in rat.*

	HumanRF	MouseBP	HumanBP	**HumanBP with adjustments used in this thesis**
datalowerlim	-6	40	0	0
dataupperlim	6	200	300	300
datajmp	0.25	10	100	100
timeshiftbar	0.5	120	100	100
Ratemin	6	400	40	**230**
Ratemax	60	800	180	**550**
Attlim_density	-1	3	-1	-1
Dspreadcolourlim	0.0005	0.002	0.002	0.002
Attlim_plot	-1	3	-1	-1
Colourlim_plot	0.0005	-1	0.002	0.002
Rdensityrange_plot	-0.1	-0.1	-1	-1
Units	Flow (L/s)	mmHg	mmHg	mmHg

8.2. VEGFR2 sequence

MQSKVLLAVALWLCVETRAASVGLPSVSLDLPRLSIQKDILTIKANTTLQITCRGQRDLD
WLWPNNQSGSEQRVEVTECSDGLFCKTLTIPKVIGNDTGAYKCFYRETDLASVIYVYVQD
YRSPFIASVSDQHGVVYITENKNKTVVIPCLGSISNLNVSLCARYPEKRFVPDGNRISWD
SKKGFTIPSYMISYAGMVFCEAKINDESYQSIMYIVVVVGYRIYDVVLSPSHGIELSVGE
KLVLNCTARTELNVGIDFNWEYPSSKHQHKKLVNRDLKTQSGSEMKKFLSTLTIDGVTRS
DQGLYTCAASSGLMTKKNSTFVRVHEKPFVAFGSGMESLVEATVGERVRIPAKYLGYPPP
EIKWYKNGIPLESNHTIKAGHVLTIMEVSERDTGNYTVILTNPISKEKQSHVVSLVVYVP
PQIGEKSLISPVDSYQYGTTQTLTCTVYAIPPPHHIHWYWQLEEECANEPSQAVSVTNPY
PCEEWRSVEDFQGGNKIEVNKNQFALIEGKNKTVSTLVIQAANVSALYKCEAVNKVGRGE
RVISFHVTRGPEITLQPDMQPTEQESVSLWCTADRSTFENLTWYKLGPQPLPIHVGELPT
PVCKNLDTLWKLNATMFSNSTNDILIMELKNASLQDQGDYVCLAQDRKTKKRHCVVRQLT
VLERVAPTITGNLENQTTSIGESIEVSCTASGNPPPQIMWFKDNETLVEDSGIVLKDGNR
NLTIRRVRKEDEGLYTCQACSVLGCAKVEAFFIIEGAQEKTNLEIIILVGTAVIAMFFWL
LLVIILRTVKRANGGELKTGYLSIVMDPDELPLDEHCERLPYDASKWEFPRDRLKLGKPL
GRGAFGQVIEADAFGIDKTATCRTVAVKMLKEGATHSEHRALMSELKILIHIGHHLNVVN
LLGACTKPGGPLMVIVEFCKFGNLSTYLRSKRNEFVPYKTKGARFRQGKDYVGAIPVDLK
RRLDSITSSQSSASSGFVEEKSLSDVEEEEAPEDLYKDFLTLEHLICYSFQVAKGMEFLA
SRKCIHRDLAARNILLSEKNVVKICDFGLARDIYKDPDYVRKGDARLPLKWMAPETIFDR
VYTIQSDVWSFGVLLWEIFSLGASPYPGVKIDEEFCRRLKEGTRMRAPDYTTPEMYQTML
DCWHGEPSQRPTFSELVEHLGNLLQANAQQDGKDYIVLPISETLSMEEDSGLSLPTSPVS
CMEEEEVCDPKFHYDNTAGISQYLQNSKRKSRPVSVKTFEDIPLEEPEVKVIPDDNQTDS
GMVLASEELKTLEDRTKLSPSFGGMVPSKSRESVASEGSNQTSGYQSGYHSDDTDTTVYS
SEEAELLKLIEIGVQTGSTAQILQPDSGTTLSSPPV

VEGFR2-sequence (taken from UniProt.org)

- In red: split kinase domain is indicated in red: N-terminal lobe (amino acid 834 – 930) and C-terminal lobe (amino acid 999 – 1162)
- In yellow: activation loop of kinase domain
- In **bold**: Y1054 and Y1059 are important in autophosphorylation of the receptor

(McTigue et al., 1999; X. Wang et al., 2020)

8.3. SPAR metrics extracted from Doppler attractors

Table 23: Each BP attractor measures analysed in this Chapter, with its corresponding change in attractor and wave, and its physiological relevance.

BLOOD PRESSURE			
Measure	**Change in attractor**	**Change in waveform**	**Physiological interpretation**
maxden	Represents the number of data points in the highest density bin ('reddest' bin) of the attractor. The redder the attractor, the lower the waveform variability, thus, the redder the highest density bin, the lower the waveform variability. Low maxden = low density (blue) High maxden = high density (red)	Low maxden = high variability High maxden = low variability	Some drugs might affect variability, indicating activation of several autoregulating mechanisms to maintain blood flow to vital organs.
dspread3	Density in attractor High dspread3 = high density, lot of red Low dspread3 = low density, lot of blue	Low dspread3 = high variability High dspread3 = low variability	
rQ5	Metric extracted from the radial density plot; radial position that includes 5% of data, indication of how data points are spread over attractor. Low rQ5 = closed attractor = high density points close to centre, e.g. high density arms are large or data are evenly spread over attractor. High rQ5 = open attractor = high density points at outer sides of the attractor, e.g. in small high density arms.	Low rQ5 = wave is more symmetrical, followed by flat interbeat interval. High rQ5 = reflected waveform affects entire downstroke rather than only the last part of diastole.	Increase in rQ5 indicates vasoconstriction

Vwmedianradius_heightdiff	This metric is taken from the polar map of the attractor, generated as shown in Figure 90. On the attractor, at each angle a radius (white arrows, Figure 90A) is drawn and at each angle, the minimum radial values, maximum radial value (both shown in blue in the polar map, Figure 90B), and median (red) and mean (pink) value are determined. The metric vwmedianradio_heightdiff is measured as the difference in height between the maximum median radius, and minimum median radius (white arrow in Figure 90B). Low vwmedianradio_heightdiff = open attractor High vwmedianradio_heightdiff = closed attractor	An example is shown in Figure 91, indicating a decrease vwmedianradius_heightdiff is related to an increase in waveform reflection.	Decrease in vwmedianradius_heightdiff indicates vasoconstriction.

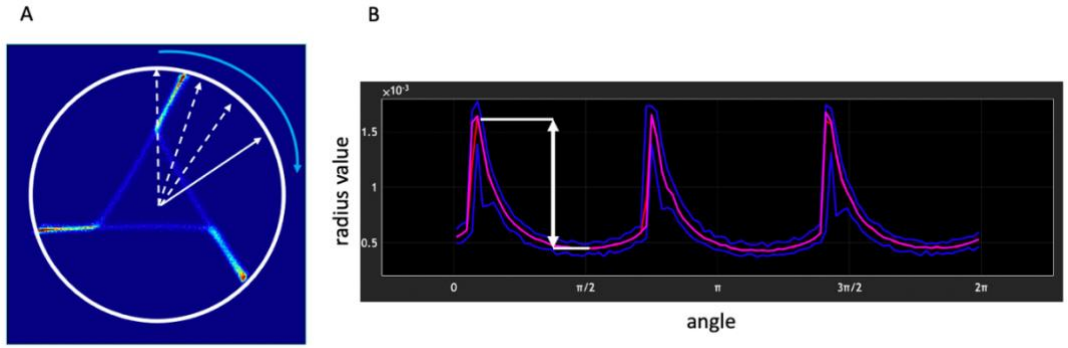

Figure 89: Creation of the polar map of an attractor. *On the attractor, a radius from the centre of the attractor to each point of the attractor is drawn (white arrows, **A**). At each angle, the minimum radial values, maximum radial value (both shown in blue in the polar map, **B**), and median (red, **B**) and mean (pink, **B**) radial values are plotted. The metric vwmedianradio_heightdiff is measured as the difference in height between the maximum median radius and minimum median radius (white arrow in **B**).*

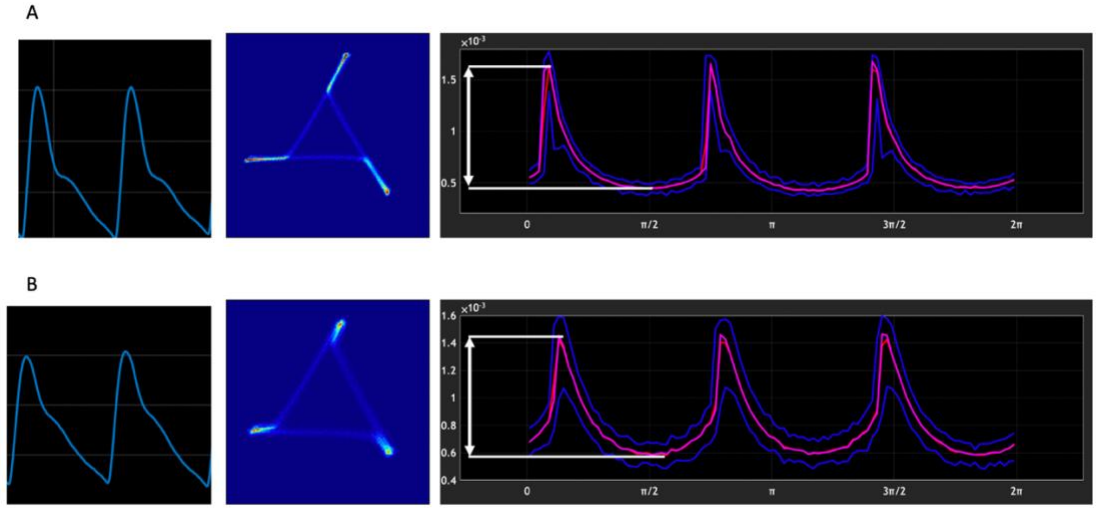

Figure 90: A decrease in vwmedianradius_heightdiff is correlated with an opening of the attractor and an increase in BP wave reflection. (A) *Waveform, attractor and polar map from baseline recording. A vwmedianradio_heightdiff of approximately 1.1 * 10^3 units was measured. **(B)** Waveform, attractor and polar map from the same animal, 30 min after sunitinib bolus dosing. Vwmedianradio_heightdiff decreased (approximately 0.8 * 10^3 units). This was associated with a more open attractor and, in the waveform, a higher contribution of wave reflection in the pressure profile (i.e. the entire downstroke is affected by wave reflection compared to the waveform in A, where wave reflection effects are observed only in the second half of downstroke).*

Table 24: Each renal flow attractor measures analysed in this Chapter, with its corresponding change in attractor and wave, and its physiological relevance.

RENAL FLOW			
Measure	**Change in attractor**	**Change in waveform**	**Physiological interpretation**
Maxrden	This metric is derived from the radial density plot and indicates the maximum radial density. Low maxden = low density (blue) High maxden = high density (red)	Low maxden = high variability High maxden = low variability	Some drugs might affect variability, indicating activation of several autoregulating mechanisms to maintain blood flow to vital organs, here the kidney.
Dspread1	Density in attractor High dspread1 = low density, lot of blue Low dspread1 = low density, lot of red	High dspread1 = high variability Low dspread1 = low variability	
vwmedianradius_bandwidth	This metric is extracted from the polar map of the attractor and is calculated as the average of difference between minimum and maximum radial value in the polar map, as presented by the yellow lines in Figure 92 and Figure 93. The narrower the attractor (more attractor loops are overlapping), the lower vwmedianradius_bandwidth. The broader the sides and arms of the attractor (less overlap between the loops), the higher vwmedianradius_bandwidth.	Thus, bandwidth is directly related to the waveform variability. High bandwidth = high variability Low bandwidth = low variability	

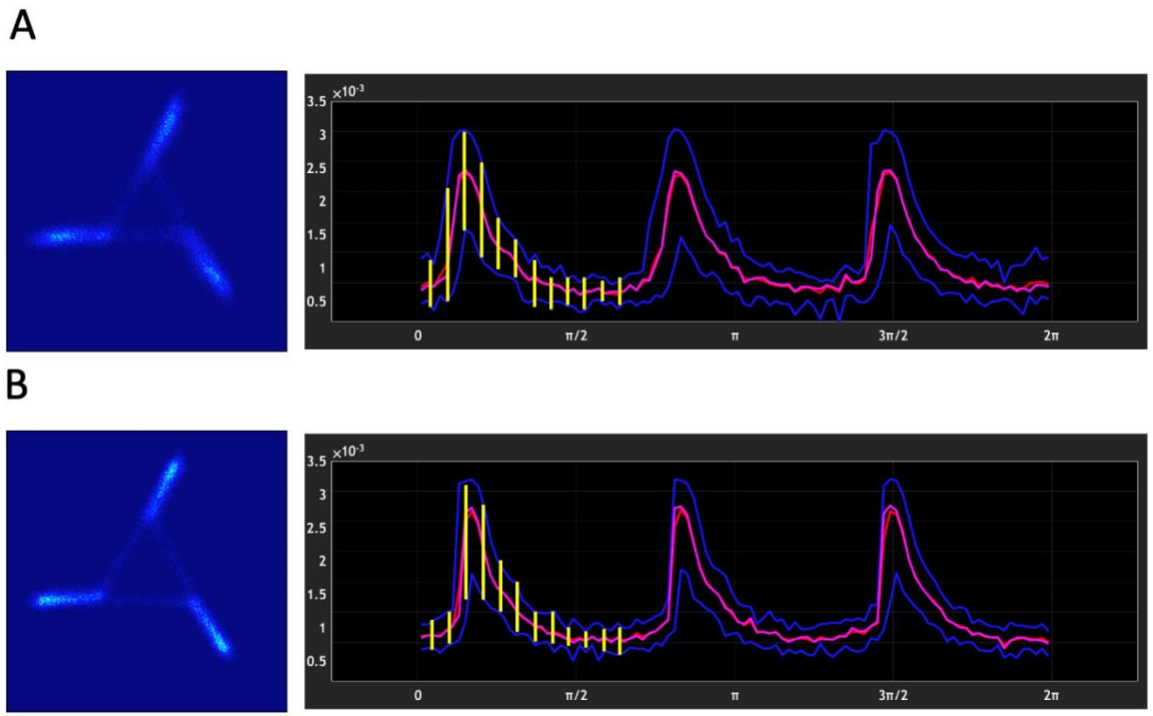

Figure 91: Example of decrease in polar map bandwidth. *A decrease in bandwidth (mean of differences between minimum and maximum radial value at every angle, indicated by yellow lines in the polar map) from 0.24 normalised units in (A) to 0.18 normalised units in (B), is associated with a narrowing of the attractor, indicating a decrease in wave-to-wave variability. Attractors taken from a sunitinib-treated animal, baseline versus 5h after dosing.*

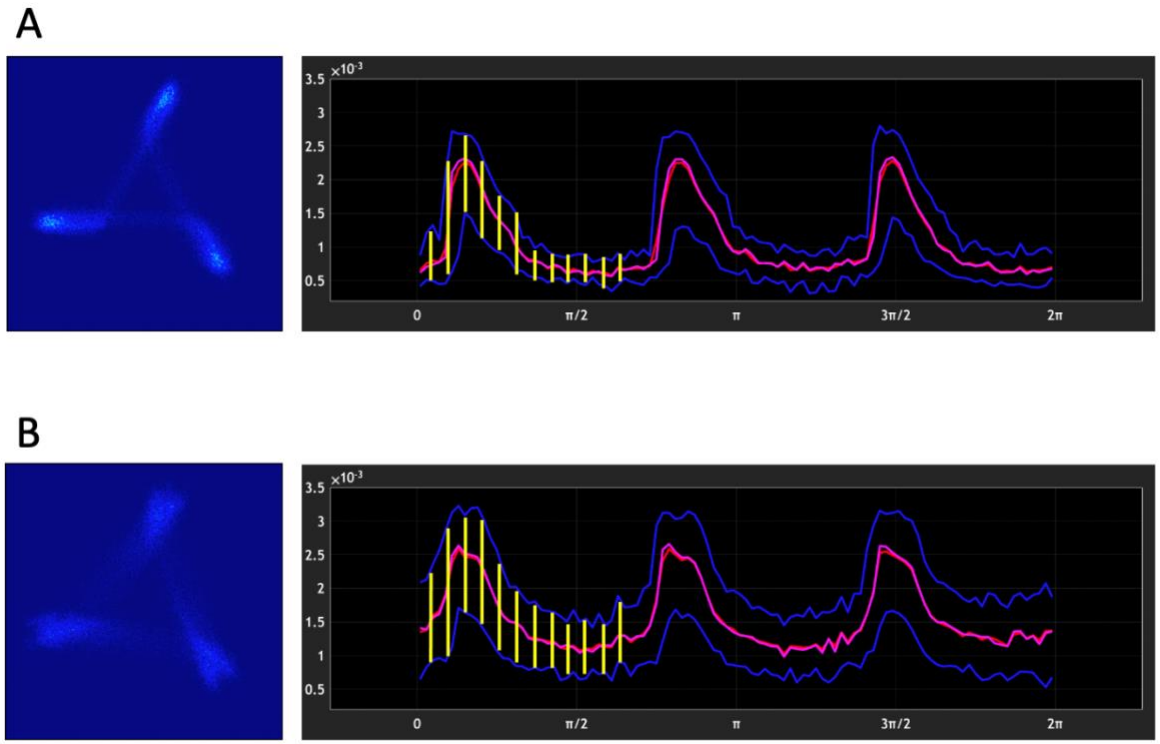

Figure 92: Example of increase in polar map bandwidth*. A decrease in bandwidth (mean of differences between minimum and maximum radial value, indicated by yellow lines in the polar map) from 0.25 units in (A) to 0.31 units in (B), is associated with a broadening of the attractor, indicating an increase in wave-to-wave variability. Attractors taken from an entospletinib-treated animal, baseline versus 5h after dosing.*

Table 25: Each mesenteric flow attractor measures analysed in this Chapter, with its corresponding change in attractor and wave, and its physiological relevance.

MESENTERIC FLOW			
Measure	**Change in attractor**	**Change in waveform**	**Physiological interpretation**
maxden	Represents the number of data points in the highest density bin ('reddest' bin) of the attractor. The redder the attractor, the lower the waveform variability, thus, the redder the highest density bin, the lower the waveform variability. Low maxden = low density (blue) High maxden = high density (red)	Low maxden = high variability High maxden = low variability	Some drugs might affect variability, indicating activation of several autoregulating mechanisms to maintain blood flow to vital organs.
avPP	The metric avPP is calculated as the mean size of the attractor, directly related to the average amplitude of the wave. This metric was originally developed for the analysis of a BP wave, indicating the amplitude of the signal. Similarly, the amplitude of a blood flow wave can be measured. An illustrative example is shown in Figure 94. High avPP = large attractor Low avPP = small attractor	High avPP = high amplitude Low avPP = low amplitude	High avPP = decrease of the minimum flow indicating an increase in flow wave reflection and thus a vasoconstriction. Low avPP = increase of the minimum flow, indicating less wave reflection, and thus a vasodilation in the downstream vascular bed (Nichols et al., 2022).
rQ75	Metric extracted from the radial density plot; radial position that includes 75% of data, indication of how data points are spread over attractor. High rQ75 = closing of the mesenteric attractor, higher density points at the outer edges of the attractor (illustrated by example in Figure 95).	High rQ75 = flattening of the interbeat interval of the mesenteric flow waveform.	High rQ75 indicates a vasoconstriction.

vwmediannorm	This metric indicates the rotational symmetry of the attractor and is determined from the polar map of the attractor as followed: several polar maps are created, starting at different angles in the attractor, and these polar maps are superimposed on one another. Vwmediannorm represents the average of differences in median radial values between the superimposed polar maps. The lower vwmediannorm, the more circular the attractor, as a perfect circle will have overlapping polar maps and thus zero differences in median values (i.e. infinite rotational symmetry). An attractor with lower rotational symmetry (e.g. a more triangular attractor) yields higher vwmediannorm values. Low vwmediannorm = opening of attractor (high rotational symmetry) An example is shown in Figure 96.	Low vwmediannorm = flat interbeat interval in the mesenteric flow waveform.	Low vwmediannorm indicates a vasoconstriction.

A. Baseline recording (avPP = 5.52 * 10^{-3} normalised units)

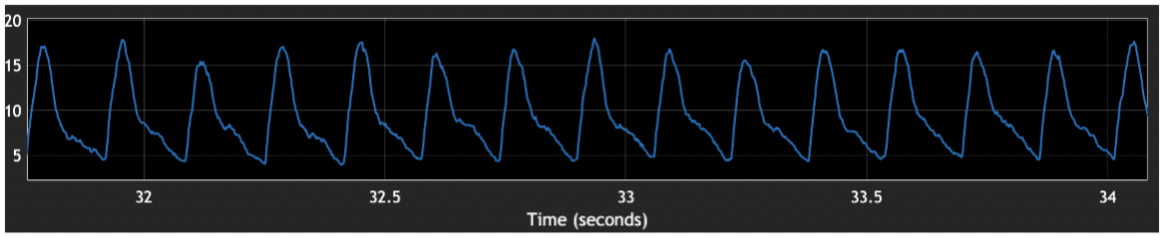

B. 5h post sunitinib bolus-administration (avPP = 9.68 * 10^{-3} normalised units)

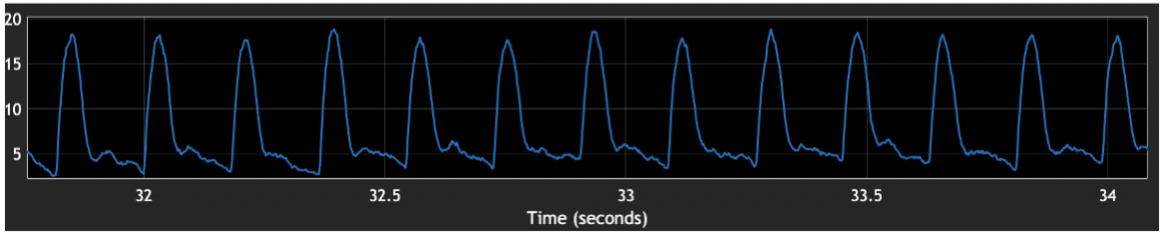

Figure 93: Metric avPP is related to the amplitude of the flow wave. (A) *shows the mesenteric flow wave before drug administration.* ***(B)*** *shows the mesenteric flow wave of the same animal, 5h after the bolus dose of sunitinib. In B, higher wave reflection effects are observed, presenting as a faster downstroke and lower minimum values, compared to the gradual downstroke in (A). This waveform change is linked to an increase in amplitude (metric avPP).*

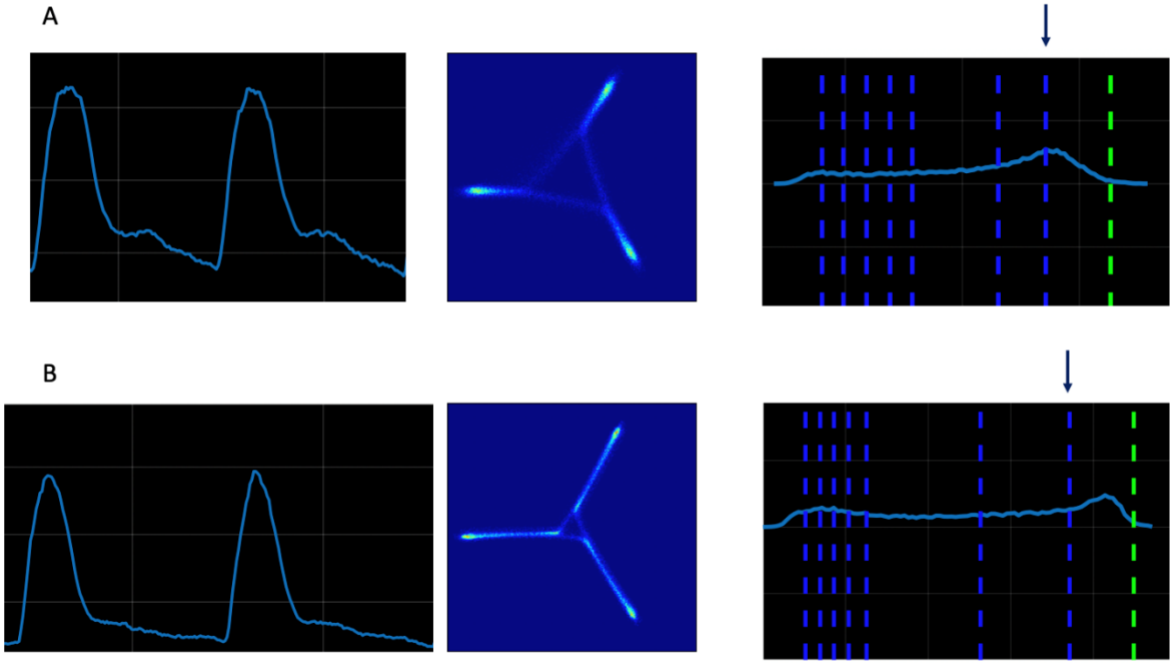

Figure 94: Metric rQ75 is related to wave morphology. (A) *shows mesenteric flow wave, corresponding attractor and radial density plot of an animal before drug administration,* ***(B)*** *shows the flow wave, attractor and radial density plot of the same animal, 5h post sunitinib-bolus dosing. In the radial density plot, the position of rQ75 is indicated with a blue arrow. rQ75 is increased in (B) (7.42 * 10^{-3} units versus 5.43 * 10^{-3} units in (A). This increase in rQ75 was linked to a closing of the mesenteric attractor, higher density points at the outer edges of the attractor (as demonstrated in the radial density plots), and a flattening of the interbeat interval in the wave form.*

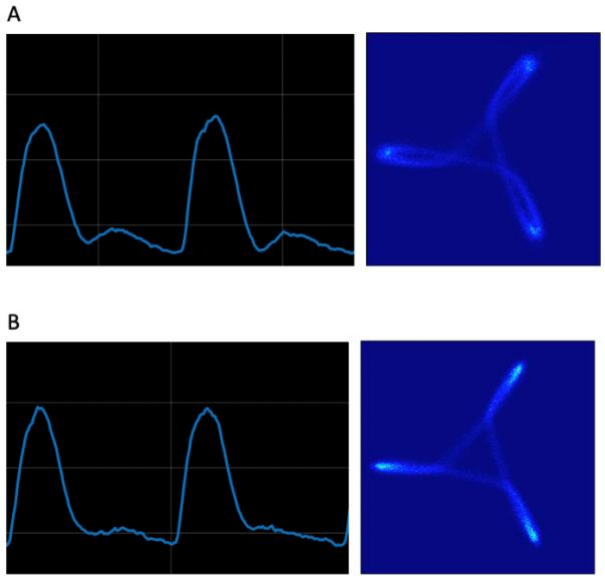

Figure 95: The metric vwmediannorm is related to the rotational symmetric of the attractor. (A) *shows the mesenteric flow wave and attractor of an animal during the baseline recording. Overlapping polar maps of this attractor yielded a vwmediannorm of 0.11 units.* ***(B)*** *shows the mesenteric flow wave and attractor of the same animal, 30 min post bolus dosing of entospletinib. Overlapping the polar maps of this attractor yielded in a vwmediannorm of 0.08 units. The decrease in vwmediannorm indeed was linked to an 'opening' of the attractor towards a more circular shape (i.e. more rotational symmetry). This was associated with a flattening of the interbeat interval of the flow wave.*

Table 26: Each hindquarter (abdominal aorta) flow attractor measures analysed in this Chapter, with its corresponding change in attractor and wave, and its physiological relevance wher e understood.

MESENTERIC FLOW			
Measure	**Change in attractor**	**Change in waveform**	**Physiological interpretation**
Maxrden	This metric is derived from the radial density plot and indicates the maximum radial density. Low maxden = low density (blue) High maxden = high density (red)	Low maxden = high variability High maxden = low variability	Some drugs might affect variability, indicating activation of several autoregulating mechanisms to maintain blood flow to vital organs, in this case the hindquarters.
dspread3	Density in attractor High dspread3 = high density, lot of red Low dspread3 = low density, lot of blue	Low dspread3 = high variability High dspread3 = low variability	
rQ25	Metric extracted from the radial density plot; radial position that includes 25% of data, indication of how data points are spread over attractor. Low rQ25 = high density points close to centre High rQ25 = lower density in the centre of the attractor	No clear link to changes in waveform (see discussion of metrics, Chapter 5, section 5.4.2.1.) Potentially: low rQ25 = large diastolic nadir, indicating increased wave reflection, illustrative example in Figure 97.	?
vwmaxnorm	This metric is extracted from stacked polar maps. Polar maps at different angles of the attractor are stacked and the average of difference between the maximum radial values between the maps is determined. Low vwmaxnorm = small differences between the maximum values of the polar maps = high the rotational symmetry of the attractor. An illustrative example is shown in Figure 98.	No clear link to changes in waveform (see discussion of metrics, Chapter 5, section 5.4.2.1.). Potentially, in the aortic wave, a low vwmaxnorm = flat interbeat interval (Figure 98), indicating an increase in wave reflection.	

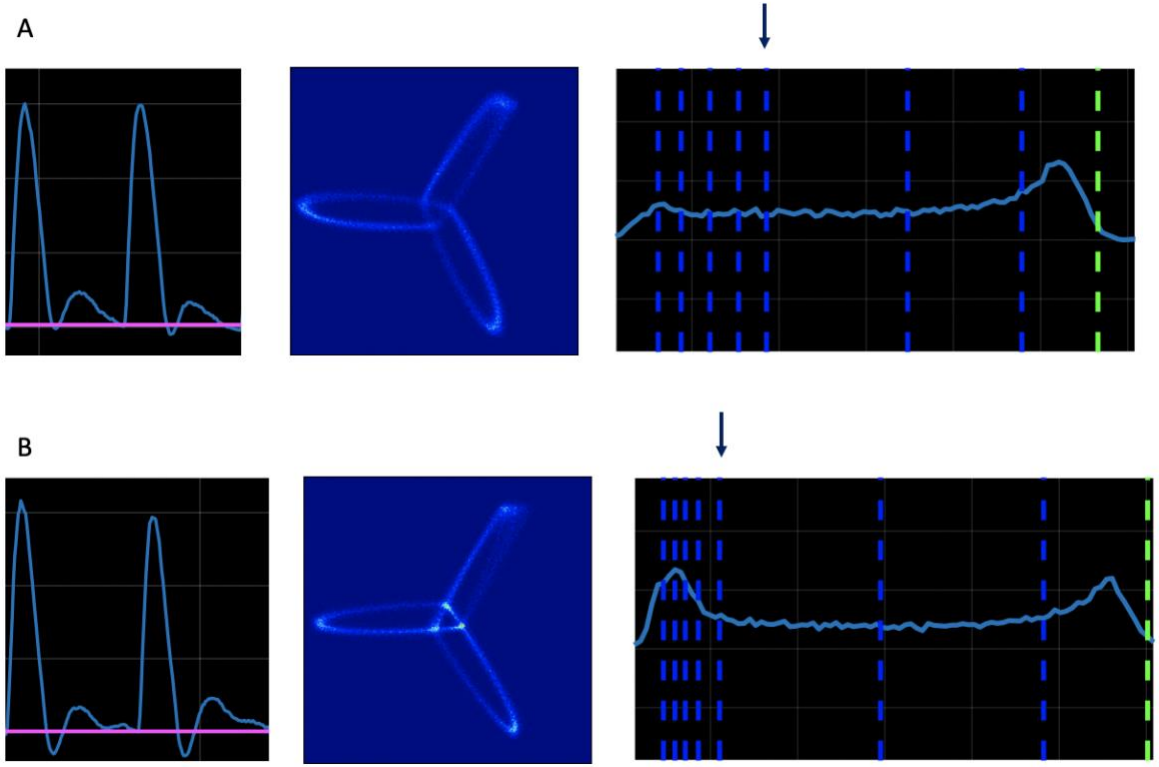

Figure 96: Example of decrease in metric rQ25 in the aortic flow wave. (A) *shows the wave, attractor and radial density plot of an animal during the baseline recording.* ***(B)*** *shows the wave, attractor and radial density plot of the same animal, 5h post sunitinib-bolus dosing. The decrease in rQ25 (3.71 * 10^{-3} units in (A) to 2.21 * 10^{-3} units in (B) was indeed linked with an increase in density in the centre of the attractor. In the waveform, an increase in wave reflection (demonstrated by a large decrease in flow in the downstroke, below the purple line) was observed, indicating a vasoconstriction downstream of the probe.*

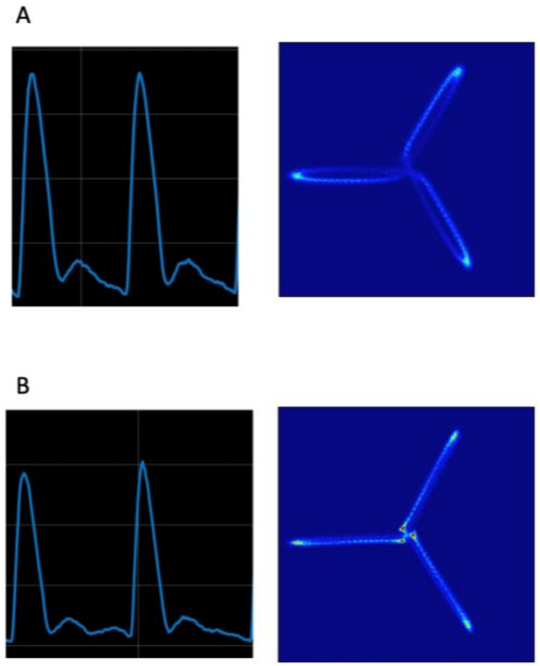

Figure 97: Example of decrease in metric vwmaxnorm in the aortic flow. (A) *shows the wave and attractor of an animal during the baseline recording.* ***(B)*** *shows the wave and attractor of the same animal, 5h post sunitinib-bolus dosing. The decrease in vwmaxnorm (0.27 units in (A) to 0.21 units in (B), indicating increase in rotational symmetry) was linked with an increase in wave reflection, demonstrated by flatter interbeat interval instead of distinct second peak in the downstroke of the wave.*

9. References

Abdel-Qadir, H., Ethier, J. L., Lee, D. S., Thavendiranathan, P., & Amir, E. (2017). Cardiovascular toxicity of angiogenesis inhibitors in treatment of malignancy: A systematic review and meta-analysis. *Cancer Treatment Reviews*, *53*, 120–127. https://doi.org/10.1016/j.ctrv.2016.12.002

Abram, C. L., & Lowell, C. A. (2007). The expanding role for ITAM-based signaling pathways in immune cells. *Science's STKE*, *2007*(377), re2–re2. https://doi.org/10.1126/stke.3772007re2

Abtahian, F., Guerriero, A., Sebzda, E., Lu, M., Zhou, R., Myers, E. E., Huang, B., Jackson, D. G., Ferrari, V. A., Lowell, C. A., Lepore, J. J., Koretzky, G. A., & Kahn, M. L. (2003). Regulation of blood and lymphatic vascular separation by signaling proteins SLP-76 and Syk. *Science*, *299*(5604), 247–251. https://doi.org/10.1126/science.1079477

Acharya, U. R., Joseph, K. P., Kannathal, N., Lim, C. M., & Suri, J. S. (2006). Heart rate variability: A review. *Medical and Biological Engineering and Computing*, *44*(12), 1031–1051. https://doi.org/10.1007/s11517-006-0119-0

AD Instruments, & Williams, E. (2022, February 1). *Solid-state vs. fluid-filled pressure catheters: know the difference*. https://m-cdn.adinstruments.com/Blogs/Fluid-Filled vs Solid-State Catheters Whitepaper PDF A4.pdf

Adini, A., Kornaga, T., Firoozbakht, F., & Benjamin, L. E. (2002). Placental growth factor is a survival factor for tumor endothelial cells and macrophages. *Cancer Research*, *62*(10), 2749–2752.

Agarwal, M., Thareja, N., Benjamin, M., Akhondi, A., & Mitchell, G. D. (2018). Tyrosine kinase inhibitor-induced hypertension. *Current Oncology Reports*, *20*(8), 65.

Aiello, L. P., Pierce, E. A., Foley, E. D., Takagi, H., Chen, H., Riddle, L., Ferrara, N., King, G. L., & Smith, L. E. H. (1995). Suppression of retinal neovascularization in vivo by inhibition of vascular endothelial growth factor (VEGF) using soluble VEGF-receptor chimeric proteins. *Proceedings of the National Academy of Sciences of the United States of America*, *92*(23), 10457–10461. https://doi.org/10.1073/PNAS.92.23.10457

Alastruey, J., Xiao, N., Fok, H., Schaeffter, T., & Figueroa, C. A. (2016). On the impact of modelling assumptions in multi-scale, subject-specific models of aortic haemodynamics.

Journal of the Royal Society Interface, *13*(119). https://doi.org/10.1098/rsif.2016.0073

Aljubran, A., Elshenawy, M. A., Kandil, M., Zahir, M. N., Shaheen, A., Gad, A., Alshaer, O., Alzahrani, A., Eldali, A., & Bazarbashi, S. (2019). Efficacy of regorafenib in metastatic colorectal cancer: A multi-institutional retrospective study. *Clinical Medicine Insights: Oncology*, *13*. https://doi.org/10.1177/1179554918825447

Allegra, C. J., Yothers, G., O'Connell, M. J., Sharif, S., Petrelli, N. J., Lopa, S. H., & Wolmark, N. (2013). Bevacizumab in stage II-III colon cancer: 5-year update of the National Surgical Adjuvant Breast and Bowel Project C-08 trial. *Journal of Clinical Oncology : Official Journal of the American Society of Clinical Oncology*, *31*(3), 359–364. https://doi.org/10.1200/JCO.2012.44.4711

Altomare, I., Markovtsov, V. V., Todd, L., Weerasinghe, D., Numerof, R. P., Tong, S., Masuda, E., & Bussel, J. B. (2019). Potential anti-thrombotic effect without accompanying hemorrhage with fostamatinib use in patients with Immune thrombocytopenia. *Blood*, *134*(Supplement_1), 4889. https://doi.org/10.1182/BLOOD-2019-126558

Apostolidis, S. A., Sarkar, A., Giannini, H. M., Goel, R. R., Mathew, D., Suzuki, A., Baxter, A. E., Greenplate, A. R., Alanio, C., Abdel-Hakeem, M., Oldridge, D. A., Giles, J. R., Wu, J. E., Chen, Z., Huang, Y. J., Belman, J., Pattekar, A., Manne, S., Kuthuru, O., … Wherry, E. J. (2022). Signaling Through FcγRIIA and the C5a-C5aR Pathway Mediate Platelet Hyperactivation in COVID-19. *Frontiers in Immunology*, *13*, 834988. https://doi.org/10.3389/fimmu.2022.834988

Arcondéguy, T., Lacazette, E., Millevoi, S., Prats, H., & Touriol, C. (2013). VEGF-A mRNA processing, stability and translation: a paradigm for intricate regulation of gene expression at the post-transcriptional level. *Nucleic Acids Research*, *41*(17), 7997–8010. https://doi.org/10.1093/NAR/GKT539

Arias-Palomo, E., Recuero-Checa, M. A., Bustelo, X. R., & Llorca, O. (2007). 3D structure of Syk kinase determined by single-particle electron microscopy. *Biochimica et Biophysica Acta*, *1774*(12), 1493–1499. https://doi.org/10.1016/J.BBAPAP.2007.10.008

Arnall, B., Rotar, V., Pitsillides, K., Sosa, M., Garg, V., & Callahan, M. F. (2017). A new biotelemetry system to monitor true volumetric blood flow, blood pressure and temperature in small animals: Preliminary test data in rats. *The FASEB Journal*, *31*, 836.21. https://doi.org/10.1096/FASEBJ.31.1_SUPPLEMENT.836.21

Aston, P. J., Christie, M. I., Huang, Y. H., & Nandi, M. (2018). Beyond HRV: Attractor

reconstruction using the entire cardiovascular waveform data for novel feature extraction. *Physiological Measurement*, *39*(2). https://doi.org/10.1088/1361-6579/aaa93d

Aston, P. J., Nandi, M., Christie, M. I., & Huang, Y. H. (2014). Comparison of attractor reconstruction and HRV methods for analysing blood pressure data. *Computing in Cardiology*, *41*(January), 437–440.

AstraZeneca. (2013). *AstraZeneca announces top-line results from OSKIRA-1 Phase III study of fostamatinib in rheumatoid arthritis*. https://www.astrazeneca.com/media-centre/press-releases/2013/astrazeneca-oskira-1-study-results-fostamatinib-rheumatoid-arthritis-05042013.html

Athaya, T., & Choi, S. (2022). A review of noninvasive methodologies to estimate the blood pressure waveform. *Sensors*, *22*(10), 3953. https://doi.org/10.3390/S22103953

Atukorala, I., & Hunter, D. J. (2013). Valdecoxib : the rise and fall of a COX-2 inhibitor. *Expert Opinion on Pharmacotherapy*, *14*(8), 1077–1086. https://doi.org/10.1517/14656566.2013.783568

Avolio, A. P., Van Bortel, L. M., Boutouyrie, P., Cockcroft, J. R., McEniery, C. M., Protogerou, A. D., Roman, M. J., Safar, M. E., Segers, P., & Smulyan, H. (2009). Role of pulse pressure amplification in arterial hypertension: Experts' opinion and review of the data. *Hypertension*, *54*(2), 375–383. https://doi.org/10.1161/HYPERTENSIONAHA.109.134379

Barr, P. M., Wei, C., Roger, J., Schaefer-Cutillo, J., Kelly, J. L., Rosenberg, A. F., Jung, J., Sanz, I., & Friedberg, J. W. (2012). Syk inhibition with fostamatinib leads to transitional B lymphocyte depletion. *Clinical Immunology*, *142*(3), 237–242. https://doi.org/10.1016/J.CLIM.2011.12.012

Barter, P. J., Caulfield, M., Eriksson, M., Grundy, S. M., Kastelein, J. J. P., Komajda, M., Lopez-Sendon, J., Mosca, L., Tardif, J.-C., Waters, D. D., Shear, C. L., Revkin, J. H., Buhr, K. A., Fisher, M. R., Tall, A. R., & Brewer, B. (2007). Effects of torcetrapib in patients at high risk for coronary events. *New England Journal of Medicine*, *357*(21), 2109–2122. https://doi.org/10.1056/nejmoa0706628

Bates, D. O., Hillman, N. J., Williams, B., Neal, C. R., & Pocock, T. M. (2002). Regulation of microvascular permeability by vascular endothelial growth factors. *Journal of Anatomy*, *200*(6), 581–597. https://doi.org/10.1046/J.1469-7580.2002.00066.X

Bates, David O., Cui, T. G., Doughty, J. M., Winkler, M., Sugiono, M., Shields, J. D., Peat, D.,

Gillatt, D., & Harper, S. J. (2002). VEGF165b, an inhibitory splice variant of vascular endothelial growth factor, is down-regulated in renal cell carcinoma. *Cancer Research*, *62*(14), 4123–4131.

Bauer, B., & Steinle, A. (2017). HemITAM: A single tyrosine motif that packs a punch. *Science Signaling*, *10*(508). https://doi.org/10.1126/SCISIGNAL.AAN3676

Behnen, M., Leschczyk, C., Möller, S., Batel, T., Klinger, M., Solbach, W., & Laskay, T. (2014). Immobilized immune complexes induce neutrophil extracellular trap release by human neutrophil granulocytes via FcγRIIIB and Mac-1. *Journal of Immunology*, *193*(4), 1954–1965. https://doi.org/10.4049/JIMMUNOL.1400478

Bendickova, K., Tidu, F., & Fric, J. (2017). Calcineurin–NFAT signalling in myeloid leucocytes: new prospects and pitfalls in immunosuppressive therapy. *EMBO Molecular Medicine*, *9*(8), 990. https://doi.org/10.15252/EMMM.201707698

Bennett, T., Mahajan, R. P., March, J. E., Kemp, P. A., & Gardiner, S. M. (2004). Regional and temporal changes in cardiovascular responses to norepinephrine and vasopressin during continuous infusion of lipopolysaccharide in conscious rats. *British Journal of Anaesthesia*, *93*(3), 400–407. https://doi.org/10.1093/bja/aeh214

Bennouna, J., Sastre, J., Arnold, D., Österlund, P., Greil, R., Van Cutsem, E., von Moos, R., Viéitez, J. M., Bouché, O., Borg, C., Steffens, C. C., Alonso-Orduña, V., Schlichting, C., Reyes-Rivera, I., Bendahmane, B., André, T., & Kubicka, S. (2013). Continuation of bevacizumab after first progression in metastatic colorectal cancer (ML18147): A randomised phase 3 trial. *The Lancet Oncology*, *14*(1), 29–37. https://doi.org/10.1016/S1470-2045(12)70477-1

Bergers, G., & Hanahan, D. (2008). Modes of resistance to anti-angiogenic therapy. *Nature Reviews. Cancer*, *8*(8), 592–603. https://doi.org/10.1038/NRC2442

Bergstrand, R., Vedin, A., Wilhelmsson, C., Peterson, L. E., Chamberlain, J., Dell, D., Stevens, L. A., & Ostrowski, J. (1984). Intravenous and oral administration of molsidomine, a pharmacodynamic and pharmacokinetic study. *European Journal of Clinical Pharmacology*, *27*(2), 203–208. https://doi.org/10.1007/BF00544046

Bettinger, J., Quevedo, H. B., & Cleary, J. (2021). Emerging pharmacologic mechanisms of buprenorphine to explain experience of analgesia versus adverse effects. *Journal of Opioid Management*, *17*(7), 21–31. https://doi.org/10.5055/JOM.2021.0639

Beurskens, D. M. H., Huckriede, J. P., Schrijver, R., Hemker, H. C., Reutelingsperger, C. P., &

Nicolaes, G. A. F. (2020). The anticoagulant and nonanticoagulant properties of heparin. *Thrombosis and Haemostasis*, *120*(10), 1371–1383. https://doi.org/10.1055/S-0040-1715460/ID/JR200068-6/BIB

Bhatt, S., Northcott, C., Wisialowski, T., Li, D., & Steidl-Nichols, J. (2019). Preclinical to clinical translation of hemodynamic effects in cardiovascular safety pharmacology studies. *Toxicological Sciences*, *169*(1), 272–279. https://doi.org/10.1093/toxsci/kfz035

Blood Pressure Lowering Treatment Trialists Collarobation. (2008). Effects of different regimens to lower blood pressure on major cardiovascular events in older and younger adults: meta-analysis of randomised trials. *BMJ (Clinical Research Ed.)*, *336*(7653), 1121–1123. https://doi.org/10.1136/BMJ.39548.738368.BE

Boccadifuoco, A., Mariotti, A., Capellini, K., Celi, S., & Salvetti, M. V. (2018). validation of numerical simulations of thoracic aorta hemodynamics: comparison with in vivo measurements and stochastic sensitivity analysis. *Cardiovascular Engineering and Technology*, *9*(4), 688–706. https://doi.org/10.1007/S13239-018-00387-X

Bonet-Luz, E., Lyle, J. V., Huang, C. L. H., Zhang, Y., Nandi, M., Jeevaratnam, K., & Aston, P. J. (2020). Symmetric Projection Attractor Reconstruction analysis of murine electrocardiograms: Retrospective prediction of Scn5a+/- genetic mutation attributable to Brugada syndrome. *Heart Rhythm O2*, *1*(5), 368–375. https://doi.org/10.1016/J.HROO.2020.08.007

Bono, P., Rautiola, J., Utriainen, T., & Joensuu, H. (2011). Hypertension as predictor of sunitinib treatment outcome in metastatic renal cell carcinoma. *Acta Oncologica*, *50*(4), 569–573. https://doi.org/10.3109/0284186X.2010.543696

Borate, U., Li, R., Huang, Y., Swords, R. T., Traer, E., Stein, E., Foran, J. M., Baer, M. R., Duong, V. H., Stock, W., Odenike, O., Patel, P., Collins, R. H., Madanat, Y. F., Kovacsovics, T., Deininger, M. W., Smith, C., Olin, R. L., Arellano, M. L., … Mims, A. S. (2022). Entospletinib (ENTO) in combination with cytarabine (Ara-C) and daunorubicin (DNR) in newly diagnosed (ND) adult patients with NPM1-mutated and FLT3-ITD wild-type acute myeloid leukemia (AML) is associated with good response and survival: A Phase 2 Sub-St. *Blood*, *140*(Supplement 1), 6200–6203. https://doi.org/10.1182/BLOOD-2022-167316

Bots, M. L., Visseren, F. L., Evans, G. W., Riley, W. A., Revkin, J. H., Tegeler, C. H., Shear, C. L., Duggan, W. T., Vicari, R. M., Grobbee, D. E., & Kastelein, J. J. (2007). Torcetrapib and

carotid intima-media thickness in mixed dyslipidaemia (RADIANCE 2 study): a randomised, double-blind trial. *Lancet*, *370*(9582), 153–160. https://doi.org/10.1016/S0140-6736(07)61088-5

Braselmann, S., Taylor, V., Zhao, H., Wang, S., Sylvain, C., Baluom, M., Qu, K., Herlaar, E., Lau, A., Young, C., Wong, B. R., Lovell, S., Sun, T., Park, G., Argade, A., Jurcevic, S., Pine, P., Singh, R., Grossbard, E. B., … Masuda, E. S. (2006). R406, an orally available spleen tyrosine kinase inhibitor blocks Fc receptor signaling and reduces immune complex-mediated inflammation. *Journal of Pharmacology and Experimental Therapeutics*, *319*(3), 998–1008. https://doi.org/10.1124/jpet.106.109058

Brijs, J., Sandblom, E., Axelsson, M., Sundell, K., Sundh, H., Kiessling, A., Berg, C., & Gräns, A. (2019). Remote physiological monitoring provides unique insights on the cardiovascular performance and stress responses of freely swimming rainbow trout in aquaculture. *Scientific Reports*, *9*(1). https://doi.org/10.1038/S41598-019-45657-3

Brockway BP, Mills PA, A. S. (1991). A new method for continuous chronic measurement and recording of blood pressure, heart rate and activity in the rat via radio-telemetry. *Clin Exp Hypertens A.*, *13*(5), 885–895. https://doi.org/10.3109/10641969109042094

Broxmeyer, H. E., Cooper, S., Li, Z. H., Lu, L., Song, H. Y., Kwon, B. S., Warren, R. E., & Donner, D. B. (1995). Myeloid progenitor cell regulatory effects of vascular endothelial cell growth factor. *International Journal of Hematology*, *62*(4), 203–215. https://doi.org/10.1016/0925-5710(95)00412-2

Broxterman, H. J., Gotink, K. J., & Verheul, H. M. W. (2009). Understanding the causes of multidrug resistance in cancer: a comparison of doxorubicin and sunitinib. *Drug Resist Updat.*, *12*(4–5), 114–126. https://doi.org/10.1016/J.DRUP.2009.07.001

Budnitz, D. S., Pollock, D. A., Weidenbach, K. N., Mendelsohn, A. B., Schroeder, T. J., & Annest, J. L. (2006). National surveillance of emergency department visits for outpatient adverse drug events. *JAMA*, *296*(15), 1858–1866. https://doi.org/10.1001/JAMA.296.15.1858

Burger, R. A., Brady, M. F., Bookman, M. A., Fleming, G. F., Monk, B. J., Huang, H., Mannel, R. S., Homesley, H. D., Fowler, J., Greer, B. E., Boente, M., Birrer, M. J., & Liang, S. X. (2011). Incorporation of Bevacizumab in the Primary Treatment of Ovarian Cancer. *Https://Doi.Org/10.1056/NEJMoa1104390*, *365*(26), 2473–2483. https://doi.org/10.1056/NEJMOA1104390

Burke, J. M., Shustov, A., Essell, J., Patel-Donnelly, D., Yang, J., Chen, R., Ye, W., Shi, W.,

Assouline, S., & Sharman, J. (2018). An open-label, Phase II trial of entospletinib (GS-9973), a selective spleen tyrosine kinase inhibitor, in diffuse large B-cell lymphoma. *Clinical Lymphoma, Myeloma and Leukemia*, *18*(8), e327–e331. https://doi.org/10.1016/j.clml.2018.05.022

Bussel, J., Arnold, D. M., Grossbard, E., Mayer, J., Treliński, J., Homenda, W., Hellmann, A., Windyga, J., Sivcheva, L., Khalafallah, A. A., Zaja, F., Cooper, N., Markovtsov, V., Zayed, H., & Duliege, A. M. (2018). Fostamatinib for the treatment of adult persistent and chronic immune thrombocytopenia: Results of two phase 3, randomized, placebo-controlled trials. *American Journal of Hematology*, *93*(7), 921–930. https://doi.org/10.1002/AJH.25125

Buus, N. H., VanBavel, E., & Mulvany, M. J. (1994). Differences in sensitivity of rat mesenteric small arteries to agonists when studied as ring preparations or as cannulated preparations. *British Journal of Pharmacology*, *112*(2), 579–587. https://doi.org/10.1111/j.1476-5381.1994.tb13114.x

Bye, A. P., Hoepel, W., Mitchell, J. L., Jégouic, S., Loureiro, S., Sage, T., Vidarsson, G., Nouta, J., Wuhrer, M., de Taeye, S., van Gils, M., Kriek, N., Cooper, N., Jones, I., den Dunnen, J., & Gibbins, J. M. (2021). Aberrant glycosylation of anti-SARS-CoV-2 spike IgG is a prothrombotic stimulus for platelets. *Blood*, *138*(16), 1481–1489. https://doi.org/10.1182/BLOOD.2021011871

Caletti, S., Paini, A., Coschignano, M. A., Ciuceis, C. De, Nardin, M., Zulli, R., Muiesan, M. L., Salvetti, M., & Rizzoni, D. (2018). *Management of VEGF-Targeted Therapy-Induced Hypertension*. *20*(68). https://doi.org/10.1007/s11906-018-0871-1

Camarda, N., Travers, R., Yang, V. K., London, C., & Jaffe, I. Z. (2022). VEGF Receptor Inhibitor-Induced Hypertension: Emerging Mechanisms and Clinical Implications. *Current Oncology Reports*, *24*(4), 463–474. https://doi.org/10.1007/s11912-022-01224-0

Cambier, J. C. (1995). Antigen and Fc receptor signaling. The awesome power of the immunoreceptor tyrosine-based activation motif (ITAM). *The Journal of Immunology*, *155*(7), 3281–3285. https://doi.org/10.4049/JIMMUNOL.155.7.3281

Capey, S. (2007). Isoflurane. In *xPharm: The Comprehensive Pharmacology Reference* (pp. 1–4). StatPearls Publishing. https://doi.org/10.1016/B978-008055232-3.61958-0

Carlström, M., Wilcox, C. S., & Arendshorst, W. J. (2015). Renal autoregulation in health and disease. *Physiological Reviews*, *95*(2), 405.

https://doi.org/10.1152/PHYSREV.00042.2012

Carmeliet, P. (2005). Angiogenesis in life, disease and medicine. *Nature*, *438*(7070), 932–936. https://doi.org/10.1038/nature04478

Carter, J. J., Fretwell, L. V., & Woolard, J. (2017). Effects of 4 multitargeted receptor tyrosine kinase inhibitors on regional hemodynamics in conscious, freely moving rats. *FASEB Journal*, *31*(3), 1193–1203. https://doi.org/10.1096/fj.201600749R

Carter, J. J., Wheal, A. J., Hill, S. J., & Woolard, J. (2015). Effects of receptor tyrosine kinase inhibitors on VEGF165a- and VEGF165b-stimulated gene transcription in HEK-293 cells expressing human VEGFR2. *British Journal of Pharmacology*, *172*(12), 3141–3150. https://doi.org/10.1111/bph.13116

Catino, A. B., Hubbard, R. A., Chirinos, J. A., Townsend, R., Keefe, S., Haas, N. B., Puzanov, I., Fang, J. C., Agarwal, N., Hyman, D., Smith, A. M., Gordon, M., Plappert, T., Englefield, V., Narayan, V., Ewer, S., ElAmm, C., Lenihan, D., & Ky, B. (2018). Longitudinal assessment of vascular function with sunitinib in patients with metastatic renal cell carcinoma. *Circulation. Heart Failure*, *11*(3), e004408. https://doi.org/10.1161/CIRCHEARTFAILURE.117.004408

Chakraborty, S., Inukai, T., Fang, L., Golkowski, M., & Maly, D. J. (2019). Targeting dynamic ATP-binding site features allows discrimination between highly homologous protein kinases. *ACS Chemical Biology*, *14*(6), 1249. https://doi.org/10.1021/ACSCHEMBIO.9B00214

Chander, V., & Chopra, K. (2005). Effect of molsidomine and L-arginine in cyclosporine nephrotoxicity: Role of nitric oxide. *Toxicology*, *207*(3), 463–474. https://doi.org/10.1016/j.tox.2004.10.018

Chang, C. Y., Chang, R. W., Hsu, S. H., Wu, M. S., Cheng, Y. J., Kao, H. L., Lai, L. C., Wang, C. H., & Chang, K. C. (2017). Defects in vascular mechanics due to aging in rats: Studies on arterial wave properties from a single aortic pressure pulse. *Frontiers in Physiology*, *8*(JUL), 503. https://doi.org/10.3389/FPHYS.2017.00503/BIBTEX

Chang, R. W., Chang, C. Y., Lai, L. C., Wu, M. S., Young, T. H., Chen, Y. S., Wang, C. H., & Chang, K. C. (2017). Determining arterial wave transit time from a single aortic pressure pulse in rats: Vascular impulse response analysis. *Scientific Reports*, *7*(40998). https://doi.org/10.1038/srep40998

Charlton, P. H., Camporota, L., Smith, J., Nandi, M., Christie, M., Aston, P. J., & Beale, R. (2015).

Measurement of cardiovascular state using attractor reconstruction analysis. *2015 23rd European Signal Processing Conference, EUSIPCO 2015*, 444–448. https://doi.org/10.1109/EUSIPCO.2015.7362422

Charlton, Peter H., Harana, J. M., Vennin, S., Li, Y., Chowienczyk, P., & Alastruey, J. (2019). Modeling arterial pulse waves in healthy aging: a database for in silico evaluation of hemodynamics and pulse wave indexes. *American Journal of Physiology - Heart and Circulatory Physiology*, *317*(5), H1062–H1085. https://doi.org/10.1152/AJPHEART.00218.2019

Chen, H. X., & Cleck, J. N. (2009). Adverse effects of anticancer agents that target the VEGF pathway. *Nature Reviews Clinical Oncology*, *6*(8), 465–477. https://doi.org/10.1038/nrclinonc.2009.94

Chen, L., Monti, S., Juszczynski, P., Ouyang, J., Chapuy, B., Neuberg, D., Doench, J. G., Bogusz, A. M., Habermann, T. M., Dogan, A., Witzig, T. E., Kutok, J. L., Rodig, S. J., Golub, T., & Shipp, M. A. (2013). SYK inhibition modulates distinct PI3K/AKT- dependent survival pathways and cholesterol biosynthesis in diffuse large B cell lymphomas. *Cancer Cell*, *23*(6), 826–838. https://doi.org/10.1016/J.CCR.2013.05.002

Chen, X. L., Lei, Y. H., Liu, C. F., Yang, Q. F., Zuo, P. Y., Liu, C. Y., Chen, C. Z., & Liu, Y. W. (2013). Angiogenesis inhibitor bevacizumab increases the risk of ischemic heart disease associated with chemotherapy: a meta-analysis. *PLoS ONE*, *8*(6), e66721. https://doi.org/10.1371/journal.pone.0066721

Chen, Y., Liu, H., Huang, Y., Lin, S., Yin, G., & Xie, Q. (2021). The cardiovascular risks of fostamatinib in patients with rheumatoid arthritis: a systematic review and meta-analysis. *Frontiers in Pharmacology*, *12*(July), 1–9. https://doi.org/10.3389/fphar.2021.632551

Cheng, H., & Force, T. (2010). Molecular mechanisms of cardiovascular toxicity of targeted cancer therapeutics. *Circulation Research*, *106*(1), 21–34. https://doi.org/10.1161/CIRCRESAHA.109.206920

Christenson, L. K., & Stouffer, R. L. (1997). Follicle-stimulating hormone and luteinizing hormone/chorionic gonadotropin stimulation of vascular endothelial growth factor production by macaque granulosa cells from pre- and periovulatory follicles. *The Journal of Clinical Endocrinology and Metabolism*, *82*(7), 2135–2142. https://doi.org/10.1210/JCEM.82.7.4169

Chu, L. Y., Ramakrishnan, D. P., & Silverstein, R. L. (2013). Thrombospondin-1 modulates VEGF signaling via CD36 by recruiting SHP-1 to VEGFR2 complex in microvascular endothelial cells. *Blood*, *122*(10), 1822–1832. https://doi.org/10.1182/blood-2013-01-482315

Cisbio. (2023a). *HTRF Dasatinib-Red | Cisbio*. https://www.cisbio.net/dasatinib-red-43216

Cisbio. (2023b). *HTRF Sunitinib-Red | Cisbio*. https://www.cisbio.net/sunitinib-red-43217

Cobleigh, M. A., Langmuir, V. K., Sledge, G. W., Miller, K. D., Haney, L., Novotny, W. F., Reimann, J. D., & Vassel, A. (2003). A Phase I/II dose-escalation trial of bevacizumab in previously treated metastatic breast cancer. *Seminars in Oncology*, *30*(5 SUPPL. 16), 117–124. https://doi.org/10.1053/j.seminoncol.2003.08.013

Coffey, G., Betz, A., DeGuzman, F., Pak, Y., Inagaki, M., Baker, D. C., Hollenbach, S. J., Pandey, A., & Sinha, U. (2014). The novel kinase inhibitor PRT062070 (Cerdulatinib) demonstrates efficacy in models of autoimmunity and B-Cell cancer. *Journal of Pharmacology and Experimental Therapeutics*, *351*(3), 538–548. https://doi.org/10.1124/jpet.114.218164

Colafella, K. M. M., Neves, K. B., Montezano, A. C., Garrelds, I. M., Veghel, R. Van, Vries, R. De, Uijl, E., Baelde, H. J., Van Den Meiracker, A. H., Touyz, R. M., Danser, A. H. J., & Versmissen, J. (2020). Selective ETA vs. dual ETA/B receptor blockade for the prevention of sunitinib-induced hypertension and albuminuria in WKY rats. *Cardiovascular Research*, *116*(10), 1779–1790. https://doi.org/10.1093/CVR/CVZ260

Collins, T. A., Rolf, M. G., & Pointon, A. (2020). Current and future approaches to nonclinical cardiovascular safety assessment. *Drug Discovery Today*, *25*(7), 1129–1134. https://doi.org/10.1016/J.DRUDIS.2020.03.011

Collins, T., Gray, K., Bista, M., Skinner, M., Hardy, C., Wang, H., Mettetal, J. T., & Harmer, A. R. (2018). Quantifying the relationship between inhibition of VEGF receptor 2, drug-induced blood pressure elevation and hypertension. *British Journal of Pharmacology*, *175*(4), 618–630. https://doi.org/10.1111/bph.14103

Conchon, M., Moura, C. M. B. de F., Rego, M. A. do C., & Braga, J. W. R. (2011). Dasatinib - Clinical trials and management of adverse events in imatinib resistant/ intolerant chronic myeloid leukemia. *Revista Brasileira de Hematologia e Hemoterapia*, *33*(2), 131–139. https://doi.org/10.5581/1516-8484.20110034

Connell, N. T., & Berliner, N. (2019). Fostamatinib for the treatment of chronic immune thrombocytopenia. *Blood*, *133*(19), 2027–2030. https://doi.org/10.1182/blood-2018-11-852491

Connolly, D. T., Heuvelman, D. M., Nelson, R., Olander, J. V., Eppley, B. L., Delfino, J. J., Siegel, N. R., Leimgruber, R. M., & Feder, J. (1989). Tumor vascular permeability factor stimulates endothelial cell growth and angiogenesis. *The Journal of Clinical Investigation*, *84*(5), 1470–1478. https://doi.org/10.1172/JCI114322

Conrad, M. E. (1992). Cytarabine and cardiac failure. *American Journal of Hematology*, *41*(2), 143–144. https://doi.org/10.1002/AJH.2830410219

Cook, D., Brown, D., Alexander, R., March, R., Morgan, P., Satterthwaite, G., & Pangalos, M. N. (2014). Lessons learned from the fate of AstraZeneca's drug pipeline: A five-dimensional framework. *Nature Reviews Drug Discovery*, *13*(6), 419–431. https://doi.org/10.1038/nrd4309

Cooper, N., Ghanima, W., Hill, Q. A., Nicolson, P. L. R., Markovtsov, V., & Kessler, C. (2022). Recent advances in understanding spleen tyrosine kinase (SYK) in human biology and disease, with a focus on fostamatinib. *Platelets*, *34*(1), 1–13. https://doi.org/10.1080/09537104.2022.2131751

Cooper, S. L., Carter, J. J., March, J., & Woolard, J. (2019). Long-term cardiovascular effects of vandetanib and pazopanib in normotensive rats. *Pharmacology Research and Perspectives*, *7*(3), 1–13. https://doi.org/10.1002/prp2.477

Cooper, S. L., March, J., Sabbatini, A. R., Hill, S. J., Jörg, M., Scammells, P. J., & Woolard, J. (2020). The effect of two selective A1-receptor agonists and the bitopic ligand VCP746 on heart rate and regional vascular conductance in conscious rats. *British Journal of Pharmacology*, *177*(2), 346–359. https://doi.org/10.1111/bph.14870

Cooper, S. L., Wragg, E. S., Pannucci, P., Soave, M., Hill, S. J., & Woolard, J. (2022). Regionally selective cardiovascular responses to adenosine A2A and A2B receptor activation. *FASEB Journal*, *36*(4), 1–19. https://doi.org/10.1096/fj.202101945R

Coxon, A., Bready, J., Kaufman, S., Estrada, J., Osgood, T., Canon, J., Wang, L., Radinsky, R., Kendall, R., Hughes, P., & Polverino, A. (2012). Anti-tumor activity of motesanib in a medullary thyroid cancer model. *Journal of Endocrinological Investigation*, *35*(2), 181–190. https://doi.org/10.3275/7609

Crestani, C. C., Tavares, R. F., Alves, F. H. F., Resstel, L. B. M., & Correa, F. M. A. (2010). Effect of acute restraint stress on the tachycardiac and bradycardiac responses of the baroreflex in rats. *Stress*, *13*(1), 61–72. https://doi.org/10.3109/10253890902927950

Crowley, M. T., Costello, P. S., Fitzer-Attas, C. J., Turner, M., Meng, F., Lowell, C., Tybulewicz,

V. L. J., & DeFranco, A. L. (1997). A critical role for Syk in signal transduction and phagocytosis mediated by Fcgamma receptors on macrophages. *The Journal of Experimental Medicine*, *186*(7), 1027–1039. https://doi.org/10.1084/JEM.186.7.1027

Curigliano, G., Mayer, E. L., Burstein, H. J., Winer, E. P., & Goldhirsch, A. (2010). Cardiac toxicity from systemic cancer therapy: a comprehensive review. *Progress in Cardiovascular Diseases*, *53*(2), 94–104. https://doi.org/10.1016/J.PCAD.2010.05.006

Currie, K. S., Kropf, J. E., Lee, T., Blomgren, P., Xu, J., Zhao, Z., Gallion, S., Whitney, J. A., Maclin, D., Lansdon, E. B., Maciejewski, P., Rossi, A. M., Rong, H., Macaluso, J., Barbosa, J., Di Paolo, J. A., & Mitchell, S. A. (2014). Discovery of GS-9973, a selective and orally efficacious inhibitor of spleen tyrosine kinase. *Journal of Medicinal Chemistry*, *57*(9), 3856–3873. https://doi.org/10.1021/jm500228a

da Silva, G. M., da Silva, M. C., Nascimento, D. V. G., Lima Silva, E. M., Gouvêa, F. F. F., de França Lopes, L. G., Araújo, A. V., Ferraz Pereira, K. N., & de Queiroz, T. M. (2021). Nitric oxide as a central molecule in hypertension: focus on the vasorelaxant activity of new nitric oxide donors. *Biology 2021, Vol. 10, Page 1041*, *10*(10), 1041. https://doi.org/10.3390/BIOLOGY10101041

Danilov, A. V, Herbaux, C., Walter, H. S., Hillmen, P., Rule, S. A., Kio, E. A., Karlin, L., Dyer, M. J. S., Mitra, S. S., Yi, P. C., Humeniuk, R., Huang, X., Zhou, Z., Bhargava, P., J Urgensmeier, J. M., & Fegan, C. D. (2020). Phase Ib study of tirabrutinib in combination with idelalisib or entospletinib in previously treated chronic lymphocytic leukemia. *Clinical Cancer Research*, *26*(12), 2810–2818. https://doi.org/10.1158/1078-0432.CCR-19-3504

Davis, M. I., Hunt, J. P., Herrgard, S., Ciceri, P., Wodicka, L. M., Pallares, G., Hocker, M., Treiber, D. K., & Zarrinkar, P. P. (2011). Comprehensive analysis of kinase inhibitor selectivity. *Nature Biotechnology*, *29*(11), 1046–1051. https://doi.org/10.1038/nbt.1990

De Castro, R. O., Zhang, J., Jamur, M. C., Oliver, C., & Siraganian, R. P. (2010). Tyrosines in the carboxyl terminus regulate Syk kinase activity and function. *The Journal of Biological Chemistry*, *285*(34), 26674–26684. https://doi.org/10.1074/JBC.M110.134262

DeMers, D., & Wachs, D. (2019). Physiology, Mean Arterial Pressure. In *StatPearls*. StatPearls Publishing.

Detry, J. M. R., Melin, J., Brasseur, L. A., Cosyns, J., & Rousseau, M. F. (1981). Hemodynamic effects of molsidomine at rest and during submaximal and maximal exercise in patients with coronary artery disease limited by exertional angina pectoris. *The American Journal*

of Cardiology, *47*(1), 109–115. https://doi.org/10.1016/0002-9149(81)90298-8

Dey, N., De, P., & Brian, L.-J. (2015). Evading anti-angiogenic therapy: resistance to anti-angiogenic therapy in solid tumors. *American Journal of Translational Research*, *7*(10), 1675.

Dhakam, Z., Yasmin, McEniery, C. M., Burton, T., Brown, M. J., & Wilkinson, I. B. (2008). A comparison of atenolol and nebivolol in isolated systolic hypertension. *Journal of Hypertension*, *26*(2), 351–356. https://doi.org/10.1097/HJH.0B013E3282F283C9

Dong, J. G. (2016). The role of heart rate variability in sports physiology (Review). *Experimental and Therapeutic Medicine*, *11*(5), 1531–1536. https://doi.org/10.3892/ETM.2016.3104/HTML

DuBridge, R. B., Tang, P., Hsia, H. C., Leong, P.-M., Miller, J. H., & Calos, M. P. (1987). Analysis of mutation in human cells by using an Epstein-Barr virus shuttle system. *Molecular and Cellular Biology*, *7*(1), 379–387. https://doi.org/10.1128/mcb.7.1.379-387.1987

Duliege, A.-M., Arnold, D. M., Boccia, R., Boxer, M., Cooper, N., Hill, Q. A., Liles, D. K., Sholzberg, M., Zayed, H., Tong, S., & Bussel, J. B. (2018). Two-year safety and efficacy outcomes with fostamatinib in adult patients with immune thrombocytopenia (ITP): Open-label extension to Phase 3 trial program. *Blood*, *132*(Supplement 1), 736–736. https://doi.org/10.1182/BLOOD-2018-99-110482

Eechoute, K., Van Der Veldt, A. A. M., Oosting, S., Kappers, M. H. W., Wessels, J. A. M., Gelderblom, H., Guchelaar, H. J., Reyners, A. K. L., Van Herpen, C. M. L., Haanen, J. B., Mathijssen, R. H. J., & Boven, E. (2012). Polymorphisms in endothelial nitric oxide synthase (eNOS) and vascular endothelial growth factor (VEGF) predict sunitinib-induced hypertension. *Clinical Pharmacology and Therapeutics*, *92*(4), 503–510. https://doi.org/10.1038/CLPT.2012.136

El-Dabh, A., & Acharya, D. (2019). Pulmonary hypertension with dasatinib and other tyrosine kinase inhibitors. *Pulmonary Circulation*, *9*(3). https://doi.org/10.1177/2045894019865704

Ellis, L., & Hicklin, D. J. (2008). Pathways mediating resistance to vascular endothelial growth factor-targeted therapy. *Clinical Cancer Research : An Official Journal of the American Association for Cancer Research*, *14*(20), 6371–6375. https://doi.org/10.1158/1078-0432.CCR-07-5287

Eremina, V., Jefferson, J. A., Kowalewska, J., Hochster, H., Haas, M., Weisstuch, J., Richardson,

C., Kopp, J. B., Kabir, M. G., Backx, P. H., Gerber, H.-P., Ferrara, N., Barisoni, L., Alpers, C. E., & Quaggin, S. E. (2008). VEGF inhibition and renal thrombotic microangiopathy. *New England Journal of Medicine*, *358*(11), 1129–1136. https://doi.org/10.1056/nejmoa0707330

Eremina, V., Sood, M., Haigh, J., Nagy, A., Lajoie, G., Ferrara, N., Gerber, H. P., Kikkawa, Y., Miner, J. H., & Quaggin, S. E. (2003). Glomerular-specific alterations of VEGF-A expression lead to distinct congenital and acquired renal diseases. *Journal of Clinical Investigation*, *111*(5), 707. https://doi.org/10.1172/JCI17423

Faivre, S., Demetri, G., Sargent, W., & Raymond, E. (2007a). Molecular basis for sunitinib efficacy and future clinical development. *Nature Reviews Drug Discovery*, *6*(9), 734–745. https://doi.org/10.1038/nrd2380

Faivre, S., Demetri, G., Sargent, W., & Raymond, E. (2007b). Molecular basis for sunitinib efficacy and future clinical development. *Nature Reviews. Drug Discovery*, *6*(9), 734–745. https://doi.org/10.1038/NRD2380

Falloon, B. J., Stephens, N., Tulip, J. R., & Heagerty, A. M. (1995). Comparison of small artery sensitivity and morphology in pressurized and wire-mounted preparations. *American Journal of Physiology - Heart and Circulatory Physiology*, *268*(2 37-2), H670-8. https://doi.org/10.1152/ajpheart.1995.268.2.h670

Felmeden, D. C., Blann, A. D., & Lip, G. Y. H. (2003). Angiogenesis: basic pathophysiology and implications for disease. *European Heart Journal*, *24*(7), 586–603. https://doi.org/10.1016/S0195-668X(02)00635-8

Feng, Y., Chen, S., Li, Z., Gu, Z., Xu, S., Ban, X., Hong, Y., Cheng, L., & Li, C. (2021). A review of controlled release from cyclodextrins: release methods, release systems and application. *Critical Reviews in Food Science and Nutrition*, *63*(20), 4744–4756. https://doi.org/10.1080/10408398.2021.2007352

Fernández-Suárez, M., & Ting, A. Y. (2008). Fluorescent probes for super-resolution imaging in living cells. *Nature Reviews Molecular Cell Biology*, *9*(12), 929–943. https://doi.org/10.1038/nrm2531

Ferrara, N. (2004). Vascular endothelial growth factor: Basic science and clinical progress. *Endocrine Reviews*, *25*(4), 581–611. https://doi.org/10.1210/er.2003-0027

Ferrara, N., & Adamis, A. P. (2016). Ten years of anti-vascular endothelial growth factor therapy. *Nature Reviews Drug Discovery*, *15*(6), 385–403.

https://doi.org/10.1038/nrd.2015.17

Fine, B. A., Valente, P. T., Feinstein, G. I., & Dey, T. (2000). VEGF, flt-1, and KDR/flk-1 as prognostic indicators in endometrial carcinoma. *Gynecologic Oncology*, *76*(1), 33–39. https://doi.org/10.1006/GYNO.1999.5658

Flecknell, P. (2015). *Laboratory Animal Anaesthesia* (4th ed.). Elsevier. https://doi.org/https://doi.org/10.1016/C2013-0-13494-0

Fluckiger, J. P., Sonnay, M., Boillat, N., & Atkinson, J. (1985). Attenuation of the baroreceptor reflex by general anesthetic agents in the normotensive rat. *European Journal of Pharmacology*, *109*(1), 105–109. https://doi.org/10.1016/0014-2999(85)90545-X

Folkman, J. (2007). Is angiogenesis an organizing principle in biology and medicine? *Journal of Pediatric Surgery*, *42*(1), 1–11. https://doi.org/10.1016/j.jpedsurg.2006.09.048

Forrest, M. J., Bloomfield, D., Briscoe, R. J., Brown, P. N., Cumiskey, A. M., Ehrhart, J., Hershey, J. C., Keller, W. J., Ma, X., McPherson, H. E., Messina, E., Peterson, L. B., Sharif-Rodriguez, W., Siegl, P. K. S., Sinclair, P. J., Sparrow, C. P., Stevenson, A. S., Sun, S. Y., Tsai, C., … Woltmann, R. F. (2008). Torcetrapib-induced blood pressure elevation is independent of CETP inhibition and is accompanied by increased circulating levels of aldosterone. *British Journal of Pharmacology*, *154*(7), 1465–1473. https://doi.org/10.1038/BJP.2008.229

Fossa, A. A., Langdon, G., Couderc, J. P., Zhou, M., Darpo, B., Wilson, F., Wallis, R., & Davis, J. D. (2011). The use of beat-to-beat electrocardiogram analysis to distinguish QT/QTc interval changes caused by moxifloxacin from those caused by vardenafil. *Clinical Pharmacology and Therapeutics*, *90*(3), 449–454. https://doi.org/10.1038/CLPT.2011.139

Frank, S., Hübner, G., Breier, G., Longaker, M. T., Greenhalgh, D. G., & Werner, S. (1995). Regulation of Vascular Endothelial Growth Factor Expression in Cultured Keratinocytes. *Journal of Biological Chemistry*, *270*(21), 12607–12613. https://doi.org/10.1074/jbc.270.21.12607

Friedberg, J. W., Sharman, J., Sweetenham, J., Johnston, P. B., Vose, J. M., LaCasce, A., Schaefer-Cutillo, J., De Vos, S., Sinha, R., Leonard, J. P., Cripe, L. D., Gregory, S. A., Sterba, M. P., Lowe, A. M., Levy, R., & Shipp, M. A. (2010). Inhibition of Syk with fostamatinib disodium has significant clinical activity in non-Hodgkin lymphoma and chronic lymphocytic leukemia. *Blood*, *115*(13), 2578–2585. https://doi.org/10.1182/blood-2009-08-236471

Friesen, G. M., Jannett, T. C., Jadallah, M. A., Yates, S. L., Quint, S. R., & Nagle, H. T. (1990). A comparison of the noise sensitivity of nine QRS detection algorithms. *IEEE Transactions on Bio-Medical Engineering*, *37*(1), 85–98. https://doi.org/10.1109/10.43620

Fritz, M., Köppl, T., Oden, J. T., Wagner, A., Wohlmuth, B., & Wu, C. (2022). A 1D–0D–3D coupled model for simulating blood flow and transport processes in breast tissue. *International Journal for Numerical Methods in Biomedical Engineering*, *38*(7), e3612. https://doi.org/10.1002/cnm.3612

Frommeyer, G., & Eckardt, L. (2016). Drug-induced proarrhythmia: Risk factors and electrophysiological mechanisms. *Nature Reviews Cardiology*, *13*(1), 36–47. https://doi.org/10.1038/nrcardio.2015.110

Fuchs, F. D., & Whelton, P. K. (2020). High blood pressure and cardiovascular disease. *Hypertension*, *75*(2), 285–292. https://doi.org/10.1161/HYPERTENSIONAHA.119.14240

Fuh, G., Garcia, K. C., & De Vos, A. M. (2000). The interaction of neuropilin-1 with vascular endothelial growth factor and its receptor flt-1. *The Journal of Biological Chemistry*, *275*(35), 26690–26695. https://doi.org/10.1074/JBC.M003955200

Fukumura, D., Gohongi, T., Kadambi, A., Izumi, Y., Ang, J., Yun, C. O., Buerk, D. G., Huang, P. L., & Jain, R. K. (2001). Predominant role of endothelial nitric oxide synthase in vascular endothelial growth factor-induced angiogenesis and vascular permeability. *Proceedings of the National Academy of Sciences of the United States of America*, *98*(5), 2604–2609. https://doi.org/10.1073/pnas.041359198

Gabe, I. T., Gault, J. H., Ross, J., Mason, D. T., Mills, C. J., Schillingford, J. P., & Braunwald, E. (1969). Measurement of instantaneous blood flow velocity and pressure in conscious man with a catheter-tip velocity probe. *Circulation*, *40*(5), 603–614. https://doi.org/10.1161/01.CIR.40.5.603

Gabrilovich, D. I., Chen, H. L., Girgis, K. R., Cunningham, H. T., Meny, G. M., Nadaf, S., Kavanaugh, D., & Carbone, D. P. (1996). Production of vascular endothelial growth factor by human tumors inhibits the functional maturation of dendritic cells. *Nature Medicine*, *2*(10), 1096–1103. https://doi.org/10.1038/nm1096-1096

Gabrilovich, D., Ishida, T., Oyama, T., Ran, S., Kravtsov, V., Nadaf, S., & Carbone, D. P. (1998). Vascular endothelial growth factor inhibits the development of dendritic cells and dramatically affects the differentiation of multiple hematopoietic lineages in vivo. *Blood*, *92*(11), 4150–4166. https://doi.org/10.1182/blood.v92.11.4150

Ganta, V. C., Choi, M., Farber, C. R., & Annex, B. H. (2019). Antiangiogenic VEGF165b regulates macrophage polarization via S100A8/S100A9 in peripheral artery disease. *Circulation*, *139*(2), 226–242. https://doi.org/10.1161/CIRCULATIONAHA.118.034165

Gardiner, S. M., & Bennett, T. (1988). Regional hemodynamic responses to adrenoceptor antagonism in conscious rats. *American Journal of Physiology - Heart and Circulatory Physiology*, *255*(4). https://doi.org/10.1152/ajpheart.1988.255.4.h813

Gardiner, S. M., Compton, A. M., Bennett, T., & Hartley, C. J. (1990). Can pulsed Doppler technique measure changes in aortic blood flow in conscious rats? *American Journal of Physiology-Heart and Circulatory Physiology*, *259*(2), H448–H456. https://doi.org/10.1152/ajpheart.1990.259.2.H448

Gardiner, S. M., Kemp, P. A., March, J. E., & Bennett, T. (1996). Temporal differences between the involvement of angiotensin II and endothelin in the cardiovascular responses to endotoxaemia in conscious rats. *British Journal of Pharmacology*, *119*(8), 1619–1627. https://doi.org/10.1111/j.1476-5381.1996.tb16081.x

Geahlen, R. L. (2014). Getting Syk: spleen tyrosine kinase as a therapeutic target. *Trends in Pharmacological Sciences*, *35*(8), 414–422. https://doi.org/10.1016/J.TIPS.2014.05.007

Genovese, M. C., Kavanaugh, A., Weinblatt, M. E., Peterfy, C., Dicarlo, J., White, M. L., O'Brien, M., Grossbard, E. B., & Magilavy, D. B. (2011). An oral Syk kinase inhibitor in the treatment of rheumatoid arthritis: A three-month randomized, placebo-controlled, phase II study in patients with active rheumatoid arthritis that did not respond to biologic agents. *Arthritis and Rheumatism*, *63*(2), 337–345. https://doi.org/10.1002/art.30114

Genovese, M. C., Van Der Heijde, D. M., Keystone, E. C., Spindler, A. J., Benhamou, C., Kavanaugh, A., Fudman, E., Lampl, K., O'Brien, C., Duffield, E. L., Poiley, J., & Weinblatt, M. E. (2014). A phase III, multicenter, randomized, double-blind, placebo-controlled, parallel-group study of 2 dosing regimens of fostamatinib in patients with rheumatoid arthritis with an inadequate response to a tumor necrosis factor-α antagonist. *Journal of Rheumatology*, *41*(11), 2120–2128. https://doi.org/10.3899/jrheum.140238

George, S., Reichardt, P., Lechner, T., Li, S., Cohen, D. P., & Demetri, G. D. (2012). Hypertension as a potential biomarker of efficacy in patients with gastrointestinal stromal tumor treated with sunitinib. *Annals of Oncology*, *23*(12), 3180–3187. https://doi.org/10.1093/annonc/mds179

Ghatalia, P., Morgan, C. J., Je, Y., Nguyen, P. L., Trinh, Q. D., Choueiri, T. K., & Sonpavde, G.

(2015). Congestive heart failure with vascular endothelial growth factor receptor tyrosine kinase inhibitors. *Critical Reviews in Oncology/Hematology*, *94*(2), 228–237. https://doi.org/10.1016/J.CRITREVONC.2014.12.008

Ghiadoni, L., Versari, D., & Taddei, S. (2008). Phosphodiesterase 5 inhibition in essential hypertension. *Current Hypertension Reports*, *10*(1), 52–57. https://doi.org/10.1007/S11906-008-0011-4

Giantonio, B. J., Catalano, P. J., Meropol, N. J., O'Dwyer, P. J., Mitchell, E. P., Alberts, S. R., Schwartz, M. A., & Benson, A. B. (2007). Bevacizumab in combination with oxaliplatin, fluorouracil, and leucovorin (FOLFOX4) for previously treated metastatic colorectal cancer: results from the Eastern Cooperative Oncology Group Study E3200. *Journal of Clinical Oncology : Official Journal of the American Society of Clinical Oncology*, *25*(12), 1539–1544. https://doi.org/10.1200/JCO.2006.09.6305

Gliki, G., Abu-Ghazaleh, R., Jezequel, S., Wheeler-Jones, C., & Zachary, I. (2001). Vascular endothelial growth factor-induced prostacyclin production is mediated by a protein kinase C (PKC)-dependent activation of extracellular signal-regulated protein kinases 1 and 2 involving PKC-delta and by mobilization of intracellular Ca2+. *The Biochemical Journal*, *353*(Pt 3), 503–512. https://doi.org/10.1042/0264-6021:3530503

Gobessi, S., Laurenti, L., Longo, P. G., Carsetti, L., Berno, V., Sica, S., Leone, G., & Efremov, D. G. (2009). Inhibition of constitutive and BCR-induced Syk activation downregulates Mcl-1 and induces apoptosis in chronic lymphocytic leukemia B cells. *Leukemia*, *23*(4), 686–697. https://doi.org/10.1038/LEU.2008.346

Goldie, L. C., Nix, M. K., & Hirschi, K. K. (2008). Embryonic vasculogenesis and hematopoietic specification. *Organogenesis*, *4*(4), 257. https://doi.org/10.4161/ORG.4.4.7416

Goldman, C. K., Kendall, R. L., Cabrera, G., Soroceanu, L., Heike, Y., Gillespie, G. Y., Siegal, G. P., Mao, X., Bett, A. J., Huckle, W. R., Thomas, K. A., & Curiel, D. T. (1998). Paracrine expression of a native soluble vascular endothelial growth factor receptor inhibits tumor growth, metastasis, and mortality rate. *Proceedings of the National Academy of Sciences of the United States of America*, *95*(15), 8795–8800. https://doi.org/10.1073/PNAS.95.15.8795

González-clemente, J. M., Cano, A., Albert, L., Giménez-palop, O., Romero, A., Berlanga, E., Vendrell, J., & Llauradó, G. (2021). Arterial stiffness in type 1 diabetes: The case for the arterial wall itself as a target organ. In *Journal of Clinical Medicine* (Vol. 10, Issue 16, p.

3616). Multidisciplinary Digital Publishing Institute. https://doi.org/10.3390/jcm10163616

Gordon, M. S., Margolin, K., Talpaz, M., Sledge, J., Holmgren, E., Benjamin, R., Stalter, S., Shak, S., & Adelman, D. C. (2001). Phase I safety and pharmacokinetic study of recombinant human anti-vascular endothelial growth factor in patients with advanced cancer. *Journal of Clinical Oncology : Official Journal of the American Society of Clinical Oncology*, *19*(3), 843–850. https://doi.org/10.1200/JCO.2001.19.3.843

Gotink, K. J., & Verheul, H. M. W. (2010). Anti-angiogenic tyrosine kinase inhibitors: what is their mechanism of action? *Angiogenesis*, *13*(1), 1. https://doi.org/10.1007/S10456-009-9160-6

Grädler, U., Schwarz, D., Dresing, V., Musil, D., Bomke, J., Frech, M., Greiner, H., Jäkel, S., Rysiok, T., Müller-Pompalla, D., & Wegener, A. (2013). Structural and biophysical characterization of the Syk activation switch. *Journal of Molecular Biology*, *425*(2), 309–333. https://doi.org/10.1016/J.JMB.2012.11.007

Greene, A. N., Clapp, S. L., & Alper, R. H. (2007). Timecourse of recovery after surgical intraperitoneal implantation of radiotelemetry transmitters in rats. *Journal of Pharmacological and Toxicological Methods*, *56*(2), 218–222. https://doi.org/10.1016/J.VASCN.2007.04.006

Grund, E., Mueller-Ruchholtz, E. R., & Lapp, E. R. (1978). Comparative study of nitroglycerin and molsidomine. Effects on the integrated systemic venous bed and the arterial pressure in dogs. *Arzneimittel-Forschung*, *28*(9), 1624–1628.

Gu, J. W., Manning, R. D., Young, E., Shparago, M., Sartin, B., & Bailey, A. P. (2009). Vascular endothelial growth factor receptor inhibitor enhances dietary salt-induced hypertension in Sprague-Dawley rats. *American Journal of Physiology - Regulatory Integrative and Comparative Physiology*, *297*(1), 142–148. https://doi.org/10.1152/ajpregu.90972.2008

Guignabert, C., Phan, C., Seferian, A., Huertas, A., Tu, L., Thuillet, R., Sattler, C., Hiress, M. Le, Tamura, Y., Jutant, E. M., Chaumais, M. C., Bouchet, S., Manéglier, B., Molimard, M., Rousselot, P., Sitbon, O., Simonneau, G., Montani, D., & Humbert, M. (2016). Dasatinib induces lung vascular toxicity and predisposes to pulmonary hypertension. *The Journal of Clinical Investigation*, *126*(9), 3207–3218. https://doi.org/10.1172/JCI86249

Guns, P. J. D., Guth, B. D., Braam, S., Kosmidis, G., Matsa, E., Delaunois, A., Gryshkova, V., Bernasconi, S., Knot, H. J., Shemesh, Y., Chen, A., Markert, M., Fernández, M. A.,

Lombardi, D., Grandmont, C., Cillero-Pastor, B., Heeren, R. M. A., Martinet, W., Woolard, J., … Valentin, J. P. (2020). INSPIRE: A European training network to foster research and training in cardiovascular safety pharmacology. *Journal of Pharmacological and Toxicological Methods*, *105*(May), 106889. https://doi.org/10.1016/j.vascn.2020.106889

Günther, A., Salzmann, I., Nowack, S., Schwab, M., Surber, R., Hoyer, H., Witte, O. W., & Hoyer, D. (2012). Heart rate variability - a potential early marker of sub-acute post-stroke infections. *Acta Neurologica Scandinavica*, *126*(3), 189–196. https://doi.org/10.1111/j.1600-0404.2011.01626.x

Gupta, R., & Maitland, M. L. (2011). Sunitinib, hypertension, and heart failure: A model for kinase inhibitor-mediated cardiotoxicity. *Current Hypertension Reports*, *13*(6), 430–435. https://doi.org/10.1007/s11906-011-0229-4

Gurevich, F., & Perazella, M. A. (2009). Renal effects of anti-angiogenesis therapy: Update for the internist. *The American Journal of Medicine*, *122*(4), 322–328. https://doi.org/10.1016/J.AMJMED.2008.11.025

Hakim, T. S., Gilbert, E., & Camporesi, E. M. (1994). Blood flow, volume, and transit time in the pulmonary microvasculature using laser-Doppler. *Journal of Applied Physiology (Bethesda, Md. : 1985)*, *76*(6), 2643–2650. https://doi.org/10.1152/JAPPL.1994.76.6.2643

Hall, M. P., Unch, J., Binkowski, B. F., Valley, M. P., Butler, B. L., Wood, M. G., Otto, P., Zimmerman, K., Vidugiris, G., MacHleidt, T., Robers, M. B., Benink, H. A., Eggers, C. T., Slater, M. R., Meisenheimer, P. L., Klaubert, D. H., Fan, F., Encell, L. P., & Wood, K. V. (2012). Engineered luciferase reporter from a deep sea shrimp utilizing a novel imidazopyrazinone substrate. *ACS Chemical Biology*, *7*(11), 1848–1857. https://doi.org/10.1021/cb3002478

Hallare, J., & Gerriets, V. (2020). *Half Life*. StatPearls Publishing.

Hametner, B., & Wassertheurer, S. (2017). Pulse waveform analysis: is it ready for prime time? *Current Hypertension Reports*, *19*(9), 1–7. https://doi.org/10.1007/s11906-017-0769-3

Hametner, B., Wassertheurer, S., Kropf, J., Mayer, C., Holzinger, A., Eber, B., & Weber, T. (2013). Wave reflection quantification based on pressure waveforms alone—Methods, comparison, and clinical covariates. *Computer Methods and Programs in Biomedicine*, *109*(3), 250–259. https://doi.org/10.1016/J.CMPB.2012.10.005

Hamnvik, O.-P. R., Choueiri, T. K., Turchin, A., McKay, R. R., Goyal, L., Davis, M., Kaymakcalan, M. D., & Williams, J. S. (2015). Clinical risk factors for the development of hypertensoin in patients treated with inhibitors of the VEGF signaling pathway. *Cancer*, *121*(2), 311–319. https://doi.org/10.1002/cncr.28972

Hartley, C. J., & Cole, J. S. (1974). An ultrasonic pulsed Doppler system for measuring blood flow in small vessels. *Journal of Applied Physiology*, *37*(4), 626–629. https://doi.org/10.1152/jappl.1974.37.4.626

Hasanzadeh, N., Ahmadi, M. M., & Mohammadzade, H. (2020). Blood pressure estimation using photoplethysmogram signal and its morphological features. *IEEE Sensors Journal*, *20*(8), 4300–4310. https://doi.org/10.1109/JSEN.2019.2961411

Hashimoto, J., & Ito, S. (2010). Pulse pressure amplification, arterial stiffness, and peripheral wave reflection determine pulsatile flow waveform of the femoral artery. *Hypertension*, *56*(5), 926–933. https://doi.org/10.1161/HYPERTENSIONAHA.110.159368

Hatton, O., Lambert, S. L., Krams, S. M., & Martinez, O. M. (2012). Src Kinase and Syk Activation Initiate PI3K Signaling by a Chimeric Latent Membrane Protein 1 in Epstein-Barr Virus (EBV)+ B Cell Lymphomas. *PLOS ONE*, *7*(8), e42610. https://doi.org/10.1371/JOURNAL.PONE.0042610

Hayashi, N., Someya, N., Endo, M. Y., Miura, A., & Fukuba, Y. (2006). Vasoconstriction and blood flow responses in visceral arteries to mental task in humans. *Experimental Physiology*, *91*(1), 215–220. https://doi.org/10.1113/EXPPHYSIOL.2005.031971

Hayman, S. R., Leung, N., Grande, J. P., & Garovic, V. D. (2012). VEGF inhibition, hypertension, and renal toxicity. *Current Oncology Reports*, *14*(4), 285–294. https://doi.org/10.1007/s11912-012-0242-z

Haywood, J. R., Shaffer, R. A., & Fastenow, C. (1981). Regional blood flow measurement with pulsed Doppler flowmeter in conscious rat. *American Journal of Physiology - Heart and Circulatory Physiology*, *10*(2), 273–278. https://doi.org/10.1152/ajpheart.1981.241.2.h273

Herman, S. E. M., Barr, P. M., McAuley, E. M., Liu, D., Wiestner, A., & Friedberg, J. W. (2013). Fostamatinib inhibits B-cell receptor signaling, cellular activation and tumor proliferation in patients with relapsed and refractory chronic lymphocytic leukemia. *Leukemia*, *27*(8), 1769. https://doi.org/10.1038/LEU.2013.37

Hermeling, E., Reesink, K. D., Kornmann, L. M., Reneman, R. S., & Hoeks, A. P. G. (2009). The

dicrotic notch as alternative time-reference point to measure local pulse wave velocity in the carotid artery by means of ultrasonography. *Journal of Hypertension*, *27*(10), 2028–2035. https://doi.org/10.1097/HJH.0b013e32832f5890

Herrmann, J., Yang, E. H., Iliescu, C. A., Cilingiroglu, M., Charitakis, K., Hakeem, A., Toutouzas, K., Leesar, M. A., Grines, C. L., & Marmagkiolis, K. (2016). Vascular toxicities of cancer therapies: The old and the new - An evolving avenue. *Circulation*, *133*(13), 1272–1289. https://doi.org/10.1161/CIRCULATIONAHA.115.018347

Hewlin, R. L., & Kizito, J. P. (2018). Development of an experimental and digital cardiovascular arterial model for transient hemodynamic and postural change studies: "A preliminary framework analysis." *Cardiovascular Engineering and Technology*, *9*(1), 1–31. https://doi.org/10.1007/S13239-017-0332-Z

Hill, S. J., Baker, J. G., & Rees, S. (2001). Reporter-gene systems for the study of G-protein-coupled receptors. *Current Opinion in Pharmacology*, *1*(5), 526–532. https://doi.org/10.1016/S1471-4892(01)00091-1

Hoeksel, S. A. A. P., Jansen, J. R. C., Blom, J. A., & Schreuder, J. J. (1997). Detection of dicrotic notch in arterial pressure signals. *Journal of Clinical Monitoring*, *13*(5), 309–316. https://doi.org/10.1023/A:1007414906294

Holland, C. K., Brown, J. M., Scoutt, L. M., & Taylor, K. J. W. (1998). Lower extremity volumetric arterial blood flow in normal subjects. *Ultrasound in Medicine and Biology*, *24*(8), 1079–1086. https://doi.org/10.1016/S0301-5629(98)00103-3

Holmes, K., Roberts, O. L., Thomas, A. M., & Cross, M. J. (2007). Vascular endothelial growth factor receptor-2: structure, function, intracellular signalling and therapeutic inhibition. *Cellular Signalling*, *19*(10), 2003–2012. https://doi.org/10.1016/J.CELLSIG.2007.05.013

Honkalampi, K., Järvelin-Pasanen, S., Tarvainen, M. P., Saaranen, T., Vauhkonen, A., Kupari, S., Perkiö-Mäkelä, M., Räsänen, K., & Oksanen, T. (2021). Heart rate variability and chronotype–a systematic review. *Chronobiology International*, *38*(12), 1786–1796. https://doi.org/10.1080/07420528.2021.1939363

Houck, K. A., Leung, D. W., Rowland, A. M., Winer, J., & Ferrara, N. (1992). Dual regulation of vascular endothelial growth factor bioavailability by genetic and proteolytic mechanisms. *Journal of Biological Chemistry*, *267*(36), 26031–26037. https://doi.org/10.1016/S0021-9258(18)35712-0

Huang, D., Zhou, T., Lafleur, K., Nevado, C., & Caflisch, A. (2010). Kinase selectivity potential

for inhibitors targeting the ATP binding site: a network analysis. *Bioinformatics*, *26*(2), 198–204. https://doi.org/10.1093/BIOINFORMATICS/BTP650

Huang, Y. H., Lyle, J. V., Ab Razak, A. S., Nandi, M., Marr, C. M., Huang, C. L. H., Aston, P. J., & Jeevaratnam, K. (2022). Detecting paroxysmal atrial fibrillation from normal sinus rhythm in equine athletes using Symmetric Projection Attractor Reconstruction and machine learning. *Cardiovascular Digital Health Journal*, *3*(2), 96–106. https://doi.org/10.1016/J.CVDHJ.2022.02.001

Hughes, C. E., Pollitt, A. Y., Mori, J., Eble, J. A., Tomlinson, M. G., Hartwig, J. H., O'Callaghan, C. A., Fütterer, K., & Watson, S. P. (2010). CLEC-2 activates Syk through dimerization. *Blood*, *115*(14), 2947–2955. https://doi.org/10.1182/BLOOD-2009-08-237834

Hughes, D., Blevins, F., Shah, B., Sarosiek, S., Lerner, A., & Sloan, J. M. (2019). Real-world experience with fostamatinib in patients with immune thrombocytopenia at an academic medical center. *Blood*, *134*(Supplement_1), 4912–4912. https://doi.org/10.1182/blood-2019-124740

Hwan, M. L., Won, K. J., Kim, J., Park, H. J., Hyo, J. K., Hui, Y. R., So, H. L., Lee, C. K., & Kim, B. (2007). Endothelin-1 induces contraction via a Syk-mediated p38 mitogen-activated protein kinase pathway in rat aortic smooth muscle. *Journal of Pharmacological Sciences*, *103*(4), 427–433. https://doi.org/10.1254/JPHS.FP0070039

Inatome, R., Yanagi, S., Takano, T., & Yamamura, H. (2001). A critical role for Syk in endothelial cell proliferation and migration. *Biochemical and Biophysical Research Communications*, *286*(1), 195–199. https://doi.org/10.1006/bbrc.2001.5355

International Conference on Harmonisation. (2001). *S7A Safety Pharmacology Studies for Human Pharmaceuticals*.

International Conference on Harmonisation. (2005). *S7B The nonclinical Evaluation of the Potential for delayed Ventricular Repolarization (QT Interval Prolongation) by Human Pharmaceuticals*.

Isobe, T., Komatsu, R., Honda, M., Kuramoto, S., Shindoh, H., & Tabo, M. (2014). Estimating the clinical risk of hypertension from VEGF signal inhibitors by a non-clinical approach using telemetered rats. *Journal of Toxicological Sciences*, *39*(2), 237–242. https://doi.org/10.2131/jts.39.237

Itatani, Y., Kawada, K., Yamamoto, T., & Sakai, Y. (2018). Resistance to anti-angiogenic therapy in cancer-alterations to anti-VEGF pathway. *International Journal of Molecular Sciences*,

19(4), 1232. https://doi.org/10.3390/IJMS19041232

Ito, S. (2011). Pharmacokinetics 101. *Paediatrics & Child Health*, *16*(9), 535. https://doi.org/10.1093/PCH/16.9.535

Iversen, N. K., Frische, S., Thomsen, K., Laustsen, C., Pedersen, M., Hansen, P. B. L., Bie, P., Fresnais, J., Berret, J. F., Baatrup, E., & Wang, T. (2013). Superparamagnetic iron oxide polyacrylic acid coated γ-Fe2O3 nanoparticles do not affect kidney function but cause acute effect on the cardiovascular function in healthy mice. *Toxicology and Applied Pharmacology*, *266*(2), 276–288. https://doi.org/10.1016/j.taap.2012.10.014

Izzedine, H., Ederhy, S., Goldwasser, F., Soria, J. C., Milano, G., Cohen, A., Khayat, D., & Spano, J. P. (2009). Management of hypertension in angiogenesis inhibitor-treated patients. *Annals of Oncology*, *20*(5), 807–815. https://doi.org/10.1093/annonc/mdn713

Izzedine, H., Escudier, B., Lhomme, C., Pautier, P., Rouvier, P., Gueutin, V., Baumelou, A., Derosa, L., Bahleda, R., Hollebecque, A., Sahali, D., & Soria, J. C. (2014). Kidney diseases associated with anti-vascular endothelial growth factor (VEGF): An 8-year observational study at a single center. *Medicine (United States)*, *93*(24), 333–339. https://doi.org/10.1097/MD.0000000000000207

Jain, R. K. (2014). Antiangiogenesis strategies revisited: from starving tumors to alleviating hypoxia. *Cancer Cell*, *26*(5), 605–622. https://doi.org/10.1016/j.ccell.2014.10.006

Jakeman, L. B., Winer, J., Bennett, G. L., Anthony Altar, C., & Ferrara, N. (1992). Binding sites for vascular endothelial growth factor are localized on endothelial cells in adult rat tissues. *The Journal of Clinical Investigation*, *89*(1), 244–253. https://doi.org/10.1172/JCI115568

James, W. P. T., Caterson, I. D., Coutinho, W., Finer, N., Van Gaal, L. F., Maggioni, A. P., Torp-Pedersen, C., Sharma, A. M., Shepherd, G. M., Rode, R. A., & Renz, C. L. (2010). Effect of sibutramine on cardiovascular outcomes in overweight and obese subjects. *The New England Journal of Medicine*, *363*(10), 905–917. https://doi.org/10.1056/NEJMOA1003114

Janić, M., Lunder, M., & Šabovič, M. (2014). Arterial stiffness and cardiovascular therapy. *BioMed Research International*, *2014*. https://doi.org/10.1155/2014/621437

Järvelin-Pasanen, S., Sinikallio, S., & Tarvainen, M. P. (2019). Heart rate variability and occupational stress— systematic review. *Industrial Health*, *56*(6), 500–511. https://doi.org/10.2486/indhealth.2017-0190

Jeroncic, A., Gunjaca, G., Mrsic, D. B., Mudnic, I., Brizic, I., Polasek, O., & Boban, M. (2016). Normative equations for central augmentation index: Assessment of inter-population applicability and how it could be improved. *Scientific Reports*, *6*(1), 1–9. https://doi.org/10.1038/srep27016

Jesus-Gonzalez, N. de, Robinson, E., Moslehi, J., & Humphreys, B. D. (2012). Management of Antiangiogenic Therapy-Induced Hypertension. *Hypertension*, *60*(3), 907–615. https://doi.org/10.1161/HYPERTENSIONAHA.112.196774

Jin, J., Geng, X., Zhang, Y., Zhang, H., & Ye, T. (2023). Pulse wave analysis method of cardiovascular parameters extraction for health monitoring. *International Journal of Environmental Research and Public Health*, *20*(3), 2597. https://doi.org/10.3390/IJERPH20032597

Johnson, S. A., Pleiman, C. M., Pao, L., Schneringer, J., Hippen, K., & Cambier, J. C. (1995). Phosphorylated immunoreceptor signaling motifs (ITAMs) exhibit unique abilities to bind and activate Lyn and Syk tyrosine kinases. *The Journal of Immunology*, *155*(10), 4596–4603. https://doi.org/10.4049/JIMMUNOL.155.10.4596

Joukov, V., Pajusola, K., Kaipainen, A., Chilov, D., Lahtinen, I., Kukk, E., Saksela, O., Kalkkinen, N., & Alitalo, K. (1996). A novel vascular endothelial growth factor, VEGF-C, is a ligand for the Flt4 (VEGFR-3) and KDR (VEGFR-2) receptor tyrosine kinases. *The EMBO Journal*, *15*(2), 290–298. https://doi.org/10.1002/j.1460-2075.1996.tb00359.x

Joy, T. R., & Hegele, R. A. (2008). The failure of torcetrapib: What have we learned? *British Journal of Pharmacology*, *154*(7), 1379–1381. https://doi.org/10.1038/bjp.2008.248

Kamba, T., Tam, B. Y. Y., Hashizume, H., Haskell, A., Sennino, B., Mancuso, M. R., Norberg, S. M., O'Brien, S. M., Davis, R. B., Gowen, L. C., Anderson, K. D., Thurston, G., Joho, S., Springer, M. L., Kuo, C. J., & McDonald, D. M. (2006). VEGF-dependent plasticity of fenestrated capillaries in the normal adult microvasculature. *American Journal of Physiology - Heart and Circulatory Physiology*, *290*(2), 560–576. https://doi.org/10.1152/ajpheart.00133.2005

Kappers, M. H. W., De Beer, V. J., Zhou, Z., Danser, A. H. J., Sleijfer, S., Duncker, D. J., Van Den Meiracker, A. H., & Merkus, D. (2012). Sunitinib-induced systemic vasoconstriction in swine is endothelin mediated and does not involve nitric oxide or oxidative stress. *Hypertension*, *59*(1), 151–157. https://doi.org/10.1161/HYPERTENSIONAHA.111.182220

Karim, N., Hasan, J. A., & Ali, S. S. (2011). Heart rate variability: A review. *Journal of Basic and*

Applied Sciences, *7*(1), 71–77.

Karkkainen, M. J., Mäkinen, T., & Alitalo, K. (2002). Lymphatic endothelium: a new frontier of metastasis research. *Nature Cell Biology*, *4*(1), E2–E5. https://doi.org/10.1038/NCB0102-E2

Kazerounian, S., Duquette, M., Reyes, M. A., Lawler, J. T., Song, K., Perruzzi, C., Primo, L., Khosravi-Far, R., Bussolino, F., Rabinovitz, I., & Lawler, J. (2011). Priming of the vascular endothelial growth factor signaling pathway by thrombospondin-1, CD36, and spleen tyrosine kinase. *Blood*, *117*(17), 4658–4666. https://doi.org/10.1182/blood-2010-09-305284

Keating, G. M., & Scott, L. J. (2003). Vardenafil: A review of its use in erectile dysfunction. *Drugs*, *63*(23), 2673–2702. https://doi.org/10.2165/00003495-200363230-00010

Keck, P. J., Hauser, S. D., Krivi, G., Sanzo, K., Warren, T., Feder, J., & Connolly, D. T. (1989). Vascular Permeability Factor, an endothelial cell mitogen related to PDGF. *Science*, *246*(4935), 1309–1312. https://doi.org/10.1126/SCIENCE.2479987

Kee, D., & Zalcberg, J. R. (2012). Current and emerging strategies for the management of imatinib-refractory advanced gastrointestinal stromal tumors. *Therapeutic Advances in Medical Oncology*, *4*(5), 255. https://doi.org/10.1177/1758834012450935

Kelly, R., Hayward, C., Avolio, A., & O'Rourke, M. (1989). Noninvasive determination of age-related changes in the human arterial pulse. *Circulation*, *80*(6), 1652–1659. https://doi.org/10.1161/01.CIR.80.6.1652

Kenakin, T. P. (2014). *A Pharmacology Primer: Techniques for more effective and strategic drug discovery* (4th editio). Elsevier Science & Technology.

Kendall, R. L., & Thomas, K. A. (1993). Inhibition of vascular endothelial cell growth factor activity by an endogenously encoded soluble receptor. *Proceedings of the National Academy of Sciences of the United States of America*, *90*(22), 10705–10709. https://doi.org/10.1073/PNAS.90.22.10705

Keragala, C. B., & Medcalf, R. L. (2021). Plasminogen: an enigmatic zymogen. *Blood*, *137*(21), 2881–2889. https://doi.org/10.1182/BLOOD.2020008951

Kiefer, F., Brumell, J., Al-Alawi, N., Latour, S., Cheng, A., Veillette, A., Grinstein, S., & Pawson, T. (1998). The Syk protein tyrosine kinase Is essential for Fcγ receptor signaling in macrophages and neutrophils. *Molecular and Cellular Biology*, *18*(7), 4209. https://doi.org/10.1128/MCB.18.7.4209

Kikukawa, Y., Watanabe, Y., Shimomura, T., & Suzushima, H. (2012). 4 cases of acute cardiac dysfunction induced by high-dose cytarabine chemotherapy. *Annals of Oncology*, *23*(S11), xi166–xi167. https://doi.org/10.1016/S0923-7534(20)32537-0

Kilpatrick, L. E., Friedman-Ohana, R., Alcobia, D. C., Riching, K., Peach, C. J., Wheal, A. J., Briddon, S. J., Robers, M. B., Zimmerman, K., Machleidt, T., Wood, K. V., Woolard, J., & Hill, S. J. (2017). Real-time analysis of the binding of fluorescent VEGF165a to VEGFR2 in living cells: Effect of receptor tyrosine kinase inhibitors and fate of internalized agonist-receptor complexes. *Biochemical Pharmacology*, *136*, 62–75. https://doi.org/10.1016/j.bcp.2017.04.006

Kim, K. J., Li, B., Winer, J., Armanini, M., Gillett, N., Phillips, H. S., & Ferrara, N. (1993). Inhibition of vascular endothelial growth factor-induced angiogenesis suppresses tumour growth in vivo. *Nature*, *362*(6423), 841–844. https://doi.org/10.1038/362841a0

Kips, J. G., Rietzschel, E. R., De Buyzere, M. L., Westerhof, B. E., Gillebert, T. C., Van Bortel, L. M., & Segers, P. (2009). Evaluation of noninvasive methods to assess wave reflection and pulse transit time from the pressure waveform alone. *Hypertension*, *53*(2), 142–149. https://doi.org/10.1161/HYPERTENSIONAHA.108.123109

Kistangari, G., & McCrae, K. R. (2013). Immune thrombocytopenia. *Hematology/Oncology Clinics of North America*, *27*(3), 495. https://doi.org/10.1016/J.HOC.2013.03.001

Kittai, A. S., Best, S., Thurlow, B., Lam, V., Hashiguchi, T., Goodyear, S., Persky, D. O., Okada, C., Park, B., Spurgeon, S. E., & Danilov, A. V. (2021). Entospletinib and obinutuzumab in patients with relapsed/refractory chronic lymphocytic leukemia and B-cell malignancies. *Haematologica*, *106*(7), 2022–2025. https://doi.org/10.3324/HAEMATOL.2020.270298

Klarhöfer, M., Csapo, B., Balassy, C., Szeles, J. C., & Moser, E. (2001). High-resolution blood flow velocity measurements in the human finger. *Magnetic Resonance in Medicine*, *45*(4), 716–719. https://doi.org/10.1002/MRM.1096

Koch, S., Tugues, S., Li, X., Gualandi, L., & Claesson-Welsh, L. (2011). Signal transduction by vascular endothelial growth factor receptors. *Biochemical Journal*, *437*(2), 169–183. https://doi.org/10.1042/BJ20110301

Kougias, P., Weakley, S. M., Yao, Q., Lin, P. H., & Chen, C. (2010). Arterial baroreceptors in the management of systemic hypertension. *Medical Science Monitor*, *16*(1), 1–8.

Kramer, K., & Kinter, L. B. (2003). Evaluation and applications of radiotelemetry in small laboratory animals. *Physiological Genomics*, *13*(3), 197–205.

https://doi.org/10.1152/physiolgenomics.00164.2002

Krejza, J., Ustymowicz, A., Szylak, A., Tomaszewski, M., Hryniewicz, A., & Jawad, A. (2005). Assessment of variability of renal blood flow Doppler parameters during the menstrual cycle in women. *Ultrasound in Obstetrics and Gynecology*, *25*(1), 60–69. https://doi.org/10.1002/UOG.1771

Ku, D. D., Zaleski, J. K., Liu, S., & Brock, T. A. (1993). Vascular endothelial growth factor induces EDRF-dependent relaxation in coronary arteries. *The American Journal of Physiology*, *265*(2 Pt 2). https://doi.org/10.1152/AJPHEART.1993.265.2.H586

Ku, D. N. (1997). Blood flow in arteries. *Annual Review of Fluid Mechanics*, *29*, 399–434. https://doi.org/10.1146/annurev.fluid.29.1.399

Kuang, H., Lv, F., Ma, X., & Liu, X. (2022). Efficient spatiotemporal attention network for remote heart rate variability analysis. *Sensors*, *22*(3), 1010. https://doi.org/10.3390/S22031010

Kukovetz, W. R., Holzmann, S., & Romanin, C. (1987). Mechanism of vasodilation by nitrates: role of cyclic GMP. *Cardiology*, *74 Suppl 1*(SUPPL. 1), 12–19. https://doi.org/10.1159/000174258

Künnapuu, J., Bokharaie, H., & Jeltsch, M. (2021). Proteolytic cleavages in the VEGF family: Generating diversity among angiogenic VEGFs, essential for the activation of lymphangiogenic VEGFs. *Biology*, *10*(2), 167. https://doi.org/10.3390/BIOLOGY10020167

Kunwar, S., Devkota, A. R., & Ghimire, D. K. C. (2016). Fostamatinib, an oral spleen tyrosine kinase inhibitor, in the treatment of rheumatoid arthritis: a meta-analysis of randomized controlled trials. *Rheumatology International*, *36*(8), 1077–1087. https://doi.org/10.1007/s00296-016-3482-7

Lagunoff, M., Lukac, D. M., & Ganem, D. (2001). Immunoreceptor tyrosine-based activation motif-dependent signaling by Kaposi's sarcoma-associated Herpesvirus K1 protein: Effects on lytic viral replication. *Journal of Virology*, *75*(13), 5891. https://doi.org/10.1128/JVI.75.13.5891-5898.2001

Lam, V., Best, S., Kittai, A., Orand, K., Spurgeon, S. E., Liu, T., Danilov, A. V, & Alexey Danilov, C. V. (2021). Proapoptotic and immunomodulatory effects of SYK inhibitor entospletinib in combination with obinutuzumab in patients with chronic lymphocytic leukaemia. *British Journal of Clinical Pharmacology*, *88*(2), 836–841.

https://doi.org/10.1111/bcp.14962

Lankhorst, S., Baelde, H. J., Kappers, M. H. W., Smedts, F. M. M., Hansen, A., Clahsen-Van Groningen, M. C., Sleijfer, S., Mathijssen, R. H. J., Danser, A. H. J., & Van Den Meiracker, A. H. (2015). Greater sensitivity of blood pressure than renal toxicity to tyrosine kinase receptor inhibition with sunitinib. *Hypertension*, *66*(3), 543–549. https://doi.org/10.1161/HYPERTENSIONAHA.115.05435

Lankhorst, S., Kappers, M. H. W., Van Esch, J. H. M., Danser, A. H. J., & Van Den Meiracker, A. H. (2014). Hypertension during vascular endothelial growth factor inhibition: focus on nitric oxide, endothelin-1, and oxidative stress. *Antioxidants & Redox Signaling*, *20*(1), 135–145. https://doi.org/10.1089/ARS.2013.5244

Laurent, P., Albaladejo, P., Blacher, J., Rudnichi, A., Smulyan, H., & Safar, M. E. (2003). Heart rate and pulse pressure amplification in hypertensive subjects. *American Journal of Hypertension*, *16*(5 Pt 1), 363–370. https://doi.org/10.1016/S0895-7061(03)00063-3

Laurent, P., Safar, M. E., Meaune, S., & Blacher, J. (2003). Influence of l-nitro-arginine methyl ester, acetylcholine, and adenosine on mean blood pressure, pulse pressure, and pulse pressure amplification in rats. *Journal of Cardiovascular Pharmacology*, *41*(2), 210–218. https://doi.org/10.1097/00005344-200302000-00009

Laurent, S., Cockcroft, J., Van Bortel, L., Boutouyrie, P., Giannattasio, C., Hayoz, D., Pannier, B., Vlachopoulos, C., Wilkinson, I., & Struijker-Boudier, H. (2006). Expert consensus document on arterial stiffness: Methodological issues and clinical applications. *European Heart Journal*, *27*(21), 2588–2605. https://doi.org/10.1093/eurheartj/ehl254

Laverty, H. G., Benson, C., Cartwright, E. J., Cross, M. J., Garland, C., Hammond, T., Holloway, C., McMahon, N., Milligan, J., Park, B. K., Pirmohamed, M., Pollard, C., Radford, J., Roome, N., Sager, P., Singh, S., Suter, T., Suter, W., Trafford, A., … Valentin, J. P. (2011). How can we improve our understanding of cardiovascular safety liabilities to develop safer medicines? *British Journal of Pharmacology*, *163*(4), 675–693. https://doi.org/10.1111/j.1476-5381.2011.01255.x

Leach, B. (2012, September 27). *FDA Approves Regorafenib for Advanced Colorectal Cancer*. https://www.onclive.com/view/fda-approves-regorafenib-for-advanced-colorectal-cancer

Lengel, D., Lamm Bergström, E., Barthlow, H., Oldman, K., Musgrove, H., Harmer, A., Valentin, J. P., Duffy, P., Braddock, M., & Curwen, J. (2015). Prevention of fostamatinib-induced

blood pressure elevation by antihypertensive agents. *Pharmacology Research and Perspectives*, *3*(5), 1–10. https://doi.org/10.1002/prp2.176

Leone, M., Asfar, P., Radermacher, P., Vincent, J. L., & Martin, C. (2015). Optimizing mean arterial pressure in septic shock: a critical reappraisal of the literature. *Critical Care*, *19*(1). https://doi.org/10.1186/S13054-015-0794-Z

Lewington, S., Clarke, R., Qizilbash, N., Peto, R., & Collins, R. (2002). Age-specific relevance of usual blood pressure to vascular mortality: A meta-analysis of individual data for one million adults in 61 prospective studies. *Lancet*, *360*(9349), 1903–1913. https://doi.org/10.1016/S0140-6736(02)11911-8

Li, M., Wang, P., Zou, Y., Wang, W., Zhao, Y., Liu, M., Wu, J., Zhang, Y., Zhang, N., & Sun, Y. (2023). Spleen tyrosine kinase (SYK) signals are implicated in cardio-cerebrovascular diseases. *Heliyon*, *9*(5), e15625. https://doi.org/10.1016/J.HELIYON.2023.E15625

Liu, B., Ding, F., Liu, Y., Xiong, G., Lin, T., He, D., Zhang, Y., Zhang, D., & Wei, G. (2016). Incidence and risk of hypertension associated with vascular endothelial growth factor receptor tyrosine kinase inhibitors in cancer patients: a comprehensive network meta-analysis of 72 randomized controlled trials involving 30013 patients. *Oncotarget*, *7*(41), 67661–67673. https://doi.org/10.18632/oncotarget.11813

Liu, D., & Mamorska-Dyga, A. (2017). Syk inhibitors in clinical development for hematological malignancies. *Journal of Hematology and Oncology*, *10*(1), 1–7. https://doi.org/10.1186/s13045-017-0512-1

Liu, J. F., Barry, W. T., Birrer, M., Lee, J.-M., Buckanovich, R. J., Fleming, G. F., Rimel, B., Buss, M. K., Nattam, S., Hurteau, J., Luo, W., Quy, P., Whalen, C., Obermayer, L., Lee, H., Winer, E. P., Kohn, E. C., Ivy, S. P., & Matulonis, U. A. (2014). A randomized phase 2 study of combination cediranib and olaparib versus olaparib alone as recurrence therapy in platinum-sensitive ovarian cancer. *Lancet Oncology*, *15*(11), 1207–1214. https://doi.org/10.1016/S1470-2045(14)70391-2

Liu, Y., Cox, S. R., Morita, T., & Kourembanas, S. (1995). Hypoxia regulates vascular endothelial growth factor gene expression in endothelial cells. Identification of a 5’ enhancer. *Circulation Research*, *77*(3), 638–643. https://doi.org/10.1161/01.RES.77.3.638

Lorenz, E. N. (1963). Deterministic nonperiodic flow. *Journal of the Atmospheric Sciences*, *20*, 130–141. https://doi.org/10.1175/1520-0469(1963)020<0130:DNF>2.0.CO;2

Lu, J., Lin, W. H., Chen, S. Y., Longnecker, R., Tsai, S. C., Chen, C. L., & Tsai, C. H. (2006). Syk

tyrosine kinase mediates Epstein-Barr virus latent membrane protein 2A-induced cell migration in epithelial cells. *The Journal of Biological Chemistry*, *281*(13), 8806–8814. https://doi.org/10.1074/JBC.M507305200

Lyle, D. P., Bancroft, W. H., Tucker, M., & Eddleman, E. E. (1971). Slopes of the carotid pulse wave in normal subjects, aortic valvular diseases, and hypertrophic subaortic stenosis. *Circulation*, *43*(3), 374–381. https://doi.org/10.1161/01.CIR.43.3.374

Lyle, J. V., Charlton, P. H., Bonet-Luz, E., Chaffey, G., Christie, M., Nandi, M., & Aston, P. J. (2017). Beyond HRV: Analysis of ECG signals using attractor reconstruction. *Computing in Cardiology*, *44*, 1–4. https://doi.org/10.22489/CinC.2017.091-096

Mabeta, P., & Steenkamp, V. (2022). The VEGF/VEGFR axis revisited: implications for cancer therapy. *International Journal of Molecular Sciences*, *23*(24). https://doi.org/10.3390/IJMS232415585

Maffei, A., & Lembo, G. (2009). Nitric oxide mechanisms of nebivolol. *Therapeutic Advances in Cardiovascular Disease*, *3*(4), 317–327. https://doi.org/10.1177/1753944709104496

Malecaze, F., Clamens, S., Simorre Pinatel, V., Mathis, A., Chollet, P., Favard, C., Bayard, F., & Plouet, J. (1994). Detection of vascular endothelial growth factor messenger RNA and vascular endothelial growth factor-like activity in proliferative diabetic retinopathy. *Archives of Ophthalmology*, *112*(11), 1476–1482. https://doi.org/10.1001/ARCHOPHT.1994.01090230090028

Mallat, Z., Lobo, S. M., Malik, A., & Tong, S. (2021). Phase 3 trial of fostamatinib for the treatment of COVID-19: Repurposing an immunomodulatory drug previously approved for immune thrombocytopenia. *Open Forum Infectious Diseases*, *8*(Suppl 1), S382. https://doi.org/10.1093/OFID/OFAB466.759

Mamer, S. B., Wittenkeller, A., & Imoukhuede, P. I. (2020). VEGF-A splice variants bind VEGFRs with differential affinities. *Scientific Reports*, *10*(1). https://doi.org/10.1038/S41598-020-71484-Y

Manni, S., Kisko, K., Schleier, T., Missimer, J., & Ballmer-Hofer, K. (2014). Functional and structural characterization of the kinase insert and the carboxy terminal domain in VEGF receptor 2 activation. *FASEB Journal*, *28*(11), 4914–4923. https://doi.org/10.1096/fj.14-256206

Marcus, R., Davies, A., Ando, K., Klapper, W., Opat, S., Owen, C., Phillips, E., Sangha, R., Schlag, R., Seymour, J. F., Townsend, W., Trněný, M., Wenger, M., Fingerle-Rowson, G., Rufibach,

K., Moore, T., Herold, M., & Hiddemann, W. (2017). Obinutuzumab for the first-line treatment of follicular lymphoma. *New England Journal of Medicine*, *377*(14), 1331–1344. https://doi.org/10.1056/NEJMoa1614598

Masuda, M., Emoto, T., Suzuki, A., Akutagawa, M., Kitawaki, T., Kitaoka, K., Tanaka, H., Obara, S., Yoshizaki, K., Konaka, S., & Kinouchi, Y. (2013). Evaluation of blood flow velocity waveform in common carotid artery using multi-branched arterial segment model of human arteries. *Biomedical Signal Processing and Control*, *8*(6), 509–519. https://doi.org/10.1016/j.bspc.2013.05.005

Matsukane, R., Suetsugu, K., Hirota, T., & Ieiri, I. (2022). Clinical pharmacokinetics and pharmacodynamics of fostamatinib and its active moiety R406. *Clinical Pharmacokinetics*, *61*(7), 955–972. https://doi.org/10.1007/S40262-022-01135-0

Matsumoto, S., Hanai, T., Uemura, H., & Levin, R. M. (2009). Effects of chronic treatment with vardenafil, a phosphodiesterase 5 inhibitor, on female rat bladder in a partial bladder outlet obstruction model. *BJU International*, *103*(7), 987–990. https://doi.org/10.1111/J.1464-410X.2008.08185.X

Mayer, E. L., Dallabrida, S. M., Rupnick, M. A., Redline, W. M., Hannagan, K., Ismail, N. S., Burstein, H. J., & Beckman, J. A. (2011). Contrary effects of the receptor tyrosine kinase inhibitor vandetanib on constitutive and flow-stimulated nitric oxide elaboration in humans. *Hypertension*, *58*(1), 85–92. https://doi.org/10.1161/HYPERTENSIONAHA.110.168120

McEniery, C. M., Yasmin, McDonnell, B., Munnery, M., Wallace, S. M., Rowe, C. V., Cockcroft, J. R., & Wilkinson, I. B. (2008). Central pressure: Variability and impact of cardiovascular risk factors the anglo-cardiff collaborative trial II. *Hypertension*, *51*(6), 1476–1482. https://doi.org/10.1161/HYPERTENSIONAHA.107.105445

McKenney, J. M., Davidson, M. H., Shear, C. L., & Revkin, J. H. (2006). Efficacy and safety of torcetrapib, a novel cholesteryl ester transfer protein inhibitor, in individuals with below-average high-density lipoprotein cholesterol levels on a background of atorvastatin. *Journal of the American College of Cardiology*, *48*(9), 1782–1790. https://doi.org/10.1016/J.JACC.2006.06.066

McNarry, M. A., & Lewis, M. J. (2012). Interaction between age and aerobic fitness in determining heart rate dynamics. *Physiological Measurement*, *33*(6), 901. https://doi.org/10.1088/0967-3334/33/6/901

McTigue, M. A., Wickersham, J. A., Pinko, C., Showalter, R. E., Parast V, C., Tempczyk-Russell, A., Gehring, M. R., Mroczkowski, B., Chen-Chen, K., Villafranca, J. E., & Appelt, K. (1999). Crystal structure of the kinase domain of human vascular endothelial growth factor receptor 2: a key enzyme in angiogenesis. *Structure*, *7*(3), 319–330. https://doi.org/10.1016/S0969-2126(99)80042-2

Mehta, A. R., Kefela, A., Toste, C., & Sweet, D. (2022). Real-world use of fostamatinib in patients with immune thrombocytopenia and thrombotic risk. *Acta Haematologica*, *145*(2), 221–228. https://doi.org/10.1159/000520438

Mejía-Mejía, E., May, J. M., Elgendi, M., & Kyriacou, P. A. (2021). Differential effects of the blood pressure state on pulse rate variability and heart rate variability in critically ill patients. *Npj Digital Medicine*, *4*(1), 1–11. https://doi.org/10.1038/s41746-021-00447-y

Meltzer, E. O., Berkowitz, R. B., & Grossbard, E. B. (2005). An intranasal Syk-kinase inhibitor (R112) improves the symptoms of seasonal allergic rhinitis in a park environment. *Journal of Allergy and Clinical Immunology*, *115*(4), 791–796. https://doi.org/10.1016/j.jaci.2005.01.040

Messerli, F. H., Rimoldi, S. F., & Bangalore, S. (2017). The transition from hypertension to heart failure: contemporary update. *JACC: Heart Failure*, *5*(8), 543–551. https://doi.org/10.1016/j.jchf.2017.04.012

Millasseau, S. C., Patel, S. J., Redwood, S. R., Ritter, J. M., & Chowienczyk, P. J. (2003). Pressure wave reflection assessed from the peripheral pulse: Is a transfer function necessary? *Hypertension*, *41*(5), 1016–1020. https://doi.org/10.1161/01.HYP.0000057574.64076.A5

Millauer, B., Wizigmann-Voos, S., Schnürch, H., Martinez, R., Møller, N. P. H., Risau, W., & Ullrich, A. (1993). High affinity VEGF binding and developmental expression suggest Flk-1 as a major regulator of vasculogenesis and angiogenesis. *Cell*, *72*(6), 835–846. https://doi.org/10.1016/0092-8674(93)90573-9

Mills, P. A., Huetteman, D. A., Brockway, B. P., Zwiers, L. M., Gelsema, A. J. M., Schwartz, R. S., & Kramer, K. (2000). A new method for measurement of blood pressure, heart rate, and activity in the mouse by radiotelemetry. *Journal of Applied Physiology*, *88*(5), 1537–1544. https://doi.org/10.1152/jappl.2000.88.5.1537

Minchenko, A., Salceda, S., Bauer, T., & Caro, J. (1994). Hypoxia regulatory elements of the human vascular endothelial growth factor gene. *Cellular & Molecular Biology Research*,

40(1), 35–39.

Mkaddem, S. Ben, Murua, A., Flament, H., Titeca-Beauport, D., Bounaix, C., Danelli, L., Launay, P., Benhamou, M., Blank, U., Daugas, E., Charles, N., & Monteiro, R. C. (2017). Lyn and Fyn function as molecular switches that control immunoreceptors to direct homeostasis or inflammation. *Nature Communications*, *8*(1), 1–13. https://doi.org/10.1038/s41467-017-00294-0

Mócsai, A., Ruland, J., & Tybulewicz, V. L. J. (2010). The SYK tyrosine kinase: A crucial player in diverse biological functions. *Nature Reviews Immunology*, *10*(6), 387–402. https://doi.org/10.1038/nri2765

Møller, N. B., Budolfsen, C., Grimm, D., Krüger, M., Infanger, M., Wehland, M., & Magnusson, N. E. (2019). Drug-induced hypertension caused by multikinase inhibitors (sorafenib, sunitinib, lenvatinib and axitinib) in renal cell carcinoma treatment. *International Journal of Molecular Sciences*, *20*(19). https://doi.org/10.3390/ijms20194712

Monaghan, R. M., Page, D. J., & Keavney, B. D. (2021). The physiological and pathological functions of VEGFR3 in cardiac and lymphatic development and related diseases. *Cardiovascular Research*, *117*(8), 1877. https://doi.org/10.1093/CVR/CVAA291

Montani, D., Bergot, E., Günther, S., Savale, L., Bergeron, A., Bourdin, A., Bouvaist, H., Canuet, M., Pison, C., MacRo, M., Poubeau, P., Girerd, B., Natali, D., Guignabert, C., Perros, F., O'Callaghan, D. S., Jaïs, X., Tubert-Bitter, P., Zalcman, G., … Humbert, M. (2012). Pulmonary arterial hypertension in patients treated by dasatinib. *Circulation*, *125*(17), 2128–2137. https://doi.org/10.1161/CIRCULATIONAHA.111.079921

Morgan, P., Brown, D. G., Lennard, S., Anderton, M. J., Barrett, J. C., Eriksson, U., Fidock, M., Hamrén, B., Johnson, A., March, R. E., Matcham, J., Mettetal, J., Nicholls, D. J., Platz, S., Rees, S., Snowden, M. A., & Pangalos, M. N. (2018). Impact of a five-dimensional framework on R&D productivity at AstraZeneca. *Nature Reviews Drug Discovery*, *17*(3), 167–181. https://doi.org/10.1038/nrd.2017.244

Morschhauser, F., S Dyer, M. J., Walter, H. S., Danilov, A. V, Ysebaert, L., James Hodson, D., Fegan, C., Rule, S. A., Radford, J., Cartron, G., Bouabdallah, K., John Davies, A., Spurgeon, S., Rajakumaraswamy, N., Li, B., Humeniuk, R., Huang, X., Bhargava, P., Jürgensmeier, J. M., & Salles, G. (2021). Phase 1b study of tirabrutinib in combination with idelalisib or entospletinib in previously treated B-cell lymphoma. *Leukemia*, *35*, 2108–2113. https://doi.org/10.1038/s41375-020-01108-x

Motzer, R. J., Hutson, T. E., Tomczak, P., Michaelson, M. D., Bukowski, R. M., Rixe, O., Oudard, S., Negrier, S., Szczylik, C., Kim, S. T., Chen, I., Bycott, P. W., Baum, C. M., & Figlin, R. A. (2007). Sunitinib versus interferon alfa in metastatic renal-cell carcinoma. *The New England Journal of Medicine*, *356*(2), 115–124. https://doi.org/10.1056/NEJMOA065044

Mullard, A. (2018). FDA approves first-in-class SYK inhibitor. *Nature Reviews. Drug Discovery*, *17*(6), 385. https://doi.org/10.1038/nrd.2018.96

Mynard, J. P., Kondiboyina, A., Kowalski, R., Cheung, M. M. H., & Smolich, J. J. (2020). Measurement, analysis and interpretation of pressure/flow waves in blood vessels. *Frontiers in Physiology*, *11*(August), 1–26. https://doi.org/10.3389/fphys.2020.01085

Nagy, J. A., Feng, D., Vasile, E., Wong, W. H., Shih, S. C., Dvorak, A. M., & Dvorak, H. F. (2006). Permeability properties of tumor surrogate blood vessels induced by VEGF-A. *Laboratory Investigation*, *86*(8), 767–780. https://doi.org/10.1038/labinvest.3700436

Nakashima, H., Natsugoe, S., Ishigami, S., Okumura, H., Matsumoto, M., Hokita, S., & Aikou, T. (2006). Clinical significance of nuclear expression of spleen tyrosine kinase (Syk) in gastric cancer. *Cancer Letters*, *236*(1), 89–94. https://doi.org/10.1016/J.CANLET.2005.05.022

Namasivayam, M., McDonnell, B. J., McEniery, C. M., & O'Rourke, M. F. (2009). Does wave reflection dominate age-related change in aortic blood pressure across the human life span? *Hypertension*, *53*(6), 979–985. https://doi.org/10.1161/HYPERTENSIONAHA.108.125179

Nandi, M., Anton, M., & Lyle, J. V. (2022). Cardiovascular waveforms - can we extract more from routine signals? *JRSM Cardiovascular Disease*, *11*. https://doi.org/10.1177/20480040221121438

Nandi, M., & Aston, P. J. (2020). Extracting new information from old waveforms: Symmetric projection attractor reconstruction: Where maths meets medicine. *Experimental Physiology*, *105*(9), 1444–1451. https://doi.org/10.1113/EP087873

Nandi, M., Venton, J., & Aston, P. J. (2018). A novel method to quantify arterial pulse waveform morphology: Attractor reconstruction for physiologists and clinicians. *Physiological Measurement*, *39*(10). https://doi.org/10.1088/1361-6579/aae46a

Nayak B, P., Minaz, N., & Pasha, K. (2021). Molsidomine ameliorates diabetic peripheral neuropathy complications in Wistar rats. *Animal Models and Experimental Medicine*, *4*(3), 243–248. https://doi.org/10.1002/ame2.12162

Neagoe, P. E., Lemieux, C., & Sirois, M. G. (2005). Vascular endothelial growth factor (VEGF)-A165-induced prostacyclin synthesis requires the activation of VEGF Receptor-1 and -2 heterodimer. *Journal of Biological Chemistry*, *280*(11), 9904–9912. https://doi.org/10.1074/JBC.M412017200

Neary, J. M., Mendenhall, V., & Santana, D. (2017). Surgical placement of a wireless telemetry device for cardiovascular studies of bovine calves. *F1000Research*, *6*(1061). https://doi.org/10.12688/F1000RESEARCH.11785.1

Neuendorff, N. R., Loh, K. P., Mims, A. S., Christofyllakis, K., Soo, W. K., Bölükbasi, B., Oñoro-Algar, C., Hundley, W. G., & Klepin, H. D. (2020). Anthracycline-related cardiotoxicity in older patients with acute myeloid leukemia: a Young SIOG review paper. *Blood Advances*, *4*(4), 762–775. https://doi.org/10.1182/BLOODADVANCES.2019000955

Neves, K. B., Montezano, A. C., Lang, N. N., & Touyz, R. M. (2020). Vascular toxicity associated with anti-angiogenic drugs. *Clinical Science*, *134*(18), 2503–2520. https://doi.org/10.1042/CS20200308

Neves, K. B., Rios, F. J., Van Der Mey, L., Alves-Lopes, R., Cameron, A. C., Volpe, M., Montezano, A. C., Savoia, C., & Touyz, R. M. (2018). VEGFR (vascular endothelial growth factor receptor) inhibition induces cardiovascular damage via redox-sensitive processes. *Hypertension*, *71*(4), 638–647. https://doi.org/10.1161/HYPERTENSIONAHA.117.10490

Newland, A., Lee, E. J., McDonald, V., & Bussel, J. B. (2018). Fostamatinib for persistent/chronic adult immune thrombocytopenia. *Immunotherapy*, *10*(1), 9–25. https://doi.org/10.2217/imt-2017-0097

Newland, A., & McDonald, V. (2020). Fostamatinib: A review of its clinical efficacy and safety in the management of chronic adult immune thrombocytopenia. *Immunotherapy*, *12*(18), 1325–1340. https://doi.org/10.2217/imt-2020-0215

Nichols, W. W. ., O'Rourke, M. F. ., Edelman, E. R. ., & Vlachopoulos, C. (2022). *McDonald's blood flow in arteries : theoretical, experimental and clinical principles* (W. W. Nichols, M. F. O'Rourke, E. R. Edelman, & C. Vlachopoulos (eds.); Seventh edition.) [Book]. CRC Press.

Nichols, W. W., Denardo, S. J., Wilkinson, I. B., McEniery, C. M., Cockcroft, J., & O'Rourke, M. F. (2008). Effects of arterial stiffness, pulse wave velocity, and wave reflections on the central aortic pressure waveform. *The Journal of Clinical Hypertension*, *10*(4), 295. https://doi.org/10.1111/J.1751-7176.2008.04746.X

Niemeyer, J. E. (2016). Telemetry for small animal physiology. *Lab Animal*, *45*(7), 255–257. https://doi.org/10.1038/laban.1048

Nirmalan, M., & Dark, P. M. (2014). Broader applications of arterial pressure wave form analysis. *Continuing Education in Anaesthesia, Critical Care and Pain*, *14*(6), 285–290. https://doi.org/10.1093/bjaceaccp/mkt078

Nissen, S. E., Tardif, J.-C., Nicholls, S. J., Revkin, J. H., Shear, C. L., Duggan, W. T., Ruzyllo, W., Bachinsky, W. B., Lasala, G. P., & Tuzcu, E. M. (2007). Effect of torcetrapib on the progression of coronary atherosclerosis. *New England Journal of Medicine*, *356*(13), 1304–1316. https://doi.org/10.1056/NEJMoa070635

Nowak-Sliwinska, P., Weiss, A., Van Beijnum, J. R., Wong, T. J., Kilarski, W. W., Szewczyk, G., Verheul, H. M. W., Sarna, T., Van Den Bergh, H., & Griffioen, A. W. (2015). Photoactivation of lysosomally sequestered sunitinib after angiostatic treatment causes vascular occlusion and enhances tumor growth inhibition. *Cell Death and Disease*, *6*(2). https://doi.org/10.1038/cddis.2015.4

Nugent, D., McMillan, R., Nichol, J. L., & Slichter, S. J. (2009). Pathogenesis of chronic immune thrombocytopenia: increased platelet destruction and/or decreased platelet production. *British Journal of Haematology*, *146*(6), 585–596. https://doi.org/10.1111/J.1365-2141.2009.07717.X

Nunan, D., Sandercock, G. R. H., & Brodie, D. A. (2010). A quantitative systematic review of normal values for short-term heart rate variability in healthy adults. *Pacing and Clinical Electrophysiology*, *33*(11), 1407–1417. https://doi.org/10.1111/J.1540-8159.2010.02841.X

O'Rourke, M. F., & Jiang, A. P. X. J. (2001). Pulse wave analysis. *British Journal of Clinical Pharmacology*, *51*(6), 507. https://doi.org/10.1046/J.0306-5251.2001.01400.X

O'Rourke, M. F., O'Brien, C., & Edelman, E. R. (2016). Arterial stiffening in perspective: Advances in physical and physiological science over centuries. *American Journal of Hypertension*, *29*(7), 785–791. https://doi.org/10.1093/ajh/hpw019

Obara, S., Hayashi, S., Hazama, A., Murakawa, M., & Katsuda, S. I. (2009). Correlation between augmentation index and pulse wave velocity in rabbits. *Journal of Hypertension*, *27*(2), 332–340. https://doi.org/10.1097/HJH.0B013E32831AC951

Olsson, A. K., Dimberg, A., Kreuger, J., & Claesson-Welsh, L. (2006). VEGF receptor signalling - In control of vascular function. *Nature Reviews Molecular Cell Biology*, *7*(5), 359–371.

https://doi.org/10.1038/nrm1911

Olufsen, M. S., Peskin, C. S., Kim, W. Y., Pedersen, E. M., Nadim, A., & Larsen, J. (2000). Numerical simulation and experimental validation of blood flow in arteries with structured-tree outflow conditions. *Annals of Biomedical Engineering*, *28*(11), 1281–1299. https://doi.org/10.1114/1.1326031

Otsuka, T., Kawada, T., Katsumata, M., & Ibuki, C. (2006). Utility of second derivative of the finger photoplethysmogram for the estimation of the risk of coronary heart disease in the general population. *Circulation Journal*, *70*(3), 304–310. https://doi.org/10.1253/CIRCJ.70.304

Pacheco, M., Knowles, T. G., Hunt, J., Slingsby, L. S., Taylor, P. M., & Murrell, J. C. (2020). Comparing paracetamol/codeine and meloxicam for postoperative analgesia in dogs: a non-inferiority trial. *The Veterinary Record*, *187*(8). https://doi.org/10.1136/VR.105487

Pagès, G., & Pouysségur, J. (2005). Transcriptional regulation of the Vascular Endothelial Growth Factor gene--a concert of activating factors. *Cardiovascular Research*, *65*(3), 564–573. https://doi.org/10.1016/J.CARDIORES.2004.09.032

Pang, C. C. Y. (2001). Autonomic control of the venous system in health and disease: effects of drugs. *Pharmacology & Therapeutics*, *90*(2–3), 179–230. https://doi.org/10.1016/S0163-7258(01)00138-3

Papaioannou, T. G., Protogerou, A. D., Vrachatis, D., Konstantonis, G., Aissopou, E., Argyris, A., Nasothimiou, E., Gialafos, E. J., Karamanou, M., Tousoulis, D., & Sfikakis, P. P. (2016). Mean arterial pressure values calculated using seven different methods and their associations with target organ deterioration in a single-center study of 1878 individuals. *Hypertension Research 2016 39:9*, *39*(9), 640–647. https://doi.org/10.1038/hr.2016.41

Park, J. E., Keller, G. A., & Ferrara, N. (1993). The vascular endothelial growth factor (VEGF) isoforms: differential deposition into the subepithelial extracellular matrix and bioactivity of extracellular matrix-bound VEGF. *Molecular Biology of the Cell*, *4*(12), 1317–1326. https://doi.org/10.1091/MBC.4.12.1317

Park, S. R., Speranza, G., Piekarz, R., Wright, J. J., Kinders, R. J., Wang, L., Pfister, T. D., Trepel, J. B., Lee, M.-J., Alarcon, S., Steinberg, S. M., Collins, J., Doroshow, J. H., & Kummar, S. (2013). A multi-histology trial of fostamatinib in patients with advanced colorectal, non-small cell lung, head and neck, thyroid, and renal cell carcinomas, and pheochromocytomas. *Cancer Chemother Pharmacol.*, *71*(4), 981–990.

https://doi.org/10.1007/s00280-013-2091-3

Parker, K. H. (2009). An introduction to wave intensity analysis. *Medical & Biological Engineering & Computing*, *47*(2), 175–188. https://doi.org/10.1007/S11517-009-0439-Y

Parragh, S., Hametner, B., Bachler, M., Weber, T., Eber, B., & Wassertheurer, S. (2015). Non-invasive wave reflection quantification in patients with reduced ejection fraction. *Physiological Measurement*, *36*(2), 179–190. https://doi.org/10.1088/0967-3334/36/2/179

Pascual, M. S., Huang, Y., Aston, P., Steier, J., Rafferty, G. F., & Nandi, M. (2021, September 5). SPAR (Symmetric Projection Attractor Reconstruction): Identifying novel respiratory biomarkers from waveform morphology and variability. *European Respiratory Journal*. https://doi.org/10.1183/13993003.congress-2021.pa3217

Peach, C. J., Mignone, V. W., Arruda, M. A., Alcobia, D. C., Hill, S. J., Kilpatrick, L. E., & Woolard, J. (2018). Molecular pharmacology of VEGF-A isoforms: Binding and signalling at VEGFR2. *International Journal of Molecular Sciences*, *19*(4). https://doi.org/10.3390/ijms19041264

Pepper, M. S. (2001). Extracellular proteolysis and angiogenesis. *Thrombosis and Haemostasis*, *86*(1), 346–355. https://doi.org/10.1055/s-0037-1616232

Pertovaara, L., Kaipainen, A., Mustonen, T., Orpana, A., Ferrara, N., Saksela, O., & Alitalo, K. (1994). Vascular endothelial growth factor is induced in response to transforming growth factor-beta in fibroblastic and epithelial cells. *The Journal of Biological Chemistry*, *269*(9), 6271–6274. https://doi.org/10.1016/s0021-9258(17)37365-9

Phan, T. S., Li, J. K. J., Segers, P., Reddy-Koppula, M., Akers, S. R., Kuna, S. T., Gislason, T., Pack, A. I., & Chirinos, J. A. (2016). Aging is associated with an earlier arrival of reflected waves without a distal shift in reflection sites. *Journal of the American Heart Association: Cardiovascular and Cerebrovascular Disease*, *5*(9). https://doi.org/10.1161/JAHA.116.003733

Phillips, H. S., Armani, M. P., Stayrou, D., Ferrara, N., & Westphal, M. (1993). Intense focal expression of vascular endothelial growth-factor messenger-RNA in human intracranial neoplasms - association with regions of necrosis. *International Journal of Oncology*, *2*(6), 913–919. https://doi.org/10.3892/IJO.2.6.913

Pine, P. R., Chang, B., Schoettler, N., Banquerigo, M. L., Wang, S., Lau, A., Zhao, F., Grossbard, E. B., Payan, D. G., & Brahn, E. (2007). Inflammation and bone erosion are suppressed in

models of rheumatoid arthritis following treatment with a novel Syk inhibitor. *Clinical Immunology*, *124*(3), 244–257. https://doi.org/10.1016/j.clim.2007.03.543

Pires, S. L. S., Barrès, C., Sassard, J., & Julien, C. (2001). Renal blood flow dynamics and arterial pressure lability in the conscious rat. *Hypertension*, *38*(1), 147–152. https://doi.org/10.1161/01.HYP.38.1.147

Piscitelli, S. C., Pavel, A. B., McHale, K., Jett, J. E., Collins, J., Gillmor, D., Tabolt, G., Li, R., Song, T., Zhang, N., Tallman, A. M., & Guttman-Yassky, E. (2021). A Phase 1b, randomized, single-center trial of topical cerdulatinib (DMVT-502) in patients with mild-to-moderate atopic dermatitis. *The Journal of Investigative Dermatology*, *141*(7), 1847–1851. https://doi.org/10.1016/J.JID.2020.11.031

Plummer, C., Michael, A., Shaikh, G., Stewart, M., Buckley, L., Miles, T., Ograbek, A., & McCormack, T. (2019). Expert recommendations on the management of hypertension in patients with ovarian and cervical cancer receiving bevacizumab in the UK. *British Journal of Cancer*, *121*(2), 109–116. https://doi.org/10.1038/s41416-019-0481-y

Podolanczuk, A., Lazarus, A. H., Crow, A. R., Grossbard, E., & Bussel, J. B. (2009). Of mice and men: an open-label pilot study for treatment of immune thrombocytopenic purpura by an inhibitor of Syk. *Blood*, *113*(14), 3154–3160. https://doi.org/10.1182/blood-2008-07-166439

Polverino, A., Coxon, A., Starnes, C., Diaz, Z., DeMelfi, T., Wang, L., Bready, J., Estrada, J., Cattley, R., Kaufman, S., Chen, D., Gan, Y., Kumar, G., Meyer, J., Neervannan, S., Alva, G., Talvenheimo, J., Montestruque, S., Tasker, A., … Kendall, R. (2006). AMG 706, an oral, multikinase inhibitor that selectively targets vascular endothelial growth factor, platelet-derived growth factor, and kit receptors, potently inhibits angiogenesis and induces regression in tumor xenografts. *Cancer Research*, *66*(17), 8715–8721. https://doi.org/10.1158/0008-5472.CAN-05-4665

Post, E. H., & Vincent, J. L. (2018). Renal autoregulation and blood pressure management in circulatory shock. *Critical Care*, *22*(1), 1–9. https://doi.org/10.1186/s13054-018-1962-8

Proescholdt, M. A., Heiss, J. D., Walbridge, S., Mühlhauser, J., Capogrossi, M. C., Oldfield, E. H., & Merrill, M. J. (1999). Vascular endothelial growth factor (VEGF) modulates vascular permeability and inflammation in rat brain. *Journal of Neuropathology and Experimental Neurology*, *58*(6), 613–627. https://doi.org/10.1097/00005072-199906000-00006

Pucci, G., Battista, F., & Schillaci, G. (2014). Effects of antihypertensive drugs on central blood

pressure: new evidence, more challenges. *Hypertension Research*, *37*(1), 10–12. https://doi.org/10.1038/hr.2013.125

Pugh, C. W., & Ratcliffe, P. J. (2003). Regulation of angiogenesis by hypoxia: role of the HIF system. *Nature Medicine*, *9*(6), 677–684. https://doi.org/10.1038/NM0603-677

Qasem, A., & Avolio, A. (2008). Determination of aortic pulse wave velocity from waveform decomposition of the central aortic pressure pulse. *Hypertension*, *51*(2), 188–195. https://doi.org/10.1161/HYPERTENSIONAHA.107.092676

Quek, L. S., Pasquet, J.-M., Hers, I., Cornall, R., Knight, G., Barnes, M., Hibbs, M. L., Dunn, A. R., Lowell, C. A., & Watson, S. P. (2000). Fyn and Lyn phosphorylate the Fc receptor γ chain downstream of glycoprotein VI in murine platelets, and Lyn regulates a novel feedback pathway. *Blood*, *96*(13), 4246–4253. https://doi.org/10.1182/BLOOD.V96.13.4246

Qureshi, Z. P., Seoane-Vazquez, E., Rodriguez-Monguio, R., Stevenson, K. B., & Szeinbach, S. L. (2011). Market withdrawal of new molecular entities approved in the United States from 1980 to 2009. *Pharmacoepidemiology and Drug Safety*, *20*, 772–777. https://doi.org/10.1002/pds.2155

Ramanathan, S., Di Paolo, J. A., Jin, F., Shao, L., Sharma, S., Robeson, M., & Kearney, B. P. (2017). Pharmacokinetics, pharmacodynamics, and safety of entospletinib, a novel pSYK inhibitor, following single and multiple oral dosing in healthy volunteers. *Clin Drug Investig*, *2017*(37), 195–205. https://doi.org/10.1007/s40261-016-0476-x

Raymond, E., Dahan, L., Raoul, J.-L., Bang, Y.-J., Borbath, I., Lombard-Bohas, C., Valle, J., Metrakos, P., Smith, D., Vinik, A., Chen, J.-S., Hörsch, D., Hammel, P., Wiedenmann, B., Van Cutsem, E., Patyna, S., Lu, D. R., Blanckmeister, C., Chao, R., & Ruszniewski, P. (2011). Sunitinib malate for the treatment of pancreatic neuroendocrine tumors. *New England Journal of Medicine*, *364*(6), 501–513. https://doi.org/10.1056/NEJMoa1003825

Reis Brandão, S., Carvalho, F., Amado, F., Ferreira, R., & Marisa Costa, V. (2022). Insights on the molecular targets of cardiotoxicity induced by anticancer drugs: A systematic review based on proteomic findings. *Metabolism*, *134*, 155250. https://doi.org/10.1016/j.metabol.2022.155250

Reth, M., & Alarcon B Wileman, C. H. (1989). Antigen receptor tail clue. *Nature 1989 338:6214*, *338*(6214), 383–384. https://doi.org/10.1038/338383b0

Ried, M., Neua, R., Lehle, K., Großer, C., Szöke, T., Lang, G., Hofmann, H. S., & Hoenicka, M.

(2017). Superior vasodilation of human pulmonary vessels by vardenafil compared with tadalafil and sildenafil: additive effects of bosentan. *Interactive CardioVascular and Thoracic Surgery*, *25*(2), 254–259. https://doi.org/10.1093/ICVTS/IVX108

Rieux, E. (2008). Trends in telemetry monitoring: more data and improved animal welfare. *Proceedings of Measuring Behavior 2008*.

Rijavec, E., Genova, C., Barletta, G., Biello, F., Dal Bello, M. G., Coco, S., Truini, A., Vanni, I., Alama, A., Boccardo, F., & Grossi, F. (2014). Efficacy of motesanib diphosphate in non-small-cell lung cancer. *Expert Opinion on Pharmacotherapy*, *15*(12), 1771–1780. https://doi.org/10.1517/14656566.2014.938639

Risau, W. (1997). Mechanisms of angiogenesis. *Nature*, *386*(6626), 671–674. https://doi.org/10.1038/386671A0

Risau, W, & Flamme, I. (1995). Vasculogenesis. *Annual Review of Cell and Developmental Biology*, *11*(1), 73–91. https://doi.org/10.1146/annurev.cb.11.110195.000445

Risau, Werner, & Flamme, I. (1995). Vasculogenesis. *Annual Review of Cell and Developmental Biology*, *11*, 73–91. https://doi.org/10.1146/ANNUREV.CB.11.110195.000445

Rixe, O., Bukowski, R. M., Michaelson, M. D., Wilding, G., Hudes, G. R., Bolte, O., Motzer, R. J., Bycott, P., Liau, K. F., Freddo, J., Trask, P. C., Kim, S., & Rini, B. I. (2007). Axitinib treatment in patients with cytokine-refractory metastatic renal-cell cancer: a phase II study. *The Lancet. Oncology*, *8*(11), 975–984. https://doi.org/10.1016/S1470-2045(07)70285-1

Robertson, G. A., & Morais-Cabral, J. H. (2020). hERG Function in Light of Structure. *Biophysical Journal*, *118*(4), 790–797. https://doi.org/10.1016/J.BPJ.2019.10.010

Robinson, C. J., & Stringer, S. E. (2001). The splice variants of vascular endothelial growth factor (VEGF) and their receptors. *Journal of Cell Science*, *114*(Pt 5), 853–865. https://doi.org/10.1242/JCS.114.5.853

Robinson, E. S., Khankin, E. V., Karumanchi, S. A., & Humphreys, B. D. (2010). Hypertension Induced by VEGF Signaling Pathway Inhibition: Mechanisms and Potential Use as a Biomarker. *Seminars in Nephrology*, *30*(6), 591. https://doi.org/10.1016/J.SEMNEPHROL.2010.09.007

Robinson, E. S., Matulonis, U. A., Ivy, P., Berlin, S. T., Tyburski, K., Penson, R. T., & Humphreys, B. D. (2010). Rapid development of hypertension and proteinuria with cediranib, an oral vascular endothelial growth factor receptor inhibitor. *Clinical Journal of the American Society of Nephrology*, *5*(3), 477–483. https://doi.org/10.2215/CJN.08111109

Rocchiccioli, C., Saad, M. A. A., & Elghozi, J. L. (1989). Attenuation of the baroreceptor reflex by propofol anesthesia in the rat. *Journal of Cardiovascular Pharmacology*, *14*(4), 631–635. https://doi.org/10.1097/00005344-198910000-00015

Rolf, M. G., Curwen, J. O., Veldman-Jones, M., Eberlein, C., Wang, J., Harmer, A., Hellawell, C. J., & Braddock, M. (2015). In vitro pharmacological profiling of R406 identifies molecular targets underlying the clinical effects of fostamatinib. *Pharmacology Research and Perspectives*, *3*(5), 1–12. https://doi.org/10.1002/prp2.175

Rosenkranz, B., Winkelmann, B. R., & Parnham, M. J. (1996). Clinical pharmacokinetics of molsidomine. *Clinical Pharmacokinetics*, *30*(5), 372–384. https://doi.org/10.2165/00003088-199630050-00004/METRICS

Rosenzweig, S. A. (2018). Acquired resistance to drugs targeting tyrosine kinases. *Advances in Cancer Research*, *138*, 71–98. https://doi.org/10.1016/bs.acr.2018.02.003

Russell, W. C., Graham, F. L., Smiley, J., & Nairn, R. (1977). Characteristics of a human cell line transformed by DNA from human adenovirus type 5. *Journal of General Virology*, *36*(1), 59–72. https://doi.org/10.1099/0022-1317-36-1-59

Sada, K., Takano, T., Yanagi, S., & Yamamura, H. (2001). Structure and function of Syk protein-tyrosine kinase. *The Journal of Biochemistry*, *130*(2), 177–186. https://doi.org/10.1093/OXFORDJOURNALS.JBCHEM.A002970

Safar, M. E., Blacher, J., Pannier, B., Guerin, A. P., Marchais, S. J., Guyonvarc, P., & London, G. M. (2002). Central pulse pressure and mortality in end-stage renal disease. *Hypertension*, *39*(3), 735–738.

Sager, P., Heilbraun, J., Turner, J. R., Gintant, G., Geiger, M. J., Kowey, P. R., Mansoor, G. A., Mendzelevski, B., Michelson, E. L., Stockbridge, N., Weber, M. A., & White, W. B. (2013). Assessment of drug-induced increases in blood pressure during drug development: report from the Cardiac Safety Research Consortium. *American Heart Journal*, *165*(4), 477–488. https://doi.org/10.1016/J.AHJ.2013.01.002

Sammito, S., Sammito, W., & Böckelmann, I. (2016). The circadian rhythm of heart rate variability. *Biological Rhythm Research*, *47*(5), 717–730. https://doi.org/10.1080/09291016.2016.1183887

Samosir, S. M., Utamayasa, I. K. A., Andarsini, M. R., Rahman, M. A., Ontoseno, T., Hidayat, T., Ugrasena, I. D. G., Larasati, M. C. S., & Cahyadi, A. (2021). Risk factors of daunorubicine induced early cardiotoxicity in childhood acute lymphoblastic leukemia: A retrospective

study. *Asian Pacific Journal of Cancer Prevention*, *22*(5), 1407. https://doi.org/10.31557/APJCP.2021.22.5.1407

Sandler, A., Gray, R., Perry, M. C., Brahmer, J., Schiller, J. H., Dowlati, A., Lilenbaum, R., & Johnson, D. H. (2006). Paclitaxel-carboplatin alone or with bevacizumab for non-small-cell lung cancer. *The New England Journal of Medicine*, *355*(24), 2542–2550. https://doi.org/10.1056/NEJMOA061884

Sarazan, R. D., Mittelstadt, S., Guth, B., Koerner, J., Zhang, J., & Pettit, S. (2011). Cardiovascular function in nonclinical drug safety assessment: Current issues and opportunities. *International Journal of Toxicology*, *30*(3), 272–286. https://doi.org/10.1177/1091581811398963

Sassi, R., Cerutti, S., Lombardi, F., Malik, M., Huikuri, H. V., Peng, C.-K., Schmidt, G., Yamamoto, Y., Reviewers:, D., Gorenek, B., Lip, G. Y. H., Grassi, G., Kudaiberdieva, G., Fisher, J. P., Zabel, M., & Macfadyen, R. (2015). Advances in heart rate variability signal analysis: joint position statement by the e-Cardiology ESC Working Group and the European Heart Rhythm Association co-endorsed by the Asia Pacific Heart Rhythm Society. *EP Europace*, *17*(9), 1341–1353. https://doi.org/10.1093/EUROPACE/EUV015

Schroeder, E. C., Lefferts, W. K., Hilgenkamp, T. I. M., & Fernhall, B. (2019). Acute systemic inflammation reduces both carotid and aortic wave reflection in healthy adults. *Physiological Reports*, *7*(15). https://doi.org/10.14814/PHY2.14203

Schutz, F. A. B., Je, Y., Richards, C. J., & Choueiri, T. K. (2012). Meta-analysis of randomized controlled trials for the incidence and risk of treatment-related mortality in patients with cancer treated with vascular endothelial growth factor tyrosine kinase inhibitors. *Journal of Clinical Oncology : Official Journal of the American Society of Clinical Oncology*, *30*(8), 871–877. https://doi.org/10.1200/JCO.2011.37.1195

Scott, L. J. (2015). Lenvatinib: First global approval. *Drugs*, *75*(5), 553–560. https://doi.org/10.1007/s40265-015-0383-0

Segers, P., O'Rourke, M. F., Parker, K., Westerhof, N., Hughes, A., Aguado-Sierra, J., Aizawa, K., Alastruey, J., Allen, J., Avolio, A., Chen, C. H., Cheng, H. min, Faita, F., Fraser, A., Gavish, B., Greenwald, S., Hametner, B., Holewijn, S., Di Lascio, N., … Westerhof, B. E. (2017). Towards a consensus on the understanding and analysis of the pulse waveform: Results from the 2016 Workshop on Arterial Hemodynamics: Past, present and future. *Artery Research*, *18*(December), 75–80. https://doi.org/10.1016/j.artres.2017.03.004

Senger, D. R., Galli, S. J., Dvorak, A. M., Perruzzi, C. A., Susan Harvey, V., & Dvorak, H. F. (1983). Tumor cells secrete a vascular permeability factor that promotes accumulation of ascites fluid. *Science*, *219*(4587), 983–985. https://doi.org/10.1126/SCIENCE.6823562

Series, J., Ribes, A., Garcia, C., Souleyreau, P., Bauters, A., Morschhauser, F., Jürgensmeier, J. M., Sié, P., Ysebaert, L., & Payrastre, B. (2020). Effects of novel Btk and Syk inhibitors on platelet functions alone and in combination in vitro and in vivo. *Journal of Thrombosis and Haemostasis*, *18*(12), 3336–3351. https://doi.org/10.1111/JTH.15098

Serna-Pascual, M., D'Cruz, R. F., Volovaya, M., Jolley, C. J., Hart, N., Rafferty, G. F., Steier, J., Aston, P. J., & Nandi, M. (2023, June 29). Novel breathing pattern analysis: Symmetric Projection Attractor Reconstruction (SPAR) improves identification of impending COPD re-exacerbations. A retrospective cohort analysis. *ERJ Open Research*. https://doi.org/10.1183/23120541.00164-2023

Shah, J., Votta-Velis, E. G., & Borgeat, A. (2018). New local anesthetics. *Best Practice & Research. Clinical Anaesthesiology*, *32*(2), 179–185. https://doi.org/10.1016/J.BPA.2018.06.010

Sharman, J., & Di Paolo, J. (2016). Targeting B-cell receptor signaling kinases in chronic lymphocytic leukemia: the promise of entospletinib. *Therapeutic Advances in Hematology*, *7*(3), 157–170. https://doi.org/10.1177/2040620716636542

Sharman, J. E., Davies, J. E., Jenkins, C., & Marwick, T. H. (2009). Augmentation index, left ventricular contractility, and wave reflection. *Hypertension*, *54*(5), 1099–1105. https://doi.org/10.1161/HYPERTENSIONAHA.109.133066

Sharman, J., Hawkins, M., Kolibaba, K., Boxer, M., Klein, L., Wu, M., Hu, J., Abella, S., & Yasenchak, C. (2015). An open-label phase 2 trial of entospletinib (GS-9973), a selective spleen tyrosine kinase inhibitor, in chronic lymphocytic leukemia. *Blood*, *125*(15), 2336–2343.

Sharp, J. L., Zammit, T. G., Azar, T. A., & Lawson, D. M. (2002). Stress-like responses to common procedures in male rats housed alone or with other rats. *Contemporary Topics in Laboratory Animal Science*, *41*(4), 8–14.

Shen, H., Clauss, M., Ryan, J., Schmidt, A. M., Tijburg, P., Borden, L., Connolly, D., Stern, D., & Kao, J. (1993). Characterization of vascular permeability factor/vascular endothelial growth factor receptors on mononuclear phagocytes. *Blood*, *81*(10), 2767–2773. https://doi.org/10.1182/blood.v81.10.2767.bloodjournal81102767

Shibuya, M., Yamaguchi, S., Yamane, A., Ikeda, T., Tojo, A., Matsushime, H., & Sato, M. (1990). Nucleotide sequence and expression of a novel human receptor-type tyrosine kinase gene (flt) closely related to the fms family. *Oncogene*, *5*(4), 519–524.

Shibuya, Masabumi. (2011). Vascular endothelial growth factor (VEGF) and its receptor (VEGFR) signaling in angiogenesis: A crucial target for anti- and pro-angiogenic therapies. *Genes and Cancer*, *2*(12), 1097–1105. https://doi.org/10.1177/1947601911423031

Shifren, J. L., Mesiano, S., Taylor, R. N., Ferrara, N., & Jaffe, R. B. (1998). Corticotropin regulates vascular endothelial growth factor expression in human fetal adrenal cortical cells. *The Journal of Clinical Endocrinology and Metabolism*, *83*(4), 1342–1347. https://doi.org/10.1210/JCEM.83.4.4730

Shimokawa, A., Kunitake, T., Takasaki, M., & Kannan, H. (1998). Differential effects of anesthetics on sympathetic nerve activity and arterial baroreceptor reflex in chronically instrumented rats. *Journal of the Autonomic Nervous System*, *72*(1), 46–54. https://doi.org/https://doi.org/10.1016/S0165-1838(98)00084-8

Singh, R., Masuda, E. S., & Payan, D. G. (2012). Discovery and development of spleen tyrosine kinase (SYK) inhibitors. *Journal of Medicinal Chemistry*, *55*(8), 3614–3643. https://doi.org/10.1021/jm201271b

Skinner, M., Philp, K., Lengel, D., Coverley, L., Lamm Bergström, E., Glaves, P., Musgrove, H., Prior, H., Braddock, M., Huby, R., Curwen, J. O., Duffy, P., & Harmer, A. R. (2014). The contribution of VEGF signalling to fostamatinib-induced blood pressure elevation. *British Journal of Pharmacology*, *171*(9), 2308–2320. https://doi.org/10.1111/bph.12559

Skinner, Matt, Ceuppens, P., White, P., & Prior, H. (2019). Social-housing and use of double-decker cages in rat telemetry studies. *Journal of Pharmacological and Toxicological Methods*, *96*(October 2018), 87–94. https://doi.org/10.1016/j.vascn.2019.02.005

Smulyan, H. (2019). The Computerized ECG: Friend and Foe. *The American Journal of Medicine*, *132*(2), 153–160. https://doi.org/10.1016/J.AMJMED.2018.08.025

Soker, S., Fidder, H., Neufeld, G., & Klagsbrun, M. (1996). Characterization of novel vascular endothelial growth factor (VEGF) receptors on tumor cells that bind VEGF165 via its exon 7-encoded domain. *The Journal of Biological Chemistry*, *271*(10), 5761–5767. https://doi.org/10.1074/JBC.271.10.5761

Soker, S., Takashima, S., Miao, H. Q., Neufeld, G., & Klagsbrun, M. (1998). Neuropilin-1 is expressed by endothelial and tumor cells as an isoform-specific receptor for vascular

endothelial growth factor. *Cell*, *92*(6), 735–745. https://doi.org/10.1016/S0092-8674(00)81402-6

Speed, B., Bu, H. Z., Pool, W. F., Peng, G. W., Wu, E. Y., Patyna, S., Bello, C., & Kang, P. (2012). Pharmacokinetics, distribution, and metabolism of [14C]sunitinib in rats, monkeys, and humans. *Drug Metabolism and Disposition: The Biological Fate of Chemicals*, *40*(3), 539–555. https://doi.org/10.1124/DMD.111.042853

Steeghs, N., Rabelink, T. J., Op 't Roodt, J., Batman, E., Cluitmans, F. H. M., Weijl, N. I., de Koning, E., & Gelderblom, H. (2010). Reversibility of capillary density after discontinuation of bevacizumab treatment. *Annals of Oncology*, *21*(5), 1100–1105. https://doi.org/10.1093/ANNONC/MDP417

Stephan, F. K., & Zucker, I. (1972). Circadian rhythms in drinking behavior and locomotor activity of rats are eliminated by hypothalamic lesions. *Proceedings of the National Academy of Sciences of the United States of America*, *69*(6), 1583–1586. https://doi.org/10.1073/PNAS.69.6.1583

Stevens, J. L., & Baker, T. K. (2009). The future of drug safety testing: expanding the view and narrowing the focus. *Drug Discovery Today*, *14*(3–4), 162–167. https://doi.org/10.1016/J.DRUDIS.2008.11.009

Stoddart, L. A., Kilpatrick, L. E., & Hill, S. J. (2018). NanoBRET Approaches to Study Ligand Binding to GPCRs and RTKs. *Trends in Pharmacological Sciences*, *39*(2), 136–147. https://doi.org/10.1016/j.tips.2017.10.006

Strich, J. R., Ramos-Benitez, M. J., Randazzo, D., Stein, S. R., Babyak, A., Davey, R. T., Suffredini, A. F., Childs, R. W., & Chertow, D. S. (2021). Fostamatinib inhibits neutrophils extracellular traps induced by COVID-19 patient plasma: A potential therapeutic. *The Journal of Infectious Diseases*, *223*(6), 981–984. https://doi.org/10.1093/INFDIS/JIAA789

Strich, J. R., Tian, X., Samour, M., King, C. S., Shlobin, O., Reger, R., Cohen, J., Ahmad, K., Brown, A. W., Khangoora, V., Aryal, S., Migdady, Y., Kyte, J. J., Joo, J., Hays, R., Collins, A. C., Battle, E., Valdez, J., Rivero, J., … Nathan, S. D. (2022). Fostamatinib for the treatment of hospitalized adults with Coronavirus disease 2019: A randomized trial. *Clinical Infectious Diseases*, *75*(1), E491–E498. https://doi.org/10.1093/cid/ciab732

Su, J., Hughes, A. D., Simonsen, U., & Howard, L. S. (2018). Nitric oxide attenuates arterial pulse wave reflection in a vasodilator responding pulmonary arterial hypertension patient. *Circulation: Cardiovascular Interventions*, *11*(3), 6242.

https://doi.org/10.1161/CIRCINTERVENTIONS.117.006242

Sun, L., Liang, C., Shirazian, S., Zhou, Y., Miller, T., Cui, J., Fukuda, J. Y., Chu, J. Y., Nematalla, A., Wang, X., Chen, H., Sistla, A., Luu, T. C., Tang, F., Wei, J., & Tang, C. (2003). Discovery of 5-[5-fluoro-2-oxo-1,2-dihydroindol-(3Z)-ylidenemethyl]-2, 4-dimethyl-1H-pyrrole-3-carboxylic acid (2-diethylaminoethyl)amide, a novel tyrosine kinase inhibitor targeting vascular endothelial and platelet-derived growth factor receptor tyrosin. *Journal of Medicinal Chemistry*, *46*(7), 1116–1119. https://doi.org/10.1021/jm0204183

Sweeny, D. J., Li, W., Clough, J., Bhamidipati, S., Singh, R., Park, G., Baluom, M., Grossbard, E., & Lau, D. T. W. (2010). Metabolism of fostamatinib, the oral methylene phosphate prodrug of the spleen tyrosine kinase inhibitor R406 in humans: contribution of hepatic and gut bacterial processes to the overall biotransformation. *Drug Metabolism and Disposition: The Biological Fate of Chemicals*, *38*(7), 1166–1176. https://doi.org/10.1124/DMD.110.032151

Sweeny, D. J., Li, W., Grossbard, E., & Lau, D. T. W. (2010). Contribution of gut bacteria to the metabolism of the spleen tyrosine kinase (Syk) inhibitor R406 in cynomolgus monkey. *Xenobiotica*, *40*(6), 415–423. https://doi.org/10.3109/00498251003734244

Tabeling, C., Herbert, J., Hocke, A. C., Lamb, D. J., Wollin, S. L., Erb, K. J., Boiarina, E., Movassagh, H., Scheffel, J., Doehn, J. M., Hippenstiel, S., Maurer, M., Gounni, A. S., Kuebler, W. M., Suttorp, N., & Witzenrath, M. (2017). Spleen tyrosine kinase inhibition blocks airway constriction and protects from Th2-induced airway inflammation and remodeling. *Allergy*, *72*(7), 1061–1072. https://doi.org/10.1111/ALL.13101

Tabeling, Christoph, Herbert, J., Boiarina, E., Hocke, A. C., Sewald, K., Lamb, D. J., Wollin, S.-L., Fehrenbach, H., Kuebler, W. M., Braun, A., Suttorp, N., Weissmann, N., & Witzenrath, M. (2018). Syk expression and function in the pulmonary vasculature. *European Respiratory Journal*, *52*(suppl 62), PA2175. https://doi.org/10.1183/13993003.CONGRESS-2018.PA2175

Takada, Y., & Aggarwal, B. B. (2004). TNF activates Syk protein tyrosine kinase leading to TNF-induced MAPK activation, NF-kappaB activation, and apoptosis. *Journal of Immunology*, *173*(2), 1066–1077. https://doi.org/10.4049/JIMMUNOL.173.2.1066

Takens, F. (1981). Detecting strange attractors in turbulence. In *Dynamical Systems and Turbulence, Warwick 1980* (pp. 366–381). Springer, Berlin, Heidelberg. https://doi.org/https://doi.org/10.1007/BFb0091924

Tan, E., Chin, C. S. H., Lim, Z. F. S., & Ng, S. K. (2021). HEK293 cell line as a platform to produce recombinant proteins and viral vectors. *Frontiers in Bioengineering and Biotechnology*, *9*. https://doi.org/10.3389/fbioe.2021.796991

Tanne, J. H. (2006). Pfizer stops clinical trials of heart drug. *BMJ : British Medical Journal*, *333*(7581), 1237. https://doi.org/10.1136/BMJ.39059.438044.DB

Tarkin, J. M., & Kaski, J. C. (2018). Nicorandil and long-acting nitrates: vasodilator therapies for the management of chronic stable angina pectoris. *European Cardiology Review*, *13*(1), 23. https://doi.org/10.15420/ECR.2018.9.2

Taylor, P. C., Genovese, M. C., Greenwood, M., Ho, M., Nasonov, E., Oemar, B., Stoilov, R., Vencovsky, J., & Weinblatt, M. (2015). OSKIRA-4: a phase IIb randomised, placebo-controlled study of the efficacy and safety of fostamatinib monotherapy. *Annals of the Rheumatic Diseases*, *74*(12), 2123–2129. https://doi.org/10.1136/annrheumdis-2014-205361

Tebbutt, N. C., Murphy, F., Zannino, D., Wilson, K., Cummins, M. M., Abdi, E., Strickland, A. H., Lowenthal, R. M., Marx, G., Karapetis, C., Shannon, J., Goldstein, D., Nayagam, S. S., Blum, R., Chantrill, L., Simes, R. J., & Price, T. J. (2011). Risk of arterial thromboembolic events in patients with advanced colorectal cancer receiving bevacizumab. *Annals of Oncology*, *22*(8), 1834–1838. https://doi.org/10.1093/annonc/mdq702

Terman, B. I., Carrion, M. E., Kovacs, E., Rasmussen, B. A., Eddy, R. L., & Shows, T. B. (1991). Identification of a new endothelial cell growth factor receptor tyrosine kinase. *Oncogene*, *6*(9), 1677–1683.

The Human Protein Atlas. (2023). *Subcellular - SYK - The Human Protein Atlas*. https://www.proteinatlas.org/ENSG00000165025-SYK/subcellular

Thickett, D. R., Armstrong, L., & Millar, A. B. (1999). Vascular endothelial growth factor (VEGF) in inflammatory and malignant pleural effusions. *Thorax*, *54*(8), 707–710. https://doi.org/10.1136/THX.54.8.707

Thijs, A. M. J., Van Herpen, C. M. L., Verweij, V., Pertijs, J., Van Den Broek, P. H. H., Van Der Graaf, W. T. A., & Rongen, G. A. (2015). Impaired endothelium-dependent vasodilation does not initiate the development of sunitinib-associated hypertension. *Journal of Hypertension*, *33*(10), 2075–2082. https://doi.org/10.1097/HJH.0000000000000662

Thomas, P., & Smart, T. G. (2005). HEK293 cell line: A vehicle for the expression of recombinant proteins. *Journal of Pharmacological and Toxicological Methods*, *51*(3

SPEC. ISS.), 187–200. https://doi.org/10.1016/j.vascn.2004.08.014

Thompson, C. A. (2007). Novartis suspends tegaserod sales at FDA's request. *American Journal of Health-System Pharmacy*, *64*(10), 1020. https://doi.org/10.2146/NEWS070044

Tidu, F., De Zuani, M., Jose, S. S., Bendíčková, K., Kubala, L., Caruso, F., Cavalieri, F., Forte, G., & Frič, J. (2021). NFAT signaling in human mesenchymal stromal cells affects extracellular matrix remodeling and antifungal immune responses. *IScience*, *24*(6), 102683. https://doi.org/10.1016/J.ISCI.2021.102683

Tomisawa, M., Tokunaga, T., Oshika, Y., Tsuchida, T., Fukushima, Y., Sato, H., Kijima, H., Yamazaki, H., Ueyama, Y., Tamaoki, N., & Nakamura, M. (1999). Expression pattern of vascular endothelial growth factor isoform is closely correlated with tumour stage and vascularisation in renal cell carcinoma. *European Journal of Cancer*, *35*(1), 133–137. https://doi.org/10.1016/S0959-8049(98)00278-0

Tomita, T., Kato, M., & Hiratsuka, S. (2021). Regulation of vascular permeability in cancer metastasis. *Cancer Science*, *112*(8), 2966–2974. https://doi.org/10.1111/CAS.14942

Touyz, R. M., Herrmann, S. M. S., & Herrmann, J. (2018). Vascular toxicities with VEGF inhibitor therapies–focus on hypertension and arterial thrombotic events. *Journal of the American Society of Hypertension*, *12*(6), 409–425. https://doi.org/10.1016/j.jash.2018.03.008

Touyz, R. M., Lang, N. N., Herrmann, J., Van Den Meiracker, A. H., & Danser, A. H. J. (2017a). Recent advances in hypertension and cardiovascular toxicities with vascular endothelial growth factor inhibition. *Hypertension*, *70*(2), 220–226. https://doi.org/10.1161/HYPERTENSIONAHA.117.08856

Touyz, R. M., Lang, N. N., Herrmann, J., Van Den Meiracker, A. H., & Danser, A. H. J. (2017b). Recent Advances in Hypertension and Cardiovascular Toxicities with Vascular Endothelial Growth Factor Inhibition. *Hypertension*, *70*(2), 220–226. https://doi.org/10.1161/HYPERTENSIONAHA.117.08856

Townsend, R. R., Black, H. R., Chirinos, J. A., Feig, P. U., Ferdinand, K. C., Germain, M., Rosendorff, C., Steigerwalt, S. P., & Stepanek, J. A. (2015). Clinical use of pulse wave analysis: proceedings from a symposium sponsored by north american artery. *Journal of Clinical Hypertension*, *17*(7), 503–513. https://doi.org/10.1111/jch.12574

Trihan, J. E., Mahé, G., Laroche, J. P., Dauzat, M., Perez-Martin, A., Croquette, M., & Lanéelle, D. (2023). Arterial blood-flow acceleration time on Doppler ultrasound waveforms: What

are we talking about? *Journal of Clinical Medicine*, *12*(3). https://doi.org/10.3390/jcm12031097

Trudeau, L. (2014). Central blood pressure as an index of antihypertensive control: Determinants and potential value. *Canadian Journal of Cardiology*, *30*(5 S). https://doi.org/10.1016/J.CJCA.2014.03.010

Tsang, E., Giannetti, A. M., Shaw, D., Dinh, M., Tse, J. K. Y., Gandhi, S., Ho, A., Wang, S., Papp, E., & Bradshaw, J. M. (2008). Molecular mechanism of the Syk activation switch. *Journal of Biological Chemistry*, *283*(47), 32650–32659. https://doi.org/10.1074/JBC.M806340200

TSE systems. (2020). *Stellar Telemetry • A wide range of research studies*. https://www.tse-systems.com/service/stellar-telemetry/

Turner, M., Schweighoffer, E., Colucci, F., Di Santo, J. P., & Tybulewicz, V. L. (2000). Tyrosine kinase SYK: essential functions for immunoreceptor signalling. *Immunology Today*, *21*(3), 148–154. https://doi.org/10.1016/S0167-5699(99)01574-1

Tyler, T. (2012). Axitinib: newly approved for renal cell carcinoma. *Journal of the Advanced Practitioner in Oncology*, *3*(5), 333–335. https://doi.org/10.6004/jadpro.2012.3.5.7

U.S. Food & Drug Administration. (2004, February 26). *Drug Approval Package: Avastin*. https://www.accessdata.fda.gov/drugsatfda_docs/nda/2004/STN-125085_Avastin.cfm

Valentin, J. P., & Leishman, D. (2023). 2000–2023 over two decades of ICH S7A: has the time come for a revamp? *Regulatory Toxicology and Pharmacology*, *139*(2023). https://doi.org/10.1016/j.yrtph.2023.105368

Vallerio, P., Orenti, A., Tosi, F., Maistrello, M., Palazzini, M., Cingarlini, S., Colombo, P., Bertuzzi, M., Spina, F., Amatu, A., Lombardo, R., Prata, I., Scaglione, F., Vighi, G. D., Severgnini, B., Siena, S., Giannattasio, C., Boracchi, P., & Sartore-Bianchi, A. (2022). Major adverse cardiovascular events associated with VEGF-targeted anticancer tyrosine kinase inhibitors: a real-life study and proposed algorithm for proactive management. *ESMO Open*, *7*(1), 100338. https://doi.org/10.1016/J.ESMOOP.2021.100338

Van Cutsem, E., Vervenne, W. L., Bennouna, J., Humblet, Y., Gill, S., Van Laethem, J. L., Verslype, C., Scheithauer, W., Shang, A., Cosaert, J., & Moore, M. J. (2009). Phase III trial of bevacizumab in combination with gemcitabine and erlotinib in patients with metastatic pancreatic cancer. *Journal of Clinical Oncology*, *27*(13), 2231–2237. https://doi.org/10.1200/JCO.2008.20.0238

Van Dorst, D. C. H., Dobbin, S. J. H., Neves, K. B., Herrmann, J., Herrmann, S. M., Versmissen, J., Mathijssen, R. H. J., Danser, A. H. J., & Lang, N. N. (2021). Hypertension and prohypertensive antineoplastic therapies in cancer patients. *Circulation Research*, *128*(7), 1040–1061. https://doi.org/10.1161/CIRCRESAHA.121.318051

Van Ravenswaaij-Arts, C. M. A., Kollee, L. A. A., Hopman, J. C. W., Stoelinga, G. B. A., & Van Geijn, H. P. (1993). Heart rate variability. *Annals of Internal Medicine*, *118*(6), 436–447. https://doi.org/10.7326/0003-4819-118-6-199303150-00008

Van Wynsberghe, M., Flejeo, J., Sakhi, H., Ollero, M., Sahali, D., Izzedine, H., & Henique, C. (2021). Nephrotoxicity of anti-angiogenic therapies. *Diagnostics*, *11*(4), 640. https://doi.org/10.3390/DIAGNOSTICS11040640

Vergis, N., Phillips, R., Cornelius, V., Katsarou, A., Youngstein, T., Cook, L., Willicombe, M., Pilay, C., Shturova, T., Almonte, M., Charania, A., Turner, R., Kon, O. M., Cooke, G., Thursz, M., Cherlin, S., Wason, J., Milojkovic, D., Innes, A. J., & Cooper, N. (2021). Multi-arm Trial of Inflammatory Signal Inhibitors (MATIS) for hospitalised patients with mild or moderate COVID-19 pneumonia: a structured summary of a study protocol for a randomised controlled trial. *Trials*, *22*(1), 270. https://doi.org/10.1186/s13063-021-05190-z

Veronese, M. L., Mosenkis, A., Flaherty, K. T., Gallagher, M., Stevenson, J. P., Townsend, R. R., & O'Dwyer, P. J. (2006). Mechanisms of hypertension associated with BAY 43-9006. *Journal of Clinical Oncology*, *24*(9), 1363–1369. https://doi.org/10.1200/JCO.2005.02.0503

Vicente-Manzanares, M., & Sánchez-Madrid, F. (2004). Role of the cytoskeleton during leukocyte responses. *Nature Reviews Immunology*, *4*(2), 110–122. https://doi.org/10.1038/nri1268

Vicente, J., Zusterzeel, R., Johannesen, L., Mason, J., Sager, P., Patel, V., Matta, M. K., Li, Z., Liu, J., Garnett, C., Stockbridge, N., Zineh, I., & Strauss, D. G. (2018). Mechanistic model-informed proarrhythmic risk assessment of drugs: Review of the "CiPA" initiative and design of a prospective clinical validation study. *Clinical Pharmacology and Therapeutics*, *103*(1), 54–66. https://doi.org/10.1002/CPT.896

Villaseñor, A. G., Kondru, R., Ho, H., Wang, S., Papp, E., Shaw, D., Barnett, J. W., Browner, M. F., & Kuglstatter, A. (2009). Structural insights for design of potent spleen tyrosine kinase inhibitors from crystallographic analysis of three inhibitor complexes. *Chemical Biology*

& Drug Design, *73*(4), 466–470. https://doi.org/10.1111/J.1747-0285.2009.00785.X

Vitolo, U., Trneny, M., Belada, D., Burke, J. M., Carella, A. M., Chua, N., Abrisqueta, P., Demeter, J., Flinn, I., Hong, X., Kim, W. S., Pinto, A., Shi, Y. K., Tatsumi, Y., Oestergaard, M. Z., Wenger, M., Fingerle-Rowson, G., Catalani, O., Nielsen, T., … Sehn, L. H. (2017). Obinutuzumab or rituximab plus cyclophosphamide, doxorubicin, vincristine, and prednisone in previously untreated diffuse large b-cell lymphoma. *Journal of Clinical Oncology*, *35*(31), 3529–3537. https://doi.org/10.1200/JCO.2017.73.3402

Walker, A. R., Byrd, J. C., Blachly, J. S., Bhatnagar, B., Mims, A. S., Orwick, S., Lin, T. L., Crosswell, H. E., Zhang, D., Minden, M. D., Munugalavadla, V., Long, L., Liu, J., Pan, Y., Oellerich, T., Serve, H., Rao, A. V, & Blum, W. G. (2020). Entospletinib in combination with induction chemotherapy in previously untreated acute myeloid leukemia: Response and predictive significance of HOXA9 and MEIS1 expression. *Clinical Cancer Research*, *26*, 5852–5859. https://doi.org/10.1158/1078-0432.CCR-20-1064

Wang L, Devarajan E, He J, Reddy SP, D. J. (2005). Transcription repressor activity of spleen tyrosine kinase mediates breast tumor suppression. *Cancer Res.*, *65*(22), 10289–10297. https://doi.org/10.1158/0008-5472.CAN-05-2231

Wang, L., Aschenbrenner, D., Zeng, Z., Cao, X., Mayr, D., Mehta, M., Capitani, M., Warner, N., Pan, J., Wang, L., Li, Q., Zuo, T., Cohen-Kedar, S., Lu, J., Ardy, R. C., Mulder, D. J., Dissanayake, D., Peng, K., Huang, Z., … Muise, A. M. (2021). Gain-of-function variants in SYK cause immune dysregulation and systemic inflammation in humans and mice. *Nature Genetics*, *53*(4), 500–510. https://doi.org/10.1038/s41588-021-00803-4

Wang, X., Bove, A. M., Simone, G., & Ma, B. (2020). Molecular bases of VEGFR-2-mediated physiological function and pathological role. *Frontiers in Cell and Developmental Biology*, *8*(November), 1–12. https://doi.org/10.3389/fcell.2020.599281

Waring, M. J., Arrowsmith, J., Leach, A. R., Leeson, P. D., Mandrell, S., Owen, R. M., Pairaudeau, G., Pennie, W. D., Pickett, S. D., Wang, J., Wallace, O., & Weir, A. (2015). An analysis of the attrition of drug candidates from four major pharmaceutical companies. *Nature Reviews Drug Discovery*, *14*(7), 475–486. https://doi.org/10.1038/nrd4609

Weatherald, J., Chaumais, M., Savale, L., Jaïs, X., Seferian, A., Canuet, M., Bouvaist, H., Magro, P., Bergeron, A., Guignabert, C., Sitbon, O., Simonneau, G., Humbert, M., & Montani, D. (2017). Long-term outcomes of dasatinib-induced pulmonary arterial hypertension: a population-based study. *European Respiratory Journal*, *50*.

https://doi.org/10.1183/13993003.00217-2017

Weaver, R. J., & Valentin, J. P. (2019a). Today's challenges to de-risk and predict drug safety in human "mind-the-gap." *Toxicological Sciences*, *167*(2), 307–321. https://doi.org/10.1093/toxsci/kfy270

Weaver, R. J., & Valentin, J. P. (2019b). Today's Challenges to De-Risk and Predict Drug Safety in Human "mind-The-Gap." *Toxicological Sciences*, *167*(2), 307–321. https://doi.org/10.1093/toxsci/kfy270

Weber, T., Auer, J., O'Rourke, M. F., Kvas, E., Lassnig, E., Berent, R., & Eber, B. (2004). Arterial stiffness, wave reflections, and the risk of coronary artery disease. *Circulation*, *109*(2), 184–189. https://doi.org/10.1161/01.CIR.0000105767.94169.E3

Weber, T., O'Rourke, M. F., Lassnig, E., Porodko, M., Ammer, M., Rammer, M., & Eber, B. (2010). Pulse waveform characteristics predict cardiovascular events and mortality in patients undergoing coronary angiography. *Journal of Hypertension*, *28*(4), 797–805. https://doi.org/10.1097/HJH.0b013e328336c8e9

Weinblatt, M E, Kavanaugh, A., Genovese, M. C., Musser, T. K., Grossbard, E. B., & Magilavy, D. B. (2010). An oral spleen tyrosine kinase (Syk) inhibitor for rheumatoid arthritis. *New England Journal of Medicine*, *363*(14), 1303–1312. https://doi.org/10.1056/NEJMoa1000500

Weinblatt, Michael E., Genovese, M. C., Ho, M., Hollis, S., Rosiak-Jedrychowicz, K., Kavanaugh, A., Millson, D. S., Leon, G., Wang, M., & Van Der Heijde, D. (2014). Effects of fostamatinib, an oral spleen tyrosine kinase inhibitor, in rheumatoid arthritis patients with an inadequate response to methotrexate: Results from a phase iii, multicenter, randomized, double-blind, placebo-controlled, parallel-group study. *Arthritis and Rheumatology*, *66*(12), 3255–3264. https://doi.org/10.1002/art.38851

Weinblatt, Michael E., Kavanaugh, A., Burgos-Vargas, R., Dikranian, A. H., Medrano-Ramirez, G., Morales-Torres, J. L., Murphy, F. T., Musser, T. K., Straniero, N., Vicente-Gonzales, A. V., & Grossbard, E. (2008). Treatment of rheumatoid arthritis with a Syk kinase inhibitor: A twelve-week, randomized, placebo-controlled trial. *Arthritis and Rheumatism*, *58*(11), 3309–3318. https://doi.org/10.1002/art.23992

Weiss, R. (2006). Nebivolol: A novel beta-blocker with nitric oxide-induced vasodilatation. *Vascular Health and Risk Management*, *2*(3), 303. https://doi.org/10.2147/VHRM.2006.2.3.303

Wenceslau, C. F., McCarthy, C. G., Earley, S., England, S. K., Filosa, J. A., Goulopoulou, S., Gutterman, D. D., Isakson, B. E., Kanagy, N. L., Martinez-Lemus, L. A., Sonkusare, S. K., Thakore, P., Trask, A. J., Watts, S. W., & Clinton Webb, R. (2021). Guidelines in Cardiovascular Research: Guidelines for the measurement of vascular function and structure in isolated arteries and veins. *American Journal of Physiology - Heart and Circulatory Physiology*, *321*(1), H77. https://doi.org/10.1152/AJPHEART.01021.2020

Wessel, N., Malberg, H., Heringer-Walther, S., Schultheiss, H. P., & Walther, T. (2007). The angiotensin-(1-7) receptor agonist AVE0991 dominates the circadian rhythm and baroreflex in spontaneously hypertensive rats. *Journal of Cardiovascular Pharmacology*, *49*(2), 67–73. https://doi.org/10.1097/FJC.0B013E31802CFFE9

Westbroek, M. L., & Geahlen, R. L. (2017). Modulation of BCR dignaling by the induced dimerization of receptor-associated SYK. *Antibodies*, *6*(4), 23. https://doi.org/10.3390/ANTIB6040023

Westerhof, B. E., Guelen, I., Westerhof, N., Karemaker, J. M., & Avolio, A. (2006). Quantification of wave reflection in the human aorta from pressure alone: A proof of principle. *Hypertension*, *48*(4), 595–601. https://doi.org/10.1161/01.HYP.0000238330.08894.17

Westerhof, N., Sipkema, P., Bos, G. C. V. Den, & Elzinga, G. (1972). Forward and backward waves in the arterial system. *Cardiovascular Research*, *6*(6), 648–656. https://doi.org/10.1093/CVR/6.6.648

Wilkinson, I. B., Mohammad, N. H., Tyrrell, S., Hall, I. R., Webb, D. J., Paul, V. E., Levy, T., & Cockcroft, J. R. (2002). Heart rate dependency of pulse pressure amplification and arterial stiffness. *American Journal of Hypertension*, *15*(1), 24–30. https://doi.org/10.1016/S0895-7061(01)02252-X/2/AJH.24.F3.JPEG

Willemet, M., & Alastruey, J. (2015). Arterial pressure and flow wave analysis using time-domain 1-D hemodynamics. *Annals of Biomedical Engineering*, *43*(1), 190–206. https://doi.org/10.1007/s10439-014-1087-4

Willemet, M., Vennin, S., & Alastruey, J. (2016). Computational assessment of hemodynamics-based diagnostic tools using a database of virtual subjects: Application to three case studies. *Journal of Biomechanics*, *49*(16), 3908–3914. https://doi.org/10.1016/J.JBIOMECH.2016.11.001

Willett, C. G., Boucher, Y., Di Tomaso, E., Duda, D. G., Munn, L. L., Tong, R. T., Chung, D. C.,

Sahani, D. V., Kalva, S. P., Kozin, S. V., Mino, M., Cohen, K. S., Scadden, D. T., Hartford, A. C., Fischman, A. J., Clark, J. W., Ryan, D. P., Zhu, A. X., Blaszkowsky, L. S., … Jain, R. K. (2004). Direct evidence that the VEGF-specific antibody bevacizumab has antivascular effects in human rectal cancer. *Nature Medicine*, *10*(2), 145–147. https://doi.org/10.1038/NM988

Woolard, J., Bennett, T., Dunn, W. R., Heal, D. J., Aspley, S., & Gardiner, S. M. (2004). Acute cardiovascular effects of sibutramine in conscious rats. *J Pharmacol Exp Ther.*, *308*(3), 1102–1110. https://doi.org/10.1124/jpet.103.061259

Woolard, J., Hale, T. M., Bushfield, T. L., & Adams, M. A. (2003). Persistent lowering of arterial pressure after continuous and intermittent therapy. *Journal of Hypertension*, *21*(4), 813–820. https://doi.org/10.1097/00004872-200304000-00026

Woolard, J., Wang, W. Y., Bevan, H. S., Qiu, Y., Morbidelli, L., Pritchard-Jones, R. O., Cui, T. G., Sugiono, M., Waine, E., Perrin, R., Foster, R., Digby-Bell, J., Shields, J. D., Whittles, C. E., Mushens, R. E., Gillatt, D. A., Ziche, M., Harper, S. J., & Bates, D. O. (2004). VEGF165b, an inhibitory vascular endothelial growth factor splice variant: mechanism of action, in vivo effect on angiogenesis and endogenous protein expression. *Cancer Research*, *64*(21), 7822–7835. https://doi.org/10.1158/0008-5472.CAN-04-0934

Wragg, E. S., Pannucci, P., Hill, S. J., Woolard, J., & Cooper, S. L. (2022). Involvement of β-adrenoceptors in the cardiovascular responses induced by selective adenosine A2A and A2B receptor agonists. *Pharmacology Research and Perspectives*, *10*(3), 1–16. https://doi.org/10.1002/prp2.975

Wu, S., Chen, J. J., Kudelka, A., Lu, J., & Zhu, X. (2008). Incidence and risk of hypertension with sorafenib in patients with cancer: a systematic review and meta-analysis. *The Lancet Oncology*, *9*(2), 117–123. https://doi.org/10.1016/S1470-2045(08)70003-2

Yamashita, M., Niisato, M., Kawasaki, Y., Karaman, S., Robciuc, M. R., Shibata, Y., Ishida, Y., Nishio, R., Masuda, T., Sugai, T., Ono, M., Tuder, R. M., Alitalo, K., & Yamauchi, K. (2022). VEGF-C/VEGFR-3 signalling in macrophages ameliorates acute lung injury. *The European Respiratory Journal*, *59*(4). https://doi.org/10.1183/13993003.00880-2021

Yang, J. C., Haworth, L., Sherry, R. M., Hwu, P., Schwartzentruber, D. J., Topalian, S. L., Steinberg, S. M., Chen, H. X., & Rosenberg, S. A. (2003). A randomized trial of bevacizumab, an anti–vascular endothelial growth factor antibody, for metastatic renal cancer. *New England Journal of Medicine*, *349*(5), 427–434.

https://doi.org/10.1056/nejmoa021491

Yang, R., Thomas, G. R., Bunting, S., Ko, A., Ferrara, N., Keyt, B., Ross, J., & Jin, H. (1996). Effects of vascular endothelial growth factor on hemodynamics and cardiac performance. *Journal of Cardiovascular Pharmacology*, *27*(6), 838–844. https://doi.org/10.1097/00005344-199606000-00011

Yang, Y., Li, S., Wang, Y., Zhao, Y., & Li, Q. (2022). Protein tyrosine kinase inhibitor resistance in malignant tumors: molecular mechanisms and future perspective. *Signal Transduction and Targeted Therapy*, *7*(1), 329. https://doi.org/10.1038/s41392-022-01168-8

Yeh, E. T. H., Tong, A. T., Lenihan, D. J., Yusuf, S. W., Swafford, J., Champion, C., Durand, J. B., Gibbs, H., Zafarmand, A. A., & Ewer, M. S. (2004). Cardiovascular complications of cancer therapy. *Circulation*, *109*(25), 3122–3131. https://doi.org/10.1161/01.CIR.0000133187.74800.B9

Yim, D. S. (2018). Five years of the CiPA project (2013-2018): what did we learn? *Translational and Clinical Pharmacology*, *26*(4), 145–149. https://doi.org/10.12793/TCP.2018.26.4.145

Zanettini, R., Antonini, A., Gatto, G., Gentile, R., Tesei, S., & Pezzoli, G. (2007). Valvular heart disease and the use of dopamine agonists for Parkinson's disease. *The New England Journal of Medicine*, *356*(1), 39–46. https://doi.org/10.1056/NEJMOA054830

Zhang, Z. F., Wang, T., Liu, L. H., & Guo, H. Q. (2014). Risks of proteinuria associated with vascular endothelial growth factor receptor tyrosine kinase inhibitors in cancer patients: A systematic review and meta-analysis. *PLoS ONE*, *9*(3), e90135. https://doi.org/10.1371/journal.pone.0090135

Zheng, D., Xia, L., Ji, H., Jin, Z., & Bai, Y. (2020). A cyclodextrin-based controlled release system in the simulation of in vitro small intestine. *Molecules*, *25*(5), 1212. https://doi.org/10.3390/MOLECULES25051212

Zheng, T. J., Lofurno, E. R., Melrose, A. R., Lakshmanan, H. H. S., Pang, J., Phillips, K. G., Fallon, M. E., Kohs, T. C. L., Ngo, A. T. P., Shatzel, J. J., Hinds, M. T., McCarty, O. J. T., & Aslan, J. E. (2021). Assessment of the effects of Syk and BTK inhibitors on GPVI-mediated platelet signaling and function. *American Journal of Physiology. Cell Physiology*, *320*(5), C902–C915. https://doi.org/10.1152/AJPCELL.00296.2020

Zhou, W., Liu, K., Zeng, L., He, J., Gao, X., Gu, X., Chen, X., Jing Li, J., Wang, M., Wu, D., Cai, Z., Claesson-Welsh, L., Ju, R., Wang, J., Zhang, F., & Chen, Y. (2022). Targeting VEGF-

A/VEGFR2 Y949 signaling-mediated vascular permeability alleviates hypoxic pulmonary hypertension. *Circulation*, *146*(24), 1855–1881. https://doi.org/10.1161/CIRCULATIONAHA.122.061900

Zhu, X., Stergiopoulos, K., & Wu, S. (2009). Risk of hypertension and renal dysfunction with an angiogenesis inhibitor sunitinib: Systematic review and meta-analysis. *Acta Oncologica*, *48*(1), 9–17. https://doi.org/10.1080/02841860802314720

Zou, A. P., & Cowley, A. W. (1999). Role of nitric oxide in the control of renal function and salt sensitivity. *Current Hypertension Reports*, *1*(2), 178–186. https://doi.org/10.1007/S11906-999-0016-7/METRICS

Zufferey, A., Kapur, R., & Semple, J. W. (2017). Pathogenesis and therapeutic mechanisms in immune thrombocytopenia (ITP). *Journal of Clinical Medicine*, *6*(2). https://doi.org/10.3390/JCM6020016

Zukowska-Grojec, Z., Dayao, E. K., Karwatowska-Prokopczuk, E., Hauser, G. J., & Doods, H. N. (1996). Stress-induced mesenteric vasoconstriction in rats is mediated by neuropeptide Y Y1 receptors. *The American Journal of Physiology*, *270*(2 Pt 2). https://doi.org/10.1152/AJPHEART.1996.270.2.H796